

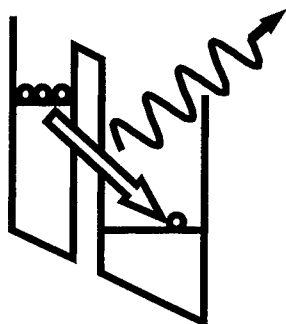
VOLUME 7, Nos. 1&2
APRIL 2000

ISSN 1386-9477

PHYSICA

E

**LOW-DIMENSIONAL SYSTEMS
& NANOSTRUCTURES**



Proceedings of the Fifth International
Conference on Intersubband Transitions
in Quantum Wells

ITQW '99

held in Bad Ischl, Austria
7-11 September 1999

Guest Editors:

M. Helm
K. Unterrainer

NOW included in your subscription:
**ELECTRONIC
ACCESS**
www.elsevier.nl/locate/elecacc

NORTH-HOLLAND

<http://www.elsevier.nl/locate/physe>

PHYSICA E

An interdisciplinary journal of research on low-dimensional systems and nanostructures

Editors:

T. Ando, Institute of Solid State Physics, University of Tokyo, 7-22-1 Roppongi, Minato-ku, Tokyo 106, Japan

Fax: + 81-3-3402-7326; E-mail: ando@issp.u-tokyo.ac.jp

T. Chakraborty, Institute of Mathematical Sciences, Taramani, Chennai 600 113, India

E-mail: tapash@imsc.ernet.in

B.D. McCombe, Department of Physics, SUNY at Buffalo, Buffalo, NY 14260-1500, USA

Fax: + 1-716-645-2507; E-mail: mcombe@acsu.buffalo.edu

M.A. Reed, Department of Electrical Engineering, Yale University, P.O. Box 208284, New Haven, CT 06520-8284, USA

Fax: + 1-203-432-6420; E-mail: mark.reed@yale.edu

D. Weiss, Universität Regensburg, Experimentelle und Angewandte Physik, Universitätstrasse 31, D-93040 Regensburg, Germany

Fax: + 49-941-943-3196; E-mail: dieter.weiss@physik.uni-regensburg.de

Advisory Editorial Board:

G. Abstreiter, Garching

S. Bending, Bath

M. Buttiker, Geneva

H. Fukuyama, Tokyo

A. Geim, Nijmegen

A.C. Gossard, Santa Barbara, CA

C. Hamaguchi, Osaka

P. Hawrylak, Ottawa

D. Lockwood, Ottawa

A. Pinczuk, Murray Hill

K. Richter, Dresden

H. Sakaki, Tokyo

B.V. Shanabrook, Washington, DC

Aims and scope

Physica E (Low-dimensional systems and nanostructures) contains papers and review articles on the fundamental and applied aspects of physics in low-dimensional systems, including semiconductor heterostructures, mesoscopic systems, quantum wells and superlattices, two-dimensional electron systems, and quantum wires and dots. Both theoretical and experimental contributions are invited. Topics suitable for publication in this journal include optical and transport properties, many-body effects, integer and fractional quantum Hall effects, single electron effects and devices, and novel phenomena.

Abstracted/indexed in:

Current Contents: Physical, Chemical and Earth Sciences; Aluminium Industry Abstracts, EI Compendex Plus, Engineered Materials Abstracts, Engineering Index, INSPEC, Metals Abstracts, Physics Briefs

Subscription information

Physica E (ISSN 1386-9477) is published monthly, except in January, June, August, October and November. For 2000, volumes 6–7 are scheduled for publication. Subscription prices

are available upon request from the Publisher. A combined subscription with *Physica A*, *Physica B*, *Physica C* and *Physica D* is available at a reduced rate.

Subscriptions are accepted on a prepaid basis only and are entered on a calendar year basis. Issues are sent by surface mail except to the following countries where air delivery via SAL is ensured: Argentina, Australia, Brazil, Canada, China, Hong Kong, India, Israel, Japan, Malaysia, Mexico, New Zealand, Pakistan, Singapore, South Africa, South Korea, Taiwan, Thailand, USA. For all other countries air mail rates are available upon request. Please address all enquiries regarding orders or subscriptions to:

Elsevier Science B.V.

Customer Support Department

P.O. Box 211, 1000 AE Amsterdam

The Netherlands

Telephone: + 31-20-485 3757; Fax: + 31-20-485 3432

Claims for issues not received should be made within six months of our publication (mailing) date.

US Mailing Notice

Physica E (ISSN 1386-9477) is published monthly, except in January, June, August, October and November by Elsevier Science B.V., P.O. Box 211, 1000 AE Amsterdam, The Netherlands. The annual subscription price in the USA is US\$ 654 (valid in North, Central and South America only), including air speed delivery. Application to mail at periodical postage rate is pending at Jamaica, NY 11431.

USA postmaster: Send address change to *Physica E*, Publications Expediting Inc., 200 Meacham Avenue, Elmont, NY 11003.

Airfreight and mailing in the USA by Publications Expediting Inc., 200 Meacham Avenue, Elmont, NY 11003.

© The paper used in the publication meets the requirements of ANSI/NISO Z39.48-1992 (Permanence of Paper).



North-Holland, an imprint of Elsevier Science

Printed in The Netherlands

REPORT DOCUMENTATION PAGE

Form Approved OMB No. 0704-0188

Public reporting burden for this collection of information is estimated to average 1 hour per response, including the time for reviewing instructions, searching existing data sources, gathering and maintaining the data needed, and completing and reviewing the collection of information. Send comments regarding this burden estimate or any other aspect of this collection of information, including suggestions for reducing this burden to Washington Headquarters Services, Directorate for Information Operations and Reports, 1215 Jefferson Davis Highway, Suite 1204, Arlington, VA 22202-4302, and to the Office of Management and Budget, Paperwork Reduction Project (0704-0188), Washington, DC 20503.

1. AGENCY USE ONLY (Leave blank)		2. REPORT DATE 2000		3. REPORT TYPE AND DATES COVERED 7-11 September 1999 Conference Proceedings - Final Report	
4. TITLE AND SUBTITLE International Conference on Intersubband Transitions in Quantum Wells (5 th) ITQW'99 Held in Bad Ischl, Austria, on 7-11 September 1999. Proceedings.				5. FUNDING NUMBERS N00014-99-1-1049	
6. AUTHOR(S) Manfred Helm and Karl Unterrainer, Editors					
7. PERFORMING ORGANIZATION NAME(S) AND ADDRESS(ES) Johannes Kepler Universitat Linz Institut fur Halbleiterphysik A-4040 Linz, Austria				8. PERFORMING ORGANIZATION REPORT NUMBER ISSN 1386-9477	
9. SPONSORING/MONITORING AGENCY NAME(S) AND ADDRESS(ES) Office of Naval Research, European Office PSC 802 Box 39 FPO AE 09499-0039				10. SPONSORING/MONITORING AGENCY REPORT NUMBER	
11. SUPPLEMENTARY NOTES Published in Physica E (Low Dimensional Systems and Nanostructures), Vol. 7, Nos 1&2, April 2000. Published by North-Holland, Elsevier Science, PO Box 211, 1000 AE Amsterdam, The Netherlands. This work relates to Department of the Navy Grant issued by the Office of Naval Research International Field Office. The United States has a royalty free license throughout the world in all copyrightable material contained herein. See also ADA389287.					
12a. DISTRIBUTION/AVAILABILITY STATEMENT Approved for Public Release; Distribution Unlimited. U.S. Government Rights License. All other rights reserved by the copyright holder.				12b. DISTRIBUTION CODE A	
13. ABSTRACT (Maximum 200 words) This volume contains papers presented at the 5 th International Conference on Intersubband Transitions in Quantum Wells (ITQW'99) held 7-11 September in Bad Ischl, Austria. The field of intersubband transitions in quantum wells has experienced impressive growth in the early '90s and has now stabilized and matured. As a consequence, there are two directions in research: (1) application of intersubband transitions in "real" devices" and (2) investigation of the basic intersubband physics. The list of topics presented includes: intersubband detectors and lasers, intersubband emission in the far-infrared or THz range, and intersubband transitions in quantum dots. Additional topics include infrared band-gap lasers and Bloch oscillation. See http://www.hlphys.uni-linz.ac.at/hl/itqw1999.htm#Anker323348					
14. SUBJECT TERMS ONRIFO, Foreign reports, Conference Proceedings, Intersubband transitions, Quantum wells, Quantum theory and relativity				15. NUMBER OF PAGES	
				16. PRICE CODE	
17. SECURITY CLASSIFICATION OF REPORT UNCLASSIFIED	18. SECURITY CLASSIFICATION OF THIS PAGE UNCLASSIFIED	19. SECURITY CLASSIFICATION OF ABSTRACT UNCLASSIFIED	20. LIMITATION OF ABSTRACT UL		

NSN 7540-01-280-5500

Standard Form 298 (Rev. 2-89)
Prescribed by ANSI Std. Z39-18
298-102

PHYSICA E

ADVISORY EDITORIAL BOARD

G. Abstreiter, Garching
S. Bending, Bath
M. Buttiker, Geneva
H. Fukuyama, Tokyo
A. Geim, Nijmegen

A.C. Gossard, Santa Barbara, CA
C. Hamaguchi, Osaka
P. Hawrylak, Ottawa
D. Lockwood, Ottawa

A. Pinczuk, Murray Hill
K. Richter, Dresden
H. Sakaki, Tokyo
B.V. Shanabrook, Washington, DC

PHYSICA is published in five sections:

PHYSICA A (*Statistical mechanics and its applications*) publishes research in the field of statistical mechanics and its applications. Statistical mechanics sets out to explain the behaviour of macroscopic systems by studying the statistical properties of their microscopic constituents. Applications of the techniques of statistical mechanics are widespread, and including applications to physical systems such as solids, liquids and gases; applications to chemical and biological systems (colloids, interfaces, complex fluids, polymers and biopolymers, cell physics); and other interdisciplinary applications to biological, economical and sociological systems.

PHYSICA B (*Condensed matter*) contains papers and review articles in the realm of physics of condensed matter. Both experimental and theoretical contributions are invited, although theoretical papers should preferably be related to experimental results. (For example "A theory on nuclear spin relaxation in metals" would be more suitable for Physica B, while a theoretical discussion on "Screening effects in the electron gas" is more fitting for Physica A.)

PHYSICA C (*Superconductivity*) serves as a rapid channel for publications on superconductivity and related subjects. This includes theoretical papers on the fundamental issues raised by high- T_c superconductivity, reports on measurements of a wide variety of physical properties of high- T_c superconductors, on new materials and new preparation techniques, on thin-film and device-oriented work and on theoretical results pertinent to such experiments. New results in the traditional areas of superconductivity as well as on novel phenomena (e.g. heavy-electron superconductivity) will also be included.

PHYSICA D (*Nonlinear phenomena*) contains papers and review articles reporting experiments, techniques and ideas which, although they may be derived and explained in the context of a particular field, advance the understanding of nonlinear phenomena in general. Contributions of this type in the recent literature have dealt with: wave motion in physical, chemical and biological systems; chaotic motion in models relevant to turbulence; quantum and statistical mechanics governed by nonlinear field equations; instability, bifurcation, pattern formation and cooperative phenomena.

PHYSICA E (*Low-dimensional systems and nanostructures*) contains papers and review articles on the fundamental and applied aspects of physics in low-dimensional systems, including semiconductor heterostructures, mesoscopic systems, quantum wells and superlattices, two-dimensional electron systems, and quantum wires and dots. Both theoretical and experimental contributions are invited. Topics suitable for publication in this journal include optical and transport properties, many-body effects, integer and fractional quantum Hall effects, single electron effects and devices, and novel phenomena.

VOLUME 7, 2000

PHYSICA E

LOW-DIMENSIONAL SYSTEMS & NANOSTRUCTURES

Editors:

T. ANDO
T. CHAKRABORTY
B.D. McCOMBE
M.A. REED
D. WEISS

20011130 013

U.S. Government Rights License

This work relates to Department of the Navy
Grant or Contract issued by Office of Naval
Research (ONR) International Field Office-
Europe. The United States Government has a
royalty-free license throughout the world in all
copyrightable material contained herein.

NORTH-HOLLAND

AQ F02-02-0290

© 2000 Elsevier Science B.V. All rights reserved.

This journal and the individual contributions contained in it are protected by the copyright of Elsevier Science B.V., and the following terms and conditions apply to their use:

Photocopying

Single photocopies of single articles may be made for personal use as allowed by national copyright laws. Permission of the Publisher and payment of a fee is required for all other photocopying, including multiple or systematic copying, copying for advertising or promotional purposes, resale, and all forms of document delivery. Special rates are available for educational institutions that wish to make photocopies for non-profit educational classroom use.

Permissions may be sought directly from Elsevier Science Global Rights Department, PO Box 800, Oxford OX5 1DX, UK; phone: (+44) 1865 843830, fax: (+44) 1865 853333, e-mail: permissions@elsevier.co.uk. You may also contact Global Rights directly through Elsevier's home page (<http://www.elsevier.nl>), selecting first 'Customer Support', then 'General Information', then 'Permissions Query Form'.

In the USA, users may clear permissions and make payment through the Copyright Clearance Center Inc., 222 Rosewood Drive, Danvers, MA 01923, USA; phone: (978) 7508400; fax: (978) 7504744, and in the UK through the Copyright Licensing Agency Rapid Clearance Service (CLARCS), 90 Tottenham Court Road, London W1P 0LP, UK; phone: (+44) 171 436 5931; fax: (+44) 171 436 3986. Other countries may have a local reprographic rights agency for payments.

Derivative works

Subscribers may reproduce tables of contents or prepare lists of articles including abstracts for internal circulation within their institutions.

Permission of the Publisher is required for resale or distribution outside the institution.

Permission of the Publisher is required for all other derivative works, including compilations and translations.

Electronic storage or usage

Permission of the Publisher is required to store or use electronically any material contained in this journal, including any article or part of an article. Contact the Publisher at the address indicated.

Except as outlined above, no part of this publication may be reproduced, stored in a retrieval system or transmitted in any form or by any means, electronic, mechanical, photocopying, recording or otherwise, without prior written permission of the Publisher.

Address permissions request to: Elsevier Science Global Rights Department, at the mail, fax and e-mail addresses noted above.

Notice

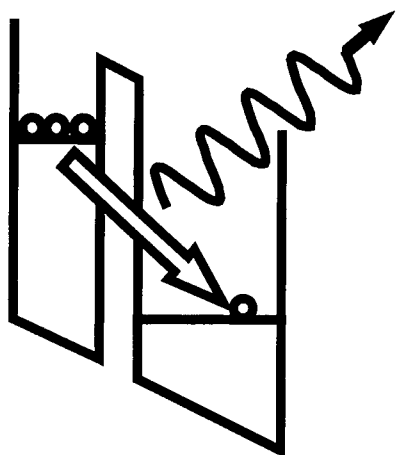
No responsibility is assumed by the Publisher for any injury and/or damage to persons or property as a matter of products liability, negligence or otherwise, or from any use or operation of any methods, products, instructions or ideas contained in the material herein. Although all advertising material is expected to conform to ethical (medical) standards, inclusion in this publication does not constitute a guarantee or endorsement of the quality or value of such product or of the claims made of it by its manufacturer.

ⓧ The paper used in this publication meets the requirements of ANSI/NISO Z39.48-1992 (Permanence of Paper).

Proceedings of the Fifth International
Conference on Intersubband Transitions
In Quantum Wells

ITQW '99

held in Bad Ischl, Austria
7–11 September 1999



Guest Editors:

Manfred Helm

*Institut für Halbleiterphysik
Universität Linz
A-4040 Linz, Austria*

Karl Unterrainer

*Institut für Festkörperelektronik
TU Wien, A-1040 Wien, Austria*



ELSEVIER

This work relates to Department of the Navy Grant N00014-99-1-1049 issued by the Office of Naval Research International Field Office – Europe. The United States has a royalty-free license throughout the world in all copyrightable material contained herein. The content does not necessarily reflect the position or the policy of the United States Government.

Preface

This volume contains papers presented at the 5th International Conference on Intersubband Transitions in Quantum Wells (ITQW '99), held from 7 to 11 September 1999 in Bad Ischl, Austria. The ITQW '99 was the 5th in a series which started in Cargese, Corsica, France in 1991 as a NATO workshop and has been successfully continued in Whistler, Canada (1993), Ginosar, Israel (1995) and Tainan, Taiwan (1997). 79 papers were presented at the conference, 14 of which were invited talks, 36 contributed talks, and 29 posters. 63 of these are published in this volume.

The field of intersubband transitions in quantum wells has experienced an impressive growth in the early 90s and has now stabilized on a very solid level. In a sense the field has also matured, since IR cameras based on intersubband transitions are commercially being sold and quantum cascade lasers fabricated from different material systems have been demonstrated in several laboratories worldwide. As a consequence we can presently observe two directions in intersubband research: (1) application of intersubband transitions in "real" devices and (2) investigation of the basic intersubband physics. The latter is still a rich field with novel exciting phenomena being discovered. Here we would like to mention many-body physics and quantum optics of intersubband transitions and even their mutual interaction. For example, electromagnetically induced transparency in quantum wells was reported for the first time at this conference. Surprisingly also, the community has become aware that to date there is no rigorous theory for such a fundamental quantity as the linewidth of intersubband transitions. Intense research has also widened the spectral range of possible applications of intersubband transitions from below $2\text{ }\mu\text{m}$ to above $100\text{ }\mu\text{m}$. According to the above, the list of topics at this conference includes intersubband detectors and lasers, with a special section on intersubband emission in the far-infrared or THz range, intersubband transitions in quantum dots, ultrafast effects and intersubband relaxation, and nonlinear and coherent as well as many-body effects. In an attempt to open the conference to "non-intersubband" topics, which however are still somewhat related to the field, the organizers decided to also hold sessions on infrared band-gap (especially antimonide) lasers and Bloch oscillations.

With over 90 participants from 16 countries this conference has been the largest so far in this series. The represented nations, in descending order, were Germany, USA, UK, Israel, Austria, Switzerland, Japan, France, Italy, Russia, Canada, Poland, Singapore, Spain, Sweden, and Ukraine. Despite this relatively large number, we think it was possible to maintain the traditional relaxed atmosphere with strong interactions of the participants. This was of course partly thanks to the pleasant location of the Kurhotel with the surrounding gentle Salzkammergut mountains. In addition, the unexpectedly (but hoped for!) warm and sunny weather during the conference completed the boundary conditions.

The organizers are very grateful to the province government of Upper Austria (Amt der OÖ Landesregierung), the Microelectronics Society of Austria (GMe), to the Office of Naval Research and the European Research Office of the US Army, London, and Bruker Optik GmbH for their generous support. Special thanks are to Klaus Rabeder and Karin Hammerschmid for their help in the organization of the conference. Finally, we would like to thank the staff of Elsevier, in particular E. van Wezenbeek and J. van Leest for the fruitful collaboration during publication of this volume.

Manfred Helm
Karl Unterrainer
Guest Editors

Conference Information

Program Committee

M. Helm, University of Linz, Austria (chair)
K. Unterrainer, Technical University Vienna,
Austria (co-chair)
J. Faist, Université de Neuchâtel, Switzerland
F. Julien, Université de Paris-Sud, Orsay, France

H.C. Liu, National Research Council, Ottawa,
Canada
A. Sa'ar, Hebrew University, Jerusalem, Israel
M.S. Sherwin, University of California at Santa
Barbara, USA

Advisory Committee

F. Capasso, Lucent Technologies, Murray Hill,
USA
E. Ehrenfreund, Technion, Haifa, Israel
S. Gunapala, Jet Propulsion Laboratory,
Pasadena, USA

S.S. Li, University of Florida, Gainesville, USA
H. Ohno, Tohoku University, Sendai, Japan
H. Schneider, IAF, Freiburg, Germany
Y.K. Su, National Cheng-Kung University,
Tainan, Taiwan

Organizing Committee

M. Helm, University of Linz, Austria
K. Unterrainer, Technical University Vienna,
Austria

Local Organization

Klaus Rabeder, University of Linz, Austria
Karin Hammerschmid, University of Linz, Austria

Acknowledgements

The organizers gratefully acknowledge substantial support by:

Amt der Oberösterreichischen Landesregierung, Linz, Austria
Gesellschaft für Mikroelektronik, Wien, Austria
Office of Naval Research International Field Office (ONRIFO) – Europe, London, UK
European Research Office of the US Army (USARDSG), London, UK
Bruker Optik GmbH, Karlsruhe, Germany
Tourismusverband Oberösterreich, Linz, Austria

Contents

Preface	vii
Conference Information	viii
 Chapter 1. Quantum cascade lasers	
Intersubband and interminiband GaAs/AlGaAs quantum cascade lasers G. Strasser, S. Gianordoli, L. Hvozdar, W. Schrenk and E. Gornik	1
Improved performance from GaAs-AlGaAs quantum cascade lasers with enhanced upper laser level confinement P.T. Keightley, L.R. Wilson, J.W. Cockburn, M.S. Skolnick, J.C. Clark, R. Grey, G. Hill and M. Hopkinson	8
High-power tunable quantum fountain unipolar lasers O. Gauthier-Lafaye, B. Seguin-Roa, F.H. Julien, P. Collot, C. Sirtori, J.Y. Duboz and G. Strasser	12
Theoretical study, modeling and simulation of SL quantum cascade lasers S. Tortora, F. Compagnone, A. Di Carlo and P. Lugli	20
Edge- and surface-emitting 10.1 μm quantum cascade distributed feedback lasers D. Hofstetter, J. Faist, M. Beck, A. Müller and U. Oesterle	25
GaAs/AlGaAs microresonator quantum cascade lasers S. Gianordoli, L. Hvozdar, G. Strasser, T. Maier, N. Finger, K. Unterrainer and E. Gornik	29
Long-wavelength ($\lambda \sim 10.5 \mu\text{m}$) quantum cascade lasers based on a photon-assisted tunneling transition in strong magnetic field S. Blaser, L. Diehl, M. Beck and J. Faist	33
GaAs/AlGaAs quantum cascade laser – a source for gas absorption spectroscopy L. Hvozdar, S. Gianordoli, G. Strasser, W. Schrenk, K. Unterrainer, E. Gornik, Ch.S.S. Murthy, M. Kraft, V. Pustogow and B. Mizaikoff	37
High-confinement waveguides for mid-IR devices P. Holmström	40
 Chapter 2. THz emission	
Electrically pumped Terahertz quantum well sources M. Rochat, J. Faist, M. Beck and U. Oesterle	44

Monte Carlo modelling of far-infrared intersubband lasers R.W. Kelsall, P. Kinsler and P. Harrison	48
Waveguide design optimization for a quantum cascade laser emitting at 77 μm V.M. Menon, W.D. Goodhue, A.S. Karakashian and L.R. Ram-Mohan	52
Resonant tunneling and intersubband population inversion effects in asymmetric wide quantum-well structures V.N. Murzin, Yu.A. Mityagin, V.A. Chuenkov, A.L. Karuzskii, A.V. Perestoronin and L.Yu. Shchurova	58
Inter-subband plasmon-emission-based THz Lasers P. Bakshi and K. Kempa	63
 Chapter 3. Antimonide lasers	
Interband cascade lasers: progress and challenges R.Q. Yang, J.D. Bruno, J.L. Bradshaw, J.T. Pham and D.E. Wortman	69
Antimonide interband and intersubband mid-IR and terahertz lasers I. Vurgaftman, J.R. Meyer and L.R. Ram-Mohan	76
Mid-infrared intersubband electroluminescence in InAs/GaSb/AlSb type-II cascade structures K. Ohtani and H. Ohno	80
Designs for a quantum cascade laser using interband carrier extraction V.J. Hales, A.J. Poulter and R.J. Nicholas	84
 Chapter 4. New materials	
Intersubband and interminiband transitions in CdS/ZnSe heterostructures M. Göppert, R. Becker, S. Petillon, M. Grün, C. Maier, A. Dinger and C. Klingshirn	89
Intersubband transitions in InAs/GaSb superlattices in a parallel magnetic field R.H.J. De Meester, F.M. Peeters, M. Lakrimi, R.J. Nicholas, A.J.L. Poulter, N.J. Mason and P.J. Walker	93
Self-assembled ErAs islands in GaAs for THz applications C. Kadow, A.W. Jackson, A.C. Gossard, J.E. Bowers, S. Matsuura and G.A. Blake	97
 Chapter 5. Infrared detectors (QWIPs)	
QWIP FPAs for high-performance thermal imaging H. Schneider, M. Walther, C. Schönbein, R. Rehm, J. Fleissner, W. Pletschen, J. Braunstein, P. Koidl, G. Weimann, J. Ziegler and W. Cabanski	101
Recent developments and applications of quantum well infrared photodetector focal plane arrays S.D. Gunapala, S.V. Bandara, A. Singh, J.K. Liu, E.M. Luong, J.M. Mumolo and P.D. LeVan	108
New designs and applications of corrugated QWIPs K.K. Choi, C.J. Chen, K.L. Bacher and D.C. Tsui	112
Optical interference and nonlinearities in quantum-well infrared photodetectors M. Ershov, H.C. Liu, A.G.U. Perera and S.G. Matsik	115
Monte Carlo particle modeling of electron transport and capture processes in AlGaAs/GaAs multiple quantum-well infrared photodetectors M. Ryzhii and V. Ryzhii	120

Noise current investigations of g-r noise limited and shot noise limited QWIPs R. Rehm, H. Schneider, C. Schönbein and M. Walther	124
Effects of traps on the dark current transients in GaAs/AlGaAs quantum-well infrared photodetectors A.G.U. Perera, S.G. Matsik, M. Ershov, Y.W. Yi, H.C. Liu, M. Buchanan and Z.R. Wasilewski	130
Circuit model for quantum-well infrared photodetectors and its comparison with experiments Y.H. Chee and G. Karunasiri	135

Chapter 6. Quantum dots

Quantum dot infrared photodetectors in new material systems E. Finkman, S. Maimon, V. Immer, G. Bahir, S.E. Schacham, O. Gauthier-Lafaye, S. Herriot, F.H. Julien, M. Gendry and J. Brault	139
Mid-infrared photocurrent measurements on self-assembled Ge dots in Si C. Miesner, O. Röthig, K. Brunner and G. Abstreiter	146
Femtosecond mid-infrared study of electron dynamics in InAs/InAlAs quantum dots E. Péronne, J.F. Lampin, A. Alexandrou, O. Gauthier-Lafaye, F.H. Julien, J. Brault and M. Gendry	151
Second-harmonic generation in InAs/GaAs self-assembled quantum dots T. Brunhes, P. Boucaud, S. Sauvage, A. Lemaître, J.-M. Gérard, V. Thierry-Mieg, F. Glotin, R. Prazeres and J.-M. Ortega	155

Chapter 7. Nonlinear and coherent effects

Coherent control of electron intersubband transitions by frequency-detuned light fields W. Pötz	159
Observation of electromagnetically induced transparency and measurements of subband dynamics in a semiconductor quantum well C.C. Phillips, E. Paspalakis, G.B. Serapiglia, C. Sirtori and K.L. Vodopyanov	166
Fano profile in intersubband transitions in InAs quantum dots Ph. Lelong, S.-W. Lee, K. Hirakawa and H. Sakaki	174
Inhomogeneous broadening of intersubband absorption bands of quantum well structures investigated by hole burning S. Schmidt, J. Kaiser and A. Seilmeier	179
Absorption saturation of near-infrared intersubband transition in lattice-matched InGaAs/AlAsSb quantum wells A. Neogi, H. Yoshida, T. Mozume, N. Georgiev, T. Akiyama and O. Wada	183
First-order coherent THz optical sideband generation from asymmetric QW intersubband transitions C. Phillips, M.Y. Su, J. Ko, L. Coldren and M.S. Sherwin	187

Chapter 8. Many-body effects and disorder

Collective effects in intersubband transitions R.J. Warburton, K. Weilhammer, C. Jabs, J.P. Kotthaus, M. Thomas and H. Kroemer	191
Direct observation of dynamical screening of the intersubband resonance S. Graf, H. Sigg, K. Köhler and W. Bächtold	200

Linewidth and dephasing of THz-frequency collective intersubband transitions in a GaAs/AlGaAs quantum well J.B. Williams, M.S. Sherwin, K.D. Maranowski, C. Kadow and A.C. Gossard	204
Nonlinear intersubband optical response of multiple-quantum-well structures M. Załuźny and C. Nalewajko	208
Second-harmonic generation in quantum wells: the role of many-body effects V. Bondarenko and M. Załuźny	212
Subband selective disorder in a quasi-2D system and its effect on the intersubband spectrum M. Hackenberg, C. Metzner, M. Hofmann and G.H. Döhler	216
Absorption of in-plane polarized light in quasi-2D systems enabled by strong potential fluctuations C. Steen, C. Metzner, M. Hofmann and G.H. Döhler	220

Chapter 9. Intersubband relaxation – Theory

Inter-subband relaxation due to electron–electron scattering in quantum well structures K. Kempa, P. Bakshi, J.R. Engelbrecht and Y. Zhou	225
The intrasubband and intersubband relaxation of nonequilibrium electron populations in wide semiconductor quantum wells S.-C. Lee and I. Galbraith	229
Electron energy relaxation in silicon quantum dots by acoustic and optical phonon scattering M. Dür and S.M. Goodnick	233

Chapter 10. Optical experiments

Time-resolved intersubband optical transitions in resonantly optically pumped semiconductor lasers I. Shtrichman, U. Mizrahi, D. Gershoni, E. Ehrenfreund, K.D. Maranowski and A.C. Gossard	237
Emission of mid-infrared radiation and intersubband population inversion in near-infrared laser QW structures L.E. Vorobjev, D.A. Firsov, V.A. Shalygin, Zh.I. Alferov, N.N. Ledentsov, V.M. Ustinov, Yu.M. Shernyakov and V.N. Tulupenko	241
Modulated resonant Raman and photoluminescence spectroscopy of Bragg confined asymmetric coupled quantum wells M. Levy, R. Kapon, A. Sa'ar, R. Beserman, V. Thierry-Mieg and R. Planel	245
Intersubband electro-absorption and retardation in coupled quantum wells: the role of interface scattering R. Kapon, N. Cohen, V. Thierry-Mieg, R. Planel and A. Sa'ar	250
Thermal relaxation processes in $\text{Si}_{1-x}\text{Ge}_x/\text{Si}$ quantum wells studied by inter-subband and inter-valence band spectroscopy B. Adoram, D. Krapf, M. Levy, R. Beserman, S. Thomas, K.L. Wang, J. Shappir and A. Sa'ar	255
Investigation of electric-field-dependent population properties in a GaAs/(Al,Ga)As multiple, asymmetric double quantum well structure by photoluminescence spectroscopy L. Schrotke, R. Hey and H.T. Grahn	259
Pico-second non-linear optical transmission in an asymmetric triple quantum well structure N. Sawaki, H.S. Ahn, K. Mizutani and M. Yamaguchi	263

Chapter 11. Bloch oscillations and superlattices

Coherent dynamics of photoexcited semiconductor superlattices in homogeneous electric fields T. Meier, H.J. Kolbe, A. Thränhardt, G. Weiser, P. Thomas and S.W. Koch	267
Interminiband spectroscopy of biased superlattices M. Helm, W. Hilber, G. Strasser, R. De Meester, F.M. Peeters and A. Wacker	274
Coupled Bloch-phonon oscillations in GaAs/AlGaAs superlattices: theory and experiment T. Dekorsy, A. Bartels, H. Kurz, A.W. Ghosh, L. Jönsson, J.W. Wilkins, K. Köhler, R. Hey and K. Ploog	279
Generation and manipulation of Bloch wave packets F. Löser, M. Sudzius, B. Rosam, V.G. Lyssenko, Y. Kosevich, M.M. Dignam, K. Köhler and K. Leo	285
Evolution of energy levels of a GaAs/AlGaAs superlattice under the influence of a strong magnetic field T. Bauer, A.B. Hummel, H.G. Roskos and K. Köhler	289
Negative differential resistance of a 2D electron gas in a 1D miniband R.A. Deutschmann, W. Wegscheider, M. Rother, M. Bichler and G. Abstreiter	294
Dynamics of electric field domain walls in semiconductor superlattices D. Sánchez, M. Moscoso, L.L. Bonilla, G. Platero and R. Aguado	299



ELSEVIER

Physica E 7 (2000) 1–7

PHYSICA E

www.elsevier.nl/locate/physa

Intersubband and interminiband GaAs/AlGaAs quantum cascade lasers

G. Strasser*, S. Gianordoli, L. Hvozdar, W. Schrenk, E. Gornik

Institut für Festkörperelektronik, TU Wien, A-1040 Wien, Austria

Abstract

Electrically pumped injection lasers based on the GaAs/AlGaAs material system are investigated. Intersubband transitions in coupled quantum wells and intraband transitions in a finite superlattice are used to demonstrate lasing. The laser emission wavelength is 10 μm for the intersubband lasers and 12.9 μm for the laser structure having a finite superlattice as an active cell. Utilizing ridge waveguide laser bars at a heat-sink temperature of 10 K, peak optical powers of the intersubband quantum cascade lasers exceed 300 mW (interminiband: 100 mW). The maximum operating temperature is 160 K (interminiband: 50 K). Cylindrical micro-cavities show single-mode behavior with a side mode suppression ratio better than 25 dB for both kinds of lasers. © 2000 Elsevier Science B.V. All rights reserved.

Keywords: Semiconductor lasers; Quantum cascade lasers; Superlattices; Micro-cavities

Since the development of unipolar semiconductor lasers based on intersubband transitions in quantum wells [1], continuous progress in device operation and performance of the so-called quantum cascade lasers has been achieved, reaching from the realization of superlattice lasers based on interminiband transitions [2,3] up to non-cascaded structures with only one single-optical transition [4]. However, till 1998 lasing was restricted to a single material-system, InGaAs/InAlAs lattice matched to InP. The realization of unipolar light emitter based on the model material system GaAs/AlGaAs showing electrolumi-

nescence [5–7], optically [8,9] pumped and finally electrically pumped lasing in GaAs/AlGaAs intersubband structures [10] was reported. Recently, we showed electrically pumped lasing in GaAs/AlGaAs interminiband structures [11].

Micro-cavity lasers show improved resonator properties because the total internal reflection of "whispering-gallery modes" (WGM) guarantees a reflectivity near unity. A consequence of the increase of the reflectivity is a decrease of the threshold current density of lasers based on these special kinds of resonators. Electrically pumped micro-cavity lasers based on intersubband transitions in the InGaAs/InAlAs/InP were demonstrated in 1996 [12] and investigated in greater detail in 1998 [13]. Recently, we have demonstrated the first micro-cavity

* Corresponding author. Tel.: +43-1-58801-362-18; fax: +43-1-58801-362-99.

E-mail address: gottfried.strasser@tuwien.ac.at (G. Strasser)

lasers based on a GaAs/AlGaAs intersubband quantum cascade structure [14]. Different sizes and shapes of these micro-cavities are demonstrated and will be published [15].

In this work the design, growth and operation of unipolar semiconductor lasers based on the material system GaAs/AlGaAs is presented. Coherent emitter based on intersubband transitions in coupled quantum wells as well as laser based on interminiband transitions in a finite superlattice have been realized. We report on the performance of ridge waveguide lasers as well of as micro-cavity lasers.

The GaAs/AlGaAs intersubband quantum cascade laser structure consists of a three-quantum well active region comparable to the one given by Sirtori et al. [10]. The active cells are separated by miniband funnel injectors and 30 repetitions of the whole structure are embedded in the conducting cladding layers to ensure proper electron injection and waveguiding. Fig. 1 shows one period of the active zone of this intersubband laser; the thicknesses of the different layers are given in the figure captions. The conduction band of one active region embedded into two injectors regions is calculated self-consistently, and the figure includes the squared wave functions of the coupled quantum wells. Applying an external electrical field of about 45 kV/cm (as shown in the plot) lets the states line up and leads to the radiative transition as indicated by an arrow. The structure was designed to emit photons at 10 μm in good agreement with the experimental findings. The aluminum concentration in the AlGaAs barriers was chosen to be 30%. This ensures that the AlGaAs barrier is a direct band-gap material and that the transfer of injected electrons from the Γ point to the X point is not very likely. On the other hand, the band offset is only 250 meV and it escapes from hot electrons into the Γ -continuum hinders lasing at elevated temperatures. The bridging region between the active cells is n-doped about $3\text{--}5 \times 10^{11} \text{ cm}^{-2}$ per period to prevent band bending. This gain medium is sandwiched between two heavily doped GaAs layers acting as waveguide structures using a plasmon-enhanced confinement [16,17]. The 1 μm thick n^+ layers are set back on either side from the active region by a low-doped core layer. These core layers are doped in the mid 10^{16} cm^{-3} range, a tradeoff between freeze out on the low and free carrier absorption losses on the high-doped side. Epitaxy

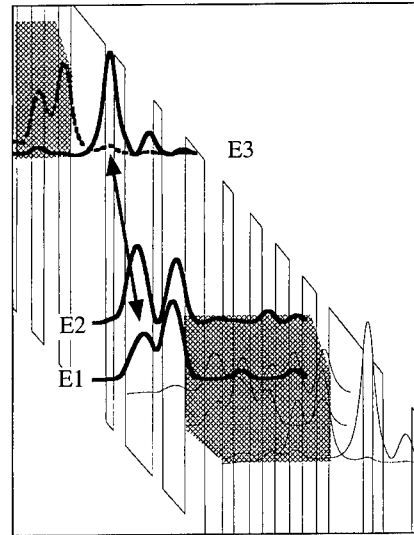


Fig. 1. Calculated conduction band structure of an active cell embedded between two injectors for the intersubband laser structure. A bias of 45 kV/cm is applied. The shaded areas indicate the miniband region in the injector. The relevant squared wave functions are shifted to the corresponding transition energy levels, respectively. The highlighted states (E1, E2, E3) are all the involved intersubband states within the well/barrier limits; the dotted state represents the injector state. One active zone consists of GaAs (nm)/Al_{0.3}Ga_{0.7}As (nm): 1.5/2/4.9/1.7/4/3.4/3.2/2/2.8/2.3/2.3/2.5/2.3/2.5/2.1/5.8; 2 wells and 2 barriers (underlined) in the center of the injector are doped ($2 \times 10^{17} \text{ cm}^{-3}$).

was done with a solid source MBE system; highly n-doped (100) GaAs wafers were used as substrates.

To achieve lasing at longer wavelength than 10 μm we designed an interminiband quantum cascade structure. The main advantage of a superlattice active region is the high oscillator strength of the radiative transitions between the two minibands. The oscillator strength has a maximum at the mini-Brillouin zone boundary ($k_z = \pi/d$) where the injected electrons are located in the upper miniband, while in the lower miniband the states at the zone boundary are empty. A detailed study of superlattice lasers in the InGaAs/InAlAs lattice matched to InP was done by the Bell group [2,3]. To prevent electric field penetration and the resulting breaking of the minibands into a Wannier–Stark ladder [18], the first active superlattice regions (Scarmacio et al., Refs. [2,3]) were doped uniformly. Two competing doping techniques

were invented by Tredicucci et al. [19,20] to improve the device performance. In the first technique the dopants are located inside the injector regions and by an applied external electric field negative electrons are separated from the positive ionized donors to compensate for the applied external electric field across the active superlattice region [19]. The latter design compensates for the electric field by using a variation in the superlattice period as well as in the SL duty cycle [20]. With this compensation flat minibands with extended states can be achieved at high external bias conditions without high doping concentrations by the so-called chirped superlattice. In the InGaAs/InAlAs system long-wavelength operation up to 17 μm has been demonstrated [2,3].

We used the chirped superlattice approach for the realization of the first GaAs-based interminiband laser [11]. In Fig. 2 a self-consistent calculation of the conduction band for this active superlattice region, sandwiched between two bridging superlattice regions, including that for the radiative transition relevant squared wave functions is plotted. At an applied external electrical field of ~ 25 kV/cm the built in asymmetry is compensated. This is shown in Fig. 2 for this particular field, where the relevant wave functions are extended and a miniband similar to a miniband in a periodic superlattice at flatband conditions is formed. The radiative transition is designed to emit photons at 12.5 μm (arrow in Fig. 2) in fair agreement with the experimental findings at about 12.9 μm .

The thicknesses of the layered structure are given in the figure captions. The finite superlattice consists of 6 wells; the same number of wells is used for the bridging region that acts as a funnel injector. To prevent band bending the center wells of the injector are n-doped in the lower 10^{17}cm^{-3} range, leaving the active cells and the barriers on top and below the active cells nominally undoped. During growth, the aluminum concentration in the barriers was kept at 30%, n^+ GaAs (100) with a doping concentration of $n_{\text{si}} = 1.5\text{--}2 \times 10^{18}\text{cm}^{-3}$ acting as substrates. A cascade of 30 repetitions of the active zone results in a total thickness of 2.5 μm . The nominally identical Al-free cladding structure as for the intersubband laser described above was used to ensure waveguiding.

In the intersubband quantum cascade laser structure (Fig. 1) the optical matrix element for the radiative

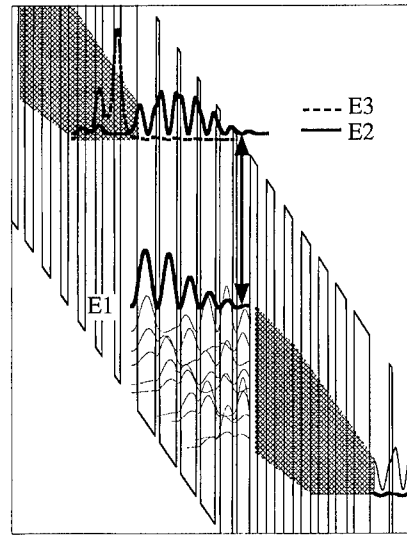


Fig. 2. Calculated conduction band structure of an active cell embedded between two injectors for the interminiband structure, the external bias being ~ 25 kV/cm; the shaded areas indicate the miniband region in the injector. The relevant squared wave functions are shifted to the corresponding transition energy levels. The highlighted states are the lowest state in the upper miniband (E2) and the highest state in the lower miniband (E1) the radiative transition (E2–E1) is shown by an arrow. The dotted state represents the lowest injector state (E3). One active zone consists of GaAs (nm)/AlGaAs (nm): 6.5/1.1/6.1/1.2/5.7/1.2/5.1/1.3/4.5/1.4/4.3/2.5/3/2/3/2.8/3/3/2.6/3/2/2.5/3.3/2.3/3.8/2.2/5.5; 3 wells and 2 barriers (underlined) in the center of the injector are doped ($2 \times 10^{17}\text{cm}^{-3}$).

transition (E3–E2) is 16 Å. At low temperatures we compute a total lifetime of the upper state E3 of 1.4 ps, limited by electron–phonon scattering. The non-radiative relaxation time from E3 to E2 is 2.2 ps and the total lifetime of the state E2 is less than 0.3 ps. All these values are consistent with the values given by Sirtori et al. [10] due to the fact that this intersubband structure is a copy of their design with minor changes to achieve lasing at longer wavelength (10 μm).

In the superlattice quantum cascade laser structure (Fig. 2) the dipole matrix element for the interminiband transition (E2–E1) is 35 Å, while for the diagonal transition from the lowest injector state (dashed thick line: E3) to the highest miniband state in the lower band (E3–E1) the matrix element is 5 Å. The lowest state of the second miniband has a total lifetime $\tau_{\text{fl}} = 0.35$ ps and a nonradiative relaxation time to

the uppermost state of the first miniband of $\tau_{\text{IL},1} = 3.0$ ps; the total lifetime of the highest state in the lowest miniband (τ_1) is calculated to be ≈ 0.2 ps. These values are valid for the design given in Fig. 2 having a radiative transition of $12.5 \mu\text{m}$.

An optical mode intensity profile calculation for the intersubband QCL structure assuming a laser wavelength of $10 \mu\text{m}$ gives a total waveguide loss of $\alpha_w = 16 \text{ cm}^{-1}$, while the calculated confinement factor for the waveguide design described above is $\Gamma = 26\%$, the effective refractive index being $n_{\text{eff}} = 3.209$. For the superlattice QCL structure and an assumed wavelength of $13 \mu\text{m}$ the calculated waveguide losses are $\alpha_w = 30 \text{ cm}^{-1}$, the confinement factor is $\Gamma = 0.45$ and the effective refractive index $n_{\text{eff}} = 3.15$. The higher losses in the superlattice structure compared to the intersubband QCL are due to the increased free carrier absorption at longer wavelength. The high confinement factor takes into account the fact that for the same number of periods the active gain medium is slightly thicker for the superlattice than for the intersubband QCL.

From the same wafer material ridge waveguide lasers and micro-cavity lasers are processed. Wet chemical etching is used to define the dimensions of ridge waveguide lasers, typically $25 \mu\text{m}$ wide. The substrate is thinned to $100\text{--}150 \mu\text{m}$; Ge/Au/Ni/Au is evaporated onto the back and forms the back contact (alloyed). After the deposition of an insulation layer (PECVD: Si_3N_4) the top of the ridges is opened again and electrical contact metals are sputtered. Sequentially, the ridge waveguides are cleaved into $1.5\text{--}2.5$ mm long laser bars. Uncoated cleave facets serve as laser mirrors.

To process micro-cavity lasers the contact pads for the top contact are sputtered. The radius of the circular top metal contact has to be smaller than the cylinder radius to prevent the damping of the whispering-gallery modes. Sequentially the surface is coated with a $1 \mu\text{m}$ thick SiN etching mask (PECVD). Circular reactive ion-etched SiN pads centered at the top metal contacts with a defined overlap act as masks during the definition of the cylinders (RIE: SiCl_4 & Ar). Perpendicular side walls with deviations less than 1° ensure high lasing performance. Sequentially the active region and both cladding layers were removed, adding up to more than a $10 \mu\text{m}$ deep etching. Finally the SiN-mask is removed. The back contact for

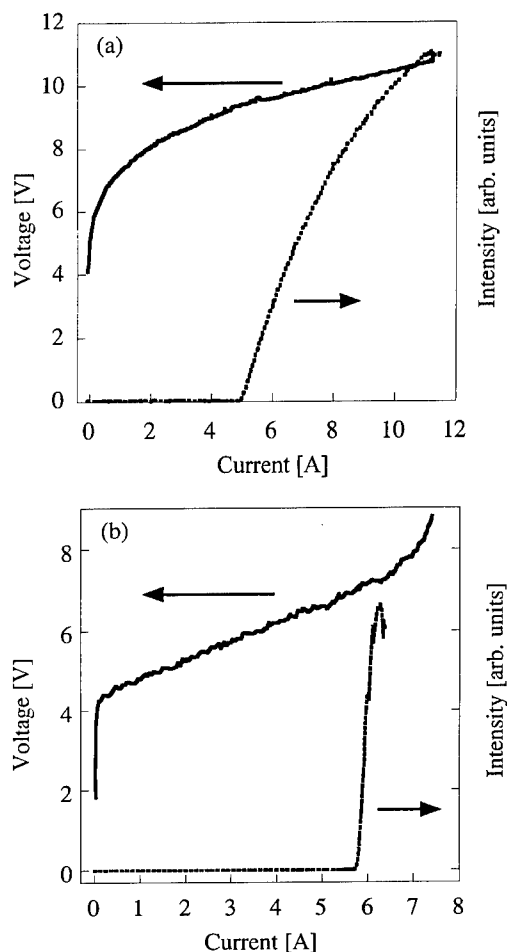


Fig. 3. Voltage and integral optical output versus current characteristic of a ridge waveguide bar at 10 K: (a) intersubband QC laser structure; (b) interminiband QC laser structure.

the micro-cavities is done in the same way as for the ridge waveguide lasers. On the very end the samples are soldered on a copper holder, wire bonded and mounted on a temperature-controlled cold head.

All laser structures are analyzed by measuring current-voltage characteristics as well as integral and spectral optical outputs. Spectral measurements are performed using a Fourier-transform step-scan spectrometer. Light is collected using $f/0.7$ optics and focused on a LN_2 cooled HgCdTe detector.

In Fig. 3 typical current-voltage curves of a laser bar at 10 K are shown; Fig. 3a shows the data of the intersubband QCL, while in Fig. 3b the intermini-

band data are plotted. To prevent heating, all data are taken in a pulsed mode at a low repetition rate. The pulsed light–current (LI) characteristics are taken at the same run with a liquid-nitrogen-cooled MCT detector to measure the threshold current. At these sampling rates (0.05% duty cycle; 5 kHz) for ridge waveguide lasers, the electroluminescence below the laser threshold is not detectable, thus, a flat line below the lasing onset is seen. The LI for the intersubband structure is shown in Fig. 3a (interminiband (IMB): Fig. 3b) and a low-temperature threshold current density of 9.0 kA/cm² for the intersubband QCL (IMB: 9.7 kA/cm²) for this particular laser ridge is achieved.

Following the literature, the threshold condition of a QCL [21] can be written as

$$J_{\text{th}} = \frac{(\alpha_m + \alpha_w) \epsilon_0 \lambda n L_p 2\gamma}{\tau_{\text{II}}(1 - \tau_{\text{I}}/\tau_{\text{II},1}) 4\pi e \Gamma z^2}.$$

For the intersubband quantum cascade laser structure (interminiband QCL structure) described above and a given laser wavelength of $\lambda = 10 \mu\text{m}$ (IMB: $\lambda = 13 \mu\text{m}$) this accounts to a threshold current density of $J_{\text{th}} = 3.9 \text{ kA/cm}^2$ (IMB: $J_{\text{th}} = 6.0 \text{ kA/cm}^2$); we assumed mirror losses $\alpha_m = 7 \text{ cm}^{-1}$, waveguide losses $\alpha_w = 16 \text{ cm}^{-1}$ (IMB: $\alpha_w = 30 \text{ cm}^{-1}$), effective refractive index $n = 3.21$ (IMB: $n = 3.15$), the length of one cascade $L_p = 45 \text{ nm}$ (IMB: $L_p = 83 \text{ nm}$), the FWHM (from electroluminescence measurements) $2\gamma \approx 15 \text{ meV}$, the confinement factor Γ and the non-radiative lifetimes of the subband (miniband) states and the transition dipole matrix elements are given above. The discrepancy between the measured and the computed threshold current density can be explained by the underestimation of the waveguide losses as well as additional losses in the SiN insulation layers.

Assuming a collection efficiency of $\approx 40\text{--}50\%$ for the ridges we estimated the total optical peak power at 10 K to be about 300 mW (IMB: 100 mW). The laser operates up to a temperature of about 140 K (IMB: 50 K).

Fig. 4a shows a typical current–voltage curve of a micro-cavity intersubband QCL structure (IMB: Fig. 4b) at 10 K. Again, the pulsed light–current (LI) characteristics are taken at the same run. The threshold current density for the intersubband micro-cavities (minimum value: 6.5 kA/cm²) is smaller than the threshold for the ridge laser bars made from the same material (9.0 kA/cm²); this is due to reduced mirror

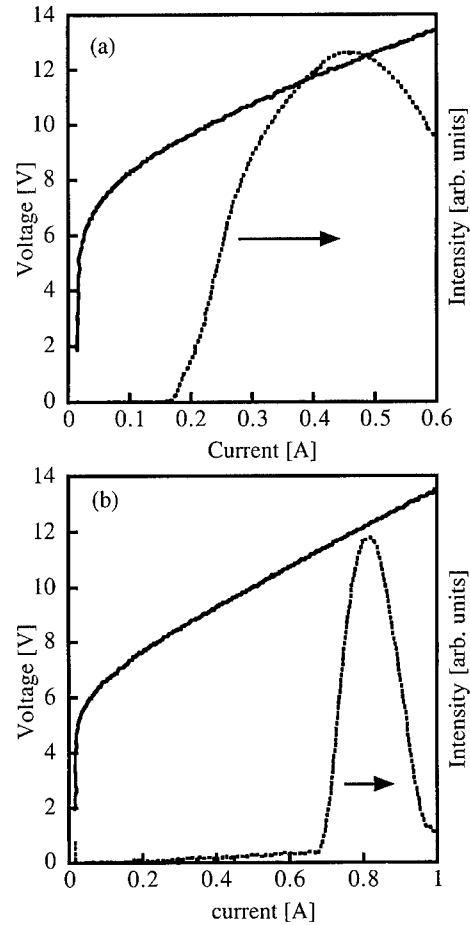


Fig. 4. Voltage and integral optical output versus current characteristic of a micro-cavity at 10 K: (a) intersubband QC laser structure; (b) interminiband QC laser structure.

losses as mentioned above. Decreasing the size of the micro-cylinders leads to a strong increase of the threshold current density for disk radii below 50 μm [14,15]. The I – V shown in Fig. 4a is the smallest GaAs micro-cavity that showed lasing. The threshold current for this particular micro-cylinder with a radius of 22 μm is the lowest threshold current reported for that material system (170 mA), giving a threshold current density of 12.5 kA/cm². The radius of the interminiband QC micro-cylinder shown in Fig. 4b is 50 μm , with a measured threshold current of 700 mA. This accounts to a current density of 8.9 kA/cm²; as expected, this value is below the value for the ridge waveguide bar.

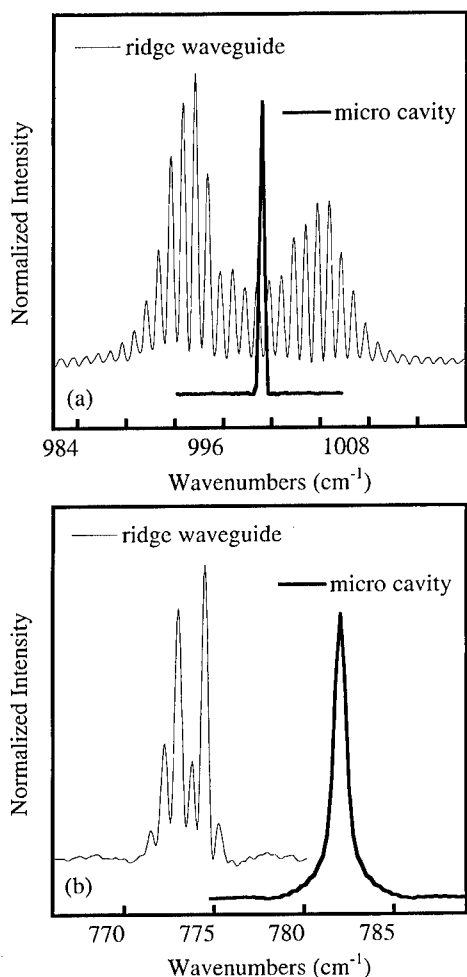


Fig. 5. Comparison of typical emission spectra of a ridge waveguide structure and a micro-cavity at 10 K; (a) intersubband QC laser structure; (b) interminiband QC laser structure.

In Fig. 5a (Fig. 5b) the spectral behavior of the intersubband (IMB) QC laser structure is shown for a ridge waveguide and a micro-cavity laser. All spectra shown here are taken at a heat-sink temperature of 10 K. The resolution of the measurement is limited by the resolution of the step scan FTIR spectrometer (0.5 wave numbers). Both, cylinders and ridges, are characterized using the same measurement set-up. The ridge waveguide structures show the typical multi-mode spectra for ridge laser bars with longitudinal modes. The mode spacing of the spectra agrees with the length of the laser bars and the re-

fractive index of the structures. For the intersubband structure (Fig. 5a) the Fabry–Perot modes of the ridge waveguide can be resolved between 9.9 and 10.15 μm (985–1010 wave numbers). This is in excellent agreement with the designed wavelength of 10 μm . The micro-cavity laser shows a single peak at 10.008 μm (999 wave numbers). For this particular cylinder with a radius of 60 μm the mode spacing can be calculated using the the following equation [22,23]:

$$\Delta\lambda = \lambda^2 / 2\pi R n_{\text{eff}}.$$

The mode spacing $\Delta\lambda$ for whispering-gallery modes amounts to $\approx 0.08 \mu\text{m}$; the radial mode spacing is larger by a factor π . The spectral response (Fig. 5a) of the intersubband micro-cavity shows clearly a single-mode behavior with a side mode suppression ratio (SMSR) greater than 25 dB; this upper value is given by the background noise of our setup.

The mode spectrum of a ridge waveguide laser, based on interminiband transitions, is shown in Fig. 5b. Different modes between 772 and 776 cm^{-1} ($\approx 12.9 \mu\text{m}$) can clearly be seen. The small deviation in the calculated wavelength (12.5 μm) may be due to uncertainties in the growth calibration (layer thickness) as well as changes in the doping concentration in the layers and thickness fluctuations over the wafer. This is supported by the fact, that the wavelength of the micro-cavity processed from the same material is shifted by 8–9 wave numbers to higher energies from the Fabry–Perot modes of the ridges. A single-mode spectrum of a micro-cavity laser with a radius of 70 μm is shown in Fig. 5b. For this particular laser the modespacing $\Delta\lambda$ for whispering-gallery modes amounts to $\sim 0.12 \mu\text{m}$ (≈ 7 wave numbers); the SMSR is again better than 25 dB.

In summary, we have reported on GaAs-based quantum cascade lasers. Active regions with intersubband and interminiband transitions have been investigated. GaAs/AlGaAs quantum cascade micro-cavity lasers have been successfully processed and compared to ordinary ridge waveguide lasers made from the very same materials. Threshold current densities for the micro-cavity lasers are significantly smaller than threshold current densities of the ridge waveguides. Single-mode emission with more than 25 dB side mode suppression has been observed for the micro-cavities. In conclusion we have demonstrated the first operation of a quantum cascade

interminiband micro-cavity laser in the GaAs/AlGaAs material system. The operating wavelength of this superlattice laser is found to be about 13 μm . This is the longest wavelength reported for an electrically pumped GaAs/AlGaAs laser so far.

Acknowledgements

This work was partly supported by a Brite Euram III project (UNISEL), the Austrian Federal Ministry of Science, the FWF Austria, and the Society for Microelectronics (GMe, Austria).

References

- [1] J. Faist, F. Capasso, D.L. Sivco, C. Sirtori, A.L. Hutchinson, A.Y. Cho, *Science* 264 (1994) 553.
- [2] G. Scarmacio, J. Faist, C. Sirtori, J. Faist, A.L. Hutchinson, D.L. Sivco, A.Y. Cho, *Science* 276 (1997) 773.
- [3] A. Tredicucci, C. Gmachl, F. Capasso, D.L. Sivco, A.L. Hutchinson, A.Y. Cho, *Appl. Phys. Lett.* 74 (1999) 638.
- [4] C. Gmachl, F. Capasso, A. Tredicucci, D.L. Sivco, A.L. Hutchinson, S.N.G. Chu, A.Y. Cho, *Appl. Phys. Lett.* 73 (1998) 3830.
- [5] G. Strasser, P. Kruck, M. Helm, J.N. Heyman, L. Hvozdar, E. Gornik, *Appl. Phys. Lett.* 71 (20) (1997) 2892.
- [6] Y.B. Li, J.W. Cockburn, M.S. Skolnick, M.J. Birkett, J.P. Duck, R. Grey, G. Hill, *Electron. Lett.* 33 (1997) 1874.
- [7] P. Kruck, G. Strasser, M. Helm, L. Hvozdar, E. Gornik, *Physica E* 2 (1998) 449.
- [8] O. Gauthier-Lafaye, P. Boucaud, F.H. Julien, R. Prazeres, F. Glotin, J.-M. Ortega, V. Thierry-Mieg, R. Planel, J.-P. Leburton, V. Berger, *Appl. Phys. Lett.* 70 (1997) 3197.
- [9] O. Gauthier-Lafaye, F.H. Julien, S. Cabaret, J.M. Lourtioz, G. Strasser, E. Gornik, M. Helm, P. Bois, *Appl. Phys. Lett.* 74 (1999) 1537.
- [10] C. Sirtori, P. Kruck, S. Barbieri, P. Collot, J. Nagle, M. Beck, J. Faist, U. Oesterle, *Appl. Phys. Lett.* 73 (1998) 3486.
- [11] G. Strasser, S. Gianordoli, L. Hvozdar, W. Schrenk, K. Unterrainer, E. Gornik, *Appl. Phys. Lett.* 75 (1999) 1345.
- [12] J. Faist, C. Gmachl, M. Striccoli, C. Sirtori, F. Capasso, D.L. Sivco, A.Y. Cho, *Appl. Phys. Lett.* 69 (1996) 2456.
- [13] C. Gmachl, A. Tredicucci, F. Capasso, E.E. Narinamov, J.U. Nöckel, A.D. Stone, J. Faist, D.L. Sivco, A.Y. Cho, *Science* 280 (1998) 1556.
- [14] S. Gianordoli, L. Hvozdar, G. Strasser, W. Schrenk, K. Unterrainer, E. Gornik, *Appl. Phys. Lett.* 75 (1999) 1045.
- [15] S. Gianordoli, L. Hvozdar, G. Strasser, W. Schrenk, J. Faist, E. Gornik, Long-wavelength ($\lambda = 10 \mu\text{m}$) quadrupolar shaped GaAs/AlGaAs microlasers, *IEEE J. Quantum Electr.*, accepted.
- [16] C. Sirtori, J. Faist, F. Capasso, D.L. Sivco, A.L. Hutchinson, A.Y. Cho, *Appl. Phys. Lett.* 66 (1995) 3242.
- [17] C. Sirtori, P. Kruck, S. Barbieri, H. Page, M. Beck, J. Faist, U. Oesterle, J. Nagle, Unipolar semiconductor lasers with Al free waveguides, *Appl. Phys. Lett.* 75 (1999) 3911.
- [18] G.H. Wannier, *Elements of Solid State Theory*, Cambridge University Press, London, 1959, pp. 190–193.
- [19] A. Tredicucci, F. Capasso, C. Gmachl, D.L. Sivco, A.L. Hutchinson, A.Y. Cho, J. Faist, G. Scarmacio, *Appl. Phys. Lett.* 72 (1998) 2388.
- [20] A. Tredicucci, F. Capasso, C. Gmachl, D.L. Sivco, A.L. Hutchinson, A.Y. Cho, *Appl. Phys. Lett.* 73 (1998) 2101.
- [21] J. Faist, F. Capasso, D.L. Sivco, C. Sirtori, A.L. Hutchinson, A.Y. Cho, *Appl. Phys. Lett.* 66 (1995) 538.
- [22] A.F.J. Levi, R.E. Slusher, S.L. McCall, S.J. Pearton, W.S. Hobson, *Appl. Phys. Lett.* 62 (1993) 2021.
- [23] R.A. Mair, K.C. Zeng, J.Y. Lin, H.X. Jiang, *Appl. Phys. Lett.* 72 (1998) 1530.



ELSEVIER

Physica E 7 (2000) 8–11

PHYSICA E

www.elsevier.nl/locate/physc

Improved performance from GaAs–AlGaAs quantum cascade lasers with enhanced upper laser level confinement

P.T. Keightley^a, L.R. Wilson^{a,*}, J.W. Cockburn^a, M.S. Skolnick^a, J.C. Clark^b, R. Grey^b,
G. Hill^b, M. Hopkinson^b

^a*Department of Physics and Astronomy, University of Sheffield, Hicks Building, Hounsfield Road, Sheffield S3 7RH, UK*

^b*Department of Electronic and Electrical Engineering, University of Sheffield, Sheffield S1 3JD, UK*

Abstract

We present a comparison of the lasing characteristics for two nearly identical GaAs–AlGaAs quantum cascade lasers with an optimised InGaAs–AlInAs device operating at a similar wavelength. The effects on the laser performance resulting from modifications to the upper lasing state lifetime and optical transition matrix element for the GaAs–AlGaAs devices are investigated by selectively altering the aluminium composition of a *single* barrier within the active region. The sample containing an Al_{0.4}Ga_{0.6}As barrier exhibits a lower-threshold current density (3.75 kA/cm²) and increased slope efficiency (280 mW/A) at 10 K relative to the sample with an Al_{0.33}Ga_{0.67}As barrier, consistent with calculations. © 2000 Elsevier Science B.V. All rights reserved.

Keywords: Quantum cascade lasers; Gallium arsenide; Temperature performance

There has been considerable development of inter-subband quantum cascade (QC) lasers [1] in recent years. Whilst these mid-infrared sources were originally developed in the InGaAs–AlInAs material system, intersubband electroluminescence [2,3] (EL) and lasing [4,5] have also been demonstrated recently in GaAs–AlGaAs devices. In addition to being the most widely developed compound semiconductor materials system, GaAs–AlGaAs offers significant flexibility in QC laser design due to the good lattice matching over the full alloy composition. In this paper, we present the

lasing characteristics of dry-etched GaAs–AlGaAs QC lasers and compare their performance with that of an optimised InGaAs–AlInAs device operating at a similar wavelength. The role of the upper state confinement in determining the performance of the GaAs–AlGaAs lasers is investigated by varying the aluminium composition of a single barrier in the active region.

Fig. 1(a) shows the band profile of the GaAs–Al_{0.33}Ga_{0.67}As laser under operating conditions. The sample, grown by MBE, is based on a design published in Ref. [5] and contains 30 periods, each consisting of an active region, where the intersubband emission occurs and an injection/bridging region. The 30 period core region is sandwiched between

* Corresponding author. Fax: +44-114-2728079.

E-mail address: luke.wilson@sheffield.ac.uk (L.R. Wilson)

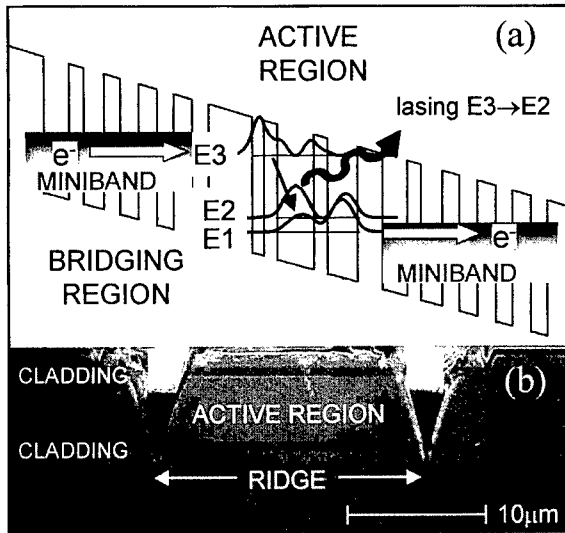


Fig. 1. (a) A section of the conduction band profile of the GaAs–Al_{0.33}Ga_{0.67}As device. (b) Cross-sectional SEM image showing the laser ridge.

Al_{0.9}Ga_{0.1}As cladding layers to form the waveguide. The wafer was processed into mesa-etched ridge waveguides of widths 10–20 μm by reactive ion etching (RIE) using SiCl₄ gas. The use of RIE allows us to define the ridge by etching narrow (< 5 μm) channels as shown in Fig. 1(b).

A section of the conduction band profile for the InGaAs–AlInAs device is shown in Fig. 2(a). The MBE-grown sample is based on the design published in Ref. [6]. An SEM of a typical, wet-etched, laser ridge is shown in Fig. 2(b).

After processing, the samples were cleaved into bars 1–3 mm long and indium-soldered epilayer up to copper holders, wire bonded and mounted on the cold finger of a closed-cycle helium cryostat. Voltage pulses of 50 ns duration with a repetition rate of 1 kHz were applied across the device and the emitted radiation was detected using a calibrated HgCdTe detector.

Fig. 3(a) shows the peak optical power from a single facet versus the injection current for an InGaAs–AlInAs device 2.5 mm long and 15 μm wide at various heatsink temperatures. A threshold current density $J_{th} = 3 \text{ kA/cm}^2$ and peak optical power up to 700 mW are measured at 10 K, and lasing is observed up to 270 K. Fig. 3(b) shows pulsed light output versus injection current measured using the same ex-

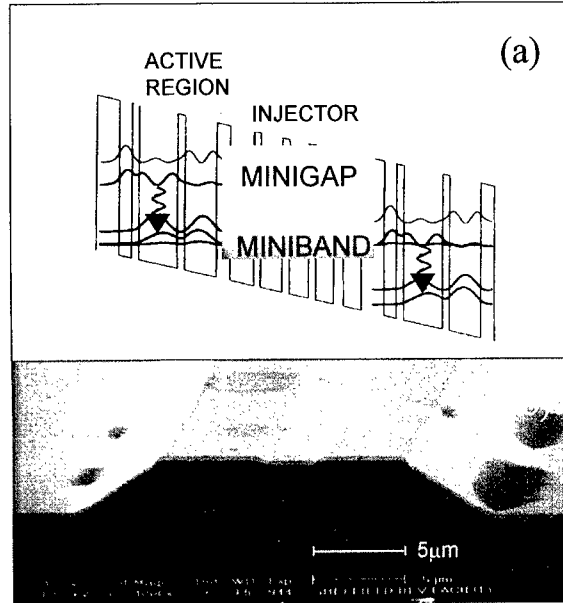


Fig. 2. (a) Conduction band diagram for the InGaAs–AlInAs structure. (b) SEM of the laser cavity.

citation conditions for a GaAs–Al_{0.33}Ga_{0.67}As device 2 mm long and 20 μm wide. A threshold current density $J_{th} = 4.6 \text{ kA/cm}^2$ and peak optical power up to 400 mW are measured at 10 K and lasing is observed up to 160 K. The larger value of J_{th} measured for the GaAs–Al_{0.33}Ga_{0.67}As device is probably due to higher waveguide losses (α_w) due to free carrier absorption in the more heavily doped cladding layers relative to the InGaAs–AlInAs sample.

The inset of Fig. 3(b) shows the temperature dependence of J_{th} for the samples. The observed increase in J_{th} by a factor of ~ 2 up to 270 K for the InGaAs–AlInAs device can be explained by the increase in non-radiative (optical phonon) scattering [7]. However, J_{th} measured for the GaAs–Al_{0.33}Ga_{0.67}As sample increases rapidly above $\sim 120 \text{ K}$ indicating that the dominant-temperature-dependent loss mechanism is not optical phonon scattering. There are a number of factors which may limit the high-temperature performance of the GaAs–Al_{0.33}Ga_{0.67}As device. It is unlikely that an increase in free carrier absorption (increasing α_w) at higher temperatures due to thermal ionisation of donors in the Al_{0.9}Ga_{0.1}As cladding is responsible for the observed behaviour. This is because a very similar temperature dependence of J_{th} is

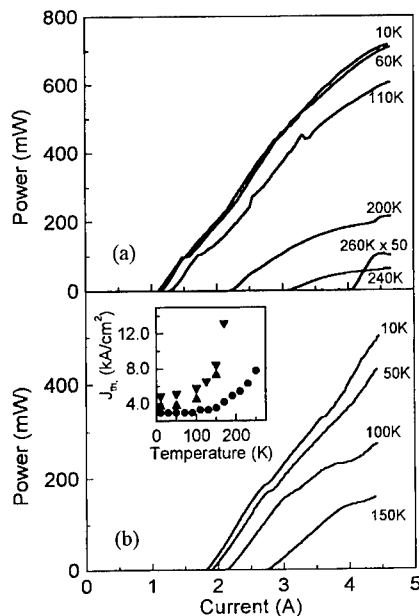


Fig. 3. Peak optical power from a single facet versus injection current at various heat sink temperatures for (a) the InGaAs–AlInAs and (b) GaAs–Al_{0.33}Ga_{0.67}As devices. The inset shows the threshold current density as a function of temperature for the InGaAs–AlInAs (●), GaAs–Al_{0.33}Ga_{0.67}As (▼) lasers and device with a single GaAs–Al_{0.4}Ga_{0.6}As barrier (▲) in the active region.

measured for GaAs–AlGaAs lasers clad with heavily doped GaAs [8] which has a donor ionisation energy ≈ 5 meV compared to ≈ 60 meV for Al_{0.9}Ga_{0.1}As. Other explanations are that the population inversion is reduced as a result of intervalley scattering of E3 electrons into the X and L valleys or thermally assisted tunnelling from E3. Both of these effects are expected to be more significant for the GaAs–Al_{0.33}Ga_{0.67}As sample due to the energetic proximity of the satellite valleys and the smaller confinement energy of the upper lasing state relative to the InGaAs–AlInAs device.

In an attempt to determine the significance of the upper lasing state (E3) confinement on laser performance we have studied another GaAs–AlGaAs sample¹ in which the aluminium composition of a single barrier in the active region has been increased. Fig. 4(a) shows the active region Γ and X conduc-

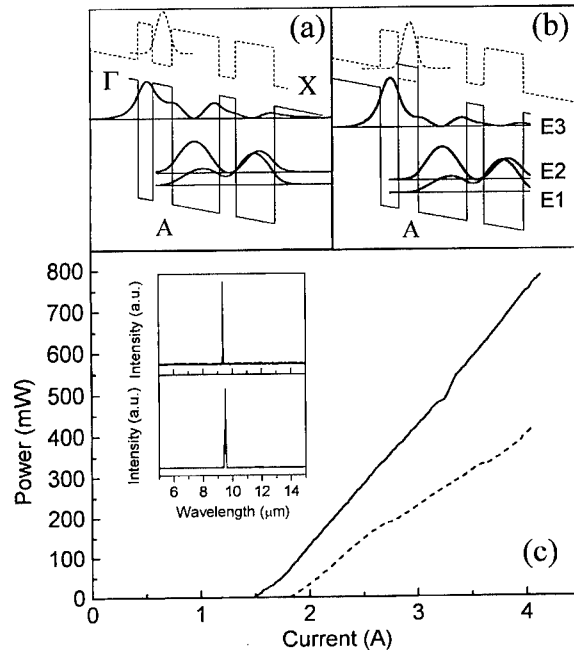


Fig. 4. Γ and X conduction band profiles and moduli squared of the wave functions for: (a) the GaAs–Al_{0.33}Ga_{0.67}As device (sample A); (b) the sample containing a single GaAs–Al_{0.4}Ga_{0.6}As barrier (sample B); (c) peak optical power from a single facet versus injection current measured at 11 K for the sample A (dashed line) and sample B (solid line). The inset shows the very similar emission wavelength for sample A (lower lasing spectrum) and sample B (upper lasing spectrum).

Table 1

Showing the calculated values of the upper state lifetime (τ_3), dipole matrix element for the E3–E2 transition (z_{32}), and threshold current density (J_{th}) for the two samples

	Sample A	Sample B
τ_3 (ps)	2.3	4.2
τ_{32} (ps)	5.2	10.0
z_{32} (Å)	11.0	8.5
J_{th} (kA/cm ²)	2.8	2.5

tion band profiles for the GaAs–Al_{0.33}Ga_{0.67}As device (sample A) and Fig. 4(b) shows those of the sample containing the Al_{0.4}Ga_{0.6}As barrier (sample B). Optical matrix elements and optical phonon scattering rates [9] have been calculated for the two structures and are summarised in Table 1.

The main effect of increasing the aluminium fraction of barrier A (Al_{0.4}Ga_{0.6}As, Fig. 4(b)) is to increase the localisation of the E3 wave function in the

¹ Approximately 10 devices fabricated from each wafer have been studied. All devices exhibit very similar trends in performance to those reported here, however the wider (20 μ m) ridges have the best characteristics for both samples.

quantum well immediately to the left of the barrier. Increasing the spatially indirect nature of the E3–E2 transition in this way doubles the upper state lifetime, $\tau_3 = (\tau_{32}^{-1} + \tau_{31}^{-1})^{-1}$, and reduces the transition matrix element, z_{32} , from 11 to 8.5 Å relative to sample A. Assuming unity injection efficiency into E3, the threshold current density can be expressed as [10]

$$J_{th} = \frac{\epsilon_0 n L_p \lambda (2\gamma_{32})(\alpha_m + \alpha_w)}{4\pi e N_p \Gamma_p (z_{32})^2 [\tau_3 \{1 - \tau_2/\tau_{32}\}]}, \quad (1)$$

where ϵ_0 is the vacuum permittivity, n is the mode refractive index, L_p is the length of each period, λ is the emission wavelength (≈ 9.5 μm for both samples), γ_{32} is the full-width at half-maximum of the spontaneous emission, α_m the mirror losses, N_p and Γ_p are the number of periods and confinement factor of each period, respectively, and $\tau_2 = 0.6$ ps the lifetime of E2. Eq. (1) predicts a 10% decrease in J_{th} for the sample B relative to sample A. In addition, a 10% increase in the slope efficiency,

$$\frac{\delta P}{\delta I} = \frac{h\nu N_p \alpha_m}{2e(\alpha_m + \alpha_w)} \left[1 - \frac{\tau_2}{\tau_{32}} \right] \quad (2)$$

is also predicted for sample B.

The peak optical power versus drive current for both devices measured at 11 K is shown in Fig. 4(c). The measured value of $J_{th} = 3.75$ kA/cm² for sample B is approximately 15% lower than J_{th} ($=4.4$ kA/cm²) measured for sample A, both values of J_{th} being larger than those calculated using Eq. (2) due to non-unity injection efficiency and parallel current paths such as those discussed above. In addition, the slope efficiency measured for sample B (280 mW/A) is approximately 20% larger than that measured for sample A (230 mW/A) in the linear regime (< 2.75 A). These measured values are in reasonable agreement with the improvements in performance calculated for sample B using Eqs. (1) and (2). The measured temperature dependence of J_{th} for the two samples is very similar (inset of Fig. 3(b)), indicating that the confinement of the E3 level is not the dominant factor affecting

the temperature performance of this sample design. We are currently investigating modifications to the design of the bridging region in an attempt to improve temperature performance.

In summary, we have compared the performance of GaAs–AlGaAs and InGaAs–AlInAs QC lasers. The threshold current density measured for the GaAs–AlGaAs laser exhibits a sudden increase above 100 K, in contrast to the InGaAs–AlInAs device. Improvements in the low-temperature performance of the GaAs–AlGaAs design have been achieved by increasing the aluminium composition of a single barrier in the active region. However, the temperature dependence of the threshold current for the modified laser is very similar, suggesting that the confinement of the upper lasing state is not the dominant factor limiting high-temperature performance.

References

- [1] J. Faist, F. Capasso, D.L. Sivco, C. Sirtori, A.L. Hutchinson, A.Y. Cho, *Science* 264 (1994) 553.
- [2] Y.B. Li, J.W. Cockburn, M.S. Skolnick, J.P. Duck, M.J. Birkett, R. Grey, G. Hill, *Electron. Lett.* 33 (1997) 22.
- [3] G. Strasser, P. Kruck, M. Helm, J.N. Heyman, L. Hvozdar, E. Gornik, *Appl. Phys. Lett.* 71 (1997) 2892.
- [4] O. Gauthier-Lafaye, P. Boucaud, F.H. Julien, S. Sauvage, S. Cabaret, J.M. Lortioz, V. Thierry-Mieg, R. Planel, *Appl. Phys. Lett.* 71 (1997) 3619.
- [5] C. Sirtori, P. Kruck, S. Barbieri, P. Collot, J. Nagle, M. Beck, J. Faist, U. Oesterle, *Appl. Phys. Lett.* 73 (1998) 3486.
- [6] C. Gmachl, A. Tredicucci, F. Capasso, A.L. Hutchinson, D.L. Sivco, J.N. Baillargeon, A.Y. Cho, *Appl. Phys. Lett.* 72 (1998) 3130.
- [7] J. Faist, F. Capasso, C. Sirtori, D.L. Sivco, J.N. Baillargeon, A.L. Hutchinson, Sung-Nee G. Chu, A.Y. Cho, *Appl. Phys. Lett.* 68 (1996) 3680.
- [8] S. Gianordoli, L. Hvozdar, G. Strasser, W. Schrenk, K. Unterrainer, E. Gornik, *Appl. Phys. Lett.* 75 (1999) 1045.
- [9] R. Ferreira, G. Bastard, *Phys. Rev. B* 40 (1989) 1074.
- [10] J. Faist, F. Capasso, C. Sirtori, D.L. Sivco, A.L. Hutchinson, A.Y. Cho, *Appl. Phys. Lett.* 66 (1994) 538.

High-power tunable quantum fountain unipolar lasers

O. Gauthier-Lafaye^{a,*}, B. Seguin-Roa^a, F.H. Julien^a, P. Collot^b, C. Sirtori^b, J.Y. Duboz^b,
G. Strasser^c

^a*Institut d'Electronique Fondamentale, UMR 8622 CNRS, Bat. 220, Université Paris-Sud, 91405 Orsay, France*

^b*Thomson-CSF, Laboratoire Central de Recherches, Domaine de Corbeville, 91404 Orsay, France*

^c*Institut für Festkörperelektronik, Technische Universität Wien, Floragasse 7/1, A-1040 Wien, Austria*

Abstract

We report on high-power GaAs/AlGaAs quantum fountain unipolar lasers emitting at 14–15 μm under optical pumping by a pulsed CO_2 laser. Two kinds of devices were investigated: edge lasers with side-facet pumping and broad-area lasers with a patterned top grating for coupling the pump at normal incidence. Collected optical powers as high as 4.16 W corresponding to an estimated power per facet of 17.6 W have been achieved in TM_{00} mode for broad-area lasers. The lasing wavelength is shown to be tunable ($\Delta\lambda/\lambda \approx 2.5\%$) by changing the pump wavelength. Broad-area lasers exhibit excellent beam quality with very low in-plane divergence in TM_{00} mode. Mode hopping is observed under intense pumping. © 2000 Published by Elsevier Science B.V. All rights reserved.

Keywords: Unipolar lasers; Long-wavelength lasers; High-power lasers; Optical pumping

1. Introduction

Unipolar emission between confined subbands in semiconductor heterostructures relies on radiative transitions of only one type of carrier. The non-radiative relaxation of electrons is largely dominated by the very efficient scattering of electrons by longitudinal optical (LO) phonons. Typical electron lifetimes in the excited state are of the order of the picosecond and an efficient injection mechanism is re-

quired for achieving population inversion. In quantum cascade (QC) lasers, efficient injection is provided by resonant tunneling of electrons between injector regions and the active quantum wells [1]. In quantum fountain (QF) lasers, selective optical excitation is used to promote electrons from the ground state to the upper state of the active quantum wells [2].

The first observation of intersubband luminescence in optically pumped quantum wells was reported by Bales and co-workers [3] using a quantum well structure designed for achieving intersubband emission at far-infrared wavelengths, i.e. at photon energies well below the optical phonon energy, in order to benefit from the long scattering times associated with acoustic phonon emission. Several studies have

* Corresponding author. Tel.: 33-(1)-69-15-40-51; fax: 33-(1)-69-15-40-90.

E-mail address: ogl@ief.u-psud.fr (O. Gauthier-Lafaye)

addressed the possibility of population inversion at these wavelengths [4–6]. The QF laser scheme for emission at energy above the LO-phonon energy was first proposed in 1995 [7]. Experimentally, intersubband spontaneous emissions have been observed at wavelengths of 14–15 μm in GaAs/AlGaAs coupled quantum wells under intersubband optical pumping by a cw CO₂ laser [8]. Observation of intersubband luminescence has also been reported under interband optical pumping at near-infrared wavelengths [9]. Population inversion in a QF laser scheme was first demonstrated in 1996 under optical pumping by an infrared free-electron laser and large stimulated gains have been measured at 12.5 μm wavelength [10,11]. Lasing action was reported at ($\lambda = 15.5 \mu\text{m}$ in 1997 under optical pumping by a CO₂ laser [2]. This first Quantum Fountain unipolar laser delivered 0.6 W optical power per facet and had a maximum operating temperature of 110 K. With no current flow, the design of a QF laser does not require doping of the cladding layers as well as metal contacts, low internal losses due to free-carrier absorption can be achieved at long wavelengths. QF lasers are then expected to exhibit better performances in terms of optical power than QC lasers at long wavelengths above 10 μm .

In this paper we review recent developments on QF lasers emitting in the 14–15 μm wavelength range under optical pumping by a pulsed CO₂ laser. We report on two kinds of GaAs/AlGaAs devices: edge lasers with side-facet pumping [12] and broad-area lasers with a patterned top grating for coupling the pump at normal incidence. Collected optical powers as high as 2.3 and 4.16 W in TM₀₀ mode have been achieved for edge and broad-area lasers, respectively. The lasing wavelength is shown to be tunable ($\Delta\lambda/\lambda \approx 2.5\%$) by changing the pump wavelength. Broad-area lasers exhibit excellent modal quality with a very low in plane divergence in TM₀₀ mode. Mode hopping is observed under intense pumping.

2. Principle of operation and sample design

The operation of the QF laser relies on the radiative transition of electrons between bound states of asymmetric coupled quantum wells (ACQW). The conduction band energy profile of AlGaAs/GaAs ACQW is shown in Fig. 1. In order to populate the ground

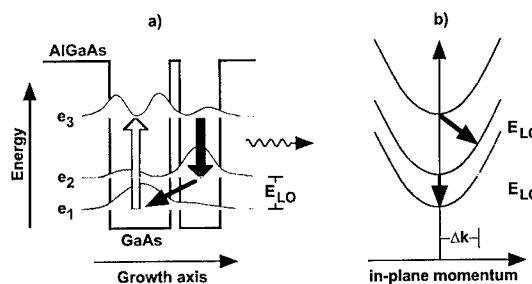


Fig. 1. (a) Conduction band profile of the active quantum wells of a quantum fountain unipolar laser, (b) corresponding subband energy dispersion diagram. The arrows indicate non-radiative relaxation channels via LO-phonon emission. The LO-phonon energy in GaAs is $E_{LO} = 36 \text{ meV}$.

electron subband, the structure is n-doped either in the wells or in the barriers (modulation doping). The structure is asymmetric to allow direct optical pumping of electrons from the ground state (e_1) to the second excited state (e_3). The emission takes place between the second and the first excited subband ($e_3 \rightarrow e_2$). Fast recycling of electrons from the first excited state into the ground state ($e_2 \rightarrow e_1$) is provided by insuring an enhanced scattering with LO phonons. The pump and emission wavelength can be tuned in the mid-infrared range through a proper choice of the thickness and composition of the five layers of the structure (the two GaAs wells, the thin AlGaAs coupling barrier and the two outermost AlGaAs confining barriers).

Population inversion in such a three-level system can be achieved if the lifetime of electrons in the e_2 subband is made shorter than the scattering time, τ_{32} , between the e_3 and e_2 subbands. As shown in Ref. [7], the scattering rate between subbands can be engineered by adjusting the subband energy separation. In particular, the structure can be designed to present an energy spacing between the first excited and ground subbands close to the LO-phonon energy. Non-radiative relaxation of one electron from e_2 to e_1 is then almost vertical in the reciprocal space, as the momentum wave vector exchanged between the phonon and the electron is small ($\Delta k = q \approx 0$). The electron–LO phonon interaction rate scales as $1/|q|^2$ in bulk semiconductors, and one can achieve a strong enhancement of the e_2 – e_1 intersubband scattering rate in this situation. A detailed analysis of the

electron–phonon interaction for engineering the scattering rates between subbands in ACQW taking into account the presence of confined phonon modes has been reported in Ref. [13]. At low carrier concentrations $\approx 1 \times 10^{11} \text{ cm}^{-2}$, typical scattering times are calculated to be $\tau_{21} \approx 0.4 \text{ ps}$ and $\tau_{32} \approx 1.9 \text{ ps}$ for an ACQW structure with $E_{21} = E_{LO}$ and $E_{31} = 125 \text{ meV}$. Although the scattering times are quite short, their large difference ensures population inversion. At larger carrier concentrations, i.e. for a Fermi energy at equilibrium above the ground subband, it is desirable to increase the energy of the second subband with respect to the ground subband in order to minimize the thermal population of the e_2 subband. Under such conditions, τ_{21} is expected to increase to $\approx 1 \text{ ps}$ but population inversion can still be maintained and large stimulated gains are predicted in optimized structures [14].

Based on these considerations, a laser sample has been designed for emission in the 14–15 μm wavelength range under optical pumping by a CO_2 laser. The active structures, separated by 20 nm thick $\text{Al}_{0.35}\text{Ga}_{0.65}\text{As}$ barriers, are asymmetric coupled quantum wells formed by a 7.9 nm thick GaAs wide well, a 1.1 nm thick $\text{Al}_{0.35}\text{Ga}_{0.65}\text{As}$ barrier and a 5.1 nm thick GaAs narrow well. The quantum wells are modulation doped resulting in a measured sheet carrier density of $2 \times 10^{11} \text{ cm}^{-2}$. The transition energies are calculated to be 127 and 86.8 meV for e_1 – e_3 and e_2 – e_3 transitions, respectively. The e_2 – e_1 energy spacing is 40.2 meV which is as desired slightly above the LO-phonon energy in GaAs (36 meV). The waveguide structure grown by molecular beam epitaxy on an n-doped GaAs substrate consists of a 5 μm thick $\text{Al}_{0.9}\text{Ga}_{0.1}\text{As}$ cladding layer, followed by a 0.75 μm thick GaAs core layer, the 5.1 μm thick multi-quantum well layer and a 1.75 μm thick GaAs cap layer. The waveguide is designed to be single mode at both the pump and the emission wavelength.

With respect to our first QF laser emitting at 15.5 μm wavelength [2], the present design is enhanced in order to improve both the net gain and the maximum operating temperature of the laser. The number of active quantum wells has been increased from 100 to 150 and the waveguide is designed to achieve a large 81.1% overlap of the emitted TM_{00} mode within the active region. To increase the operating temperature, we increased the energy separation

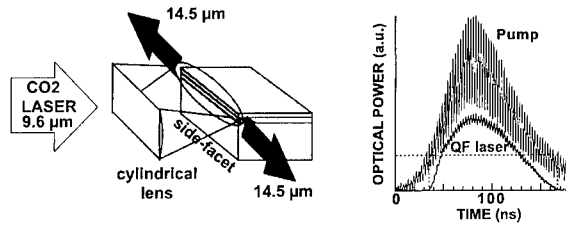


Fig. 2. (a) Side-facet optical pumping configuration. (b) Oscilloscope traces of the 9.6 μm pump (top curve) and 14.5 μm QF laser (bottom curve) pulses. The QF laser is cooled at 20 K.

between e_2 and e_1 which was set at 41 meV. Based on Fourier transform infrared (FTIR) spectroscopic measurements, we estimate the waveguide losses to be $\approx 20 \text{ cm}^{-1}$ at the 14.5 μm emission wavelength. These losses are mainly attributed to free carrier absorption in the doped MQW active region. The measurements also reveal a two-phonon absorption band at 13.8 μm , which is attributed to the mixed-mode Al–Ga optical phonons in the thick $\text{Al}_{0.9}\text{Ga}_{0.1}\text{As}$ cladding layer [15].

3. Edge lasers with side-facet pumping

Fig. 2(a) shows the experimental set-up for edge lasers with side-facet pumping. The 2.15 mm long cleaved samples are mounted on the cold finger of a variable temperature cryostat. Optical pumping is provided by a tunable Edinburgh MTL-3 mini-TEA CO_2 laser operated at 10 Hz repetition rate. The pump pulse delivered by the multimode longitudinal CO_2 laser consists of micropulses with a 2.6 ns full-width at half-maximum (FWHM) in a macropulse with 110 ns FWHM. The pump beam is focused using a cylindrical lens onto the 2.15-mm-long side-facet of the sample with a polarization parallel to the growth axis. The elliptical pump spot size is $5 \times 0.4 \text{ mm}^2$ at the sample facet with the shorter axis perpendicular to the layer plane. In this configuration, lateral confinement of the emission is provided by index guiding at the interface between the side-facet and air and by gain guiding on the other side. The lateral extent of the gain region is then of the order of the penetration length of the pump beam. For pump intensities lower than the saturation intensity of the e_1 – e_3 absorption ($\approx 1 \text{ MW cm}^{-2}$), this length is of the

order of 10 μm , and increases with pump intensity. The emission is collected from one of the cleaved facets perpendicular to the side-facet with a $f/1.2$ ZnSe lens. Time-resolved detection is performed by a helium-cooled quantum well infrared detector (QWIP) with a cut-off wavelength of 18 μm and a sensitive area of $0.45 \times 1.5 \text{ mm}^2$. This detector has a linear response even under intense irradiation [16], but its rise time is limited by electronics at 5 ns, which is too slow to resolve the multimode beatings of the pump. Part of the incident pump beam is detected for reference purposes by a room-temperature HgCdTe photoconductor with a rise time of $\approx 1 \text{ ns}$. The spectral response of both the detectors and the various optics has been carefully calibrated using our FTIR spectrometer. This side-facet pumping configuration offers the advantage of simplicity for coupling the TM polarized pump beam into the active layers. However, the pumping efficiency remains dramatically small. Based on simple geometric considerations, less than 1.5% of the incident pump energy is used to pump the QF laser. This figure may be largely overestimated since it does not account for the effective coupling of the pump into the waveguide, which is presently unknown.

Lasing action has been achieved at 20 K under optical pumping at 9.6 μm wavelength. Fig. 2(b) shows typical oscilloscope traces of the pump and laser pulses. The laser emission follows the pump signal above some threshold. The pump threshold evolution versus pump wavelength and sample temperature is reported in Fig. 3. For temperatures between 20 and 77 K, the pump threshold is of the order of 33 kW at 9.46 μm . It decreases to 12 kW (corresponding to an energy incident on the facet $\approx 1.25 \text{ mJ}$) as the pump wavelength gets in closer resonance with the e_1 – e_3 intersubband absorption near 9.6 μm . At 120 K, the minimum threshold $\approx 18 \text{ kW}$ is achieved at a longer wavelength of 9.66 μm . This slight increase of the optimum pump wavelength is due to the red-shift of the intersubband resonance with temperature. As seen, the minimum threshold is somewhat larger at 120 K than at 77 K. This increase is a consequence of the thermal population of the e_2 subband, which reduces the available gain. Above 120 K, the intersubband resonance wavelength shifts to $\lambda > 9.7 \mu\text{m}$ which is outside the tuning range of our CO_2 laser over the 9P emission branch. Thus, a maximum operating tem-

perature of 135 K has been achieved under optical pumping at 9.68 μm . We stress that the main intrinsic mechanism limiting the operating temperature is the gain reduction due to the thermal population of the second subband. Larger operating temperatures could be achieved by maintaining resonant pumping conditions. One way to increase the operating temperature is to slightly modify this structure in order to shift the pump absorption resonance to shorter wavelengths for compensating the temperature red-shift of the resonance.

To estimate the collection efficiency, we have performed output beam profile divergence measurements. Single mode TM_{00} emission is achieved in the investigated range of pump power. The divergence angle in the plane of the layer is found to be 26° , which corresponds to a beam waist at the output facet of the order of 10 μm . The divergence angle θ_z in the plane parallel to the growth axis could not be measured due to the limited aperture of the cryostat windows but is larger than 50° . Based on our calculations of the TM mode profile at the output facet, we estimate θ_z to be 60.4° following Ref. [17]. The collection efficiency is then deduced to be 35%. From the time-resolved evolution of the pump and laser pulses we can deduce the evolution of the collected power versus pump power, as shown in Fig. 3 for temperatures ranging from 20 to 120 K. The pump wavelength was 9.6 μm at 20 K and 9.68 μm at 120 K. The collected power per facet at 20 K reaches 2.3 W when the laser is operated at 7 times above the threshold. Accounting for collection efficiency, this corresponds to an emitted power as large as 6.6 W per facet at 20 K. The evolution with pump power is similar at 20 and 77 K. At 120 K, the collected power is of the order of 1.5 W (corresponding to an emitted power of 4.3 W) when the laser is operated 4 times above the threshold. The power curve slope above threshold is smaller at 120 K than at 20 K because of a reduced differential gain due to the thermal population of the e_2 subband and to the pump detuning from exact resonance.

Fig. 4 presents normalized spectra of the emission of the QF laser recorded with a 60 cm long infrared spectrometer with 0.4 cm^{-1} resolution. The QF laser was operated 2 times above threshold at a temperature of 20 K for different pump wavelengths. As seen, the laser spectrum is typical of multimode longitudinal operation with a mode spacing of 0.69 cm^{-1}

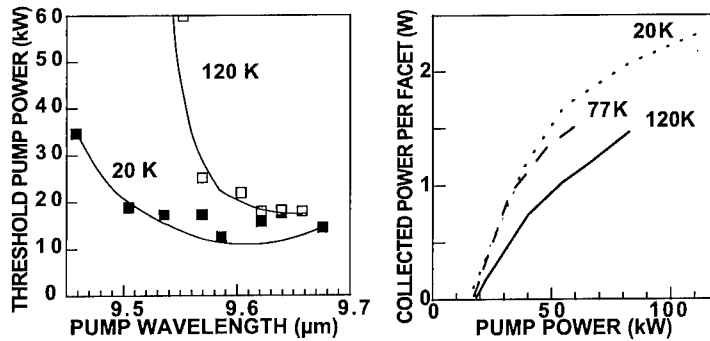


Fig. 3. Left: pump power at threshold versus pump wavelength at a temperature of 20 and 120 K. The solid curves are guide to the eye. Right: collected power per facet versus the incident pump power at a temperature of 20, 77 and 120 K.

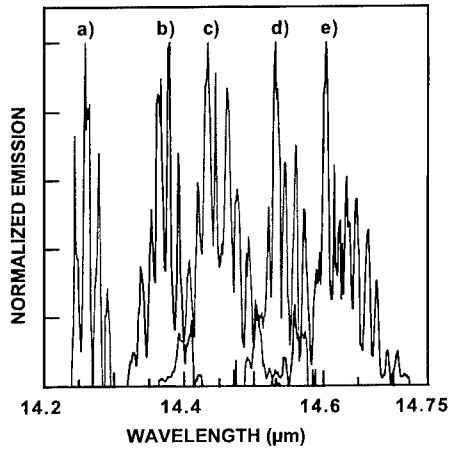


Fig. 4. Normalized emission spectra of the QF laser operated 2 times above threshold at a temperature of 20 K. The pump wavelength is: (a) 9.458 μm, (b) 9.52 μm, (c) 9.569 μm, (d) 9.640 μm and (e) 9.676 μm.

wavenumbers. Based on the device length, the group index deduced from the mode spacing is of the order of 3.4. The major result of Fig. 4 is the large tunability of the peak lasing wavelength between 14.25 and 14.61 μm ($\Delta\lambda/\lambda \approx 2.5\%$) achieved when tuning the pump wavelength between 9.458 and 9.676 μm. This tunability range is maintained at 77 K, and decreases with the pump resonance at higher temperatures. In terms of photon energies, the tunability is linear with a slope of 0.72. This excludes the possibility of a near-resonant Raman emission process which would lead to a slope equal to 1 [18]. We attribute the tunability of the QF laser to layer thickness fluctua-

tions during the long growth of the multiple quantum well layers. We have simulated the peak gain spectral position accounting for a one-monolayer thickness fluctuation of each of the quantum well layers, and assuming a Gaussian distribution centered at the nominal thickness. The model predicts a relative energy shift of 0.7 in agreement with experiments. Also seen in Fig. 4, the emission spectrum gets narrower as the emission wavelength is shifted to 14.2 μm. This is a consequence of the lower gain when the pump wavelength is tuned out of resonance. However, we cannot exclude the effect of increased internal losses as the emission wavelength gets closer to the mixed-mode Al–Ga two-phonon absorption band at 13.8 μm in the AlGaAs alloy cladding layer [15].

4. High-power broad-area lasers with normal-incidence pumping

One way to enhance the pump coupling efficiency is to use a diffraction grating patterned on top of the sample for normal-incidence coupling of the pump radiation. The diffracted waves inside the sample have a polarization component along the growth axis, which allows efficient coupling of the pump to the e_1 – e_3 intersubband transition. Besides, the normal-incidence pumping configuration is well suited for pumping broad-area lasers. The 1.75 μm thick GaAs cap layer has been used to pattern 1 mm wide transmission gratings by means of standard 3 level photolithographic and dry etching techniques. The grating period is 3.14 μm with a duty cycle of 0.7 and an etched

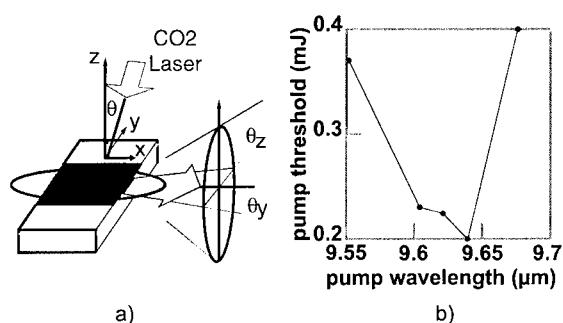


Fig. 5. (a) Experimental arrangement for broad-area QF lasers and (b) minimum threshold pump energy versus pump wavelength.

depth of $1\text{ }\mu\text{m}$. The grating efficiency (± 1 diffraction orders) is calculated to be 35% [19]. After thinning the GaAs substrate, 1.5 mm long laser samples have been cleaved and mounted on the cold-finger of a liquid-nitrogen cryostat. Fig. 5a shows the experimental arrangement. A cylindrical lens is used to focus the CO_2 laser beam onto the sample surface with a spot size of $5 \times 0.4\text{ mm}^2$. The angle of incidence θ of the pump beam on the grating can be adjusted to optimize the pump coupling. Lasing action is achieved parallel to the grooves between the cleaved facets of the sample. It should be noted that the laser is gain guided in the layer plane and that the width of the active region along the y -axis, i.e. where positive gain occurs, increases with pump intensity.

Fig. 5b shows the measured pump threshold energy as a function of pump wavelength. For each wavelength, the angle of incidence of the pump beam onto the top grating has been adjusted to minimize the threshold energy. The spectral evolution of the threshold exhibits a sharp resonance with a full-width at half-minimum of 1.8 meV . As seen, thresholds as low as $200\text{ }\mu\text{J}$ are achieved at a pump wavelength of $9.64\text{ }\mu\text{m}$. The corresponding threshold pump power is 8 kW , which is smaller than the value obtained on 2.15 mm long QF edge lasers, although the distributed optical losses in the present 1.5 mm long sample are increased from 5.6 to 8.5 cm^{-1} .

At pump energies below 1 mJ , the output mode is measured to be TM_{00} . The divergence angle in the layer plane, $\theta_y \approx 5^\circ$, is remarkably small. The beam diameter at the output facet is deduced to be $\approx 120\text{ }\mu\text{m}$. As seen, the in-plane divergence angle of

the broad-area QF laser is a factor of 5 smaller than the value obtained for edge QF lasers with side-facet pumping. This low in-plane divergence is of course a consequence of the larger spatial extent of the active region along the y -axis achieved with surface pumping with respect to side-facet pumping. Because of the strong confinement of the TM emission along the growth axis, the divergence angle along z remains very large and could not be measured due to the limited aperture of the cryostat windows. We estimate $\theta_z \approx 60.4^\circ$ as for side-facet pumped lasers. The collection efficiency is then deduced to be $\approx 53\%$ for the TM_{00} emission at low pump power, i.e. when all the emissive area is imaged on to QWIP detector. At larger pump powers, the collection efficiency drastically drops because of the limited area viewed by the detector. Fig. 6 displays the multimode pump pulse and the corresponding temporal evolution of the QF emission at $14.7\text{ }\mu\text{m}$ wavelength recorded with a $f/1.1$ lens. The pump wavelength is set at $9.64\text{ }\mu\text{m}$ and the angle of incidence has been adjusted for minimum threshold (8 kW). The pump energy incident on the sample is 1.27 mJ for a and 2.55 mJ for b and c. Not shown in Fig. 6, at pump energies below 1.2 mJ , the QWIP signal closely follows the pump pulse above threshold. At a pump energy of 1.27 mJ (curve a), the emission still follows the pump pulse above threshold but some saturation is visible at maximum. The collected power reaches 2.4 W at a pump power of 35 kW , i.e. 4.4 times above threshold. At higher pumping energies, the shape of the emission pulse radically changes. As shown by curve b, the collected power follows the pump power at the initial and final stages of the pump pulse but an opposite behavior is observed for pump powers above 35 kW . The collected power drops by almost 50% at the peak of the pump pulse (120 kW). This behavior is attributed to a mode switching at higher pump powers from TM_{00} to TM_{01} and to the limited imaging area viewed by the detector. By moving the detector along the y -axis 0.5 mm away from its on-axis position, an emission pulse is detected as shown by curve c, which corresponds to the detection of one of the TM_{01} mode emission lobe. The pump threshold is of the order of 35 kW and the emission power grows with pump power. These results give clear indication that the laser switches to higher transverse mode under intense excitation. The time-resolved emission spectrums recorded with

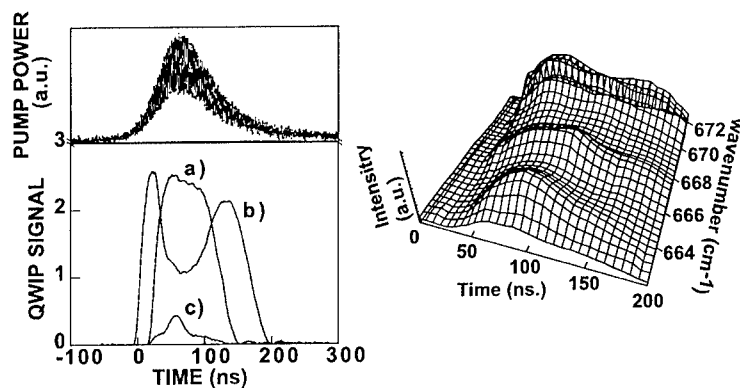


Fig. 6. Left: temporal evolution of a typical pump pulse at 9.64 μm wavelength (top curve) and of the broad-area QF laser power collected by the QWIP detector. The angle of incidence is set at 3.3° to minimize pump threshold. The pump energy is 1.27 mJ for (a) and 2.55 mJ for (b) and (c). For (c), the detector has been moved by 0.5 mm along the y -axis in the focal plane. Right: time-resolved spectrum of the QF laser recorded with a QWIP detector.

our QWIP detector through a grating monochromator of the QF emission are shown in Fig. 6. Switching from mode TM_{00} to TM_{01} is accompanied by a shift of the emission wavelength, from 671 cm^{-1} to 667 and 664 cm^{-1} respectively, larger than the longitudinal mode interval of 0.96 cm^{-1} on this sample. We attribute this behavior to an α -DFB filtering effect induced by the top grating [20].

Fig. 7 shows the collected power versus pump power for three different pump wavelengths. For each pump wavelength, the angle of incidence of the pump radiation has been adjusted to achieve maximum output power under intense pumping. As seen, the threshold pump power is increased by almost a factor of 2 with respect to measurements at an angle of incidence optimized for low-threshold operation. The collected power reaches 4.16, 3.8 and 1.7 at a pump wavelength of 9.67 μm (a), 9.64 μm (b) and 9.55 μm (c), respectively. As for side-facet pumped QF lasers, the laser wavelength is found to be dependent on pump wavelength and is measured to be 14.8, 14.7 and 14.55 μm for curves a, b and c, respectively. The saturation visible in curve a is attributed to the lower collection efficiency at large pump powers. Separate simulations accounting for the in-plane extent of the net gain region, its increase with pump intensity and for the limited field of view of the collecting optics, show that the collection efficiency drops from 53% to 23.6% when the pump power at 9.64 μm increases from 20 to 50 kW. Accounting for this factor, the

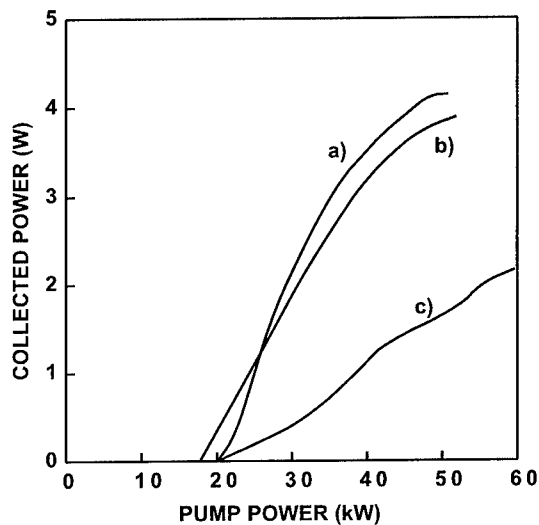


Fig. 7. Collected power versus pump power of the broad-area QF laser (full curves). The pump (emission) wavelength is 9.67 μm (14.8 μm), 9.64 μm (14.7 μm) and 9.55 μm (14.55 μm) for curves a–c, respectively. The angle of incidence $\theta \approx 2.6^\circ$ has been adjusted for achieving large output powers.

optical power per facet of the broad-area laser reaches values as high as 17.6 W at 77 K when the laser is operated at 2.5 times above threshold. This value sets a new record high for a semiconductor laser emitting at mid-IR wavelengths. It should be noted that much higher output powers can be achieved under more

intense pumping conditions. However, in this case the broad-area QF laser is multimode transverse.

5. Conclusion

In conclusion, we have reported on high-power unipolar GaAs/AlGaAs lasers emitting in the 14–15 μm wavelength range under optical pumping by a pulsed CO_2 laser. Operation of edge lasers with side-facet pumping as well as broad-area lasers with normal-incidence pumping has been demonstrated. Extended tunability of the lasing wavelength, $\Delta\lambda/\lambda \approx 2.5\%$, has been observed by varying the pump wavelength. We have shown that record high optical powers can be obtained from these quantum fountain unipolar lasers, with optical powers per facet as high as 6.6 W for edge lasers and 17.6 W for broad-area lasers in TM_{00} mode emission.

Acknowledgements

We thank Jean-Michel Lourtioz for fruitful discussions and M. Helm and P. Bois for experimental support. We acknowledge financial support by Brite-Euram program UNISEL #BE97-4072, Gaz De France, INTAS-RFBR 95-0615 and the Austrian GMe.

References

- [1] J. Faist, F. Capasso, D.L. Sivco, C. Sirtori, A.L. Hutchinson, A.Y. Cho, *Science* 264 (1994) 553.
- [2] O. Gauthier Lafaye, P. Boucaud, F.H. Julien, S. Sauvage, S. Cabaret, J.M. Lourtioz, V. Thierry Mieg, R. Planel, *Appl. Phys. Lett.* 71 (1997) 3619.
- [3] J.W. Bales, K.A. McIntosh, T. Sollner, W.D. Goodhue, E.R. Brown, *SPIE Proc.* 1283 (1990) 74.
- [4] A. Afzali-Kushaa, G.I. Haddad, T.B. Norris, *IEEE J. Quantum Electron.* 31 (1995) 912.
- [5] V. Berger, *Semicond. Sci. Technol.* 9 (1994) 1493.
- [6] G. Sun, J.B. Khurgin, *IEEE J. Quantum Electron.* 29 (1993) 1104.
- [7] F.H. Julien, A. Sa'ar, J. Wang, J.P. Leburton, *Electron. Lett.* 31 (1995) 838.
- [8] Z. Moussa, P. Boucaud, F.H. Julien, Y. Lavon, A. Sa'ar, V. Berger, J. Nagle, N. Coron, *Electron. Lett.* 31 (1995) 912.
- [9] S. Sauvage, P. Boucaud, F.H. Julien, O. Gauthier-Lafaye, V. Berger, J. Nagle, *Appl. Phys. Lett.* 71 (1997) 1183.
- [10] O. Gauthier Lafaye, S. Sauvage, P. Boucaud, F.H. Julien, R. Prazeres, F. Glotin, J.M. Ortega, V. Thierry-Mieg, R. Planel, J.P. Leburton, V. Berger, *Appl. Phys. Lett.* 70 (1997) 3197.
- [11] O. Gauthier-Lafaye, S. Sauvage, P. Boucaud, F.H. Julien, F. Glotin, R. Prazeres, J.M. Ortega, V. Thierry Mieg, R. Planel, *J. Appl. Phys.* 83 (1998) 2920.
- [12] O. Gauthier Lafaye, F.H. Julien, S. Cabaret, J.-M. Lourtioz, G. Strasser, E. Gornik, M. Helm, P. Bois, *Appl. Phys. Lett.* 74 (1999) 1537.
- [13] J. Wang, J.P. Leburton, Z. Moussa, F.H. Julien, A. Sa'ar, *J. Appl. Phys.* 80 (1996) 1970.
- [14] J. Wang, J.P. Leburton, F.H. Julien, A. Saar, *IEEE Photonics Technol. Lett.* 8 (1996) 1001.
- [15] S. Adachi, *J. Appl. Phys.* 58 (1985) R1.
- [16] J.Y. Duboz, E. Costard, J. Nagle, J.M. Berset, J.M. Ortega, J.M. Gerard, *J. Appl. Phys.* 78 (1995) 1224.
- [17] H.C. Casey, M.B. Panish, *Heterostructure Lasers*, Vol. 1, Academic Press, New York, 1978.
- [18] J.B. Khurgin, G. Sun, L.R. Friedman, R.A. Soref, *J. Appl. Phys.* 78 (1995) 7398.
- [19] J.Y. Duboz, *J. Appl. Phys.* 80 (1996) 5432.
- [20] R.J. Lang, K. Dzurko, A.A. Hardy, S. Demars, A. Schoenfelder, D.F. Welch, *IEEE J. Quantum Electron.* 34 (1998) 2196.



ELSEVIER

Physica E 7 (2000) 20–24

PHYSICA E

www.elsevier.nl/locate/physc

Theoretical study, modeling and simulation of SL quantum cascade lasers

S. Tortora¹, F. Compagnone¹, A. Di Carlo, P. Lugli^{*,1}

Department of Electronic Engineering, University of Roma "Tor Vergata", Via di Tor Vergata 110, 00133 Roma, Italy

Abstract

We present a thorough theoretical investigation of electron dynamics in superlattice quantum cascade lasers, both for the InGaAs/AlInAs and for the GaAs/AlGaAs systems. Determination of the miniband dispersion and electron wave functions and calculation of scattering rates have been performed in order to set up Monte Carlo simulations. Injection and extraction rates in the active region are calculated with a transfer matrix technique. Results are here discussed. © 2000 Published by Elsevier Science B.V. All rights reserved.

PACS: 78.20.Bh; 42.55.Px; 78.60.Fi; 85.30Vw

Keywords: Monte Carlo simulations; Quantum cascade lasers; Simulation; Electroluminescence

1. Introduction

Among all the proposed typologies of quantum cascade lasers (QCLs) [1–4] (for a recent review see Ref. [5]) the one based on superlattice (SL) structures [2,5] offers the advantages of intrinsic population inversion, simplicity of design and higher current drive capabilities. In such devices, carrier injection and transport always involve two minibands of adjacent SLs. Thus, modeling of device performance has to rely on physical models fully accounting for the miniband dispersion. Up to now, theoretical investigation on

electron dynamics in SL minibands has been very scarce.

2. Theoretical model and results

We present a theoretical investigation of electron dynamics in InGaAs/InAlAs superlattice QCL structure. A comparison with electroluminescence spectra measured in Bari SL structures will be also discussed. Our approach is the following:

(i) We first determine the miniband dispersion and electron wave functions for the SL using the Kronig–Penney nonparabolic model; (ii) We then calculate the scattering rates for electron–phonon (acoustic and optical phonons) and electron–electron interactions [6]; (iii) we choose the optimal SL (in terms of

* Corresponding author. Tel.: +39-06-72597372; fax: +39-06-2020519.

E-mail address: lugli@uniroma2.it (P. Lugli)

¹ Also at INFN.

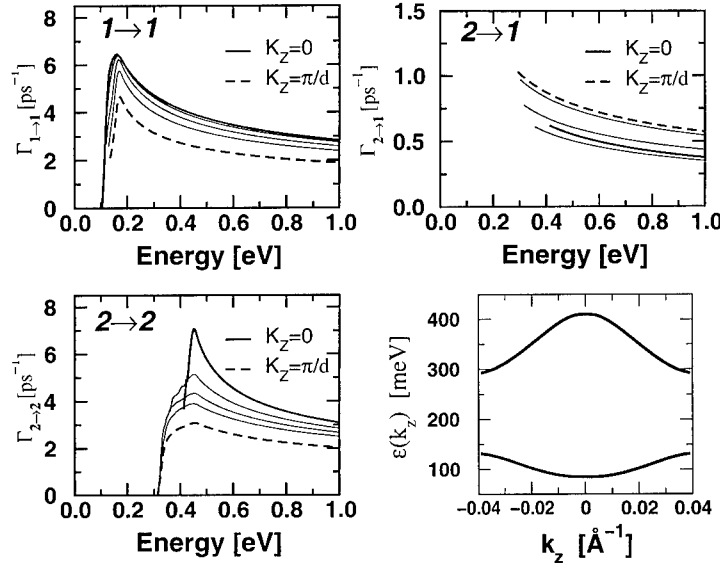


Fig. 1. Scattering rates and miniband dispersion of the InGaAs/InAlAs structure.

Table 1
Scattering rates for LO phonon emission processes

Transition	GaAs/AlGaAs	InGaAs/AlInAs
2 → 2	0.88 ps ⁻¹	1.60 ps ⁻¹
2 → 1	0.33 ps ⁻¹	0.25 ps ⁻¹
1 → 1	0.40 ps ⁻¹	0.74 ps ⁻¹

barrier and well width) on the basis of the strength of the intraminiband phonon scattering and the miniband width, both of which have to be as large as possible for the proper operation of the laser; (iv) we calculate the injection and extraction rates and energies into the active region from a transfer matrix technique; (v) we perform Monte Carlo simulations of electron dynamics based on all previous ingredients, extracting the electron distribution functions for each miniband under steady-state conditions; (vi) we calculate the emission spectra at the chosen injection condition.

The determination of the optimal SL structure is based on the consideration that (i) the width of each miniband has to be much larger than an LO phonon energy, and (ii) the intraminiband scattering times have to be much shorter than the interminiband ones. By looking at the miniband profiles and electron–LO phonon scattering rates for a variety of geometries,

we have chosen for the InGaAs/InAlAs system the values $W = 60 \text{ \AA}$ $B = 18 \text{ \AA}$ (well and barrier width, respectively). In the case of GaAs/AlGaAs condition (i) is hardly fulfilled because of the smaller band offset. Based on the scattering rate values we chose $W = 60 \text{ \AA}$ and $B = 40 \text{ \AA}$ for GaAs/AlGaAs SLs.

Fig. 1 shows the electron–LO phonon emission scattering rates and the miniband profile for the optimal InGaAs/AlInAs structure. Here, we have considered bulk phonon dispersions, as we are interested only in the overall electron dynamics and not on the detailed contribution of the various SL phonon modes to the relaxation processes. The scattering rates are plotted as a function of electron energy (measured from the bottom of the miniband) at different values of the parallel k_p and perpendicular k_z k -vector. For instance, for the $2 \rightarrow 2$ transition, the lowest curve corresponds to the maximum k_z (at the miniband edge), as only states on the k_p dispersion are involved in the transition, while the largest scattering rate is found at $k_z = 0$, that is at the top of the miniband. The reverse situation holds for the intraminiband transitions within the first miniband. A Monte Carlo simulation [7] has been set up based on the scattering rates described above. In addition to LO phonon, electron–electron scattering is included, the interaction being calculated

Table 2

Scattering rates for electron–phonon and electron–electron intraminiband scattering within the first (1 1 1) and the second (2 2 2) miniband

n_{tot}	$f_{2 \rightarrow 2}$ [ps^{-1}]	$f_{2 \rightarrow 1}$ [ps^{-1}]	$f_{1 \rightarrow 1}$ [ps^{-1}]	$f_{2 2 2 2}$ [ps^{-1}]	$f_{1 1 1 1}$ [ps^{-1}]
10^{16} cm^{-3}	0.74	0.28	1.60	0.80	2.90
10^{17} cm^{-3}	0.79	0.28	1.60	1.25	3.80
10^{18} cm^{-3}	0.73	0.25	1.63	1.70	4.80

assuming a statically screened Coulomb potential. Acoustic phonons are neglected since the corresponding rates are much lower. Pauli's exclusion principle is accounted for in the usual way [7]. In order to reach a steady-state condition in the simulation, electrons are extracted from the bottom of the first miniband at a fixed rate determined by a time constant τ_{tunn} , which is taken as an input parameter (here $\tau_{\text{tunn}} = 2 \text{ ps}$). This process mimics the tunneling from the active layer into the next injector region of the real device. For each electron which is extracted, one is injected into the second miniband. In the simplest scheme, another input parameter E_{inj} defines the energy of the injected electron (here $E_{\text{inj}} = \text{miniband top}$). A more realistic condition, which will be described below, involves the calculation of the transmission coefficient at a given bias point. As initial condition for the simulation a given electron density is distributed as an equilibrium Fermi function in the first miniband. The extraction/injection routine and the MC simulation of the electron dynamics is then performed until stationarity is reached. The stationary distribution functions for the first and second minibands for a lattice temperature of 5 K are plotted in the inset of Fig. 2. Three different densities are considered. As the density increases, the enhanced intercarrier scattering broadens the distribution functions, thus reducing the overlap in k -space between the populations of the two minibands. The effect of such a broadening on lasing capabilities of the SL can be evaluated by looking at the *inversion gain*, g_{inv} , which we define as the ratio of the electron density at the bottom of the upper miniband to the density at the top of the lower miniband. The higher the value of g_{inv} , the higher the probability that the structure will lase (and the lower the threshold current for lasing). It should be noted that, for comparable densities, the value of the inversion gain of the InGaAs/InAlAs SL is about one order of magnitude higher than that of

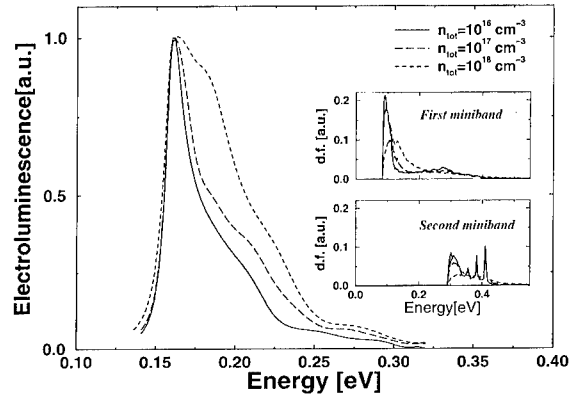


Fig. 2. Electroluminescence spectra in stationary condition. The inset shows the stationary electron distribution functions of the first and the second miniband.

the GaAs/AlGaAs structure. This is consistent with the actual rates for phonon processes that can be extracted from the simulation, presented in Table 1. Here the intraminiband $2 \rightarrow 2$, $1 \rightarrow 1$ and the interminiband $2 \rightarrow 1$ transition rates are displayed for the two SLs. It is clear that InGaAs/InAlAs does indeed promise much better performance. An interesting result is found as a function of doping density. As the density moves from 10^{16} to 10^{18} cm^{-3} , the inversion gain of the InGaAs/InAlAs structure drops from 26 to 1.2, indicating that low doping of the active region has to be preferred. The physical reason can be understood from Table 2 which shows the rates for electron–phonon and electron–electron scattering calculated during the simulation. While the phonon rate does not change appreciably (indicating that Pauli's exclusion principle does not effect the electron transport around the miniband edge, at least up to the densities considered here), the intercarrier rate increases with the electron density, both as intra and inter-miniband processes. The former contributes to the thermalization and spreading in k -space of the electrons within

each miniband, the latter causes a redistribution between minibands, in particular favoring the scattering out the upper into the lower miniband. Indeed, a significant reduction of the threshold current and room temperature operation in QCL with intrinsic SL regions has been reported [8]. The electroluminescence spectra are plotted in Fig. 2. The spectra get broader at higher densities, a direct consequence of the electron thermalization detected in the distribution functions. The influence of the various parameters of the simulation has also been tested. In short, we found that the inversion gain is higher when the injection energy is lower. This is caused by a strong reduction of the phonon scattering within the second miniband when electrons are injected closer to the miniband edge, while the interminiband $2 \rightarrow 1$ and the intraminiband $1 \rightarrow 1$ do not show any sizeable dependence on E_{inj} . This result indicates the importance of the injection condition in determining the performance of superlattice QCLs. For instance, it is possible to compensate for the loss of inversion gain characteristic of high densities by properly tuning the injection energy. A similar picture is obtained when varying τ_{tunn} : the higher its value, the higher the population of the first miniband, and therefore the lower the inversion gain.

3. Physical model for injection

Up to now the simulation was based on a simple injection model, which assumes a Fermi distribution of the injected carriers around a given energy, given as input. We have developed a more refined model which is based on the standard “transfer matrix” approach. The starting point is the 1D Schroedinger’s equation for the simulated structure, solved with the boundary conditions of bulk propagating plane waves impinging on the SL regions from a left contact. This approach allows us to calculate the transmission coefficient as a function of the energy of the incoming electron. To better account for the structure of the SL QCL, we have considered a region made up of two active SL layers, separated by the injector (see the central portion of Fig. 3).

If the Schroedinger equation is coupled to the 1D solution of the Poisson equation, the transmission coefficient can be calculated for each bias applied to the

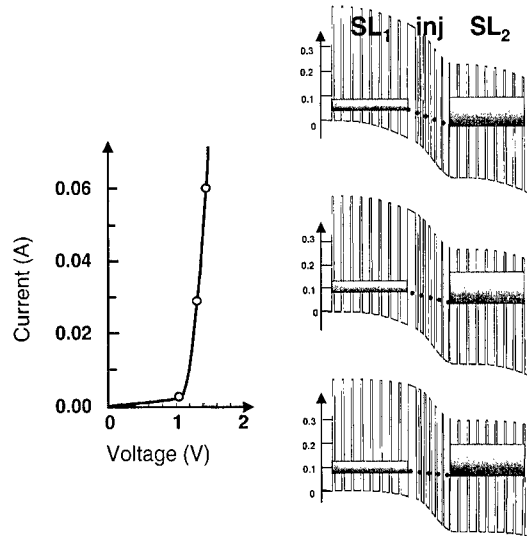


Fig. 3. Current–voltage characteristics, conduction band profile and transmission coefficient of InGaAs/InAlAs structure for three different bias voltages.

device. By integrating the product of the transmission coefficient and the electron distribution function over the k -vector parallel to the heterointerfaces of the SL, the current density is readily obtained. Fig. 3 shows the current–voltage characteristics of the InGaAs/InAlAs structure, together with the band profile and transmission coefficient for three bias points. Clearly, an efficient transmission from one SL to the other is obtained (i) if the miniband of the two SLs on the right and on the left are aligned, and (ii) if allowed energies exist in the injector providing the channel for the electron transfer. The transmission coefficient versus energy calculated for a given bias point gives directly the energy distribution of the simulated injected electrons.

4. Conclusions

We have presented a physical model for the description of superlattice QCL structures based on the Kronig–Penney model for the electronic states and on Fermi’s Golden rule for the relevant electron interaction. A Monte Carlo simulation has been set up to analyze the electron dynamics and the influence of several microscopic processes on the performance of

the QCL. In particular, we have pointed out the role of interelectron scattering, and compared different material systems.

Acknowledgements

This work was partially supported by the INFM under PRA project “SUPERLAS”, and by the European TMR Network “Ultrafast Quantum Electronics”. We gratefully acknowledge the contribution of Fausto Rossi and Mario Gulia to the development of the simulation code.

References

- [1] J. Faist, F. Capasso, D.L. Sivco, C. Sirtori, A.L. Hutchinson, A.Y. Cho, *Science* 264 (1994) 553.
- [2] G. Scamarcio, F. Capasso, C. Sirtori, J. Faist, A.L. Hutchinson, D.L. Sivco, A.Y. Cho, *Science* 276 (1997) 773.
- [3] C. Sirtori, P. Kruck, S. Barbieri, P. Collot, J. Nagle, M. Beck, J. Faist, U. Oesterle, *Appl. Phys. Lett.* 73 (1998) 3486.
- [4] A. Tredicucci, C. Gmachl, F. Capasso, D.L. Sivco, A.L. Hutchinson, A.Y. Cho, *Appl. Phys. Lett.* 74 (1999) 638.
- [5] F. Capasso, A. Tredicucci, C. Gmachl, D.L. Sivco, A.L. Hutchinson, A.Y. Cho, G. Scamarcio, *IEEE J. Selected Topics Quant. Electron.* 5 (1999) 792.
- [6] F. Rossi et al., *Phys. Rev. B* 51 (1995) 16 943.
- [7] C. Jacoboni, P. Lugli, in: S. Selberherr (Ed.), *The Monte Carlo Method for Semiconductor Device Simulation*, Springer, Berlin, 1989.
- [8] A. Tredicucci, F. Capasso, C. Gmachl, D.L. Sivco, A.L. Hutchinson, A.Y. Cho, J. Faist, G. Scamarcio, *Appl. Phys. Lett.* 72 (1998) 2388.

Edge- and surface-emitting 10.1 μm quantum cascade distributed feedback lasers

Daniel Hofstetter^{a,*}, Jérôme Faist^a, Mattias Beck^a, Antoine Müller^a, Ursula Oesterle^b

^aUniversity of Neuchâtel, Institute of Physics, 1 Rue A.-L. Breguet, Neuchâtel, CH 2000, Switzerland

^bSwiss Federal Institute of Technology, Physics Department, PHB Ecublens, Lausanne, CH 1015, Switzerland

Abstract

We present measurement results on high-power low-threshold quantum cascade-distributed feedback lasers emitting infrared radiation at 10.16 μm . A lateral current injection scheme allowed the use of a strongly coupled surface grating without metal coverage and epitaxial re-growth. Although this design resulted in a simplified processing, the fabrication of high-performance edge- and surface-emitting devices was demonstrated. For the edge-emitting laser, we used a standard first-order grating with a period of 1.57 μm , and for the surface emitter, a second-order grating with a period of 3.15 μm was used. Maximal output powers in excess of 200 mW at 85 K and 70 mW at 300 K were achieved for both configurations. The threshold current densities at 85 K (300 K) were 1.85 kA/cm² (5.4 kA/cm²) and 2.1 kA/cm² (5.6 kA/cm²) for edge and surface emitters, respectively. © 2000 Elsevier Science B.V. All rights reserved.

Keywords: Quantum cascade lasers; Distributed feedback lasers; Surface emission; Lateral current injection

Quantum cascade (QC) lasers are very promising light sources for environmental sensors in the mid-infrared spectral region [1–3]. Most of these applications require the use of single-mode light sources; be they edge- or surface-emitters. This requirement can be accomplished by using a distributed feedback (DFB) laser [4–6]. In order to achieve standard edge-emission, we fabricated devices with a first-order grating, while for the surface-emitters, a second-order grating was used [7]. Although DFB

lasers have obvious performance benefits, they usually suffer from the fact that epitaxial re-growth is necessary to complete the structure after grating fabrication. As has been recently demonstrated, one can use a lateral current injection scheme in order to fabricate a strongly coupled, low-loss grating without epitaxial re-growth [5]. These devices have a waveguide with a semiconductor lower cladding and air forming the top cladding. The heavily n-doped InGaAs cap layer, which serves as a host layer for the grating, is highly conducting to allow lateral current injection and -distribution throughout the device. This results in both a high coupling coefficient of the grating and a relatively high net gain of the laser; thus

* Corresponding author. Tel.: +41-32-718-3545; fax: +41-32-718-2901.

E-mail address: daniel.hofstetter@iph.unine.ch (D. Hofstetter)

it potentially allows the fabrication of short devices with a low threshold current.

Growth of this material was based on molecular beam epitaxy (MBE) of lattice-matched InGaAs/InAlAs layers on top of an n-doped InP (Si, $2 \times 10^{17} \text{ cm}^{-3}$) substrate. The growth process started with the lower waveguide layers (InGaAs, Si, $1 \times 10^{17} \text{ cm}^{-3}$, total thickness $1.5 \mu\text{m}$), proceeded with an active region (thickness $1.75 \mu\text{m}$) and was finished by a thicker set of upper waveguide layers (thickness $2.2 \mu\text{m}$) and a $0.7 \mu\text{m}$ thick highly n-doped cap layer on top. This cap layer was also the host layer for the grating, as mentioned earlier. The active region, which thus formed the central part of the waveguide, consisted of 35 super-lattice periods; those were alternating n-doped funnel injector regions and undoped triple quantum well active regions. The laser transition in the latter was diagonal, similar to that described in Ref. [8]. The layer sequence of the structure, in nanometers, starting from the injection barrier, is as follows: 3.9/**1.0**/3.8/**1.2**/3.7/**1.5**/3.9/**1.7**/4.0/**4.2**/3.1/**0.9**/6.4/**1.0**/6.0/**2.8** nm. $\text{In}_{0.52}\text{Al}_{0.48}\text{As}$ layers are in bold, $\text{In}_{0.53}\text{Ga}_{0.47}\text{As}$ layers are in roman, and n-doped layers (Si $2.5 \times 10^{17} \text{ cm}^{-3}$) are underlined.

The fabrication of these DFB lasers was based on holographically defining a grating with either $1.57 \mu\text{m}$ (first-order grating) or $3.15 \mu\text{m}$ period (second-order grating, $n_{\text{eff}} = 3.22$), and wet chemical etching of the grating in a $\text{H}_2\text{SO}_4/\text{H}_2\text{O}_2/\text{H}_2\text{O}$ solution to a depth of $0.6 \mu\text{m}$ (etch rate 100 nm/sec). We used a 488 nm Ar-ion laser and a 90° corner reflector mounted on a rotational stage for the grating exposure. The grating lines run along the dove-tail direction of the crystal in order to achieve non-rectangular profile and to obtain a sufficiently high first-order Fourier component. This is quite critical for the performance of the surface-emitting laser because a symmetric rectangular second-order grating contains no first-order Fourier component. In addition, the combination holography/wet etching for the fabrication of the grating involves a high risk of obtaining a duty cycle which is considerably smaller than 50%. Since a small duty cycle reduces the average refractive index and therefore also the overlap factor of the grating layer, the coupling coefficient becomes small, resulting in an even poorer efficiency of the grating.

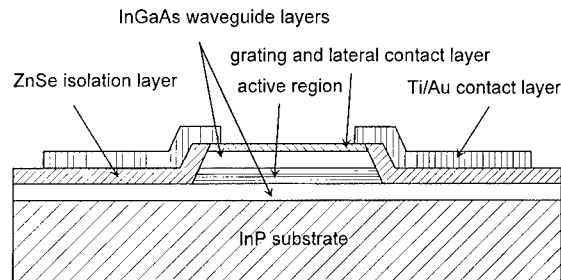


Fig. 1. Schematic cross-section through the waveguide of a DFB laser. The top metal contact covers only a small fraction on both shoulders of the waveguide.

Standard processing techniques were used to define ridge waveguides with a width of $35\text{--}55 \mu\text{m}$ (etch depth $4.5 \mu\text{m}$, $\text{HBr}/\text{HNO}_3/\text{H}_2\text{O}_2$, etch rate 800 nm/min) and a length of $1\text{--}1.5 \text{ mm}$ [5]. 300 nm of ZnSe served as an electrical passivation layer and Ti/Au ($10/400 \text{ nm}$) was used as top contact metal. Thinning, back contacting (Ge/Au/Ag/Au, $12/27/50/100 \text{ nm}$), and cleaving completed the processing. As shown by the schematic cross-section in Fig. 1, the contact metal covered only the edges (about $5 \mu\text{m}$ on each side) of the ridge to avoid large absorption losses in the waveguide, but still to allow lateral current injection. The devices, whose facets were left uncoated, were mounted ridge side up on copper heat sinks and operated at different temperatures between 85 and 300 K . The samples were then placed into a temperature-controlled N_2 flow cryostat. The light from the facet or the grating of the DFB QC laser was collected by $f/0.8$ optics and fed into a high-resolution Fourier transform spectrometer (Nicolet-type Magna-IR 860), where we detected it by using a liquid nitrogen-cooled HgCdTe detector. For the measurement of L - I curves, we measured the intensity with a calibrated $500 \times 500 \mu\text{m}^2$ room temperature HgCdTe detector. For both types of lasers, the current pulses were 100 ns long, and a pulse repetition frequency of 5 kHz was used for all temperatures. A typical L - I and I - V curve of the first-order DFB laser are presented in Fig. 2. For a 1.2 mm long and $45 \mu\text{m}$ wide laser, a maximal output power of 230 mW at 85 K and 80 mW at room temperature was seen. The device emitted single-mode radiation for all temperatures and power levels. The threshold current was 1 A at 85 K and increased to 2.9 A at

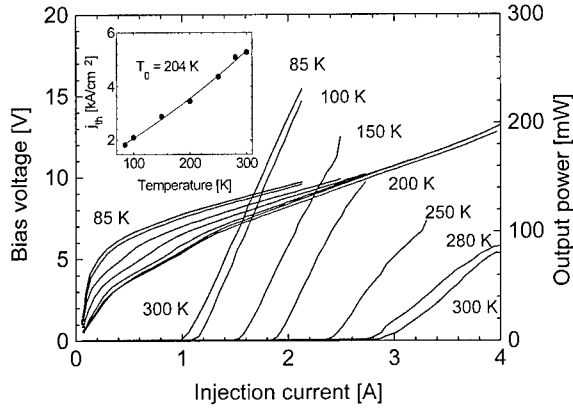


Fig. 2. L – I and I – V curve of a first-order DFB laser measured at different temperatures between 85 and 300 K. The inset shows how the threshold current changes with increasing temperature.

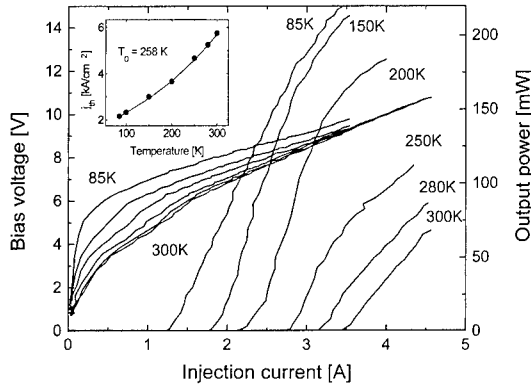


Fig. 3. L – I and I – V curve of a surface-emitting second-order DFB laser measured at temperatures between 85 and 300 K. The inset shows the threshold current change with increasing temperature.

300 K, corresponding to threshold current densities of 1.85 and 5.4 kA/cm², respectively. Edge emission L – I and I – V -curves of a 55 μ m wide and 1.125 mm long surface-emitting device are shown in Fig. 3. At low temperatures, we observed a threshold current of 1.3 A and a maximum output power of 210 mW from the facet. The slope efficiency at this temperature was 105 mW/A and a threshold current density of 2.1 kA/cm² was determined. At room temperature, we obtained 70 mW optical output power from the facet, with a slope efficiency of 70 mW/A. However, the threshold current increased to 3.45 A (threshold current density of 5.6 kA/cm²), and an operating voltage of 10.5 V was seen. From the increase in

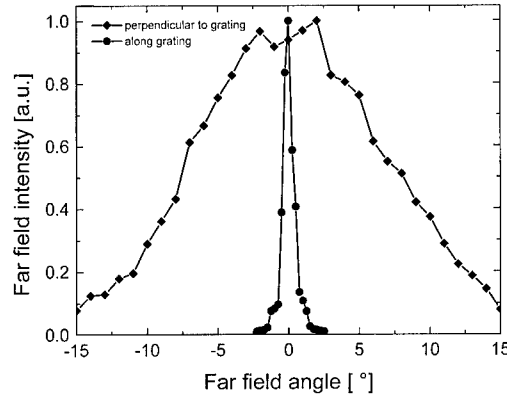


Fig. 4. Far field distribution of a surface-emitting second-order DFB laser in the directions both parallel and perpendicular to the waveguide.

threshold current, we were able to derive a characteristic temperature T_0 of 204 K for the first-order DFB laser and 258 K for the surface-emitting DFB laser.

In Fig. 4, we present the vertically emitted far-field distribution of the surface-emitter in both directions. In the direction along the waveguide, we observed, due to the wide aperture and the Bragg reflection, a very narrow far-field angle of about 1° (FWHM), whereas in the other, perpendicular direction, the far-field angle was equivalent to the one observed at the corresponding direction of the facet, namely about 14° (FWHM). Such a far field distribution will facilitate coupling into a micro-optical sensor system in the respect that a cylindrical lens instead of an aspherical one will be sufficient to achieve a parallel laser beam.

Spectral measurements below lasing threshold allowed a relatively precise measurement of the Bragg reflector's stop-bandwidth, the value obtained was 2.6 cm^{−1} for the first-order and 1.1 cm^{−1} for the second-order DFB laser. From these figures, we determined the coupling coefficients of the grating to be $\kappa = \Delta\lambda\pi n_{eff}/\lambda^2 = 28$ cm^{−1} and 12 cm^{−1}, respectively. A relatively small free carrier absorption loss of 12 cm^{−1} was calculated for both devices, whereas a laser utilizing our standard waveguide design with a 2.2 μ m thick InAlAs/InGaAs upper cladding layer and a metal-covered grating would suffer from a waveguide loss of 30 cm^{−1}. In addition, the refractive index contrast would be reduced by almost two orders of magnitude.

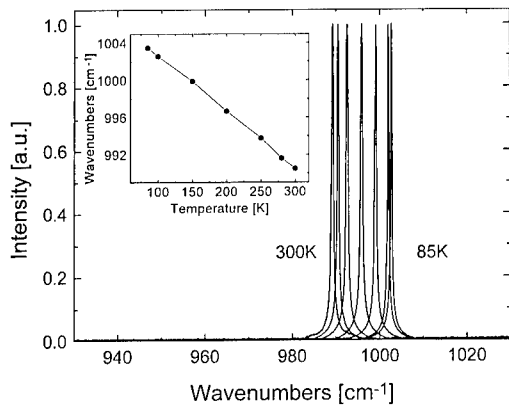


Fig. 5. Optical emission spectra of a second-order DFB laser measured at different temperatures between 85 and 300 K. The inset shows the linearity of the temperature tuning.

Finally, Fig. 5 shows the lasing spectra of the second-order DFB laser at temperatures between 85 and 300 K. We determined the line width to be of the order of 0.3 cm^{-1} , which corresponds to the resolution limit of our experimental set-up. The emission wavelength at 85 K was 1003 cm^{-1} , at room temperature, it decreased to 989 cm^{-1} . The luminescence peak was found in the vicinity of 990 cm^{-1} for all temperatures. The temperature-tuning coefficient of the lasing peak was constant over the entire temperature range, and its magnitude was $1/\lambda \times \Delta\lambda/\Delta T = 6.1 \times 10^{-5} \text{ K}^{-1}$ ($\Delta\nu/\Delta T = -0.06 \text{ cm}^{-1}/\text{K}$). These numbers are consistent with what has been reported in the literature [6].

In conclusion, we have shown device results for both first-order and second-order DFB QC lasers operating at $10.1 \mu\text{m}$. These DFB lasers function without upper cladding layer, the grating is therefore directly exposed to air. Current injection is accomplished laterally through the grating layer; this design avoids large waveguide losses due to metal absorption. At room temperature, both types of lasers emitted in excess of 70 mW optical power through the facet, the second-order device an

additional 18 mW from the grating. The corresponding numbers for 85 K were > 200 and 60 mW for facet and grating emissions, respectively. Pulsed threshold current densities of 5.4 kA/cm^2 (5.6 kA/cm^2) and 1.85 kA/cm^2 (2.1 kA/cm^2) for the first- (second-) order DFB laser were seen. For the surface-emitting laser, the far-field angle in the narrow direction along the waveguide was of the order of 1° , in the direction perpendicular to the waveguide, we observed a far field angle of 14° .

Acknowledgements

We would like to thank Stéphane Blaser, and Antoine Müller for their advice during processing, electrical and spectral measurements on these samples, and the Swiss National Science Foundation and the Science Foundation of the European Community under contract BRITE/EURAM project UNISEL (No. CT97-0557) for their financial support.

References

- [1] J. Faist, F. Capasso, D.L. Sivco, A.L. Hutchinson, A.Y. Cho, *Science* 264 (1994) 553.
- [2] J. Faist, F. Capasso, C. Sirtori, D.L. Sivco, J.N. Baillargeon, A.L. Hutchinson, S.N.G. Cho, A.Y. Cho, *Appl. Phys. Lett.* 68 (1996) 3680.
- [3] C. Sirtori, J. Faist, F. Capasso, D.L. Sivco, A.L. Hutchinson, A.Y. Cho, *Appl. Phys. Lett.* 68 (1996) 1745.
- [4] J. Faist, C. Gmachl, F. Capasso, C. Sirtori, D.L. Sivco, J.N. Baillargeon, A.Y. Cho, *Appl. Phys. Lett.* 70 (1997) 2670.
- [5] D. Hofstetter, J. Faist, A. Müller, M. Beck, U. Oesterle, *Appl. Phys. Lett.* 75 (1999) 665.
- [6] C. Gmachl, F. Capasso, J. Faist, A.L. Hutchinson, A. Tredicucci, D.L. Sivco, J.N. Baillargeon, S.N.G. Chu, A.Y. Cho, *Appl. Phys. Lett.* 72 (1998) 1430.
- [7] G.A. Evans, D.P. Bour, N.W. Carlson, J.M. Hammer, M. Lurie, J.K. Butler, S.L. Palfrey, R. Amantea, L.A. Carr, F.Z. Hawrylo, J.B. Kirk, S.K. Liew, W.F. Reichert, *Appl. Phys. Lett.* 55 (1989) 2721.
- [8] J. Faist, C. Sirtori, F. Capasso, D.L. Sivco, J.N. Baillargeon, A.L. Hutchinson, A.Y. Cho, *IEEE Photonics Technol. Lett.* 10 (1998) 1100.



ELSEVIER

Physica E 7 (2000) 29–32

PHYSICA E

www.elsevier.nl/locate/physa

GaAs/AlGaAs microresonator quantum cascade lasers

S. Gianordoli *, L. Hvozdar, G. Strasser, T. Maier, N. Finger, K. Unterrainer, E. Gornik

Institut für Festkörperelektronik, TU Wien, A-1040 Wien, Austria

Abstract

We report on the realization of electrically pumped GaAs/AlGaAs microcylinder lasers emitting at $\lambda = 10 \mu\text{m}$. The design and fabrication process of the special resonator shapes (circular- and stadium-like cross section) are presented. The active material is a 30 period sequence of injectors/active regions made of GaAs/AlGaAs quantum wells. Far-field characteristics of these special resonators are compared and the dependence of directionality of the emission on the deformation is investigated. The bow-tie mode can be resolved in the far-field pattern. A transition from the bow-tie to another mode with highly directional emission along the short axis of the resonators is shown for the first time. Single-mode emission is detected for $100 \mu\text{m}$ diameter circular microlasers with a side mode suppression exceeding 20 dB. The maximum working temperature of the microcylinder lasers is 165 K. © 2000 Elsevier Science B.V. All rights reserved.

PACS: 42.55.P; 42.55.X; 78.66; 78.66.F; 78.65; 73.20.D; 73.40; 78.30.F; 85.30.V

Keywords: GaAs-lasers; Quantum cascade lasers; Microresonator

Semiconductor lasers are realized using Fabry Perot (VCSEL, DFB laser, DBR and external cavity lasers) or circular-shaped resonators (microdisks or microcylinders). In the latter geometry a decrease of mirror losses is achieved due to an increase of the reflectivity. Total internal reflection of the so-called “whispering-gallery modes” (WGM) guarantees a reflectivity near unity and thus a decrease of the threshold current density of lasers based on these special kinds of resonators. Microdisk interband lasers with a lasing wavelength around $1 \mu\text{m}$ have been studied, e.g. on the InGaAs/InGaAsP material system [1].

In the mid-infrared regime unipolar semiconductor lasers based on intersubband transitions in quantum wells marked a breakthrough in the application of band-structure engineering [2,3]. These first quantum cascade lasers (QCL) were based on the Fabry Perot resonator geometry. Next to these classical ridge waveguide geometry disk lasers based on InGaAs/InAlAs-QC active regions emitting around $5 \mu\text{m}$ [4] and between 9.5 and $11.5 \mu\text{m}$ have been fabricated [5]. The two longer wavelength lasers show a reduction of threshold current densities as compared to ridge waveguide lasers using nominally the same gain. Compared to microdisks where the heat can mostly be dissipated over a thin pedestal, microcylinders show a better heat dissipation. Microcylinders with circular and stadium-like cross sections [6]

* Corresponding author. Tel.: +43-1-58801-36217; fax: +43-1-58801-36299.

E-mail address: stefan.gianordoli@tuwien.ac.at (S. Gianordoli)

emitting around 5 μm are also reported [7] and show higher threshold current densities (4–7 kA/cm^2) than ridge waveguide lasers with identical gain regions (1–2 kA/cm^2). QCL are unipolar lasers, thus, surface recombination, which is the major problem for disk bandgap lasers (wavelength around 1 μm), is not an issue. Additionally, due to an about 10 times longer wavelength (5–12 μm) surface roughness is not so critical.

The realization of unipolar light emitters based on the material system GaAs/AlGaAs extends the QCL field to a wider range of applications. Electroluminescence [8], optically and finally electrically pumped [9] lasing in GaAs/AlGaAs structures have been reported lately. GaAs/AlGaAs microcylinder with circular cross section emitting at 10 μm were compared to ridge waveguide lasers fabricated on the same grown laser material [10]. These circular resonators significantly improved the threshold current density ($\sim 7 \text{ kA}/\text{cm}^2$ for the microcylinder and $\sim 10 \text{ kA}/\text{cm}^2$ for the ridge waveguide lasers) and the low current consumption because of the small size. On the other hand, the emission pattern is isotropic and the emitted power is smaller compared to the ridge waveguide geometry because of scattering (on surface imperfections) as the main outcoupling mechanism [11].

We present here the results of the investigations on quadrupolar deformed microlasers based on GaAs/AlGaAs. The design of the unipolar GaAs/AlGaAs intersubband laser working at a wavelength of 10 μm is based on a three-quantum-well active cell comparable to the one given in Ref. [9]. Layer thickness and doping concentration are essentially the same, the Al content in the barrier is reduced to 30% to lower the band offset and, thus, to increase the emission wavelength to 10 μm . The active cells are separated by miniband funnel injectors and the whole structure is embedded between conducting cladding layers to ensure efficient electron injection and waveguiding. The cladding layers contain low-doped GaAs core layers between the active region and highly doped n^+ GaAs layers acting as a plasma-enhanced confinement [12,13].

The microlasers are step-wise ($\varepsilon = 0.02$) deformed starting from a circular cross section (deforming parameter $\varepsilon = 0$) to a quadrupolar cross section ($\varepsilon = 0.24$) following the quadrupolar shape given in

Ref. [14] where also the polar coordinates are defined. Starting from a radius $R = 60$ or $70 \mu\text{m}$ the radius in one direction (short axis) is step wise reduced while the radius in the other direction (long axis) is kept constant. The pattern of these deformed quadrupoles is transferred to the QCL-material via photolithography, and dry etched using a SiN mask and reactive ion etching (RIE). On the top of the $\sim 9 \mu\text{m}$ high resonators a Ti/Au contact is formed by sputtering, afterwards the Ge/Au/Ni/Au back contact is evaporated. The back contact has been alloyed for some samples and for others it has not been alloyed. There is no noticeable difference in the performance between samples with alloyed and non-alloyed contacts. The microlasers are In-soldered on a samples holder and mounted in a He-cooled flow cryostat.

For measuring the far-field pattern the mid-infrared laser beam from a microlaser is collected with a $f/2.9$ ZnSe-lense onto an LN_2 cooled MCT. The setup has a collecting angle of 19° . The samples in the flow cryostat are turned in steps of $\phi \sim 11^\circ$ in order to record the emitted intensity for different angles ϕ . The lasing spectrum gets multi mode for higher driving currents. Emission spectra are obtained using a Fourier transform infrared spectrometer. The samples are driven with 200 ns long pulses at a repetition rate of 37 kHz and at a temperature of 12 K.

In Fig. 1 the far-field patterns of two microlasers (placed on different positions on wafer) with $R = 70 \mu\text{m}$ for the long radius ($\phi = 0^\circ$), $R_1 = 53 \mu\text{m}$ for the short radius ($\phi = 90^\circ$) and a deformation of $\varepsilon = 0.16$ are depicted. The threshold current density for both is $7.6 \text{ kA}/\text{cm}^2$. To guarantee a single-mode operation the microlasers are driven at low driving currents. The maximum in the far-field pattern is located at $\phi \sim 50^\circ$, typical for a bow-tie mode. Fig. 2 shows the emission spectrum of these microlasers for high driving current in order to resolve the side modes and to measure the mode spacing. The calculated bow-tie mode spacing $\Delta\nu$ [14,15] for these lasers is $\Delta\nu = 8.16 \text{ cm}^{-1}$ for $\phi \sim 50^\circ$. The measured value $\Delta\nu = 8.2 \text{ cm}^{-1}$ agrees very well to the calculated one.

Following the considerations in Ref. [14] the bow-tie modes appear for deformations larger than $\varepsilon = 0.1$. Below this value the resonator modes are WGMs with high internal reflectivity and the low outcoupling of the lasing radiation due to evanescent leakage and

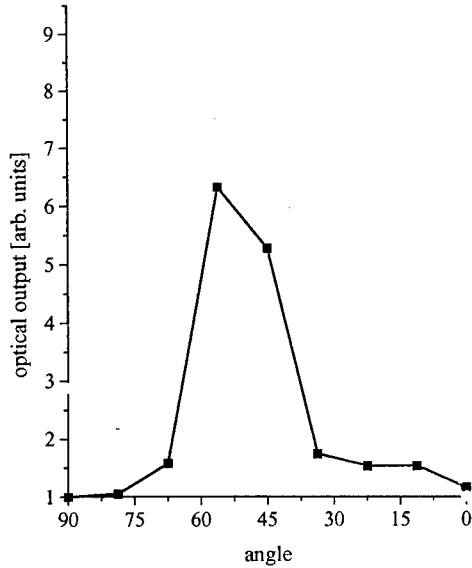


Fig. 1. Typical far-field pattern of a bow-tie mode with directional emission around 50° .

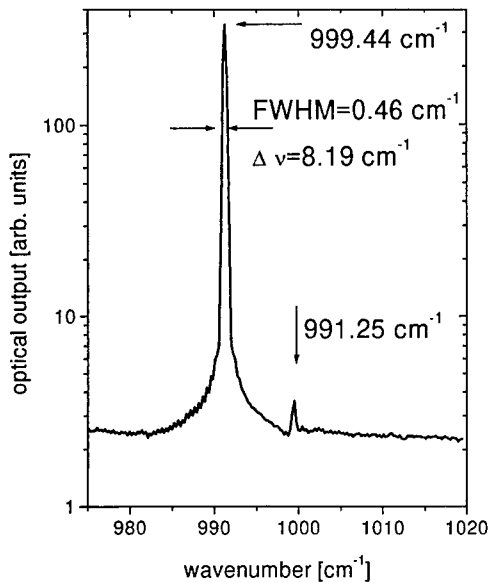


Fig. 2. Emission spectrum of an intersubband laser at $T = 10$ K measured in continuous scan mode. The FWHM derived of the main peak is 4.6 cm^{-1} .

scattering on surface imperfections. Above $\varepsilon = 0.1$ the reflectivity of the modes in the resonators decreases and the outcoupling of the radiation increases.

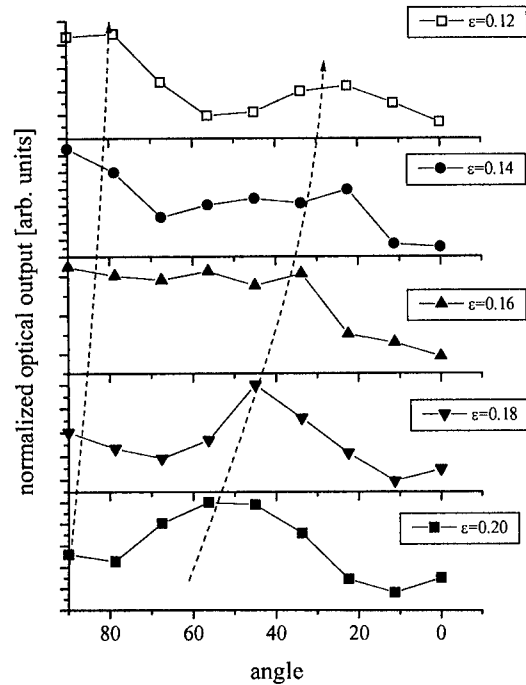


Fig. 3. Far-field pattern for different deformations. The large radius $R = 60 \text{ }\mu\text{m}$ is constant for all deformations whereas the smaller one is decreasing from 48.4 to $42.8 \text{ }\mu\text{m}$ with increasing deformation. The measured data points for the different far field are normalized to their respective maximal value.

In Fig. 3 far-field patterns for deformations ranging from $\varepsilon = 0.12$ to 0.2 are shown. The long radius for these microlasers is kept constant at $R = 60 \text{ }\mu\text{m}$ and the shorter one, R_1 , is decreased from 48.4 ($\varepsilon = 0.12$) to $42.8 \text{ }\mu\text{m}$ ($\varepsilon = 0.2$). It is remarkable that at a deformation of $\varepsilon = 0.18$ and 0.2 the bow-tie mode can be seen in the far-field pattern; but from $\varepsilon = 0.12$ to 0.16 the far-field patterns differ from that one of a simple bow-tie mode. Two maxima in the far field for the $\varepsilon = 0.12$ microlaser can be distinguished: the largest one between $\phi \sim 90^\circ$ and 80° and a smaller one between $\phi \sim 50^\circ$ and 10° . The peak around $\phi = 90^\circ$ is decreasing with increasing deformation whereas the second peak around $\phi \sim 35^\circ$ is increasing.

To discover the reason of the behaviour depicted in Fig. 3 the shape of the resonator modes (which are the origin for the different far-field patterns) in the deformed resonators have to be found.

Acknowledgements

This work was partly supported by an European Brite Euram III project and the Society for Microelectronics (GMe, Austria).

References

- [1] S.L. McCall, A.F.J. Levi, R.E. Slusher, S.J. Pearton, R.A. Logan, *Appl. Phys. Lett.* 60 (1992) 289.
- [2] J. Faist, F. Capasso, D.L. Sivco, C. Sirtori, A.L. Hutchinson, A.Y. Cho, *Science* 264 (1994) 553.
- [3] C. Gmachl, F. Capasso, A. Tredicucci, D.L. Sivco, A.L. Hutchinson, S.N.G. Chu, A.Y. Cho, *Appl. Phys. Lett.* 73 (1998) 3830.
- [4] J. Faist, C. Gmachl, M. Striccoli, C. Sirtori, F. Capasso, D.L. Sivco, A.Y. Cho, *Appl. Phys. Lett.* 69 (1996) 2456.
- [5] C. Gmachl, J. Faist, F. Capasso, C. Sirtori, D.L. Sivco, A.Y. Cho, *IEEE J. Quantum Electron.* QE-33 (1997) 1567.
- [6] J.U. Nöckel, A.D. Stone, *Nature* 385 (1997) 45.
- [7] C. Gmachl, F. Capasso, E.E. Narimanov, J.U. Nöckel, A.D. Stone, J. Faist, D.L. Sivco, A.Y. Cho, *Science* 280 (1998) 1556.
- [8] G. Strasser, P. Kruck, M. Helm, J.N. Heyman, L. Hvozdar, E. Gornik, *Appl. Phys. Lett.* 71 (1997) 2892.
- [9] C. Sirtori, P. Kruck, S. Barbieri, P. Collot, J. Nagle, M. Beck, J. Faist, U. Oesterle, *Appl. Phys. Lett.* 73 (1998) 3486.
- [10] S. Gianordoli, L. Hvozdar, G. Strasser, W. Schrenk, K. Unterrainer, E. Gornik, *Appl. Phys. Lett.* 75 (1999) 1045.
- [11] J.U. Nöckel, A.D. Stone, G. Chen, H.L. Grossman, R.K. Chang, *Opt. Lett.* 21 (1996) 1609.
- [12] C. Sirtori, J. Faist, F. Capasso, D.L. Sivco, A.L. Hutchinson, A.Y. Cho, *Appl. Phys. Lett.* 66 (1995) 3242.
- [13] C. Sirtori, P. Kruck, S. Barbieri, H. Page, M. Beck, J. Faist, U. Oesterle, J. Nagle, *Unipolar Semiconductor Lasers with Al Free Waveguides*, *Appl. Phys. Lett.* 75 (1999) 3911.
- [14] C. Gmachl, F. Capasso, E.E. Narimanov, J.U. Nöckel, A.D. Stone, J. Faist, D.L. Sivco, A.Y. Cho, *Science* 280 (1998) 1556.
- [15] S. Gianordoli, L. Hvozdar, G. Strasser, W. Schrenk, J. Faist, E. Gornik, *IEEE J. Quantum Electron.* (1999), accepted for publication.



ELSEVIER

Physica E 7 (2000) 33–36

PHYSICA E

www.elsevier.nl/locate/physa

Long-wavelength ($\lambda \sim 10.5 \mu\text{m}$) quantum cascade lasers based on a photon-assisted tunneling transition in strong magnetic field

Stéphane Blaser *, Laurent Diehl, Mattias Beck, Jérôme Faist

Institut de Physique, Université de Neuchâtel, Rue A.-L. Breguet 1, CH-2000 Neuchâtel, Switzerland

Abstract

Magnetic field studies on photon-assisted tunneling transition-based quantum cascade lasers are reported. Laser action at a wavelength of $\lambda \sim 10.5 \mu\text{m}$ is achieved by oscillator strength tuning. The characteristics of these lasers are a small threshold current at low temperature (1.1 kA/cm^2), an optical power up to 160 mW at 80 K and a maximal operation temperature of 200 K. A strong magnetic field applied perpendicularly to the layers results in a threshold current of the laser which shows several minima and maxima under increasing magnetic field. In a parallel magnetic field, electroluminescence measurements show a strong decrease, a broadening and a blue-shift of the luminescence peak. © 2000 Elsevier Science B.V. All rights reserved.

Keywords: Magnetic field; Quantum cascade lasers; Mid-infrared; Photon-assisted tunneling

Quasi-two-dimensional electron systems in magnetic field have been the subject of many experimental and theoretical studies. If the magnetic field is perpendicular to the layers, i.e. parallel to the electric field, the Hamiltonian can be separated in perpendicular and in-plane motion. The in-plane states are then localized into Landau levels. This additional localization offers the possibility of simulating a quantum box structure: the intersubband emission should occur between Landau levels instead of subbands. Quantum cascade (QC) lasers [1] based on such quantum boxes have already been proposed

[2,3]. The situation becomes more complicated if a magnetic field is applied parallel to the layers: thus we end up with a crossed electric and magnetic field system. Numerous studies have been done for such conditions: theoretically [4,5] as well as experimentally (see for example Refs. [6–8]). Here, we report measurements on a QC laser [1] based on a diagonal transition in presence of a strong magnetic field perpendicular and parallel to the layers.

The laser designed for these measurements is based on a photon-assisted tunneling transition [9] by oscillator strength tuning [10]. In contrast to QC lasers based on diagonal transitions where the threshold condition is achieved by increasing population inversion, here the lasing threshold is achieved by keeping the population inversion constant and increasing

* Corresponding author. Fax: +41-32-7182901.

E-mail addresses: stephane.blaser@iph.unine.ch (S. Blaser), jerome.faist@iph.unine.ch (J. Faist)

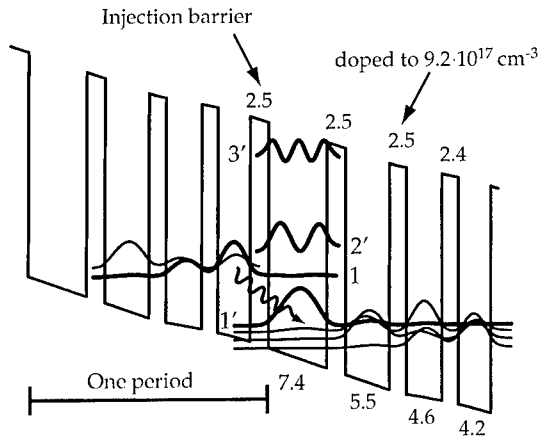


Fig. 1. Self-consistent computation of the energy band diagram of two periods of the structure under an average applied electric field of 55 kV/cm. Shown are the moduli squared of the relevant wave functions. The wavy line indicates the transition responsible for laser action. The thickness of the different layers is indicated in nanometers.

both matrix element and energy of the designed photon-assisted transition. Fig. 1 shows one period of the structure, grown by molecular beam epitaxy (MBE) lattice-matched to an InP substrate. It consists of an $\text{Al}_{0.48}\text{In}_{0.52}\text{As}/\text{Ga}_{0.47}\text{In}_{0.53}\text{As}$ superlattice and a $\text{Ga}_{0.47}\text{In}_{0.53}\text{As}$ quantum well of 7.4 nm between two $\text{Al}_{0.48}\text{In}_{0.52}\text{As}$ tunneling barriers. Under suitable applied bias, photon-assisted tunneling emission occurs across the injection barrier upstream from this quantum well. The downstream barrier allows fast electron escape into the next well by tunneling. Electroluminescence spectra without magnetic field on a structure processed in squared mesas to avoid optical feedback and gain showed a strong first-order Stark shift due to the interwell $n = 1$ to $n = 1'$ designed transition (see Fig. 1). This is due to the large spatial difference between the center of the electron probability distribution of the states 1 and $1'$. A second peak attributed to the vertical interwell transition $2'-1'$ in the 7.4 nm-wide well was also observed. The main characteristics of the laser (processed into ridge waveguides of 28 μm width by wet chemical etching) are a low threshold current of 1.1 kA/cm^2 and a maximum output power of 160 mW at 80 K in pulsed mode. The laser operates up to 200 K with up to 20 mW at 190 K, with an emission wavelength of about 10.5 μm depending on electric field and temperature. In continuous wave it

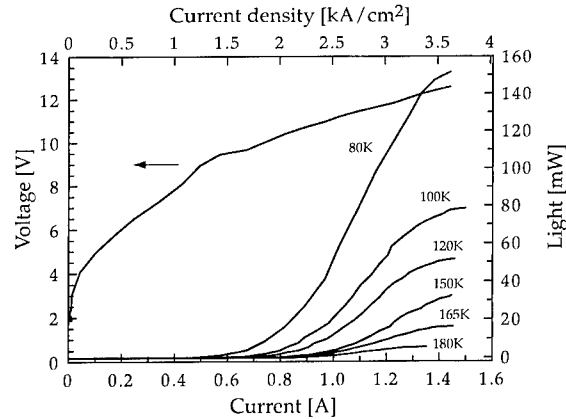


Fig. 2. $L-I$ curves of a 28- μm -wide and 1.4-mm-long QC laser measured at different temperature. Also shown is a $V-I$ curve measured at 80 K.

operates up to 40 K with a mono-mode emission just above the threshold current. Typical light ($L-I$) and voltage ($V-I$) versus current curves are displayed in Fig. 2 for a 1.4-mm-long device in pulsed mode. The intensity of light was measured with a calibrated $500 \times 500 \mu\text{m}^2$ room temperature HgCdTe detector. The curvature of the $L-I$ curves at threshold is due to the fact that laser action takes place at a smaller voltage than expected. In such a case, the losses are still too high to yield a good differential efficiency. Details on electroluminescence spectra and laser characteristics will be presented in Ref. [11].

To performed magneto-optical measurements, the samples were mounted on special holders which allowed to characterize them in a magnetic field either perpendicular or parallel to the layers. The magnetic field with a maximum strength of 14 T was produced by a superconducting magnet located in a helium cryostat. The sample temperature could be varied between 2 and 300 K using a needle flow control valve between helium bath and sample tube. Light collection was then accomplished by lenses and mirrors and the resulting beam was sent in a Fourier-transform infrared spectrometer (FTIR) Nicolet 860 to perform spectra or in a HgCdTe detector to perform $L-I$ curves.

In perpendicular magnetic field, we simulate, as mentioned in the introduction, a quantum box laser. Since the intersubband emission of the laser should occurs between Landau levels, the optical phonon emission is, in general, forbidden. Then, with applied

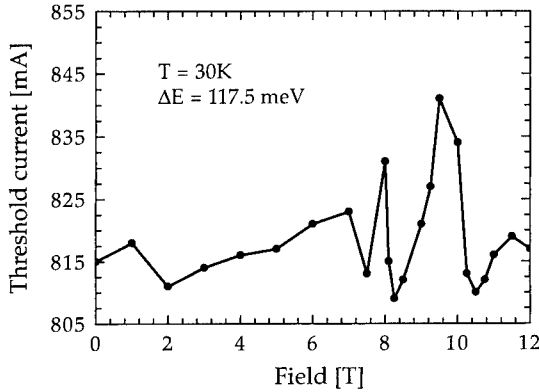


Fig. 3. Threshold current versus applied perpendicular magnetic field.

magnetic field, the threshold current should show maxima and minima when there is a resonance with the optical phonon. Fig. 3 shows experimental results of laser threshold current versus magnetic field done at $T = 30$ K. Minima and maxima are observed but the separation between them is less than the expected one. Moreover, the size of the maxima should increase at high field and this is not the case.

In parallel magnetic field, the Hamiltonian is

$$H = -\frac{\hbar^2}{2m^*} \frac{\partial^2}{\partial z^2} + V_{\text{conf}}(z) + \frac{\hbar^2}{2m^*} \times \left(k_x^2 - \frac{2eBk_x z}{\hbar} + \frac{e^2 B^2 z^2}{\hbar^2} \right) + \frac{\hbar^2}{2m^*} k_y^2, \quad (1)$$

where $V_{\text{conf}}(z)$ is the periodic potential due to the conduction-band discontinuity, e the elementary charge and m^* the effective mass.

Two terms are due to the magnetic field: the first one, $2eBk_x z/\hbar$, acting as an electric field and the second one, $e^2 B^2 z^2/\hbar^2$, being quadratic in B . To solve the Schrodinger equation with plane waves in the x - and y -directions, the magnetic field can be treated as a perturbation. The first-order correction in energy results in [4]

$$E = E_{\text{conf}}(z) + \frac{\hbar^2}{2m^*} k_y^2 + \frac{\hbar^2}{2m^*} \times \left(k_x - \frac{eBz}{\hbar} \right)^2 + \frac{e^2 B^2}{2m^*} (\langle z^2 \rangle - \langle z \rangle^2), \quad (2)$$

where $\langle z \rangle$ and $\langle z^2 \rangle$ are expectation values of the respective operators for the unperturbed wave functions

and $E_{\text{conf}}(z)$ corresponds to the energy quantification due to the potential $V_{\text{conf}}(z)$. In fact, $\langle z \rangle$ represents the position of the gravity center of the wave function with respect to the origin of the z -axis. The third term on the left-hand side of Eq. (2) changes the usual dispersion in k_x to a parabola shifted in k -space by a value called $k_{\text{shift}} = -eB\langle z \rangle/\hbar$. The fourth term is called diamagnetic shift and slightly changes the energy independently of the choice of the origin. It is clear that this effect should be observed only for diagonal transitions where $\langle z \rangle$ is different for the two states involved in the transition.

We investigated our structure in a parallel magnetic field to study the behaviour of the intersubband electroluminescence spectra in presence of such a field. The structure was processed in mesas like for the electroluminescence measurements without magnetic field. The spectra were measured using the FTIR in step-scan mode and a lock-in amplifier. Luminescence spectra at 30 K obtained at a constant voltage of 13 V for different applied magnetic fields are displayed in Fig. 4a). The main peak due to the interwell 1–1' transition at about 130 meV presents three important different behaviours in function of the applied magnetic field. First, the peak has a strong quenching of his intensity. The inset of Fig. 4a shows the decrease of the peak integral in function of the magnetic field. The light intensity is proportional to the oscillator strength and then to the squared transition matrix element. Then this latter seems to strongly decrease in a parallel magnetic field. We made computation of the energy band diagram and matrix elements of the transition taking into account the effects of the parallel magnetic field by inserting Hamiltonian 1 in our model. The inset of Fig. 4a shows the values of the transition matrix elements calculated by this model, which decrease significantly less than the experimental results.

The peak exhibits also a broadening and a blue shift of the transition energy. In contrast, besides the broadening, our model predicts a red shift of the emission, as shown in Fig. 4b. Here we made the assumption that the matrix element of the transition is constant. This explains why the peak intensity does not change in the simulation. Measurements performed at 10 V and at 200 and 300 K at 13 V have shown the same decrease of the peak integral of the luminescence peaks. This effect seems then to depend neither on the bias nor on the temperature. Although the model does not

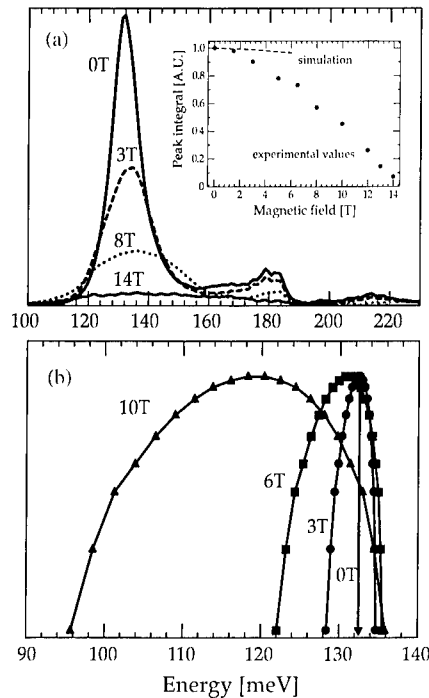


Fig. 4. (a) Luminescence spectra at different applied parallel magnetic fields at a voltage of 13 V. The inset shows the peak integral decrease versus applied magnetic field. (b) Simulated luminescence spectra predicting a broadening and a red shift of the peak.

correctly predict the observed comportment, we can see that it is in good agreement with the broadening of the luminescence peak. The blue shift and the strong decrease of the luminescence emission are still to be explained. We expect that introducing the Hall effect

and the k -space electronic distribution should refine enough the model to become predictive.

Acknowledgements

We would like to thank Daniel Hofstetter and Antoine Müller for their careful reading of the manuscript. This work was supported by the Swiss National Science Foundation.

References

- [1] J. Faist, F. Capasso, D.L. Sivco, C. Sirtori, A.L. Hutchinson, A.Y. Cho, *Science* 264 (1994) 553.
- [2] C.F. Hsu, J.S. O, P.S. Zory, D. Botez, Intersubband laser design using a quantum box array, *Proceedings of SPIE*, Vol. 3001, 1997.
- [3] S.J. Lee, J.B. Khurgin, *Appl. Phys. Lett.* 69 (1996) 1038.
- [4] F. Stern, *Phys. Rev. Lett.* 21 (1968) 1687.
- [5] W. Zawadzki, *Semicond. Sci. Technol.* 2 (1987) 550.
- [6] G. Belle, J.C. Maan, G. Weimann, *Solid State Commun.* 56 (1985) 65.
- [7] A.P. Heberle, M. Oestreich, S. Haacke, W.W. Rühle, J.C. Maan, K. Köhler, *Phys. Rev. Lett.* 72 (1994) 1522.
- [8] C. Gauer, A. Wixforth, J.P. Kotthaus, M. Kubisa, W. Zawadzki, B. Brar, H. Kroemer, *Phys. Rev. Lett.* 74 (1995) 2772.
- [9] R.F. Kazarinov, R.A. Suris, *Sov. Phys. Semicond.* 5 (1971) 707.
- [10] J. Faist, F. Capasso, C. Sirtori, D.L. Sivco, A.L. Hutchinson, A.Y. Cho, *Nature* 387 (1997) 777.
- [11] S. Blaser, L. Diehl, M. Beck, J. Faist, U. Oesterle, J.H. Xu, S. Barbieri, F. Beltman, Long-wavelength ($\lambda \sim 10 \mu\text{m}$) quantum cascade laser based on a photon-assisted tunneling transition, unpublished.



ELSEVIER

Physica E 7 (2000) 37–39

PHYSICA E

www.elsevier.nl/locate/physce

GaAs/AlGaAs quantum cascade laser – a source for gas absorption spectroscopy

L. Hvozدارa^{a,*}, S. Gianordoli^a, G. Strasser^a, W. Schrenk^a, K. Unterrainer^a, E. Gornik^a,
Ch.S.S.S. Murthy^b, M. Kraft^b, V. Pustogow^b, B. Mizaikoff^b

^a*Solid State Electronics, TU-Wien, Austria*

^b*Institute of Analytical Chemistry, Technische Universität Wien, A-1040 Wien, Austria*

Abstract

We report on an application of the recently developed electrically pumped GaAs/AlGaAs quantum cascade lasers in gas spectroscopy. Laser light with emission maximum at 10.009 μm is used to investigate the absorption in side bands of the vibrational spectrum of ethene at atmospheric pressure. Different mixtures of helium and ethene with known concentrations are flushed through an absorption cell. Laser radiation passing through the gas absorption cell is analyzed using a Fourier transform spectrometer. The laser spectrum is modulated by the ethene absorption. The experimentally obtained discrete spectrum is compared with the Hitran database, showing full agreement. © 2000 Published by Elsevier Science B.V. All rights reserved.

Keywords: Quantum cascade lasers; Gas spectroscopy; GaAs laser

Laser spectroscopy is a powerful analytic tool in many technical and scientific branches since several decades. It uses the advantage of lasers as generators of coherent radiation with extremely high spectral density. Until the last decade, most of the applications used near-infrared (NIR) or visible laser sources. Development of the mid-infrared laser spectroscopy was limited to the only available CO₂ laser. The advent of lead salt lasers and later quantum cascade lasers based on intersubband transitions in InGaAs/InAlAs/InP

heterostructures [1] significantly extended the possibilities of laser spectroscopy in the mid-infrared range.

GaAs/AlGaAs quantum cascade lasers have been introduced recently [2–4]. We report on the application of a GaAs/AlGaAs QCL, in gas spectroscopy. The laser has been fabricated following the design described in Ref. [3]. The aluminum content in the AlGaAs ternary (barrier material) is kept at 30%, in order to lower the barriers and to achieve emission at longer wavelengths. The high-resolution multimode spectrum ($\text{res} = 0.125 \text{ cm}^{-1}$) of the laser is shown in Fig. 1 (lower curve). The spectrum of the ridge waveguide laser operated in pulsed mode, is recorded at $T = 62 \text{ K}$, at a repetition rate

* Corresponding author. Tel.: + 43-1-58801-362-17; fax.: +43-1-58801-362-99.

E-mail address: lubos.hvozدارa@tuwien.ac.at (L. Hvozدارa)

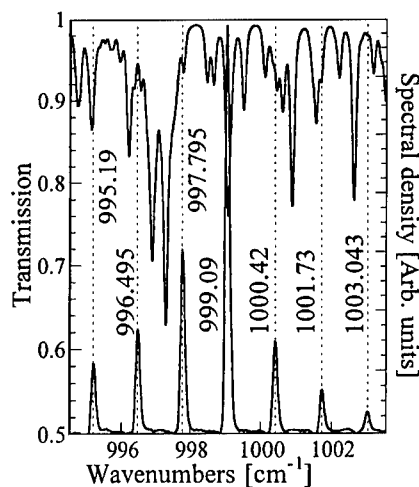


Fig. 1. Spectra of the used QCL with dominant emission maximum at 999.09 cm^{-1} (lower curve) and of ethene absorption taken from Hitran database files (upper curve). The laser is tuned by temperature to match the dominant emission peak with a strong absorption line in the ethene absorption spectrum.

$f = 5 \text{ kHz}$, a pulse duration of 100 ns and a peak current density of 18 kA/cm^2 . The laser operating at these conditions exhibits an overlap of the dominant mode with a strong absorption in the side-band of the vibrational spectrum of ethene (Fig. 1 – upper curve).

The experimental setup is depicted in Fig. 2. The absorption cell is a 400 mm tube, 1.13 mm in diameter [5]. The inner wall of the tube is silver coated. The composition of the gas mixture, consisting of helium (carrier gas) and ethene (analyte) is controlled with mass flow controllers. A stabilized flux of the defined gas mixture is flushed through the absorption cell during the measurement at a rate of $200\text{--}500 \text{ sccm/min}$. The laser bar is installed in a liquid helium cooled cryo-flow. The emitted laser radiation is collected using $f/0.75$ ZnSe meniscus lens, and focused on the inlet of the absorption gas cell. The light, passing through the cell is collected using off-axis parabolic mirrors and launched into the interferometer of a Fourier transform infrared spectrometer. An LN_2 cooled mercury–cadmium–telluride (MCT) detector is used to detect the signal.

The ethene concentration is varied in nine steps from ~ 1000 to $\sim 30\,000 \text{ ppm}$ to observe the influence of the concentration on the transmission at different lasing modes. The reference

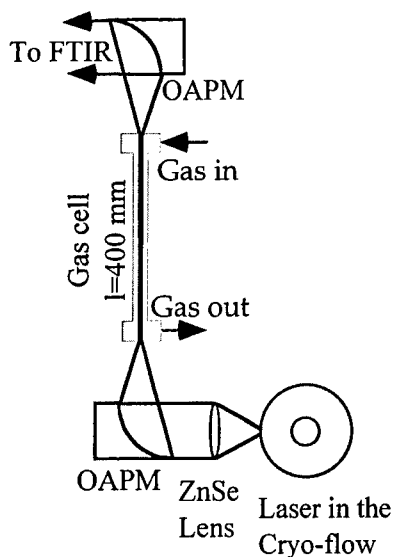


Fig. 2. Scheme of the experimental setup. Light emitted from a laser in the He cooled cryo-flow, is collected using ZnSe lens and focused by an off-axis parabolic mirror on the inlet window of the absorption cell. Light passing the cell is collected into the FTIR spectrometer.

spectrum is recorded with pure helium in the gas cell. The absorption spectrum of ethene (Fig. 1 upper curve) is taken from Hitran database.

Fig. 3a shows ten spectra of the mode with emission maximum at 997.8 cm^{-1} , recorded for ten different concentrations of the ethene mixture. Fig. 3b shows ten spectra with concentration as a parameter recorded for 999.08 cm^{-1} . The concentrations are given in the figure caption. Both Fig. 3a and b are scaled in such a way, that the spectra of maximal transmission (curves (j) – pure He) are of the same height. Spectrum recorded with pure He in the optical path serves as a background to establish the transmittance. Transmittance as a function of the concentration is plotted in Fig. 4 for both investigated frequencies. Significantly stronger absorption is observed at 999.08 cm^{-1} , compared to that at 997.8 cm^{-1} . Curves are fitted exponentially, according to the Lambert–Beer law:

$$I = I_0 \exp(-p c l)$$

where I is the transmitted light intensity, I_0 is the incident light intensity, c is concentration of the

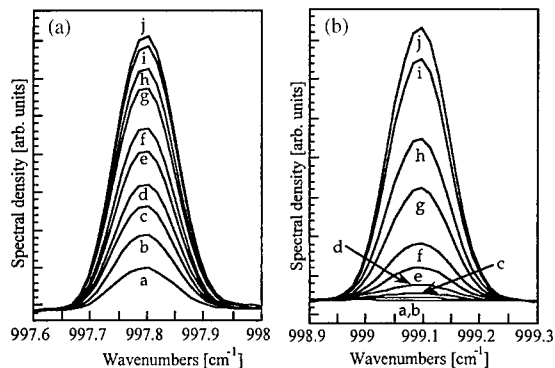


Fig. 3. Comparison of the absorption at two different modes, (a) 997.8 cm^{-1} and (b) 999.09 cm^{-1} . Spectra are recorded for different ethene concentrations: (a) 29 918 ppm, (b) 21 000 ppm, (c) 16 481 ppm, (d) 13 064 ppm, (e) 9 622 ppm, (f) 7 314 ppm, (g) 4 763 ppm, (h) 3 133 ppm, (i) 1 438 ppm, (j) pure helium (0 ppm). The modes are scaled to the same height. The 999.09 cm^{-1} mode exhibits significantly stronger absorption, compared to the 997.8 cm^{-1} mode.

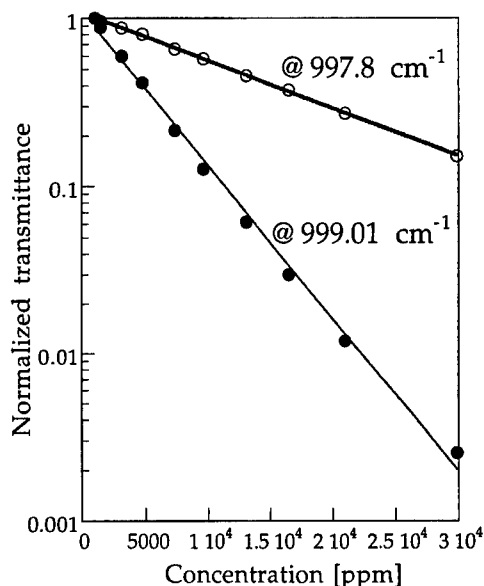


Fig. 4. Normalized transmittance, as a function of the concentration for 997.8 cm^{-1} mode (rings) and for 999.01 cm^{-1} mode (dots). The dependencies are exponentially fitted (lines).

analyte, p is the pressure of the mixture, ϵ is the extinction coefficient and l is the optical path. The value of the exponent from the exponential fit, directly expresses the absorption strength, corresponding to the investigated frequency, since the pressure and the optical path are constant, and the concentration is a variable in the plot. The exponent value of -6.495×10^{-5} for 997.08 cm^{-1} is 3.23 times larger than the exponent value of -2.1009×10^{-4} , corresponding to 999.08 cm^{-1} . The ratio of 3.218 obtained from the theoretical spectrum (Hitran data base) is in a good agreement with the results of the measurement. The small difference between the theoretical and the measured values can be assigned to the uncertainty in the emission peak position.

We have demonstrated an application of a GaAs/AlGaAs quantum cascade laser in gas spectroscopy. A laser operated at 62 K in pulsed mode, emitting a multimode spectrum of longitudinal Fabry–Perot mode, centered at 10 μm is used to measure the absorption in helium – ethene gas mixtures with different ethene concentrations. Gas mixtures are flushed through 400 mm long absorption cell. The light absorption at two modes – 997.08 cm^{-1} and 999.09 cm^{-1} is compared. The mode centered at 999.08 cm^{-1} exhibits significantly stronger absorption compared to the 997.08 cm^{-1} mode. The results are compared to the Hitran database files, showing full agreement.

Acknowledgements

This work was partly supported by a European Brite Euram III project UNISEL and the Society of Microelectronics (GMe, Austria).

References

- [1] J. Faist, F. Capasso, C. Sirtori, D.L. Sivco, A.L. Hutchinson, A.Y. Cho, *Science* 264 (1994) 553.
- [2] O. Gauthier-Lafaye, P. Boucaud, F.H. Julien, R. Prazeres, F. Glotin, J.-M. Ortega, V. Thierry-Mieg, R. Panel, J.-P. Leburton, V. Berger, *Appl. Phys. Lett.* 70 (1997) 3197.
- [3] C. Sirtori, P. Kruck, S. Barbieri, P. Collot, J. Nagle, M. Beck, J. Faist, U. Oesterle, *Appl. Phys. Lett.* 73 (1998) 3486.
- [4] G. Strasser, S. Gianordoli, L. Hvozďara, W. Schrenk, K. Unterrainer, E. Gornik, *Appl. Phys. Lett.* 75 (1999) 1345.
- [5] C. Worrell, N. Gallen, *J. Phys. D* 30 (1997) 1984.

High-confinement waveguides for mid-IR devices

P. Holmström *

*Laboratory of Photonics and Microwave Engineering, Department of Electronics, Royal Institute of Technology (KTH),
Electrum 229, S-164 40 Kista, Sweden*

Abstract

We analyze the use of heavily doped semiconductor layers as a means to tightly confine light. The very low refractive index ($n \approx 1$) that is present just above the plasma frequency renders large index steps possible. Slab waveguide structures with InP or GaAs cladding layers doped to $n_D \sim 10^{19} \text{ cm}^{-3}$ are analyzed in the mid-IR wavelength range, $\lambda = 4\text{--}15 \text{ }\mu\text{m}$. The performance of the waveguide in terms of achieved overlap with an active region of a given thickness versus the waveguide absorption, is compared to waveguides based on surface plasmons. The calculated results indicate that these plasma effect waveguides should be favourable in this respect for wavelengths $\lambda \approx 6\text{--}10 \text{ }\mu\text{m}$ using heavily doped InP as a cladding. In GaAs efficient use of the plasma effect is limited to wavelengths $\lambda \gtrsim 9 \text{ }\mu\text{m}$. Guidelines for required doping levels are given. © 2000 Elsevier Science B.V. All rights reserved.

Keywords: Waveguide; Mid-infrared; Plasma effects; Surface plasmons

A high confinement of the optical field is of vital importance for efficient operation of optical devices. The usual way to achieve waveguiding at optical frequencies is to use a slab waveguide, which is based on the relative refractive index difference between a higher-index core material and a lower index cladding material. For the commonly used wavelength of optical communication, $1.55 \text{ }\mu\text{m}$, the core thicknesses in semiconductor heterostructures are a few tenths of a micrometer. This corresponds to a reasonable number of quantum wells (≈ 10) that are required for a good overlap with the optical mode.

For mid-IR wavelengths, $\lambda \approx 4\text{--}15 \text{ }\mu\text{m}$, there is an index contrast of about 10% in ordinary material sys-

tems such as AlGaAs/GaAs and InGaAs/InP, about the same value as closer to the band edge. The required thickness of the core and cladding layers thus scales in proportion to the wavelength of the light, which may entail several disadvantages for the longer wavelengths. Thick cladding layers increase the series resistance of a device and is also time consuming to grow with MBE. With a thick core a large number of quantum wells and thus a large applied voltage is needed to have a strong interaction with the optical mode. Alternatively, if a smaller number of wells is used in a longer device, the RC time constant of the device, which often limits the speed in modulators [1] and detectors [2], is drastically increased. In order to achieve a low RC constant in conjunction with a low applied voltage, a tight confinement of the optical mode is needed.

* Fax: +46-8-752-1240.

E-mail address: petterh@ele.kth.se (P. Holmström)

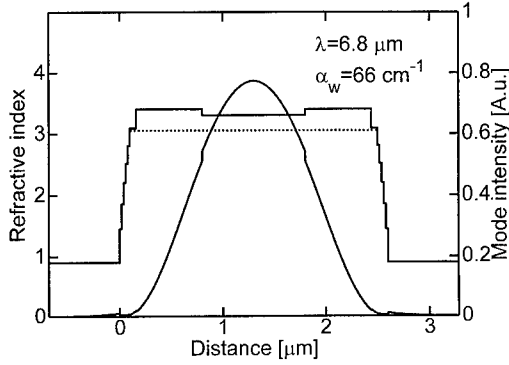


Fig. 1. Mode intensity profile of TM-polarized light and profile of the refractive index perpendicular to the growth direction in a plasma effect waveguide. The dotted line indicates the mode index. The cladding layers are InP doped at $n_D = 2 \times 10^{19} \text{ cm}^{-3}$. Indicated is also the waveguide absorption α_w .

In the mid-IR spectrum there are however two possibilities to achieve a tight confinement of the optical mode. One is to utilize the anomalously low refractive index that is experienced by light with frequencies just above the plasma frequency [3]. A slab waveguide can then be formed as shown in Fig. 1, by heavily doping ($n_D \sim 10^{19} \text{ cm}^{-3}$) the cladding layers so that the plasma frequency approaches the frequency of the guided light. We here refer to this kind of waveguide as a plasma effect waveguide (PEWG). The plasma effect has been used frequently in quantum cascade lasers to reduce cladding layer thickness, but without substantially affecting the confinement [4].

The other possibility to achieve a high confinement of the optical field is to use electro-magnetic surface waves (surface plasmons) guided by a metal/semiconductor interface [5]. Quantum cascade lasers emitting at 8.0 and 11.4 μm that rely on surface plasmons have recently been demonstrated [6].

The purpose of this paper is to evaluate and compare the achieved confinement versus waveguide loss in these two waveguide types.

The complex dielectric constant of the heavily doped layers is determined in the classical Drude model as

$$(n - ik)^2 = \epsilon = \epsilon_\infty \left[1 - \frac{\omega_p^2}{\omega^2 \eta} \left(1 + \frac{i}{\omega \tau} \right) \right], \quad (1)$$

where n and k are the real and imaginary parts of the refractive index, $1/\tau$ is the scattering rate and $\eta = 1 + 1/(\omega \tau)^2 \approx 1$ at the frequencies and doping densities

Table 1

Material parameters used in the numerical calculations for InP and GaAs ($T = 300 \text{ K}$)

	InP	GaAs
E_g (eV)	1.35	1.42
m_c/m_0	0.074	0.067
ϵ_s	12.60	12.90
ϵ_∞	9.61	10.90
$\hbar\omega_{LO}$ (eV)	0.043	0.035

considered here. The scattering rate has been determined in a quantum mechanical calculation [7], since the photon energy $\hbar\omega$ is not small compared to typical electron energies. In this paper we include the most important scattering processes [7] for free carrier absorption of mid-IR light, i.e. scattering due to LO phonons and ionized impurities.

At moderate electron densities, n_e , the plasma frequency is accurately given by $\omega_p^2 = n_e e^2 / m_c \epsilon_\infty \epsilon_0$, where m_c is the mass at the conduction band edge. At high doping densities however the non-parabolicity of the band should be accounted for. If the dependence of the scattering rate on the initial electron energy is neglected, then an effective plasma frequency can be defined as

$$\omega_p^2 = \int_0^\infty \frac{g(E)f(E)e^2}{m_c(E)\epsilon_\infty \epsilon_0} dE, \quad (2)$$

where $g(E)$ is the density of states and $f(E)$ is the Fermi distribution function. To describe the non-parabolic dispersion we use the two band Kane model, which remains adequate far above the band edge, i.e. the energy-dependent electron mass is given by $m_c(E) = m_c(1 + 2E/E_g)$, where E_g is the fundamental band gap. As a result of non-parabolicity the effective plasma frequency tends to saturate at high doping levels.

The material parameters of InP and GaAs used in the numerical calculations are given in Table 1. In Fig. 2 the calculated n and k of heavily doped InP is shown along with the absorption coefficient in bulk material, $\alpha = 4\pi k/\lambda$, where λ is the free space wavelength of the light. It is interesting to note that for a given desired index change, the magnitude of the free carrier absorption is to a large degree independent of the wavelength of the light. This is in stark

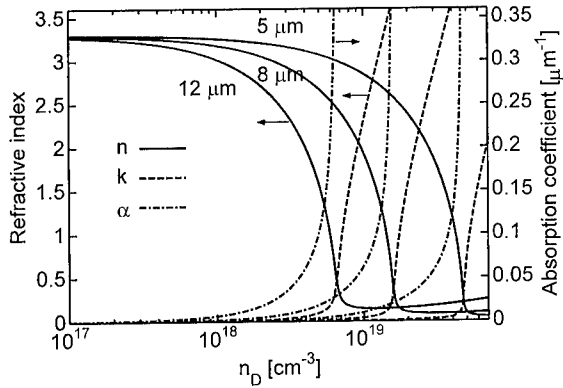


Fig. 2. Calculated real and imaginary part of the refractive index, as well as absorption coefficient of InP as a function of the doping density n_D . Results are given for three different free space wavelengths.

contrast to the absorption of surface plasmons, which is known to increase strongly with reduced wavelength.

The plasma effect is limited towards shorter wavelengths by the maximum achievable free carrier concentration. In Sn-doped InP a free electron concentration of $n_c = 3.3 \times 10^{19} \text{ cm}^{-3}$ with no compensation has been achieved using MOCVD [8], and in GaAs : Si $n_c = 1.6 \times 10^{19} \text{ cm}^{-3}$ at low compensation has been obtained [9]. Scattering processes from the central Γ -valley to the L -valley [10] have not received much attention in the literature but should become increasingly important as the Fermi level approaches the L_6 band edge. Additionally, thermal population of the high mass L -valley should effectively saturate the plasma frequency. These effects relating to the L -valley were not included, but should be considered in order to further elucidate the lower wavelength limit of the plasma effect. Conservative (low) estimates of the separation of the band edges $L_6 - \Gamma_6$ are 0.53 eV in InP and 0.29 eV in GaAs. The corresponding free carrier densities in the Γ -valley, indicated by the dotted lines in Fig. 3, are 5.8×10^{19} and $1.7 \times 10^{19} \text{ cm}^{-3}$, respectively.

With the help of Fig. 3 a suitable doping level in InP and GaAs can be found. It is evident that in order to efficiently exploit the plasma effect a high accuracy ($\approx \pm 10\%$) of the doping level must be accomplished.

The transfer matrix method has been employed to solve for TM-polarized modes, relevant for intersub-

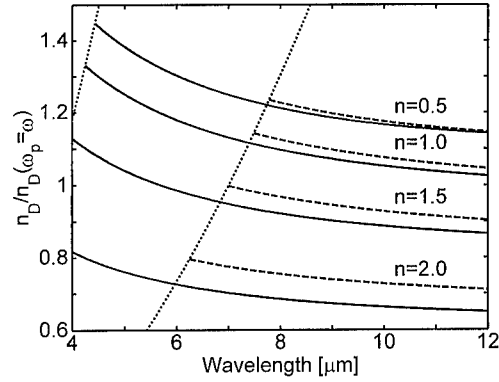


Fig. 3. Required doping levels in InP (solid) and GaAs (dashed) in order to achieve a given refractive index, $n = 0.5, 1.0, 1.5, 2.0$. The doping level is given in relation to the doping density that equilibrates the plasma frequency in a parabolic band with the light frequency, i.e. $n_D(\omega_p = \omega) = m_c \epsilon_\infty \epsilon_0 \omega^2 / e^2$, which is easily accessible. The dotted lines indicate where the Fermi level reaches the L -valley band edge, and can be taken as somewhat optimistic lower wavelength limits.

band transitions. The overlap of the optical mode with the active layer should properly be defined as [11]

$$\Gamma = \frac{\alpha_m - \alpha_w}{\alpha_a}, \quad (3)$$

where α_m is the mode absorption (negative in the case of gain) in an active device, α_w is the waveguide absorption and α_a is the absorption (negative in the case of gain) in the active material.

In order to compare InP-based PEWGs and waveguides based on surface plasmons (SPWGs) at a gold/semiconductor interface the achieved overlap, Γ , has been plotted versus the sustained waveguide absorption, α_w , in Fig. 4. Note that in the PEWGs the core thickness and the doping density in the cladding are adjusted according to the wavelength, so that the absorption dependence on the wavelength reflects the lack of change in free carrier absorption in the cladding material. The small decrease in waveguide absorption with reduced wavelength is mainly due to the assumed finite width, $0.1 \mu\text{m}$, of the interface regions between the core and the heavily doped cladding. In the PEWGs the refractive index of the core was assumed to be constant at $n = 3.35$. In the “ordinary” SPWG:s (+) $n = 3.35$ in all semiconductor layers. “Enhanced” SPWGs (\times), i.e. with an index step that strongly increases confinement and wave-

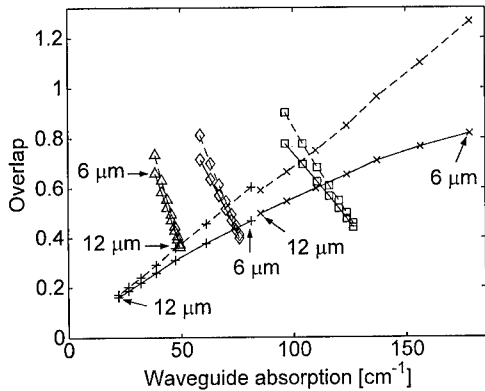


Fig. 4. The obtained overlap of the optical mode with an active layer of 1 μm thickness versus the waveguide absorption α_w (solid). Results are given for PEWG:s with core thicknesses 0.30λ (\square), 0.35λ (\diamond), 0.40λ (\triangle), for a SPWG (+), and for an "enhanced" SPWG (\times). In the PEWG:s the doping level in the cladding layers is adjusted according to wavelength to yield the refractive index $n = 1$. Indicated is also the achievable overlap per micron thickness of an active layer that is much thinner than 1 μm (dashed).

guide absorption, are also considered with an index of $n = 3.35$ in the active and buffer layers, total thickness 1.1 μm , on top of an InP substrate, $n = 3.05$. Comparing the performance of the PEWG:s and the SPWG:s at the integer wavelengths $\lambda = 6, 7, \dots, 12 \mu\text{m}$ indicated by the symbols, it is concluded that the PEWG gives a better overlap versus waveguide absorption for wavelengths $\lambda \lesssim 10 \mu\text{m}$. It can also be noted that the waveguide absorption increases much more strongly than the overlap, when the core thickness of the PEWG is reduced. The results for GaAs are very similar, but as can be concluded from Fig. 3 the small $L_6 - \Gamma_6$ separation precludes efficient use of the plasma effect below $\lambda \approx 9 \mu\text{m}$.

In summary the feasibility of tightly confining plasma effect waveguides has been investigated numerically. In particular, it was found that, with a wavelength dependent doping density that yields a given low refractive index ($n \approx 1$), the obtained free carrier absorption is to a large degree independent of the wavelength. This is in stark contrast to surface plasmons whose absorption is known to increase strongly with decreased wavelength.

In InP-based PEWG:s a better confinement versus waveguide absorption than in waveguides based on surface plasmons was deduced for wavelengths $\lambda \approx 6\text{--}10 \mu\text{m}$. In GaAs efficient use of the plasma effect is limited to $\lambda \gtrsim 9 \mu\text{m}$. We note that scattering events to the L -valley were not included in this study, and should be considered in order to further elucidate the lower wavelength limit.

Note added in proof

The scattering rate $1/\tau$ derived in Ref. [7] includes implicitly the energy dependence of the electron mass, i.e. in Eq. (1) the effective plasma frequency in Eq. (2) should be used only to obtain the real part of ϵ , while the parabolic plasma frequency (given in the text) should be used in the imaginary part of ϵ . The figures and drawn conclusions have been revised to consider this.

Acknowledgements

The author acknowledges B. Jensen for useful discussions.

References

- [1] R.P.G. Karunasiri, Y.J. Mii, K.L. Wang, IEEE Electron. Dev. Lett. 11 (1990) 227.
- [2] B.F. Levine, J. Appl. Phys. 74 1993 R1.
- [3] B. Jensen, in: E.D. Palik (Ed.), Handbook of Optical Constants of Solids, Academic Press, San Diego, 1985, pp. 169–188.
- [4] C. Sirtori, J. Faist, F. Capasso, D.L. Sivco, A.L. Hutchinson, A.Y. Cho, Appl. Phys. Lett. 66 (1995) 3242.
- [5] P. Yeh, Optical Waves in Layered Media, Wiley, New York, 1988.
- [6] C. Sirtori, C. Gmachl, F. Capasso, J. Faist, D.L. Sivco, A.L. Hutchinson, A.Y. Cho, Opt. Lett. 23 (1998) 1366.
- [7] B. Jensen, in: J. Button (Ed.), Infrared and Millimeter Waves, Vol. 8, Academic Press, New York, 1983, pp. 127–171.
- [8] C.J. Pinzone, N.D. Gerrard, R.D. Dupuis, N.T. Ha, H.S. Luftman, J. Appl. Phys. 67 (1990) 6823.
- [9] R.J. Malik, J. Nagle, M. Micovic, T. Harris, R.W. Ryan, L.C. Hopkins, J. Vac. Sci. Technol. B 10 (1992) 850.
- [10] E. Haga, H. Kimura, J. Phys. Soc. Japan 19 (1964) 1596.
- [11] T.D. Visser, H. Blok, B. Demeulenaere, D. Lenstra, IEEE J. Quant. Electron. 33 (1997) 1763.

Electrically pumped Terahertz quantum well sources

Michel Rochat^{a,*}, Jérôme Faist^a, Mattias Beck^a, Ursula Oesterle^b

^aUniversity of Neuchâtel, Institute of Physics, 1 Rue A.-L. Breguet, Neuchâtel, CH 2000, Switzerland

^bSwiss Federal Institute of Technology, Physics Department, PHB Ecublens, Lausanne, CH 1015, Switzerland

Abstract

Far infrared emission from quantum cascade structures is presented. Surface emission from a grating coupler show that the intersubband luminescence of our vertical transition structure is limited at low temperature by electron–electron scattering. As the temperature is increased, the limitation comes from the emission of optical phonons. In order to check for material gain, waveguide loss and differential gain measurements have been performed using a single-pass-type measurement. We report waveguide losses of 110 cm^{-1} and differential gain of 23 cm^{-1} . Our results strongly suggest the possibility of far-infrared lasers using the quantum cascade technology coupled to double plasmon waveguides. © 2000 Elsevier Science B.V. All rights reserved.

Keywords: Terahertz sources; Plasmon waveguide; FIR quantum cascade lasers

The recent demonstration of far-infrared intersubband emission from quantum cascade diodes opens the door to novel type of lasers in a region where the lack of efficient light sources is important [1]. Actually only few and quite inconvenient sources are available, as free-electron lasers, gas lasers, and p-Ge lasers. Besides these lasers do not have the intrinsic advantages exhibited by the quantum cascade technology, i.e. band-structure engineering. At the FIR wavelengths, because the photon energy is lower than the optical phonon energy ($\hbar\omega_{\text{LO}} = 36\text{ meV}$ in GaAs), optical phonon emission is not always the dominant intersubband non-radiative channel. Indeed, a large

spread in the values reported in the literature for the intersubband non-radiative lifetime (between 0.5 ps [2] to 1 ns [3]) reflects the complex interplay between various non-radiative channels. We show that this non-radiative lifetime can be determined by a combination of electron–electron scattering and optical phonon emission from electrons which have an excess kinetic energy larger than the optical-phonon energy.

We have grown two structures by molecular beam epitaxy on an n-doped GaAs and InP substrate that consist of 35 periods. One period of our structure consists of four GaAs, respectively, InGaAs quantum wells separated by thin AlGaAs (AlInGaAs) tunnel barriers. As in mid-infrared quantum cascade structures, each period consists of an undoped active region, in which the spontaneous emission occurs, and

* Corresponding author. Tel.: +41-32-718-2948; fax: +41-32-718-2901.

E-mail address: michel.rochat@iph.unine.ch (M. Rochat)

a graded-gap injector. The active region consists of a 28 nm GaAs (respectively, 38 nm InGaAs) quantum well coupled through a 2.5 nm AlGaAs (resp., 1.4 nm AlInAs) barrier to an 18 nm GaAs (25.5 nm InGaAs) well. The emission occurs in the 28 nm (resp., 38 nm) well through a vertical transition. For the experiments, the samples were processed into $450 \times 450 \mu\text{m}$ mesas and Ti/Au contacts were provided to the n^+ contact layers on the periphery of the mesa. In order to couple the light out from the structure, we also evaporated a Ti/Au metal grating with a $15 \mu\text{m}$ periodicity. Samples were mounted on the cold finger of a He flow cryostat, and the temperature was controlled with a LakeShore 330 temperature controller. The injected current was provided by a HP-33120A function generator programmed to deliver bursts of $1.93 \mu\text{s}$ long pulses with a duty-cycle of 80%. The repetition rate was matched with the maximum time constant of our detector for maximum response, at 413 Hz. The overall duty-cycle was 40%. The luminescence signal was collected by wide numerical aperture gold-coated parabolic off-axis mirror and sent through a FTIR. The resulting signal was then detected with a liquid-helium-cooled Si bolometer.

Temperature-dependent spectra of the luminescence have been done using the FTIR in a step-scan mode, the signal being detected with a lock-in amplifier. The temperature was varied from 10 K up to temperatures above liquid nitrogen for both samples. The injection current was chosen to be as high as possible to have the maximum output power. The maximum current injection is limited by the structure's maximum working bias before the appearance of the negative differential resistance (NDR), which was shown to arise at 1.2 V for GaAs sample and 0.8 V for the InGaAs sample. The maximum-injected currents were, respectively, 68 A (39 A/cm^2) and 50 mA (28 A/cm^2) at 10 K. Representative spectra at constant injection current and varying temperatures for both samples are given in Fig. 1. At low temperature, the electron–electron scattering is a limiting factor for the luminescence. As the temperature is increased, electrons acquire sufficient excess kinetic energy to make optical-phonon emission possible. The total non-radiative rate w_{nr} can then be expressed as

$$w_{\text{nr}} = w_{\text{ee}} + w_{\text{op}} \exp((\hbar\omega_{\text{lo}} - \Delta E_{21})/kT)$$

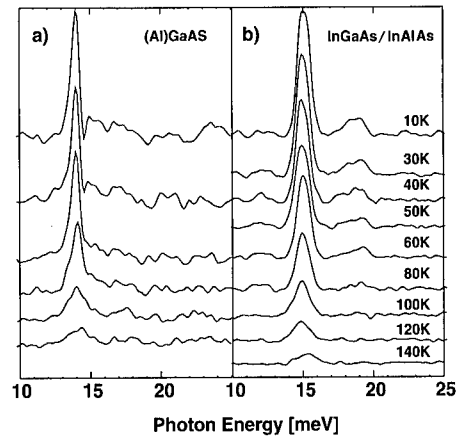


Fig. 1. Representative spectra for the (Al)GaAs (a) and the InGaAs/InAlAs (b) samples at constant injection current densities of, respectively, 39 and 28 A/cm^2 for increasing temperatures.

and is clearly temperature dependent. At high temperatures, the non-radiative depopulation channel of the upper subband is essentially provided by the emission of optical phonons through hot electrons. Activation graphs of the integrated peak intensity efficiency, taken from the spectral data and from luminescence data, are given in Fig. 2. The data obtained from the integrated peak intensity can be well fitted using the total non-radiative rate w_{nr} formula given before (see plain line) with an electron–electron scattering rate of $w_{\text{ee}} = 0.09$ and 0.07 ps^{-1} , and using the calculated optical-phonon scattering rate $w_{\text{isb}} = 1.86 \text{ ps}^{-1}$ for the GaAs and $w_{\text{isb}} = 1.31 \text{ ps}^{-1}$ for the InGaAs [4]. The energies of the $\hbar\omega_{\text{lo}}$ optical phonons used for the fit are, respectively, 36 and 33 meV for GaAs and InGaAs. At low temperatures ($T < 30 \text{ K}$), the main non-radiative channel is clearly dominated by the electron–electron scattering with fitted lifetimes of, respectively, 11 and 14 ps. As the lattice temperature is raised above $T = 30 \text{ K}$, the luminescence decreases exponentially and converges at high temperatures to the optical-phonon lifetime. The integrated luminescence data, i.e. the integrated power from the whole detectable spectrum, has been plotted for comparison. We observe that the integrated data does not follow the spectral data, indicating that it is perturbed by blackbody radiation.

The possibility to build a QC FIR laser based on this type of structure strongly relies on the ability of

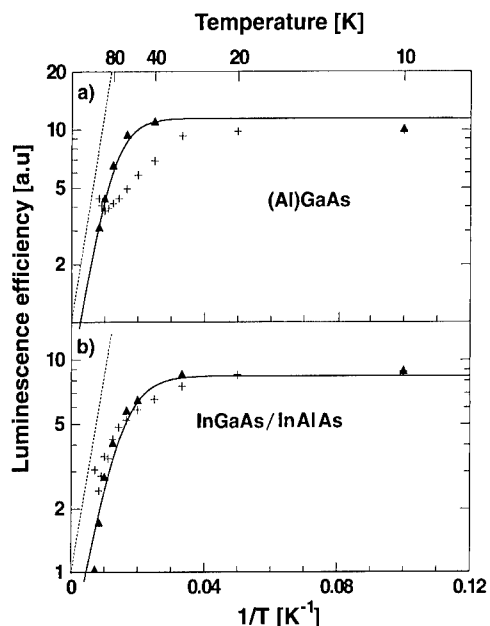


Fig. 2. Activation graphs of the integrated peak intensity efficiency for (a) (Al)GaAs and (b) InGaAs/InAlAs samples are shown (triangles). Corresponding total luminescence power are also shown for comparison (crosses). The spectral data is fitted using the w_{nr} relation (plain lines) and show, respectively, lifetimes of 14 and 11 ps at low temperature ($T = 10$ K) for the (Al)GaAs and (Al)InGaAs samples. Dotted lines show optical-phonon activation.

having gain. The second condition is the need of an efficient resonator in order to obtain laser action. In the far infrared, i.e. beyond the *reststrahlen* region ($\sim 30 \mu\text{m}$ for GaAs), several problems arise when one wants to build waveguides. At these wavelengths, free-carrier-induced absorption gets very important ($\alpha \sim \lambda^2$, Drude model) compared to the mid-infrared absorption. This can be overcome by having high gain active regions and high Q cavities. In the far infrared, waveguides based on pure dielectric confinement would require the cladding thickness to be of the order of $20 \mu\text{m}$ on both sides of the active region. Knowing that the MBE growth rate is of the order of $1 \mu\text{m/h}$, this method is not really efficient. We have chosen to confine the optical mode by providing highly doped GaAs grown on both sides of the active region, allowing us to have metal-like semiconductor interfaces leading to a double-surface plasmon-type waveguides. Waveguide losses of 51 cm^{-1} have been computed. For the experiment, the active region of our structure

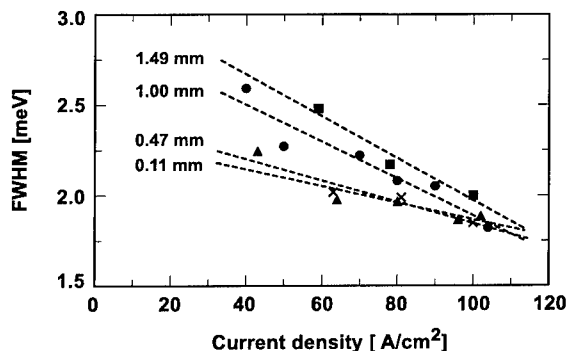


Fig. 3. FWHM of the luminescence peaks are plotted versus injected current density for different sample length.

is a 120 period MBE-grown replica of the (Al)GaAs structure described earlier. The samples were processed in $500 \mu\text{m}$ large stripes, chemically wet etched to the substrate with a $1 \text{ H}_2\text{SO}_4 : 8 \text{ H}_2\text{O}_2 : 1 \text{ H}_2\text{O}$ solution and then cleaved at different lengths ranging from $100 \mu\text{m}$ to 1.5 mm . We have measured the luminescence spectra for different waveguide length and different current densities. Fig. 3 shows the FWHM of the luminescence peaks plotted versus the injected current density for different sample length. A clear decrease of the peak FWHM is observed with increasing injected current density. The fact that the slope of this decrease is larger for longer devices is a good indication that the losses are due to the transition changes, suggesting differential gain. However, it is also clear that at fixed injected current density, the FWHM of the luminescence peak increases with increasing waveguide length, in contrary to what is expected from a transition with inverted population. We therefore believe that in all the current range in which our measurements have been carried out, the upper state population increases faster than the lower one, but population inversion has not yet been reached. The crossing of all curves at $J \sim 100 \text{ A/cm}^2$ indicates that transparency of the transition occurs and both states are equally populated. Increasing the injected current density would lead to population inversion and possible lasing action.

Measurements of waveguide properties can be done using a single-pass-type measurement [5]. The light intensity coming out of the waveguide is related to a waveguide net absorption $g - \alpha$ with the following

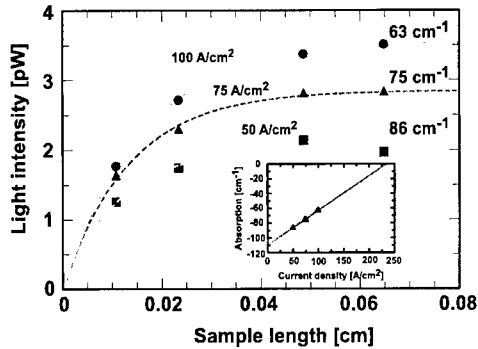


Fig. 4. Light intensity is plotted versus sample length for different injection current densities. Fitting the data gives a waveguide loss of 63 cm^{-1} at the maximum injected current density of 100 A/cm^2 . A net differential gain of 23 cm^{-1} has been measured. Extrapolation of the obtained results (inset) leads to a net waveguide loss of 110 cm^{-1} . Lasing threshold is projected to arise at a current density of 235 A/cm^2 .

relation

$$I_{\text{out}} = I_0 \int_0^l e^{(g-\alpha)x} dx = I_0 \frac{1}{(g-\alpha)} (e^{(g-\alpha)l} - 1),$$

where l being the length of the waveguide, g the gain, and α the total absorption. Performing measurement for different cavity lengths and at various injection current densities, allows to extract both g and α separately. Fig. 4 shows the light intensity plotted versus sample length for different injection current densities. The experimental data has been fitted using the previous relation. We obtain a waveguide loss of 63 cm^{-1} at the maximum injected current density of 100 A/cm^2 .

Extrapolating the obtained results for different current densities (see inset of Fig. 4) leads to a net

waveguide loss of 110 cm^{-1} and a differential gain of 23 cm^{-1} . Transparency is expected to appear at a current density of 235 A/cm^2 , which is far beyond the NDR region of our sample.

In conclusion, we have shown that the luminescence in a vertical quantum cascade light-emitting diode is limited at low temperatures by the electron–electron scattering. As the temperature is raised, the main non-radiative channel is dominated by the emission of optical phonons. We have also shown that the structure confined into a double-plasmon waveguide is able to provide optical gain. Even though no lasing has been observed, this result is very encouraging in the future realization of a far-infrared quantum cascade laser.

Acknowledgements

This work is supported by the Swiss National Science Foundation.

References

- [1] Michel Rochat, Jérôme Faist, Mattias Beck, Ursula Oesterle, Marc Illegems, *Appl. Phys. Lett.* 73 (1998) 3724.
- [2] M. Hartig, S. Haacke, P.E. Selbmann, B. Deveaud, R.A. Taylor, L. Rota, *Phys. Rev. Lett.* 80 (1998) 1940.
- [3] J.N. Heyman, K. Unterrainer, K. Craig, J. Williams, M.S. Sherwin, K. Campman, P.F. Hopkins, A.C. Gossard, B.N. Murdin, C.J.G.M. Langerak, *Appl. Phys. Lett.* 68 (1996) 3019.
- [4] R. Ferreira, G. Bastard, *Phys. Rev. B* 40 (1989) 1074.
- [5] J. Bakker G.A. Ackert, *IEEE J. Quantum Electron.* 13 (1977) 567.



ELSEVIER

Physica E 7 (2000) 48–51

PHYSICA E

www.elsevier.nl/locate/physa

Monte Carlo modelling of far-infrared intersubband lasers

R.W. Kelsall *, P. Kinsler, P. Harrison

Institute of Microwaves and Photonics, School of Electronic and Electrical Engineering, The University of Leeds, Leeds, LS2 9JT, UK

Abstract

An ensemble Monte Carlo simulation method has been used to model the carrier dynamics of optically pumped intersubband lasers. GaAs/AlGaAs asymmetric (single step) and triple quantum well structures are studied: both are 4-subband systems designed for intersubband pumping by a 10.6 μm CO₂ laser, and for far-infrared emission at 11.7 THz (25.6 μm). The simulations predict population inversion at 77 K for the asymmetric quantum well, but not at 300 K, whence intersubband electron–electron interactions cause significant re-distribution of electron kinetic energies in the 4th subband. However, simulations of the triple quantum well structure show strong inversion at 77 K, and marginal inversion at 300 K. The improved performance of the triple quantum structure in this case is attributed to stronger 3rd–2nd subband scattering (which depopulates the lower of the two laser levels) due to an anticrossing of eigenstates, and to reduced energy re-distribution effects. © 2000 Elsevier Science B.V. All rights reserved.

Keywords: Far-infrared; Monte Carlo simulation

1. Introduction

Intersubband laser operation has been reported by various groups at a wide range of wavelengths in the mid-infrared band [1]. There is now a strong interest in applying the intersubband laser concept to obtain emission at far-infrared (FIR) wavelengths, for potential applications in terahertz electronic systems and terahertz imaging, and intersubband electroluminescence at 88 μm (3.4 THz) has recently been reported [2]. Whilst the majority of attention has been focused on electrically excited quantum cascade devices, intersubband lasers can also be designed using

optical pumping schemes [3]. These devices have the advantage of a much simpler layer design, with no interaction required between adjacent active regions in a multi-period stack.

The design of successful FIR intersubband lasers is critically dependent on optimisation of both radiative and non-radiative electronic transitions. This requires detailed modelling work to calculate transition rates, subband populations, energy distributions and lifetimes. In this paper, we demonstrate the use of a Monte Carlo algorithm to simulate the intersubband carrier dynamics in optically pumped GaAs/AlGaAs asymmetric quantum well (AQW) and triple quantum well (TQW) FIR laser designs (see Figs. 1 and 2, respectively). The devices are designed for intersubband optical pumping using a 10.6 μm CO₂ laser.

* Corresponding author. Fax: +44-113-244-9451.

E-mail address: r.w.kelsall@leeds.ac.uk (R.W. Kelsall)

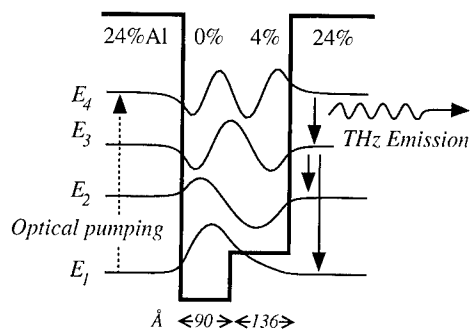


Fig. 1. Potential profile, subband-edge energies and wave functions of the 11.7 THz asymmetric quantum well FIR laser structure. The percentage figures show the aluminium content in the AlGaAs alloy layers, and the layer widths are indicated in angstroms below the profile. The vertical arrows indicate the key intersubband transitions for laser operation.

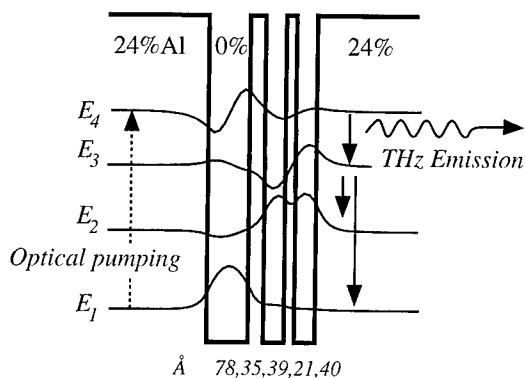


Fig. 2. Potential profile, subband-edge energies and wave functions of the 11.7 THz triple quantum well FIR laser structure. Details as for Fig. 1.

Terahertz emission is sought from transitions between subbands 4 and 3. In an attempt to optimise population inversion between these subbands, the energy separation between subbands 3 and 2 is set equal to the LO phonon energy, so that the $3 \rightarrow 2$ intersubband scattering rate, which depopulates subband 3, is maximised. Thus, the three principal design criteria are that the relationships between the zone-centre subband energies E_i , $i = 1, 4$, are: $E_4 - E_1 = 117$ meV, $E_3 - E_2 = 36$ meV and 12 meV $< E_4 - E_3 < 50$ meV (for FIR emission in the range 3–12 THz).

The Monte Carlo simulation includes the energy-dependent electron-phonon and electron-electron scattering rates for all intra- and inter-subband processes, as calculated using Fermi's Golden Rule.

Bulk-like phonon modes are assumed, as recent calculations for AQW structures showed that the subband population ratios are obtained using confined and bulk phonon modes are very similar [4,5]. Pauli exclusion effects are self-consistently included in the simulation by frequent sampling of the electron distribution. The optical pumping process is included via calculation of the exact intersubband absorption matrix element, with a Gaussian line shape assumed for the incident beam [6]. This enables us to account for de-tuning of the pump transition at different kinetic energies due to differences in the effective masses of the 1st and 4th subbands. For the results presented here, a pump laser line width of 2 meV was assumed. Additional simulations have shown that the distribution of carriers between subbands is, in fact, only weakly dependent on the pump line width. Each simulation is run until convergence to a steady state is obtained. The full ensemble state is then replicated, and used as a seed for a series of physically equivalent simulations, to facilitate estimation of the statistical errors.

2. Results and discussion

The AQW and TQW structures are both designed for emission at 11.7 THz. Fig. 3 shows simulated population ratios for both structures at 77 and 300 K.

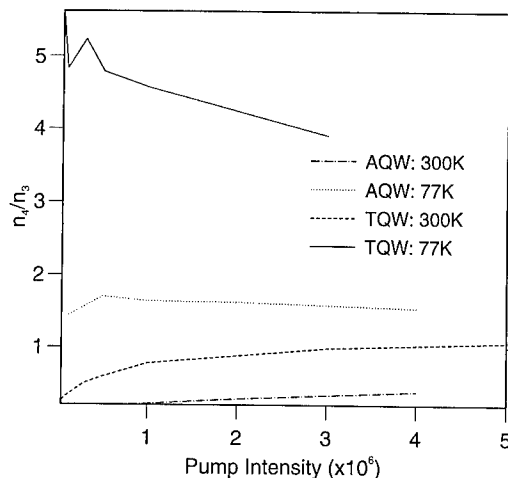


Fig. 3. Population ratios for the asymmetric (AQW) and triple (TQW) quantum well structures at 77 and 300 K, as a function of optical pump intensity. The intensity scale is expressed as a multiple of the 1st–4th subband optical absorption rate.

For the AQW structure, moderate population inversion is predicted at 77 K, and the population ratio is relatively insensitive to the optical pump intensity. However, at 300 K, population inversion is not predicted for the AQW. Our previous calculations of intersubband transition rates, based on the assumption of equilibrium Fermi–Dirac distribution functions in each subband, showed that $4 \rightarrow 3$ scattering processes — which destroy inversion, have a weaker temperature dependence than the $3 \rightarrow 2$ and $3 \rightarrow 1$ processes — which help to maintain inversion. (These temperature dependences were due primarily to the temperature dependence of the electron distribution functions, rather than the phonon populations.) Our Monte Carlo simulations show that, at 77 K, the extent to which the subband 3 and 4 distribution functions are heated is very similar, such that the balance of $4 \rightarrow 3$ and $3 \rightarrow 2$, $3 \rightarrow 1$ scattering is similar to that for the case of Fermi–Dirac distributions.

However, at a lattice temperature of 300 K, the average electron energy in the 4th subband is equivalent to a temperature of approximately 500 K — much higher than that for the 3rd subband. This localised heating of the 4th subband population preferentially raises the $4 \rightarrow 3$ scattering rates, hence destroying population inversion. The apparent cause of this heating effect is the strong interaction between the 4th and 1st subband populations at room temperature. At 300 K, the tail of the 1st subband distribution function overlaps the energy range of the 4th subband, resulting in strong electron–electron interactions, including both intersubband electron scattering ($44 \rightarrow 11$) and the $41 \rightarrow 41$ process, which changes the average kinetic energy, but not the population, of each subband. These interactions lead to a substantial broadening of the electron energy distribution in the 4th subband. The speed of the energy redistribution processes, combined with the fact that the 4th subband is continually replenished by the optical pumping, means that the broadened energy distribution is observed in the steady state — whilst ever pumping is maintained.

Previous calculations for the AQW structures based on a rate equation approximation [7], using Fermi–Dirac distributions and neglecting carrier heating, predicted population ratios of 1.4–1.6 at both 77 and 300 K. This new data thus highlights the role of electron heating in determining carrier dynamics at high lattice temperatures.

Conversely, simulation results for the TQW structure predict population inversion at both 77 and 300 K. The strong inversion at 77 K, compared to that for the AQW structure, may be ascribed to the fact that the 2nd and 3rd subband wave functions are approximately an symmetric/antisymmetric pair, thus increasing the matrix elements for $3 \rightarrow 2$ scattering. At 77 K, inversion is clearly observed in the simulations whilst, at 300 K, inversion only occurs for high pump intensities. Although the AQW and TQW structures utilise the same basic design criteria, the simulations show an important difference in carrier dynamics: in the TQW structure, the 4th subband distribution does not suffer from excessive heating, even at room temperature. This is because the overlap of the wave functions of 4th and 1st subband electrons is reduced, relative to the AQW case, leading to weaker interactions between the two subbands. Given this fact, it also follows that higher pump intensities are required to generate sufficient carrier densities in the 4th subband for the attainment of inversion.

3. Conclusion

Our Monte Carlo simulations have shown the importance of including realistic non-equilibrium electron distributions in calculations of population inversion in optically pumped intersubband lasers. Strong population inversion at 77 K, and marginal population inversion at 300 K, is predicted for CO₂ pumped triple quantum well lasers designed for emission at 11.7 THz.

Acknowledgements

This work was funded by the UK Engineering and Physical Sciences Research Council.

References

- [1] F. Capasso, C. Gmachl, D.L. Sivco, A.Y. Cho, *Physics World* 12 (6) (1999) 27.
- [2] M. Rochat, J. Faist, M. Beck, U. Oesterle, M. Illegems, *Appl. Phys. Lett.* 73 (25) (1998) 3724.
- [3] O. Gauthier-Lafaye, F.H. Julien, S. Cabaret, J.M. Lourtioz, G. Strasser, E. Gornik, M. Helm, P. Bois, *Appl. Phys. Lett.* 74 (11) (1999) 1537.

- [4] P. Kinsler, R.W. Kelsall, P. Harrison, *Physica B* 263–4 (1999) 507.
- [5] P. Kinsler, R.W. Kelsall, P. Harrison, *Superlatt. Microstruct.* 25 (1999) 163.
- [6] P. Kinsler, R.W. Kelsall, P. Harrison, *Phys. Rev. B*, submitted for publication.
- [7] P. Kinsler, P. Harrison, R.W. Kelsall, *J. Appl. Phys.* 85 (1999) 23.



ELSEVIER

Physica E 7 (2000) 52–57

PHYSICA E

www.elsevier.nl/locate/physe

Waveguide design optimization for a quantum cascade laser emitting at 77 μm

Vinod M. Menon^{a,*}, W.D. Goodhue^a, A.S. Karakashian^a, L.R. Ram-Mohan^b

^a*Photonics Center and Department of Physics and Applied Physics, University of Massachusetts Lowell, One University Avenue, Lowell, MA 01854, USA*

^b*Department of Physics and Department of Electrical and Computer Engineering, Worcester Polytechnic Institute, Worcester, MA 01609, USA*

Abstract

The dependence of waveguide design parameters on the performance of a GaAs/AlGaAs quantum cascade laser emitting at 77 μm is theoretically evaluated. We propose a new waveguiding scheme for modal confinement at such long wavelengths. An artificially tailored index layer and a plasmon enhanced layer act as the cladding at the top and bottom of the active region, respectively. The cladding layers have been made aluminum free to avoid the presence of DX centers. The waveguide design is optimized to enhance modal confinement and reduce waveguide losses. Finally, we present an optimized design of the quantum cascade laser in its entirety along with expected performance characteristics. © 2000 Published by Elsevier Science B.V. All rights reserved.

Keywords: Quantum cascade lasers; Terahertz sources; Plasmons; Waveguide

1. Introduction

Even though Kazarinov and Suris proposed using the intersubband transitions as possible terahertz (THz) sources [1], the first real experimental demonstration of an intersubband laser was the mid-infrared quantum cascade laser (QCL) [2]. More recently, far-infrared (FIR) emission (60 and 88 μm) has been observed in quantum cascade structures [3,4]. One of the earlier proposals for modal confinement in THz range was to use a heavily doped plasma reflector

[5]. The presence of such layers close to the active region may result in free carriers migrating into the active region, which degrades the device performance (adding to the loss). In this paper we explore the possibility of using an artificially tailored upper cladding layer with a predetermined effective index. The lower cladding layer (the substrate) will be a plasma reflector, which has now been distanced from the active region by the intermediate layers. The paper is organized into sections on waveguide design along with parameter optimization, a possible fabrication scheme for the waveguide design, the multiple quantum well (MQW) design for the active region, and the expected device performance characteristics.

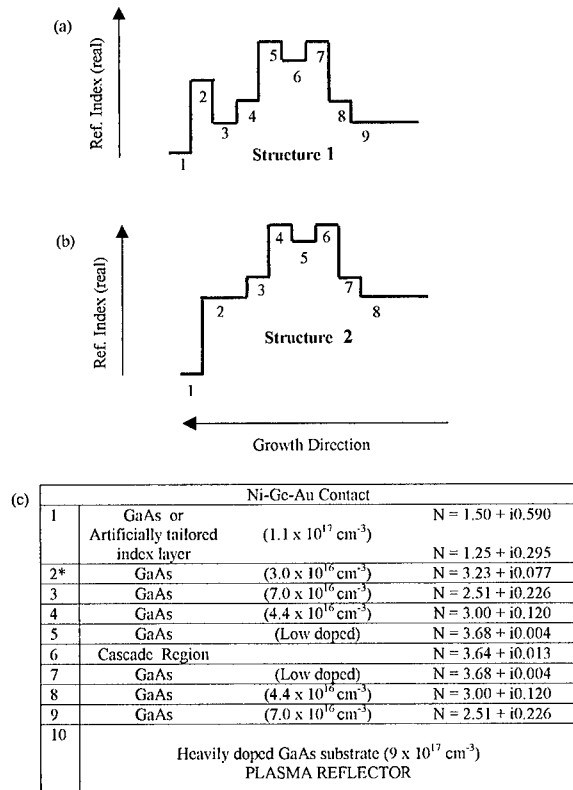
* Corresponding author. Tel.: +1-978-458-4972; fax: +1-978-934-4994.

E-mail address: vinod_menon@student.uml.edu (V.M. Menon)

2. Waveguide design

The transfer matrix method (TMM) was employed to determine the propagation constants, mode profile and confinement factors. In the analysis presented, the refractive indices of all the layers are taken to be complex since the imaginary part becomes important at high doping concentrations. The roots in the complex plane which give the propagation constants were determined using a *regula-falsa* method.

Two different epitaxial structures as shown in Fig. 1a and b were studied. For each structure, we analyzed the device characteristics with and without the artificially tailored index layer. The thickness and refractive index of these layers were optimized so as to obtain minimum loss and maximum modal confinement.



* This layer is not there in structure 2.

Fig. 1. Refractive index profiles for the two designs evaluated in the text. Layers 6 and 5 are the active regions in structures 1 and 2, respectively. Details of each layer are shown in Fig. 1c.

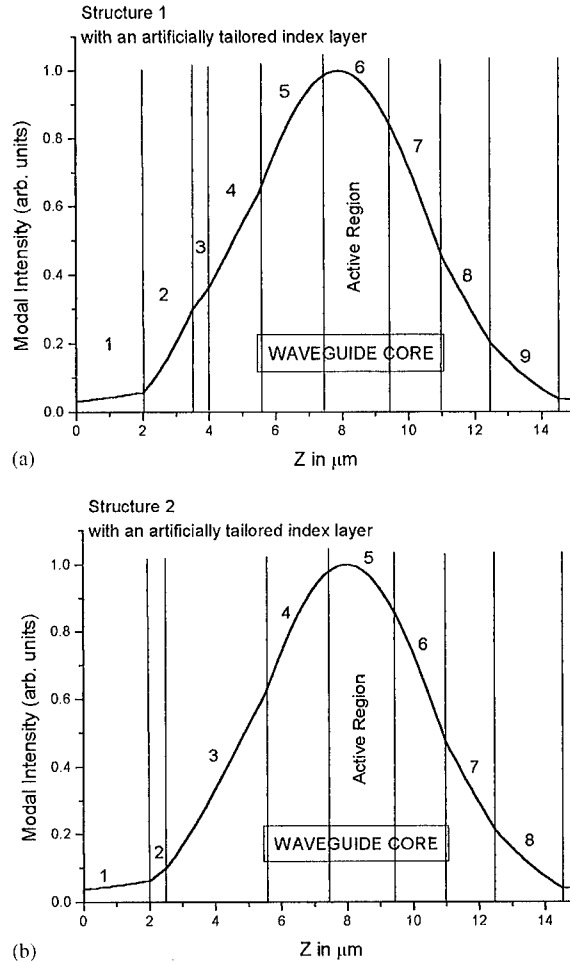


Fig. 2. Mode intensity profile of the waveguide for optimal designs.

Low doped GaAs layers are placed on either side of the active region so as to increase the net refractive index (real part) of the core. This is similar to the approach used by Sirtori and coworkers for the GaAs/AlGaAs QCL [6]. In the waveguide designs at mid-infrared, high aluminum concentration AlGaAs layers were used as cladding to enhance the refractive index contrast with the core. It has been pointed out recently that in spite of this advantage, these high aluminum content AlGaAs layers have low conductivity and have DX centers (associated with Si doping) which at low temperatures tend to reduce the number of free electrons in the conduction band [7]. Hence, we have tried to design an aluminum free cladding layer. The

Table 1

The thickness of each layer along with the effective modal indices, waveguide loss and the confinement factor

Layer thickness (μm)		Structure 1				Structure 2			
Layer no.		With double plasmon enhanced layers		With artificially tailored index layer		With double plasmon enhanced layers		With artificially tailored index layer	
		Case 1	Case 2	Case 3	Case 4	Case 5	Case 6	Case 7	Case 8
1		1.0	2.0	1.0	2.0	1.0	2.0	1.0	2.0
2		2.5	1.5	2.5	1.5	0.5	0.5	0.5	0.5
3		0.5	0.5	0.5	0.5	3.0	3.0	3.0	3.0
4		1.5	1.5	1.5	1.5	3.0	2.0	3.0	2.0
5		2.0	2.0	2.0	2.0	2.0	2.0	2.0	2.0
6		2.0	2.0	2.0	2.0	1.5	1.5	1.5	1.5
7		1.5	1.5	1.5	1.5	1.5	1.5	1.5	1.5
8		1.5	1.5	1.5	1.5	2.0	2.0	2.0	2.0
9		2.0	2.0	2.0	2.0	—	—	—	—
Total		14.5	14.5	14.5	14.5	14.5	14.5	14.5	14.5
$N_{\text{effective}}$	n	1.87	1.67	1.85	1.63	1.858	1.62	1.84	1.58
	k	0.172	0.215	0.149	0.164	0.18	0.22	0.157	0.168
Loss coeff. α_w (cm^{-1})		280.7	350.8	243.1	267.6	293.7	359.0	256.2	274.1
Confinement factor Γ		0.64	0.66	0.65	0.67	0.76 ^a	0.65	0.77 ^a	0.66

^aThe peak of the mode does not lie in the active region.

index contrast has been achieved using doped GaAs layers.

In both structures, the core (GaAs + cascade layer) is sandwiched between GaAs layers having different doping concentrations. The refractive indices along with the corresponding doping concentrations are given in Fig. 1c. In structure 1 (Fig. 1a), the role of the high index layer (layer 2) before the top layer is to decouple any metal (contact) semiconductor interface surface plasmon mode from the laser mode [8].

The artificially tailored index layer is fabricated on the n^{++} GaAs ($7.0 \times 10^{16} \text{ cm}^{-3}$). A grating-like structure with periodicity much lesser than the lasing wavelength is first fabricated on the GaAs layer. Index tailoring is achieved by introducing another material in between the GaAs pillars. For our study we have considered that the case where the gaps between the GaAs pillars have been left empty (air). The periodicity of these structures should be less than $2 \mu\text{m}$. Due to the long wavelength, the optical mode does not see the gratings, but instead a layer with an average index corresponding to the two materials. By having different materials, one can now tailor the refractive index of the layer. In our case we have a layer with an effective index corresponding to the average of the n^{++} GaAs and air.

The lower n^{++} GaAs layer ($7.0 \times 10^{16} \text{ cm}^{-3}$) is grown on a heavily doped ($9.0 \times 10^{17} \text{ cm}^{-3}$) GaAs substrate, which acts as the plasma reflector. The optimized layer thickness, effective modal index, confinement factor and waveguide loss are summarized in Table 1. The only difference between cases 1 and 2, 3 and 4, 5 and 6, and 7 and 8 is the layer thickness. Fig. 2 illustrates the mode intensity profiles of the waveguide for the two structures that gave optimal performance. Waveguide losses were evaluated from the imaginary part of the effective modal index obtained using the transfer matrix method ($\alpha = 4\pi k/\lambda$).

3. Fabrication technique

All the layers except the altered index layer can be fabricated using molecular beam epitaxy (MBE). The fabrication of the altered index layer (having air gaps) consists of six steps. Step 1: deposition of photoresist (Fig. 3a). Step 2: angle evaporation of aluminum (Fig. 3b), Step 3: reactive ion beam etching to form pillars of photoresist (Fig. 3c), Step 4: deposition of Ni Ge Au layer using electron beam deposition, followed by lift off (Fig. 3d), Step 5: ion-beam-assisted etching, which leaves a series of pillars of n^{++} GaAs with the

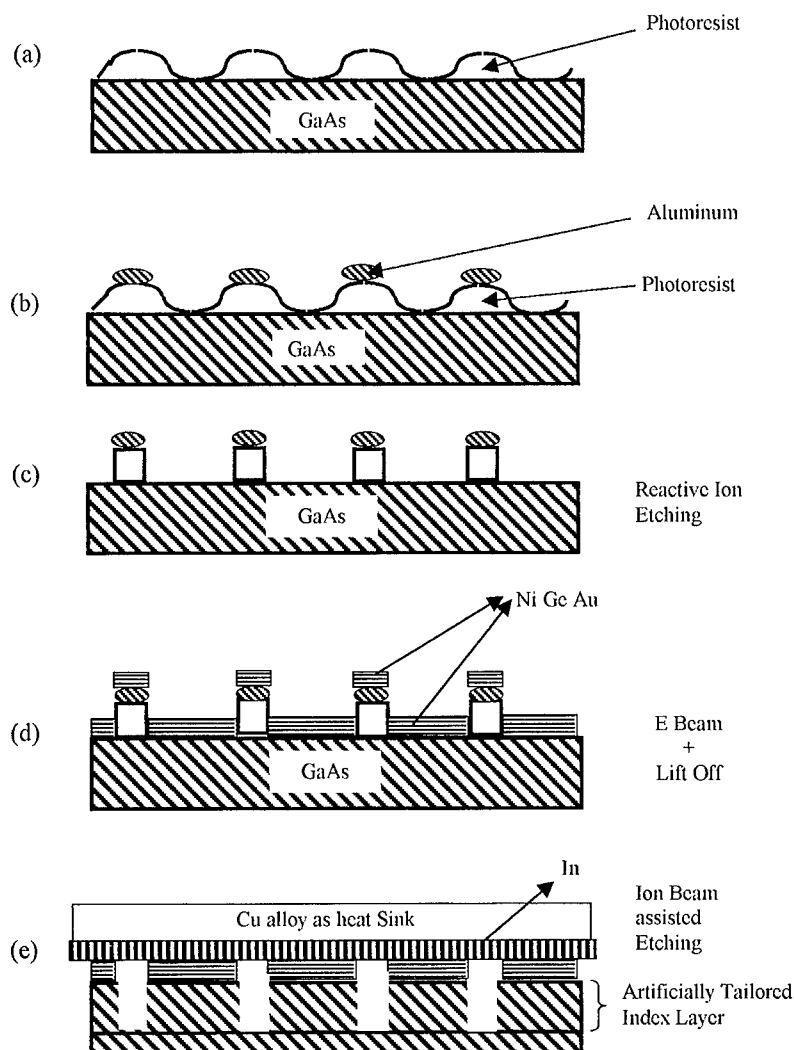


Fig. 3. Scheme for fabricating the altered index layer. Steps (a)–(e) are discussed in the text.

Ni Ge Au alloy on top (Fig. 3e). Thick indium-coated copper alloy is pressed on to the Ni Ge Au contact. The end result is a layer having alternating n^{++} GaAs and air sandwiched between the contact layer and rest of the cladding. The periodicity of the pillars could be broken slightly so as to avoid any mode build up.

4. Design of active region

The energy levels and wave functions were computed using a finite element $k \cdot p$ model. Fig. 4

illustrates the design of the multiple quantum well structure along with the subband levels and squared magnitude of the wave functions. Lasing occurs between the upper two levels (levels 3 and 2) through a vertical transition. These levels are separated by 16 meV, corresponding to a wavelength of $77 \mu\text{m}$ (3.8 THz) at a bias of 9.96 kV/cm. Levels 2 and 1 are separated by the confined LO phonon frequency to aid a fast non-radiative transition between these levels. The matrix element between level 3 and level 2 was calculated to be 3.85 nm, resulting in a radiative lifetime $\tau_{\text{rad}} = 0.8 \mu\text{s}$. The lifetime of level 3 is given

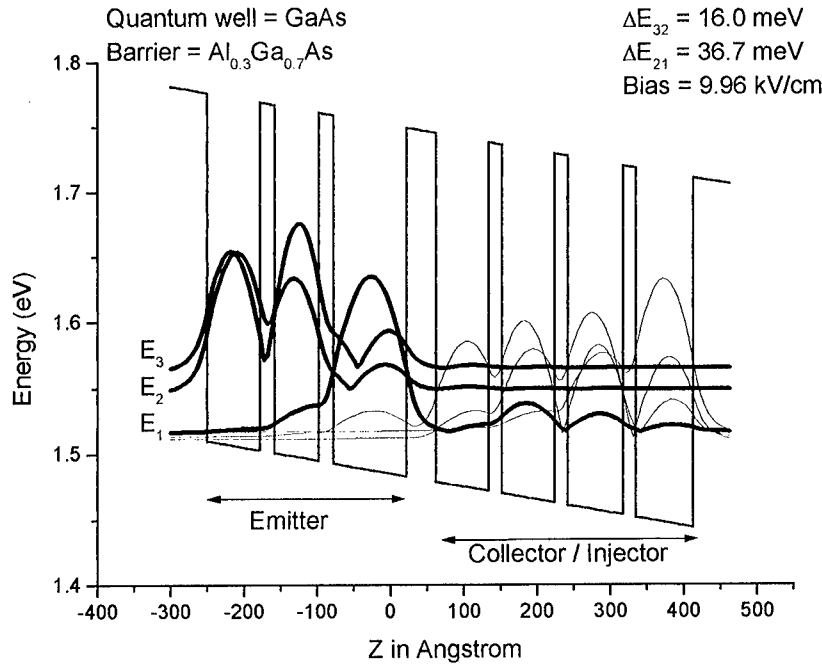


Fig. 4. Schematic conduction-band diagram of one period of our structure at the threshold bias along with the squared magnitude of the wave functions. The wells and barrier widths starting with the leftmost barrier in nm are: 5.0/7.2/2.0/6.0/10.0/4.0/7.2/1.8/7.2/1.8/7.8/1.8/7.8/5.0.

by $1/\tau_3 = 1/\tau_{32} + 1/\tau_{31}$. The non-radiative lifetime between levels 3 and 2 is primarily dominated by the electron–electron scattering which has been estimated to be ~ 2.1 ps [9]. The 3 to 1 transition is dominated by the interface LO phonon scattering time ~ 1.5 ps. The net lifetime of level 3 is $\tau_3 \sim 0.9$ ps. The lifetime of level 2 is dominated by the confined LO phonon scattering to level 1 which is estimated to be on the order of 0.4 ps. The interface and confined LO phonon scattering rates were evaluated using a scheme similar to that proposed by Kim and Strociro [10]. Since τ_3 is only greater than τ_2 by a factor of two, great care has to be taken in material quality, growth and design to attain population inversion between these levels.

5. Expected device performance

The threshold current density for a QCL can be expressed as [8]

$$J_{th} = \frac{(\alpha_M + \alpha_W) \epsilon_0 n_R (2\gamma) L_P \lambda}{4\pi e (\tau_{32} - \tau_2) (\tau_3 / \tau_{32}) |Z_{32}|^2 \Gamma},$$

where J_{th} is the threshold current density, α_M is the mirror loss $\sim 5 \text{ cm}^{-1}$, α_W is the waveguide loss,

L_P (71.6 nm) is the thickness of one period, n_R is the real part of the effective index of the mode, e is the electronic charge, ϵ_0 is the vacuum permittivity, λ (77 μm) is the lasing wavelength, z_{32} is the matrix element ~ 3.85 nm, and 2γ is the line width of the spontaneous emission spectrum ~ 0.7 meV at 5 K [4]. The threshold current density values were computed for the different cases analyzed and are presented in Table 2. The radiative efficiency $\eta_{rad} = \tau_3 / \tau_{rad} \sim 1.12 \times 10^{-6}$.

6. Summary

Different waveguiding schemes for a THz QCL were theoretically evaluated and optimized to minimize loss and maximize modal confinement. Typical losses are in the range of 250 cm^{-1} . In Tables 1 and 2, if we compare cases 1 and 3, 2 and 4, 5 and 7, and 6 and 8, it is seen that for the same layer thickness and doping concentration, the structure with the artificially tailored index layer has lower loss and therefore lower threshold current densities. Expected threshold current densities are in the order of 2.0 kA/cm^2 . We

Table 2
The threshold current density for the difference cases analyzed

Threshold current density J_{th} (kA/cm ²)	Case 1	Case 2	Case 3	Case 4	Case 5	Case 6	Case 7	Case 8
	2.25	2.43	1.9	1.79	1.97	2.45	1.68	1.8

have tried to design an aluminum free cladding layer to avoid DX centers. The lifetimes of levels 3 and 2 are both in the sub-picosecond range making it difficult to attain population inversion between these levels. The possibility of achieving gain in these devices so as to overcome all the losses seem difficult at this point, but with more efficient wave function engineering, one may be able to control these scattering rates and thereby lower the losses in the system.

Acknowledgements

We would like to thank Prof. J.P. Donnelly and Prof. T.G. Castner for helpful discussions. We also thank Quantum Semiconductor Algorithms for use of the finite-element band structure software. One of the authors (VMM) would like to acknowledge support provided by University of Massachusetts Lowell, Dept. of Physics, the Council of Federated Centers and Institutes and the organizers of ITQW'99 for providing funds to attend the conference.

References

- [1] R.F. Kazarinov, R.A. Suris, *Sov. Phys. Semicond.* 5 (1971) 707.
- [2] J. Faist, F. Capasso, D.L. Sivco, C. Sirtori, A.L. Hutchinson, A.Y. Cho, *Science* 264 (1994) 553.
- [3] B. Xu, Q. Hu, M.R. Melloch, *Appl. Phys. Lett.* 71 (1997) 440.
- [4] M. Rochat, J. Faist, M. Beck, U. Oesterle, M. Illegems, *Appl. Phys. Lett.* 73 (1998) 3724.
- [5] Q. Hu, S. Feng, *Appl. Phys. Lett.* 59 (1991) 2923.
- [6] C. Sirtori, P. Kruck, S. Barbieri, P. Collot, J. Nagle, M. Beck, J. Faist, U. Oesterle, *Appl. Phys. Lett.* 73 (1998) 3486.
- [7] C. Sirtori, S. Barbieri, P. Kruck, V. Piazza, M. Beck, J. Faist, U. Oesterle, P. Collot, J. Nagle, *IEEE Photonics Technol. Lett.* 11 (1999) 1090.
- [8] J. Faist, F. Capasso, D.L. Sivco, A.L. Hutchinson, C. Sirtori, A.N.G. Chu, A.Y. Cho, *Appl. Phys. Lett.* 65 (1994) 2901.
- [9] Per Hyldgaard, John W. Wilkins, *Phys. Rev. B* 53 (1996) 6889.
- [10] K.W. Kim, M.A. Strocio, *J. Appl. Phys.* 68 (1990) 6289.



ELSEVIER

Physica E 7 (2000) 58–62

PHYSICA E

www.elsevier.nl/locate/physe

Resonant tunneling and intersubband population inversion effects in asymmetric wide quantum-well structures

V.N. Murzin *, Yu.A. Mityagin, V.A. Chuenkov, A.L. Karuzskii, A.V. Perestoronin,
L.Yu. Shchurova

P.N. Lebedev Physical Institute, Leninsky pr. 53, 117924 Moscow, Russia

Abstract

Theoretical estimates and the results of vertical transport and optical investigations in GaAs/AlGaAs structures show that resonant tunneling can lead efficiently to selective depopulation of the levels, resulting in a population inversion and possible stimulated emission due to intersubband transitions between the lowest states in wide-quantum-well structures. © 2000 Published by Elsevier Science B.V. All rights reserved.

Keywords: Resonant tunneling; Far-infrared laser

1. Introduction

The development of physical principles of amplification and generation of electromagnetic waves over a broad infrared range remains one of the urgent problems in physics. The very prominent achievements in this direction are obviously the investigations of quantum cascade and quantum fountain lasers operating in the near- and mid-infrared regions. As to the far-infrared range, a number of schemes to realize intersubband population inversion and stimulated emission in quantum-well structures were proposed [1–3], but the problem has not yet been solved.

In this paper we discuss a version of a far-infrared (50–100 μm) resonant tunneling laser based on the

intersubband transitions in wide quantum-well structures (WQWS) with the energy spacing between the two lowest states below the longitudinal-optic (LO) phonon energy. Population inversion in these structures is achieved due to the difference in scattering relaxation processes between the lowest states with or without LO-phonon emission, and via the selective removal of carriers from the ground state by the use of resonant tunneling to the neighboring quantum well [4,5].

2. Scattering relaxation carrier life-times in wide-quantum-well structures

Several mechanisms can be proposed to produce a population inversion in lower subbands by the use of selective resonant tunneling in the regime of cur-

* Corresponding author. Fax: 007-095-938-22-51.

E-mail address: murzin@sci.lebedev.ru (V.N. Murzin)

rent injection, or in the regime of optical pumping in heterostructures with different compositions of semiconductor compounds in the neighboring quantum wells [4,5]. If the parameters of a wide quantum well are chosen in such a way that $\varepsilon_3 - \varepsilon_2 = \hbar\omega_0$ and $\varepsilon_2 - \varepsilon_1 < \hbar\omega_0$ whereas the energy spacing between the resonant $\varepsilon_{2'}$ and ground $\varepsilon_{1'}$ states in the neighboring well being of order or more than $\hbar\omega_0$ ($\hbar\omega_0$ is the optical phonon energy), then carriers injected into the ε_3 level due to resonant tunneling from a previous quantum well will rapidly relax to both lower ε_2 and ε_1 states. The relaxation between ε_2 and ε_1 will be considerably slower. Population inversion and laser transitions between ε_2 and ε_1 states arise due to resonant tunneling of carriers from the ground state to a suitable state in the next well. In the case of GaAs/Al_{0.3}Ga_{0.7}As the situation corresponds to quantum wells of width $d_w = 25$ nm ($\varepsilon_1 = 7, \varepsilon_2 = 29, \varepsilon_3 = 64, \varepsilon_4 = 113, \varepsilon_5 = 173$ meV), the lasing transitions being located at wave lengths around 60 μm . The concrete model structure investigated here consists of three wells of different thickness, 16.5/ d_b /25/ d_b /16.5 nm, with equal barrier thickness d_b . A more detailed scheme of the transitions is shown in Refs. [4,5].

2.1. Acoustical phonon and charged impurity scattering relaxation

As it follows from the theoretical estimates confirmed experimentally the optic-phonon relaxation between excited subbands results in $\tau^{\text{opt}} \approx 0.5$ ps, while the acoustic-phonon intersubband relaxation between the first excited and the ground states results in $\tau_{12}^{\text{AC}} \approx 300$ ps at low temperatures [5–7]. The value τ_{12} decreases in electric field due to ionized-impurity scattering. The relaxation time estimates in our case were made in analytical form taking into account the screening effect by free electrons that, as we show, plays a noticeable role in structures with rather wide wells. The interaction between an electron and an ionized impurity scatterer centered at $z = z_i$ is described by a potential $\varphi(\rho, z, z_i)$ which is found in quasi-two-dimensional approximation from Poisson's equations

$$\varphi(\rho, z, z_i) = \frac{e}{\varepsilon_w} \left\{ \frac{\exp(-q_0 \sqrt{\rho^2 + (z - z_i)^2})}{\sqrt{\rho^2 + (z - z_i)^2}} \right\}, \quad (1)$$

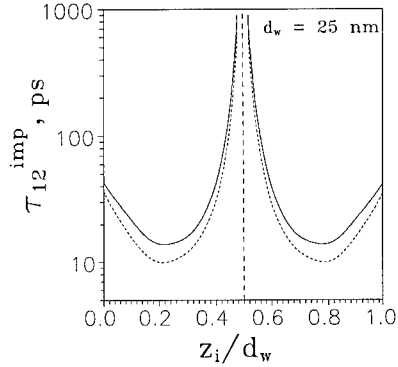


Fig. 1. Theoretically estimated charge-impurity intersubband relaxation times in GaAs/Al_{0.3}Ga_{0.7}As structures as a function of the impurity center location z_i/d_w inside the well with (full line) or without (dotted line) screening.

under approximation $q_0 d_w \gg 1$ (q_0 is the reciprocal screening length). Here $\rho^2 = x^2 + y^2$, x, y, z are the distances from the ionized impurity, z is the component in growth direction. Since the scatterers are randomly distributed in the layer the lifetime $\tau_{\text{nl}}^{\text{imp}}$ is inversely proportional to the areal concentration of static defects. The relaxation times evaluated using a standard program for the computation of the probabilities of intersubband transitions with the use of Eq. (1) for unscreened ($q_0 = 0$) and screened ionized impurities in GaAs/Al_{0.3}Ga_{0.7}As quantum wells ($d_w = 25$ nm, $d_b = 4$ nm, $N_s = 10^{10} \text{ cm}^{-2}$, $T = 4.2$ K) are presented in Fig. 1. These times depend on the impurity center location z_i/d_w inside the well. The results show that the relaxation time increases noticeably due to screening, decreases distinctly with increasing the well width depending strongly on the impurity center location due to the envelope wave function peculiarities in different subbands. The values τ_{21}^{imp} in uniformly doped wells averaged over the impurity positions are about 40 ps ($N_d = 10^{16} \text{ cm}^{-3}$, $N_s = 10^{10} \text{ cm}^{-2}$). The parameter $q_0 d_w \approx 5$ in the above situations which is quite satisfactory.

2.2. Selective doping as a method for producing long-living carriers in the second subband

As one might expect, the ionized impurity scattering governs the lifetimes of carriers on the first excited state in WQWS under the application of an electric field. This makes the realization of laser systems with

high carrier concentration rather difficult. The possible solution seems to be the use of the selective doping (in the well center where the square of the wave function in the first excited goes to zero). As it follows from Fig. 1, selective doping ($N_d = 5 \times 10^{16} \text{ cm}^{-3}$) with a profile width of 4 nm gives in ordinary pure structures τ_{21}^{imp} around 60 ps that look rather promising. The electron–electron scattering in the situation being considered ($N_s \approx 10^{10} \text{ cm}^{-2}$) does not play a decisive role, resulting in an intersubband relaxation time longer than 50 ps [8].

3. Resonant tunneling rates and space charge mismatching effects

In view of the estimates we make, the problem of resonant tunneling is extremely important and calls for particular attention.

3.1. Resonant tunneling rates and selectivity in structures with broadened energy levels

It follows from experiments that the resonant tunneling times usually estimated from the energy-level splitting $\tau_{\text{tun}}^{\text{coherent}} \cong \hbar/\delta\epsilon_{\text{split}}$ are, as a rule, essentially longer [9–11]. The main reason is the necessity of taking into account the level widths which can be caused, in particular, by carrier relaxation in a neighboring well, that makes the tunneling process incoherent [9,10]. According to the nonstationary quantum perturbation theory [10] resonant tunneling combined with the relaxation process in a neighboring well yields

$$\tau_{\text{tun}}^{\text{incoherent}} \cong \tau_{\text{opt}} + \frac{\hbar}{\delta\epsilon_{\text{split}}} \left(\frac{\gamma}{\delta\epsilon_{\text{split}}} \right) \frac{\Delta\epsilon^2 + \gamma^2}{\gamma^2} \quad (2)$$

under approximation $\delta\epsilon_{\text{split}} \ll \gamma$. Here $\Delta\epsilon$ is the mismatch of the resonant levels (ϵ_1 and $\epsilon_{2'}$), γ is the half-width of the final tunneling level ($\epsilon_{2'}$). In the case of optical phonon scattering $\gamma = \hbar/\tau_{\text{opt}} \approx 1 \text{ meV}$ ($\tau_{\text{opt}} = 0.4 \text{ ps}$). One can see that under exact resonance condition ($\Delta\epsilon = 0$) the value τ_{tun} should be proportional to $\delta\epsilon_{\text{split}}^2$ and increase with increasing of the level width as $\gamma/\delta\epsilon_{\text{split}}$. The physical sense of the effect may be simply understood in terms of the perturbation theory. This means that the tunneling transitions

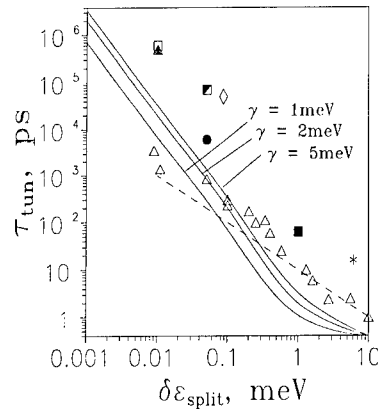


Fig. 2. Resonant tunneling times determined from photoluminescence (Δ - [11]) and from vertical transport (SL with d_w/d_b : (■) 33/4 [14]; (●) 9/7.9 [15]; (□) 25/10 [5], (▲) 35/12 [13]; (◇) 35/10 [12]; (*) 6.8/2.6 [2] nm and in the model structure: (●) 8/16.5/8/25/8/16.5/8 nm) as a function of the calculated energy splitting $\delta\epsilon_{\text{split}}$. The dotted line corresponds to model [11]; the full lines are the results of calculations using Eq. (2).

from one well to another with a broadened level happen at different moments to the states with different energies inside the level width. In other words, only a small part of the tunneling transitions may be carried out with high rates under the condition $\delta\epsilon_{\text{split}} \ll \gamma$, which obviously delays the whole tunneling process. According to this interpretation one may suggest that the model (2) can be effective also when the level widths are caused by some other mechanisms, besides relaxation, if they have a statistical nature. As can be seen from Fig. 2, where the results of vertical transport and photoluminescence investigations of resonant tunneling times in different structures are presented and compared with theoretical curves (2), the results are roughly consistent with Eq. (2) and can be used for our estimates. The resulting values τ_{tun} for the tunneling transitions $\epsilon_1 \rightarrow \epsilon_{2'}$ in the model structure are about 30 ps ($d_B = 6 \text{ nm}$), 10 ps ($d_B = 4 \text{ nm}$), 3 ps ($d_B = 2 \text{ nm}$) based on the calculated $\delta\epsilon_{\text{split}} = 0.5, 1$ and 3 meV.

According to far-infrared emission [12], photoluminescence and vertical transport investigations [4,5,13] the lowest subbands are manifested even in very long-period superlattices (SL) ($d_w \leq 35 \text{ nm}$, $\gamma_3 \approx 1\text{--}2 \text{ meV}$). Vertical-transport measurements in SL with $d_w = 25 \text{ nm}$ (Fig. 3) show that the lowest states are distinctly pronounced in the resonant tunneling structures under consideration (the data in

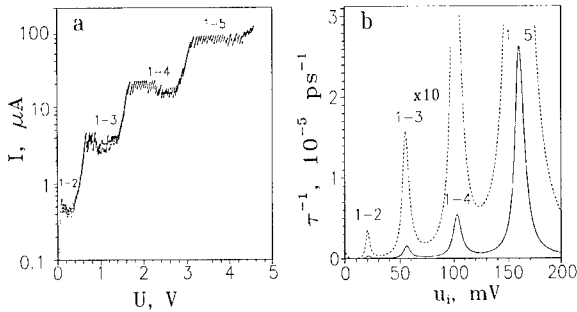


Fig. 3. (a) Current–voltage characteristics of GaAs/Al_{0.3}Ga_{0.7}As superlattice $d_w = 25$ nm, $d_b = 10$ nm, 30 periods. (b) Dependence of tunneling time $\tau_{\text{tun}}(u_i)$ calculated from experiments on the basis of resonance tunneling model [13] (u_i is the voltage between the centers of the neighboring wells).

Fig. 3 relate to SL since the theoretical model [13] allows one to determine the resonant tunneling characteristics from the experiments in the case). The data observed are a proof that resonant tunneling can be used for selective depopulation of the levels leading to a population inversion in WQWS [4,5].

3.2. Space charge mismatching of resonant levels in electric fields

The vertical transport measurements reveal a large variety of the effects that extremely change the resonant tunneling behavior and the electrical properties of the WQWS under electrical fields [4,5,12–15]. As can be seen from Fig. 3 the current–voltage characteristics of the long-period superlattices have a very complicated stepwise form with a set of plateaus having a shallow periodic structure. These peculiarities have been investigated in detail by now and, as shown, are caused by the carrier redistribution in the structures leading to a mismatch of the resonant levels, breaking the system down to the areas with different electric field strength (electric-field domains) [4,12–15]. Effects of the same type were observed equally in the WQWS [4,5]. The main result from the experiments is that the carrier redistribution leads to blocking the transformation of the resonant tunneling structure in an electric field and, at the same time, results in a mismatching of the energy levels involved in the resonance. These effects can be overcome but merit detailed consideration.

4. Optical intersubband absorption and amplification in multiple wide-quantum-well-structures

The estimates of the resonant tunneling rates and the relaxation life-times of carriers in the lowest states look suitable and combined with the large oscillator strength of optical intersubband transitions in wide-well structures make the laser problem in such systems fairly attractive. According to the analytically obtained expression [5]

$$\alpha_{12}^{\text{inter}} = \frac{512}{9} \frac{e^2(\varepsilon_F - \varepsilon_1)\Gamma}{mc\eta\omega d_w^3 [e(\varepsilon_2 - \varepsilon_1 - \hbar\omega)^2 + \Gamma^2]}. \quad (3)$$

the intersubband optical absorption coefficient for transitions between the first excited and the ground subbands in GaAs/Al_{0.3}Ga_{0.7}As structure is of order $\alpha_{12}^{\text{inter}} = 4 \times 10^3 \text{ cm}^{-1}$ at a carrier concentration of 10^{16} cm^{-3} ($d_w = 25$ nm, $d_b = 4$ nm, $\Gamma = 5$ meV, $\varepsilon_2 - \varepsilon_1 = 22$ meV, $T = 4.2$ K). Here ε_F is the Fermi energy, Γ the level width, c the light velocity, η the refractive index, ω the optical transition frequency, e and m the electron charge and the effective mass, respectively. Taking into account the estimates for free-carrier absorption at the same parameters (less than 10 cm^{-1}) [5] and for phonon absorption (less than 10 cm^{-1}) [16] in the same spectral range one can conclude that even the very small population inversion in the lowest subbands may result in a drastic increase of the intensity of emission due to transitions between these states. Combined with the fact that the tunneling heating effect under the condition $\tau_{32}^{\text{opt}} \cong \tau_{31}^{\text{opt}} \ll \tau_{\text{tun}} < \tau_{21}^{\text{imp}}$ cannot play an essential role, the above discussion appears to be stimulating for laser investigations not only in WQWS but also in multiple WQWS as well.

5. Conclusion

Theoretical estimates and the results of vertical transport and optical investigations in GaAs/AlGaAs wide-quantum-well structures, allow us to estimate the optical properties as well as the carrier relaxation lifetime and resonant tunneling rate characteristics for the structure revealing the possibility of intersubband population inversion and far-infrared stimulated

emission between the first excited and the ground states in the system.

Acknowledgements

This work is supported by RFFI (99-02-17437) and FTNS Program (97-1048).

References

- [1] J.H. Smet, C.G. Fonstad, Q. Hu, *J. Appl. Phys.* 79 (1996) 9305.
- [2] Bin Xu, Qing Hu, M.R. Melloch, *Appl. Phys. Lett.* 71 (1997) 440.
- [3] M. Rochat et al., *Appl. Phys. Lett.* 73 (1998) 3724.
- [4] V.N. Murzin, Yu.A. Mityagin, *Uspekhi Fizicheskikh Nauk* 169 (1999) 464.
- [5] V.N. Murzin, Yu.A. Mityagin, V.A. Chuenkov, *Izvestiya RAN*, in press.
- [6] W. Heiss et al., *Proceedings of 23 International Conference on Phys. Semicond.* VE 19, 1996 p. 1915.
- [7] R. Ferreira, G. Bastard, *Phys. Rev.* 40 (1989) 1074.
- [8] S.-C. Lee, I. Galbraith, private communication.
- [9] K. Leo et al., *Phys. Rev. B* 42 (1990) 7065.
- [10] S.A. Gurvitz, I. Bar-Joseph, B. Deveaud, *Phys. Rev. B* 43 (1991) 14703.
- [11] A.P. Haberle et al., *Semicond. Sci. Technol.* 9 (1994) 519.
- [12] M. Helm et al., *Phys. Rev. Lett.* 63 (1989) 74.
- [13] Yu.A. Mityagin, V.N. Murzin, *JETP Lett.* 64 (1996) 155.
- [14] B.J. Keay et al., *Phys. Rev. Lett.* 75 (1995) 4098.
- [15] S.H. Kwok et al., *Phys. Rev.* 50 (1994) 2007.
- [16] P.D. Coleman et al., *Submillimeter Waves*, vol. 20, Polytechnic Press, Brooklyn, NJ, 1970, p. 694.



ELSEVIER

Physica E 7 (2000) 63–68

PHYSICA E

www.elsevier.nl/locate/physa

Inter-subband plasmon-emission-based THz Lasers

P. Bakshi *, K. Kempa

Department of Physics, Boston College, Chestnut Hill, MA 02467, USA

Abstract

We have proposed stimulated generation of plasmons (plasma instabilities) as a novel way to generate THz radiation from low-dimensional semiconductor systems. The microcharge oscillations of such plasmons become the source of electromagnetic radiation in the THz range. This plasma-instability-based concept offers distinct advantages as it relies on a collective phenomenon, which is less susceptible to disruption due to higher temperatures and various scattering effects. Also, since the plasmons are created internally and form a (coherent) collective mode of the electron gas itself, there is no need for an external feedback mechanism. A self-consistent calculational scheme shows the feasibility of plasma instabilities in appropriately designed quantum well structures. © 2000 Published by Elsevier Science B.V. All rights reserved.

Keywords: Terahertz emission; Plasma instabilities; Plasmon lasers; Inter-subband plasmons

1. Introduction

There is an increasing interest in and need for compact, coherent and tunable sources of terahertz (THz) radiation, in view of their many possible applications. Neither conventional electronic devices nor lasers have been able to provide sources in this difficult, intermediate frequency range. The conventional electronic devices (transistors, IMPATT diodes, etc.) cannot reach this frequency range due to the so-called impedance limitation [1–4]. While the quantum cascade structures have been extended to THz frequencies, only spontaneous emission has been obtained so far [5,6]. Stimulated generation of plasmons (plasma instabilities) has been proposed by

us as a novel way to generate THz radiation from low-dimensional semiconductor systems [7].¹ The microcharge oscillations of such plasmons can become the source of electromagnetic radiation in the THz range. This mechanism is a robust phenomenon, since the microcharge oscillations are intrinsically coherent. Analogs of this phenomenon are well known in gaseous plasmas [8–10], where plasma instabilities have been studied theoretically and observed experimentally in many situations and have led to device applications [11]. Even high temperatures and various scattering effects cannot easily disrupt these coherent collective oscillations. Since the natural plasma oscillations of the carriers in typical low-dimensional semiconductor systems are in the THz range, we have

* Corresponding author. Fax: +1-617-552-8478.
E-mail address: bakshi@bc.edu (P. Bakshi)

¹ This paper provides a review of our earlier work and a perspective for future work.

systematically investigated the possibility of generating plasma instabilities in several such systems [12–21].

Nonequilibrium plasmas can spontaneously develop *growing* plasma oscillations (plasma instabilities) in many situations [8–10]. This happens because plasmons constitute a natural energy transfer channel in a plasma, and provide an easy way to relax the excess free energy of a nonequilibrium plasma. A sufficiently strong population inversion in the carrier distribution function is needed for this to happen. Such a population inversion can often be achieved by driving a constant current through the plasma. However, in solid-state plasmas the drift velocity required to achieve such a population inversion is prohibitively large, of the order of the Fermi velocity [12–17]. In contrast to the uniform systems [12–17] introducing a periodic density modulation [19] in a high mobility quantum wire leads to a dramatic reduction in the threshold drift velocity required to generate a plasma instability, making this system a suitable candidate for experimental verification of this phenomenon. Bounded plasmas offer distinct advantages [7] and can be employed as active media to generate strong plasma instabilities by selective extraction and injection of carriers [20,21].

Experimentally, radiative decays of plasmons from two-dimensional electron channels [22] and parabolic quantum wells [23] have been observed, emitting radiation in THz regime at low temperature. Emission from coherent (but decaying) plasmon oscillations even at room temperature, and in the presence of bulk doping, on a picosecond time scale has also been observed [24]. These results suggest that plasma oscillations can survive even at room temperature in doped semiconductors. If a plasma instability is generated along the ideas mentioned above, it would then provide the means to *sustain* coherent plasma oscillations and the ensuing radiation. This phenomenon can thus be used for the realization of practical semiconductor THz radiation sources.

From our investigation of plasma instabilities in various systems, we find that quantum well structures (QWS) operating under bias in a nonequilibrium steady state, with appropriate carrier injection and extraction [25,26], may be the best candidates for a realization of this idea. The simplest scenario for the generation of plasma instabilities requires [21]

a three-subband system, with the first and third subband well populated and the second nearly empty (or vice-versa). The essential instability mechanism is the resonant interaction of two plasma modes, due to the up and down depolarization shifted intersubband plasmons, in such a structure [21].

We have developed a fully self-consistent computational scheme for designing such structures. The eigenstates are determined by the Schroedinger–Poisson scheme, the subband populations by rate balance equations, inter-subband transfer rates through a RPA self-energy calculation, and the injection–extraction rates by the transfer matrix for complex energies. The feasibility of plasma instability for the resulting nonequilibrium steady state is examined for each bias, by obtaining the full spectral response in a RPA formalism. The I – V curves, and the domains of instability (as a function of bias) are obtained for any structure. Experimental results on first generation structures confirm our predictions of the dynamic conductance versus bias [25], and (spontaneous) emission frequencies [26]. Population inversion was insufficient to generate a plasma instability in these bulk-doped structures. Preliminary experimental results on the newly designed, second-generation structures, which are remote-doped, show quantitative agreement with our calculation of the current versus bias. Calculations also show that sufficient population inversion can be achieved in such structures to obtain plasma instability, and ensuing THz radiation.

2. Calculations

2.1. Non-equilibrium steady state

We use the Hartree approximation in which one solves self-consistently the Schroedinger equation of the form

$$\left[-\frac{\hbar^2}{2m^*} \frac{d^2}{dz^2} + V_{\text{ext}} + V_{\text{Hartree}} \right] \psi_j(z) = \epsilon_j \psi_j(z) \quad (1)$$

with the Hartree potential given by

$$\frac{d^2}{dz^2} V_{\text{Hartree}} = -\frac{4\pi e^2}{\kappa} \sum_j n_j |\psi_j(z)|^2, \quad (2)$$

n_j being the electron density in the j th sub-band. This calculation provides the energy levels ϵ_j and the cor-

responding wavefunctions $\psi_j(z)$, for the total potential $V_{\text{tot}} = V_{\text{ext}} + V_{\text{Hartree}}$.

2.2. Scattering and transmission rates

We have developed a full RPA formalism, and an efficient computational scheme for calculating the electron–electron scattering rates in quantum wells, which include both single particle (Auger) and collective (plasmon) processes [27,28]. The intersubband scattering rates, $\gamma_{\text{ec}}(j \rightarrow j')$, can be obtained from the imaginary part of the corresponding self-energy (see Refs. [27,28]). These rates depend on the wave functions and energies of Section 2.1.

We similarly obtain electron–phonon rates γ_{LO} due to the dominant LO phonon emission, through essentially evaluating the imaginary part of the self-energy using the unscreened phonon interaction, and assuming the “bulk” (3D) LO phonon dispersion.

The injection and extraction rates α_j and β_j are determined by the transfer matrix method [29]. The complex energy poles of the transmission coefficient, $E_j = E_{rj} - i\Gamma_j/2$, determine [30] the total widths $\Gamma_j = \alpha_j + \beta_j$ of the quasi-bound energy levels E_{rj} . This condition is equivalent to $M_{11}(E_j) = 0$ in terms of the transfer matrix M [23]. The ratio (β_j/α_j) is related to $|M_{21}(E_j)|^2$, and along with Γ_j determines the values of α_j and β_j for any given quantum well structure [29]. We determine the transfer matrix numerically from the shape of the total potential $V_{\text{tot}}(z)$ of Section 2.1

2.3. Balance equations for the subband populations

The subband populations are determined by the rate balance equations

$$\begin{aligned} \frac{dn_i}{dt} = & \alpha_i(N_i^{\text{L}} - n_i) - \beta_i(n_i - N_i^{\text{R}}) \\ & - \sum_j [\gamma^{\text{ec}}(i \rightarrow j) + \gamma^{\text{LO}}(i \rightarrow j)]n_i \\ & + \sum_j [\gamma^{\text{ec}}(j \rightarrow i) + \gamma^{\text{LO}}(j \rightarrow i)]n_j, \end{aligned} \quad (3)$$

where n_i is the population (sheet density) of the i th level in the active region, obtained by summing the distribution function over the in-plane momenta. α_i are the injection and β_i the extraction rates, N_i^{L} and

N_i^{R} the populations of the regions to the left and right of the active region. These rate equations are based on integrating over the in-plane momentum transfers, and are adequate at low temperatures. More detailed equations in terms of the distribution functions become necessary at higher temperatures.

In the steady state, $dn_i/dt = 0$. The α and β terms provide the net particle flow through each level, and the net current in the steady state is given by

$$J = e \sum_i \alpha_i(N_i^{\text{L}} - n_i) = e \sum_i \beta_i(n_i - N_i^{\text{R}}). \quad (4)$$

The γ^{ec} and γ^{LO} terms represent all the interlevel transitions through the scatterings. The matrix elements entering γ^{ec} and γ^{LO} coefficients, as well as the rates α and β depend on the nonequilibrium steady-state energies and wave functions (Section 2.1), which in turn, through the Hartree potential, depend on the subband populations n_j obtained from the balance equations. The self-consistent solution is obtained by iteration until the input n_j in Eq. (2) and the solutions n_j of Eq. (3) agree.

2.4. Response calculations

We obtain the electromagnetic response using our RPA formalism for inhomogeneous systems [25,31,32]. The energies and wave functions from the nonequilibrium steady-state calculations (Section 2.1) are used to obtain the density response of the entire system. In general, one can write the induced density as

$$\delta p(z; q_{\perp}, \omega) = \int dz' \chi_0(z, z'; q_{\perp}, \omega) V_{\text{T}}(z'; q_{\perp}, \omega), \quad (5)$$

where $\chi_0(z, z'; q_{\perp}, \omega)$ is the single-electron susceptibility given by

$$\begin{aligned} \chi_0(z, z'; q_{\perp}, \omega) = & 2 \sum_{\mathbf{k}_{\perp}} \sum_j \sum_{j'} \frac{f_{\varepsilon} - f_{\varepsilon'}}{\varepsilon - \varepsilon' + \hbar\omega} \\ & \times \psi_j(z) \psi_{j'}(z) \psi_j(z') \psi_{j'}(z'), \end{aligned} \quad (6)$$

where V_{T} is the total dynamic potential for an external perturbation at frequency ω , and includes the dynamical Hartree term. Also, $f_{\varepsilon} = f_{j, \mathbf{k}_{\perp}}$, $\varepsilon = \varepsilon_j + k_{\perp}^2/2m^*$, $\varepsilon' = \varepsilon_{j'} + (\mathbf{k}_{\perp} + \mathbf{q}_{\perp})^2/2m^*$, where \mathbf{k}_{\perp} is the electron wave vector and \mathbf{q}_{\perp} the plasmon wave vector in the perpendicular ($x - y$) plane.

The density response becomes infinite at the plasma mode frequency. Our formalism [31,32], with proper analytical continuation [32–34], allows us to study all relevant roots of the response functions in the entire complex frequency plane. Characteristics of the unstable plasma modes are determined, with imaginary part of the frequency $\gamma = \text{Im } \omega$ (when positive) representing the growth rate.

Our present calculations show that there is very little dispersion of ω with q_{\perp} , the in-plane wave vector of the plasmon, and that the growth rate γ diminishes rapidly with q_{\perp} . Thus the mode arising from “vertical transitions” ($q_{\perp} = 0$) will dominate, providing frequency coherence in spite of the in-plane electron energy continuum.

3. Comments

3.1. Plasma wave growth saturation

If, for a given applied bias, the condition for a plasma instability (i.e. $\gamma > 0$) is satisfied, the induced plasma wave density amplitude begins to grow exponentially in time, with time constant $1/\gamma$. The growing energy in the induced charge oscillation can be viewed to be due to a growing plasmon population. The larger this population becomes, the greater is the rate of creation of additional plasmons; this is why the *plasma instability* phenomenon can be described as the *stimulated generation of plasmons*.

As the instability develops, the induced plasma wave density grows sufficiently strong to affect the population inversion, through the inter-level transitions which generate the plasmons. The reduced population inversion diminishes the instantaneous growth rate γ , (Section 2.4), even as the mode amplitude keeps growing. Finally, this continuing wave-particle interaction makes $\gamma \rightarrow 0$. In this new steady state, the plasma mode has grown to a saturation level, providing a significant plasmon population in the system. Determination of the properties of this new steady state will require enlargement of the self-consistency scheme to include the full ramifications of this large amplitude coherent charge oscillation for various collision rates, and for the previous nonequilibrium steady state. If this amplitude is large enough, quasi-energy sidebands appear at multiples

of the plasma wave frequency in this new dynamic nonequilibrium oscillating state.

3.2. Radiation emission characteristics

The plasma charge oscillations in the bounded system are dipole active, and directly emit narrow width electromagnetic radiation at the same frequency. The power level of the electromagnetic radiation is related to the dipole strength, and thus to the plasma mode amplitude at saturation, determined through various loss mechanisms and the onset of nonlinear effects (Section 3.1).

Even when the conditions for a plasma instability are not met, the emissive plasma modes of the nonequilibrium plasma will couple to and decay into electromagnetic radiation at the frequencies of the plasma modes. The line widths, however, will be broader, reflecting the uncompensated loss mechanisms. The power levels will also be much lower, since there is no build-up of energy from the driving current.

3.3. Other experimental signatures

Even though our goal is the direct observation of plasma instabilities through the ensuing emission of THz radiation (Section 3.2), we can also obtain indirect evidence for an instability, through the identification and detection of specific signatures in the transport and emission characteristics. It is necessary to make these observations in small steps of the applied bias, since the predicted domains of plasma instability cover narrow bias ranges.

For some biases, the plasma instability occurs, but being damped out due to larger (intrinsic) dissipative losses in the given structure. If we do not take into account these damping effects, we would have $\gamma > 0$. However, the effective growth rate is only $\gamma_{\text{eff}} = \gamma - \nu$, where ν represents all the damping effects. So, in a regime where $\gamma > \nu$, plasma wave growth and saturation will occur, with strong radiation (Sections 3.1 and 3.2). On the other hand, if $\gamma < \nu$, the mode is effectively damped with $\nu_{\text{eff}} = \nu - \gamma$. (1) This effect will show up as line narrowing for the range of biases where $\gamma > 0$. Other neighboring lines which are due to real-emissive modes ($\gamma = 0$), will show a larger broadening corresponding to ν . (2) We find that the mode

frequency does not vary much in the range of instability. This is a general feature of the plasma instability phenomenon arising from the merging of two modes in the range of biases where the instability occurs. Thus $d\omega/dV_b$ will show a dip in that range of biases (3). Since the plasmon generation during an instability opens a new channel for transport, we can expect an enhanced current in the range of biases where an instability occurs. This can be seen in the I – V characteristics.

3.4. Concluding remarks

As shown in Ref. [26], radiation emission has been observed, in agreement with the theoretical calculation, and shows that a *population inversion has been achieved* in the previously designed structures. The next generation of structures, with no doping in the active region, should considerably reduce the broadening seen in the emission. The measured current in such structures is much larger, in agreement with the theoretical calculations. Our present self-consistent calculations show instabilities with γ upto 0.5 meV. Enhancing the growth rate to over 1 meV by varying the structure parameters should be sufficient to generate observable plasma instabilities in clean samples. The plasma instability under consideration has shown itself to be both ubiquitous and robust. Thus we expect that our designed structures will lead to a “proof of principle” for the phenomenon of plasma instability, to be detected through an abrupt increase in the current as a function of the bias potential in the measured I – V curve, by line narrowing in emission, by reduction of $d\omega/dV_b$ in the range of biases where instability occurs and finally, for a sufficiently strong plasma instability, through the ensuing electromagnetic radiation.

Acknowledgements

This work has been supported by USARO grant no. DAAG55-97-1-0021.

References

- [1] M. Tschernitz, J. Freyer, *Electron. Lett.* 31 (1995) 582.
- [2] M.E. Elta et al., *IEEE Electron Dev. Lett.* EDL-6 (1980) 694.
- [3] H. Eisele, G.C. Haddad, *IEEE Microwave Guided Wave Lett.* 5 (1995) 385.
- [4] H. Eisele, G.I. Haddad, *Electron. Lett.* 30 (1994) 1950.
- [5] M. Rochat, J. Faist, M. Beck, U. Oesterle, M. Illegems, *Appl. Phys. Lett.* 73 (1998) 3724.
- [6] B. Xu, Q. Hu, M. Melloch, *Appl. Phys. Lett.* 71 (1997) 440.
- [7] P. Bakshi, K. Kempa, *Superlattices Microstruct.* 17 (1995) 363.
- [8] A.B. Mikhailovskii, in: *Theory of Plasma Instabilities*, Vol. 1, Consultant Bureau, New York, 1974.
- [9] N. Krall, A. Trivelpiece, in: *Principles of Plasma Physics*, McGraw-Hill, New York, 1973.
- [10] S. Ichimaru, *Basic Principles of Plasma Physics – a Statistical Approach*, Benjamin/Cummings, Reading, MA, 1973.
- [11] A. Gover, A. Yariv, in: S.F. Jacobs et al. (Eds.), *Novel Sources of Coherent Radiation*, Addison-Wesley, London, 1978, p. 197.
- [12] P. Bakshi, J. Cen, K. Kempa, *J. Appl. Phys.* 64 (1988) 2243.
- [13] J. Cen, K. Kempa, P. Bakshi, *Phys. Rev. B* 38 (1988) 10051.
- [14] P. Bakshi, J. Cen, K. Kempa, *Solid State Commun.* 76 (1990) 835.
- [15] J. Cen, K. Kempa, P. Bakshi, *Solid State Commun.* 78 (1991) 433.
- [16] K. Kempa, P. Bakshi, J. Cen, H. Xie, *Phys. Rev. B* 43 (1991) 9273.
- [17] H. Xie, K. Kempa, P. Bakshi, *J. Appl. Phys.* 72 (1992) 4767.
- [18] K. Kempa, P. Bakshi, H. Xie, W.L. Schaich, *Phys. Rev. B* 47 (1993) 4532.
- [19] K. Kempa, P. Bakshi, H. Xie, *Phys. Rev. B* 48 (1993) 9158.
- [20] K. Kempa, P. Bakshi, E. Gornik, *Phys. Rev. B* 54 (1996) 8231.
- [21] P. Bakshi, K. Kempa, in: J. Clark, P. Panat (Eds.), *Condensed Matter Theories*, Vol. 12, Nova Science Publishers, New York, 1997, p. 399.
- [22] M. Vossebuerger, H.G. Roskos, F. Wolter, C. Waschke, H. Kurz, K. Hirakawa, I. Wilke, K. Yamanaka, *J. Opt. Soc. Am. B* 13 (1996) 1045.
- [23] K.D. Maranowski, A.C. Gossard, K. Unterrainer, E. Gornik, *Appl. Phys. Lett.* 69 (1996) 3522, and further experimental work in Vienna.
- [24] R. Kersting, K. Unterrainer, G. Strasser, H.F. Kauffmann, E. Gornik, *Phys. Rev. Lett.* 79 (1997) 3038.
- [25] K. Kempa, P. Bakshi, C.G. Du, G. Feng, A. Scorupsky, G. Strasser, C. Rauch, K. Unterrainer, E. Gornik, *J. Appl. Phys.* 85 (1999) 3708.
- [26] P. Bakshi, K. Kempa, A. Scorupsky, C.G. Du, G. Feng, R. Zobl, G. Strasser, C. Rauch, Ch. Pacher, K. Unterrainer, E. Gornik, *Appl. Phys. Lett.* 75 (1999) 1685.
- [27] K. Kempa, P. Bakshi, J. Engelbrecht, Y. Zhou, *Intersubband electron transitions due to electron–electron interactions in quantum well structures*, submitted.
- [28] K. Kempa, P. Bakshi, in these Proceedings (ITQW '99), *Physica E* 7 (2000).
- [29] C.G. Du, P. Bakshi, K. Kempa, *Injection and extraction rates for quantum well structures through the transfer matrix at complex energies*, to be published.

- [30] E. Merzbacher, Quantum Mechanics, 2nd Edition, Wiley, New York (Chapter 7) 1970.
- [31] K. Kempa, D.A. Broido, C. Beckwith, J. Cen, Phys. Rev. B 40 (1989) 8385.
- [32] K.D. Tsuei, E.W. Plummer, A. Liebsch, E. Phelke, K. Kempa, P. Bakshi, Surf. Sci. 247 (1991) 302.
- [33] P. Bakshi, K. Kempa, Phys. Rev. B 40 (1989) 3433.
- [34] K.D. Tsuei, E.W. Plummer, A. Liebsch, K. Kempa, P. Bakshi, Phys. Rev. Lett. 64 (1990) 44.



ELSEVIER

Physica E 7 (2000) 69–75

PHYSICA E

www.elsevier.nl/locate/physce

Interband cascade lasers: progress and challenges

Rui Q. Yang *, J.D. Bruno, J.L. Bradshaw, J.T. Pham, D.E. Wortman

US Army Research Laboratory, 2800 Powder Mill Road, Adelphi, MD 20783-1197, USA

Abstract

Interband cascade (IC) lasers take advantage of the broken-gap alignment in type-II InAs/Ga(In)Sb heterostructures to reuse electrons for sequential photon emissions from successively connected active regions; thus, they represent a new class of mid-IR light sources. In this work, we describe recent progress in IC lasers at emission wavelengths of 3.8–3.9 μm ; these lasers have exhibited significantly higher differential quantum efficiencies and peak powers than previously reported. These InAs/GaInSb type-II IC lasers were able to operate at temperatures up to 217 K, which is higher than the previous record (182 K) for an IC laser at this wavelength. We observed from several devices at temperatures above 80 K a slope greater than 750 mW/A per facet, corresponding to a differential external quantum efficiency exceeding 460%. A peak optical output power exceeding 4 W/facet and peak power efficiency of $\sim 7\%$ were observed from a device at 80 K. Also discussed are challenging issues related to the reduction of threshold currents and power dissipation to further advance this new class of lasers. © 2000 Elsevier Science B.V. All rights reserved.

Keywords: Antimonides; Diode lasers; Type-II quantum wells; Interband cascade lasers

The concept of interband cascade (IC) lasers, utilizing optical transitions between the conduction and valence bands in a staircase of Sb-based type-II quantum-well (QW) structures, was first proposed in 1994 by Yang, then at the University of Toronto, Canada [1]. IC lasers reuse injected electrons by taking advantage of the broken band-gap alignment in Sb-based type-II QWs to form cascade stages, leading to a quantum efficiency greater than the conventional limit of unity, similar to the intersubband quantum cascade (QC) laser [2]. Furthermore, IC laser designs

can circumvent the fast phonon scattering loss in intersubband QC lasers and suppress Auger recombination through band-structure engineering. Mid-IR IC lasers based on InAs/GaInSb type-II QWs are promising for obtaining high output powers.

Following the initial success in the characterization and the observation of mid-IR electroluminescence of type-II IC structures [3,4], IC lasers were first demonstrated in early 1997 [5]. Shortly thereafter, type-II IC lasers were improved, with encouraging results: ~ 0.5 W/facet peak power, relatively high quantum efficiency ($> 200\%$), and near-room-temperature operation at 3.5 μm [6–10]. However, since then, little new progress was made until this year.

Recently, we have made significant advances [11,12] in the development of type-II IC lasers in

* Corresponding author. Tel.: 001-301-394-5752; fax: +1-301-394-2103.

E-mail address: ARL07@clark.net (R.Q. Yang)

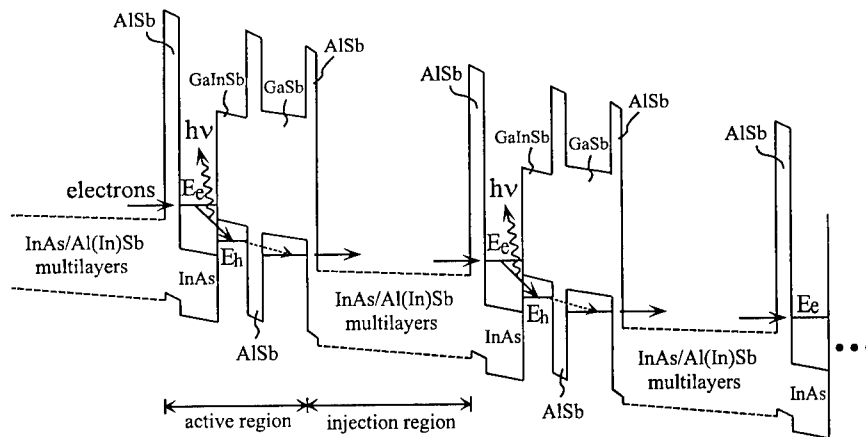


Fig. 1. Schematic band diagram of a type-II interband cascade laser structure.

terms of record-high differential quantum efficiency, peak output power, operating temperature, peak power conversion efficiency, and reproducibility. Here, we present this recent progress and discuss issues that need to be addressed in order to further advance this new class of lasers.

The IC laser structure we have studied has 23 repeated periods of active regions separated by n-type injection regions, as shown in Fig. 1, that form the waveguide core. Two n-type InAs/AlSb superlattices were used as top and bottom optical waveguide cladding layers, with thicknesses of ~ 1.6 and $2 \mu\text{m}$, respectively. Each active region comprises coupled QWs, stacked sequentially with 23 \AA AlSb, 25 \AA InAs, 36 \AA $\text{Ga}_{0.7}\text{In}_{0.3}\text{Sb}$, 15 \AA AlSb, and 58 \AA GaSb layers. Digitally graded InAs/Al(In)Sb multi-QWs were employed for the injection region, which serves both as a collector for the preceding active region and as an emitter for the following one. Under a forward bias, electrons are injected from the emitter into the E_c electron level, which is in the band-gap region of the adjacent GaInSb layer. Since the electrons at the E_c level are effectively blocked from directly tunneling out by the GaInSb, AlSb, and GaSb layers, they tend to relax to the E_h hole state in the adjacent valence-band QW, which results in the emission of photons. Electrons in the E_h state cross the thin AlSb barrier and GaSb layers by tunneling and scattering into the conduction band of the next injection region because of a strong spatial interband coupling (a unique feature of type-II heterostructures). They are

then ready for the next interband transition, which leads to sequential photon emission with a quantum efficiency greater than the conventional limit of unity.

Based on the same IC structure design, three laser samples were grown in a Varian Gen-II MBE system on two different vendor GaSb substrates. We used double-crystal X-ray diffraction (DCXRD) spectra to evaluate the quality of the epitaxial layers. For all three laser samples, we observed many sharp satellite peaks in the DCXRD spectra, indicating their high structural quality.

After the growth, samples were processed into broad-area gain-guided and mesa-stripe devices with several different widths. Au/AuGe and Au/Ti electrical contacts were deposited onto the top n-type layer and p-type substrate, respectively. Laser bars were cleaved to cavities from ~ 0.5 to 1.5 mm long with both facets left uncoated. The laser bars were glued with silver epoxy, epilayer side up, onto a chip carrier (made of Au-coated Al-alloy) and devices were wire-bonded to the pin-outs. The chip carrier was then mounted on the temperature-controlled cold finger of an optical cryostat. The optical output power was measured with a cooled InSb detector together with a lock-in amplifier calibrated by a thermopile power meter when the average power was high. For most measurements, neutral density filters were used to avoid saturating the detector.

Devices made from all three samples, labeled ICL1 (vendor A), ICL2 (vendor B), and ICL3 (vendor B),

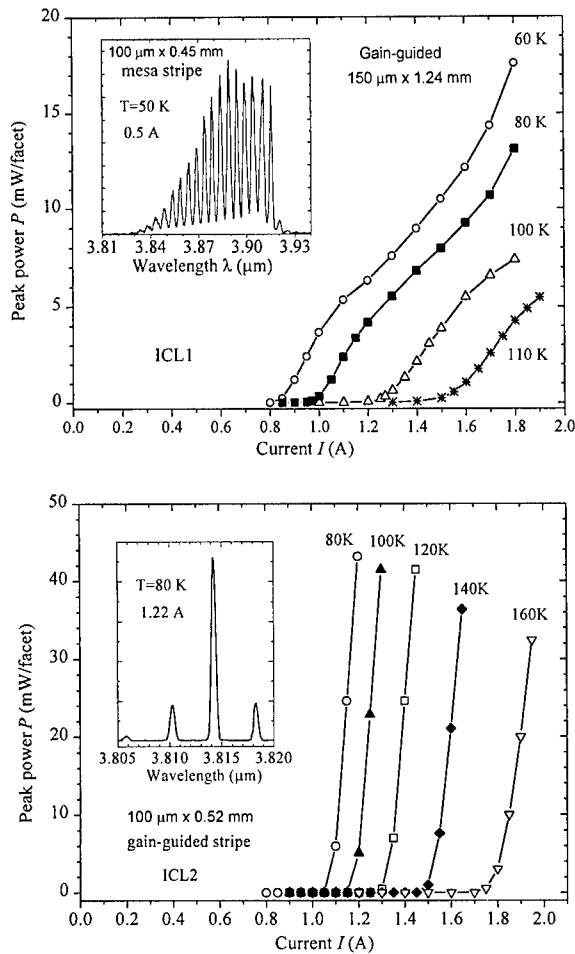


Fig. 2. L - I curves and spectra of lasers made from ICL1 (top) and ICL2 (bottom) pumped with 100 ns pulses at 1 kHz. Note that the spectrum for ICL1 is from a mesa-etched laser bar and for ICL2 is from a gain-guided device.

lased in the wavelength range from 3.8 to 3.9 μm. The lasing wavelengths agree well with the designed wavelength (~ 3.9 μm at 80 K) considering some uncertainty in the growth rates, the sample uniformity, and Stark shifts in the active regions. The lasing spectra were obtained by focusing the optical output beam into a $\frac{2}{3}$ m monochrometer. Two high-resolution spectra of lasers from ICL1 and ICL2 (given in the insets of Fig. 2) show multiple longitudinal modes with adjacent separations (~ 50 and 40 Å, respectively) that are in good agreement with the calculated values for the Fabry–Perot cavity.

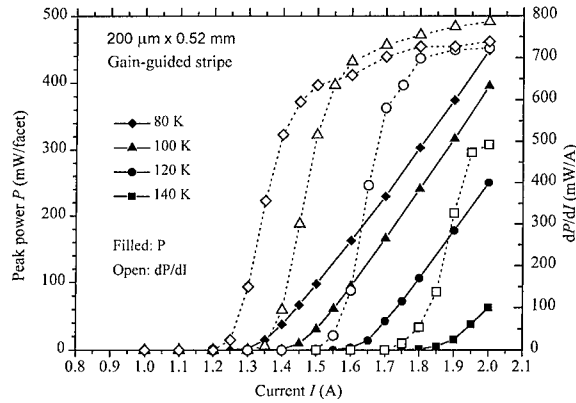


Fig. 3. Peak output power and differential external quantum efficiency versus injection current for a gain-guided (0.2 mm \times 0.52 mm) laser device with 100 ns pulses at 1 kHz.

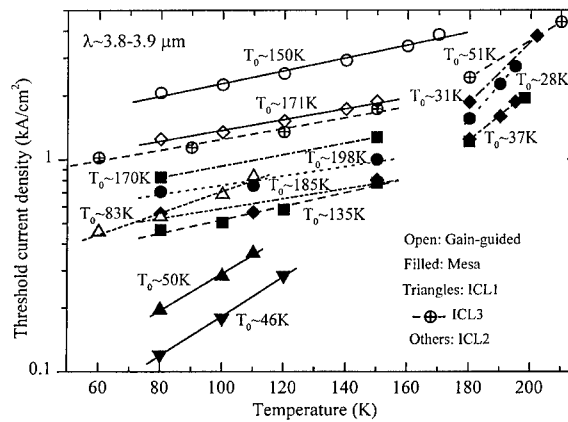


Fig. 4. Threshold current density versus the heat-sink temperature. The cavity length varies from 0.45 to 1.2 mm. The stripe width is 50 μm (down triangle), 150 μm (open triangle), 0.2 mm (diamond), and 0.1 mm (others).

Lasers made from different vendor substrates exhibited different general characteristics. In Fig. 2, peak powers observed from gain-guided devices fabricated from ICL1 and ICL2 are shown as functions of injection current. Lasers from ICL1 have much lower threshold current densities. They were able to operate at duty cycles as large as 20–30% (20–30 μs at 10 kHz). The threshold current densities of lasers from ICL1 were found to be relatively insensitive to the cavity length. This suggests that the optical loss in lasers from ICL1 was quite significant, consistent with the relatively low slope efficiencies (dP/dI) observed. Devices from ICL2 have higher threshold current densities and consequently were electrically

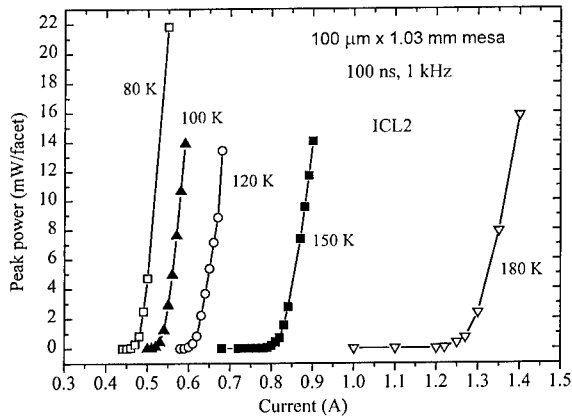


Fig. 5. Peak output power versus injection current for a mesa stripe ($0.1 \text{ mm} \times 1.03 \text{ mm}$) laser device with 100 ns pulses at 1 kHz.

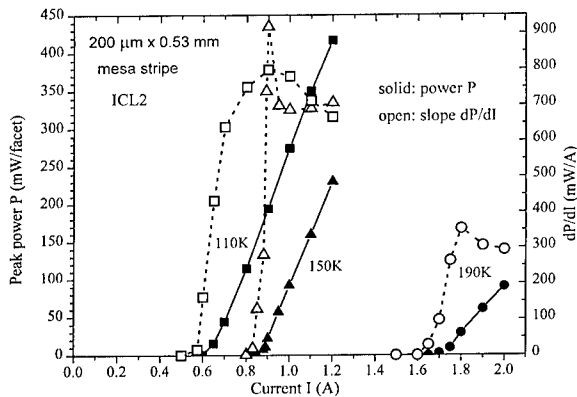


Fig. 6. Peak output power (filled) and differential external quantum efficiency (open) versus injection current for a mesa stripe ($0.2 \text{ mm} \times 0.53 \text{ mm}$) laser from ICL2 with 100 ns (200 ns at 110 K) pulses at 1 kHz.

pumped with (usually) 100 ns current pulses at repetition rates of 1–10 kHz. These lasers had larger slopes, i.e. a higher differential external quantum efficiency (DEQE). The slope efficiency was found to be weakly dependent on the temperature and to increase with the current. The weak dependence of slope efficiency on temperature was also observed from previously reported IC lasers emitting at ~ 3 and $3.5 \mu\text{m}$ [6,9]. However, with the devices reported here, we achieved significantly higher slope efficiencies. In Fig. 2, slopes greater than 350 mW/A were observed in the device from ICL2; these slopes correspond to DEQE exceeding 215% assuming two identical facets, indicating more than two photons generated

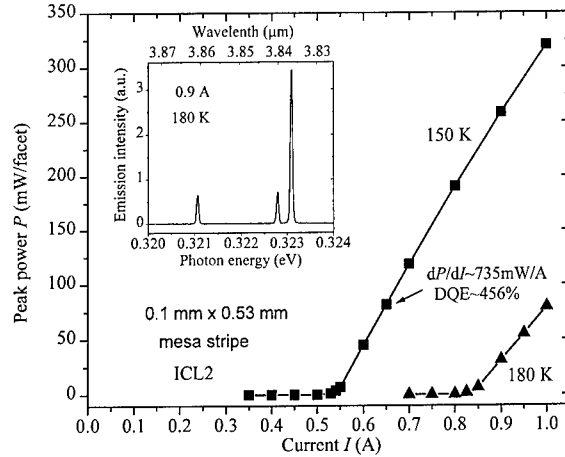


Fig. 7. Peak output power versus injection current for a mesa stripe ($0.1 \text{ mm} \times 0.53 \text{ mm}$) laser from ICL2 under 100 ns pulses at 1 kHz. The inset is a high-resolution lasing spectrum at 0.9 A.

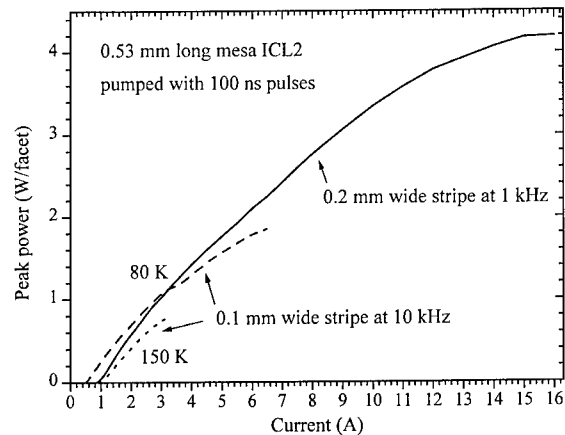


Fig. 8. The peak power observed from two mesa lasers (0.2 mm and 0.1 mm wide stripes) from ICL2 pumped by large pulsed currents at 1 and 10 kHz, respectively.

by each injected electron. However, the threshold current density was high ($> 2 \text{ kA/cm}^2$) for this device, due partially to significant current spreading. For a $200 \mu\text{m}$ wide gain-guided device from ICL2, the relative reduction of current spreading lowered the threshold current density, and a higher peak power was obtained, as shown in Fig. 3. Also, a slope efficiency as high as 786 mW/A was observed from this $200 \mu\text{m}$ wide laser at 100 K, corresponding to a DEQE of 484% ($\sim 21\%$ per stage). This value indicates an average of ~ 4.8 photons generated by

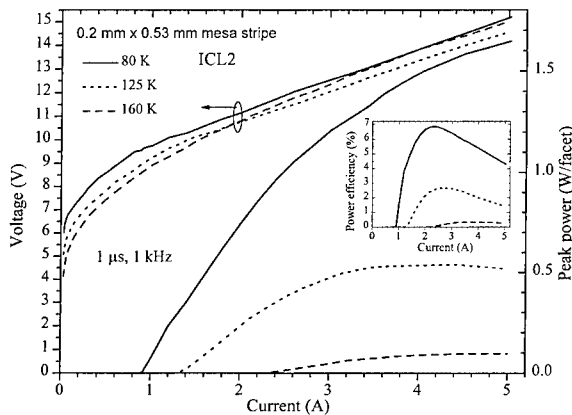


Fig. 9. Voltage and peak output power versus injection current for a mesa stripe ($0.2 \text{ mm} \times 0.53 \text{ mm}$) laser shown in Fig. 8 from ICL2 with $1 \mu\text{s}$ pulses at 1 kHz . The inset shows the power efficiency.

each injected electron, which is more than twice any value reported previously [6–10]. The peak power, operating temperature, and DEQE were limited by the maximum current (2 A) of the HP8114A pulser used in the experiment.

Using mesa structures to suppress the current spreading, the threshold current was remarkably reduced compared with gain-guided devices, as shown in Fig. 4. However, the threshold current density in the mesa-stripe varies significantly from device to device. One possible reason is that the mesas are formed by wet chemical etching down to the substrate, yielding uncontrolled rough surfaces and large fluctuations in surface recombination. In devices from ICL2 and ICL3, the threshold current densities are much larger than the previously reported value ($\sim 100 \text{ A/cm}^2$) [7,8], but rise gradually with increasing temperature when $T < 180 \text{ K}$. This results in large characteristic temperatures T_0 and may indicate the dominance of Shockley–Read recombination in this temperature range, perhaps due to high concentrations of various material defects in ICL2 and ICL3 that may be associated with substrate imperfections. When $T \geq 180 \text{ K}$, the threshold current increases rapidly with temperature, resulting in a small T_0 ($\sim 30 \text{ K}$ for ICL2 and $\sim 51 \text{ K}$ for ICL3). One possible reason for a small T_0 is that the actual device temperature is substantially higher than the heat-sink temperature in this range due to more joule heating.

Among devices from ICL2, several 1 mm long devices were able to lase at temperatures up to 210 K , which is considerably higher than the previous record (182 K) for an IC laser [8] at this wavelength. A $100 \mu\text{m}$ wide and 1.03 mm long device has the lowest threshold current density among them, and its slope is nearly insensitive to temperature from 80 to 180 K , as shown in Fig. 5. The threshold current densities of devices from ICL3 are the largest in comparison to devices from ICL1 and ICL2; however, lasers from ICL3 could be operated at the temperatures up to 217 K , the highest among any III–V diode lasers at the same wavelength. The observed DEQE from ICL3 was not high (in contrast to ICL2), probably because ICL3 had a larger leakage current. More characterization on ICL3 remains to be done.

Lasers made from ICL2 exhibited a significantly higher slope efficiency and peak power. A slope efficiency dP/dI of $\sim 800 \text{ mW/A}$ was observed from one facet of a $200 \mu\text{m}$ wide mesa device at 110 K , as shown in Fig. 6, corresponding to a DEQE of nearly 500% (if the two facets were identical), which is more than twice the largest previously reported value (214%) [8]. While there were some fluctuations in the measurements at 150 K for pulsed operation, the average of six dP/dI values was $\sim 740 \text{ mW/A/facet}$, and was nearly unchanged when the temperature was raised from 110 to 150 K . Even at 190 K , this laser displayed a slope of 354 mW/A/facet (DEQE $\sim 220\%$). For a $100 \mu\text{m}$ wide mesa laser, a high slope efficiency dP/dI of 735 mW/A (DEQE $\sim 456\%$) was also observed from one facet at 150 K , as shown in Fig. 7. At the higher temperature of 180 K , the slope efficiency was decreased, but was still as high as 483 mW/A/facet (DEQE $\sim 300\%$) in this laser (its lasing spectrum is also shown in Fig. 7).

When a high peak current pulser became available, further measurements were taken. A peak output exceeding 4 W/facet was observed from a $200 \mu\text{m}$ wide mesa laser (pumped with 100 ns pulses at 1 kHz) at 80 K , as shown in Fig. 8. This represents, to the best of our knowledge, the highest peak power yet reported among mid-IR semiconductor diode lasers at emission wavelengths beyond $3 \mu\text{m}$. A $100 \mu\text{m}$ wide mesa laser also exhibited a peak output of 1.85 W/facet at 80 K when driven with 6.5 A current pulses (100 ns at 10 kHz). Even at 150 K , a peak power as large as 0.73 W/facet was observed at 3 A , and

higher output power is still possible since we did not drive it to saturation to avoid over heating the device.

Fig. 9 shows current–voltage (I – V) and peak-power (L – I) characteristics of the 200 μm wide mesa-stripe laser (shown in Fig. 8) operated with 1 μs pulses at 1 kHz. In comparison to operation with 100 ns pulses at 80 K, the threshold current did not change, and the slope efficiency was slightly higher ($> 700 \text{ mW/A}$) at a relatively low current and then decreased at large currents due to more heating. The I – V curves clearly exhibited the sharp turn-on characteristics of a laser diode. The threshold voltage was 9.7 V at 80 K and increased with the temperature, lower than the reported value ($\sim 14 \text{ V}$) [8] for a previous 23-stage IC laser. At the threshold, the excess voltage [10] at 80 K was about 30% of the minimal bias voltage required for lasing, indicating that the applied voltage was utilized efficiently. The threshold voltage for other lasers from ICL2 with different sizes was found to be nearly consistent (9.5–10 V at 80 K). The operating voltage was increased slowly with the current after lasing because of its small differential resistance ($< 2 \Omega$). From the I – V and L – I curves in Fig. 9, we obtained the power (wall-plug) efficiency (output optical power/input electrical power) by assuming two identical facets; the power efficiency is shown in the inset and has a record-high peak of $\sim 7\%$ for the mid-IR ($> 3.7 \mu\text{m}$). This value is comparable to or even higher than the best values obtained in optically pumped mid-IR lasers [13,14] and intersubband QC lasers [15,16].

Note that the power values reported here have been corrected only for the transmission coefficients of the collection optics ($f/2.6$) and not corrected for beam divergence. If the spatial divergence of the laser beam were taken into account, the actual emitted powers, DEQE and peak power efficiencies would be considerably higher.

In contrast to previously reported IC lasers [6,8–10], most of our lasers were able to operate repeatedly without suffering from damage at high currents ($> 10 \text{ kA/cm}^2$). The threshold current density is significantly higher than theoretical predictions [17–20] and even larger than the lowest values reported from previous lasers. The possible reasons could be associated with high concentrations of defects and surface recombinations. The different characteristics of ICL1, ICL2, and ICL3 may be associated with variations in

growth conditions and substrate type. The quality of commercially available GaSb substrates is considerably less than that of GaAs and InP substrates, and the variations in quality could significantly affect the growth of Sb-based lasers and thus their performance. The improvement of GaSb substrates and their polishing and cleaning will likely affect the performance of these mid-IR lasers.

High joule heat generated by large currents is detrimental to laser performance and to achieving cw operation. One way to reduce this heat is by making small-area ridge lasers. In this regard, appropriate processing and passivation techniques of Sb-based heterostructure devices need to be developed so that leakage current and losses due to etched surfaces can be minimized. Another way is to improve device heat sinking. The lasers reported here were mounted on a chip carrier made of Al-alloy, which is not a good heat conductor, especially at low temperatures. Heat sinking can be significantly improved by the use of Cu instead of Al-alloy. In an initial attempt to reduce device heating, mesa-stripe devices (60–110 μm wide) made from ICL1 were mounted on a thin copper mount attached to the copper cold finger, but again epi-side up. These devices lased in cw at temperatures up to the cold-finger temperature of 70 K. Further experimentation with these and other devices is currently underway. We anticipate that mounting devices epilayer side down will efficiently reduce heat accumulation in the active region, making cw operation more viable at elevated temperatures.

In summary, IC lasers were demonstrated with a DEQE exceeding 460%, large peak power ($> 4 \text{ W/facet}$), peak power efficiency of $\sim 7\%$, and maximum operating temperature of 217 K. Certainly, these type-II IC lasers are still far from optimum. Considering that the Sb-based material devices and the fabrication techniques have been much less investigated than GaAs- and InP-based compound semiconductor systems, these preliminary results of IC lasers are especially stimulating. There are many aspects that can be improved to significantly advance IC laser performance. Furthermore, numerous variations of type-II cascade laser structures with other materials and their combinations are possible [21], which should provide flexibility and opportunities. It is also relatively straightforward to create type-II IC lasers with multicolor capability by stacking multiple

distinct active regions in series, which is desirable in many gas-sensing applications. With continued and extensive efforts to improve the laser design, material quality, fabrication, and deepen our understanding of the underlying physics, Sb-based type-II interband cascade lasers promise to meet the application requirements in many areas.

Acknowledgements

This work was performed while one of the authors (Yang) held a National Research Council/ARL Senior Research Associateship and was supported in part by US Air Force Research Laboratory, Kirtland AFB New Mexico.

References

- [1] R.Q. Yang, Seventh International Conference on Superlattices, Microstructures and Microdevices, Banff, Canada, August, 1994; *Superlattices Microstruct.* 17 (1995) 77.
- [2] J. Faist, F. Capasso, D.L. Sivco, C. Sirtori, A.L. Hutchinson, A.Y. Cho, *Science* 264 (1994) 553.
- [3] R.Q. Yang, C.-H. Lin, P.C. Chang, S.J. Murry, D. Zhang, S.S. Pei, S.R. Kurtz, S.N.G. Chu, F. Ren, *Electron. Lett.* 32 (1996) 1621.
- [4] R.Q. Yang, C.-H. Lin, S.J. Murry, S.S. Pei, H.C. Liu, M. Buchanan, E. Dupont, *Appl. Phys. Lett.* 70 (1997) 2013.
- [5] C.-H. Lin, R.Q. Yang, D. Zhang, S.J. Murry, S.S. Pei, A.A. Allerna, S.R. Kurtz, *Electron. Lett.* 33 (1997) 598.
- [6] C.L. Felix, W.W. Bewley, I. Vurgaftman, J.R. Meyer, D. Zhang, C.-H. Lin, R.Q. Yang, S.S. Pei, *IEEE Photon. Technol. Lett.* 9 (1997) 1433.
- [7] R.Q. Yang, B.H. Yang, D. Zhang, C.-H. Lin, S.J. Murry, H. Wu, S.S. Pei, *Appl. Phys. Lett.* 71 (1997) 2409.
- [8] B.H. Yang, D. Zhang, R.Q. Yang, C.-H. Lin, S.J. Murry, S.S. Pei, *Appl. Phys. Lett.* 72 (1998) 2220.
- [9] L.J. Olafsen, E.H. Aifer, I. Vurgaftman, W.W. Bewley, C.L. Felix, J.R. Meyer, D. Zhang, C.-H. Lin, S.S. Pei, *Appl. Phys. Lett.* 72 (1998) 2370.
- [10] R.Q. Yang, *Microelectron. J.* 30 (1999) 1043.
- [11] R.Q. Yang, J.D. Bruno, J.L. Bradshaw, J.T. Pham, D.E. Wortman, *Electron. Lett.* 35 (1999) 1254.
- [12] J.L. Bradshaw, R.Q. Yang, J.D. Bruno, J.T. Pham, D.E. Wortman, *Appl. Phys. Lett.* 75 (1999) 2362.
- [13] H.Q. Le, C.H. Lin, S.J. Murry, R.Q. Yang, S.S. Pei, *IEEE J. Quantum Electron.* 34 (1998) 1016.
- [14] H.Q. Le, G.W. Turner, J.R. Ochoa, *IEEE Photon. Technol. Lett.* 10 (1998) 663.
- [15] J. Faist, A. Tredicucci, F. Capasso, C. Sirtori, D.L. Sivco, J.N. Baillargeon, A.L. Hutchinson, A.Y. Cho, *IEEE J. Quantum Electron.* 34 (1998) 336.
- [16] C. Gmachl, A. Tredicucci, F. Capasso, A.L. Hutchinson, D.L. Sivco, J.N. Baillargeon, A.Y. Cho, *Appl. Phys. Lett.* 72 (1998) 3130.
- [17] J.R. Meyer, I. Vurgaftman, R.Q. Yang, L.R. Ram-Mohan, *Electron. Lett.* 32 (1996) 45.
- [18] I. Vurgaftman, J.R. Meyer, L.R. Ram-Mohan, *IEEE Photon. Technol. Lett.* 9 (1997) 170.
- [19] Y.-M. Mu, R.Q. Yang, *J. Appl. Phys.* 84 (1998) 5357.
- [20] R.Q. Yang, Y.-M. Mu, *Proc. SPIE* 3628 (1999) 104.
- [21] R.Q. Yang, in: M. Helm (Ed.), *Long Wavelength Infrared Emitters Based on Quantum Wells and Superlattices*, Gordon and Breach, Singapore, 1999 (Chapter 2), pp. 13–64.

Antimonide interband and intersubband mid-IR and terahertz lasers

I. Vurgaftman^{a,*}, J.R. Meyer^a, L.R. Ram-Mohan^{a,b}

^aNaval Research Laboratory, Code 5613 Washington, DC 20375, USA

^bWorcester Polytechnic Institute, Worcester, MA 01609, USA

Abstract

Antimonide semiconductor lasers for the mid-infrared and terahertz spectral regions are considered. It is predicted that optically pumped interband type-II lasers will be advantageous at long wavelengths, out to $\lambda \approx 100 \mu\text{m}$. In the mid-IR, antimonide intersubband lasers should have higher gains and longer carrier lifetimes than InGaAs/InAlAs quantum cascade lasers, and hence have prospects for room-temperature cw operation. Spin-polarized antimonide intersubband lasers with applied magnetic fields are projected to display room-temperature cw emission at $\lambda = 16 \mu\text{m}$. © 2000 Elsevier Science B.V. All rights reserved.

Keywords: Optically pumped interband “W” lasers; Antimonide quantum cascade lasers; Spin-polarized devices

Quantum cascade lasers (QCLs) based on intersubband transitions in InGaAs/InAlAs quantum wells have operated at room temperature in pulsed mode over a broad wavelength range between 5 and 12 μm [1]. The maximum reported cw operating temperature is 175 K. Pulsed operation has been achieved for emission out to $\lambda = 17 \mu\text{m}$, which is the longest for any III–V semiconductor laser [2].

However, contrary to the common perception that intersubband lasers are the only viable option at longer wavelengths, it will be seen below that interband type-II lasers with “W” active regions [3] may in fact be advantageous in the long-wavelength limit. Using optical pumping, cw operation was recently observed up to 210 K at $\lambda = 5.9 \mu\text{m}$ and to $T_{\text{max}} = 130 \text{ K}$

at 7.1 μm [4]. Furthermore, near-room-temperature (290 K) cw operation was demonstrated at 3.0 μm , and type-II W diodes emitting at 3.3 μm recently lased in pulsed mode at 300 K [5]. In this paper, we theoretically investigate several new classes of antimonide-based lasers, namely terahertz emitters ($\lambda > 25 \mu\text{m}$), quantum cascade lasers, and “spin-polarized” intersubband lasers in a magnetic field.

At THz wavelengths, optical-phonon relaxation in a QCL becomes energetically forbidden. The lifetime is instead dominated by non-activated electron–electron processes that scatter two upper-subband carriers almost elastically to the lower subband with opposite momentum transfers [6]. Hence beyond a certain point, decreasing the temperature may no longer increase the gain to the point where lasing can be achieved. However, Auger processes in an

* Corresponding author. Fax: +1-202-404-8613.

E-mail address: vurgaftm@aphrodite.nrl.navy.mil (I. Vurgaftman)

interband laser remain thermally activated when the gap is small, so that one can always attain a longer lifetime and more gain by going to sufficiently low T .

A successful THz laser must also minimize the internal loss due to free-carrier absorption, which for both interband and intersubband devices scales roughly as λ^2 in the long-wavelength limit. It follows that for a given temperature, the threshold carrier density required for lasing will be much higher than in the mid-IR. While the maximum attainable population inversion in a THz QCL may be severely limited by electron–electron scattering [7], in the interband laser we can again increase the injected carrier density by lowering the temperature to lengthen the lifetime. By employing optical pumping and thereby eliminating the need for doped cladding layers, we can also remove a substantial component of the internal loss.

We first consider a type-II W structure designed to emit at $\lambda_0 = 27 \mu\text{m}$: 58-Å InAs/30-Å $\text{Ga}_{0.75}\text{In}_{0.25}\text{Sb}$ /50-Å InAs/100-Å $\text{GaAs}_{0.25}\text{Sb}_{0.75}$, which is strain compensated for growth on an InAs substrate. The band structure, wave functions, and optical matrix elements were modeled using an 8-band finite-element kp algorithm. Intervalence transitions, which usually dominate the internal loss and Auger recombination in type-II lasers, are negligible here because the second hole subband is 240 meV below the valence band maximum. The nonradiative lifetime in should therefore be dominated by CCCH and CHHH Auger processes with final states in the same subband. Using an InAs substrate as the bottom cladding layer and a diamond heat sink as the top cladding [8], a 7- μm -thick active region results in an optical confinement factor of 67%.

At the calculated threshold carrier density under typical low-temperature operating conditions, second-order perturbation theory for TE-polarized photons and the appropriate nonparabolic dispersion yields a net cavity loss of 16 cm^{-1} if the scattering is assumed to be dominated by interface roughness [9]. However, more conservative values (nearly twice as high) from the classical Drude expression were employed in obtaining the present simulation results. Fig. 1 shows calculated pulsed and cw light–light curves for the 27 μm W emitter pumped by a 10.6 μm CO_2 laser. Although pulsed operation is predicted only up to 60 K and cw to 35 K, output powers exceeding 100 mW appear feasible.

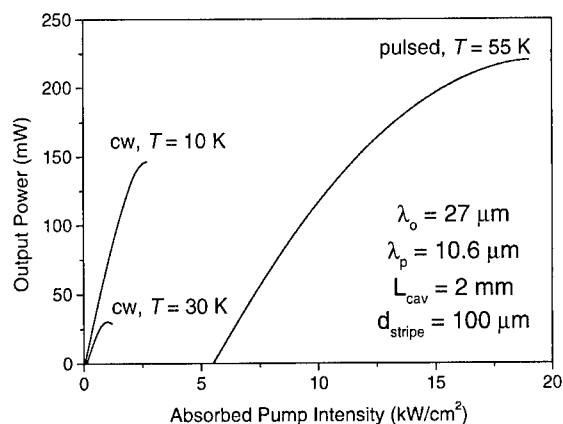


Fig. 1. Calculated pulsed and cw output powers versus absorbed pump intensity for a type-II W laser emitting at $\lambda_0 = 27 \mu\text{m}$. Results are shown for several different heatsink temperatures.

At wavelengths beyond the phonon bands in the 30–50 μm range, phonon-assisted recombination processes involving thermally excited electrons and holes in W lasers must be taken into account [10] (an analogous process for intersubband relaxation exists). To illustrate, we consider a W laser designed for emission at $\lambda_0 = 60 \mu\text{m}$: 72.5 Å InAs/30 Å GaSb /62.5 Å InAs/65 Å AlSb , which is strain-compensated for growth on a GaSb substrate. Two $\text{InAs}_{0.09}\text{Sb}_{0.91}$ regions sandwich the active region to enhance the optical confinement. The simulations predict a maximum pulsed operating temperature of 10 K, which is limited primarily by the activated phonon-assisted process above that temperature. At 10 K, the derived carrier lifetime at the threshold carrier density of $\approx 3 \times 10^{10} \text{ cm}^{-2}$ is 250 ps, which is far longer than the $\approx 1 \text{ ps}$ value that has been calculated for electron–electron scattering in an intersubband cascade laser [7]. It is estimated that pulsed lasing at 4 K should be achievable in W lasers to wavelengths as long as $\approx 100 \mu\text{m}$. Whereas optical pumping has been assumed and the projected operating temperatures are quite low, the fundamental limitations that impose these requirements may make it even more difficult for electrically pumped intersubband structures to lase at very long wavelengths.

At somewhat shorter λ in the 8–12- μm atmospheric window, intersubband cascade lasers may be preferable to interband devices. Although to date all QCLs have employed InGaAs/InAlAs or GaAs/AlGaAs [11,12] quantum wells, antimonide-based

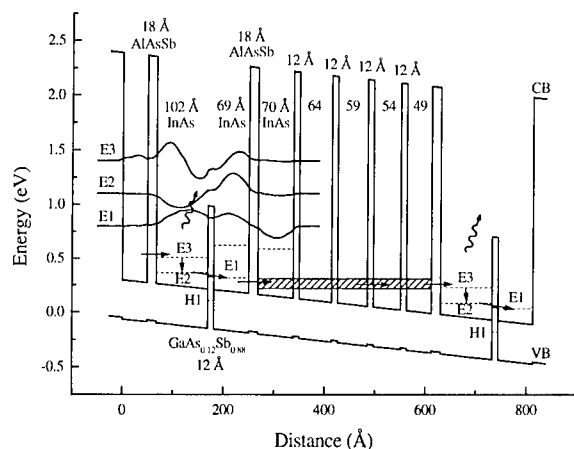


Fig. 2. Conduction-band and valence-band profiles, quantized energy levels, and selected wave functions for one period of a vertical-transition InAs/AlAs_{0.16}Sb_{0.84} QCL ($\lambda = 8.8 \mu\text{m}$). The applied electric field is 50 kV/cm, and each constituent layer is lattice matched to the InAs substrate.

intersubband lasers with InAs quantum wells may ultimately yield lower thresholds and higher cw operating temperatures. This is because a much smaller effective mass results in both a decreased rate of optical-phonon emission and an increase in the dipole matrix element [13], since wider wells are required to achieve the same intersubband transition energy.

The band diagram for an InAs/AlAsSb quantum cascade laser designed for operation at $\lambda = 8.8 \mu\text{m}$ is shown in Fig. 2. This structure is based on a “vertical” transition, in which the initial and final states are confined primarily to the same well. The lower lasing subband E2 empties on a time scale of a few hundred fs, since the separation between E2 and E1 is tuned to one InAs-like optical-phonon energy. The lifetime for the upper lasing subband E3 is calculated to be $\tau_3 = 1.0 \text{ ps}$ when the strong nonparabolicity of the conduction band is taken into account. A large dipole matrix element of 46 Å then yields a pulsed threshold current density of only 1.2 kA/cm^2 at 300 K, which compares to the best results of $> 3 \text{ kA/cm}^2$ for InGaAs/InAlAs QCLs [14,15] if the same optical loss is taken for both devices. The lower threshold may lead to room-temperature cw operation.

From the fundamental scientific standpoint, it is interesting to consider how the intersubband lasing properties are altered by the application of a growth-direction magnetic field [16]. Since the

electrons then execute cyclotron orbits in the plane, quantum confinement is effectively imposed along the other two axes and the subbands come to resemble a system of zero-dimensional quantum boxes. The fully quantized energy levels are split into two separate Landau ladders corresponding approximately to the two spin states, although, strictly speaking, spin is not a good quantum number when interband mixing is included.

Since spin relaxation times [17,18] tend to be longer than the other relevant time scales for intersubband lasers, it may be possible to selectively create a population inversion and lasing in one of the two spin systems while the other remains inert. This may be accomplished most easily in narrow-gap type-II antimonides, since the small electron mass (large g -factor) and strong interband interactions lead to much larger energy splittings between the two systems. The threshold is decreased by populating only half the states in the upper subband and tuning the discrete Landau levels so as to avoid phonon resonances. With Lorentzian broadening (a line width of 2.5 meV), we estimate that it may be possible to increase the phonon relaxation lifetime of the upper lasing level to $\approx 5 \text{ ps}$.

The four-well structure whose spin-split Landau levels are shown in Fig. 3 is designed for intersubband optical pumping, although interband pumping can also be envisioned [19]. The two InAs wells on the left (in which wave functions for the E1 and E4 electron subbands are concentrated) are strongly coupled, as are the two wells on the right (containing E2 and E3). We employ the numbering convention described in Ref. [19] and assume an applied magnetic field of $B = 10 \text{ T}$. Optical pumping by a CO₂ laser at $\lambda = 11.4 \mu\text{m}$ with an input beam polarized linearly along the growth axis produces electron intersubband transitions from the $-1'$ E1 level to the $-1'$ E3 level ($\Delta n = 0$ selection rule). On the other hand, the unprimed spin system is largely unaffected because the $0 \text{ E1} \rightarrow 0 \text{ E3}$ transition energy is out of resonance by more than 7 meV. The lasing transition $-1' \text{ E3} \rightarrow -1' \text{ E2}$ is vertical, and thus has a large dipole matrix element of 37 Å . From the $-1' \text{ E2}$ Landau level, electrons are quickly emptied back into E1, which has a Landau level that lies lower by one InAs-like optical-phonon energy. Note that neither the E4 electron states nor the H1 hole states enter directly into the pumping, lasing, or lower-level emptying for

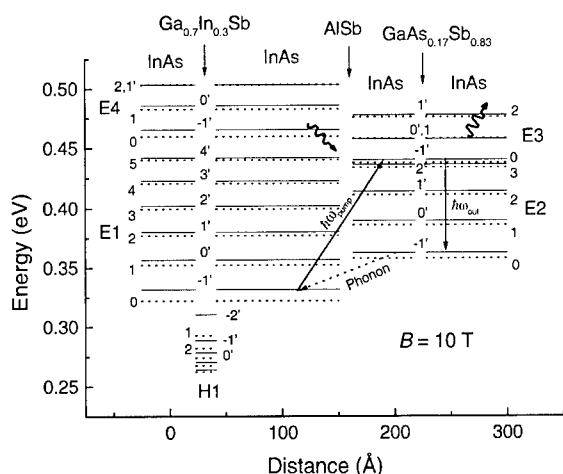


Fig. 3. Fully quantized Landau levels for one period of a spin-polarized intersubband laser structure designed for intersubband optical pumping with an applied magnetic field of $B = 10$ T. Primed (solid) and unprimed (dashed) levels are the two spin systems, which do not interact in lowest order. From left to right, the InAs wells have thicknesses: 48, 110, 55, and 72 Å; the AlSb barrier is 12 Å, the $\text{Ga}_{0.7}\text{In}_{0.3}\text{Sb}$ layer is 18.5 Å, and the $\text{GaAs}_{0.17}\text{Sb}_{0.83}$ layer is 10 Å thick. Neighboring periods are separated by thick AlSb barriers, and the entire structure is undoped.

this design. However, H1 provides interband mixing to enhance the level splitting and also a source of thermally generated electrons for pumping to E3. The leftmost InAs containing E4 spatially extends the E1 wave function to enhance its overlap with the H1 hole wave function.

A simulation of the spin-polarized intersubband laser of Fig. 3 leads to the prediction of room-temperature cw operation with an absorbed pump intensity of 8 kW/cm^2 and an output power of up to 1 W at the lasing wavelength of $16 \mu\text{m}$. This far surpasses the optimal performance of electrically pumped antimonide or InGaAs QCLs with $B = 0$ at the same wavelength.

Acknowledgements

This work was supported by the Office of Naval Research. We thank Quantum Semiconductor Algorithms for use of the finite-element band structure software.

References

- [1] J. Faist, C. Sirtori, F. Capasso, D.L. Sivco, J.N. Baillargeon, A.L. Hutchinson, A.Y. Cho, *IEEE Phot. Tech. Lett.* 10 (1998) 1100.
- [2] A. Tredicucci, C. Gmachl, F. Capasso, D.L. Sivco, A.L. Hutchinson, A.Y. Cho, *Appl. Phys. Lett.* 74 (1999) 638.
- [3] J.R. Meyer, C.A. Hoffman, F.J. Bartoli, L.R. Ram-Mohan, *Appl. Phys. Lett.* 67 (1995) 757.
- [4] C.L. Felix, W.W. Bewley, L.J. Olafsen, D.W. Stokes, E.H. Aifer, I. Vurgaftman, J.R. Meyer, M.J. Yang, *IEEE Photon. Technol. Lett.* 11 (1999) 964.
- [5] H. Lee, L.J. Olafsen, R.J. Menna, W.W. Bewley, R.U. Martinelli, I. Vurgaftman, D.Z. Garbuzov, C.L. Felix, M. Maiorov, J.R. Meyer, J.C. Connolly, A.R. Sugg, G.H. Olsen, *Electron Lett.* 36 (1999) 1743.
- [6] J.H. Smet, C.G. Fonstad, Q. Hu, *J. Appl. Phys.* 79 (1996) 9305.
- [7] P. Hyldgaard, J.W. Wilkins, *Phys. Rev. B* 53 (1996) 6889.
- [8] W.W. Bewley, C.L. Felix, I. Vurgaftman, D.W. Stokes, E.H. Aifer, L.J. Olafsen, J.R. Meyer, M.J. Yang, B.V. Shanabrook, H. Lee, R.U. Martinelli, A.R. Sugg, *Appl. Phys. Lett.* 74 (1999) 1075.
- [9] I. Vurgaftman, J.R. Meyer, *Phys. Rev. B* 60 (1999) 14277.
- [10] I. Vurgaftman, J.R. Meyer, *Appl. Phys. Lett.* 75 (1999) 899.
- [11] O. Gauthier-Lafaye, P. Boucaud, F.H. Julien, S. Sauvage, S. Cabaret, J.-M. Lourtioz, V. Thierry-Mieg, R. Planel, *Appl. Phys. Lett.* 71 (1997) 3619.
- [12] C. Sirtori, P. Kruck, S. Barbieri, P. Collot, J. Nagle, M. Beck, J. Faist, U. Oesterle, *Appl. Phys. Lett.* 73 (1998) 3486.
- [13] I. Vurgaftman, J.R. Meyer, F.H. Julien, L.R. Ram-Mohan, *Appl. Phys. Lett.* 73 (1998) 711.
- [14] S. Slivken, A. Matlis, A. Rybaltowski, Z. Wu, M. Razeghi, *Appl. Phys. Lett.* 74 (1999) 2758.
- [15] A. Tredicucci, F. Capasso, C. Gmachl, D.L. Sivco, A.L. Hutchinson, A.Y. Cho, *Appl. Phys. Lett.* 73 (1998) 2101.
- [16] Y. Arakawa, K. Vahala, A. Yariv, K. Lau, *Appl. Phys. Lett.* 47 (1985) 1142.
- [17] J.M. Kikkawa, I.P. Smorchkova, N. Samarth, D.D. Awschalom, *Science* 277 (1997) 1284.
- [18] J.M. Kikkawa, D.D. Awschalom, *Phys. Rev. Lett.* 80 (1998) 4313.
- [19] I. Vurgaftman, J.R. Meyer, L.R. Ram-Mohan, *J. Appl. Phys.* 86 (1999) 4734.



ELSEVIER

Physica E 7 (2000) 80–83

PHYSICA E

www.elsevier.nl/locate/physe

Mid-infrared intersubband electroluminescence in InAs/GaSb/AlSb type-II cascade structures

K. Ohtani *, H. Ohno

*Laboratory for Electronic Intelligent Systems, Research Institute of Electrical Communication, Tohoku University,
Katahira 2-1-1, Aoba-ku, Sendai 980-8577, Japan*

Abstract

Mid-infrared intersubband light-emitting diodes based on InAs/GaSb/AlSb type-II cascade structure have been investigated. The observed emission energy is in good agreement with calculation based on the multi-band $k \cdot p$ theory. In contrast to interband cascade structures, dominant polarization of the emitted light is perpendicular to the quantum well layers. Structure dependence of intersubband electroluminescence is also presented. © 2000 Published by Elsevier Science B.V. All rights reserved.

Keywords: Electroluminescence; Type-II InAs/GaSb/AlSb cascade structure; Antimonides

1. Introduction

Using type-I quantum well (QW) structures, high-performance lasers utilizing intersubband transitions with a wide spectrum range were realized [1,2]. The wavelength range (3.4–17 μm) covered by such lasers includes the atmospheric windows important for gas sensing and environment monitoring. Recently, high-power continuous-wave (CW) operation (~ 5 and ~ 8 μm , ~ 200 mW/facet at 80 K) was reported with high quantum efficiency due to the carrier recycling called quantum cascading [3,4]. However, so far no room-temperature CW operation has been

reported presumably because of the severe sample heating due to the fast polar optical phonon scattering. Type-II InAs/GaSb interband cascade lasers (ICL), proposed by Yang [5] and demonstrated by Lin et al. [6], utilizes interband transition to suppress the polar optical phonon scattering, while retaining the carrier recycling by the unique band alignment of InAs/GaSb heterojunction. Very recently, ICL with external efficiency $> 450\%$ has been reported [7].

Recent theoretical appraisal [8,9] of InAs/GaSb/AlSb type-II *intersubband* light emitter proposed earlier [10,11], small polar optical phonon scattering rate due to the small effective mass of InAs offers advantages over type-I intersubband light emitters. The type-II InAs/GaSb structure blocks electrons injected into the excited state in the InAs QW by the adjacent GaSb band gap as in the InAs/GaSb

* Corresponding author. Tel./fax: +81-22-217-5555.

E-mail addresses: keita@rice.tohoku.ac.jp (K. Ohtani), ohno@rice.tohoku.ac.jp (H. Ohno)

ICL, reducing the leakage current path present in type-I intersubband lasers. The injected electrons can be extracted efficiently from the ground state after intersubband transition by interband tunneling through the InAs/GaSb broken gap heterojunction. Also the InAs/AlSb heterostructure has a wide range of tunability of intersubband transition energy because of the larger conduction band offset (~ 1.35 eV) [12] compared to that of the GaInAs/AlInAs system (~ 0.5 eV). Theoretical calculations indicate that optical gain of type-II intersubband laser is more than 50% higher than that of type-I [9] and the calculated threshold current can be as low as 750 A/cm^2 at 300 K [8]. Since this value is a factor of 4 lower than the theoretical prediction for the $5 \mu\text{m}$ type-I InGaAs/AlInAs intersubband lasers [8], it is a strong candidate for achieving room-temperature CW intersubband laser operation. Recently, we reported the first observation of intersubband electroluminescence in InAs/GaSb/AlSb type-II quantum cascade structures [13]. Here we report the characteristics of intersubband electroluminescence, especially the structure dependence of intersubband electroluminescence.

2. Experimental

The intersubband quantum cascade structures (IS-BQC) were grown by molecular beam epitaxy system equipped with a compound As cell and a Sb cracker cell on undoped InAs (100) substrates. After growth of 700 nm Si-doped ($3 \times 10^{17} \text{ cm}^{-3}$) n-type InAs as a bottom contact layer, 10 periods of injector structures and active layers were grown. The injector structure consisted of digitally graded InAs/AlSb superlattices in which the InAs layers were Si-doped to $n = 2 \times 10^{17} \text{ cm}^{-3}$. The active layer consisted of an InAs/GaSb coupled QW which was made of 10 ML AlSb barrier, X ML InAs quantum well, Y ML GaSb quantum well and 5 ML AlSb barrier. To investigate the structure dependence of intersubband electroluminescence, four samples ((A) $X = 30$ ML, $Y = 25$ ML (B) $X = 33$ ML, $Y = 25$ ML (C) $X = 26$ ML, $Y = 25$ ML (D) $X = 33$ ML, $Y = 40$ ML) were grown. After growth of the injector/active layer structures, 200 nm Si-doped ($3 \times 10^{17} \text{ cm}^{-3}$) InAs layer was grown as a top contact layer.

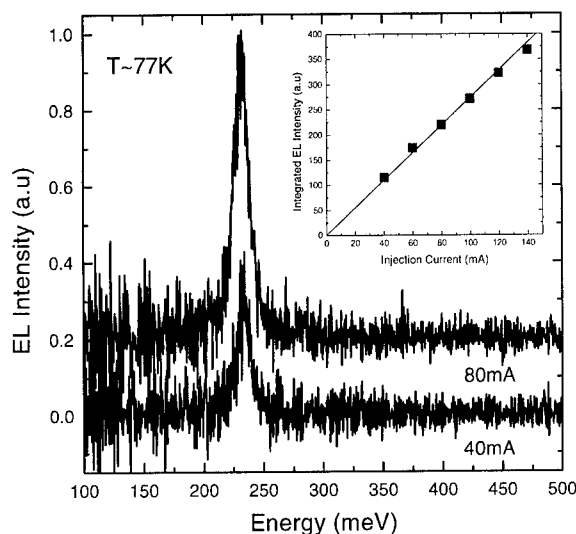


Fig. 1. Electroluminescence spectra at ~ 77 K for injection current of 40 and 80 mA (sample (A)). Inset: the integrated electroluminescence intensity against injection current.

Grown sample was processed into $300 \mu\text{m} \times 300 \mu\text{m}$ mesa structures by wet etching and photolithography. Non-alloyed Cr/Au ohmic contacts were deposited on both top and bottom contact layers. Sample edge was then polished 45° wedge for light emission. The electroluminescence measurement was performed with FT-IR spectrometer using lock-in detection technique [14]. A polarizer was inserted in the optical path to verify the polarization of the emission. Current pulse at 15 kHz with duty cycle of 50% was used for electroluminescence measurements.

3. Results and discussion

Fig. 1 shows the electroluminescence spectra of sample (A) at ~ 77 K under two different current biasing conditions. An emission peak was observed at 233 meV, corresponding to the wavelength of $5.6 \mu\text{m}$ with full-width at half-maximum (FWHM) being ~ 14 meV. The emission energy is in close agreement with the transition energy (218 meV) between E1 and E2 of InAs QW calculated using a multi-band $k \cdot p$ theory [15]. The inset of Fig. 1 shows the integrated electroluminescence intensity as a function of injection current at ~ 77 K, where a linear relationship was observed, which is consistent with a spontaneous emission process with a constant emission energy.

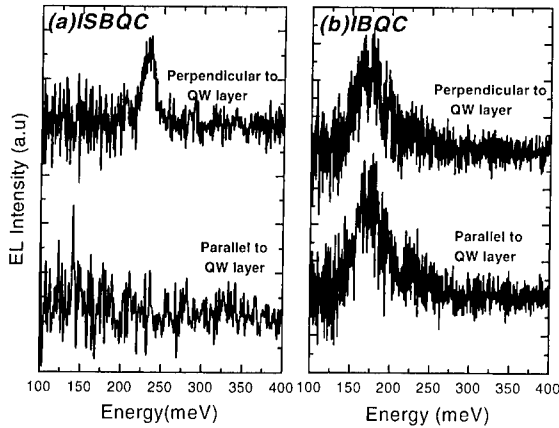


Fig. 2. (a). Polarized intersubband electroluminescence spectra at ~ 77 K for injection current of 80 mA. (b) Polarized interband electroluminescence spectra at ~ 77 K for same injection current.

Fig. 2(a) and (b) show polarization resolved electroluminescence spectra; light polarized perpendicular or parallel to the quantum well layer. As shown in Fig. 2(a), the spectrum of intersubband cascade structure (sample (A)) is polarized perpendicular to the layer, which shows that the light emission is indeed from the intersubband optical transition. Fig. 2(b) shows the same measurements of an interband cascade structure (IBQC) (InAs 4.8 nm and GaSb 12 nm), collected from 45° wedge. The intensity of the two polarizations was almost the same and is in sharp contrast to the intersubband spectra. The selection rule derived from the multi-band $k \cdot p$ theory shows that the polarization characteristic to the intersubband transition is preserved in a low band-gap semiconductor such as InAs, where band mixing is appreciable, as long as the energy separation of E1 and E2 is small compared to the band gap [15,16]. This was verified by absorption measurements in AlSb/InAs/AlSb QWs [16]. Although the calculation based on the multi-band $k \cdot p$ theory shows that the light hole component in E1 state of the InAs well in sample A (AlSb/InAs/GaSb/AlSb) increases by a factor of 2 compared to a single AlSb/InAs/AlSb QW, the ratio of polarization perpendicular to the QW layer and parallel to the QW layer remains below the error level of the present experimental setup.

Fig. 3(a) and (b) show the structure dependence of intersubband electroluminescence spectra under

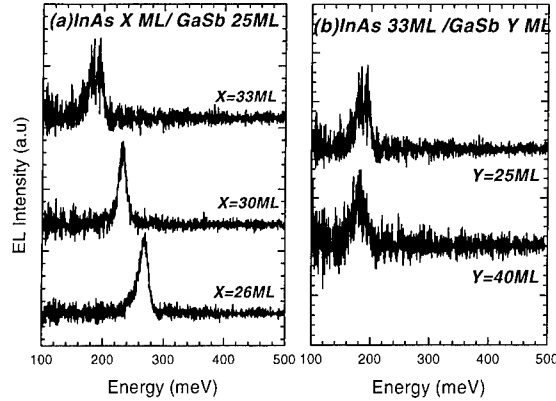


Fig. 3. (a). InAs well width dependence of intersubband electroluminescence ($X = 30$ ML (sample (A)), $X = 33$ ML (sample (B)), $X = 26$ ML (sample (C))) at ~ 77 K. (b) GaSb well width dependence of intersubband electroluminescence ($Y = 25$ ML (sample (B)), $Y = 40$ ML (sample (D))) at ~ 77 K.

the same injection current (80 mA) at ~ 77 K. The InAs well width dependence of electroluminescence is shown in Fig. 3(a). By decreasing the InAs well width, the emission peak energy shifts to the higher energy, because of the increase in the transition energy between the first excited state and the ground state. On the other hand, the GaSb well width does not change the emission peak energy as shown in Fig. 3(b). These experimental results are again consistent with the observed emission being due to the intersubband optical transition in InAs QW. The temperature dependence of intersubband electroluminescence shows that the emission peak shifts to lower energy and the spectrum becomes slightly broader (by a factor of 1.5 between ~ 77 and 300 K) as temperature increases. Typical full-width at half-maximum (FWHM) of an ISBQC sample at ~ 77 K is in the range of 15–25 meV and spectrum shape is nearly symmetric, whereas the IBQC samples show asymmetric and broader FWHM (35–60 meV).

4. Conclusion

We have investigated the electroluminescence characteristics of type-II InAs/GaSb/AlSb intersubband light-emitting diodes. The observed emission energies were in good agreement with the results of a multi-band $k \cdot p$ calculation. The spectrum was polar-

ized perpendicular to QW layer, whereas the intensity of perpendicular and horizontal polarization was almost the same for the interband cascade structures. This electroluminescence polarization as well as the InAs and GaSb well widths dependence establish that the luminescence is from the intersubband optical transition in InAs QW.

Acknowledgements

The authors thank Y. Ohno, H.C. Liu and T. Dietl for helpful discussions. This work was partly supported by a Grant-in-Aid for Scientific Research (A) (No. 11355012) from the Ministry of Education, Science, Sports and Culture, Japan and by 'Research for the Future Program' from the Japan Society for the promotion of Science (JSPS-RFTF 97P00202).

References

- [1] J. Faist, F. Capasso, D.L. Sivco, A.L. Hutchinson, A.Y. Cho, *Science* 264 (1994) 553.
- [2] F. Capasso, J. Faist, C. Sirtori, A.Y. Cho, *Solid State Commun.* 102 (1997) 231.
- [3] J. Faist, A. Tredicucci, F. Capasso, C. Sirtori, D.L. Sivco, J.N. Baillargeon, A.L. Hutchinson, A.Y. Cho, *IEEE J. Quantum Electron.* 34 (1998) 336.
- [4] C. Gmachl, A. Tredicucci, F. Capasso, A.L. Hutchinson, D.L. Sivco, J.N. Baillargeon, A.Y. Cho, *Appl. Phys. Lett.* 72 (1998) 3130.
- [5] R.Q. Yang, *Superlattices Microstruct.* 17 (1995) 77.
- [6] C.-H. Lin, R.Q. Yang, D. Zhang, S. Murry, S.S. Pei, A.A. Allerman, S.R. Kurtz, *Electron. Lett.* 33 (1997) 598.
- [7] R.Q. Yang, J.D. Bruno, J.L. Bradshaw, J.T. Pham, D.E. Wortman, *Electron. Lett.* 35 (1999) 1254.
- [8] I. Vurgaftman, J.R. Meyer, F.H. Julien, L.R. Ram-Mohan, *Appl. Phys. Lett.* 73 (1998) 711.
- [9] J.L. Jimenez, E.E. Mendez, *Solid State Commun.* 110 (1999) 537.
- [10] H. Ohno, L. Esaki, E.E. Mendez, *Appl. Phys. Lett.* 60 (1992) 3153.
- [11] R.Q. Yang, J.M. Xu, *Appl. Phys. Lett.* 59 (1991) 181.
- [12] A. Nakagawa, H. Kroemer, J.H. English, *Appl. Phys. Lett.* 54 (1989) 1893.
- [13] K. Ohtani, H. Ohno, *Appl. Phys. Lett.* 74 (1999) 1409.
- [14] J. Faist, F. Capasso, C. Sirtori, D.L. Sivco, A.L. Hutchinson, S.N.G. Chu, A.Y. Cho, *Appl. Phys. Lett.* 63 (1994) 1354.
- [15] R.Q. Yang, J.M. Xu, M. Sweeny, *Phys. Rev. B* 50 (1994) 7474.
- [16] R.J. Warburton, C. Gauer, A. Wixforth, J.P. Kotthaus, B. Brar, H. Kroemer, *Phys. Rev. B* 53 (1996) 7903.

Designs for a quantum cascade laser using interband carrier extraction

V.J. Hales^{a,*}, A.J. Poulter^b, R.J. Nicholas^a

^a*Department of Physics, Clarendon Laboratory, Parks road, Oxford OX1 3PU, UK*

^b*CNRS-MPI, 25 Avenue des Martyrs, BP 166 Grenoble, Cedex 9, France*

Abstract

We have performed band structure calculations on intersubband cascade lasers using interband extraction, based on type II InAs/GaSb superlattices. The band structure under high electric field biasing was calculated using four-band $\mathbf{k} \cdot \mathbf{p}$ theory. We show that the broken gap system should enable emission beyond 10 μm without leakage of carriers from the active well. Design of the structures allows us to enhance or suppress electric field tunability. © 2000 Elsevier Science B.V. All rights reserved.

Keywords: InAs/GaSb superlattice; Interband extraction; Tunability; Quantum cascade lasers

1. Introduction

There has been much progress in the area of intersubband lasers in the past five years since the successful development of the quantum cascade laser (QCL) [1–5]. The type-I QC laser utilises photon emission between subbands in coupled AlInAs/GaInAs QWs, in which each carrier undergoes the same transition a number of times. However, the QC laser has a high leakage rate and low radiative efficiency due to non-radiative intersubband relaxation via optical phonon scattering. The interband cascade laser (ICL), proposed by Yang [6,7] use the type II broken gap

InAs/GaInSb system to overcome fast phonon scattering whilst retaining cascaded tunnelling injection.

It has recently been shown that intersubband emission may be combined with interband processes for carrier extraction [8]. Ohtani [9] has demonstrated intersubband electroluminescence from InAs/GaSb/AlSb type II structures, grown by MBE.

In this paper we explore structures based only on InAs/GaSb, looking for ways to extend the possible wavelength range and making the structures easier to grow by MOVPE, by eliminating the AlSb layer.

The major advantage of the InAs/GaSb system is the crossed-gap alignment, which presents a strong tunnel barrier to electrons injected into the excited state in the InAs QW, reducing the leakage current path present in type I QCLs. As shown in Fig. 1. Lasing occurs via a normal intersubband transition within a single InAs well, but the device utilises interband

* Corresponding author. Tel.: +44-01865-272299; fax: +44-01865-272400.

E-mail address: v.hales1@physics.ac.uk (V.J. Hales)

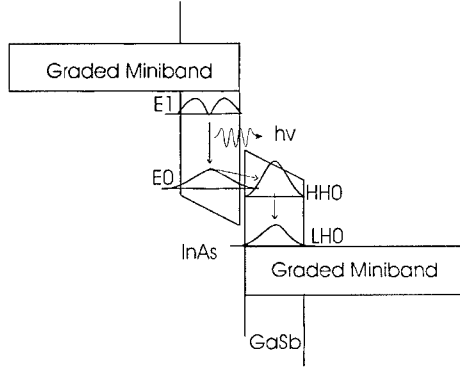


Fig. 1. Schematic band diagram of the InAs/GaSb-type II intersubband laser.

coupling to quickly remove electrons from the QW ground state by annihilation with holes in the adjacent GaSb barrier.

We have examined ways to optimise the structures by modelling the detailed band structure under high electric field biasing by using four-band $\mathbf{k} \cdot \mathbf{p}$ calculations and the momentum matrix technique [10].

2. Momentum matrix method

Existing $\mathbf{k} \cdot \mathbf{p}$ methods are restricted to flat band edge heterostructures, when modelled using the matrix transfer approach, so that modelling structures with high electric fields requires many separate layers. In order to model cascade structures under electric field biasing we have used a new procedure which was recently been developed within the framework of the envelope function approximation (EFA), termed the momentum matrix method. The technique constructs a matrix that represents the propagation of the wave function in momentum space and thus is ideally suited for modelling slowly varying potentials such as electric fields. The starting point of the momentum matrix method is to describe the wave function in terms of the EFA. The Schrödinger equation is simply

$$H\varphi(r) = [k_z H_2 k_z + \frac{1}{2}(H_1 k_z + k_z H_1) + H_0]\varphi(r) = E\varphi(r), \quad (1)$$

where the bulk Hamiltonian is separated into the coefficients of k_z the momentum operator along the growth direction (z), H_1 , H_2 and H_0 .

Instead of solving Eq. (1) in real space, the structure is assumed to be periodic. The $\mathbf{k} \cdot \mathbf{p}$ Hamiltonian (H_j), potential (V) and envelope functions (f) are periodic in real space with the periodicity of the structure modelled, d . A Fourier expansion of those functions is formed in terms of reciprocal lattice vectors, $G_n = 2\pi n/d$

$$H_j(z) = \sum T_{i,n} e^{iG_n z}, \quad (2a)$$

$$V(z) = \sum V_n e^{iG_n z}, \quad (2b)$$

$$f(z) = \sum f_n e^{iG_n z}, \quad j = 0, 1, 2, \dots, FF, \quad (2c)$$

where n denotes the n th Kane state and FF is the number of Fourier components used in the calculation.

The Fourier equations are fed into Eq. (1) and the resulting Matrix eigenvalue equation is

$$M(q)F = EF, \quad (3)$$

where the elements of eigenvector F are the Fourier coefficients on the envelope function f_n , and the matrix $M(q)$ is defined

$$M_{ij}(q) = (q + G_i)(q + G_j)T_{2,i-j} + (q + \frac{1}{2}(G_i + G_j))T_{1,ij} + T_{0,i-j} + V_{i-j}. \quad (4)$$

The electronic structure of the superlattice is derived by diagonalizing the matrix $M(q)$ at given $k_{||}$ and q . The eigenvalues of the matrix are the eigenenergies and the corresponding eigenvectors are the Fourier coefficients of the envelope function.

In this present case, the band structure is modelled over four repeats of the cascade structure and the electric field is added as a periodic potential to the entire structure. The conduction and three p-like valence bands are included with higher band interactions as correlation terms. Only the central section of the model can be studied to avoid edge effects at the ends.

3. Interband extraction

The basic principles of the device involve the use of superlattice injection followed by an intersubband transition from E_1 to E_0 . The widths of the active well and extraction barrier are carefully controlled to ensure E_0 lies above the GaSb valence band level, HH_0 . The

tailored electron miniband is formed from a set of four coupled QWs with carefully controlled thicknesses. The widths are graded such that the electron wave function at the bottom of the miniband has a high probability density in the active well.

A population inversion is maintained between the two well states E_1 and E_0 , by the rapid removal of electrons from E_0 , via interband extraction to HH_0 . The extraction energy is tailored to match LO phonon emission and further shorten the lifetime of carriers in state E_0 . The heavy hole state then rapidly empties into the light hole barrier state, LH_0 which is strongly coupled to the tailored electron miniband. The miniband thus serves as both collector and emitter regions of the device.

4. Band structure

The first structures modelled have four periods of a 10-layer device. Calculations were performed on three structures, qc11, qc12, and qc13, shown in Fig. 2, with the active well and barriers thicknesses, 110/100 Å, 120/90 Å, 140/90 Å, respectively. The wave functions and band profile under 0.5 V bias per period are plotted in Fig. 2a for the device qc11, with well and barrier widths 110/100 Å.

The strong wave function overlap within the tailored electron miniband provides the current path for injection into the active region and excited state E_1 . The intersubband transition occurs between states E_1 and E_0 , which have a strong spatial overlap within the active well. The emission wavelength is 7.4 μm . The calculation shows that a strong overlap does exist between the E_0 and HH_0 state. The light hole-state LH_0 is also strongly coupled to the top of the tailored electron miniband to recycle the electrons.

Structures qc12 and qc13 exhibited the same strong overlap between the E_0 and HH_0 states. The effect of widening the active well to 120 and 140 Å is to lower the electron confined states, E_1 and E_0 and hence lengthen the emission wavelength. In order to retain the ordering and strong coupling the hole levels were also lowered by thinning the GaSb barrier.

The limitations of this device lie with retaining the barrier to tunnelling. It was found that the GaSb barrier could only by thinned to a minimum width of

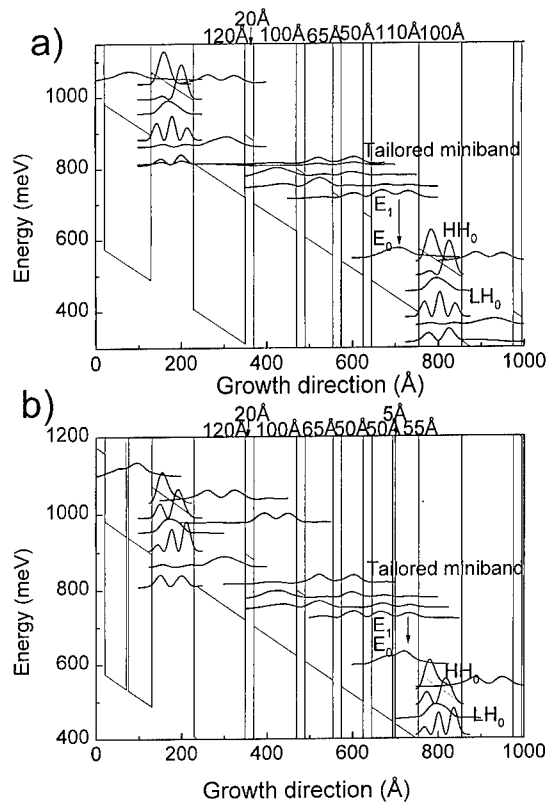


Fig. 2. Calculation performed on (a) structure qc11 with well and barrier widths 110/100 Å and (b) structure qc14, both under 0.5 V bias/period.

90 Å, before more than 10% of the E_1 wave function was found to propagate through the barrier. With this structure a maximum emission wavelength of 9 μm could be attained.

In an attempt to raise the electron ground state in the active well to access emission beyond 9 μm , a different structure, qc14 was modelled. Based on the previous design, an additional thin (5 Å) barrier was inserted into the centre of the active well, to form a 12-layer device. The wave functions and band profiles of the structure under 0.5 V bias per period are plotted in Fig. 2b.

The results show that the thin GaSb barrier does indeed raise the energy of the ground state electrons in E_0 by approximately 50 meV but the excited state E_1 by only 8 meV. The emission wavelength can then be extended beyond 10 μm .

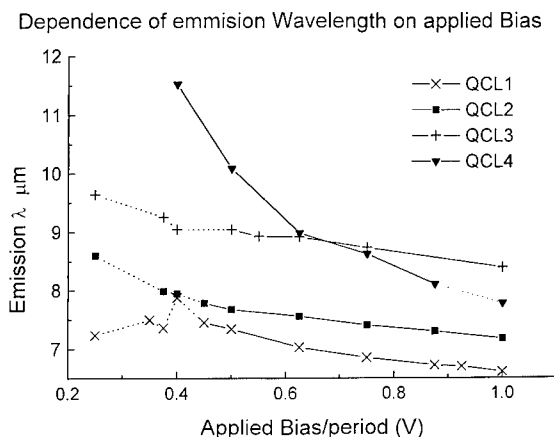


Fig. 3. The dependence of emission wavelength on applied bias for operational laser (solid line) and non-operational laser (dotted line).

5. Laser tunability

The main advantage of the broken gap system in cascade structures is the large barrier to tunnelling provided by the GaSb layer. It should therefore be possible to operate the laser over a wide range of biases without substantial leakage of carriers. An investigation into the tunability of the four structures was carried out.

The results are classified as operational or non-operational lasers. A number of criteria were defined for a device to be classified as operational. Firstly, there must be sufficient overlap between the wave function of the well and barrier states. A limit of 60 meV on the electron-hole energy separation ($E_1 - HH_0$) was defined for sufficient interband extraction. The excited electron state, E_1 must lie at the bottom of the tailored miniband to ensure that all carriers are funnelled into the active well.

The results are displayed in Fig. 3. For the single well structures the emission energies are relatively insensitive to bias and cover the range 6.5–9 μm . The structure containing the additional thin barrier, qcl4, however, could operate over a much wider range of biases producing emission between 8 and 12 μm . All four devices emit at wavelengths that cover the atmospheric window (8–14 μm).

Calculations were also performed on qcl4 structures with 10 and 15 Å wide additional barriers, to

try and lift the electron confined states further. However, the excited and ground electron states became localised on opposite sides of the thin barrier and thus the spatial overlap between the states was reduced.

6. Potential advantages

This structure has many potential advantages over more conventional structures. Firstly, the broken gap system allows extraction from the lower level directly into the adjacent layer without the need for conventional tunnelling, whilst maintaining a large barrier to inhibit tunnelling from the upper state. Secondly, it has been demonstrated that the energy levels in the active well can be tailored for a wide range of emission wavelengths, without substantial leakage of carriers into the adjacent well.

Finally, the InAs/GaSb intersubband laser has an additional advantage over the type I AlInAs/GaInAs intersubband devices. A recent theoretical study of Sb-based intersubband lasers showed that the small InAs effective mass reduces the optical phonon relaxation rate of the excited state and also increases the oscillator strength of the intersubband transition [11]. Room-temperature threshold currents five times lower than required for type I QCLs have been predicted. One potential disadvantage, however, is that interband absorption from E_0 to HH_0 across the InAs/GaSb interface could also present a possible additional loss mechanism [12].

7. Concluding remarks

We have presented designs for an intersubband laser using interband carrier extraction. We have demonstrated that the device could operate over a wavelength range within the (6–12 μm) atmospheric window. The designs show significant advantages over existing cascade laser structures.

References

- [1] F. Capasso, J. Faist, D.L. Sivco, C. Sirtori, A.L. Hutchinson, A.Y. Cho, *Science* 246 (1994) 553.
- [2] J. Faist, F. Capasso, C. Sirtori, D.L. Sivco, A.L. Hutchinson, A.Y. Cho, *Appl. Phys. Lett.* 66 (1994) 538.

- [3] F. Capasso, J. Faist, D.L. Sivco, C. Sirtori, A.L. Hutchinson, S.-N.G. Chu, A.Y. Cho, *Appl. Phys. Lett.* 68 (1996) 1745.
- [4] J. Faist, F. Capasso, C. Sirtori, D.L. Sivco, J.N. Baillargeon, A.L. Hutchinson, S.-N.G. Chu, A.Y. Cho, *Appl. Phys. Lett.* 68 (1996) 1745.
- [5] J. Faist, C. Gmachl, M. Striccoli, C. Sirtori, F. Capasso, D.L. Sivco, A.Y. Cho, *Appl. Phys. Lett.* 69 (1996) 2456.
- [6] R.Q. Yang, S.S. Pei, *J. Appl. Phys.* 79 (1996) 8197.
- [7] R.Q. Yang, C.-H. Lin, S.J. Murray, S.S. Pei, H.C. Liu, M. Buchanan, E. Dupont, *Appl. Phys. Lett.* 70 (1997) 2013.
- [8] E.E. Mendez, J.L. Jimenez, *Bull. Am. Phys. Soc.* 43 (1998) 647.
- [9] K. Ohtani, H. Ohno, *Appl. Phys. Lett.* 74 (10) (1999) 1409.
- [10] T.A. Vaughan, A.J. Poulter, R.J. Nicholas, C.C. Chang, submitted.
- [11] I. Vurgaftman, J.R. Meyer, F.H. Julien, L.R. Ram-Mohan, *Appl. Phys. Lett.* 73 (1998) 711.
- [12] I. Vurgaftman, J.R. Meyer, L.R. Ram-Mohan, *IEEE Photon. Technol. Lett.* 9 (2) (1997) 170.



ELSEVIER

Physica E 7 (2000) 89–92

PHYSICA E

www.elsevier.nl/locate/physce

Intersubband and interminiband transitions in CdS/ZnSe heterostructures

M. Göppert*, R. Becker, S. Petillon, M. Grün, C. Maier, A. Dinger, C. Klingshirn

Institut für Angewandte Physik, Universität Karlsruhe, 76128 Karlsruhe, Germany

Abstract

We report on the first investigation of intersubband and interminiband transitions in CdS/ZnSe multiple quantum wells and superlattices. The cubic heterostructures with type II band alignment were grown by molecular beam epitaxy on semi-insulating GaAs (001) substrates using CdS and ZnSe compound sources. The transmission spectra of n-type doped CdS/ZnSe heterostructures recorded in waveguide geometry show strong absorption lines in the mid-infrared. These absorption structures are attributed to intersubband (interminiband) transitions from the first to the second subband (miniband). The strong absorption is a direct consequence of the different refraction indices of the GaAs substrate and the wide-gap II–VI semiconductor heterostructure. Furthermore, first results of pump-probe experiments performed on lightly doped and undoped multiple quantum wells are presented. The photoinduced absorption was studied in dependence on the laser power. Thereby, the pump intensity was varied over three orders of magnitude. © 2000 Elsevier Science B.V. All rights reserved.

Keywords: CdS/ZnSe heterostructures; Interminiband; Photoinduced absorption

1. Introduction

In the last decade infrared absorption due to intersubband and interminiband transitions in multiple quantum wells (MQWs) and superlattices (SLs) has attracted much attention because of their potential applications as infrared detectors and lasers. So far, the intersubband (interminiband) investigations have

been mainly concentrated on Si/SiGe (see for example Ref. [1]) and III–V semiconductor heterostructures (see for example [2]). Less attention has been paid to intersubband (interminiband) transitions in II–VI structures. To the best of our knowledge there are only publications about intersubband transitions in the narrow-gap II–VI semiconductor system HgCdTe [3]. We present in this work first results of intersubband (interminiband) transition investigations on wide-gap II–VI CdS/ZnSe quantum films. The CdS/ZnSe QWs have a type II band alignment with a conduction band offset of (0.8 ± 0.1) eV, as determined from the analysis of photoluminescence data of undoped

* Corresponding author. Tel.: +49-721-6083417; fax: +49-721-607593.

E-mail address: markus.goeppert@physik.uni-karlsruhe.de (M. Göppert)

single quantum wells [4]. The occupation of the lowest subband (miniband) can be achieved by doping or interband photo-excitations [5]. Both CdS as well as ZnSe can be n-type doped with chlorine. In CdS and ZnSe free carrier concentrations of up to 8×10^{19} and $1 \times 10^{19} \text{ cm}^{-3}$ have been reached, respectively [6]. Therefore, the two-dimensional electron density in the CdS/ZnSe MQWs is tunable up to about 10^{13} cm^{-2} [7].

2. Experiment

The CdS/ZnSe MQWs and SLs were grown by molecular-beam epitaxy on semi-insulating (001)-oriented GaAs substrates using CdS and ZnSe compound sources [8]. In all the samples only the CdS QWs are doped continuously in order to minimize band bending effects. The sample parameters of the investigated MQWs and SLs are given in Table 1. For the infrared measurements which were performed in waveguide geometry by a Bruker IFS113v Fourier spectrometer two parallel facets were prepared at an angle α to the QW or SL plane. The different refraction indices in the middle infrared of the GaAs substrate ($n_{\text{GaAs}} \approx 3.3$) and the CdS/ZnSe heterostructure ($n_{\text{CdS}} \approx 2.3$, $n_{\text{ZnSe}} \approx 2.3$) lead to a totally reflected infrared beam at the GaAs–ZnSe interface for $\alpha \geq 44^\circ$. In order to avoid this total reflection the waveguides were prepared with $\alpha = 40^\circ$. The radiation coupled into the samples undergoes approximately one or two internal reflections, depending on the sample size. In the pump-probe experiments the electron occupation number for the lowest subband was changed by illumination of the QWs with the 488 nm (2.54 eV) line of an Ar⁺ laser.

3. Results and discussion

The position of the Fermi level even in the highly n-doped CdS : Cl/ZnSe MQWs is well below the second subband level E_2 . Thus only the lowest subband is occupied. According to the selection rules only the electric field component perpendicular to the layer planes couples to the $E_1 \rightarrow E_2$ transition. Therefore, the ratio of the transmitted intensities of p- and s-polarized radiation, where the electric field is parallel and perpendicular to the plane of incidence,

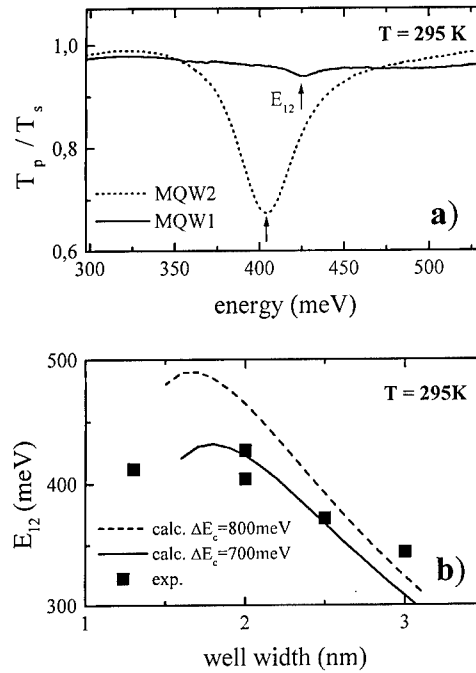


Fig. 1. (a) Transmission spectra of a highly and lightly doped MQW sample which have the same nominal well and barrier width. (b) The calculated and measured intersubband transition energies in CdS : Cl/ZnSe multiple quantum wells as a function of the well width.

respectively, has a minimum at the $E_1 \rightarrow E_2$ transition energy E_{12} . Therefore we plot for normalization purposes the ratio T_p/T_s as a function of $\hbar\omega$.

The transmission minima shown in Fig. 1a are attributed to intersubband transitions from the first to the second subband. For the lightly and highly doped MQWs (sample parameters are given in Table 1) the full-width at half-maximum (FWHM) of the intersubband absorption line is 16.7 and 38 meV, respectively. Since in both samples the CdS layers are n-type doped, the larger FWHM of MQW2 can be explained by the higher concentration of ionized donors in the well causing a shorter phase relaxation. The energy difference of about 23 meV between the absorption peaks of MQW1 and MQW2 is probably due to slightly different actual well widths. As expected, the integrated absorption intensities correspond to the two-dimensional free carrier densities of the two samples. Fig. 1b shows the calculated and measured intersubband transition energies in

CdS : Cl/ZnSe multiple quantum wells as a function of the well width. The numerical calculations are based within the envelope function approximation on the solution for a finite square potential [9]. Due to the high quantization energies non-parabolicity effects in the bulk materials were considered by using energy-dependent effective electron masses [10]. The parameters used in the calculation are as follows [4]: as adjustable parameter the conduction band offset ΔE_c ; as fixed parameters for ZnSe, $E_g = 2.8$ eV and $m_{\text{eff}} = 0.16 m_e$, and for cubic CdS $E_g = 2.5$ eV and $m_{\text{eff}}(\text{CdS}) = 0.19 m_e$. The effective electron mass of cubic CdS (0.19 ± 0.04) m_e has been determined by a combination of Hall effect and infrared reflectance measurements on n-type-doped cubic CdS-layers grown on GaAs (001) substrates. Using a conduction band offset of 0.7 eV (straight line in Fig. 1b) the deviation between theoretical and experimental values becomes smaller than for $\Delta E_c = 0.8$ eV (dashed line in Fig. 1b), the value previously obtained from CdS/ZnSe single quantum wells [4]. The reason for this discrepancy is as follows: The doped CdS/ZnSe MQWs and SLs investigated here were grown at a substrate temperature around 130°C higher than the samples investigated in Ref. [4]. This higher growth temperature probably causes some alloying in the CdS QWs which decreases the conduction band offset. Furthermore, the interface composition may be changed which also may influence the offset [11]. The smaller band offset in the samples investigated here in comparison to that grown at $T_{\text{Sub}} = 170^\circ\text{C}$ is indicated by a blue shift of the excitonic luminescence compared to that of the samples in Ref. [4].

Fig. 2a shows the photoinduced absorption T_{p*}/T_p of the lightly doped CdS/ZnSe MQW1. T_{p*} is the transmission for the p-polarized infrared beam with laser illumination. With increasing pump intensity tuned from about 7 mW/cm^2 to 7 W/cm^2 the absorption structure becomes stronger. In comparison to the intersubband absorption of MQW1 without illumination, as shown in Fig. 1a, the photoinduced absorption has the same line shape and is also on the same energetic position. This means that in case of MQWs there is no experimental evidence for excitonic or band bending effects in the investigated density regime. The excitation-induced absorption was observable down to pump intensities of about $70\text{ }\mu\text{W/mm}^2$. This is a consequence of (i) the relatively long life times

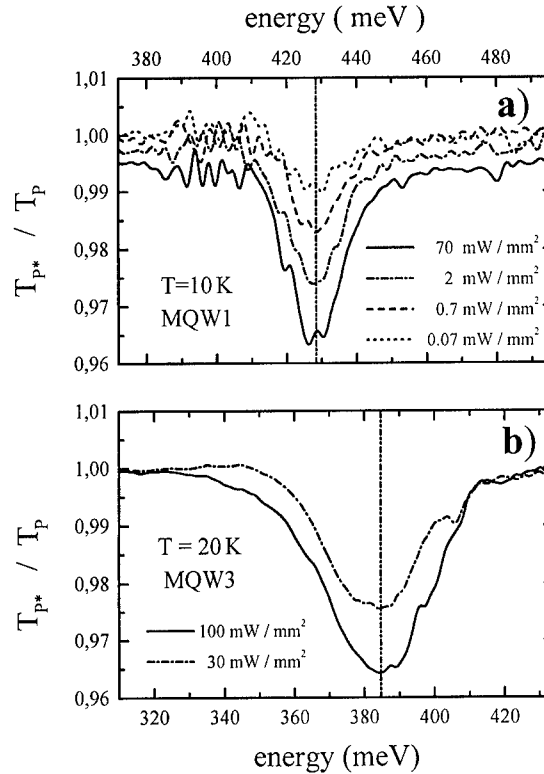


Fig. 2. The photoinduced intersubband absorption of (a) MQW1 and (b) MQW2 for different pump intensities at $\lambda_{\text{exc}} = 488\text{ nm}$.

of the photo-generated electron-hole pairs in the type II heterostructure allowing to reach substantial densities of carriers in the well and (ii) the different indices of refraction causing an enhanced electric field component parallel to the growth direction. Fig. 2b shows the photoinduced absorption spectra of the undoped MQW3. Because of its larger well widths, the intersubband absorption in MQW3 is at a lower energy. The broader FWHM of MQW3 is attributed to larger well-width fluctuations. The strength of the photoinduced absorption in MQW1 and MQW3 is nearly the same.

In case of the superlattices the wave functions in the neighboring quantum wells have considerable overlap causing the formation of minibands. Fig. 3 shows the calculated miniband dispersion scheme and the interminiband absorption of the CdS : Cl/ZnSe superlattice SL1. The sample parameters are given in Table 1. The miniband dispersion for the electrons was calculated by solving the transcendental equation

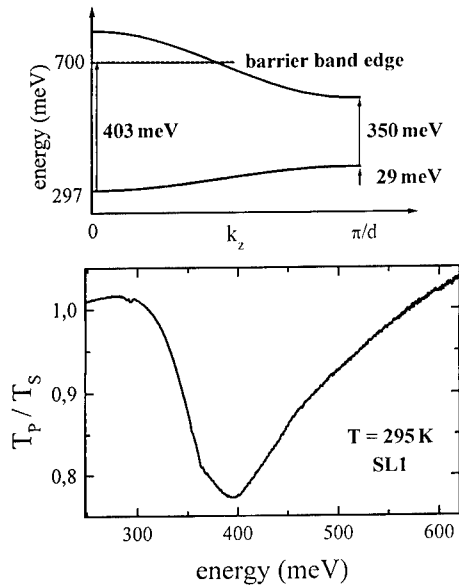


Fig. 3. The calculated miniband dispersion scheme and the measured interminiband absorption spectrum of superlattice SL1.

Table 1

Sample parameters of the investigated multiple quantum wells and superlattices, where d_b , d_w and d_{bu} are the nominal thicknesses of the ZnSe barrier, the CdS well and the ZnSe buffer. N_w is the nominal free carrier concentration in the well

Sample	SL1	MQW1	MQW2	MQW3
d_b (nm)	2.0	30	30	26.0
d_w (nm)	2.0	2.0	2.0	3.4
d_{bu} (nm)	300	300	300	300
N_w (10^{19} cm^{-3})	0.8	0.03	1.2	—
Number of periods	140	20	20	20

derived within the envelope function approximation [9]. As in case of the subband calculations for MQWs the non-parabolicity of the CdS and ZnSe conduction bands have also been taken into account by using an energy-dependent effective electron mass. Band-bending effects have been neglected. For the lowest miniband the theoretical miniband width is 29 meV. The second miniband overlaps partly with the continuum states (see Fig. 3). In agreement with

theoretical expectations [12] the observed miniband absorption structure shows a strong asymmetry to the high-energy side. The transmission minimum in Fig. 3 is at 395 meV and is attributed to transitions from $E_1(k = \pi/d)$ to $E_2(k = \pi/d)$. Assuming $\Delta E_c = 0.7 \text{ eV}$, the calculated value is 350 meV and is in relatively good agreement to the experimentally determined value.

4. Conclusions

It has been shown that the intersubband transition energies in CdS : Cl/ZnSe MQWs can be tuned from 430 to 340 meV by increasing the well width from 2 to 3 nm. The strong intersubband absorption lines have been explained by the different indices of refraction of the GaAs substrate and the wide band gap II–VI semiconductor heterostructure. In case of CdS : Cl/ZnSe superlattices a strong asymmetric interminiband absorption structure has been observed in agreement with theory. The photoinduced intersubband absorption has been studied in dependence on the laser pump intensity over three orders of magnitude.

Acknowledgements

This work was supported by the Deutsche Forschungsgemeinschaft.

References

- [1] T. Fromherz et al., Phys. Rev. B 50 (1994) 15 073.
- [2] Qin-Sheng Zhu et al., Phys. Rev. B 57 (1998) 12 388.
- [3] A.M. de Paula et al., Phys. Rev. B 59 (1999) 10 158.
- [4] A. Dinger et al., Semicond. Sci. Technol. 14 (1999) 595.
- [5] M. Olszakier et al., Phys. Rev. Lett. 62 (1989) 2997.
- [6] M. Grün et al., J. Crystal Growth 201/202 (1999) 457.
- [7] V. Kazukauskas et al., Appl. Phys. Lett. 74 (1999) 395.
- [8] S. Petillon et al., J. Crystal Growth 201/202 (1999) 453.
- [9] G. Bastard, Wave Mechanics Applied to Semiconductor Heterostructures, Les Editions de Physique, 1988.
- [10] P. Harrison et al., Physica E 2 (1998) 468.
- [11] M. Nagelstrasser et al., J. Appl. Phys. 83 (1998) 4253.
- [12] M. Helm, Semicond. Sci. Technol. 10 (1995) 557.



ELSEVIER

Physica E 7 (2000) 93–96

PHYSICA E

www.elsevier.nl/locate/physa

Intersubband transitions in InAs/GaSb superlattices in a parallel magnetic field

R.H.J. De Meester^{a,*}, F.M. Peeters^a, M. Lakrimi^b, R.J. Nicholas^b, A.J.L. Poulter^b,
N.J. Mason^b, P.J. Walker^b

^aDepartement Natuurkunde, Universiteit Antwerpen (UIA), B-2610 Antwerpen, Belgium

^bClarendon Laboratory, Department of Physics, University of Oxford, Parks Road, Oxford OX1 3PU, UK

Abstract

We present a theoretical study of intersubband transitions (IST) in InAs/GaSb superlattices in the presence of a parallel magnetic field. Starting from a model describing a single electron in a single quantum well and extending it to include many-body effects and the non-parabolicity of the InAs conduction band we are able to explain the recent cyclotron resonance experiments on narrow and wide InAs/GaSb quantum wells. © 2000 Elsevier Science B.V. All rights reserved.

Keywords: InAs/GaSb; Intersubband transition; Plasmon shift; Non-parabolicity

1. Introduction

InAs/GaSb heterostructures have been the subject of many theoretical [1] and experimental [2] investigations for the past few decades because of their characteristic band structure in which the top of the GaSb valence band is about 150 meV higher than the bottom of the InAs conduction band. For wide (> 150 Å) superlattice periods these InAs/GaSb superlattices are such that a transfer of electrons from GaSb to InAs gives rise to a two-dimensional electron gas in InAs and a two-dimensional hole gas in GaSb without extrinsic doping.

In this paper we will calculate the intersubband transitions of such systems. We will compare our results with the experiments performed at the university of Oxford [3] on a wide range of samples with well widths (W) varying from 100 Å to 540 Å. Magnetic fields up to 14 T were applied parallel to the layer surfaces. These experiments reveal three general classes of behaviour depending on well-width thickness. Discussion of all classes would bring us beyond the scope of this paper. Hence, we will compare our theoretical results on two samples which exhibit characteristic behaviour, to the experimental results.

2. Simple model

In our simple model the Schrödinger equation describing an electron in a one-dimensional potential

* Corresponding author. Tel.: +32-3-820-2478; fax: +32-3-820-2245.

E-mail address: roelddm@uia.ua.ac.be (R.H.J. De Meester)

$U(z)$ in the presence of a parallel magnetic field is given by

$$\left\{ \frac{-\hbar^2}{2m} \frac{d^2}{dz^2} + \frac{1}{2m} \left(\hbar k_x + \frac{e}{c} B_y z \right)^2 + U(z) \right\} \psi_{k_x}(z) = E_n(k_x) \psi_{k_x}(z), \quad (1)$$

with $m = m_{\text{InAs}} = 0.023m_c$ the effective mass of the electrons in InAs ($m_{\text{GaSb}} = 0.047m_c$), $U(z)$ the conduction potential derived from eight-band $\mathbf{k} \cdot \mathbf{p}$ calculations performed by Poulter [3] and $E_n(k_x)$ the energy levels of the system depending on the wave vector k_x due to the presence of a magnetic field B_y . The equation is solved using finite element techniques. Although the effect of a mass mismatch [4] between the electrons in GaSb and InAs can be significant for QW structures in a parallel field configuration [5] we found that it can be neglected in the InAs/GaSb systems studied in this paper.

Knowing the energy spectrum we calculate the density of states which give us information about the filling of the levels. Assuming zero temperature we know that states with energy higher (lower) than the Fermi energy are empty (filled). At zero magnetic field we calculated that the narrow ($W = 30$ nm) sample had two levels filled, with the first excited state being depleted by a magnetic field of $B = 4$ T. However, experimental results show that only the ground state is filled for all magnetic fields. For the wide ($W = 46$ nm) sample we find that the first excited state is depleted at $B = 8$ T, and experimentally this is the magnetic field at which the low-energy peak disappears.

We assumed that the IST at $k_x = 0$ gives the main contribution to the absorption and supposed that the energy difference between the initial state and the final state equals the position of the absorption peak. These results are shown in the figures as a full curve.

3. Many-body effects

Up to now we considered only a single electron. Due to the high density of the 2D electron gas we have to take into account many-body effects. The high density leads to a dynamic screening of electrons giving rise to a depolarisation shift which shifts the resonance peak to higher energy. To calculate the shift of the intersubband transition we first have to calculate

the plasma energy E_{pl} , needed to deduce the new transition energy $\tilde{E}_{if}^2 = E_{if}^2 + E_{\text{pl}}^2$. The plasma energy is given by [6] $E_{\text{pl}}^2 = 2e^2 n_e S_{if} E_{if} / \epsilon$ with $\epsilon = 15.5$ the permittivity of the system and S_{if} the depolarisation integral which is equal to $S_{if} = \int_{-\infty}^{+\infty} dz [\int_{-\infty}^z \psi_{f,k_x}(z') \psi_{i,k_x}(z') dz']$. In all samples and for all transitions we see an upshift of the transition energy compared to the simple model as expected by the definition of the new transition energy. The peak positions calculated using this model are shown by the dashed curves in all figures.

4. Non-parabolicity

In our previous calculations we assumed the InAs conduction band to be parabolic such that the mass of the electrons is the same for all energy levels. But due to the fact that InAs has a rather small energy gap ($E_g = 418$ meV) this is not the case and we have taken the non-parabolicity into account using a simple two band Kane model which describes this effect by entering an energy-dependent mass $m(E) = m_f(1 + 2E/E_g)$, in Eq. (1), with $m_f = m_{\text{InAs}}$, i.e. the mass of the electrons in bulk InAs and E_g the bandgap between the bulk InAs conduction and valence band. This requires an iterative calculation. We start by solving Eq. (1) using $m = m_f$ and the energy found is used to calculate a new mass m' . This mass is again entered in Eq. (1) giving a new energy and thus also a new mass m'' . After a few steps both the mass and the energy have converged, respectively, to a larger mass and lower energy. The difference between the converged energy and starting energy is larger for higher energy levels and as such the difference between subsequent levels will decrease. This effect must be added to the many-body effect and will most strongly affect the theoretical results for the narrow sample. The dotted curves in all the three figures show the theoretical results for the three samples including the depolarisation shift and the down shift due to the band non-parabolicity.

5. Results

Due to the limited space we will only discuss the results for the final model which are shown as dotted

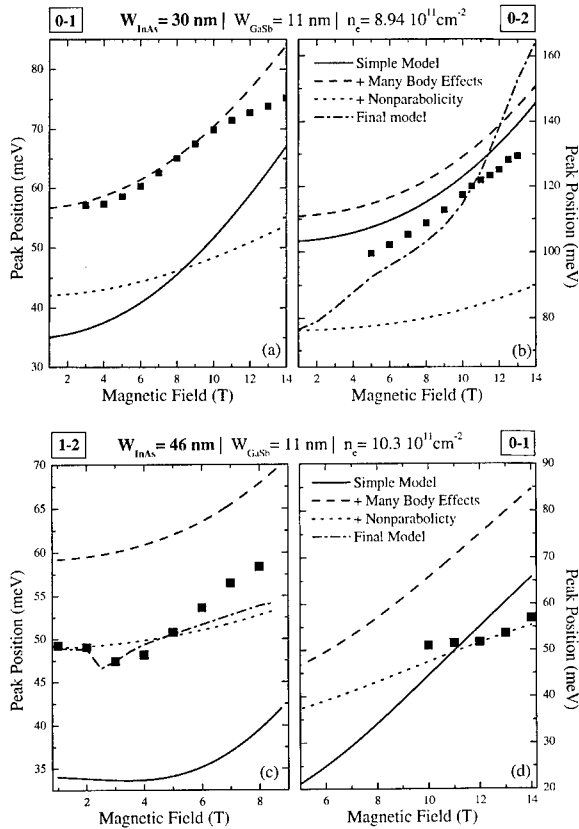


Fig. 1. Calculated peak positions for the (a) $0 \rightarrow 1$ IST and (b) $0 \rightarrow 2$ IST for the narrow-well sample and (c) $1 \rightarrow 2$ IST and (d) $0 \rightarrow 1$ IST for the wide sample. Results from the simple model (full), including many-body effects (dashed) and also including the band non-parabolicity (dotted) are shown. The dash-dotted curve shows the results from the same model as the dotted curve but taking the peak position at the maximum of the absorption spectrum instead of at $k_x = 0$. The measured (square symbols) peak positions are also shown.

curves in Fig. 1(a)–(d). The narrow sample shows experimentally two peaks, with the strength of the high-energy IST a few percent of the low-energy IST. Theoretically, we find that the $0 \rightarrow 2$ IST is about 5% of the $0 \rightarrow 1$ and therefore we believe that the experimental ISTs can be attributed to the $0 \rightarrow 1$ and $0 \rightarrow 2$ IST. We see that the peak position of the $0 \rightarrow 1$ IST (dotted curve in (a)) has about the same increasing trend as the experimental peak position but lies about 15–20 meV below these results. The $0 \rightarrow 2$ IST (dotted curve in (b)) shifts only slightly to higher energy (12 meV) compared to the experimental shift (30

meV) and furthermore the theoretical peak position at $B = 5$ T lies about 20 meV below the experimental peak position. These peak positions were calculated assuming that the peak in the absorption spectra results from transitions at zero wave vector. However, we hence calculated that the main contribution to the spectrum comes from transitions at higher (i.e. Fermi) wave vector. Therefore, we have calculated the total absorption at each magnetic field and then searched for the peak in the absorption spectrum. These peak positions are shown as the dash-dotted curve in (b), and these peak positions have a much higher diamagnetic shift which is in good agreement with the experimental results in the range ($B = 6$ –12 T). The wide sample shows experimentally two peaks which exchange intensity with increasing magnetic field. As explained for the previous sample we have calculated the position of the peak for the $1 \rightarrow 2$ IST (dash-dotted curve in (c)) at low fields, which agrees with the experiment since both the decrease of transition energy at $B = 3$ T and the depletion of the second excited state at $B = 8$ T are predicted by our final theory. The transition at higher fields is believed to correspond to an $0 \rightarrow 1$ IST and the peak positions resulting from our model (dotted curve in (d)) coincide very well with the experimental data. The dash-dotted curve is not shown in Fig. 1(a) and (d) because calculations show that for the $0 \rightarrow 1$ IST in both samples, the states at $k_x = 0$ are most responsible for the peak and thus the dash-dotted curve would be not much different from the dotted curve.

Acknowledgements

RDM is supported by IWT and FMP is a Research Director of the Fund for Scientific Research – Flanders (Belgium) (FWO). Part of this work is supported by the Flemish-British collaborative program and by FWO and IUAP.

References

- [1] M. Lakrimi, S. Khym, R.J. Nicholas, D.M. Symons, F.M. Peeters, N.J. Mason, P.J. Walker, Phys. Rev. Lett. 79 (1997) 3034.
- [2] D.M. Symons, M. Lakrimi, R.J. Warburton, R.J. Nicholas, N.J. Mason, P.J. Walker, M.I. Eremets, G. Hill, Phys. Rev. B 49 (1994) 16 614.

- [3] A.J.L. Poulter, M. Lakrimi, R.J. Nicholas, N.J. Mason, P. Walker, *Phys. Rev. B* 59 (1999) 10 785.
- [4] Gerald Bastard, *Wave Mechanics Applied to Semiconductor Heterostructures*, Les éditions de physique, Les Ulis, France, 1988.
- [5] R.H.J. De Meester, F.M. Peeters, *J. Phys.: Condens. Matter* 11 (1999) 6207.
- [6] R.J. Warburton, C. Gauer, A. Wixforth, J.P. Kotthaus, *Superlatt. Microstruct.* 19 (1996) 365.



ELSEVIER

Physica E 7 (2000) 97–100

PHYSICA E

www.elsevier.nl/locate/physce

Self-assembled ErAs islands in GaAs for THz applications

Christoph Kadow^{a,*}, Andrew W. Jackson^a, Arthur C. Gossard^{a,b}, John E. Bowers^b,
Shuji Matsuura^c, Geoffrey A. Blake^c

^aMaterials Department, University of California Santa Barbara, Santa Barbara, CA 93106-5050, USA

^bDepartment of Electrical and Computer Engineering, University of California Santa Barbara, Santa Barbara, CA 93106, USA

^cDivision of Geological and Planetary Science, California Institute of Technology, Pasadena, CA 91109, USA

Abstract

This paper concerns self-assembled ErAs islands in GaAs grown by molecular beam epitaxy. The nucleation of ErAs on GaAs occurs in an island growth mode leading to spontaneous formation of nanometer-sized islands. Pump–probe measurements indicate that the ErAs islands capture photogenerated carriers on a subpicosecond time scale. This together with the high resistivity of the material allows us to use it as a fast photoconductor. The performance of photomixer devices made from this material is discussed. © 2000 Published by Elsevier Science B.V. All rights reserved.

Keywords: ErAs islands; Carrier dynamics; THz source

1. Introduction

The sub-millimeter wave region is interesting for many applications, such as molecular spectroscopy, astronomy, pollution monitoring and last but not least semiconductor spectroscopy. A promising approach for the generation of sub-millimeter waves is photomixing. This approach requires a photoconductive material with a response time in the subpicosecond range. The response time is a crucial parameter for device design and performance, and engineering control over this time is desirable. Brown et al. [1] demonstrated photomixer devices based on low-temperature grown GaAs (LTG-GaAs), which is the most widely

used ultrafast photoconductor. Subsequently, the usefulness of these devices for molecular spectroscopy was shown [2].

Here we report on an alternative material with the desired properties based on self-assembled ErAs islands in GaAs. Other motivations for this research besides the generation of sub-millimeter waves are to study the growth and the properties of heterostructures of very dissimilar materials.

2. Sample structure

A cross-section of the sample structure is outlined schematically in Fig. 1. All samples are superlattices; they consist of equidistant layers, which contain ErAs islands embedded in a GaAs matrix. The material was

* Corresponding author. Fax: +1-805-893-8971.

E-mail address: kadow@engineering.ucsb.edu (C. Kadow)

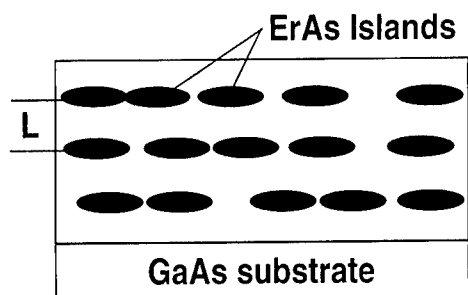


Fig. 1. Schematic cross-section of the sample structure.

grown on semi-insulating (100) GaAs substrates by molecular beam epitaxy (MBE) using a Varian Gen II solid source MBE machine. The GaAs was grown under standard growth conditions. The ErAs was grown at the same temperature of 535°C as the GaAs matrix; the ErAs growth rate was typically 0.039 monolayers (ML)/s. The nucleation of ErAs on GaAs occurs in an island growth mode (for a review on growth of rare earth arsenides see for example Ref. [3]), which results in the spontaneous formation of nanometer-sized ErAs islands. It is possible to overgrow the ErAs islands with GaAs of high quality, and complete recovery of the reflection high-energy electron diffraction (RHEED) pattern is observed after a few nanometers of overgrowth.

X-ray rocking curves around the (004) GaAs peak show that the superlattice period is well defined. Plan view transmission electron micrographs show that the diameter of the islands is between 1 and 2 nm and the island density on the order of 10^{12} cm^{-2} . A more detailed discussion of the MBE growth is given in Ref. [4].

3. Pump-probe measurements

Time-resolved differential reflectance measurements were performed on samples grown under several different growth conditions. The experimental setup is a pump-probe arrangement using short laser pulses generated by a mode-locked Ti:sapphire laser. The laser pulses are centered at wavelengths ranging from 800 to 860 nm. They are between 80 and 140 fs long. The pump and the probe pulses are polarized orthogonally to each other. The $\Delta R/R$ signals

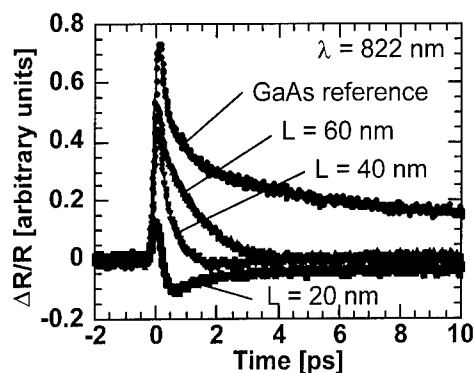


Fig. 2. Results of pump-probe experiments for three ErAs containing samples and a GaAs reference sample.

are on the order of 10^{-4} . For their measurement, lock-in detection employing an RF front end is used. All wavelengths used are shorter than the wavelength corresponding to the GaAs band gap of 870 nm at room temperature. Linear absorption measurements on similar samples show that the position of the band gap is not affected by the presence of the ErAs islands [5]. In the wavelength range used in our experiments, the absorption coefficient is approximately 25% higher than for a GaAs reference sample. We estimate that each pump pulse injects approximately $5 \times 10^{17} \text{ cm}^{-3}$ carriers into the GaAs matrix.

In Fig. 2, results from three samples that contain ErAs-islands and a GaAs reference sample are compared. The GaAs reference sample is a 1.2 μm thick GaAs film on a GaAs substrate grown under the same conditions as the ErAs containing films. All four samples are grown on the same day. The ErAs containing samples differ from each other by the period of the superlattice L ($L = 20, 40$ and 60 nm). The three samples have the following structures: $20 \times (1.2 \text{ ML ErAs}, 60 \text{ nm GaAs})$, $40 \times (1.2 \text{ ML ErAs}, 40 \text{ nm GaAs})$, $60 \times (1.2 \text{ ML ErAs}, 20 \text{ nm GaAs})$. The data shows that first, having the ErAs-islands changes the observed signal significantly. After an initial positive transient the signal returns to a value close to the baseline within a few picoseconds in contrast to the GaAs reference. Second, the different periods L of the superlattice structures change both the magnitude and the decay time of this initial transient response seen in all three ErAs containing samples. Third, the $\Delta R/R$ trace for the sample

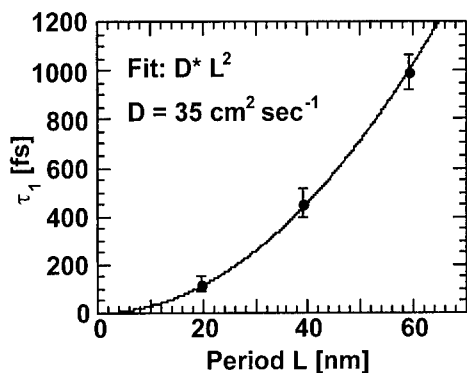


Fig. 3. Time constant τ_1 of the initial transient decay as a function of the superlattice period L .

with the 20 nm period in Fig. 2 contains an additional negative term.

The $\Delta R/R$ traces taken at several different wavelengths are fit with either a single exponential function or the sum of two exponential terms to obtain the different time constants involved. The fits are started approximately 50 fs after the pump pulse has arrived at the sample. The time constant of the initial decay τ_1 shows little dependence on the wavelengths used and also on ErAs depositions between 0.6 and 2.3 ML. However, it does depend strongly on the period L of the superlattice. Fig. 3 shows this dependence of the time constant τ_1 on the superlattice period L . The data is from the three samples described before. The error bars indicate the variation of τ_1 with wavelength. It can be seen that τ_1 increases in a superlinear fashion with L . A fit with a quadratic function is shown in Fig. 3.

Our interpretation of the dependence seen in Fig. 3 is as follows. The carriers are generated in the GaAs matrix and recombine in the ErAs islands or defects located at these islands. We believe that the response is limited by the time the photogenerated carriers need to reach the ErAs containing layers and not the relaxation processes at the capture site. The quadratic dependence seen in Fig. 3 would be consistent with diffusional transport. If the recombination process at the capture site were the limiting factor, a linear dependence on the superlattice period would be expected. Currently, it is neither known why the relaxation processes at the capture site are so fast nor which transitions are involved.



Fig. 4. Top view on a photomixer device showing the interdigitated gate electrodes at the center of a spiral antenna.

4. Photomixer devices

The subpicosecond response time together with the high resistivity of the material allows us to fabricate photomixer [1] devices from it. The purpose of a photomixer is to generate sub millimeter waves by heterodyne conversion at the difference frequency between two laser beams, which have optical frequencies. A top view on the device structure is shown in Fig. 4. On the surface of the photoconductive material a planar log-spiral antenna and at its vortex a pair of interdigitated electrodes are fabricated. During device operation a DC bias is applied to the interdigitated electrodes and the two laser beams with slightly different wavelength are focussed onto the interdigitated electrodes. The center wavelength of the two laser beams is typically 800 nm. The laser light generates charge in the photoconductor with the beat frequency. This results in a photocurrent with the same frequency, which drives the antenna structure. The sub-mm waves are radiated through the substrate into free space. In our experiment the output power is coupled into a Si bolometer. More details on the experimental setup are given in Refs. [1,2].

The material used for the devices we fabricated is nominally identical to one of the samples used for pump-probe measurements. Its structure is $60 \times$ (1.2 ML ErAs, 20 nm GaAs), resulting in a $1.2 \mu\text{m}$ thick active layer. The response time as measured in pump-probe experiments is 120 fs. The metalization is

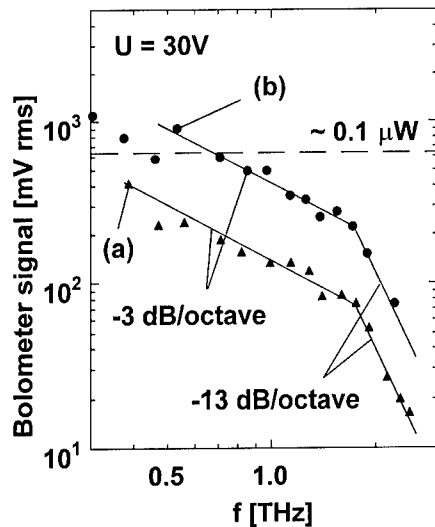


Fig. 5. Output power as a function of frequency for a photomixer device.

fabricated in two steps by electron beam and optical lithography. The finger width is $0.2 \mu\text{m}$, and the gaps are $1.8 \mu\text{m}$ wide.

Under illumination the I - V characteristic of the devices is S-shaped on a log-log plot. At intermediate bias the DC-photocurrent I_{DC} follows a power law with exponents around 1.8. At high bias the DC-photocurrent saturates and at low bias it follows a power law with a smaller exponent. The THz output power is expected to have a quadratic dependence on the laser power. Experimentally, we find power laws with somewhat smaller exponents between 1.7 and 1.8. The measured characteristics are similar to devices made on LTG-GaAs material [6].

Fig. 5 shows the frequency response of one device for two different laser powers. A frequency corner can clearly be seen at 1.7 THz. At higher frequencies the power decays with -13 dB/octave , and at smaller frequencies the power decreases with approximately -3 dB/octave . Photomixer theory predicts two corner frequencies f_1 and f_2 , each resulting in a power decay of -6 dB/octave [7]. f_1 is at $1/(2\pi\tau)$ where τ is the carrier life time. f_2 equals $1/(2\pi RC)$ where C is the capacitance of the interdigitated electrodes and R is the radiation resistance of the spiral antenna, which is

72Ω . Assuming for our devices $f_1 = f_2 = 1.7 \text{ THz}$, yields $\tau = 94 \text{ fs}$ and $C = 1.3 \text{ fF}$. This value for τ is in agreement with the value of 120 fs from the pump-probe measurements considering that the pump-probe measurement is close to its resolution limit. The value for the capacitance is somewhat higher than what is expected for the interdigitated electrodes. We believe that the additional capacitance is due to the interconnecting metal. The roll-off with 3 dB/octave at frequencies smaller than 1.7 THz is unexpected and currently not understood. Overall the devices behave very close to expectations and perform comparably to devices made from LTG-GaAs.

5. Summary

In summary we investigated the MBE growth and selected properties of self-assembled ErAs islands in GaAs. The carrier dynamics were investigated by pump-probe experiments on a subpicosecond time scale, which reveal response times as short as 120 fs . Photomixer devices fabricated from this material show characteristics similar to devices made from LTG-GaAs. The device results confirm that the material is a fast photoconductor with response times in the subpicosecond range.

References

- [1] E.R. Brown, K.A. McIntosh, K.B. Nichols, M.J. Manfra, C.L. Dennis, Proceedings of the SPIE, Vol. 2145, 1994, p. 200.
- [2] P. Chen et al., Appl. Phys. Lett. 71 (1997) 1601.
- [3] T. Sands, C.J. Palmstrom, J.P. Harbison, V.G. Keramidas, N. Tabatabaie, T.L. Cheeks, R. Ramesh, Y. Silberberg, Mater. Sci. Rpts. 5 (3) (1990) 99.
- [4] C. Kadow, S.B. Fleischer, J.P. Ibbetson, J.E. Bowers, A.C. Gossard, J.W. Dong, C.J. Palmstrom, Appl. Phys. Lett. 75 (1999) 3548.
- [5] S. Tautz, private communication.
- [6] E.R. Brown, K.A. McIntosh, F.W. Smith, K.B. Nichols, M.J. Manfra, C.L. Dennis, J.P. Mattia, Appl. Phys. Lett. 64 (1994) 3311.
- [7] E.R. Brown, F.W. Smith, K.A. McIntosh, J. Appl. Phys. 73 (1993) 1480.



ELSEVIER

Physica E 7 (2000) 101–107

PHYSICA E

www.elsevier.nl/locate/physce

QWIP FPAs for high-performance thermal imaging

H. Schneider^{a,*}, M. Walther^a, C. Schönbein^a, R. Rehm^a, J. Fleissner^a, W. Pletschen^a,
J. Braunstein^a, P. Koidl^a, G. Weimann^a, J. Ziegler^b, W. Cabanski^b

^a*Fraunhofer-Institut für Angewandte Festkörperphysik, Tullastrasse 72, D-79108 Freiburg, Germany*

^b*AEG Infrarot Module GmbH, Theresienstrasse 2, 74072 Heilbronn, Germany*

Abstract

System properties of focal plane array (FPA) cameras based on GaAs/AlGaAs quantum well infrared photodetectors (QWIPs) operating in the long-wavelength infrared are analyzed. Due to the limited charge storage capacity of available readout circuits, a small photoconductive gain improves the noise-equivalent temperature difference (NE Δ T) of the sensor. We have demonstrated several camera systems based on conventional photoconductive QWIPs with NE Δ T < 10 mK and NE Δ T < 20 mK for FPAs with 256 \times 256 and 640 \times 512 pixels, respectively. A small photoconductive gain is obtained by operating the QWIP at very small electric fields (< 3 kV/cm). Finally, we discuss the possibility of reducing the NE Δ T even further by using QWIP structures in which the photoexcited carrier mean free path is controlled by the incorporation of additional epitaxial layers. We thus obtain a high detectivity at very small signal and noise currents, which is useful in particular for large arrays with reduced pixel sizes. In addition, these detectors are shot-noise limited since the recombination noise is suppressed. The performance of FPA sensors based on these detectors will be addressed. © 2000 Elsevier Science B.V. All rights reserved.

Keywords: QWIP camera; Focal plane array; Noise-equivalent temperature difference

1. Introduction

Quantum well infrared photodetectors (QWIPs) find increasing attention for imaging applications in the 8–12 μ m long-wavelength infrared atmospheric window. After the first demonstration of a 128 \times 128 focal plane array (FPA) camera based on GaAs/AlGaAs QWIPs [1], a variety of systems with increasing complexity and performance has been

developed (see, e.g., Refs. [2,3]). The latest trend goes towards two-color systems with simultaneous detection at different wavelengths [4,5].

In the last few years, we have demonstrated several camera systems based on FPAs comprising QWIP detector arrays hybridized to silicon readout integrated circuits (ROIC). Thermal resolutions better than 10 and 20 mK were obtained with 256 \times 256 and 640 \times 512 QWIP FPAs, respectively [6–9]. In addition to the excellent temperature resolution, more than 99.9% of the pixels were working properly without any cluster defect. Large GaAs-based QWIP FPAs can be

* Corresponding author. Fax: +49-761-5159-359.

E-mail address: hschneider@iaf.fhg.de (H. Schneider)

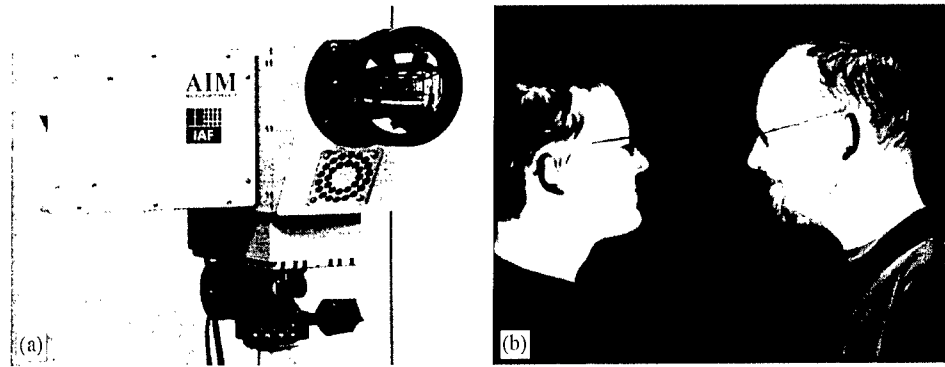


Fig. 1. (a) Camera housing and optics. (b) Far-infrared image recorded by a QWIP camera in a 640×486 video format.

produced on a stable technological platform and represent a promising approach for high-performance thermal imaging. In our cameras, the QWIP FPA is kept at a standard operation temperature of 65 K, which is provided by a Stirling cooler. The cameras are operated at a 50 Hz frame rate with an integration time between 10 and 20 ms. Such a QWIP camera and a long-wavelength infrared image are shown in Fig. 1.

We have recently developed a different class of QWIP structures where the capture of the photoexcited carriers is controlled by the incorporation of additional epitaxial layers [10]. In these low-noise QWIPs, the photoconductive gain is drastically reduced while maintaining a high detectivity. In addition, these new detectors provide the possibility to suppress the recombination noise [11]. Both properties make low-noise QWIPs highly attractive for applications in camera systems operating in the long-wavelength infrared.

In this paper, we analyze some system properties of thermal-imaging cameras and relate them with the specific characteristics of the detector structure used in our 256×256 and 640×512 QWIP cameras. In particular, we show that a small photoconductive gain is useful to improve the noise-equivalent temperature difference ($NE\Delta T$). For this reason, our QWIP cameras are operated at a bias voltage below 0.3 V in order to reduce the gain for optimized temperature resolution. This low-bias operation allows us to increase the integration time while maintaining a high detectivity. Finally, we address the potential of low-noise QWIPs for further enhancement of the temperature resolution and dynamic range of far-infrared cameras,

taking into account the limited charge storage capacity of the ROIC.

2. System considerations

In order to calculate the required responsivity for a detector in a thermal-imaging camera, we consider a detector of area A which is located behind a cold shield with the f -number f . The spectral power density dP_ν associated with the thermal background at the photon energy $h\nu$ incident on the detector is then given by [12]

$$dP_\nu = \frac{A}{4f^2 + 1} \frac{2\pi h^3 \nu^3 d\nu}{c^2 (\exp(h\nu/k_B T_B) - 1)}, \quad (1)$$

where c is the speed of light and T_B the background temperature.

Let us assume that the detector is sensitive between 8 and 9 μm . The power P_1 within this spectral regime at $T = 300$ K is obtained as $P_1 = A/(4f^2 + 1)29 \text{ W/m}^2$. Values of P_1 obtained for the pixel geometries of our FPAs are given in Table 1.

We now define the *critical responsivity* R_c by the condition that the detected photocharge within the integration time τ equals the storage capacity Q_c of the readout cell. In addition to the case $T_B = 300$ K, Table 1 also summarizes the R_c -values at an upper scene temperature of 45°C (318 K), where P_1 is about 40% higher than at 300 K. Since the resulting responsivities are easily achieved with most detectors, it is clear that readout limitation is an important issue for two-dimensional FPAs. Additional constrictions appear if there is a significant dark current, since the

Table 1
Characteristic parameters of the 256×256 and 640×512 QWIP FPA sensors

Parameter	Symbol	256×256	640×512
Pitch		40 μm	24 μm
Pixel area	A	$37 \times 37 \mu\text{m}^2$	$22 \times 22 \mu\text{m}^2$
Filling factor		85%	84%
f -number	f	2.0	2.0
Frame rate		50 Hz	50 Hz
Integration time	τ	< 20 ms	< 20 ms
Storage capacity	Q_c	$4.5 \times 10^7 \text{ e}$	$8 \times 10^6 \text{ e}$
Incident power at 300 K	P_1	2.3 nW	0.82 nW
Critical responsivity	R_c		
300 K scene		156 mA/W	78 mA/W
318 K scene		113 mA/W	58 mA/W
Temperature resolution	NE ΔT	< 10 mK	< 20 mK

system performance of the camera usually degrades more strongly due to the extra charging of the ROIC by the dark current than by the reduced detectivity of the detector.

The *noise-equivalent temperature difference* (NE ΔT) is defined as [12] $\text{NE}\Delta T = i_n / R(dP_1/dT_B)$, where R is the responsivity and i_n the noise current. For the photon energies considered here, the Bose–Einstein distribution function in Eq. (1) can be approximated by an exponential dependence, such that

$$\frac{dP_1}{dT_B} = \frac{hv}{k_B T_B^2} P_B. \quad (2)$$

The noise current i_n of a QWIP with N periods is given to a good approximation by [13]

$$i_n^2 = 4e \left(g - \frac{1}{2N} \right) I \Delta f = \frac{4e}{N p_c} \left(1 - \frac{p_c}{2} \right) I \Delta f. \quad (3)$$

Here p_c is the probability for excited electrons to be captured in a quantum well, $g = 1/N p_c$ the noise gain, I the total current, and Δf the bandwidth of the noise measurement. In the case of a conventional photoconductive QWIP, we have $p_c \ll 1$, such that Eq. (3) is reduced to the conventional [14,15] expression $4egI\Delta f$ for the generation-recombination noise. The full equation (3) will be used in Section 4.

We now use the standard expression $R = eng/hv$ with the quantum efficiency η and obtain

$$\text{NE}\Delta T_{\text{DET}} = 2k_B T_B^2 \sqrt{\frac{\Delta f}{hv\eta P_1}} \quad (4)$$

for the *detector-limited* NE ΔT of a photoconductive QWIP. Assuming a rectangular gate function for the detection process, Δf is related with the integration time τ via [12] $\Delta f = 1/2\tau$. In actual circuits, the bandwidth Δf for a given τ is usually larger than in this relation, which results in a somewhat higher value of the NE ΔT .

Different restrictions apply in the case that the responsivity of the detector exceeds R_c , since the integration time has to be reduced according to the storage capacity Q_c of the ROIC. Assuming a 100% background limited detection, we thus obtain in the *readout-limited* case

$$\text{NE}\Delta T_{\text{RL}} = \frac{k_B T^2}{hv} \sqrt{\frac{2eg}{Q_c}}. \quad (5)$$

The relation $\text{NE}\Delta T_{\text{RL}} \sim \sqrt{g/Q_c}$ implies that a reduced g increases the effective storage capacity of the sensor. In fact, each detected photon charges the readout capacitor by g electrons, such that a reduced gain implies a reduced number of noise electrons and an improved dynamic range of the sensor. Small responsivities can thus be tolerated for camera applications if the gain is small and if snapshot capability with very short integration times is not required.

In addition to the limits associated with the detectivity and the charge storage capacity, the temperature resolution of actual cameras is also influenced by the noise due to input amplifiers and analog-to-digital converters (ADC). Moreover, cameras are mostly operated at only 50–60% of the full storage capacity in order to maintain a reasonable dynamic range, since P_1 increases by 100% if T is raised from 300 to 340 K. In the case of a 14-bit ADC, one least significant bit then corresponds to a 5 mK temperature difference, which imposes an additional limit on the temperature resolution.

For these reasons, and because of the above-mentioned uncertainty in the relation between the bandwidth Δf and the integration time τ , the prediction of temperature resolutions for actual camera systems is beyond the scope of the present paper. Nevertheless, Eqs. (4) and (5) are useful for the purpose of detector optimization and to compare the performance of specific detector structures.

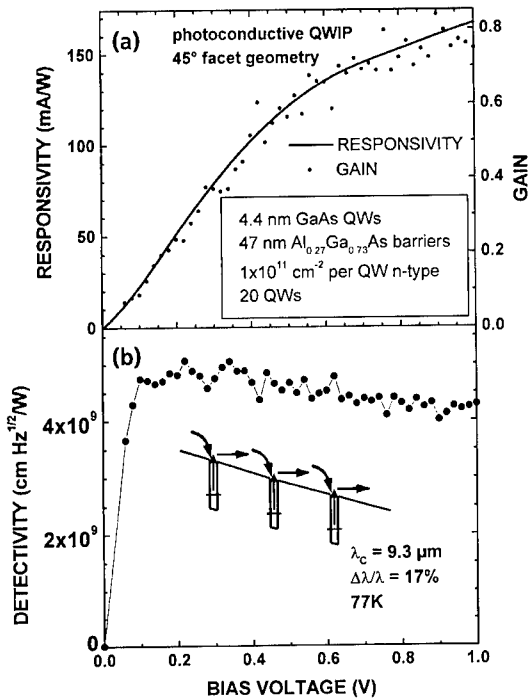


Fig. 2. (a) Peak responsivity R , gain g , and (b) peak detectivity D^* of a photoconductive QWIP versus bias voltage.

3. Photoconductive QWIPs for camera applications

In order to match the QWIP to the ROIC, bound-to-quasibound QWIPs with 50 periods have been used previously [3] since these devices exhibit very large photocurrent/darkcurrent ratios, resulting in high operating temperatures. However, the detectivity of these devices is maximized at relatively large electric fields where the photoconductive gain is high.

In contrast, we have decided to operate the QWIP at very small electric fields (typically below 3 kV/cm) where the photoconductive gain is small. Low-bias operation is possible without sacrificing detectivity for bound-to-continuum QWIPs since the emission probability saturates at small fields. In order to illustrate this behavior, we have plotted in Fig. 2 the responsivity, gain and peak detectivity of such a QWIP structure. The noise current and gain measurements have been described elsewhere [16]. In Fig. 2a, the gain is strictly proportional to the peak responsivity, thus indicating a saturation of the emission probability. The ratio R/g yields a peak quantum effi-

ciency of $\eta = 3\%$. The detectivity is fully developed already at 100 mV applied bias where the gain is only 10%.

About six times higher values for R , η , and D^* as compared to the 45° facet geometry used in Fig. 2 are observed for devices with two-dimensional grating couplers. This enhancement is caused by the high coupling efficiency of the grating [17].¹ It is therefore clear from the previous section that a bias voltage of 150–300 mV is sufficient for operating the QWIP array in combination with an ROIC.

In this way, excellent temperature resolution is obtained already for a relatively thin active region of only $N = 20$ QWIP periods, thus facilitating detector processing. The process technology for the fabrication of QWIP FPAs has been described in detail elsewhere [7,9]. Fig. 3 shows secondary electron emission micrographs of QWIP arrays as used in our camera systems. The individual mesas of the 256×256 array are defined by wet-chemical etching, with a pixel size of about $37 \times 37 \mu\text{m}^2$. Dry etching is used for the $22 \times 22 \mu\text{m}^2$ mesas of the 640×512 array in order to keep a high filling factor (see Table 1). The arrays are covered by a silicon nitride passivation layer with openings in the center of each mesa. Here an additional bond metallization provides electrical contacts for connection with the ROIC via indium solder bumps. Also visible are etched two-dimensional diffraction gratings, which have been covered by a mirror metallization before depositing the passivation. Geometrical parameters of both FPAs are listed in Table 1.

4. Low-noise QWIPs for further enhancement of the temperature resolution

While Eqs. (4) and (5) are valid for a *photoconductive* detector, the $\text{NE}\Delta T$ is further reduced by a factor of $\sqrt{2}$ in the case of a particular type of (photo-voltaic) QWIPs, where i_n arises from shot noise rather than from generation-recombination noise [11,16]. The physical reason for the improved noise behavior

¹ This grating-induced enhancement factor relates to the case that the 45° facet device does not contain an additional 1 μm thick GaAs top layer (which may be used to produce the grating). A different enhancement factor (about 2.5) is observed if this top layer is present. (see Ref. [17]).

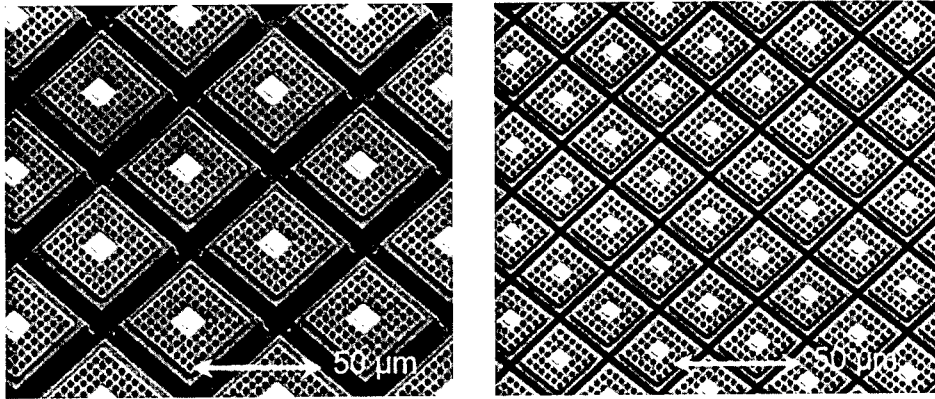


Fig. 3. Scanning electron microscope pictures of detector pixels of the 256×256 FPA (left) and of the 640×512 FPA (right).

of these *low-noise QWIPs* can be understood from the fact that the photoexcited carriers have a high probability p_c (close to 100%) to be captured into the adjacent period of the detector structure, such that the noise induced by statistical variations of the drift length ('recombination noise') is suppressed. As a consequence, the noise current of such a device is reduced by a factor of $\sqrt{2}$, which can also be seen by inserting $p_c = 1$ into Eq. (3). Therefore, a reduced NE ΔT is expected to be obtained by using low-noise QWIPs, in particular for large FPA sensors.

The photoconduction mechanism of a low-noise QWIP is indicated in the inset of Fig. 4b. Each period of the detector is composed of four zones (1)–(4) with different functions. In the excitation zone (1), carriers are optically excited and emitted into the quasi-continuum of the drift zone (2). These two zones are in analogy to the barrier and well of the conventional QWIP. Moreover, two additional zones are present in order to control the relaxation of the photoexcited carriers, namely a capture zone (3) and a tunneling zone (4). The tunneling zone has two functions. First, it blocks the carriers in the quasi-continuum, such that they can be captured efficiently into the capture zone. Second, it transmits carriers from the ground state of the capture zone into the excitation zone of the subsequent period. Because of this layout, the detector structure has also been called four-zone QWIP [10].

Fig. 4 summarizes the detection properties of a typical low-noise QWIP. A detailed description of the

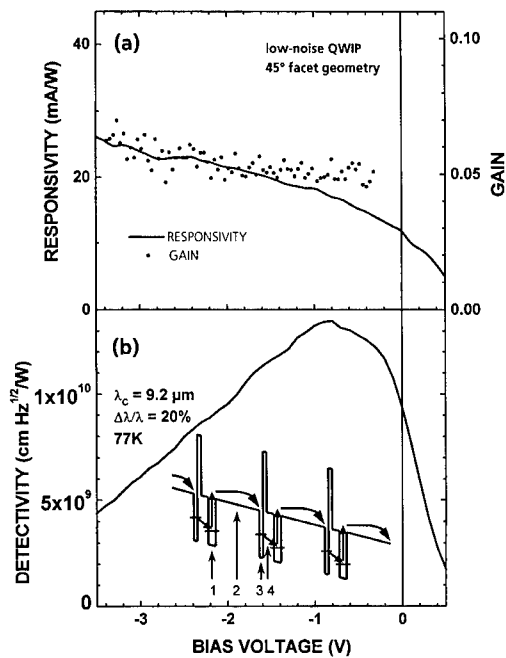


Fig. 4. (a) Peak responsivity R , gain g , and (b) peak detectivity D^* of a low-noise QWIP versus bias voltage.

20-period device is given in Refs. [10,18]. The peak responsivity² is 11 mA/W at 0 V applied bias and

² In contrast to previous measurements [10] which use a fixed scaling factor to relate the responsivity measured at a wavelength of 9.2 μm to the value at the peak wavelength, we have taken here into account the variation of this scaling factor with the bias voltage.

about 22 mA/W in the range between -2 and -3 V (see Fig. 4a). We associate the latter bias region with the field regime where complete emission of the photoexcited electrons occurs, whereas the emitted carriers are still captured efficiently [10,18]. This results in a photocarrier mean free path of one period, i.e., a photoconductive gain of $1/N = 0.05$. This interpretation is further supported by the behavior of the noise current i_n . As indicated in Fig. 4a, a gain of 5% is obtained from noise measurements [11,16] via Eq. (3). From these data we calculate an internal peak quantum efficiency of $\eta = 7\%$.

The bias dependence of the detectivity obtained from the measured responsivity and noise current is shown in Fig. 4b. The detectivity has its maximum at around -0.8 V. About 70% of this value is still obtained at 0 V (photovoltaic operation). The detectivity strongly depends on the sign of the bias voltage due to the asymmetric nature of the transport process. This behavior is in strong contrast to that of a conventional QWIP where the detectivity vanishes at 0 V (see Fig. 2).

Let us now address the potential of these low-noise QWIPs in the context of detector arrays. Again, about six times higher quantum efficiencies as compared to the present test device are expected for devices with grating coupler [17]. A responsivity of about 0.1 A/W is therefore expected for a low-noise QWIP FPA. According to Table 1, this value is quite suitable for multiplexers.

Fig. 5 shows peak detectivities of both conventional and low-noise QWIP structures as a function of the cutoff wavelength. A good description of the functional dependence is obtained within a thermionic emission model (dashed line). The low-noise QWIPs show similar detectivities as the conventional ones. Since these detectivities are limited by the dark current and not by the background photocurrent, the improvement due to the suppression of the recombination noise is not prominent in Fig. 5. In fact, the low-noise QWIPs were grown with much higher carrier densities than the conventional QWIPs (4×10^{11} and 1×10^{11} cm $^{-2}$ per QW, respectively), which results in a decrease of the activation energy. In addition, the spectral line width of the responsivity in low-noise QWIPs is typically 10–20% larger than for the conventional QWIPs, such that the peak detectivity is reduced correspondingly. However, in contrast

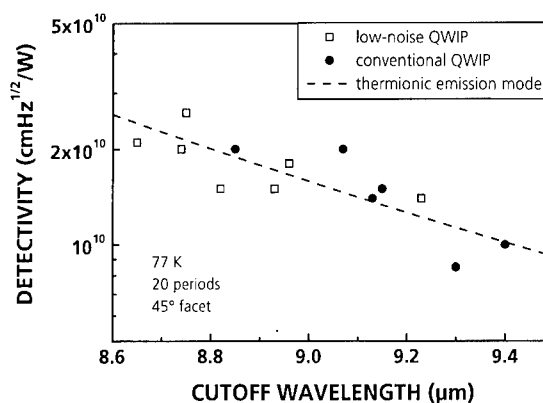


Fig. 5. Peak detectivity of low-noise QWIPs and conventional QWIPs at 77 K versus cutoff wavelength.

to the dark detectivities of Fig. 5, the suppression of the recombination noise does have an influence on the background-limited detectivity which determines the temperature resolution of a camera. In fact, preliminary measurements indicate a temperature resolution of 7.2 mK for a 256×256 QWIP camera prototype comprising a low-noise QWIP FPA.

5. Conclusion

System considerations concerning focal plane array sensors for the long-wavelength infrared indicate that readout-limited detection is obtained at responsivities above 0.1–0.2 A/W at 20 ms integration time. In this case, the temperature resolution and the dynamical range of the sensor only depends on the noise performance. We have therefore optimized photoconductive GaAs/AlGaAs QWIP structures for low-bias operation, which results in a small photoconductive gain and an accordingly reduced noise. Excellent temperature resolutions of better than 10 and 20 mK have been obtained in this way for 256×256 and 640×512 infrared sensors based on QWIP FPAs.

Further improvement of the temperature resolution is achievable using low-noise QWIPs. In addition to the doped quantum well and the thermionic barrier, which are also present in the conventional QWIP, each period of this novel device contains a capture zone followed by a tunneling barrier. In this way, the capture process can be controlled, giving rise to a small

photoconductive gain and to a suppression of the recombination noise. Using this detector, an improved thermal resolution can be obtained in particular in the case of large FPA sensors with limited charge storage capacity.

Acknowledgements

We are grateful to E. Diwo and K. Schwarz for expert technical assistance. The detector development was supported by the German Ministry of Defense.

References

- [1] B.F. Levine, C.G. Bethea, K.G. Glogovsky, J.W. Stayt, R.E. Leibenguth, *Semicond. Sci. Technol.* 6 (1991) C114.
- [2] W.A. Beck, J.W. Little, A.C. Goldberg, T.S. Faska, in: H.C. Liu, B.F. Levine, J.Y. Andersson (Eds.), *Quantum Well Intersubband Transition Physics and Devices*, NATO ASI Series Vol. E 270, Kluwer Academic Publishers, Dordrecht, 1994, p. 55.
- [3] S.D. Gunapala, J. Bandara, J.K. Liu, W. Hong, M. Sundaram, R. Carralejo, C.A. Shott, P.D. Maker, R.E. Muller, *Proc. SPIE* 3061 (1997) 382.
- [4] D. Scribner, J. Schuler, P. Warren, M. Satyshur, M. Kruer, *Proc. SPIE* 3379 (1998) 2.
- [5] S.D. Gunapala, S.V. Bandara, J.K. Liu, E.M. Luong, S.B. Rafol, J.M. Mumolo, N.Q. Tran, J.D. Vincent, C.A. Shott, J. Long, A. Singh, P.D. LeVan, *Proc. SPIE* 3698 (1999) 687.
- [6] R. Breiter, W. Cabanski, R. Koch, W. Rode, J. Ziegler, K. Eberhardt, R. Oelmaier, *Proc. SPIE* 3379 (1998) 423.
- [7] M. Walther, F. Fuchs, H. Schneider, J. Schmitz, W. Pletschen, J. Braunstein, J. Ziegler, W. Cabanski, P. Koidl, G. Weimann, *Proc. SPIE* 3436 (1998) 348.
- [8] R. Breiter, W. Cabanski, R. Koch, W. Rode, J. Ziegler, K. Eberhardt, R. Oelmaier, M. Walther, *Proc. SPIE* 3698 (1999) 397.
- [9] M. Walther, J. Fleissner, H. Schneider, C. Schönbein, W. Pletschen, E. Diwo, K. Schwarz, J. Braunstein, P. Koidl, J. Ziegler, W. Cabanski, *Proceedings of the International Symposium on Compound Semiconductors (ISCS'99)*, Berlin, 22–26 August 1999.
- [10] H. Schneider, C. Schönbein, M. Walther, K. Schwarz, J. Fleissner, P. Koidl, *Appl. Phys. Lett.* 71 (1997) 246.
- [11] C. Schönbein, H. Schneider, R. Rehm, M. Walther, *Appl. Phys. Lett.* 73 (1998) 1251.
- [12] R.H. Kingston, in: D.L. Mac Adam (Ed.), *Detection of Optical and Infrared Radiation*, Springer Series in Optical Sciences, Vol. 10, Springer, Berlin, 1978.
- [13] W.A. Beck, *Appl. Phys. Lett.* 63 (1993) 3589.
- [14] B. Levine, *J. Appl. Phys.* 74 (1993) R1.
- [15] H.C. Liu, *Appl. Phys. Lett.* 61 (1992) 2703.
- [16] R. Rehm, H. Schneider, C. Schönbein, M. Walther, *Physica E*, 1999, this volume.
- [17] H. Schneider, C. Schönbein, M. Walther, P. Koidl, G. Weimann, *Appl. Phys. Lett.* 74 (1999) 16.
- [18] C. Schönbein, H. Schneider, R. Rehm, M. Walther, in: S.S. Li, M.Z. Tidrow, S.D. Gunapala, H.C. Liu (Eds.), *Long Wavelength Infrared Detectors and Arrays: Physics and Applications*, Electrochemical Society Proceedings Vol. 98-21, 1999, p. 158.



ELSEVIER

Physica E 7 (2000) 108–111

PHYSICA E

www.elsevier.nl/locate/physce

Recent developments and applications of quantum well infrared photodetector focal plane arrays

S.D. Gunapala^{a,*}, S.V. Bandara^a, A. Singh^b, J.K. Liu^a, E.M. Luong^a, J.M. Mumolo^a,
P.D. LeVan^b

^a*Jet Propulsion Laboratory, Centre for Space Microelectronics Technology, California Institute of Technology,
M/S 302-306, Pasadena, CA 91109, USA*

^b*Air Force Research Laboratory, Kirtland Air Force Base, NM 87117, USA*

Abstract

One of the simplest device realizations of the classic particle-in-the-box problem of basic quantum mechanics is the quantum well infrared photodetector (QWIP). In this paper we discuss the optimization of the detector design, material growth and processing that has culminated in realization of large format long-wavelength QWIP cameras, holding forth great promise for many applications in 6–25 μm wavelength range in science, medicine, defense and industry. In addition, we present the recent developments in long-wavelength/very long-wavelength dualband QWIP imaging camera for various applications. © 2000 Published by Elsevier Science B.V. All rights reserved.

Keywords: Infrared photodetector; Detectors; Multi-color camera; Arrays

1. 640×486 Long-wavelength QWIP camera

In order to detect long-wavelength infrared (LWIR) radiation we have designed the following multi-quantum well (MQW) structure. Each period of the MQW structure consists of a 45 Å well of GaAs (doped $n = 4 \times 10^{17} \text{ cm}^{-3}$) and a 500 Å barrier of $\text{Al}_{0.3}\text{Ga}_{0.7}\text{As}$. Stacking many identical quantum wells (typically 50) together increases photon absorption. This photosensitive MQW structure is sandwiched

between 0.5 μm GaAs top and bottom contact layers doped $n = 5 \times 10^{17} \text{ cm}^{-3}$, grown on a semi-insulating GaAs substrate by molecular beam epitaxy (MBE). Then a 0.7 μm thick GaAs cap layer on top of a 300 Å $\text{Al}_{0.3}\text{Ga}_{0.7}\text{As}$ stop-etch layer was grown in situ on top of the device structure to fabricate the light coupling optical cavity.

The responsivity spectrum is shown in Fig. 1. The responsivity of the detector peaks at 8.5 μm and the peak responsivity (R_p) of the detector is 300 mA/W at bias $V_B = -3 \text{ V}$. The spectral width and the cutoff wavelength are $\Delta\lambda/\lambda = 10\%$ and $\lambda_c = 8.9 \mu\text{m}$, respectively. The peak quantum efficiency was 6.9% at bias $V_B = -1 \text{ V}$ for a 45° double pass. The lower quantum efficiency is due to the lower well doping density

* Corresponding author. Tel.: 001-818-354-1880; fax: +1-818-393-4540.

E-mail address: sarath.d.gunapala@jpl.nasa.gov (S.D. Gunapala)

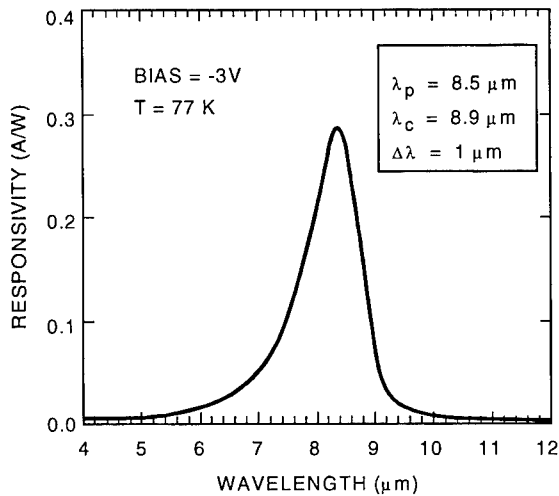


Fig. 1. Responsivity spectrum of a bound-to-quasibound LWIR QWIP test structure at temperature $T = 77$ K. The spectral response peak is at $8.4 \mu\text{m}$ and the long wavelength cutoff is at $8.9 \mu\text{m}$.

($5 \times 10^{17} \text{ cm}^{-3}$) as it is necessary to suppress the dark current at the highest possible operating temperature [1].

After the 2-D grating array was defined by the photolithography and dry etching, the photoconductive QWIPs of the 640×486 focal plane arrays (FPAs) were fabricated by wet chemical etching through the photosensitive GaAs/ $\text{Al}_x\text{Ga}_{1-x}\text{As}$ MQW layers into the $0.5 \mu\text{m}$ thick doped GaAs bottom contact layer. The pitch of the FPA is $25 \mu\text{m}$ and the actual pixel size is $18 \times 18 \mu\text{m}^2$. The cross gratings on top of the detectors were then covered with Au/Ge and Au for Ohmic contact and reflection. A single QWIP FPA was chosen and hybridized to a 640×486 direct injection silicon readout multiplexer and biased at $V_B = -2.0$ V. The FPA was back-illuminated through the flat thinned substrate membrane (thickness $\approx 1300 \text{ \AA}$). This thinned GaAs FPA membrane has completely eliminated the thermal mismatch between the silicon CMOS readout multiplexer and the GaAs-based QWIP FPA. Basically, the thinned GaAs based QWIP FPA membrane adapts to the thermal expansion and contraction coefficients of the silicon readout multiplexer. Therefore, this thinning has played an extremely important role in the fabrication of large area FPA hybrids. In addition, this thinning has completely eliminated the pixel-to-pixel

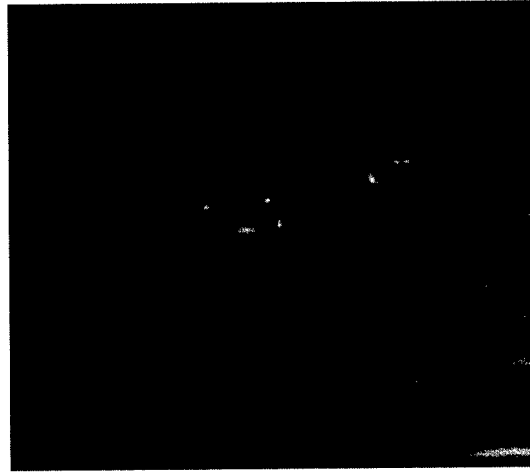


Fig. 2. This picture was taken in the night (around midnight) and it clearly shows where automobiles were parked during the day time. This image demonstrates the high sensitivity of the 640×486 long-wavelength QWIP staring array camera.

optical cross-talk of the FPA. This initial array gave excellent images with 99.9% of the pixels working, demonstrating the high yield of GaAs technology.

A 640×486 QWIP FPA hybrid was mounted onto a 84-pin lead-less chip carrier and installed into a laboratory dewar which is cooled by liquid nitrogen to demonstrate a LWIR imaging camera [2]. The experimentally measured mean noise equivalent temperature difference ($\text{NE}\Delta T$) of the QWIP camera is 36 mK at an operating temperature of $T = 70$ K and bias $V_B = -2$ V at 300 K background. This agrees reasonably with our estimated value of 25 mK based on single element test structure data. The uncorrected $\text{NE}\Delta T$ non-uniformity of the 640×486 FPA is about 5.6% ($= \text{sigma/mean}$).

Video images were taken at a frame rate of 30 Hz at temperatures as high as $T = 70$ K using a readout circuit (ROC) capacitor having a charge capacity of 9×10^6 electrons. The non-uniformity after two-point (17° and 27°C) correction improves to an impressive 0.03%. Fig. 2 shows a frame of video image taken with this long-wavelength 640×486 QWIP camera. This image demonstrates the high sensitivity of the 640×486 long-wavelength QWIP staring array camera [2]. As mentioned earlier, this high yield is due to the excellent GaAs growth uniformity and the mature GaAs processing technology.

2. 640×486 Long-wavelength dualband imaging camera

The LWIR and very long-wavelength infrared (VLWIR) dualband QWIP device structure described in this section processed into interlace simultaneously readable dualband FPAs (i.e., odd rows for one color and the even rows for the other color) [3].

The device structure consists of a 30 periods stack, of VLWIR QWIP structure and a second 18 periods stack of LWIR QWIP structure separated by a heavily doped $0.5 \mu\text{m}$ thick intermediate GaAs contact layer. The first stack (VLWIR) consists of 30 periods of a 500 \AA $\text{Al}_x\text{Ga}_{1-x}\text{As}$ barrier and a 60 \AA GaAs well. Since the dark current of this device structure is dominated by the longer wavelength portion of the device structure, the VLWIR QWIP structure has been designed to have a bound-to-quasibound intersubband absorption [1] peak at $14.5 \mu\text{m}$. The second stack (LWIR) consists of 18 periods of a 500 \AA $\text{Al}_x\text{Ga}_{1-x}\text{As}$ barrier and a narrow 40 \AA GaAs well. This LWIR QWIP structure has been designed to have a bound-to-continuum intersubband absorption peak at $8.5 \mu\text{m}$, since photocurrent and dark current of the LWIR device structure is relatively small compared to the VLWIR portion of the device structure. This whole dualband QWIP structure is then sandwiched between $0.5 \mu\text{m}$ GaAs top and bottom contact layers doped with $n = 5 \times 10^{17} \text{ cm}^{-3}$, and has been grown on a semi-insulating GaAs substrate by MBE. Then a 300 \AA $\text{Al}_{0.3}\text{Ga}_{0.7}\text{As}$ stop-etch layer and a $1.0 \mu\text{m}$ thick GaAs cap layer were grown in situ on top of the device structure. GaAs wells of the LWIR and VLWIR stacks were doped with $n = 6 \times 10^{17}$ and $2.5 \times 10^{17} \text{ cm}^{-3}$, respectively. All contact layers were doped to $n = 5 \times 10^{17} \text{ cm}^{-3}$. The GaAs well doping density of the LWIR stack was intentionally increased by a factor of two to compensate for the reduced number of quantum wells in the LWIR stack [3]. It is worth noting that, the total (dark current + photocurrent) current of each stack can be independently controlled by carefully designing the position of the upper state, well doping densities, and the number of periods in each MQW stack. All of these features were utilized to obtained approximately equal total currents from each MQW stack.

Simultaneously measured responsivity spectra of these vertically integrated dualband QWIPs are shown

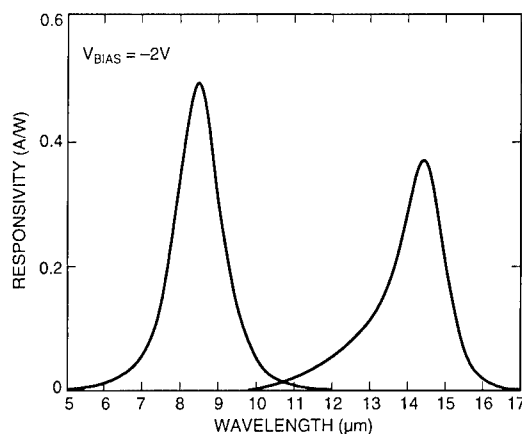


Fig. 3. Simultaneously measured responsivity spectrum of vertically integrated LWIR and VLWIR dualband QWIP detector.

in Fig. 3. Based on single element test detector data, the LWIR detectors show BLIP at bias $V_B = -2 \text{ V}$ and temperature $T = 72 \text{ K}$ for a 300 K background with $f/2$ cold stop. The VLWIR detectors show BLIP under the same operating conditions at 45 K operating temperature [3]. Two different 2-D periodic grating structures were designed to independently couple the $8\text{--}9$ and $14\text{--}15 \mu\text{m}$ radiation into detector pixels in even and odd rows of the FPAs. The FPA fabrication process is described elsewhere [3].

These dualband FPAs were tested at a background temperature of 300 K , with $f/2$ cold stop, and at 30 Hz frame rate. As expected (due to BLIP), the estimated and experimentally obtained $\text{NE}\Delta T$ values of the LWIR detectors do not change significantly at temperatures below 65 K . The estimated $\text{NE}\Delta T$ of LWIR and VLWIR detectors at 40 K are 36 and 44 mK , respectively (see Fig. 4). These estimated $\text{NE}\Delta T$ values based on the test detector data agree reasonably well with the experimentally obtained values. The experimental LWIR $\text{NE}\Delta T$ value is lower than the estimated $\text{NE}\Delta T$ value of 36 mK . This improvement is attributed to the 2-D periodic grating light coupling efficiency. On the other hand, the experimental VLWIR $\text{NE}\Delta T$ value is higher than the estimated $\text{NE}\Delta T$ value of 44 mK . The authors believe this degradation is due to the inefficient light coupling at $14\text{--}15 \mu\text{m}$ region, readout multiplexer noise, and noise of the proximity electronics. At 40 K the performance of both LWIR and VLWIR detector pixels of this dualband FPA are limited by photocurrent noise and readout noise.

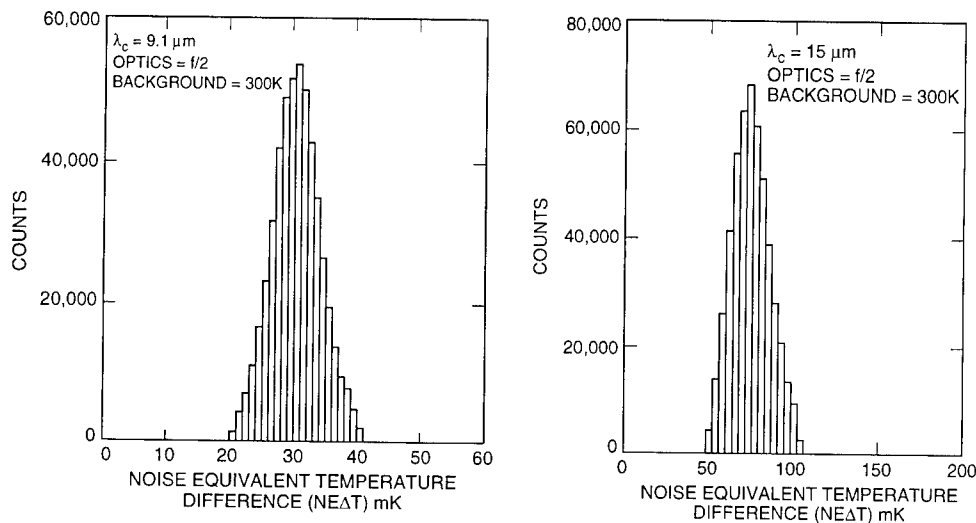


Fig. 4. The uncorrected noise equivalent temperature difference (NEΔT) histogram of 8–9 μm detector pixels of the 640×486 dualband FPA. The mean NEΔT is 29 mK. The uncorrected noise equivalent temperature difference (NEΔT) histogram of 14–15 μm detector pixels of the 640×486 dualband FPA. The mean NEΔT is 74 mK.

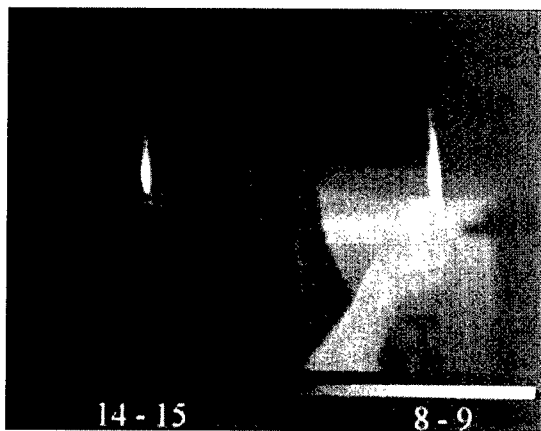


Fig. 5. Both pictures show (Flame – simultaneously acquired) two-color images with the 640×486 two-color QWIP camera. Image on the left is from 14–15 μm infrared and the image on the right is from 8–9 μm infrared. Pixel pitch of the FPA is 25 μm . The 14–15 μm image is less sharp due to the diffraction limited spot size being larger than the pixel pitch of the FPA.

Video images were taken at a frame rate of 30 Hz, at temperatures as high as $T = 74 \text{ K}$, using a ROC capacitor having a charge capacity of 9×10^6 electrons (the maximum number of photoelectrons and dark electrons that can be counted in the time taken to read each detector pixel). Fig. 5 shows simultane-

ously acquired 8–9 and 14–15 μm images using this two-color camera [3].

3. Summary

In summary, we have demonstrated 648×486 LWIR imaging camera, and the first 640×486 LWIR/VLWIR dualband imaging camera.

Acknowledgements

The research described in this paper was performed by the Center for Space Microelectronics Technology, Jet Propulsion Laboratory, California Institute of Technology, and was jointly sponsored by the Ballistic Missile Defense Organization/Exo-atmospheric Interceptor Technology office, and the Air Force Research Laboratory.

References

- [1] S.D. Gunapala, S.V. Bandara, in: Semiconductors and Semimetals, Vol. 62, Academic Press, New York, 1999, pp. 197–282.
- [2] S.D. Gunapala et al., SPIE 3061 (1997) 722.
- [3] S.D. Gunapala et al., SPIE 3698 (1999) 687.



ELSEVIER

Physica E 7 (2000) 112–114

PHYSICA E

www.elsevier.nl/locate/physa

New designs and applications of corrugated QWIPs

K.K. Choi^{a,*}, C.J. Chen^b, K.L. Bacher^c, D.C. Tsui^b^a*US Army Research Laboratory, Attn: AMSRL-SE-EI, 2800 Powder Mill Road, Adelphi MD 20783, USA*^b*Department of Electrical Engineering, Princeton University, NJ 08544, USA*^c*Quantum Epitaxial Designs, Inc., Bethlehem, PA 18015, USA*

Abstract

Corrugated QWIPs are sensitive to only one polarization of light. We used two C-QWIPs with their corrugations oriented in orthogonal directions for polarization-sensitive detection. By measuring the photocurrent ratio from these two detectors, the polarization-state of the radiation rather than its intensity can be sensed; the detection is useful in scenes with extremely small or large intensity contrast. Using C-QWIPs for detector characterization, we obtained the intensity decay function of light propagating nearly parallel to the layers, with which the absorption coefficient can be measured. New C-QWIPs have been designed to improve the detector performance. In one approach, additional vertical trenches are etched into C-QWIP structures. In another approach, the entire corrugated area is covered with a conformal dielectric and a metal. Both approaches prove effective. © 2000 Elsevier Science B.V. All rights reserved.

Keywords: Infrared detector; Light coupling; Polarization-sensitive detection

In certain circumstances, the utility of infrared imaging is limited by the low thermal contrast. On the other hand, the polarization of thermal radiation can have high contrast, depending on the nature of the target and the background. The use of IR detectors, which can capture both polarization and intensity data, will lead to significant improvement in target recognition functions.

Since C-QWIPs with linear corrugations are sensitive to only one polarization, detectors with different corrugation orientations can be used to detect both the intensity and the polarization of a radiation [1].

Fig. 1 shows the photocurrent of three C-QWIPs oriented at 90° (detector A), 0° (detector B) and 45° (detector C) as a function of the polarization angle θ relative to the [0 1 1] axis. As expected, the signal from detectors A and B is 90° out of phase. If we take the photocurrent ratio $r = J_A/J_B$ from these two detectors, it is maximized at $\theta = 0^\circ$ and decreases toward $\pm 90^\circ$ as shown in Fig. 1(b). This ratio is independent of the target intensity, as the figure shows, for two blackbody temperatures. Therefore, from the value of r , one can determine the angle θ . However, when the radiation is only partially polarized, the ratio r depends on the degree of polarization as well as θ of the polarized component. Nevertheless, the r contrast remains finite as long as there is a certain degree of polarization. It

* Corresponding author. Tel.: +1-301-394-0495; fax: +1-301-394-1746.

E-mail address: kchoi@arl.mil (K.K. Choi)

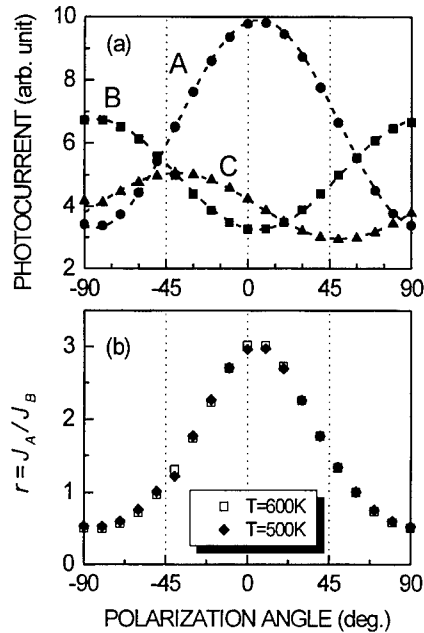


Fig. 1. (a) Photoresponse of C-QWIPs with orientation at 90° (A), 0° (B), and 45° (C), as a function of polarization angle. (b) The ratio of photocurrent from detectors A and B.

can be used in target recognition functions that do not require complete knowledge of the polarization state.

The surface corrugations in C-QWIP structures are also useful in detector characterization. They can be used to measure the absorption coefficient α and the photoconductive gain g of a QWIP material under typical operating conditions. In this approach, a batch of C-QWIPs with different V-groove periods P is prepared. The normal incident light reflected at the slanted sidewalls travels nearly parallel to the layers. The s-polarization of the incident radiation can then be absorbed, and it decays exponentially as light propagates away from these sidewalls. As a function of P , the responsivity $R(P)$ is first increasing with P , since there is more active material in the detector. However, when P increases beyond $1/\alpha$, the material at the center of a corrugation unit receives little reflected light, while the total number of reflecting sidewalls is reduced. $R(P)$ thus decreases. The functional form of $R(P)$ is therefore determined by α . The value of g determines the overall magnitude of R . Therefore, by fitting $R(P)$ as a function of P , the values of α and g can be uniquely determined.

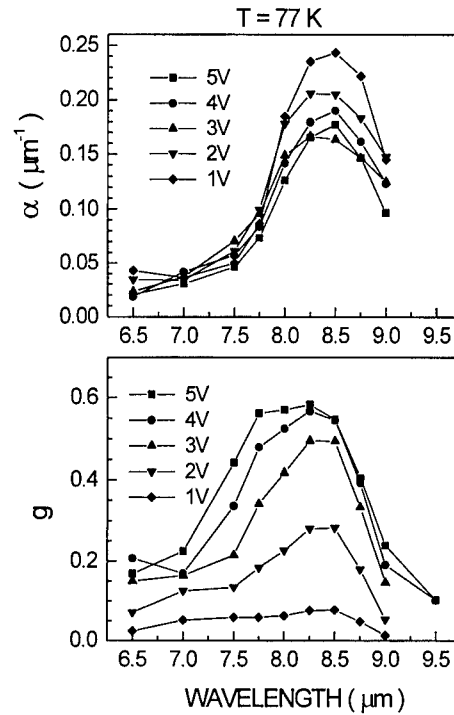


Fig. 2. The values of α and g of a typical QWIP at different wavelengths and biases.

Fig. 2 shows the results of α and g for a typical QWIP material. Despite the observed increase of R with the bias V , the value of α actually decreases, up to 38% at 5 V. This decrease can be explained by the carrier depletion in the QWs in the presence of an applied bias. The absorption is peaked at the same location as R , at which $\alpha = 0.22 \mu\text{m}^{-1}$ at 2 V, corresponding to a decay length of $4.5 \mu\text{m}$. The parameter g , on the other hand, increases monotonically with V , as expected. At low bias, g is approximately constant across the spectrum. However, the value of g increases rapidly around $8.5 \mu\text{m}$, creating a strong peak at large bias.

The peak value of g is plotted against V in Fig. 3, along with the noise gains of the background photocurrent and the 77 K dark current. At low bias, the three parameters are nearly the same. At high bias, they become different when g is sensitive to the electron energy. The measured values of the noise gains thus depend on the average electron energy distribution at large bias.

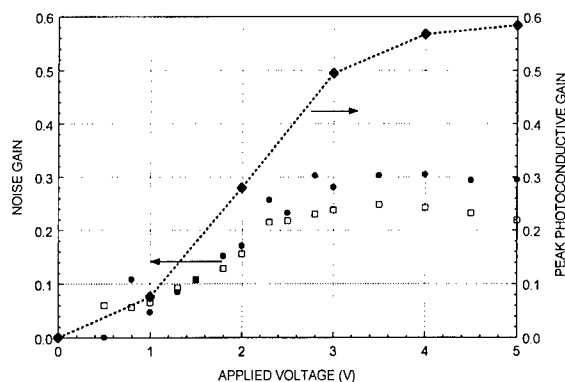


Fig. 3. The noise gain of the 77 K dark current (squares), the noise gain of the 300 K background photocurrent (circles) and the peak value of the photoconductive gain at different biases.

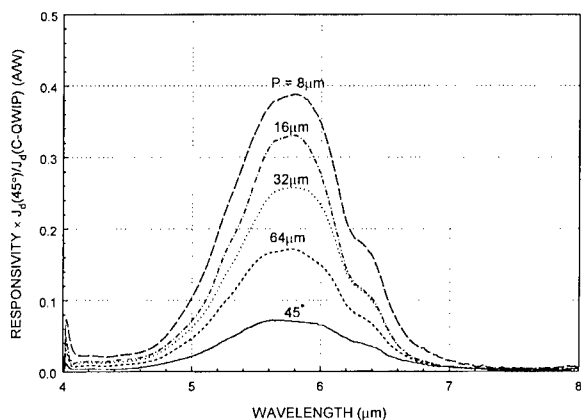


Fig. 4. The normalized responsivity for C-QWIPs having $\text{SiO}_2/\text{metal}$ coverage.

In order to improve the C-QWIP performance, we covered the entire C-QWIP with a thin dielectric film and a metal layer [2]. The metal provides a better confinement of light within the detector active region, thereby increasing the detector responsivity. Fig. 4 shows the normalized responsivity NR achieved under this approach. For the smallest $P = 8 \mu\text{m}$ tested, NR is 5.4 times larger than the edge coupling.

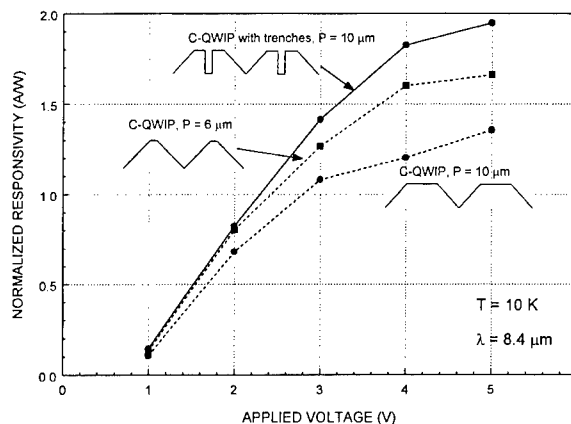


Fig. 5. The normalized responsivity for C-QWIPs with and without vertical trenches.

Based on parity symmetry of electromagnetic interaction, one can conclude that the vertical optical intensity is necessarily zero at the center of any symmetric corrugation profile. As a result, the center region produces no photocurrent, and better detector performance can be achieved if this region is removed. Fig. 5 shows that the NR of a C-QWIP with $2 \mu\text{m}$ trenches is 44% higher than that without at $V = 5 \text{ V}$. Even compared with a regular C-QWIP with a smaller P , there is a 15% improvement. This design is particularly useful when the pixel pitch can only fit one or two corrugation units.

In summary, we applied C-QWIPs in polarization-sensitive detection and detector characterization. The sensitivity of a C-QWIP can be improved by dielectric/metal coverage or with additional vertical trenches.

References

- [1] C.J. Chen, K.K. Choi, L. Rohinson, W.H. Chang, D.C. Tsui, *Appl. Phys. Lett.* 74 (1999) 862.
- [2] K.K. Choi, K.L. Bacher, Y. Wu, in: Li, Liu, Tidrow, Gunapala (Eds.), *Proceedings of the Sixth International Symposium on Long Wavelength Infrared Detectors and Arrays: Physics and Applications*, The Electro Chemical Society, Inc., NJ, 1998, p. 71.



ELSEVIER

Physica E 7 (2000) 115–119

PHYSICA E

www.elsevier.nl/locate/physa

Optical interference and nonlinearities in quantum-well infrared photodetectors

M. Ershov^{a,*}, H.C. Liu^b, A.G.U. Perera^a, S.G. Matsik^a

^aDepartment of Physics and Astronomy, Georgia State University, 29 Peachtree Center Avenue, Atlanta, GA 30303-3083, USA

^bInstitute for Microstructural Sciences, National Research Council, Ottawa, Ontario, K1A 0R6, Canada

Abstract

The effects of optical interference in quantum-well infrared photodetectors (QWIPs) caused by reflection of radiation from the metal contact are investigated. It is shown that interference leads to strong deterioration of QWIP characteristics (responsivity, noise, and noise equivalent power (NEP)) if signal photocurrent is larger than the dark current or background current. This is caused by the nonuniform distribution of the photogeneration rate, electric field, and all other microscopic physical quantities. As a result, the photocurrent gain and photoionization efficiency are decreased, while the noise gain is increased with respect to their values for uniform excitation. Several puzzling experimental effects – a strong increase of the QWIP NEP for high-power heterodyne operation and temperature dependence of QWIP responsivity – can be explained by the model described above. © 2000 Elsevier Science B.V. All rights reserved.

Keywords: Quantum-well infrared photodetectors; Nonlinearity; Optical interference; Responsivity

1. Introduction

Photoconductivity of quantum-well infrared photodetectors (QWIPs) is determined by the carrier photogeneration from the QWs and their transport in the QW structure [1]. Conventional QWIP theories assume that the electric field and photogeneration rate are constant across QWIP structure. Therefore, it is commonly believed that QWIP characteristics (responsivity, detectivity, etc.) are independent of temperature and incident infrared power. It has been shown recently [2,3] that QWIPs with *small*

number of QWs can display nonlinear photoresponse at relatively high infrared power. The decrease of responsivity occurs due to the voltage drop on the injection barrier and modulation of the electric field in the bulk of QWIP. These phenomena, however, cannot explain several puzzling experimental effects in QWIPs with *large* number of QWs. One of these effects observed recently is an unexpected large value of the QWIP noise equivalent power (NEP) in heterodyne mode of operation [4]. The observed value of the NEP exceeded the value $NEP(0) = 2\hbar\omega\Delta f/\eta$ (predicted by conventional heterodyne theories [5]) by a factor of 10 (!). Another effect reported recently is temperature dependence of QWIP responsivity [6].

* Corresponding author. Fax: +1-404-651-1427.

E-mail address: mershov@gsu.edu (M. Ershov)

We believe that these nonlinear effects can be explained by the non-uniform distribution of the infrared radiation intensity (and photoexcitation rate) in QWIPs. The nonuniformity of light distribution due to attenuation in QWIPs and other photodetectors has been studied in Refs. [7–10]. The influence of the radiation interference on detector characteristics has been reported in Refs. [11,12].

The nonuniformity of the light intensity in QWIP caused by the reflection from the metal contact and interference was demonstrated experimentally [13]. If the photoexcitation rate from the QWs exceeds the thermoionization rate, the nonuniformity leads to the modulation of the electric field and other physical quantities in the bulk of QWIP, resulting in deterioration of QWIP characteristics. The present paper reports detailed investigation of these effects.

2. Numerical model

Numerical simulation of QWIP operation was performed using a one-dimensional simulator [14] solving self-consistently equations describing physical processes in QWIP – Poisson equation, current continuity equation in the drift-diffusion approximation, and rate equations for capture and emission in QWs. The physical parameters of the model – field-dependent electron mobility, thermoionization rate from the QWs, and photoexcited electron escape probability – were fitted to the experimental dark current–voltage and responsivity–voltage characteristics, which is necessary to obtain realistic simulation results. The escape probability has been described by a model proposed in Ref. [15]. Calculation of QWIP characteristics has been done as follows. Dark current regime was simulated first, followed by simulation of illuminated conditions corresponding to various levels of incident infrared power. The responsivity was calculated as a difference of the total current at a given infrared power and the dark current, normalized to the power level. The photocurrent gain is given by the ratio of the photocurrent to total QW excitation rate caused by illumination. The photoionization efficiency is calculated as the ratio of the QW photoexcitation rate to incident photon flux. Note that with this definition of gain and efficiency the photoexcited carrier escape probability is included into the photo-

ionization efficiency. The noise has been evaluated according a model proposed in Ref. [16]. The noise power spectral density can be represented in a conventional form $S_I = 4eg_nI$, where I is the total current and g_n is the noise gain given by the expressions:

$$g_n = \frac{\sum_{i=1}^N z_i^2 (1 - p_i/2)/p_i}{(\sum_{i=1}^N z_i)^2}, \quad (1)$$

where z_i is the impedance of the i th barrier and p_i is the capture probability of the i th QW. Local impedance has been calculated as $z_i = \Delta V_i/\Delta I$, where ΔV_i is the change of the voltage drop across i th barrier to the change of current in QWIP upon application of a small voltage step (5 mV).

The noise equivalent power (NEP) (for heterodyne regime) is given by the expression

$$\text{NEP}(P) = \text{NEP}(0) \times [\eta(0)/\eta(P)] \times (g_p/g_n), \quad (2)$$

where $\text{NEP}(0) = 2\hbar\omega\Delta f/\eta$ is the low-power NEP value, and $\hbar\omega$ is the photon energy.

Calculations have been performed for GaAs/Al_{0.26}Ga_{0.74}As QWIPs with 32 QWs of 60 Å width, separated by barriers of 232 Å width. The barriers were undoped, and the QWs were center δ -doped with silicon to about $9 \times 10^{11} \text{ cm}^{-2}$. The GaAs contacts were doped at $1.5 \times 10^{18} \text{ cm}^{-3}$. These QWIPs were studied in detail both experimentally and theoretically earlier [2,17,18]. Optical excitation rate was assumed to be proportional to $\cos^2(kx)$, where k is the x -component of the wave vector, and x is the coordinate perpendicular to the QW plane ($x = 0$ corresponds to the metal–semiconductor interface). This distribution corresponds to 45° illumination geometry and perfect reflection from the metal contact [13].

3. Results

Fig. 1 shows the dependence of the responsivity, photocurrent gain, and photoionization efficiency on incident infrared power at temperature $T = 77 \text{ K}$ and applied bias $V = 1 \text{ V}$. Responsivity is constant at low-power, decreases with power, and saturates at low value for high infrared power. The responsivity is decreased by a factor of 5 at high power. The onset of the responsivity degradation occurs when the photocurrent exceeds the dark current. Responsivity is determined by the product of the photocurrent gain g_p and

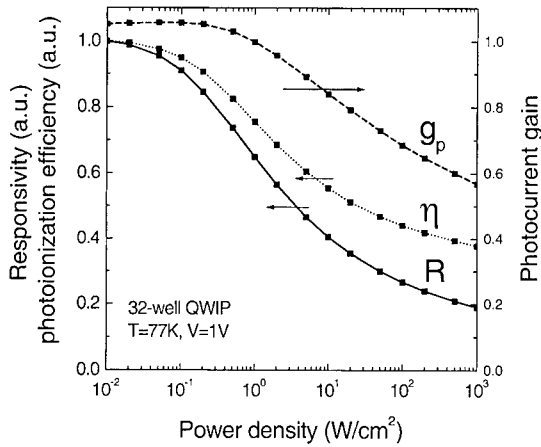


Fig. 1. Photoresponsivity R , photocurrent gain g_p , and photoionization efficiency η versus incident infrared power for 32-well QWIP at temperature $T = 77$ K and applied voltage $V = 1$ V. The dashed-dotted line shows the distribution of optical power.

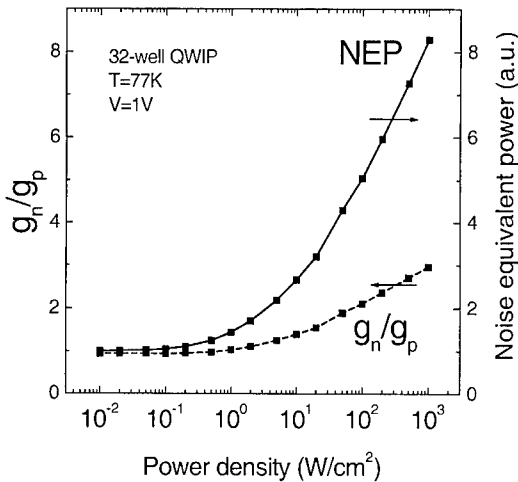


Fig. 2. Power dependence of the noise equivalent power NEP and noise gain-to-photocurrent gain ratio.

photoionization efficiency η : $R = e\eta/(\hbar\omega)$, where e is the electron charge. The decrease of the responsivity is caused by the degradation of both g_p and η , the reasons of which will be clear from the analysis of spatial distributions of physical quantities in QWIP.

Power dependence of the noise gain-to-photocurrent gain ratio and NEP are plotted in Fig. 2. The gain ratio is increased by a factor of 3, while the NEP is

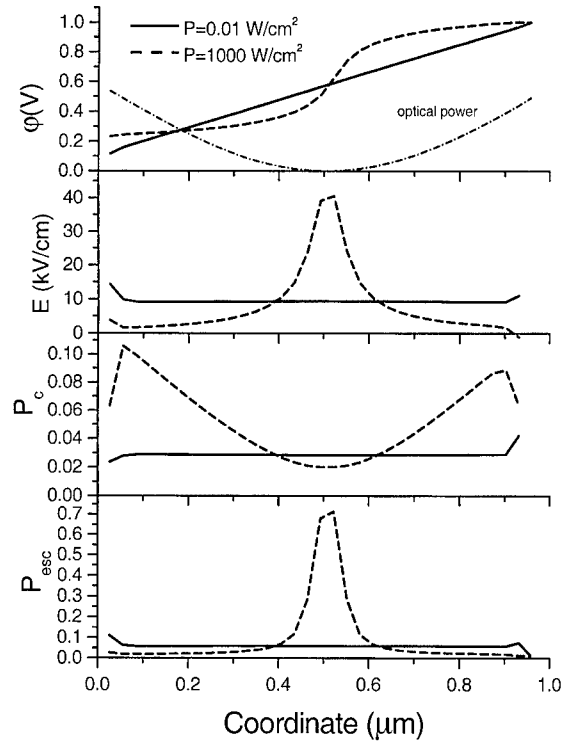


Fig. 3. Coordinate dependence of (a) potential, (b) electric field, (c) QW capture probability, and (d) photoexcited electron escape probability for low-power (solid line) and high-power (dashed line) densities.

enhanced by about an order of magnitude (!) with respect to their low-power values.

Fig. 3 illustrates the distributions of physical quantities in QWIP in the dark regime and under high-power illumination. At low power, the potential is almost linear with coordinate, indicating the uniformity of the electric field and other relevant quantities. However, at high power, the electric field is distributed nonuniformly across QWIP. This is caused by the nonuniform optical generation rate, having a minimum near the center of QWIP structure. To keep the total current constant in each cross-section, the QWs are recharged to provide higher electric field in unilluminated regions. As a result, the electric field in illuminated regions is decreased, causing the lowering of the drift electron velocity, photoexcited carrier escape probability, and increasing the capture probability. In unilluminated region, the increased electric field results in enhancement of the tunneling-assisted

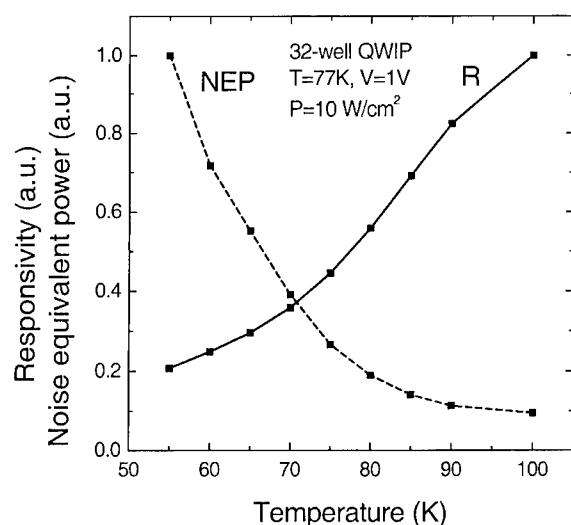


Fig. 4. Temperature dependence of responsivity and noise equivalent power for 32-well QWIP at incident power density of $P = 10 \text{ W/cm}^2$.

thermal ionization, which effectively plays the role of the photoexcitation.

The temperature dependence of the responsivity and NEP at incident power density $P = 10 \text{ W/cm}^2$ is plotted in Fig. 4. The effect of the temperature increase on the QWIP characteristics is equivalent to that of the lowering of infrared power – both R and NEP are improved with temperature (compare with Figs. 1 and 2). Thus, the nonlinearity of QWIP characteristics is determined primarily by the ratio of the thermal excitation rate to (nonuniform) optical excitation rate, rather than by particular value of incident infrared power.

Fig. 5 shows the voltage dependence of QWIP responsivity and ratio $R(P)/R(0)$. The voltage increase helps to minimize the ratio $R(P)/R(0)$, i.e. to suppress the nonlinear effects. This is due to a strong enhancement of thermal excitation rate with applied voltage.

4. Conclusions

We have shown that optical interference effect can lead to strong nonlinearities of the QWIP characteristics. Responsivity, NEP, and gain ratio are deteriorated when the nonuniform optical excitation rate exceeds the thermal ionization or background excitation rates. These effects are caused by the nonuniform electric

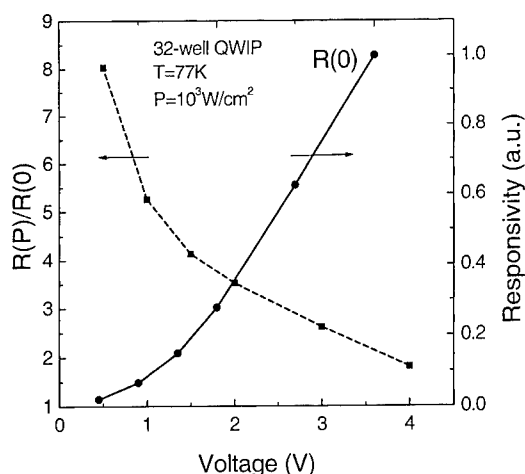


Fig. 5. Low-power responsivity and high-to-low power responsivities ratio for 32-well QWIP at $T = 77 \text{ K}$.

field distribution. They can play an important role for heterodyne (or other high-power) operation, and for low-temperature/low-background applications.

Acknowledgements

This work has been partially supported by NSF (grant #ECS 9809746).

References

- [1] B.F. Levine, J. Appl. Phys. 74 (1993) R1.
- [2] M. Ershov, H.C. Liu, M. Buchanan, Z.R. Wasilewski, V. Ryzhii, Appl. Phys. Lett. 70 (1997) 414.
- [3] C. Mermelstein, H. Schneider, A. Sa'ar, C. Schönbein, M. Walter, G. Bihlman, Appl. Phys. Lett. 71 (1997) 2011.
- [4] R.K. Richards, D.P. Hutchinson, C.A. Bennett, M.L. Simpson, H.C. Liu, M. Buchanan, Proceedings of the Sixth International Symposium on Long Wavelength Infrared Detectors and Arrays: Physics and Applications, 1998.
- [5] R.H. Kingston, Detection of Optical and Infrared Radiation, Springer, Berlin, 1979.
- [6] A.C. Goldberg, J.F. Little, S.W. Kennerly, D.W. Beekman, R.P. Leavitt, Proceedings of the Sixth International Symposium on Long Wavelength Infrared Detectors and Arrays: Physics and Applications, 1998.
- [7] F. Szmulowicz, K.T. Bloch, F.L. Madarasz, J. Appl. Phys. 60 (1986) 4300.
- [8] F. Szmulowicz, F.L. Madarasz, J. Diller, J. Appl. Phys. 62 (1987) 310.

- [9] I.K. Blokhin, V.A. Kholodnov, *Sov. Phys. Semicond.* 26 (1992) 417.
- [10] V.D. Shadrin, V.V. Mitin, V.A. Kochelap, K.K. Choi, *J. Appl. Phys.* 77 (1995) 1771.
- [11] D.D. Coon, A.G.U. Perera, *Solid-State Electron.* 29 (1986) 929.
- [12] Y.A. Kozlovskiy, L.N. Neustroev, V.V. Osipov, *Radioeng. Electron.* 8 (1989) 1729.
- [13] H. Schneider, C. Schönbein, M. Walther, P. Koidl, G. Weigmann, *Appl. Phys. Lett.* 74 (1999) 16.
- [14] M. Ershov, V. Ryzhii, C. Hamaguchi, *Appl. Phys. Lett.* 67 (1995) 3147.
- [15] E. Rosencher, B. Vinter, F. Luc, L. Thibaudau, P. Bois, J. Nagle, *IEEE J. Quantum Electron.* 30 (1994) 2875.
- [16] L. Thibaudau, P. Bois, J.Y. Duboz, *J. Appl. Phys.* 79 (1996) 446.
- [17] A.G. Steele, H.C. Liu, M. Buchanan, Z.R. Wasilewski, *J. Appl. Phys.* 72 (1992) 1062.
- [18] M. Ershov, *Appl. Phys. Lett.* 73 (3432) 1998.



ELSEVIER

Physica E 7 (2000) 120–123

PHYSICA E

www.elsevier.nl/locate/physce

Monte Carlo particle modeling of electron transport and capture processes in AlGaAs/GaAs multiple quantum-well infrared photodetectors

M. Ryzhii *, V. Ryzhii

Computer Solid State Physics Laboratory, University of Aizu, Aizu-Wakamatsu 965-8580, Japan

Abstract

We study steady-state and transient electron transport and capture effects in n-AlGaAs/GaAs multiple quantum-well infrared photodetectors utilizing bound-to-continuum transitions using an ensemble Monte Carlo particle modeling. It is shown that nonequilibrium distributions of electrons over the conduction band valleys essentially determine the characteristics of these devices. The macroscopic capture parameter is calculated as a function of the electric field. We show also that monotonic electric-field distributions can be unstable with the excitation of the wave of quantum-well recharging. As a result of the instability, quasi-periodic domain structures in quantum-well infrared photodetectors can be formed. © 2000 Elsevier Science B.V. All rights reserved.

Keywords: Infrared detector; Transport; Capture; Domain structure

1. Introduction

Electron transport and capture processes play important roles in the performance of quantum-well infrared photodetectors (QWIPs) [1,2]. The dark current in QWIPs, their responsivity, and photoelectric gain are determined by the probability of the electron capture into QWs. The dependence of the capture probability on the electric field strongly affects the spatial distribution of the self-consistent electric field in QWIPs [3–6].

The dominant mechanism of the capture of electrons in QW structures is associated with the electron transitions from the continuum states into the bound states in the QWs due to the optical phonon emission [7–10]. Thus, the capture rate depends not only on the microscopic probability of the electron continuum-to-bound transitions, but on the number of electrons having the energy ε less than the optical phonon energy ε_0 as well. As a result, the capture rate essentially depends on the energy distribution of electrons in the continuum states. This distribution changes with varying electric field. Because the capture rate into a QW depends on the energy distribution of the electrons in the vicinity of this QW, which, in turn, is determined by the electric field in some region around the QW (the size of the

* Corresponding author. Fax: +81-242-37-2596.
E-mail address: m-ryzhii@u-aizu.ac.jp (M. Ryzhii)

region is on the order of the energy relaxation length), nonlocal effects can be important. These effects can substantially influence the capture processes when the electric field is nonuniform. They can lead to the instability of the states with monotonic electric-field distributions resulting in the formation of quasi-periodic domain structures.

In this paper, we present the results of the study of steady-state and transient electron phenomena in QWIPs using an ensemble Monte Carlo (MC) particle modeling. We calculated the macroscopic capture parameter p_c (microscopic capture probability [2]) as a function of the electric field in the case when the latter is nearly uniform. The evolution of the electric-field and charge distributions and the transient photocurrent were also calculated. The MC technique implemented in this work was described and used previously [11–14]. In particular, the microscopic probability of the capture processes associated with the continuum-to-bound transitions of electrons crossing QWs and emitting optical phonons was adjusted to the experimental data [10]. The QWIPs under consideration are based on n-type $\text{Al}_{0.22}\text{Ga}_{0.78}\text{As}/\text{GaAs}$ heterostructures with the width of QWs $L_w = 5$ nm. The width of the barriers was chosen to be in the range $L_b = 30$ –100 nm. The donor sheet concentration in the QWs and the donor concentration in the barriers were assumed to be in the ranges $\Sigma_d = (0.5\text{--}1) \times 10^{12} \text{ cm}^{-2}$ and $N_d = 1 \times 10^{15}$ – $5 \times 10^{16} \text{ cm}^{-3}$, respectively. All calculations were performed for the temperature $T = 77$ K.

2. Electric-field dependence of the capture parameter

When the diffusion current in a QWIP is negligible in comparison to the drift current, the QW capture rate C and the current density j are related to each other as $C = p_c j/e$, where e is the electron charge. In QWIPs with a large number of QWs, the electric field can be nearly uniform except relatively narrow region adjacent to the emitter contact (see, for example, Refs. [3,4,6]). The microscopic capture parameter for QWs in the QWIP bulk where the electric field is uniform was calculated using the following method [14]. We calculated by the MC procedures the number of electrons passed several QWs in the QWIP bulk (the

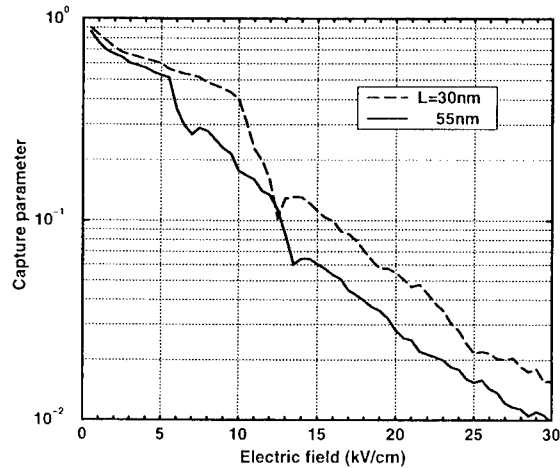


Fig. 1. Capture parameter as a function of the electric field for QWIPs with $N_d = 1 \times 10^{15} \text{ cm}^{-3}$ and different periods $L = L_w + L_b$.

number of the QWs in question $N^* < N$, where N is the total number of QWs in a QWIP) and the number of electrons captured in these QWs during a certain period of time. Under steady-state conditions, the numbers of captured and thermoexcited (or photoexcited) electrons are equal to each other. After that, we calculated the “current gain” G^* as the ratio of the numbers of passed and excited electrons. Then, the capture parameter was found from the following formula [2]: $p_c = (1 + G^* N^*)^{-1}$. In the case when electric field is generally nonuniform but the scale of its nonuniformity is large in comparison to the QW structure period (i.e., when the electric field is smooth), the obtained p_c – E relations can be considered as the dependences of the capture parameter on the local electric field. The calculated dependences of the capture parameter p_c on the electric field for QWIPs with low donor concentrations in the barriers are shown in Fig. 1.

These dependences exhibit a dramatic drop of the capture parameter with increasing electric field. This effect is attributed to a significant decrease of the number of electrons which can be captured, i.e., the Γ -electrons with the energies $\varepsilon < \varepsilon_0$ as the electric field increases (see Fig. 2).

As seen from Fig. 1, the QWIP with a larger period L (wider barriers) correspond to larger values of the capture parameter in a wide range of the

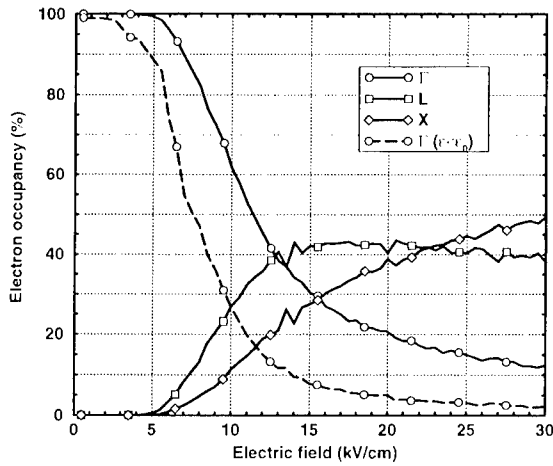


Fig. 2. Occupancy of Γ -, L-, and X-valleys by electrons for $L = 55$ nm. Dashed line shows the fraction of the Γ -electrons with $v < v_0$.

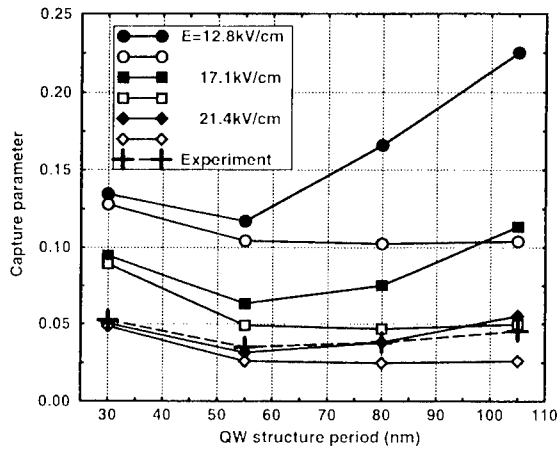


Fig. 3. Capture parameter versus period for different electric fields for $N_d = 1 \times 10^{16} \text{ cm}^{-3}$ (open markers) and $N_d = 2.5 \times 10^{16} \text{ cm}^{-3}$ (solid markers). Crosses connected by dashed line correspond to experimental data extracted from Ref. [15].

electric field. This is in agreement with the experimental results (see, for example Ref. [15]). However, the capture parameter as a function of the barrier width reaches a minimum at a certain value of the barrier width and begins to increase with further widening of the barriers [15]. Such a behavior was qualitatively explained previously [16]. Fig. 3 shows the calculated dependences of the capture parameter as a function

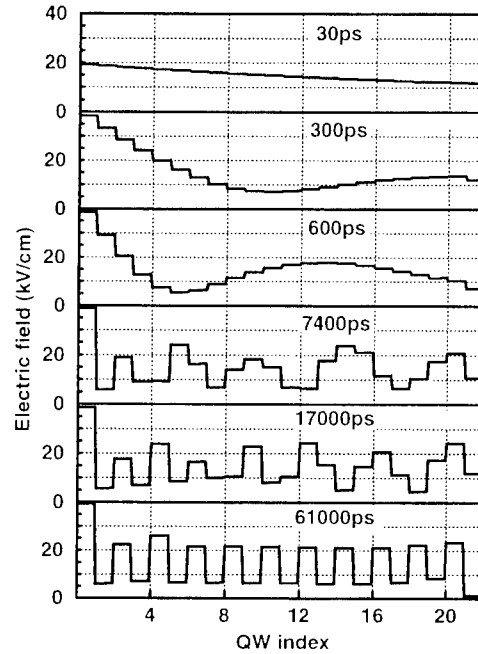


Fig. 4. Evolution of electric-field distribution and formation of domain structure in QWIP with 21 QWs.

of the QW structure period at different electric fields as well as the experimental data (marked by crosses). As seen from Fig. 3, these dependences are monotonically decreasing when the barrier donor concentration is moderate, but they exhibit the nonmonotonic behavior in the case of relatively high doping of the barriers (compare the curves with open and solid markers).

3. Instability and domain structures

The above results correspond to the conditions when the electric field is nearly constant in a wide region of a QWIPs (in its bulk). However, at least in some cases, such distributions are unstable. This effect was revealed in our MC simulations of QWIPs under relatively strong powers of incident infrared radiation. The results of the study of the transient processes in a QWIP with $N = 21$ and $\Sigma_d = 1 \times 10^{12} \text{ cm}^{-2}$ as a response to a step-like pulse of radiation with the intensity $I = 10^{23} \text{ cm}^{-2} \text{ s}^{-1}$ are shown in Fig. 4. It is seen from Fig. 4 that the electric-field distribution does not tend to a monotonic distribution. On the contrary, it clearly exhibits wavy behavior. It is of interest that the

wavelength of the excited wave of the self-consistent electric field (and related wave of the charges in QWs) gradually decreases. As a result of the instability a quasi-periodic stable distribution establishes late in the development. Such an electric-field distribution corresponds to a dipole domain structure in which neighboring QWs are charged oppositely. A marked difference in the electric fields in different barriers results in a change of the total (or average) capture rate compared to that when the electric field is uniform or, at least, uniform in the main part of a QWIP. Very similar structures were found in QWIPs with different numbers of QWs ($N = 5\text{--}50$) in wide ranges of the intensities ($I = 10^{21}\text{--}10^{24} \text{ cm}^{-2}\text{s}^{-1}$) and the average electric fields ($E = 5\text{--}20 \text{ kV/cm}$). The instability and domain structures in question can be attributed to the nonlocality of the dependence of the hot electron capture rate into QWs on the electric field [6]. These effects have the same origin as those predicted many years ago for compensated semiconductors with deep traps [17]. The formation of the quasi-periodic domain structures in QWIP can markedly affect their characteristics (see also Ref. [18]). Due to relatively slow processes of the QW recharging the duration of the instability nonlinear development and domain structures formation varies from tens of nanoseconds to several microseconds depending on the number of QWs and the intensity. Because of this, the computation time in some cases was fairly long (up to few months on the SUN Ultrasparc workstations).

4. Conclusion

We calculated the capture parameter as a function of the electric field for QWIPs with different structure periods and doping levels of QWs and the barriers, using the developed ensemble MC particle method. A steep drop of the capture parameter with increasing local electric field is attributed to the decrease of the number of electrons with the energies lower than the optical phonon energy as the electric field becomes stronger. The sag of the conduction band edge in the

barriers due to their donor space charge influences the electron capture processes because it affects the electron energy distributions. The calculated dependences are in agreement with the experimental results. We predicted that monotonic electric-field distributions in QWIPs can be unstable with respect to the excitation of the recharging waves. The instability can lead to the formation of stable quasi-periodic electric-field distributions corresponding to dipole domain structures.

Acknowledgements

The authors thank Profs. M. Willander, R. Suris, C. Hamaguchi, and Dr. I. Khmyrova for helpful discussions.

References

- [1] B.F. Levine, *J. Appl. Phys.* 74 (1993) R1.
- [2] H.C. Liu, *Appl. Phys. Lett.* 60 (1992) 1507.
- [3] M. Ershov, V. Ryzhii, C. Hamaguchi, *Appl. Phys. Lett.* 67 (1995) 3147.
- [4] L. Thibaudau, P. Bois, J.Y. Duboz, *J. Appl. Phys.* 79 (1995) 446.
- [5] V. Ryzhii, *J. Appl. Phys.* 81 (1997) 6442.
- [6] V. Ryzhii, H.C. Liu, *Jpn. J. Appl. Phys.* 38 (1999) 10.
- [7] J.A. Brum, G. Bastard, *Phys. Rev. B* 33 (1986) 1420.
- [8] P.W.M. Blom, C. Smit, J.E.M. Haverkort, J.H. Wolter, *Phys. Rev. B* 47 (1993) 2072.
- [9] D. Morris, D. Deveaud, A. Regreny, P. Auvray, *Phys. Rev. B* 47 (1993) 6819.
- [10] J.M. Gerard, B. Deveaud, A. Regreny, *Appl. Phys. Lett.* 63 (1993) 240.
- [11] M. Ryzhii, V. Ryzhii, *Appl. Phys. Lett.* 72 (1997) 842.
- [12] M. Ryzhii, I. Khmyrova, V. Ryzhii, *Jpn. J. Appl. Phys.* 37 (1998) 78.
- [13] M. Ryzhii, V. Ryzhii, M. Willander, *J. Appl. Phys.* 84 (1998) 3403.
- [14] M. Ryzhii, V. Ryzhii, *Jpn. J. Appl. Phys.* 38 (1999) 5922.
- [15] E. Rosencher, F. Luc, P. Bois, J. Nagle, Y. Cordier, *Appl. Phys. Lett.* 63 (1993) 3312.
- [16] K.K. Choi, *The Physics of Quantum Well Infrared Photodetectors*, World Scientific, Singapore, 1997.
- [17] R.A. Suris, B.I. Fuks, *Sov. Phys. Semicond.* 7 (1974) 1039.
- [18] M. Ryzhii, V. Ryzhii, R. Suris, C. Hamaguchi, *Jpn. J. Appl. Phys.* 38 (1999) L1388.

Noise current investigations of g–r noise limited and shot noise limited QWIPs

R. Rehm*, H. Schneider, C. Schönbein, M. Walther

Fraunhofer-Institut für Angewandte Festkörperphysik, Tullastrasse 72, 79108 Freiburg, Germany

Abstract

We report on the experimental determination of the different contributions to the noise current in quantum-well infrared photodetectors (QWIPs). A detailed description of the measurement set-up and experimental methods is given. The noise properties of conventional bound-to-continuum QWIPs and four-zone QWIPs will be discussed. The noise current of these devices is dominated by g–r noise and by shot noise, respectively. © 2000 Elsevier Science B.V. All rights reserved.

Keywords: Quantum-well infrared detectors; Johnson noise; g–r noise; Infrared detector

1. Introduction

GaAs/AlGaAs-based quantum-well infrared photodetectors (QWIPs) operating in the 8–12 μm spectral range are finding increasing application in thermal imaging systems due to the excellent homogeneity and temperature resolution of two-dimensional detector arrays. Noise-equivalent temperature differences (NETD) of less than 10 mK and below 20 mK have been achieved with QWIP cameras with 256×256 and 640×512 pixels, respectively [1,2]. The NETD of the system is critically determined by the signal and noise currents of the QWIP. Furthermore, noise measurements give important experimental clues

for the understanding of the charge carrier transport properties.

2. Detector structures and device operation

Two types of QWIP structures have been analysed. The conduction band-edge distribution and the appropriate carrier transport mechanisms of both samples are summarised in Fig. 1. Sample A (Fig. 1a) represents a conventional photoconductive QWIP based on bound-to-continuum intersubband transitions [3]. The active region contains $N = 50$ n-type GaAs quantum wells embedded between 48 nm thick $\text{Al}_{0.26}\text{Ga}_{0.74}\text{As}$ barriers. The width of the quantum wells is 4.1 nm. The wells are Si-doped to a sheet concentration of $4 \times 10^{11} \text{ cm}^{-2}$.

Sample B (Fig. 1b) is a novel type of QWIP with an asymmetric potential distribution. The active region consists of $N = 20$ periods. As indicated

* Corresponding author. Fax: +49-761-5159-851.

E-mail address: rehm@iaf.fhg.de (R. Rehm)

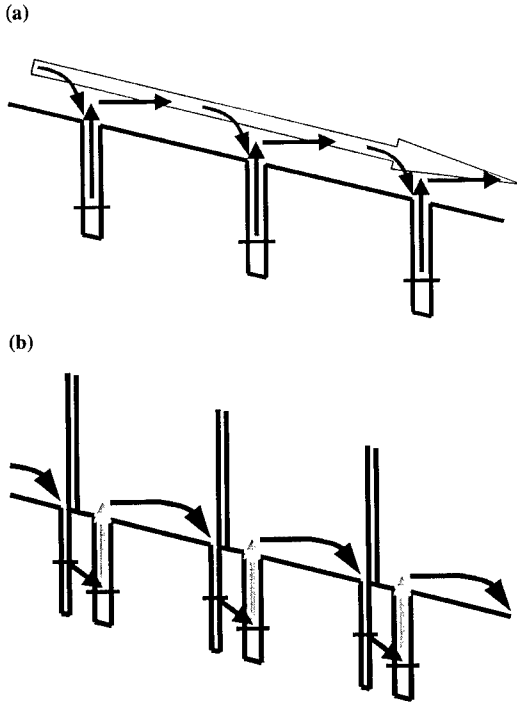


Fig. 1. Potential distribution of the conduction band edge of (a) a conventional bound-to-continuum QWIP and (b) a four-zone QWIP.

by the arrows, the carriers are emitted from a 4.8 nm wide, Si-doped ($4 \times 10^{11} \text{ cm}^{-2}$) GaAs quantum well. Subsequently, they drift across a 45 nm wide $\text{Al}_{0.24}\text{Ga}_{0.76}\text{As}$ barrier. A narrow barrier containing two 0.6 nm wide AlAs spikes blocks further carrier transport in the continuum. The carriers are thus captured into a narrow, undoped quantum well region adjacent to the barriers. The captured electrons tunnel through the narrow barrier and reach the subsequent period. As apparent from the described transport process four separate zones can be distinguished in this class of QWIPs, namely the emission zone, the drift zone, the capture zone and the tunneling zone. These QWIPs have therefore been called four-zone QWIPs [4]. As long as the AlAs barriers efficiently block the carrier transport in the continuum, the drift length of the excited carriers corresponds to exactly one period. In this case the carrier capture probability p_c is equal to unity. Further details concerning the detector structures can be found in Refs. [5,4], respectively.

3. Noise contributions

The noise behaviour of QWIPs is determined by two basic contributions, namely Johnson noise and generation–recombination (g–r) noise. Johnson noise [6,7] is caused by the random thermal motion of charge carriers, which leads to local gradients in the charge carrier density. The corresponding noise current I_J at the bias voltage U can be expressed as

$$I_J^2 = 4k_B T \frac{dI_d}{dU} \Delta f, \quad (1)$$

where k_B is Boltzmann's constant, T the temperature, I_d the thermally activated dark current, dI_d/dU the differential conductivity and Δf the measurement bandwidth. Every electrical conductor exhibits temperature-dependent Johnson noise even without an applied voltage.

Similar to the noise behaviour of a photoconductor [8], g–r noise in QWIPs is the result of the fluctuating number of mobile charge carriers in multi-quantum-well structures due to statistical carrier emission and capture. A general theoretical description was given by Beck [9]. For a structure containing N periods, his deduction of the g–r noise yields

$$I_{g-r}^2 = 4eg_{ph} \left(1 - \frac{p_c}{2}\right) I_d \Delta f. \quad (2)$$

An important parameter in the description of the carrier transport mechanism is the photoconductive gain g_{ph} , which is given by

$$g_{ph} = \frac{I_d}{L} = \frac{1}{Np_c}. \quad (3)$$

Here l_d denotes the emitted carrier mean drift length and L the overall length of the multi-quantum-well region. Inserting expression (3) into Eq. (2) leads to the following relation between g_{ph} and I_{g-r} :

$$g_{ph} = \frac{I_{g-r}^2}{4eI_d \Delta f} + \frac{1}{2N}. \quad (4)$$

Actually, the widely used standard model for the description of g–r noise in QWIPs [3,10] differs from Beck's equation (2) by omitting the factor of $(1 - p_c/2)$. Consequently, within the standard model the additional term $1/(2N)$ of Eq. (4) is not present in the corresponding expression for the photoconductive gain. Note that in the case of $p_c \ll 1$, which is typical for conventional bound-to-continuum QWIPs,

the g–r noise expression of the standard model is a good approximation to Beck's equation. In four-zone QWIPs the carrier capture becomes deterministic (i.e. $p_c \approx 1$), such that the noise associated with the 'recombination process' vanishes. In contrast to the standard model, Beck's equation is able to predict this reduction of the g–r noise [11]. For a carrier capture probability of unity Beck's expression has the same form as the expression describing the shot noise of an ordinary photodiode [8].

By assuming that g–r noise and Johnson noise are statistically independent, the total noise of a quantum-well infrared photodetector is given by

$$I_n^2 = I_{g-r}^2 + I_J^2. \quad (5)$$

Apart from the situation with no applied voltage, g–r noise generally exceeds Johnson noise. Therefore the photoconductive gain can be determined by noise measurements. In frequency regimes where emitted carrier lifetimes can be ignored, the noise in QWIPs is independent of frequency.

4. Measurement set-up

Fig. 2 shows the measurement set-up used for the characterization of the dark current noise. The QWIP is mounted on a sample holder in a dewar and cooled to 77 K. Simultaneously, the sample holder acts as a Faraday cage to shield unamplified signal currents from ambient electromagnetic fields in order to avoid parasitic contributions to the measured noise. A computer controllable, battery-equipped current preamplifier (Stanford Research Systems, SR570) acts as a low noise voltage source. Noise measurements of the output voltage yielded a value of $U_{n,v.s.} = 2.6 \times 10^{-8} \text{ V/Hz}^{1/2}$. According to Ohm's law, the noise of the applied bias $U_{n,v.s.}$ induces a noise current $I_{n,v.s.}$ in the QWIP, which can be expressed as

$$I_{n,v.s.} = U_{n,v.s.} \frac{dI_d}{dU}. \quad (6)$$

Note that this term is proportional to dI_d/dU , while Johnson noise and g–r noise are proportional to $(dI_d/dU)^{1/2}$ and $I_d^{1/2}$, respectively. Within bias regimes where the sample exhibits a sufficiently high dI_d/dU , voltage-source-induced noise $I_{n,v.s.}$ exceeds Johnson noise. At high voltages, $I_{n,v.s.}$ may even ex-

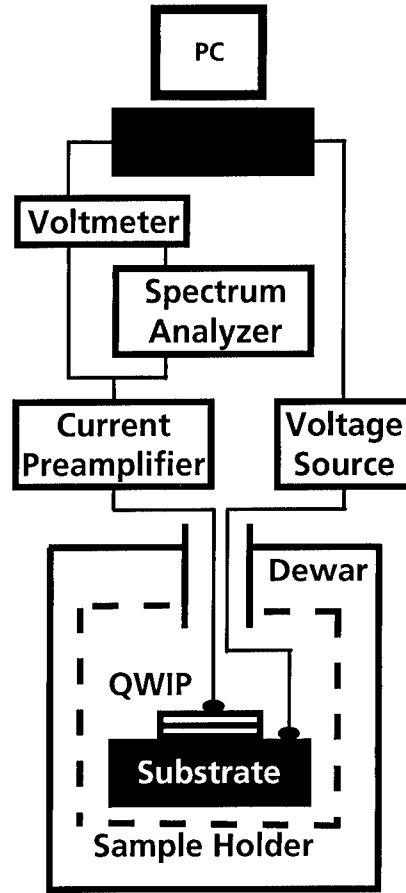


Fig. 2. Noise measurement set-up.

ceed g–r noise, if the increase of $I_d(U)$ is stronger than quadratic.

The gain of the DC-coupled low noise current preamplifier (ITHACO, Model 564) can be set to values from 10^{-4} to 10^{-8} A/V . The corresponding cut-off frequencies (–3 dB) range from 250 kHz down to 3 kHz. The preamplifier's input noise current $I_{n,amp.}$ depends on the selected amplification and limits the noise resolution of our measurement set-up. We measured a value of $1.5 \times 10^{-14} \text{ A/Hz}^{1/2}$ at an amplification of 10^{-8} A/V . The current preamplifier is placed close to the sample holder in order to reduce electromagnetic perturbation before signal amplification. In addition to the bias of the voltage source, the preamplifier provides the possibility of adding an input offset voltage in the range of 0

to 10 V. A computer-controllable digital voltmeter (Hewlett-Packard, HP3457A) measures the output voltage of the current preamplifier, which is proportional to the DC current.

We use a spectrum analyzer (Hewlett-Packard, HP3580A) to measure the noise of the current preamplifier's output signal at a fixed frequency. The digital voltmeter measures the analog output of the spectrum analyzer. For every applied voltage, the spectrum analyzer's signal output is averaged a hundred times in order to determine the noise current at the given voltage and frequency.

Summarizing all noise contributions, the measured noise $I_{n, \text{meas}}$ can be written as

$$I_{n, \text{meas}}^2 = I_{g-r}^2 + I_J^2 + I_{n, \text{v.s.}}^2 + I_{n, \text{amp.}}^2 \quad (7)$$

Thereby, contributions originating from the set-up and being constant throughout the measurement may be included into the preamplifier noise. By simultaneously measuring the noise, the current and the differential conductivity, we extract the gain by first calculating the mere g - r noise according to expression (7) and then using Eq. (4). In order to obtain reliable values for the photoconductive gain, the main contribution to the measured noise has to be given by the sample's g - r noise.

5. Negative differential gain in photoconductive QWIPS

Fig. 3 shows several contributions to the measured noise current versus bias voltage of sample A obtained at a temperature of 77 K and 1070 Hz. The sign of the applied bias refers to the voltage at the top contact. Because the preamplifier's noise contribution $I_{n, \text{amp.}}$ depends on the selected amplification range, steps in the measured noise appear when the preamplifier's gain is switched. As seen in Fig. 3, the Johnson noise is relevant at around 0 V. The noise current induced by the voltage source is mostly at least an order of magnitude below the Johnson noise within the investigated voltage range. Therefore, this contribution is practically negligible in the evaluation of the measured data shown in Fig. 3. At high applied voltages, the voltage-source-induced noise increases more strongly than the Johnson noise due to their different dependencies on the differential conductivity.

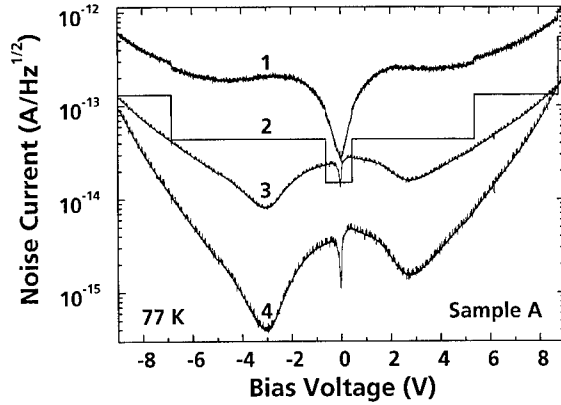


Fig. 3. Noise current contributions versus voltage of sample A measured at 1070 Hz and 77 K. The numbers indicate the measured noise (1), the preamplifier's contribution (2), the Johnson noise (3) and the noise induced by the voltage source (4).

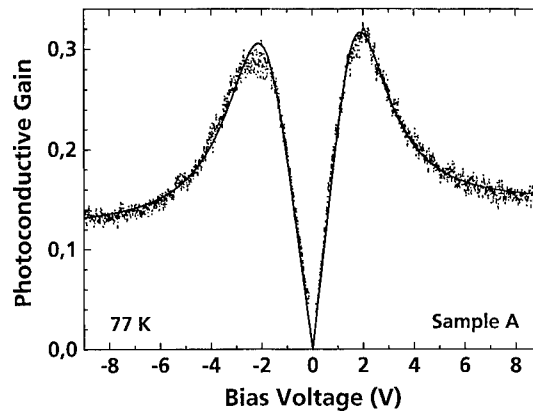


Fig. 4. Measured photoconductive gain versus voltage of sample A at a temperature of 77 K. The solid line represents a theoretical fit based on intervalley scattering.

The voltage dependence of the photoconductive gain as calculated from the measured data according to Eqs. (4) and (7) is shown in Fig. 4. At low applied fields the photoconductive gain exhibits a linear behaviour. Subsequently, the gain passes through a maximum and decreases afterwards. This negative differential behaviour has been attributed to a negative differential field dependence of the carrier drift velocity due to Γ -X and Γ -L intervalley scattering processes. The solid line shows a fit to the measured data which uses a theoretical expression describing

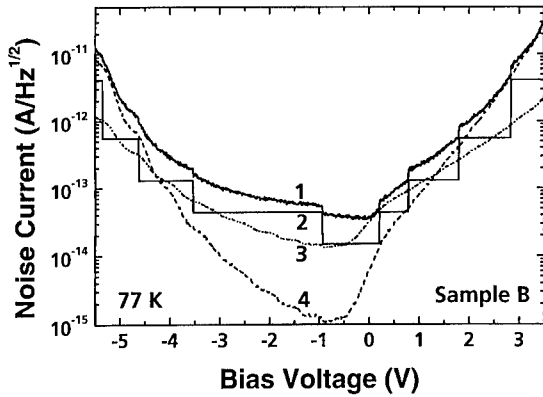


Fig. 5. Noise current contributions versus voltage of sample B measured at 1430 Hz and 77 K. The numbers are explained in the figure caption of Fig. 3.

the drift velocity in consideration of intervalley scattering. The fit yields realistic values for the characteristic field, carrier mobility and saturation velocity in $\text{Al}_{0.26}\text{Ga}_{0.74}\text{As}$, as described in more detail in Ref. [5].

6. Suppression of recombination noise in four-zone QWIPS

The measured noise, the preamplifier noise, the Johnson noise and the noise induced by the voltage source in the case of sample B are shown in Fig. 5 as a function of the applied bias. The measured noise is closer to the preamplifier's noise as compared to Fig. 3. Thus, the steps in the measured noise, which occur whenever the preamplifier is switched, are more pronounced. Since the measured noise primarily consists of Johnson noise at very low bias voltages, the photoconductive gain cannot be extracted from the measured data at around 0 V. The voltage-source-induced noise becomes the most significant part of the measured noise at high applied bias. This prevents the determination of the photoconductive gain at those voltages.

As a consequence of the blocking of the carrier transport by the AIAs barriers, the mean drift length is expected to correspond to exactly one period. Hence the photoconductive gain should equal 0.05 in a 20 period QWIP structure according to Eq. (3). A detailed evaluation of the measured photoconductive gain by different noise models has been carried out in Ref.

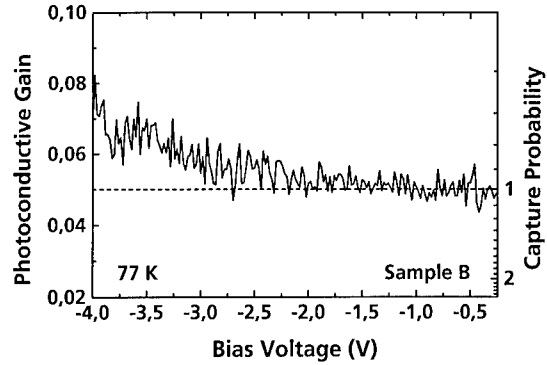


Fig. 6. Photoconductive gain and capture probability versus voltage of sample B at a temperature of 77 K.

[11], confirming the validity of Beck's model. The photoconductive gain and the related carrier capture probability, which have been obtained by the application of Beck's noise model to the experimental data, are presented in Fig. 6. The theoretically expected gain value of 0.05, which corresponds to a carrier capture probability of unity for $N = 20$ periods, is actually observed over a wide bias range. In this bias range the noise behaviour of sample B is limited by shot noise rather than g-r noise (see (2)). The increase of the photoconductive gain at high negative voltages can be explained by the less efficient blocking of the carrier transport in the continuum by the AIAs barriers, which leads to a mean drift length of more than one period.

7. Summary

We have presented a detailed description of our noise measurement set-up and the experimentally relevant noise contributions in QWIPs. Generally, Johnson noise is dominant at low bias. The noise induced by the voltage source becomes significant at high bias. In between, g-r noise or shot noise are the dominant contributions, thus the photoconductive gain can be determined. We characterized the noise behaviour of a conventional bound-to-continuum QWIP and a four-zone QWIP. The photoconductive gain of the bound-to-continuum QWIP reveals a negative differential behaviour, which can be attributed to intervalley scattering. The particular transport mechanism in a four-zone QWIP gives rise to a shot noise limited behaviour, as predicted by Beck's noise model [11].

References

- [1] R. Breiter, W. Cabanski, R. Koch, W. Rode, J. Ziegler, K. Eberhardt, R. Oelmaier, *Proc. SPIE* 3379 (1998) 423.
- [2] M. Walther, J. Fleissner, H. Schneider, C. Schönbein, W. Pletschen, E. Diwo, K. Schwarz, J. Braunstein, P. Koidl, J. Ziegler, W. Cabanski, *Proceedings of 26th International Symposium on Compound Semiconductors (ISCS'99)*, Berlin, 1999, in press.
- [3] B. Levine, *J. Appl. Phys.* 74 (1993) R1.
- [4] H. Schneider, C. Schönbein, M. Walther, K. Schwarz, J. Fleissner, P. Koidl, *Appl. Phys. Lett.* 71 (2) (1997) 246.
- [5] H. Schneider, C. Mermelstein, R. Rehm, C. Schönbein, A. Sa'ar, M. Walther, *Phys. Rev. B* 57 (1998) R15 096.
- [6] J.B. Johnson, *Phys. Rev.* 32 (1928) 97.
- [7] H. Nyquist, *Phys. Rev.* 32 (1928) 110.
- [8] R.H. Kingston, *Detection of Optical and Infrared Radiation*, in: D.L. McAdam (Ed.), *Springer Series in Optical Sciences*, Vol. 10, Springer, Berlin, 1978.
- [9] W.A. Beck, *Appl. Phys.* 63 (199) 3589.
- [10] H.C. Liu, *Appl. Phys. Lett.* 61 (1992) 2703.
- [11] C. Schönbein, H. Schneider, R. Rehm, M. Walther, *Appl. Phys. Lett.* 73 (1998) 1251.

Effects of traps on the dark current transients in GaAs/AlGaAs quantum-well infrared photodetectors

A.G.U. Perera^{a,*}, S.G. Matsik^a, M. Ershov^a, Y.W. Yi^a, H.C. Liu^b, M. Buchanan^b,
Z.R. Wasilewski^b

^aDepartment of Physics and Astronomy, Georgia State University, Atlanta, GA 30303, USA

^bInstitute for Microstructural Sciences, National Research Council, Ottawa, Canada

Abstract

In this work, experimental results showing very slow (up to 10^4 s) dark current transients in n-type GaAs/Al_{0.27}Ga_{0.73}As quantum-well photodetectors (QWIPs) are reported. The transients with amplitudes of 0.1% to 65% of the steady-state current have been observed at 77 K. These effects are believed to be associated with initially ionized deep levels acting as traps reducing the positive charge in the structure. The time constant of the dark current (transient) decreases with increasing temperature with an experimentally determined activation energy ~ 75 meV. A fitting of the capture cross section to $\sigma(T) = \sigma_0 \exp(E_c/k_B T)$ gives an estimate for the capture activation energy of $E_c \sim 35$ meV. © 2000 Elsevier Science B.V. All rights reserved.

Keywords: Dark current; quantum-well infrared detectors; Transients

1. Introduction

Variations in the dark current in quantum-well IR photodetectors (QWIPs) can have significant effects on their performance. Previously the effects of deep levels on current have been observed in the persistent photoconductivity [1,2]. This effect is believed to be due to the traps associated with deep levels in the AlGaAs barrier. In this work we present experimental results for transient dark currents in QWIPs with very long time scales on the order of minutes to

hours. These transients have amplitudes of 0.1%–65% of the steady state current and time scales of 10^3 – 10^4 s for a GaAs/Al_{0.27}Ga_{0.73}As QWIP at 77 K. At higher temperatures the time scales became much faster giving ~ 50 s time constants for 120 K. The amplitude of the transient initially increases as the temperature is increased and then decreases for temperatures above ~ 130 K.

2. Experimental data

The experiment consisted of measuring the dark current as a function of time in a QWIP at a fixed tem-

* Corresponding author. Fax: 404-651-1427.

E-mail address: uperera@gsu.edu (A.G.U. Perera)

Table 1

Parameters for the samples used in measuring the transients, the relative doping in the barrier and the growth temperature. Relative doping in the barrier is determined by integrating the dopant that migrated into the barrier [4] with samples #1127 and #1130 being taken as 1. All samples were grown at 605°C except #1327 which was grown at 550°C

Sample number	Well width (Å)	Barrier width (Å)	Number of periods	δ -doping offset	Relative doping in the barrier
#1127	59	250	4	0	1.00
#1300	59	350	25	0	1.00
#1301	59	350	25	6 Å	0.89
#1302	59	350	25	12 Å	0.79
#1327	55	250	25	0	0.00
#1328	55	250	25	11 Å	0.86
#1329	55	250	25	22 Å	0.68

perature after a fixed voltage had been applied to the sample. All current measurements were performed using a Keithley 2400 sourcemeter. The samples were cooled in a closed-cycle refrigerator, a continuous flow cryostat or by direct immersion in liquid nitrogen. Before each measurement, the samples were warmed up to room temperature to remove any accumulated space charge and have the same initial conditions. The first sample measured was designed as a 4-well QWIP (#1127) with a peak response at 8.5 μm [3]. This sample showed a strong transient whose time scale varied with temperature and field. A set of 25 well samples (see Table 1) with the same device parameters except for the δ -doping position were measured. The wells of samples #1300, #1301, and #1302 were δ -doped at the center, or off center by 6 and 12 Å (in the direction opposite to the growth direction) respectively. Samples #1327, #1328, and #1329 were doped in the center, 11 and 22 Å away from the center. These samples were previously used to study the dopant segregation effects in QWIPs [4] and were studied here to find any relationship between the transient and the dopant distribution in the structure.

Fig. 1 shows typical current–time curves for sample #1127 in the range 100–160 K when a constant voltage of 0.7 V corresponding to a field of 47 kV/cm is applied. All the curves have been normalized, with the actual currents ranging from 3 to 46 mA. The curves all show some similarities, with an initial increase in the current for the first ~ 100 s which could be due to heating of the sample. The absence of this increase for samples immersed in liquid nitrogen supports this ex-

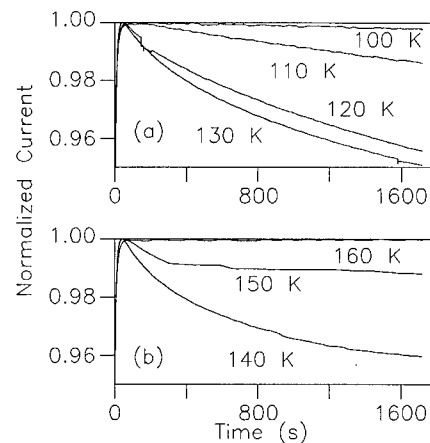


Fig. 1. Transient current in the 4-well sample for (a) $T = 100$ –130 K and (b) $T = 140$ –160 K at a field of 47 kV/cm. Note the increasing strength of the transient up to ~ 130 K followed by a decrease with the transient almost disappearing at 160 K. The time scale for the transient also decreases as the temperature rises.

planation. After this heating transient, the current decreases until it eventually reaches a steady state value. The small variations on these general trends seen in the curves are due to the small temperature fluctuations on the order of ~ 0.01 K in the cooling system. It is possible to fit the current for $t > 500$ s to

$$I = I_0 + \Delta I \exp(-t/\tau), \quad (1)$$

where I_0 is the steady-state current, ΔI is the amplitude of the transient current and τ is a time constant related to the capture process, which was determined

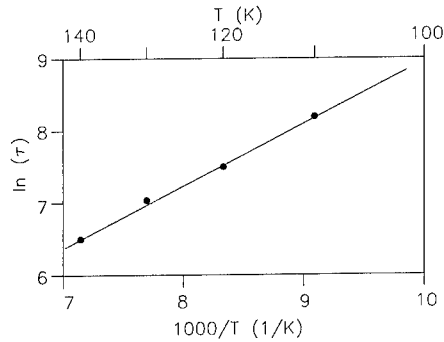


Fig. 2. Decay time for the transient versus $1/T$ for the temperature range 100–140 K indicating an activation energy of 75 meV. When the increase in current with temperature is included the capture energy was found to be ~ 35 meV.

over a range of temperatures from 77 to 170 K. In the region of 100–140 K it was possible to determine an activation energy of 75 meV by plotting $\ln(\tau)$ versus $1/T$ (see Fig. 2). Below 100 K, τ became very long ($> 10^3$ s) making determination of τ imprecise. However, estimations based on measurements over 1–2 h agree in order of magnitude with the extrapolations of Fig. 2.

The time constant for charge capture should obey the equation

$$\tau = 1/nv\sigma, \quad (2)$$

where n is the carrier density, v is the carrier velocity and σ is the capture cross section. Since nv is proportional to the current, the temperature dependence of nv can be obtained from the steady state dark current measurements. This allows the extraction of the temperature dependence of σ . A fit to the expression

$$\sigma(T) = \sigma_0 \exp(E_c/k_B T), \quad (3)$$

gives the capture energy $E_c \sim 35 \pm 5$ meV which is close to the LO phonon energy. Sample #1302 gave a similar value of 37 ± 5 meV. This value is smaller than observed thermal and capture energies of ~ 200 meV for DX centers in AlGaAs for Al fraction $x = 0.26$ [5]. However, the capture barrier can be much smaller than the thermal activation energy for other traps. Capture energies are not readily available in the literature for deep traps in AlGaAs. However, in GaAs $E_c = 40$ meV has been observed [6] for a deep level with 330 meV activation energy while other traps have

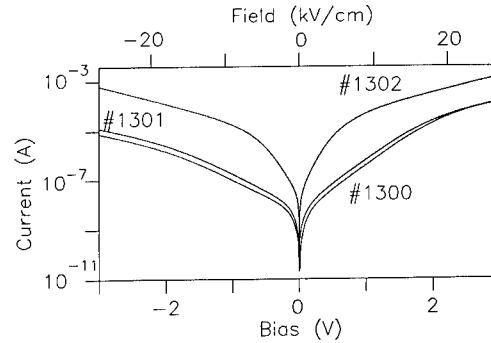


Fig. 3. Dark current for samples #1300, #1301 and #1302 showing the reduced dopant segregation in #1302.

capture energies up to several hundred meV. Although the addition of Al will change the various capture energies, AlGaAs can be expected to have traps with similar energies, which is confirmed by our results.

To determine how the transient was related to dopant segregation, measurements were made on the samples (#1300, #1301, #1302, 1327, 1328 and 1329) with known dopant segregation. The sample in which the doping was at the center of the well (#1300) showed an asymmetric dark current indicating that there was migration of dopants in the growth direction. It showed a transient of $\sim 3\%$ for a field of 9 kV/cm with electron flow in the growth direction but none for electron flow in the opposite direction. When the field on the sample was increased the time scale of the transient increased and the transient appears to become smaller. Above 28 kV/cm field the transient begins to increase again, and by 47 kV/cm reached 4%. Sample #1301 showed a more symmetric I - V and had similar behavior with a 2% transient at 9 kV/cm that initially decreased then began to increase as the fields was increased above 18 kV/cm. The sample with the largest doping shift (#1302) showed a larger and more symmetric dark current [see Fig. 3(a)] which is consistent with previous measurements of the same sample [4]. For sample #1302 the observed transient is strong (up to 7% at 77 K) for electron flow in the growth direction and nonexistent for electron flow in the opposite direction at fields of 14 kV/cm (see Fig. 4). The forward transient in this sample increased at fields of 9 kV/cm and continued increasing for fields up to 23 kV/cm.

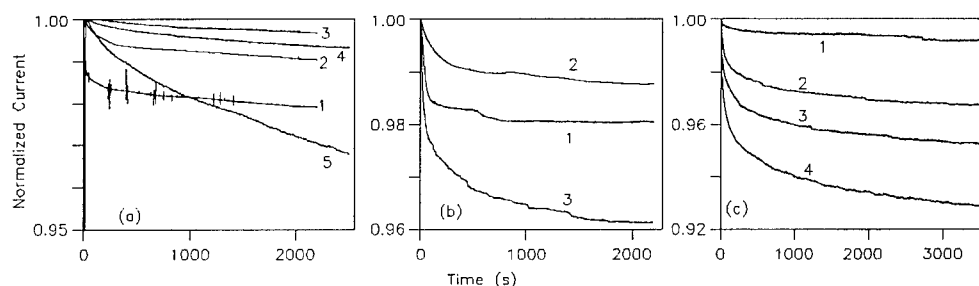


Fig. 4. Comparison of three samples with identical device parameters except for doping location. (a) #1300 center-doped sample, (b) #1301 shifted 6 Å opposite to growth direction and (c) #1302 shifted 12 Å. The fields in (a) and (b) are (1) 9, (2) 18, (3) 28, (4) 37 and (5) 47 kV/cm. The fields in (c) are (1) 9, (2) 14, (3) 18 and (4) 23 kV/cm.

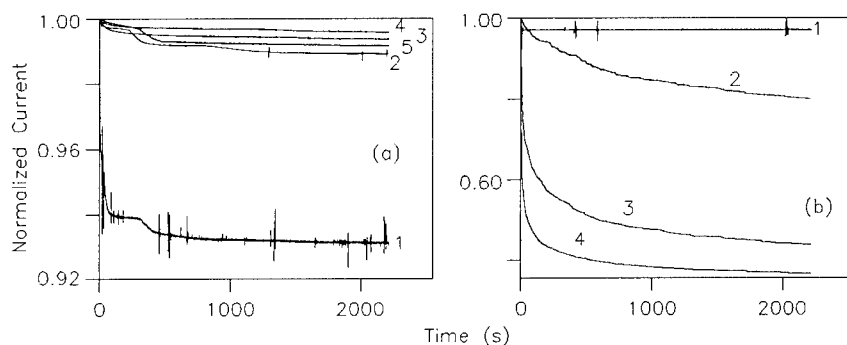


Fig. 5. Comparison of two samples with identical device parameters except for doping location. (a) #1328 shifted 11 Å opposite to growth direction and (b) #1329 shifted 22 Å. The fields are (1) 9, (2) 18, (3) 28, (4) 37 and (5) 47 kV/cm.

If the transient was only due to the enhanced number of traps in the barrier caused by dopant segregation sample #1300, which had the more asymmetric I - V , was expected to show the largest transient, with the transient decreasing in #1301 and #1302. However, sample #1302 showed the largest transient as well as having a transient at lower fields than the other two samples.

Similar behavior is seen in samples #1328 and #1329 (see Fig. 5) sample #1328 with a more asymmetric current showed a small transient that decreased as the bias was increased and then started to increase at 47 kV/cm. Sample #1329 showed only a small ($\sim 0.5\%$) transient at 9 kV/cm. For fields above 9 kV/cm the transient amplitude increased rapidly, reaching 65% for fields of 38 kV/cm.

Sample #1327 which was grown at lower temperature and had no significant dopant migration into the

barrier showed no transient at any temperature even for fields above 47 kV/cm. This indicates that dopant migration may play some role in generating the traps related to the transient.

3. Conclusion

The presence of transient currents in QWIPs when electric fields above 9 kV/cm are applied has been experimentally demonstrated. Based on the temperature dependence of the transient the capture activation energy is estimated to be ~ 35 meV. Measurements on samples with and without dopant segregation in the wells indicate that the traps responsible for the transient may be associated with migration of the dopant into the AlGaAs barriers. However, measured activation energies do not seem to

correspond with any known defects so further measurements are required to confirm the trap location and nature. Due to the small number of capture activation energies for traps in Al-GaAs it is not possible to directly identify the “defect” associated with the trap. The lowering of the critical field at which transients become significant indicates that while shifting the location of the doping can reduce the current asymmetry caused by dopant segregation this also leads to large transients occurring at operating fields in the devices. These large transients could degrade the performance of the detectors in cases where high temporal uniformity is important.

Acknowledgements

The authors thank Dr. K.K. Choi for performing independent measurements on some of these samples. Work was supported in part by NSF grant #ECS 9809746.

References

- [1] V.N. Ovsyuk, M.A. Dem'yanenko, V.V. Shashkin, A.I. Toropov, *Semiconductors* 32 (1998) 1082.
- [2] V.I. Borosov, V.A. Sablikov, I.V. Borisova, A.I. Chmil', *Semiconductors* 33 (1999) 60.
- [3] A.G. Steele, H.C. Liu, M. Buchanan, Z.R. Wasilewski, *J. Appl. Phys.* 71 (1992) 1062.
- [4] H.C. Liu, Z.R. Wasilewski, M. Buchanan, H. Chu, *Appl. Phys. Lett.* 63 (1993) 761.
- [5] K. Yamanaka, S. Naurituska, K. Kanamoto, M. Mihara, M. Ishii, *J. Appl. Phys.* 61 (1987) 5062.
- [6] K.W. Nauka, in: E.R. Weber (Ed.), *Imperfections in III/V Materials*, Academic Press Inc, Boston, 1993, pp. 343–396.



ELSEVIER

Physica E 7 (2000) 135–138

PHYSICA E

www.elsevier.nl/locate/physa

Circuit model for quantum-well infrared photodetectors and its comparison with experiments

Y.H. Chee, G. Karunasiri *

Department of Electrical Engineering, Center for Optoelectronics, National University of Singapore, 10 Kent Ridge Crescent, Singapore 119260, Singapore

Abstract

This paper presents a PSPICE model for quantum-well infrared photodetectors (QWIP). Bias dependence of the dark current and photocurrent is accurately described by the model with the aid of analogue behaviour modelling (ABM) technique in PSPICE. The model can be easily integrated with the readout electronics for circuit optimisation. In addition, we have also incorporated the temperature dependence of dark current into the model for analysing the effects of operating temperature on the performance. The various design parameters of the QWIP can be fed into the model as user-defined inputs to simulate the detector performance. Experimental data of different QWIP structures were compared with the simulated results and their good agreement verifies the accuracy of the PSPICE model. © 2000 Elsevier Science B.V. All rights reserved.

Keywords: Quantum-well infrared photodetector; Readout electronics; PSPICE modelling

1. Introduction

The rapid development of quantum-well infrared photodetectors (QWIPs) has prompted its application in focal plane arrays [1]. Such applications require the integration of readout electronics with the detectors. For the optimisation of the readout electronics, it is necessary to simulate the circuit along with the QWIP. The operation of a QWIP is usually described by a set of equations based on its device physics [1]. How-

ever, these equations cannot be used directly when the detector is connected with its readout electronics for circuit simulation. To overcome this difficulty, a simplified model using a few current sources in parallel with the device resistance has been recently employed [2]. However, this model does not provide the bias and temperature dependence of the dark current and hence it is not applicable for a wide range of operating conditions. In this paper, we describe a PSPICE model for QWIPs, which can be used under different operating conditions. The operation of QWIP can be represented by two equations that take into account the dark current and photocurrent as a function of bias across the device and operating temperature. These equations

* Corresponding author. Tel.: 00-65-874-2162; fax: 00-65-779-1103.

E-mail address: elekg@nus.edu.sg (G. Karunasiri)

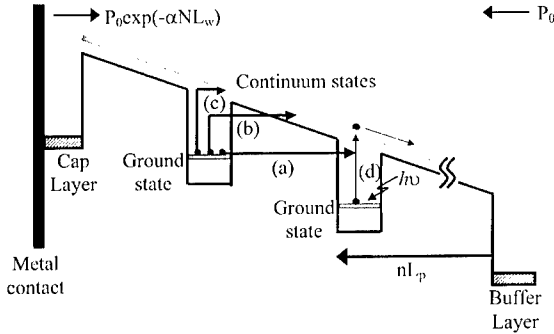


Fig. 1. Origin of dark current (a) ground state sequential tunnelling, (b) thermally assisted tunnelling, and (c) thermionic emission. Also shown is the photoexcitation process (d) in a QWIP.

can conveniently be incorporated for circuit simulation using the analogue behaviour modelling (ABM) technique in PSPICE.

2. Dark current

It is well known that the dark current of a QWIP originates from three main sources (a) sequential tunnelling of ground state electrons from well to well, (b) thermally assisted tunnelling, and (c) thermionic emission of ground state electrons into the continuum states as illustrated schematically in Fig. 1. The QWIP is normally operated at low temperature with a relatively low bias across the device to reduce the dark current. Under these conditions, the dominant mechanism responsible for the dark current is the thermionic emission of electrons in the well [3].

The effective number of electrons that are thermally excited to the continuum states $n_{th}(V)$, is given by [3]

$$n_{th}(V) = \frac{m_w^*}{\pi \hbar^2 L_p} \int_{E_1}^{\infty} f(E) T(E, V) dE, \quad (1)$$

where m_w^* is the effective mass of electrons in the well, L_p is period of the quantum well, E_1 is the ground state energy, V is the applied bias, $T(E, V)$ is the tunnelling probability of an electron through the barrier and $f(E)$ is the Fermi–Dirac distribution function. For typical bias used in QWIPs, the tunnelling probability $T(E, V)$ can be approximated as zero for $E < E_b$ and unity for $E \geq E_b$, where E_b is the barrier height

measured from the ground state [4,5]. With these approximations, $n_{th}(V)$ is evaluated as

$$n_{th}(V) = \frac{m_w^* kT}{\pi \hbar^2 L_p} \exp \left[\frac{-(E_c - E_F)}{kT} \right], \quad (2)$$

where $E_c = E_b - E_1$ is the spectral cut-off energy. The Fermi level $E_F = \pi \hbar^2 N_D L_w / m_w^*$, where N_D is the doping concentration in the well and L_p is the well width. Thus, the dark current, I_d , can be calculated as

$$I_d = n_{th}(V) A v(V) e, \quad (3)$$

where A is the cross-sectional area of the QWIP and $v(V) = \mu F / \sqrt{1 + (\mu F / v_s)^2}$ is the electron drift velocity [6]. In this expression, v_s is the saturated drift velocity of electrons and F is the average electric field in the active region of the QWIP.

3. Photocurrent

In a QWIP, optical transition occurs when an electron in the ground state of the well absorbs a photon and make a transition to the continuum band. These excited electrons can drift towards the contact under an external bias, resulting in a photocurrent, which is proportional to the incident infrared power. The photocurrent can be estimated by summing the contributions from each quantum well and taking into account the capturing of the excited electrons by another quantum well during their drift towards the contact. Thus, the photocurrent can be estimated as the product of the number of photogenerated carriers and their probability of reaching the contact. Considering the absorption due to both the incident and reflected infrared from the top metal contact, the photocurrent, I_p , can be expressed as [7]

$$I_p(V) = \sum_{n=1}^N \frac{e P_0}{\hbar \nu} [e^{-\alpha(n-1)L_w} - e^{-\alpha n L_w} + e^{-\alpha(2N-n)L_w} - e^{-\alpha(2N-n+1)L_w}] e^{-n L_p / v(V) \tau}, \quad (4)$$

where P_0 is the incident infrared power, $\hbar \nu$ is the photon energy, α is the absorption coefficient assuming the absorption of light occurs only in the well, N is the number of quantum wells and τ is the excited carrier lifetime. The terms in the square bracket of Eq. (4) represent the absorption of the incident light and reflected light from the metal contact. In the case

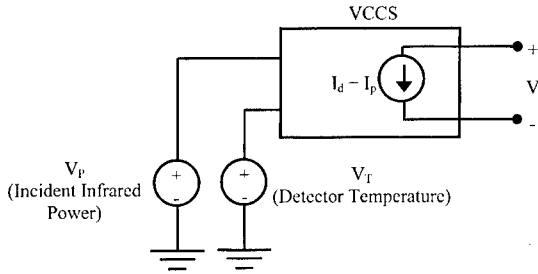


Fig. 2. PSPICE model for the QWIP. The two voltage sources V_p and V_T are used to input incident infrared power and detector temperature, respectively, to the model. In analogue behaviour modelling, the dark current and photocurrent given by Eqs. (3) and (5) can be incorporated using a VCCS.

of QWIPs, $\alpha L_w < 1$ and under typical operating bias, the mean free path is much greater than the period of the multiple quantum wells (i.e., $v(V)\tau > L_p$) [3]. Using these approximations, Eq. (4) can be simplified as

$$I_p(V) \approx \frac{2eP_0}{h\nu} \alpha L_w \frac{v(V)\tau}{L_p}. \quad (5)$$

4. PSPICE model and results

It can be seen from Eq. (3) that the dark current is dependent of both the bias and temperature while the photocurrent is mainly a function of the bias as given in Eq. (5). These two equations can be conveniently implemented by PSPICE using the analogue behaviour modelling technique [8] using a voltage controlled current source (VCCS). The circuit model that we have constructed for the simulation of QWIP characteristics is shown in Fig. 2. The operating temperature of the detector and the incident infrared power are represented by two voltage sources V_T and V_p attached to the VCCS, respectively. These voltages can be varied in the simulation to analyse the effects of temperature and incident infrared power on the detector performance. The PSPICE model is verified by comparing the simulated results with the experimental data of two different QWIPs as described below.

The first QWIP [9] consists of 50 periods of $\text{In}_{0.3}\text{Ga}_{0.7}\text{As}/\text{GaAs}$ quantum wells with well width of 40 Å, barrier thickness of 300 Å and area of $3.41 \times 10^{-8} \text{ m}^2$. Fig. 3 shows the simulated and experimental dark current as a function of bias across the QWIP. The device parameters used for the simulation are

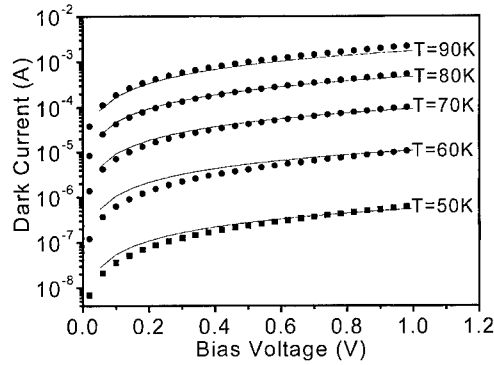


Fig. 3. Simulated (solid lines) and experimental [6] (solid circles) dark current for the $\text{In}_{0.3}\text{Ga}_{0.7}\text{As}/\text{GaAs}$ QWIP.

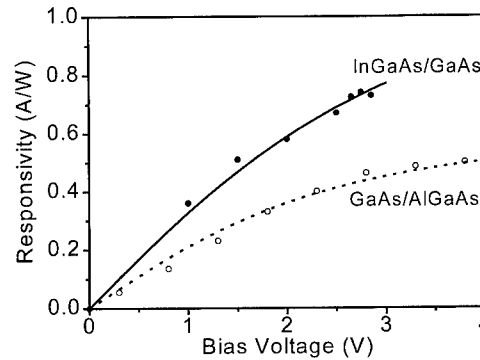


Fig. 4. Simulated (solid line) and experimental (solid circles) responsivity for the $\text{In}_{0.3}\text{Ga}_{0.7}\text{As}/\text{GaAs}$ QWIP [9]. Also shown in the simulated (dash line) and experimental (open circles) responsivity for the $\text{Al}_{0.25}\text{Ga}_{0.75}\text{As}/\text{GaAs}$ QWIP [10].

$N_D = 2 \times 10^{18} \text{ cm}^{-3}$, $v_s = 4.5 \times 10^7 \text{ cm s}^{-1}$, $\mu = 2200 \text{ cm}^2 \text{ V}^{-1} \text{ s}^{-1}$ and $m_w^* = 0.054m_0$, where m_0 is the free electron mass. The experimental data fits well when $E_c = 108 \text{ meV}$ which is in close agreement with the reported value of about 110 meV. Fig. 4 shows the simulated and experimental responsivity (I_p/P_0) of the $\text{InGaAs}/\text{GaAs}$ QWIP. The measured absorption coefficient $\alpha = 1.4 \times 10^4 \text{ cm}^{-1}$ at wavelength $\lambda = 9.8 \mu\text{m}$ and the responsivity data as a function of bias were obtained from Ref. [9]. The experimental data fits well with a carrier lifetime (τ) of 1 ps which falls within the typical carrier lifetime of QWIPs [10,11].

The second QWIP [3,12] composed of 50 periods of $\text{Al}_{0.25}\text{Ga}_{0.75}\text{As}/\text{GaAs}$ quantum wells having

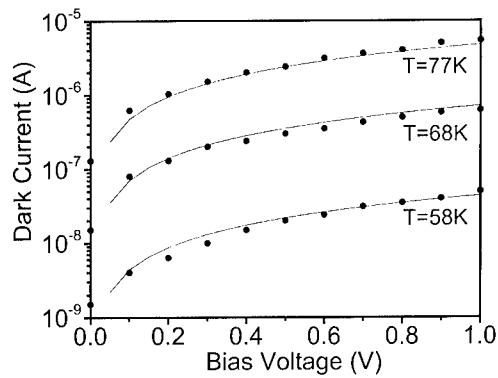


Fig. 5. Simulated (solid lines) and experimental [3] (solid circles) dark current for the $\text{Al}_{0.25}\text{Ga}_{0.75}\text{As}/\text{GaAs}$ QWIP.

well width of 40 \AA , barrier thickness of 480 \AA and area of $3.14 \times 10^{-8} \text{ m}^2$. Fig. 5 shows the simulated and experimental dark current as a function of bias across the GaAs/AlGaAs QWIP. The values used for simulation are $N_D = 1.2 \times 10^{18} \text{ cm}^{-3}$, $v_s = 1 \times 10^7 \text{ cm s}^{-1}$, $\mu = 1000 \text{ cm}^2 \text{ V}^{-1} \text{ s}^{-1}$ and $m_w^* = 0.067m_0$. The experimental data gives a good agreement with $E_c = 106 \text{ meV}$ which is in close to the reported value of 98 meV . Fig. 4 shows the simulated and experimental responsivity of the QWIP. The measured absorption coefficient $\alpha = 1.1 \times 10^4 \text{ cm}^{-1}$ at wavelength $\lambda = 9.7 \text{ \mu m}$ and the responsivity data were obtained from Ref. [10]. The simulated responsivity agrees well with the experimental data with a carrier lifetime of 4 ps .

5. Conclusion

In conclusion, a PSPICE model for quantum well infrared photodetectors is developed. By using the

device parameters, bias dependence of the dark current and photocurrent is completely described by the model. Temperature dependence of the dark current is also incorporated into the model. Simulated results obtained from the model are in close agreement with experimental data in a wide range of operating conditions verifying the validity of the model. This model can be easily integrated with the readout electronics for circuit simulations.

Acknowledgements

This research was supported in part by a NSTB grant GR6471.

References

- [1] B.F. Levine, *J. Appl. Phys.* 74 (1993) and references therein.
- [2] E. Costard, P.F. Bois, F. Audier, E. Herniou, *Proc. SPIE* 3436 (1998) 228.
- [3] B.F. Levine, C.G. Bethea, G. Hasnain, V.O. Shen, E. Pelve, R.R. Abbott, S.J. Hsieh, *Appl. Phys. Lett.* 56 (1990) 851.
- [4] M.A. Kinch, A. Yariv, *Appl. Phys. Lett.* 55 (1989) 2093.
- [5] S.D. Gunapala, B.F. Levine, L. Pfeiffer, K. West, *J. Appl. Phys.* 69 (1991) 6517.
- [6] D.M. Caugley, R.E. Thomas, *Proc. IEEE* 55 (1967) 2192.
- [7] G. Karunasiri, *Jpn. J. Appl. Phys.* 33 (1994) 2401.
- [8] MicroSim Pspice A/D & Basics + User Guide, 1997, 6–1.
- [9] G. Karunasiri, J.S. Park, J. Chen, R. Shih, J.E. Scheihing, M.A. Dodd, *Appl. Phys. Lett.* 67 (1995) 2600.
- [10] A. Seilmeier, H.J. Hubner, G. Abstreiter, G. Weimann, W. Schlapp, *Phys. Rev. Lett.* 59 (1987) 1345.
- [11] M.C. Tatham, J.F. Ryan, C.T. Foxon, *Phys. Rev. Lett.* 63 (1989) 1637.
- [12] B.F. Levine, A. Zussman, S.D. Gunapala, M.T. Asom, J.M. Kuo, W.S. Hobson, *J. Appl. Phys.* 72 (1992) 4429.



ELSEVIER

Physica E 7 (2000) 139–145

PHYSICA E

www.elsevier.nl/locate/physce

Quantum dot infrared photodetectors in new material systems

E. Finkman^{a,*}, S. Maimon^a, V. Immer^a, G. Bahir^a, S.E. Schacham^b, O. Gauthier-Lafaye^c,
S. Herriot^c, F.H. Julien^c, M. Gendry^d, J. Brault^d

^aDepartment of Electrical Engineering and Solid State Institute, Israel Institute of Technology, Technion, Haifa 32000, Israel

^bDepartment of Electrical and Electronic Engineering, College of Judea and Samaria, Ariel 44837, Israel

^cInstitut d'Electronique Fondamentale, CNRS, Univervite Paris-XI, 91405 Orsay, France

^dLaboratoire d'Electronique-LEOM, UMR CNRS 5512, Ecole Centrale de Lyon, 69131 Ecully, France

Abstract

Infrared detectors were implemented on InAs self-assembled quantum dots fabricated using Stranski–Krastanov growth mode on InAlAs matrix, lattice matched to InP (001) substrates. These dots grow with a shape of small elongated boxes, with their long axis along the $[110]$ direction, and with a high concentration of $7 \times 10^{10} \text{ cm}^{-2}$. Photoconductive measurements were performed in all three polarizations. Rich spectra in the range of 50–500 meV, with different polarization selection rules were observed. The bias dependence of peak intensity of the intraband transitions serves as an additional tool to identify their origin. Some of the peaks, which increase linearly with bias, are attributed to bound-to-continuum transitions. Others, which appear only at larger biases, and increase superlinearly, are due to bound-to-bound transitions. The magnitude of detector responsivity at normal-incidence is similar to that obtained for polarization normal to the layers, and is comparable to that achieved in QWIPs. BLIP conditions prevail at 77 K for integral photocurrent response at $F\#1$. The effect of unintentional doping is discussed. It is shown that this doping can be destructive for detector operation unless the density of dots is large. © 2000 Elsevier Science B.V. All rights reserved.

Keywords: Quantum dots; Intraband transitions; Infrared detectors

1. Introduction

Recent studies have shown the potential advantages in using quantum dot infrared photodetectors (QDIPs) rather than quantum well infrared photodetectors (QWIPs) to implement detectors [1–5]. There

are two major potential advantages of quantum dots over quantum wells as photodetectors, namely:

1. Intersubband absorption may be allowed at normal incidence. In QWIPs only transitions polarized perpendicular to the growth direction are allowed, due to absorption selection rules. The selection rules in QDIPs are inherently different, and normal incidence absorption is, indeed, observed.

2. Thermal generation of electrons is significantly reduced due to the energy quantization in all three

* Corresponding author. Tel.: +972-4-294-686; fax: 972-4-832-3041.

E-mail address: finkman@ee.technion.ac.il (E. Finkman)

dimensions. Generation by LO phonons is prohibited unless the gap between the discrete energy levels equals exactly to that of the phonon. This prohibition does not apply to quantum wells, since the levels are quantized only in the growth direction and a continuum exists in the other two. Hence thermal-generation or recombination by LO phonons results, with a capture time of few picoseconds. Thus, it is expected that S/N ratio in QDIPs will be significantly larger than that of QWIPs.

In this paper we present a study on two material systems of QDIPs. We first present a study on a promising structure for this application, based on InAs/InAlAs/InP material system [6]. In the second study, the more traditional system of InAs/GaAs dots is used to demonstrate the significance of the residual, unintentional, doping in affecting the performance of detectors based on intraband transitions.

2. InAs/ InAlAs/ InP QDIPs

2.1. Experimental set-up

In this work, we investigate InAs self-assembled quantum dots. These structures were grown using Stranski–Krastanov growth mode in an MBE Riber 2300 reactor. They were composed of ten layers of self-assembled InAs dots, separated by 400 Å InAlAs barrier layers, lattice matched to semi-insulating (0 0 1) InP substrate [6]. The layer combination resulted in a high concentration of elongated QDs with a unique shape. These dots grow with a shape of a flattened ellipsoids, around 500 Å long, 300 Å wide and 20 Å high, with their long axis along the $[\bar{1}10]$ direction, and with a high dot concentration of $7 \times 10^{10} \text{ cm}^{-2}$ (see Fig. 1). The barriers were delta-doped in their center by Si at a sheet concentration of $5 \times 10^{11} \text{ cm}^{-2}$. InGaAs contact layers, 5000 Å thick, n-doped with Si at a concentration of $1 \times 10^{18} \text{ cm}^{-3}$ and $8 \times 10^{18} \text{ cm}^{-3}$, were grown on the top and the bottom of the structure, respectively. The dots seem rather flat, but their exact shape is not accurately yet determined from the AFM image, as the AFM images were taken on uncapped dot layers, grown under the same conditions. It is reasonable to assume that the dots shapes and sizes are only slightly modified after the deposition of the $\text{In}_{0.52}\text{Al}_{0.48}\text{As}$

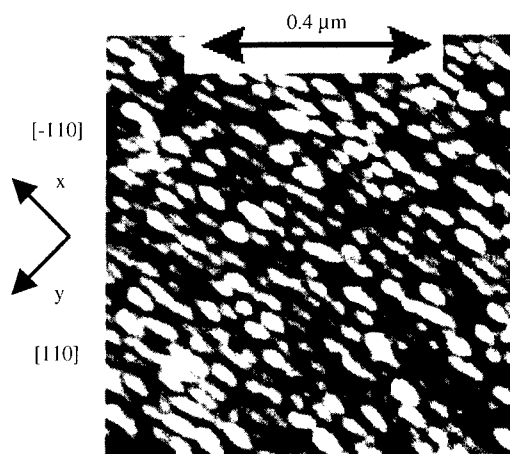


Fig. 1. Typical ex situ surface morphology of the InAs/InAlAs/InP dots.

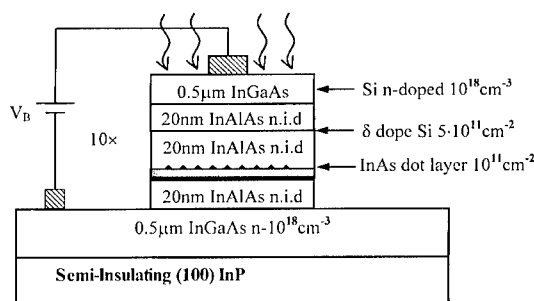


Fig. 2. Schematic view of MBE grown layer structure and photoconductive intersubband mesa detector.

cap layers, due to a low interdiffusion of the element III atoms, since the As concentration is the same in the dots and in the cap layers.

Photoluminescence (PL) and normal-incidence infrared absorption measurements were previously studied on similar dots [7]. A structured broad PL peak was interpreted as an evidence to a distribution of dot size in the sample. A single strong in-plane intraband absorption in such dots, peaked around 90 meV was observed, with a remarkably large oscillator strength ($f = 10$). This peak is polarized perpendicular to the dot length.

Mesa structure detectors were fabricated with an area of $200 \times 200 \mu\text{m}^2$. $50 \times 50 \mu\text{m}^2$ Ti/Au contacts were evaporated on the InGaAs contact layers (see

Fig. 2). Two illumination geometries were used. In the first, normal incidence (front illumination) photoconductive spectra were taken. Light is polarized either in the $[110]$ direction, defined as the x -axis, in which the electric field is along the width of the dot, or in the $[\bar{1}10]$ direction, the y -axis, where the electric field is along the length of the dot. It must be emphasized that, due to the elongated shape of the dots, absorption of radiation polarized in the x -axis could differ from that at the y -axis.

In the second configuration, the samples were cleaved along the $[110]$ and the $[\bar{1}10]$ directions, and were illuminated through a 45° -wedge, polished along the $[110]$ direction. In this configuration, two polarizations of the incoming IR beam are possible. In the s-polarization (TE), the electric field is parallel to the width of the dots, the x -axis. In p-polarization (TM), due to the 45° wedge, 50% of the component of the electric field is along the growth $[001]$ direction, z -axis, and 50% is in-plane. Thus, the observed transitions are polarized both in the y and z directions. Here we record spectra for polarization along the height of the dot, which is not available in the front illumination.

2.2. Experimental results

Photoconductive spectra at 24 K were measured using a Mattson Cygnus 25 FTIR. Spectra were taken at various biases and polarizations. Front illumination spectra are shown in Fig. 3a and b for both possible polarizations. At low bias voltages, the dominant photoconductive peaks appear at about 250 and 340 meV, denoted as (c) and (d), respectively. At low biases these peaks are hardly affected by polarization. The relative intensity of the peak (c) with respect to that of (d) is reduced as the bias is increased, and both seem to merge into one.

With increasing bias, two additional peaks emerge. The first, marked as (a), at 100 meV. The other, denoted as (b), varied in position for different detectors on the same wafer at the range of 150–165 meV. The 100 meV line, (a), is strongly polarized along the width of the dot (along the x -axis). The second peak, (b), is present at both polarizations. While the dependence of the low-energy peak (a) on bias is superlinear throughout, the responsivity of the second,

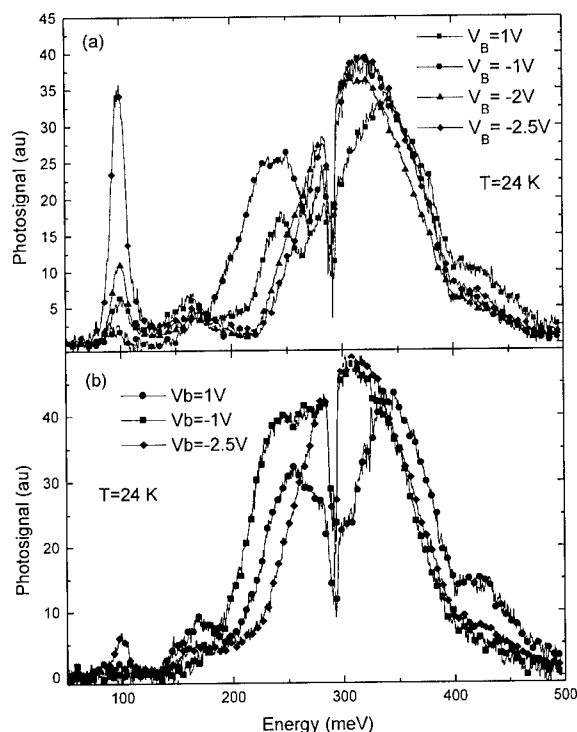


Fig. 3. QDIP spectra for front illumination: (a) x -axis polarization; (b) y -axis polarization.

(b), changes from superlinear to linear at larger biases.

The spectra obtained with wedge illumination are presented in Fig. 4a and b. Again the measurements were taken at various bias voltages. The strong voltage dependence of the polarized peak (a) present at front illumination is more pronounced in this configuration. While at low biases it is practically absent, it becomes by far the dominant at the largest bias. Once again, when the radiation is polarized along the length of the dots (y -axis), this peak is absent. Here, peak (b) is absent at lower bias, while at larger biases it increases linearly. In the p-polarization the dominant peak at larger energies is peak (c), and its shape hardly depends on bias.

The detector dark current, as a function of bias voltage, for various temperatures in the range of 50–110 K, is presented in Fig. 5. Also shown is the current due to background radiation at $F\#1$, at front illumination, with the detector at $T = 40$ K. By comparing the background curve to the dark curves, it is possible to conclude that background limited in performance

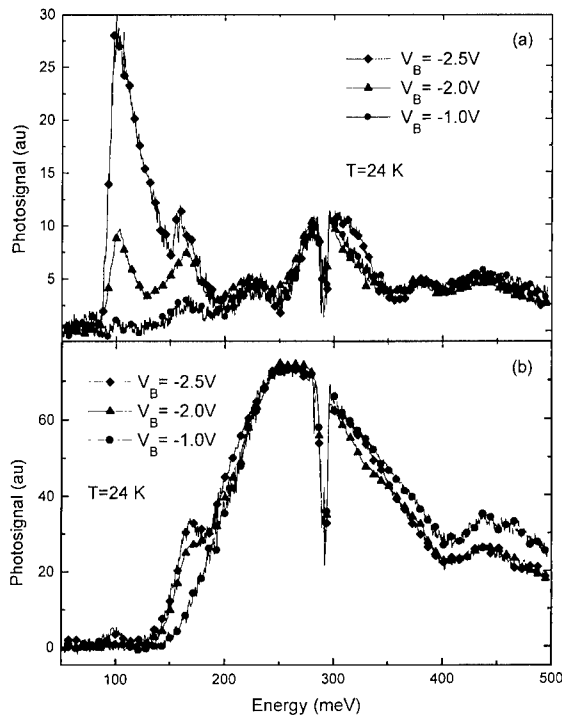


Fig. 4. QDIP spectra for wedge illumination: (a) x -axis polarization; (b) $y + z$ -axes polarization.

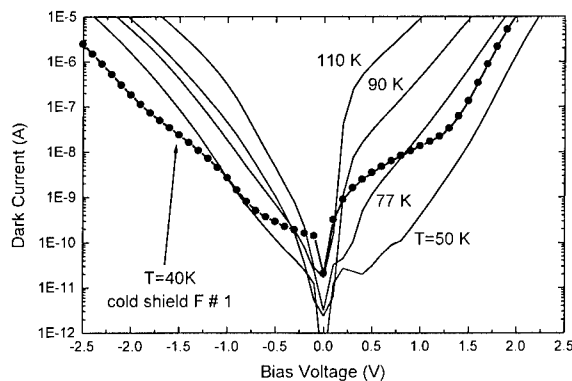


Fig. 5. Dark currents and background current characteristics.

(BLIP) conditions prevail up to 77 K for integral response at $F\#1$ illumination.

2.3. Analysis and discussion

All the confined energy levels in the dots are not degenerated, as a result of their non-symmetric shape.

Thus, two electrons at the most may populate each. The number of electrons per dot can be estimated from the ratio of the doping concentration in the barrier to the dot concentration, assuming all free electrons reside in the dots. Accordingly for the structure analyzed in this work the average number of electrons per dot is about 7. Thus, the 3–4 lowest levels are occupied at low temperatures. The highest of them may be partially populated, due to the variation in dot size. In the most basic approach it is possible to assign three quantum numbers to each level, n_x , n_y , n_z , associated with the x , y and z directions. Assuming, to a first approximation, that separation of variables applies, and that the dots have the shape of parallelepiped boxes, one may create a schematic representation of the confined energy levels in the conduction band of the dots. This scheme is presented in Fig. 6, together with the allowed transitions that result from this simplistic approach. This diagram gives a plausible interpretation to the origin of the observed peaks. Qualitatively, this scheme resembles the results of Dekel et al. [8], which are based on an eight-band model.

All photoconductive signals are due to carriers escaping the dots into the continuum and swept by the bias. The various peaks can be divided into two groups. The first group is generated by bound to continuum transitions. Its peaks increase linearly with bias. The second group consists of peaks, which appear only at larger biases, and their amplitude shows a superlinear dependence. This group should be associated with bound to bound transitions, followed by tunneling.

Peak (a) arises undoubtedly from the same transition as the one reported by Weber et al. [7]. It is strongly polarized along the width of the dots, the x -axis, and shows a super linear dependence on the bias. Thus it is reasonable to associate it with a bound to bound $e2 \rightarrow e5$ transition, that agrees with the observed polarization. Its energy is almost unchanged in all samples under all experimental conditions. In contrast, the other peaks have slightly different energies for different detector elements, which is interpreted as a difference in average dot sizes along the wafer. Dot dimensions should less affect the positions of deep levels in the dots than those of the shallow levels, a further verification of this interpretation.

The interpretation of line (b) is less obvious. The bias dependence turns linear, it is broader, and is

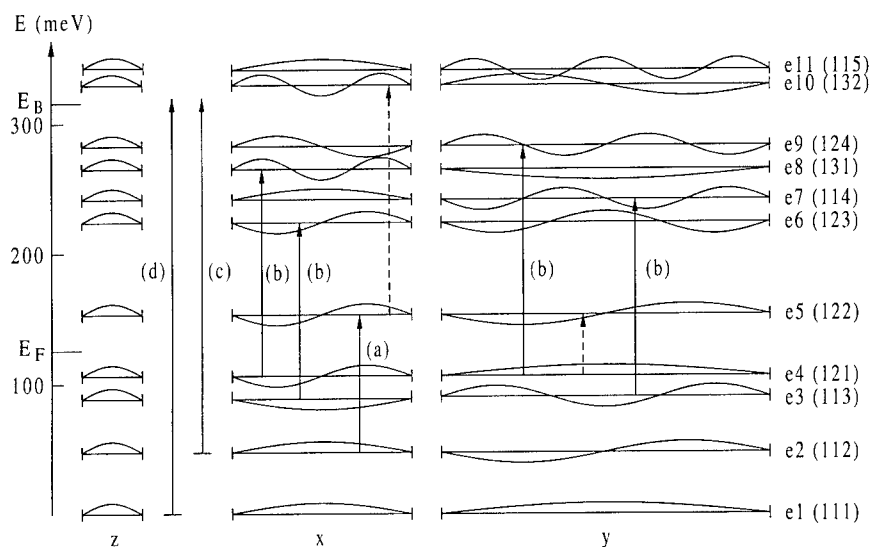


Fig. 6. Simplified schematic representations of the first possible energy levels in the QD. Arrows represent allowed transitions with appropriate polarizations. Only transitions from occupied to unoccupied transitions are indicated. Peaks are polarized in the directions in which the arrows appear. Tentative assignment of arrows corresponds to peaks described in text.

asymmetric. Thus it is probably associated with more than one transition from deep to a shallow bound state. Tentative transitions, e3–e6 and e4–e7 are x-polarized, and e3–e7 and e4–e9 are y-polarized, as marked in Fig. 6.

Both lines (c) and (d) are assigned to bound-to-continuum transitions, since they are basically linearly dependent on the bias, and their polarization selection rules are not as strict. Peak (d) is associated with electrons excited from the ground state e1, while peak (c) is due to transitions from the partially populated e3, e4, and possibly e5 states. The effects of polarization and bias on the structured spectra in the higher-energy range of peaks (c) and (d) are not completely understood yet. Model calculations are in the working.

3. Residual doping in QDIPs

3.1. Sample structure

An experimental structure of InAs/GaAs self-assembled QD was prepared. The sample was not rotated during the QD growth, thus a gradient in the

dot density was formed across the surface. Samples were grown with 10 layers of InAs QDs separated by 50 nm GaAs barriers. GaAs contact layers were grown on the bottom and the top of the quantum structure. There was no intentional doping in the entire quantum structure, except for the contact layers.

200 × 200 μm^2 mesa detectors, similar in structure to those described in Section 2.1 were implemented on three different sites on the wafer. The concentration of dots varies between the groups: high density (HD, $2\text{--}4 \times 10^{10} \text{ cm}^{-2}$), medium density (MD, $\sim 10^9 \text{ cm}^{-2}$), and low density (LD, $\sim 10^8 \text{ cm}^{-2}$). Alloyed AuGe/Ni/Au 100 × 100 μm^2 contacts were formed on top and bottom of the structure.

3.2. Experimental results

Photoluminescence spectra of the HD sample taken at 77 K show a strong peak at 1.32 eV due to inter-band transition in the dots, and a weaker one 1.44 eV, attributed to recombination in the wetting layer. The GaAs luminescence line appears at 1.51 eV. Similar peak transition energies, but with narrower linewidths, were found for samples MD and LD, showing that average dot sizes are similar in all samples.

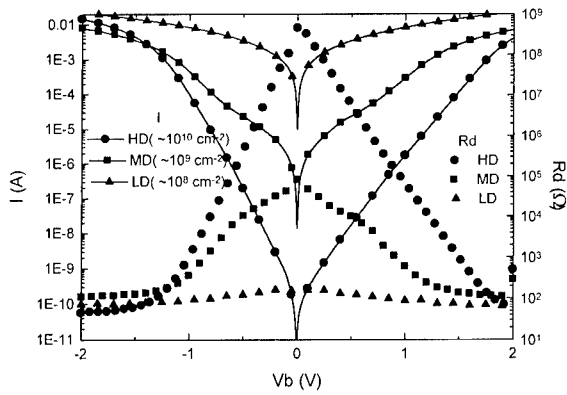


Fig. 7. I - V characteristics, and differential resistance of high density (HD, $\sim 10^{10} \text{ cm}^{-2}$), medium density (MD, $\sim 10^9 \text{ cm}^{-2}$), and low density (LD, $\sim 10^8 \text{ cm}^{-2}$) InAs/GaAs QDs.

The resistance of the three detectors varies greatly with dot density. The HD group shows, at 77 K, a uniform resistance of about 300 M Ω at zero bias. For MD samples the measured resistances is much lower, and much more dispersed, in the range of 50 k Ω to 50 M Ω , mostly in the lower end. The resistance of the LD samples is again lower by several orders of magnitude and it is in the range of 100 Ω to 100 k Ω .

Current and differential resistance as a function of voltage are shown in Fig. 7 for three detectors, one from each group. The HD sample, shows a clear back-to-back diode characteristic, while the LD detector shows almost ohmic behavior.

Spectral response measurements at 77 K were taken both for front and wedge illuminations. Typical spectra for the HD and MD samples are shown in Fig. 8. The spectra of the MD samples consist of a single peak, centered at about 0.2 eV, while those of the HD samples show a double peak. The first peak is identical to that of the MD sample, and the second is located at about 0.22 eV. This indicates that while the dot size in the MD samples is quite uniform, there is double distribution of dot size in the HD samples. The spectra are completely unpolarized, with the same waveform obtained in all configurations. No signal could be observed for the LD sample. The low resistivity generated a large noise current, prohibiting observation of a signal.

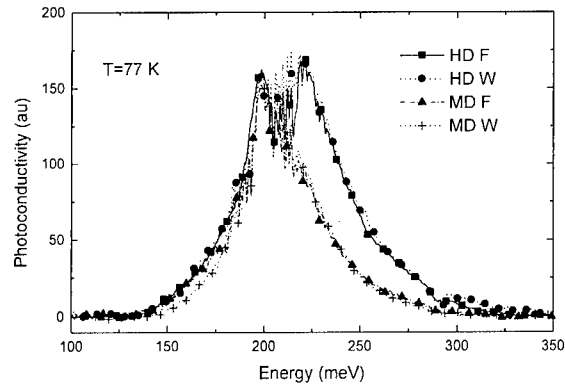


Fig. 8. Spectral response of HD and MD samples with front (F) and wedge (W) illuminations.

3.3. Discussion

This set of experiments is aimed at emphasizing the importance of unintentional background doping on device performance. It is shown that in samples with low dot density, the presence of unintentional doping can be destructive and prevent the use of the device. Optimization of doping and dot concentration is essential in order to achieve the desired performance.

4. Conclusions

Intraband transitions in quantum dots were studied by implementing infrared detectors and studying their photoconductivity as a function of applied bias and polarization. Both perpendicular and wedge illuminations were investigated. Complex spectra show different types of lines, attributed to both bound-to-continuum, and bound-to-bound followed by tunneling, transitions.

The present results are compared to absorption measurements performed on similar structures, in which only one bound-to-bound polarized transition was observed. The combination of photoconductivity and photo-induced absorption gives complementary information. It is easier to identify bound-to-bound transitions and estimate their oscillator strengths using IR transmission. On the other hand, photoconductivity spectrum is usually richer, giving easier access to bound-to-continuum transitions as well.

A tentative assignment of the transitions is based on a simplified model based on separation of wavefunctions. A more thorough analysis has to be completed, using a more comprehensive eight-band $k \cdot p$ model. Unlike QWIPs, it is obvious that infrared detectors based on quantum dots can perform well with front illumination.

The effect of residual doping must be taken into consideration when designing QDIPs. In epitaxial layers in GaAs/AlAs systems the unintentional doping is frequently in the range of 10^{15} cm^{-3} or higher. Under such conditions, it is possible that the concentration of carriers, which remains in the barrier, due to saturation of the dots, is large enough to effectively shorten the device. Hence, the dark current increases to the extent that the signal cannot be observed. Moreover, filling lower levels in the dots changes the observable transitions and the spectral response of the detectors. All these must be taken into account when designing QDIPs.

References

- [1] E. Finkman, S. Maimon, G. Bahir, S.E. Schacham, P.M. Petroff, in: S.S. Li, Y-K. Su (Eds.), *Intersubband Transitions in Quantum Well: Physics and Devices* (ITQW97, Tainan, Taiwan, December 1997), Kluwer Academic, Boston, 1998, p. 133.
- [2] S. Maimon, E. Finkman, G. Bahir, S.E. Schacham, J.M. Garcia, P.M. Petroff, *Appl. Phys. Lett.* 73 (1998) 2003.
- [3] S. Maimon, E. Finkman, G. Bahir, S.E. Schacham, L. Fonseca, J. Shumway, J.P. Leburton, J.M. Garcia, P.M. Petroff, ICPS-24, Jerusalem, August, 1998.
- [4] D. Pan, E. Towe, S. Kennerly, *Appl. Phys. Lett.* 73 (1998) 1937.
- [5] N. Horiguchi, T. Futatsugi, Y. Nakata, N. Yokoyama, T. Mankad, P.M. Petroff, *Jpn. J. Appl. Phys. Part 1* 38 (1999) 2559.
- [6] J. Brault, M. Gendry, G. Grenet, G. Hollinger, Y. Desieres, T. Benyatou, *Appl. Phys. Lett.* 73 (1998) 2932.
- [7] A. Weber, O. Gauthier-Lafaye, F.H. Julien, J. Brault, M. Gendry, Y. Desieres, T. Benyatou, *Appl. Phys. Lett.* 74 (1999) 413.
- [8] E. Dekel, D. Gershoni, E. Ehrenfreund, D. Spector, J.M. Garcia, P.M. Petroff, *Phys. Rev. Lett.* 80 (1998) 4991.



ELSEVIER

Physica E 7 (2000) 146–150

PHYSICA E

www.elsevier.nl/locate/physa

Mid-infrared photocurrent measurements on self-assembled Ge dots in Si

C. Miesner *, O. Röthig, K. Brunner, G. Abstreiter

Walter Schottky Institut, Technische Universität München, Am Coulombwall, D-85748 Garching, Germany

Abstract

We report on mid-infrared photocurrent spectroscopy of p-doped Ge quantum dots in Si. The Ge dots were fabricated by self-assembling in the Stranski–Krastanov growth mode using molecular beam epitaxy. Cross-sectional transmission electron microscopy reveals a lens-like dot shape with a lateral size of about 70 nm. Photocurrent is obtained between 200 meV (6.2 μm) and 600 meV (2.1 μm) in waveguide as well as normal incidence geometry for measurement temperatures up to 100 K. The strong high-energy tail is mainly attributed to intravalence band transitions from states bound in the Ge dots to continuum states. This is supported by the polarization dependence of the photocurrent as well as by interband photoluminescence. © 2000 Elsevier Science B.V. All rights reserved.

Keywords: Self-assembled quantum dots; Intersubband photocurrent; Quantum dot infrared photodetectors

The mid-infrared spectral range is very interesting for applications such as pollution monitoring, thermography and telecommunication. The earth atmosphere has two major transmission windows in the range of about 3–5 and of 8–14 μm . The development of lasers and detectors for this spectral range has thus been a major topic in applied semiconductor research during the last few years. Efficient quantum well infrared photodetectors (QWIPs) have been developed mainly on III–V-semiconductor materials [1–3] using intersubband transitions between confined states in the conduction band. A major limitation of such QWIPs

based on an electron system is the weakness of normal incidence absorption without grating couplers. This limitation is not very serious for highly p-doped QWIPs utilizing hole transitions between confined states in the valence band [4,5]. The efficiency may be further enhanced in quantum dot infrared photodetectors (QDIPs), where the confinement potential is three dimensional. Such QDIPs were predicted to have some important advantages over QWIPs such as a reduced dark current and higher electric gain [6]. Recently, some QDIPs on the InGaAs/GaAs material system have been presented. The intrinsic capability of normal incidence detection could be demonstrated [7,8], but concerning other important features such as responsivity or dark current, these devices need further improvement.

* Corresponding author. Tel.: +49-89-28912776; fax: +49-89-3206620.

E-mail address: christian.miesner@wsi.tu-muenchen.de (C. Miesner)

Self-assembled quantum dots can also be grown with Ge on Si in the Stranski–Krastanov growth mode because of the 4% difference in the lattice constants [9,10]. However, small dots are difficult to grow in this material system. Typical dot sizes range between 50 and 200 nm. Therefore, such dots do not represent a real zero-dimensional system as they do not have a strong confinement in all three dimensions. Nevertheless, Ge dots exhibit a much larger valence band discontinuity than quantum wells because of the higher Ge content in the dots. The large band discontinuity makes Ge dots an ideal system for normal incidence infrared detection in the wavelength range around 4 μm .

In this paper, we report on photocurrent (PC) measurements on Ge dots in Si structures in normal incidence and waveguide geometry. Photocurrent associated with transitions from bound hole states in the Ge dots to excited states is obtained for measuring temperatures up to 100 K without a significant decrease of the responsivity compared to $T = 20$ K. The maximum of the PC is at about 4 μm and undergoes a strong red shift with biasing.

Three samples were grown by molecular beam epitaxy (MBE) at a substrate temperature of $T = 550^\circ\text{C}$ in a commercial Riber Siva 32 chamber. The active region of the samples consists of 10 periods of doped Ge dots separated by undoped Si spacers of $L = 50$ nm thickness. The Ge dots were grown by deposition of 8 monolayers of Ge at a rate of 0.1 $\text{\AA}/\text{s}$. To provide carriers for intersubband absorption, boron was homogeneously supplied during Ge deposition. The boron concentrations for the three samples are 5.0×10^{18} (sample A), 2.5×10^{18} (sample B) and 0.9×10^{18} (sample C) cm^{-3} , respectively. For the electrical measurements, this active region was enclosed between two heavily boron-doped ($p = 4.2 \times 10^{18}/\text{cm}^{-3}$) contact layers with thicknesses of 300 nm for the bottom contact and 100 nm for the top contact. Mesa structures of $550 \times 550 \mu\text{m}^2$ were fabricated by standard photolithography and wet chemical etching. For the bottom contact, a standard AlAu metallization was used whereas TiAu was used for the top contact to avoid Al spiking through the active region. A $250 \times 250 \mu\text{m}^2$ window was left open in the top contact for light coupling in normal incidence geometry. For measurements in waveguide geometry, a 38° facet was polished to the samples after processing.

For structural characterization, atomic force microscopy (AFM) measurements and high-resolution transmission electron microscopy (HRTEM) were performed. For the AFM measurements, a reference sample was grown at which the Ge dots were left uncapped. They reveal a typical dot diameter of about 75 nm and a dot height of 7.5 nm. The density is determined to be $4.4 \times 10^9 \text{ cm}^{-2}$. Together with the nominal doping concentrations, the number of dopant atoms per dot is 133, 65 and 23 for the samples A, B and C.

A HRTEM image is shown in Fig. 1. From HRTEM, the diameter of the overgrown dots was determined to be about 70 nm and the height 6.5 nm. No dislocations were found in the samples. In the HRTEM image, the different quality of the Si/Ge interface at the bottom and at the top side of the dot is visible. Whereas the bottom interface is sharp, the top interface is smeared out due to segregation during overgrowth.

Fig. 2 shows a photoluminescence (PL) spectrum of sample A taken at $T = 6$ K. Beneath the Si related luminescence between 1.0 and 1.2 eV, Ge dot related luminescence is observed at 0.82 eV. Since Ge dot luminescence is regarded as a spatially type-II transition, the recombination occurs between the hole ground state of the Ge dots and the Si conduction band edge. Thus, assuming that the dot luminescence mainly arises from a no-phonon transition, the energy difference between the ground state of the dot and the Si valence band edge is about 340 meV. The FWHM of the luminescence is about 70 meV, reflecting the size distribution of the dots.

For the photocurrent measurement a set-up consisting of a glow bar coupled to a grating monochromator was used. Light was focussed onto the sample using KRS5 optics and a gold mirror. To avoid absorption from ambient air, the beam path was purged with dry nitrogen. The sample was mounted on the cold finger of a He flow cryostat equipped with a KRS5 window. A current amplifier and standard lock-in technique were used to detect the photocurrent. The raw spectra were normalized by the lamp spectrum recorded with a calibrated pyroelectric detector with flat spectral response.

Fig. 3 shows normal incidence PC spectra of sample B for different bias voltages taken at $T = 20$ K. At the low-energy side of the spectra, the photocurrent



Fig. 1. HRTEM image of a Ge dot in Si. The dimensions of the dot are about 70 nm diameter and 6.5 nm height. The white marker bar corresponds to $L = 20$ nm.

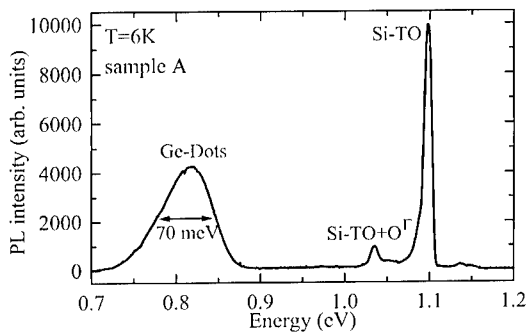


Fig. 2. PL spectrum of sample A taken at $T = 6$ K. The FWHM of the dot related PL at 0.82 eV is 70 meV. The Si-related peaks arise from recombination processes involving a TO-phonon (1.10 eV) and a TO as well as a Γ -phonon (1.04 eV).

intensity increases rapidly whereas it gradually decreases on the high-energy side.

To get a better understanding on the nature of this normal incidence photocurrent spectra, measurements with polarized light were carried out in waveguide geometry (see Ref. [11]). For TM polarized light, an intense maximum is observed at about 330 meV which is attributed to transitions from the ground state of the dots to the states near the Si valence band edge. The transition energy observed is consistent with the results obtained from PL. On the low-energy side, the PC intensity decreases quickly whereas an exponential decrease on the high-energy

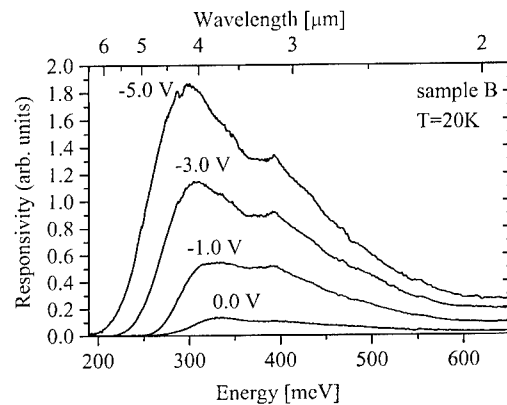


Fig. 3. Intersubband photocurrent spectra of sample B taken at $T = 20$ K for different bias voltages. With increasing bias, the photocurrent spectra undergo a strong red shift. Note the nonvanishing photocurrent for 0 V bias.

side is observed. For geometrical reasons, the TM mode contains z as well as xy -polarized components of the electromagnetic field. For TE polarized light, the photocurrent obtained is nearly constant over a range from about 330 to more than 450 meV and drops only slightly for energies up to 600 meV. The spectrum is very similar to the spectra obtained in normal incidence geometry. Note that the ratio between the PC intensity in TM and in TE polarization is about 2:1 for our Ge dot samples.

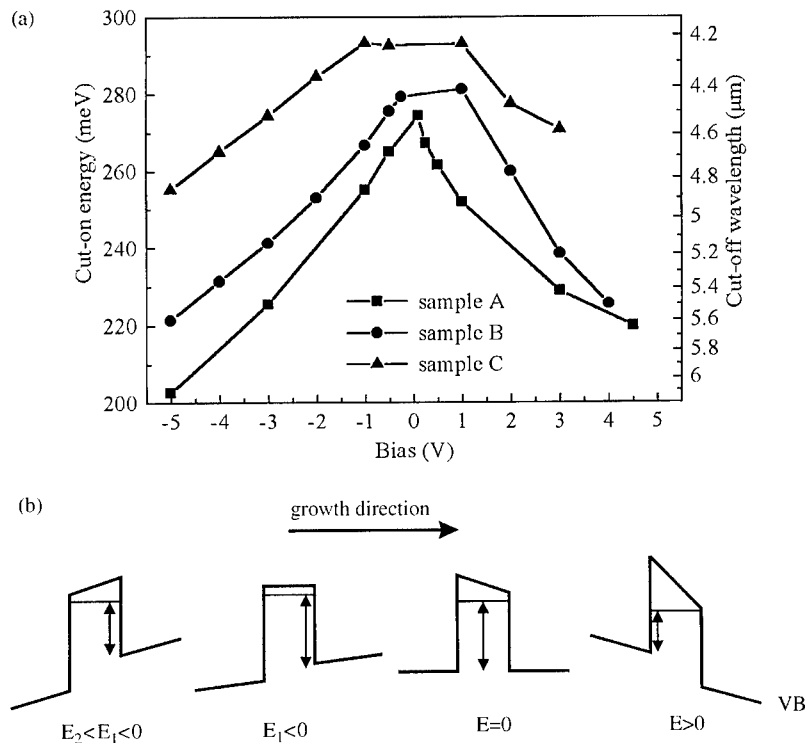


Fig. 4. (a) Bias dependence of the cut on energy of the photocurrent for samples A, B and C. (b) Schematic picture of the asymmetric valence band offsets of Ge dots in different electric fields.

In Fig. 3 a clear red shift of the PC maximum as well as of the cut on energy is observed when the bias is increased. This red-shift occurs for both polarities. The cut on energy at normal incidence is plotted in Fig. 4(a) as a function of bias for all the three samples at $T = 20$ K. For positive applied bias, the red-shift is a little stronger for all samples then for negative. A possible explanation for this behavior is the quantum-confined Stark-effect in combination with band bending in the electric field when the Ge dots are treated as asymmetric local quantum wells with a quasi-two-dimensional density of states. As depicted in Fig. 4(b), the band offset at the top interface of the dot is smaller than on the bottom side due to segregation and the dot shape. For negative electric field, i.e. if negative voltage is applied to the top contact with respect to flat band conditions, the asymmetry of the dots has to be compensated by the field and the red-shift is not so strong as that for positive electric field.

In Fig 4(a), the influence of the doping level on the photocurrent spectra can also be seen: With increasing doping level within the dot, the cut on energy of the photocurrent decreases. This is explained by band filling assuming that the cut on energy corresponds to the energy difference between the Fermi level within the dot and the Si valence band edge. In a simplified model we calculated the Fermi level of a dot with 70 nm diameter assuming a two-dimensional density of states and only one subband. We find that changing the number of holes per dot from 65 to 133 leads to an increase of the Fermi level of about 10 meV, which is of the same order of magnitude as the differences in the cut on energies determined experimentally.

Photocurrent in normal incidence has been measured for temperatures of 20, 50 and 100 K. It shows that the responsivity does not significantly decrease even at $T = 100$ K. No temperature-related shift of the PC peaks is observed.

Dark current measurements were performed for temperatures between 5 and 120 K. For all temperatures, the dark current flowing for positive applied bias is lower than for negative. At $T = 5$ K, the dark current is below 10 pA for voltages smaller than ± 5 V. At $T = 80$ K, the dark current does not exceed 1 nA for voltages below ± 1 V. The dark current spectra for temperatures between 5 and 100 K show characteristic kinks. Below the voltage V_m at which the kink occurs, the dark current only increases slightly whereas it increases exponentially with voltage for $V > V_m$. With increasing temperature, the voltage V_m at which the kink occurs decreases. For 120 K, no kink is observed anymore. Similar kinks were observed by Xu et al. for InGaAs dots [12].

In summary, mid-infrared photocurrent measurements on Ge dots in Si structures were performed. The obtained transition energies strongly depend on bias voltage and on the doping level within the dot. The results may be qualitatively described by a model of local asymmetric quantum wells with a quasi-two-dimensional density of states. Nevertheless, our samples exhibit some features characteristic of quantum dots such as reduced dark current, nearly equal PC intensities for TM and TE polarized light in waveguide geometry and a very good temperature stability of PC. All these features make Ge dots in Si a very promising system for normal incidence quantum dot infrared photodetectors.

Acknowledgements

We are grateful to H. Cerva, Infineon Technologies AG, Munich who gave us the opportunity to perform the TEM measurements in his laboratories. This work was financially supported by the DFG via grant No. Ab 35/3-1.

References

- [1] L.C. West, S.J. Eglash, *Appl. Phys. Lett.* 46 (1985) 1156.
- [2] B.F. Levine, C.G. Bethea, G. Hasnain, V.O. Shen, E. Pelve, R.R. Abbott, S.J. Hsieh, *Appl. Phys. Lett.* 56 (1990) 851.
- [3] B.F. Levine, *J. Appl. Phys.* 74 (1993) R1.
- [4] B.F. Levine, S.D. Gunapala, J.M. Kuo, S.S. Pei, S. Hui, *Appl. Phys. Lett.* 59 (1991) 1864.
- [5] J.S. Park, R.P.G. Karunasiri, K.L. Wang, *Appl. Phys. Lett.* 60 (1992) 103.
- [6] V. Ryzhii, *Semicond. Sci. Technol.* 11 (1996) 759.
- [7] D. Pan, E. Towe, S. Kennerly, *Appl. Phys. Lett.* 73 (1998) 1937.
- [8] L. Chu, A. Zrenner, G. Böhm, G. Abstreiter, *Appl. Phys. Lett.* 75 (1999) 3599.
- [9] D.E. Eaglesham, M. Cerulle, *Phys. Rev. Lett.* 64 (1990) 1943.
- [10] P. Schittenhelm, M. Gail, J. Brunner, J.F. Nützel, G. Abstreiter, *Appl. Phys. Lett.* 67 (1995) 1292.
- [11] C. Miesner, O. Röthig, K. Brunner, G. Abstreiter, *Appl. Phys. Lett.*, submitted for publication.
- [12] S.J. Xu, S.J. Chua, T. Mei, X.C. Wang, X.H. Zhang, G. Karunasiri, W.J. Fan, C.H. Wang, J. Jiang, S. Wang, X.G. Xie, *Appl. Phys. Lett.* 73 (1998) 3153.



ELSEVIER

Physica E 7 (2000) 151–154

PHYSICA E

www.elsevier.nl/locate/physica

Femtosecond mid-infrared study of electron dynamics in InAs/InAlAs quantum dots

E. Péronne^{a,*}, J.F. Lampin^{a,1}, A. Alexandrou^a, O. Gauthier-Lafaye^b, F.H. Julien^b,
J. Brault^c, M. Gendry^c

^aLaboratoire d'Optique Appliquée, ENSTA-Ecole Polytechnique-CNRS UMR 7639, F-91761 Palaiseau, France

^bInstitut d'Electronique Fondamentale, Université Paris-XI, CNRS URA 22, F-91405 Orsay, France

^cLaboratoire d'Electronique-LEOM, Ecole Centrale de Lyon, CNRS UMR 5512, F-69131 Ecully, France

Abstract

We present pump-mid-infrared-probe measurements in InAs/InAlAs self-organized quantum dots allowing to isolate the electron dynamics. By tuning the probe to an intraband transition in the conduction band at 13 μm , we measured a characteristic time of 3 ps for the electron capture from the barrier to the ground state of the dots at low excitation densities. At higher densities, this capture time decreases to 1.5 ps indicating the contribution of Auger-like processes. © 2000 Elsevier Science B.V. All rights reserved.

Keywords: Capture; Relaxation; Mid-infrared femtosecond measurements; InAs/InAlAs quantum dots

The Stranski–Krastanov growth mode provides high-quality semiconductor quantum dots (QD). Intensive investigations in these dots have been motivated by promising QD properties such as the δ -function-like density of states and by the perspective of realizing QD devices like low-threshold QD lasers. The physics of carrier dynamics is of particular importance for devices especially because of the predicted “phonon bottleneck” effect [1,2], a drastic slow-down of the relaxation process due to the discrete nature of the electronic energy levels.

However, short capture and relaxation times have been measured in QD structures and explained in terms of Coulomb collisions between electrons or electrons and holes [3,4].

In this work, we study the *electron* dynamics, for different carrier densities, in self-organized InAs/InAlAs quantum dots at room temperature using femtosecond pump-mid-infrared-probe transmission experiments. The pump excites electron–hole pairs in the barrier, while the probe is tuned in the mid-infrared range to the transition between the ground state (E_1) and an excited electronic state of the QDs (see Fig. 1). In contrast to other differential transmission [3] or photoluminescence reports [5], where the signal reflects the dynamics of both electrons and

* Corresponding author. Fax: +33-1-69-31-99-96.

E-mail address: peronne@ensta.fr (E. Péronne)

¹ Present address: IEMN-Dpt. ISEN, BP 69, 59652 Villeneuve d'Ascq Cedex, France.

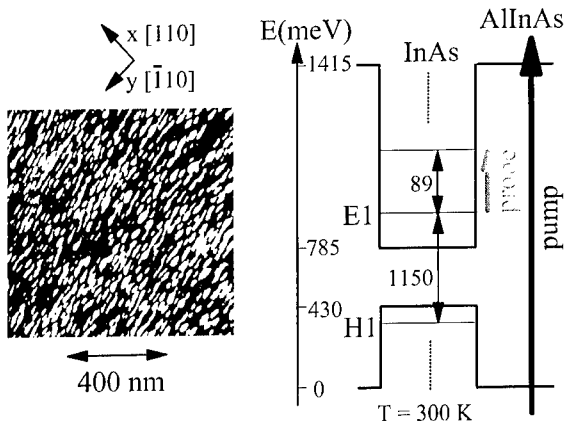


Fig. 1. Left: Typical atomic-force-microscopy image of an uncapped QD plane. Right: Schematic diagram of the QD potential. The interband transition energy (E_1-H_1) was determined by cw photoluminescence [7], while the intraband transition energy was obtained from photo-induced absorption [7] as well as photocurrent [8] measurements.

holes, these experiments are sensitive to the capture and relaxation of electrons only.

The sample was grown at 525°C on a semi-insulating InP (001) substrate using solid-source molecular beam epitaxy. A 0.5- μm thick $\text{In}_{0.52}\text{Al}_{0.48}\text{As}$ buffer layer is followed by ten undoped planes of 3 monolayers (ML) InAs separated by 50-nm $\text{In}_{0.52}\text{Al}_{0.48}\text{As}$ barriers. The 3% lattice mismatch, which is two times smaller than that in the well-studied InAs/GaAs system, the InAlAs surface morphology and the growth conditions (3×10^{-6} torr arsenic pressure and 0.22 ML/s growth rate) lead to a full coverage of the surface with InAs islands [6]. The atomic-force-microscopy (AFM) image (see Fig. 1) shows a $7 \times 10^{10} \text{ cm}^{-2}$ density of elongated islands aligned in the $[-110]$ direction with an average in-plane size of $56 \pm 11 \text{ nm}$ along the $[-110]$ (y -axis) and $31 \pm 6 \text{ nm}$ along the $[110]$ (x -axis) and with a broad height distribution centered at 1.5 nm, 0.6-nm wide at half maximum.

In our previous work, the cw optical properties of this sample have been characterized by means of photoluminescence, photoluminescence excitation spectroscopy and photo-induced infrared absorption spectroscopy [7]. The sample exhibits mid-infrared QD absorption around 89 meV, strongly polarized along the x -axis, corresponding to an intraband transition in the conduction band [7]. The width of the

intraband absorption peak was attributed to the size distribution of the QDs. The electronic nature of the transition was confirmed by the fact that this absorption occurs only in n-doped samples and not in p-doped ones. Photoconductivity experiments have confirmed the existence of this intraband transition and attributed it to a bound-to-bound transition [8]. Fig. 1 depicts the energy diagram of the QDs at 300 K. The oscillator strength associated with this intraband transition was estimated to be around 10.7, which is comparable to that of conduction intersubband transitions in the GaAs quantum wells [7].

To directly probe this intraband transition, we use a 200-kHz Ti:sapphire regenerative amplifier (Coherent RegA) which produces 4- μJ pulses at 808 nm. The output is split into two. The first beam generates a white-light continuum used to seed a double-stage optical parametric amplifier which is pumped by the second beam. A difference-frequency-generation stage follows: the signal (1.2–1.6 μm) and idler (1.6–2.4 μm) are focused in a type-II AgGaS₂ crystal to produce 3–13 μm tunable mid-infrared pulses [9,10]. We mechanically chopped the pump and the probe beams and used a lock-in detection to measure the differential transmission (DT) signal. While the carriers are injected in the barrier by an 808 nm pump, the probe is tuned to the intraband transition around 13 μm (see Fig. 1). The pump and probe durations were about 200 fs.

Fig. 2 shows the DT for two different QD-sample orientations. Based on the cw infrared absorption observed in doped samples [7], we estimated the carrier density to be around 0.5 electrons per dot for a pump energy of 0.1 nJ. When the probe is polarized along the y -axis, the signal is composed of a rapid rise followed by a slow decay. We attribute this signal to free-carrier (FC) absorption (in the buffer and barrier layers and the substrate) and its decay time of about 120 ps to free-carrier recombination. This is confirmed by the quite similar DT of a bulk InP sample (see inset of Fig. 2). A 300-fs resolution was deduced from the rise time of the DT in InP. As expected from our previous results [7], when the probe is x -polarized, the DT signal is seven times stronger than in the case of a y -polarized probe. The difference between the two polarizations is due to the QD absorption at the intraband transition and is visible through the rising signal superimposed on the FC step-like signal. Thus

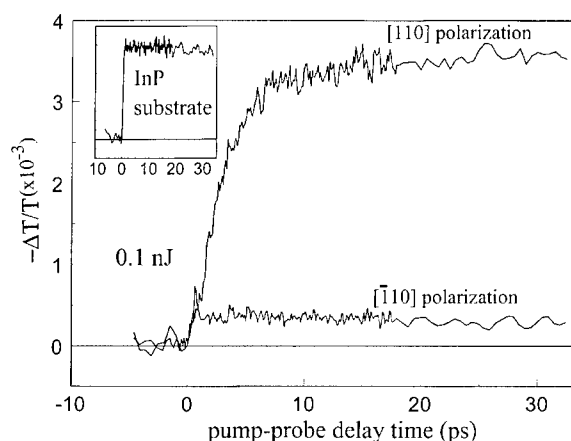


Fig. 2. Differential transmission of the QD-sample as a function of pump-probe delay for a probe wavelength of 13 μm and for probe polarizations along x and y . The pump pulse energy was 0.1 nJ. The inset shows the differential transmission of an InP substrate.

we have direct access to the population difference between the two QD electron states. The fact that the signal remains practically constant at long delay times shows that the intraband transition occurs between the ground electron state E_1 and an excited electron state. This is further confirmed by the observation of this transition under continuous excitation [7].

We expect the electrons excited in the barrier to be captured in the excited confined QD states and then relax to the ground state E_1 (Capture directly to E_1 was predicted to be less probable [11].) Thus, the rise time of the x -polarized DT reflects an effective capture time from the barrier into the ground state via capture and subsequent relaxation from the excited states to the ground state. It is in this sense that the word capture will be used in the following.

In order to confirm the above results, we performed the experiment at different probe wavelengths. Fig. 3 shows the x -polarized DT signal for a 0.5-nJ pump energy and three different wavelengths: one is tuned far from the absorption region, at 7.1 μm , a second on the high-energy side of the absorption peak, at 10.5 μm , and the third is tuned to the absorption maximum at 13 μm . At 7.1 μm , the signal is due only to FC absorption, is polarization independent, and has the same shape as those for InP and the y -polarized DT (see Fig. 2). The signal at 13 μm is much larger than at 10.5 μm . Even though the FC absorption also grows

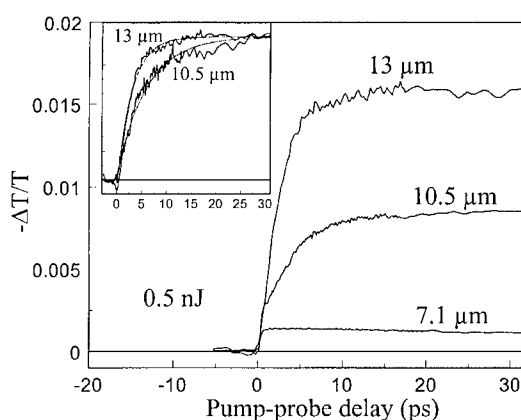


Fig. 3. Differential transmission as a function of pump-probe delay for a pump pulse energy of 0.5 nJ and for three different probe wavelengths: 7.1, 10.5, and 13 μm . The probe polarization was along x . The inset shows the signals at 10.5 and 13 μm after subtraction of the y -polarized differential transmission together with exponential fits using time constants of 6 and 3 ps, respectively.

with wavelength, this signal increase is mainly due to the increase of the QD absorption. We have subtracted the y -polarized DT from the x -polarized one in order to eliminate the polarization-independent FC signal and isolate the QD contribution and measure the capture time.

The capture time from the barrier to the ground state varies from 6 ps at 10.5 μm to 3 ps at 13 μm (see inset of Fig. 3). Larger dots exhibit lower-energy intraband transitions, and this seems to indicate that the capture is faster in larger dots. However, we cannot exclude the contribution of different intraband transitions to the width of the QD absorption peak. These times are surprisingly short for the capture and subsequent relaxation between levels separated by more than the LO-phonon energy. Short capture and relaxation times have been observed before [3,4] and have been attributed to Auger-like electron-hole [3] or electron-electron scattering [4]. Recently, a continuum background of states was observed in InGaAs/GaAs quantum dots and was used to explain the efficient carrier relaxation [12]. Another possible explanation in our system would be a quantum-wire-like rather than quantum-dot potential as proposed in Ref. [7] in order to explain the mid-infrared absorption results in n -doped samples.

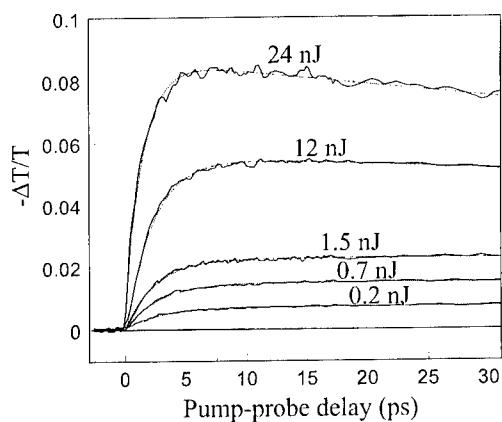


Fig. 4. Differential transmission for a probe wavelength of 13 μm and for different pump pulse energies. In order to isolate the contribution of the QD absorption, we show the difference between the x - and y -polarized signal. The dashed lines are exponential fits with time constants 3, 2.8, 2.5, 2.3, and 1.5 ps, respectively.

In order to study the effect of carrier density on the capture dynamics of the QDs, we performed experiments with a pump-pulse energy varying from 0.1 to 24 nJ for an x - and y -polarized probe at 13 μm . The difference of the DT signals in the two probe polarizations (x and y) for several pump-pulse energies is depicted in Fig. 4 together with a mono-exponential fit. For the two highest pump-pulse energies a second exponential (with time constants 370 and 200 ps) had to be used in order to describe the slow decay time observed. This decay time is probably due to electron–hole recombination. It should be noted, however, that its existence does not modify the extracted capture time. Below 0.5 nJ, we measured a constant 3-ps rise

time which then starts to decrease with pump intensity. When the pump-pulse energy is fifty times higher, the rise time is divided by two to obtain 1.5 ps. This decrease of the capture time at high excitation densities indicates the contribution of Auger-like processes such as Auger capture involving scattering with barrier electrons [13] or intradot relaxation through the ejection of a carrier from the QD [14].

References

- [1] U. Bockelmann, G. Bastard, *Phys. Rev. B* 42 (1990) 8947.
- [2] H. Benisty, C.M. Sottomayor-Torres, C. Weisbuch, *Phys. Rev. B* 44 (1991) 10945.
- [3] T.S. Sosnowski, T.B. Norris, H. Jiang, J. Singh, K. Kamath, P. Bhattacharya, *Phys. Rev. B* 57 (1998) R9423.
- [4] S. Sauvage, P. Boucaud, F. Glotin, R. Prazeres, J.-M. Ortega, A. Lemaître, J.-M. Gérard, V. Thierry-Mieg, *Appl. Phys. Lett.* 73 (1998) 3818.
- [5] B. Ohnesorge, M. Albrecht, J. Oshinowo, A. Forchel, Y. Arakawa, *Phys. Rev. B* 54 (1996) 11532.
- [6] J. Brault, M. Gendry, G. Grenet, G. Hollinger, Y. Desières, T. Benyattou, *Appl. Phys. Lett.* 73 (1998) 2932.
- [7] A. Weber, O. Gauthier-Lafaye, F.H. Julien, J. Brault, M. Gendry, Y. Desières, T. Benyattou, *Appl. Phys. Lett.* 74 (1999) 413.
- [8] E. Finkman, S. Maimon, V. Immer, G. Bahir, S.E. Schacham, O. Gauthier-Lafaye, S. Herriot, F.H. Julien, J. Brault, M. Gendry, *Physica E*, present volume.
- [9] M.K. Reed, M.K. Steiner Shepard, *IEEE J. Quantum Electron.* 32 (1996) 1273.
- [10] B. Golubovic, M.K. Reed, *Opt. Lett.* 23 (1998) 1760.
- [11] U. Bockelmann, T. Egeler, *Phys. Rev. B* 46 (1992) 15574.
- [12] Y. Toda, O. Moriwaki, M. Nishioka, Y. Arakawa, *Phys. Rev. Lett.* 82 (1999) 4114.
- [13] A.V. Uskov, F. Adler, H. Schweizer, M.H. Pilkuhn, *J. Appl. Phys.* 81 (1997) 7895.
- [14] R. Ferreira, G. Bastard, *Appl. Phys. Lett.* 74 (1999) 2818.

Second-harmonic generation in InAs/GaAs self-assembled quantum dots

T. Brunhes^a, P. Boucaud^{a,*}, S. Sauvage^a, A. Lemaître^b, J.-M. Gérard^b, V. Thierry-Mieg^b,
F. Glotin^c, R. Prazeres^c, J.-M. Ortega^c

^a*Institut d'Électronique Fondamentale, UMR CNRS 8622, Bâtiment 220, Université Paris-Sud, 91405 Orsay, France*

^b*Groupement Scientifique CNET-CNRS, 196 Av. H. Ravaud, 92225 Bagneux, France*

^c*CLIO/LURE, Bât. 209D, Université Paris-Sud, 91405 Orsay, France*

Abstract

We have studied second-harmonic generation at midinfrared wavelengths in InAs/GaAs semiconductor self-assembled quantum dots. We show that resonant second-harmonic generation associated with the intraband transitions of the quantum dots can be achieved in p-type samples. Frequency doubling is observed both for a TM- and a TE-polarized infrared excitation. A peak susceptibility value of 2×10^{-7} m/V at 168 meV is deduced for one quantum dot layer. The peak susceptibility results from the achievement of the double resonance between the optical pump field and the h_1-h_8 and h_1-h_{29} intraband transitions. © 2000 Elsevier Science B.V. All rights reserved.

PACS: 78.66. Fd; 42.65. Ky; 85.30 Vw

Keywords: Self-assembled quantum dots; Intraband transitions; Second-harmonic generation

Midinfrared second-order nonlinear susceptibilities associated with intersubband transitions have attracted a considerable interest in recent years. Two factors explain the enhancement of the nonlinear susceptibility in two-dimensional heterostructures by comparison with bulk semiconductors: (i) the large dipole matrix elements associated with the intersubband transitions; (ii) the wave function engineering which allows the achievement of double resonance

conditions (i.e. resonance between the pump and harmonic energies and the intersubband transitions) in asymmetric structures. Second-harmonic generation at a wavelength close to 10 μ m was first reported by Fejer et al. in GaAs quantum wells under an electric field [1]. This demonstration was shortly followed by the report of second-harmonic generation in asymmetric quantum wells [2], InP-based quantum wells [3] or by the demonstration of second-harmonic generation at longer wavelengths [4]. Frequency doubling at midinfrared wavelengths was also reported in the valence band of GaAs quantum wells [5] and SiGe/Si quantum wells [6].

* Corresponding author. Present address: Quantum Institute, University of California, Santa Barbara, CA 93106-9530, USA. Tel.: +33-1-69-41-62-99; fax: 805-893-4170.

E-mail address: boucaud@qi.ucsb.edu (P. Boucaud)

Semiconductor quantum dots appear as promising candidates to achieve large nonlinear susceptibilities in the midinfrared. By analogy with intersubband transitions, the dipole matrix elements associated with the intraband transitions of the quantum dots can be large, with typical dipole matrix element ranging from a fraction of nm to a few nm [7,8]. Both *z*-polarized and in-plane polarized intraband transitions are optically active in the conduction band and in the valence band. Self-assembled quantum dots are naturally asymmetrical in shape, thus providing the necessary symmetry breaking to observe second-order nonlinear susceptibility. Finally, the intrinsic homogeneous line width of the intraband transitions is predicted to be very narrow, which is a key feature for the susceptibility enhancement when the double resonance condition is achieved [9].

In this communication, we report on second-harmonic generation in p-type InAs/GaAs self-assembled quantum dots. The p-type quantum dot sample, grown by molecular beam epitaxy, consists of 40 InAs quantum dot layers separated by 35 nm GaAs barriers. The quantum dot layers are grown in the middle of a midinfrared waveguide epitaxially deposited on a n^+ -doped GaAs substrate. The midinfrared waveguide consists of a 5.5 μm thick GaAs core grown above a 5 μm thick $\text{Al}_{0.9}\text{Ga}_{0.1}\text{As}$ cladding layer. The dot density is around $4 \times 10^{10} \text{ cm}^{-2}$. The quantum dots are p-doped with a Beryllium δ -doping layer ($6 \times 10^{10} \text{ cm}^{-2}$) located 2 nm above each InAs layer. The quantum dots are lens-shaped and exhibit a much stronger confinement along the *z* growth axis direction. A reference sample with undoped quantum dots was separately used to calibrate the nonlinear susceptibility with the second-order nonlinear susceptibility of bulk GaAs.

Nonlinear optical experiments were performed with the free-electron laser CLIO. The experiments were performed at room-temperature. The free-electron laser pump beam was injected through the cleaved edge along the (110) direction of a 3 mm long sample. The maximum average power was 1.5 mW and the injected intensity around 200 MW cm^{-2} . Two polarizers were set in front of the sample. The first polarizer was set at an angle of 45° while the second polarizer could be rotated, providing a method to adjust the incoming polarization. TM (TE) polarization corresponds to an electric field along the *z*-growth axis

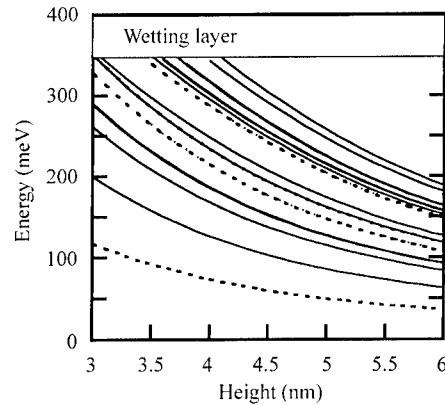


Fig. 1. Energy of the 20 first confined states in the valence band as a function of the quantum dot height. The aspect ratio (height/diameter) of the dots is 0.2. The levels involved in the experimentally observed harmonic conversion are emphasized.

(in the layer plane), respectively. A sapphire window was placed in front of the InSb photodetector to reject the pump.

The confined energy states in the quantum dots were calculated in the effective-mass approximation. The three-dimensional Schrödinger equation was solved for the lens-shaped quantum dot geometry by a finite difference method. The energies of the confined states in the valence band are shown in Fig. 1 as a function of the quantum dot height. Several intraband transitions involving the ground state are allowed. Starting from the ground state, the largest dipole matrix element is associated with the h_1 – h_2 transition (3.45 nm) and is oriented in the layer plane. The next allowed transition is the h_1 – h_4 transition with a 0.75 nm dipole matrix element along the *z* growth axis. The h_1 – h_7 transition is *z*-polarized with a typical 0.36 nm dipole matrix element. Experimentally, this transition is found to dominate the midinfrared absorption spectrum at energies larger than 90 meV [10]. The h_1 – h_8 transition is in-plane polarized (0.15 nm dipole length). A weak *z*-polarized h_1 – h_{29} intraband transition is also predicted. Although the number of confined states is quite large, only few transitions with non-vanishing dipole matrix elements can satisfy or be close to the double resonance condition. As shown below, the h_1 – h_8 , h_8 – h_{29} and h_1 – h_{29} intraband transitions are associated with the largest component of the second-order susceptibility $\chi_{zxx}^{(2)}$.

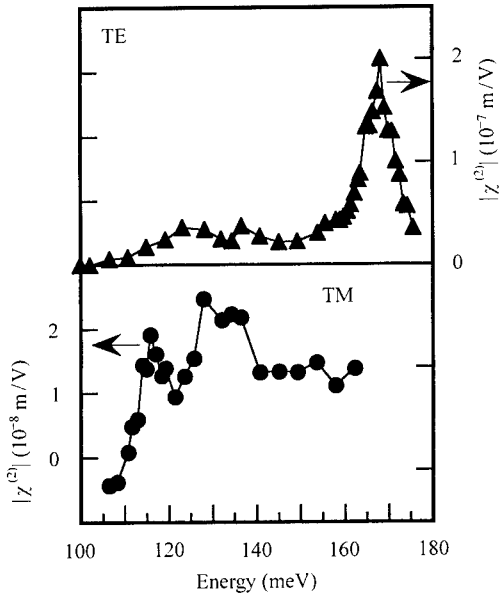


Fig. 2. Spectral dependence of the second-order nonlinear susceptibility measured for a TE-polarized pump (triangles) and a TM-polarized pump (circles). Note the two different vertical scales.

Fig. 2 shows a comparison between the nonlinear susceptibilities measured in TE and TM polarizations for the p-doped quantum dot sample. Similar experiments were performed with the undoped reference sample. No resonances were observed in the latter case for both polarizations. The resonances observed in the nonlinear susceptibility in Fig. 2 are therefore associated with the intraband transitions. The largest value of the nonlinear susceptibility is obtained for a TE-polarized infrared excitation with a dominant resonance at 168 meV. The peak susceptibility in TM polarization is roughly decreased by a factor of 10 as compared to the one obtained for a TE-polarized pump. Note that the second-harmonic power exhibits, as expected, a quadratic dependence with the pump power.

The susceptibility amplitude has been calibrated by reference to the susceptibility of bulk GaAs [11]. Because of the weak overlap of the quantum dots with the optimal mode, we have neglected the influence of the InAs layers on the bulk susceptibility. The second-harmonic power was measured for the undoped and doped quantum dot sample as a function of the second polarizer angle. The pump energy

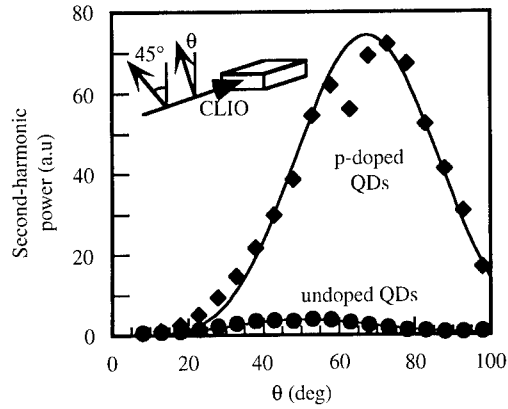


Fig. 3. Amplitude of the second-harmonic power as a function of the angle of the polarizer set in front of the sample. The diamonds (dots) correspond to the p-doped (undoped) quantum dot sample. The full lines correspond to Eqs. (1) and (2). The inset shows a schematic diagram of the experimental configuration.

was set at 168 meV. For the undoped sample, only the susceptibility of bulk GaAs contributes to the frequency-doubled signal. The angular dependence of the second-harmonic power is shown in Fig. 3. The two curves exhibit resonances at different angles. The second-harmonic power can be expressed following Eqs. (1) and (2) for the doped and undoped sample, respectively,

$$P_{2\omega} \propto |\chi_{zxx}^{(2)}|^2 \sin^4 \theta \cos^4(\theta - 45) P_{\omega}^2, \quad (1)$$

$$P_{2\omega} \propto |\chi_{zxy}^{(2)}|^2 (1 + 3 \cos^2 \theta) \sin^2 \theta \cos^4(\theta - 45) P_{\omega}^2, \quad (2)$$

where θ is the angle of the second polarizer ($\theta = 0$ corresponds to the TM direction). These expressions are plotted as the full curves in Fig. 3. The quantum dot nonlinear susceptibility $|\chi_{zxx}^{(2)}|$ can be directly deduced from the data presented in Fig. 3. Assuming $|\chi_{zxx}^{(2)}| = 1.9 \times 10^{-10}$ m/V for bulk GaAs [12], one finds $|\chi_{zxx}^{(2)}| = 1.2 \times 10^{-9}$ m/V for the p-doped quantum dot sample. Considering that the overlap factor between the 40 dot layers and the midinfrared confined optical mode is around 6×10^{-3} , the experimental nonlinear susceptibility for a single-quantum dot layer is found as large as 2×10^{-7} m/V. The peak susceptibility per quantum dot layer is three orders of magnitude larger than the bulk GaAs susceptibility. The susceptibility amplitude is similar to the susceptibilities reported so far for intersubband transitions in quantum wells.

The spectral dependence of the second-order non-linear susceptibility of the quantum dots can be calculated from the energy dependence of the quantum dot levels as reported in Fig. 1. Only the second-order processes starting from the ground state are considered. When the pump field and the second harmonic field are in close resonance with the E_i-E_j and E_j-E_k intraband transitions, the second-order susceptibility $\chi_{kji}^{(2)}$ at an energy $\hbar\omega$ can be written for a given quantum dot height h according to

$$\chi_{kji}^{(2)}(h) = \frac{e^2 N_{3D}}{\epsilon_0} \times \frac{\langle d_{ij} \rangle \langle d_{jk} \rangle \langle d_{ik} \rangle}{(\hbar\omega - E_{ij}(h) - i\Gamma_{ij})(2\hbar\omega - E_{ik}(h) - i\Gamma_{ik})}, \quad (3)$$

where e is the electronic charge, ϵ_0 the vacuum permittivity, Γ_{ij} the homogeneous line width (half-width at half-maximum) of the different intraband transitions. Γ_{ij} was taken equal to 0.2 meV. N_{3D} is the three-dimensional carrier density in the quantum dots which is obtained by dividing the equivalent 2D population of the dots by the thickness of the deposited InAs (2 monolayers). d_{ij} are the intraband dipole matrix elements corresponding to the E_i-E_j transition.

The dot size dispersion is given by a Gaussian distribution. The mean dot height (4.6 nm) is chosen in order to fit the h_1-h_7 intraband energy which is experimentally found to dominate the midinfrared absorption spectrum [10]. The spectral dependence of the different components of the nonlinear susceptibility can be calculated by integrating the susceptibility over the quantum dot size distribution for the distinct dipole allowed intraband transitions.

Fig. 4 shows the spectral dependence of the $|\chi_{zxx}^{(2)}|$ component of the susceptibility. This component has to be compared with the susceptibility measured in TE polarization. The dominant contribution which involves the h_1-h_2 and h_1-h_4 intraband transitions has been omitted. The theoretical susceptibility is dominated by a narrow peak at high energy. This resonance involves the h_1-h_8 and the h_8-h_{29} intraband transitions, which are in-plane polarized, and the z -polarized h_1-h_{29} intraband transition. The narrow line width indicates that the double resonance is achieved for a

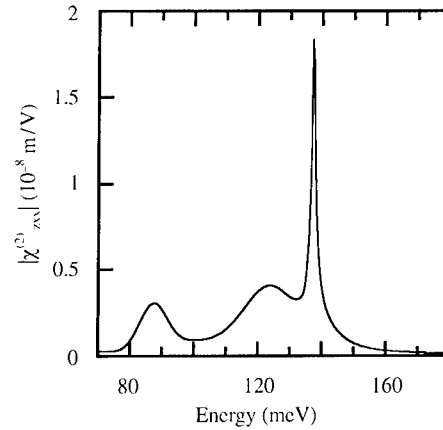


Fig. 4. Theoretical susceptibility $|\chi_{zxx}^{(2)}|$ of one quantum dot layer.

fraction of the quantum dots. The peaks at lower energy involve the h_1-h_8 and the h_1-h_{12} intraband transitions. A comparison with the experimental spectrum shows that the same features are observed experimentally. The theoretical peak susceptibility is predicted at lower energy as compared to the experimental one. This can be explained by the fact that the h_1-h_8 transition is predicted to occur at 140 meV whereas it is found experimentally to have its maximum at 160 meV. The amplitude of the experimental susceptibility is around one order of magnitude larger than the calculated one. This is most likely attributed to an overestimation of the homogeneous broadening of the intraband transitions or an underestimation of the dipole matrix elements. A 20 μ eV homogeneous broadening would account for the difference.

References

- [1] M. Fejer et al., Phys. Rev. Lett. 62 (1989) 1041.
- [2] P. Boucaud et al., Appl. Phys. Lett. 57 (1990) 215.
- [3] C. Sirtori et al., Appl. Phys. Lett. 60 (1992) 151.
- [4] J.N. Heyman et al., Phys. Rev. Lett. 72 (1994) 2183.
- [5] M.J. Shaw et al., Phys. Rev. B 50 (1994) 18395.
- [6] M. Seto et al., Appl. Phys. Lett. 65 (1994) 2969.
- [7] H. Drexler et al., Phys. Rev. Lett. 73 (1994) 2252.
- [8] S. Sauvage et al., Phys. Rev. B 58 (1998) 10562.
- [9] X-Qi Li et al., Phys. Rev. B 60 (1999) 1915.
- [10] S. Sauvage et al., Phys. Rev. B 59 (1999) 9830.
- [11] T. Brunhes et al., Appl. Phys. Lett. 75 (1999) 835.
- [12] Z. Levine et al., Phys. Rev. Lett. 66 (1991) 42.



ELSEVIER

Physica E 7 (2000) 159–165

PHYSICA E

www.elsevier.nl/locate/physa

Coherent control of electron intersubband transitions by frequency-detuned light fields

Walter Pötz *

University of Illinois at Chicago, Physics Department, Chicago, IL 60607, USA

Abstract

We present a brief overview over some of our recent theoretical results regarding coherent control in semiconductor heterostructures. Three potential schemes for optical coherent control of electron intersubband transitions in semiconductor heterostructures are reviewed. They use the relative phase between two external light fields to manipulate fundamental physical properties, such as absorption, optical gain, final-state population, phonon emission rates, and emission of THz radiation. In this paper we focus on the coherent control of absorption (exciton formation) using two frequency-detuned light fields in asymmetric GaAs/AlGaAs double wells. We show that in the short-pulse regime the change of relative phase amounts to pulse shaping which, in conjunction with excitonic effects, allows substantial control of inter(sub)band transitions. In the long-pulse regime this phase sensitivity is lost, however, charge oscillations between wells can be induced. © 2000 Elsevier Science B.V. All rights reserved.

Keywords: Coherent control; Semiconductor quantum well; Excitons; Photoabsorption

1. Introduction

Coherent control uses the principle of quantum interference to manipulate the dynamics of a quantum system. The basic idea is contained in Fermi's golden rule (as well as Young's double slit experiment), which says that in the quantum regime (wave regime) the response of a system in the presence of two perturbations is, in general, not equal to the sum of the responses to the individual perturbations, i.e.,

$$|\langle i|H_1 + H_2|f\rangle|^2 \neq |\langle i|H_1|f\rangle|^2 + |\langle i|H_2|f\rangle|^2, \quad (1)$$

where the Hamiltonians H_1 and H_2 account for two different external perturbations which can take the system from state $|i\rangle$ to $|f\rangle$. Rather, there is an interference term which can be manipulated by adjusting the relative phase between H_1 and H_2 .

In semiconductors, coherent control has been demonstrated experimentally for a variety of situations. Several coherent control schemes have been explored and/or suggested for semiconductors. Three such elementary schemes that we and others have explored are shown in Fig. 1. Adopted from atomic physics, interference between single- and multi-photon absorption in Fig. 1(a) has been used to control the symmetry of final states and transition cross sections [1]. In semiconductors, this scheme has

* Fax: 312-996-9016.

E-mail address: wap@uic.edu (W. Pötz).

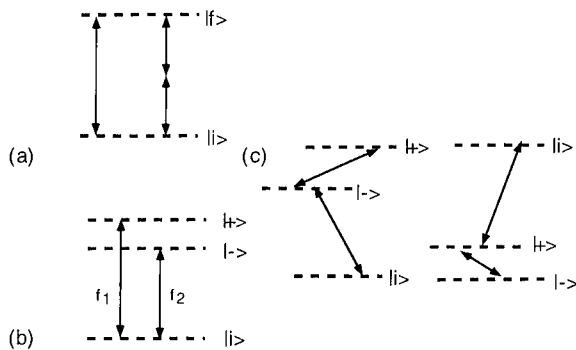


Fig. 1. Illustration of three elementary schemes for optically induced coherent control: (a) Conventional scheme based on interference between single- and multiple-phonon absorption, (b) scheme which uses two light fields of similar frequency and pulse shape with variable time-delay and polarization, (c) three-level scheme which uses one pump-field and one control field. The latter couples the band doublet $+/-$.

been used to control photocurrents [2,3]. We have proposed this scheme to control charge oscillations in double-quantum wells and the associated THz radiation [4]. The basic idea here is to control the rate of electron–hole formation which directly controls the amplitude of charge oscillations. Another scheme, Fig. 1(b) uses two coherent light fields of variable time-delay, polarization, and/or frequency detuning. Heberle and coworkers have used this scheme (with variable time-delay and relative polarizations, but equal frequencies) to coherently control exciton formation (optical absorption) and Faraday rotation [5]. A control scheme based on a driven three-level system has been used to demonstrate stimulated Raman adiabatic processes in atomic systems, [6] as well as electromagnetically induced transparency in various media [7–9]. In semiconductor heterostructures, this scheme has been predicted to provide a variety of coherent control phenomena, once high-intensity coherent microwave (mw) fields become available. These include coherent control of final-state population, optical absorption, optical gain, and LO phonon emission associated with electron intersubband transitions [10–13]. The physical mechanism behind this scheme is that interband polarization f_{+-} between the doublet $+/-$ enters the kinetic equations for interband polarization between the doublet and the third subband (i), i.e., $f_{\pm i}$. The latter govern transitions between i and the doublet. Hence, when the Rabi

period associated with the driven doublet is larger than a pump (or probe) pulse coupling subband i to the subband doublet, the phase of the driving field matters. In case of coherent control of LO phonon emission in interband transitions, the electron–phonon coupling plays the role of the probe field, making this an effect without counterpart in atomic systems [13].

Another application of Eq. (1) uses structural engineering of semiconductor nanostructures to exhibit Fano resonances [14]. These arise when there are two or more excitation pathways from a bound state to a continuum. Various structural design studies have been offered to evaluate the potential of semiconductors to exhibit Fano resonances in the absorption line shape [15–19]. Fano line shapes have been used in model studies to explore the possibility of manipulation of optical gain in semiconductors [20].

In this paper we first give a brief account of the theory we employ in our calculations. Then we present recent results on optical excitation of a biased GaAs/AlGaAs double well using two frequency-detuned pulses. In the short-pulse regime, it will be shown that a significant variation in absorption (exciton formation) can be achieved by variation of the relative phase of the two pulses. The phase sensitivity is intricately linked to excitonic effects in the system. This phase sensitivity disappears when the pulse duration begins to exceed characteristic frequencies of this electronic multi-subband system. However in this case, charge oscillations between the two wells can be induced by proper choice of light fields.

2. Theoretical background

A theoretical description of coherent phenomena and coherent control in a semiconductor clearly requires a theory which goes beyond the standard Boltzmann equation which has been so useful in the rate-equation regime of transport and optical processes. The two most common approaches used are non-equilibrium Green's functions methods and the density matrix approach [21–23]. Both approaches require approximations. Hence, the most useful approach depends on the particular application. The kinetic equations used in our work were originally derived within the Keldysh Green's function formal-

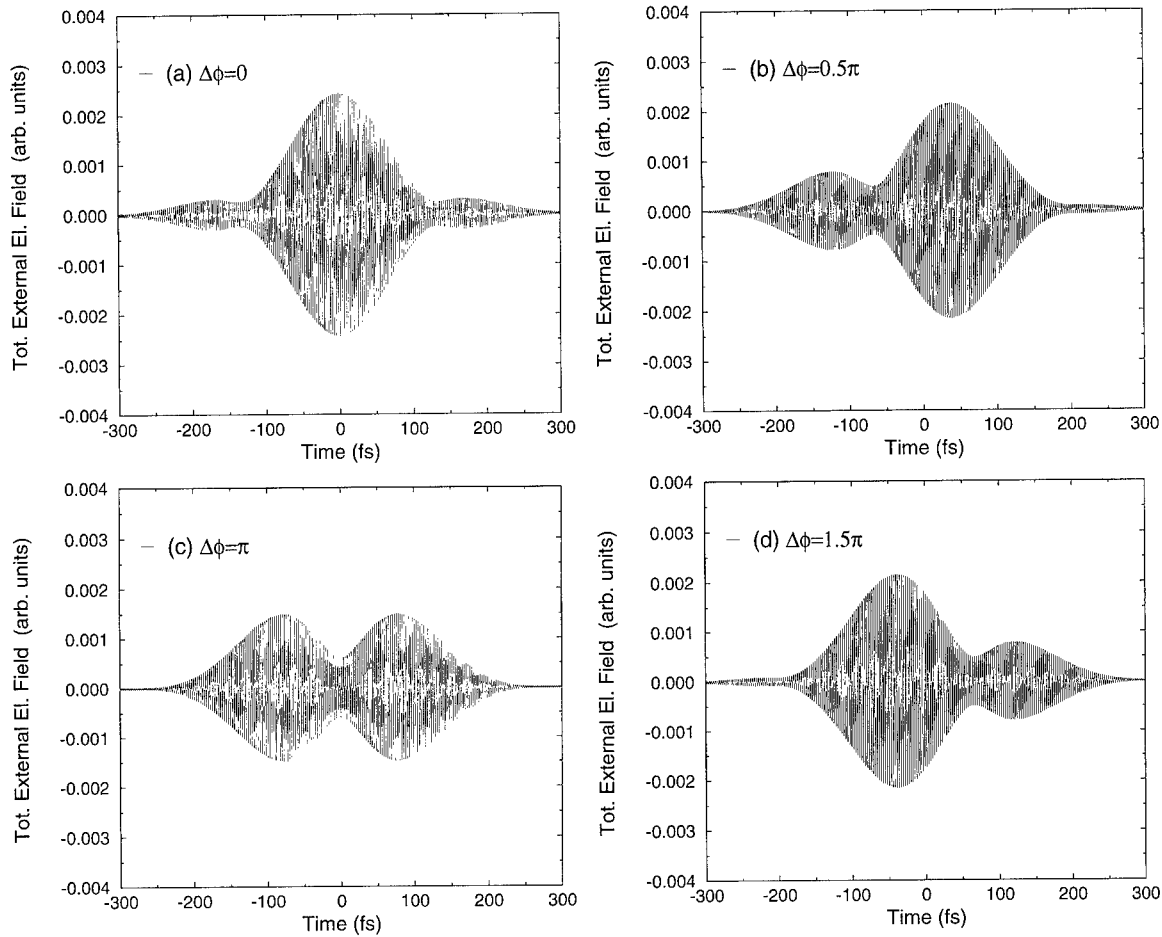


Fig. 2. Total external electric field versus time for two Gaussian pulses of 200 fs duration with zero time delay. Relative phase of the lower- to the higher-frequency pulse is (a) $\Delta\phi = 0$, (b) $\Delta\phi = \pi/2$, (c) $\Delta\phi = \pi$, and (d) $\Delta\phi = 1.5\pi$.

ism, but, may equally well be obtained within the density matrix approach [24,25]. They account for the exact coherent single-particle dynamics as given by the free-particle Hamiltonian and the external light field(s). In most of our calculations the former is for an asymmetric GaAs–AlGaAs–GaAs double well whose electron subband splitting is controlled by a static electric field, similar to the structure originally used to demonstrate coherent charge oscillations [26]. The free-particle dynamics in the double well is described within a multi-subband approximation, accounting for the subbands involved in the optical transitions.

The system is exposed to at least two external light fields, with examples illustrated in Fig. 1. The light fields are treated classically and their coupling to the

carriers is incorporated within the dipole approximation using a Hamiltonian of the form

$$H_{\text{e-LF}} = \sum_{i,f;k} \{ a_{fi}(k,t) \cos(\omega_{\text{LF}}t + \phi_{\text{LF}}) \times \hat{b}_f(k)^\dagger \hat{b}_i(k) + \text{h.c.} \}.$$

Here $a_{\text{e-LF}}(k,t)$ are proportional to the dipole matrix elements between initial (i) and final state (f) subbands. In case of resonant multi-photon absorption, they account for k -dependent mixing of $|s\rangle$ and $|p\rangle$ states in valence and conduction band Bloch functions [27]. ϕ_i is the phase of light field i . Within this Hamiltonian, the light fields are treated exactly. In case of resonant intersubband coupling where splittings

$E_f - E_i$ are small (tens of meV), the rotating-wave approximation is avoided.

The carrier–carrier Coulomb interaction is treated within the screened Hartree–Fock approximation, allowing us to account for excitonic effects, as well as scattering-induced phase breaking. Excitonic effects and Coulomb enhancement are generally important because of the relatively low 2-d carrier densities ($\leq 5 \times 10^{10} \text{ cm}^{-2}$) required to suppress carrier–carrier scattering on a picosecond time scale. In many cases, subband splitting, temperature, and time scales are designed such that LO phonon scattering may be neglected. Where coupling via LO phonons is relevant, we have included LO phonon scattering within the standard Markov and adiabatic approximation. This approximation can be considered valid for time scales ≥ 100 fs. If shorter time scales are relevant, a numerical evaluation of the time-convolution integrals which arise from memory effects may be necessary [28].

The present unavailability of intense coherent mw sources required for scheme Fig. 1(c) makes desirable the development of alternative control schemes. One possibility follows the versatile scheme of Fig. 1(b) in which two phase-locked coherent light fields are used to manipulate carrier absorption, as well as inter-well tunneling. As the two light fields differ in frequency a change in relative phase allows manipulation of the effective pulse shape. Hence one may consider this form of coherent control most naturally as control by manipulation of pulse shapes. To provide a specific example, we consider an asymmetric, biased double well in which the electron subband associated with the narrow well is tuned to lie 10 meV below the one associated with the wide one. We choose a GaAs/AlGaAs structure with well thicknesses of 14 and 8 nm and a barrier thickness of 2 nm. This assures that, by proper choice of pump frequencies, mainly the top heavy-hole subband (v), associated with the wide well, and the lowest two-electron subbands (denoted $+$ and $-$) participate in the absorption process. The two light fields are also detuned by 10 meV and are identical regarding pulse shape and polarization. Field amplitudes of the two pulses are of the same order of magnitude. They are basically adjusted such that both pulses independently give the same final number of photo-excited carriers.

Using, for example, the density matrix formalism one obtains a coupled set of Boltzmann–Bloch equa-

tions in the density matrix elements $f_{ij}(k)$, where i and j label band indices and k is the magnitude of the two-dimensional k -vector [29]. Here we account for the free-particle dynamics and the two external light fields, as discussed above, as well as the carrier–carrier Coulomb interaction within the Hartree–Fock mean-field approximation. As we consider optical excitation across the main energy gap and light fields of moderate intensity, the rotating-wave approximation is applied here. For the interband polarizations between valence and conduction subbands $f_{cv}(k)$, $c = +, -$, one obtains

$$\begin{aligned} i\hbar \dot{f}_{cv}(k) = & [(e_v(k) + H_v^{(v)}(k) - F_v^{(v)}(k)) \\ & - (e_c(k) + H_c^{(c)}(k) - F_c^{(c)}(k))] f_{cv}(k) \\ & - [\mathbf{P}^{(c)}(k)^* \cdot (\mathbf{E}_1(t)e^{i\omega_1 t} + \mathbf{E}_2(t)e^{i\omega_2 t}) \\ & - F_r^{(c)}(k)](1 - f_{cc}(k) - f_{vv}(k)) \\ & - \sum_{c' (\neq c)} [(H_{c'}^{(c)}(k) - F_{c'}^{(c)}(k)) f_{c'v}(k) \\ & + F_r^{(c')}(k) f_{cc'}(k)]. \end{aligned} \quad (2)$$

$e_x(k)$ is the energy of the free particle state (x, k) , $\mathbf{P}^{(c)}$ is proportional to the dipole matrix element between c and v , $\mathbf{E}_i(t)$ is the envelope of light field i , and ω_i is the frequency of light field i .

Hartree terms are given by

$$H_\beta^{(\alpha)}(k) = \sum_{\gamma\delta k'} v_{\alpha\gamma\beta\delta}(0) f_{\gamma\delta}(k') \zeta_{\gamma\delta}.$$

Fock terms are given by

$$F_\beta^{(\alpha)}(k) = \sum_{\gamma\delta k'} v_{\beta\gamma\delta\alpha}(k - k') f_{\gamma\delta}(k') \zeta_{\gamma\delta},$$

where $v_{\beta\gamma\delta\alpha}$ are Coulomb matrix elements and $\zeta_{\gamma\delta} = -1$, for $\gamma = \delta = v$, and $\zeta_{\gamma\delta} = 1$ otherwise.

Similar equations arise for the first time-derivative of all other density matrix elements. When compared to the Boltzmann equation, additional terms containing interband polarizations appear. It is important to note, that the Coulomb interaction renormalizes the externally applied light fields and also leads to *additional* coupling terms to other density matrix elements, such as the last sum in Eq. (2).

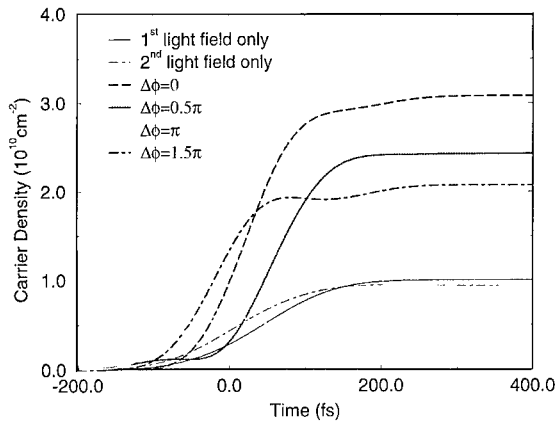


Fig. 3. Density of photo-generated electron–hole pairs as a function of time for several phase differences $\Delta\phi$. Thin lines for single pulses, thick lines for two pulses. Pulse duration is 200 fs.

3. Results

In the first excitation study we consider short pump pulses of Gaussian shape with a duration of 200 fs, peaks at $t = 0$, and zero time-delay. The first pulse has a photon energy of $hf_1 = E_-(k=0) - E_v(k=0) - 20$ meV and is close to the indirect exciton peak. $hf_2 = \hbar\omega_1 + 10$ meV, i.e. near the direct exciton peak. Light field intensities are such that individual pulses lead to a final number of about 1×10^{10} per cm^2 . Change of the relative phase between these two fields provides a simple means for “pulse-shaping” of the net excitation pulse for short pulses. If, on the other hand, the pulse duration is large compared to $2/\delta f$, where $\delta f = f_2 - f_1$, one gets the usual beating phenomenon which does not provide phase sensitivity to the net absorption. The pulse shapes for $\Delta\Phi = 0, 0.5\pi, \pi$, and 1.5π are shown in Fig. 2(a)–(d), respectively. Here, $\Delta\Phi$ is the phase of the lower-frequency pulse relative to the higher-frequency pulse. Note that coherent control by optical means can either be interpreted within the photon picture, which is the most commonly used, or the (semi-classical) pulse shaping picture used here. Fig. 3 gives the corresponding total number of electron–hole pairs versus time, including the two cases of excitation by individual light fields (thin lines). Significant variation in the final number of photo-excited carriers is evident. A cosine fit to the final number of electron–hole pairs shows the expected 2π periodicity displayed in

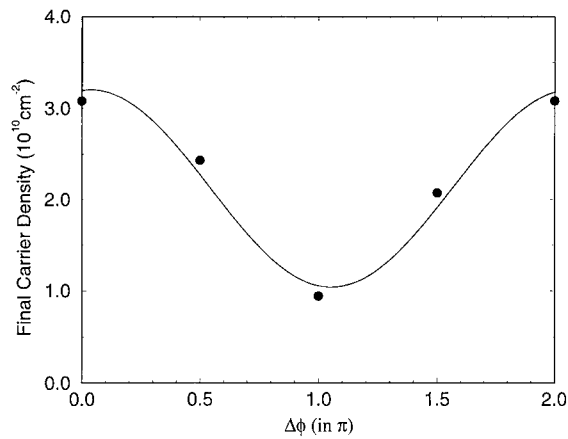


Fig. 4. Density of photo-generated electron–hole pairs versus relative phase $\Delta\phi$ between the lower- relative to the higher-frequency pulse. Dots give numerical results. Solid line is a cosine fit.

Fig. 4. It is important to note that additional coupling terms provided by the electron–electron Coulomb interaction (“excitonic effects”) play an essential role regarding this phase sensitivity. Eq. (2) shows that through the latter the time evolution of f_{+v} , f_{-v} , and f_{+-} becomes coupled. If we neglect excitonic effects, i.e. the correlation of photoexcited carriers, the phase sensitivity of the absorption process is lost. Then photogenerated electron–hole pairs act as individually driven two-level systems. The adjustment of relative phase simply leads to a phase change in the interband polarization with no influence on the final number of carriers. In fact, this phase sensitivity does not require excitation into a doublet of electron subbands, but also occurs if the possible final states lie within one subband only. In this case, phase sensitivity arises from interference of f_{cv} from two different regions in k -space.

Data for a pair of 400 fs pulses are shown in Fig. 5 which gives the number of electron–hole pairs versus time for $\Delta\Phi = 0, 0.5\pi, \pi$, and 1.5π . As expected, the phase sensitivity has decreased quite a bit. Inspection of the interwell dynamics by monitoring the number of carriers in the wide and narrow well shows that in this case tunneling between left and right well is stronger than in the short-pulse case. This trend can be confirmed for increasing pulse duration. The beating field which is tuned near resonance to the direct-indirect exciton transition drives charge

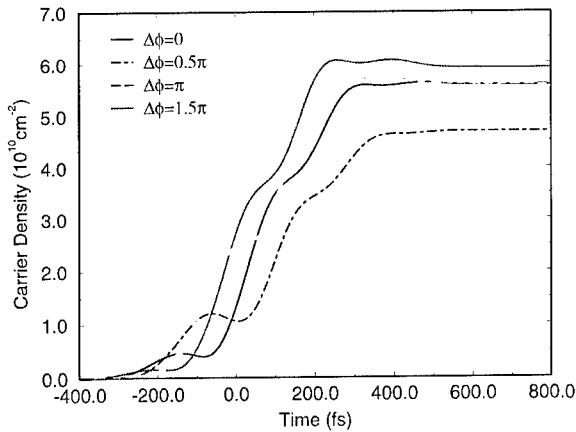


Fig. 5. Density of photo-generated electron–hole pairs as a function of time for several phase differences $\Delta\phi$. Pulse duration is 400 fs.

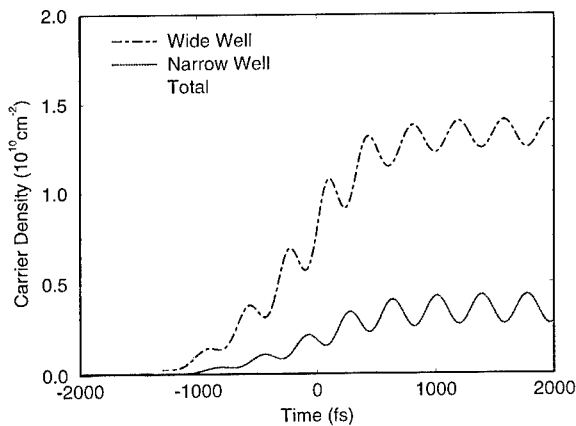


Fig. 6. Density of electrons in wide well (dot-dashed line) and narrow well (dotted line), as well as total number of electron–hole pairs as a function of time. The pulse duration is 1600 fs.

oscillations between narrow and wide wells. While the relative phase of these charge oscillations changes with the relative phase between the two light fields, there is neither phase sensitivity in the *amplitude* of charge oscillations nor in the total number of photogenerated carriers in this long-pulse limit. This is illustrated in Fig. 6 for a pulse duration $\tau_p = 1.6$ ps. The beating in the total light field leads to an oscillatory rise in the total number of carriers, as well as an induction of tunneling of electrons between wide and narrow well. For the data in Fig. 6, the intensity of the light-field that predominantly couples to the indirect exciton was chosen four times higher than that

for the field which is resonant with the direct exciton. Moreover, carrier–carrier scattering was neglected.

4. Summary

In summary, we have very briefly presented three elementary schemes with potential application for coherent control in semiconductors. We focused on the case of photoabsorption in a semiconductor double well using two detuned phase-locked light fields. We have found that in the short-pulse limit, excitonic effects in conjunction with pulse shaping by adjustment of the relative phase between the two pump fields allows control of the final number of photoexcited carriers. In the long-pulse regime, the beating in the total driving field allows the induction of electron charge oscillations between the two wells when the beating frequency is tuned near resonance to the energy between direct and indirect exciton energies. This preliminary study points at the possibility of using this scheme for the generation of THz radiation. A more detailed study regarding this effect, including an optimization of parameters for structure and light fields, is currently in progress.

Acknowledgements

Helpful discussions with W.A. Schroeder regarding experimental aspects are acknowledged. This work has been supported by the US Army Research Office.

References

- [1] R.J. Gordon, *Ann. Rev. Phys. Chem.* 48 (1997) 595.
- [2] E. Dupont, P.B. Corkum, H.C. Liu, M. Buchanan, Z.R. Wasilewski, *Phys. Rev. Lett.* 74 (1995) 3596.
- [3] A. Hachè, Y. Kostoulas, R. Atanasov, J.L.P. Hughes, J.E. Sipe, H.M. van Driel, *Phys. Rev. Lett.* 78 (1997) 306.
- [4] W. Pötz, *Appl. Phys. Lett.* 72 (1998) 3002.
- [5] A.P. Heberle, J.J. Baumberg, K. Köhler, *Phys. Rev. Lett.* 75 (1995) 2598.
- [6] U. Gaubatz, P. Rudecki, S. Schiemann, K. Bergmann, *J. Chem. Phys.* 92 (1990) 5363.
- [7] See, for example, S.E. Harris, *Phys. Today* 50 (7) (1997) 36.
- [8] Y. Zhao, *Opt. Photon. News* (1997) 30.
- [9] *Appl. Phys. Lett.* 71 (1997) 395.
- [10] W. Pötz, *Appl. Phys. Lett.* 71 (1997) 395.
- [11] W. Pötz, *Phys. Rev. Lett.* 79 (1997) 3262.

- [12] X. Hu, W. Pötz, *Appl. Phys. Lett.* 73 (1998) 876.
- [13] X. Hu, W. Pötz, *Phys. Rev. Lett.* 82 (1999) 3116.
- [14] U. Fano, *Phys. Rev.* 124 (1961) 1866.
- [15] J. Faist, C. Sirtori, F. Capasso, L.N. Pfeiffer, K.W. West, *Opt. Lett.* 21 (1996) 985.
- [16] J. Faist, F. Capasso, C. Sirtori, A.L. Hutchinson, K.W. West, L.N. Pfeiffer, *Appl. Phys. Lett.* 71 (1977) 3477.
- [17] J. Faist, F. Capasso, C. Sirtori, K.W. West, L.N. Pfeiffer, *Nature* 390 (1997) 589.
- [18] H. Schmidt, K.L. Campman, A.C. Gossard, A. Imamoglu, *Appl. Phys. Lett.* 70 (25) (1997) 3455.
- [19] W. Pötz, Structural Control of Fano resonances in semiconductor heterostructures, *Superlatt. Microstruct.*, 1999, in press.
- [20] A. Imamoglu, R.J. Ram, *Opt. Lett.* 19 (1994) 1744.
- [21] J. Rammer, H. Smith, *Rev. Mod. Phys.* 58 (1986) 323.
- [22] T. Kuhn, F. Rossi, *Phys. Rev. B* 46 (1992) 7496.
- [23] H. Haug, A.-P. Jauho, *Quantum Kinetics in Transport and Optics of Semiconductors*, Springer, Berlin, 1996.
- [24] W. Pötz, *Phys. Rev. B* 54 (1996) 5647.
- [25] U. Hohenester, W. Pötz, *Phys. Rev. B* 56 (1997) 13 177.
- [26] K. Leo, J. Shah, E.O. Göbel, T.C. Damen, S. Schmitt-Rink, W. Schäfer, K. Köhler, *Phys. Rev. Lett.* 66 (1991) 201.
- [27] E.O. Kane, *J. Phys. Chem. Solids* 1 (1957) 249; M.D. Dvorak, W.W. Schroeder, D.R. Andersen, A.L. Smirl, B.S. Wherrett, *IEEE J. Quantum Electron.* 30 (1994) 256.
- [28] X. Hu, W. Pötz, in: W. Pötz, W.A. Schroeder (Eds.), *Coherent Control in Atoms, Molecules, and Semiconductors*, Kluwer, Dordrecht, 1999.
- [29] W. Pötz, M. Žiger, P. Kocevar, *Phys. Rev. B* 52 (1995) 1959.



ELSEVIER

Physica E 7 (2000) 166–173

PHYSICA E

www.elsevier.nl/locate/physa

Observation of electromagnetically induced transparency and measurements of subband dynamics in a semiconductor quantum well

C.C. Phillips^{a,*}, E. Paspalakis^b, G.B. Serapiglia^a, C. Sirtori^c, K.L. Vodopyanov^a^a*Experimental Solid State Group, Physics Department, Imperial College, London SW7 2BZ, UK*^b*Optics Section, Physics Department, Imperial College, London SW7 2BZ, UK*^c*LCR Thomson-CSF, Domaine de Corbeville, 91404 Orsay Cedex, France*

Abstract

The phenomenon of electromagnetically induced quantum coherence is demonstrated between three confined electron subband levels in a quantum well which are almost equally spaced in energy. Applying a strong coupling field, two-photon-resonant with the 1–3 intersubband transition, produces a pronounced narrow transparency feature in the 1–2 absorption line. This result can be understood in terms of all three states being simultaneously driven into “phase-locked” quantum coherence by a single coupling field. We describe the effect theoretically with a density matrix method and an adapted linear response theory. Tuning the excitation laser to the 1–2 absorption energy allows the electron subband momentum distributions to be measured with the sample close to intersubband inversion. These are modelled to yield scattering rates and non-equilibrium phonon densities. © 2000 Elsevier Science B.V. All rights reserved.

PACS: 78.47.+p; 78.66.Fd; 42.50.Hz

Keywords: Subbands; Quantum interference; Electromagnetically induced transparency

1. Introductory remarks

The phenomenon of electromagnetically induced transparency (EIT, for reviews see Refs. [1,2]) is one of a class of intriguing quantum optical effects which rely on incident optical beams being intense enough

for their fields to significantly perturb the electron Hamiltonian which determined the original “bare” electron states of a system. Under suitable conditions a coherent superposition of the original states can be created, so that macroscopic properties like photon absorption and spontaneous and stimulated emission become determined by microscopic and essentially quantum interferences between wave function probability amplitudes within each member of an ensemble of oscillators. EIT has been known for some years but has been studied almost exclusively in atomic

* Corresponding author. Tel.: +44-171-594-7575; fax: +44-171-594-7580.

E-mail address: chris.phillips@ic.ac.uk (C.C. Phillips)

vapour systems [1–5], and defect levels in crystals [6–9]. In these narrow linewidth systems the optical perturbation energy, characterised by the Rabi frequency, $\Omega_{\text{Rabi}} = \mu E / \hbar$ (where μ is a transition dipole matrix element and E is an amplitude of the coupling EM field) can most easily be made large enough for electromagnetically induced splittings and shifts of optical transitions to be resolved spectroscopically.

EIT typically involves a three-level system of well-defined parity, having two dipole-allowed transitions ($|1\rangle \rightarrow |2\rangle$ and $|2\rangle \rightarrow |3\rangle$) and a third ($|1\rangle \rightarrow |3\rangle$) dipole forbidden (Raman) transition. Driving this with a “coupling field”, of photon energy $\hbar\omega_c \sim E_{23}$ establishes a coherent superposition of the states’ probability amplitudes and makes quantum interference possible. Absorption at the original E_{12} photon energy now involves two coherent pathways, ($|1\rangle \rightarrow |2\rangle$ and $|1\rangle \rightarrow |2\rangle \rightarrow |3\rangle \rightarrow |2\rangle$) whose probability amplitudes interfere destructively and, in the ideal case, completely cancel the original absorption at photon energy E_{12} . Once the necessary quantum coherences have been created by the “coupling” beam, both it and the “probe” beam (with $\hbar\omega_c \sim E_{12}$) can propagate without loss through a medium which would otherwise have been highly opaque to the probe.

By allowing operation close to a transition resonance (where the material would otherwise absorb strongly), EIT enables the exploitation of highly efficient resonant non-linear optical processes [10, 11]. Also, if e.g. the state $|2\rangle$ is populated incoherently, stimulated photon emission occurs at E_{12} without the corresponding absorption process being possible, leading to predicated, and, in sodium vapour, recent demonstrations [12] of lasing without inversion (LWI).

Practical EIT observations are classified, by the ordering of the energy levels, into “ Λ ” (1–3–2), “V” (2–1–3) and “ladder” or “cascade” schemes (1–2–3), where the first state has the lowest energy. Compared with atomic and crystal defect states, QW subbands have unattractively broad transitions (homogenous linewidths ~ 5 meV, corresponding to dipole dephasing rates of ~ 100 fs $^{-1}$), but have the unique and intriguing property that the transition energies, dipoles and even symmetry properties can be engineered with considerable freedom and precision. Also, because of

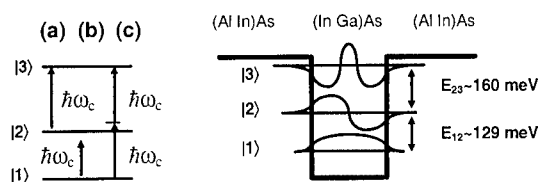


Fig. 1. Schematic of quantum well energy levels and coupling laser resonance conditions. (a) “Autler–Townes” EIT, $\omega_c \sim E_{23}$, (b) strongly driven two-level atom, $\omega_c \sim E_{12}$, (c) “phase-locked” coherence, $\omega_c \sim E_{13}/2$.

the light conduction band effective masses, QW inter-subband dipole elements, and hence Rabi frequencies, can be large.

To date there has been theoretical interest in quantum optics in QWs [13–16] but no experimental observations. On the other hand, Fano interference schemes, analogous to EIT but using strong and appropriately phased tunnelling coupling between the QW states and an adjacent continuum to establish the $|2\rangle \rightarrow |3\rangle$ coherence, have recently demonstrated the viability of quantum interference and transparency in a QW system [17–19].

In practice, observing EIT absorption cancellation depends on maintaining the phase of the overall quantum coherence between states $|1\rangle$ and $|3\rangle$. In the ideal case of continuous monochromatic coupling fields, the incorrectly phased component damps out within several Rabi periods. Practical pulsed measurements though typically require “adiabatic preparation” techniques, in which the coupling and probe pulse envelopes are chosen so that Ω_{Rabi} changes sufficiently slowly for the expectation value of the electron probability density always to correspond to state $|1\rangle$ [1, 2].

Here we study a novel three-level QW “ladder”-type system (Fig. 1), in which, for the first time, the states are close, compared with the transition linewidths, to being equally spaced in energy. In this case a single coupling field can simultaneously drive all three states into coherence with their quantum phases “locked” so as to produce an enhanced coherent transparency feature in the absorption spectrum. This allows us to observe EIT in a QW system and to demonstrate “phase-locked” quantum coherence, both for the first time.

2. Experimental details

The QW sample consists of 40 symmetric 10 nm n-doped ($n_s = 6 \times 10^{11} \text{ cm}^{-2}$) $\text{In}_{0.47}\text{Ga}_{0.53}\text{As}$ wells with 10 nm $\text{Al}_{0.48}\text{In}_{0.52}\text{As}$ barriers, lattice matched to an undoped InP substrate. It came from the same wafer as the sample of Ref. [20] but had subband transition energies slightly shifted by wafer non-uniformity. Transition energies (matrix elements) were $E_{12} \sim 129 \text{ meV}$ (2.34 nm) and $E_{23} \sim 160 \text{ meV}$ (2.64 nm). E_{12} was measured from the sample's linear absorption spectrum (Fig. 2a). At the 30 K experiment temperature only the ground subband was occupied, so E_{23} was measured using the induced absorption method of Ref. [20].

The sample was polished into a 45° wedge to allow one double pass of the beams through the QWs. Absolute transmission values, T , were obtained by ratioing spectra linearly polarised perpendicular and parallel to the QW normal since only the former couple to the ISB transitions. The interaction region was shorter than the wavelengths, rendering dispersion and propagation effects negligible.

Independently tunable ($\lambda \sim 6\text{--}12 \mu\text{m}$) synchronised coupling (ω_c) and probe (ω_p) laser pulses, were generated in separate $\text{Er}^{3+}:\text{Cr}^{3+}:\text{YSGG}$ pumped optical parametric generators [21,22] based on ZnGeP_2 and CdSe non-linear crystals (Fig. 3). They had similar overall temporal profiles (FWHM $\sim 100 \text{ ps}$), but differed in their short timescale amplitude structure arising from the OPG amplification statistics. The pulses were sufficiently narrow linewidth and long compared with the subband dephasing and relaxation times for the measurement to be effectively continuous wave and monochromatic.

Peak effective coupling field intensities, corrected for the experimental geometry, reflection losses and polarisation coupling efficiency to the subband transitions, of up to $\approx 2.6 \text{ MW cm}^{-2}$ were attained. All measurements were taken through a $300 \mu\text{m}$ pin-hole which was attached to the sample facet, and the probe was defocused to $\sim 10^{-3}$ of the coupling beam intensity with a 10° angular separation between the two. Linear absorption measurements (Fig. 2a) gave a Lorentzian line centred at $E_{12} = 129 \text{ meV}$ with a homogenous linewidth, $\gamma_{12} \sim 5 \text{ meV}$ with the sample of $T = 30 \text{ K}$.

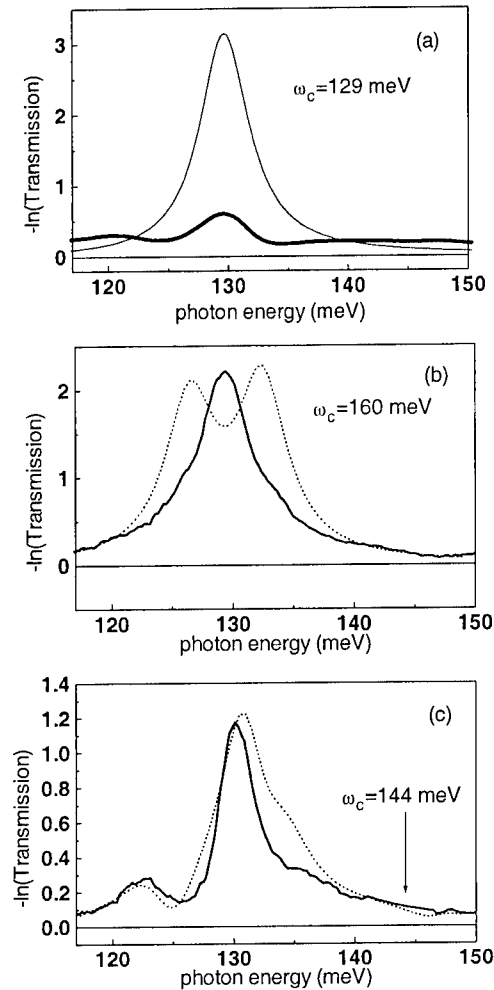


Fig. 2. Measured (heavy solid lines) and calculated (dotted lines) absorption across the 1–2 resonance for different coupling laser frequencies (a) $\omega_c \sim E_{12}$, (b) $\omega_c \sim E_{23}$, (c) $\omega_c \sim E_{13}/2$. Fig. 2a, light solid line, linear absorption spectrum.

Tuning the coupling energy to the lower transition, ($\hbar\omega_c = E_{12}$) produced, unsurprisingly, an absorption spectrum (Fig. 2a), characteristic of a strongly saturated two-level system transition. Carrier redistribution between the first two levels almost completely bleaches the original absorption, and the large absorbed laser energy heats the carrier system broadening the transitions and masking any coherent effects in the absorption spectrum.

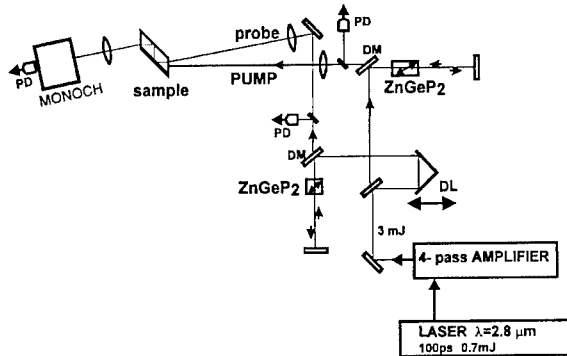


Fig. 3. Schematic of the optical parametric generator laser system used in the experiments. In this work all data was taken with zero time difference between the coupling and probe pulses and the ZnGeP₂ crystals were replaced by CdSe for some spectral ranges.

Interestingly, tuning ω_c to the E_{23} resonance, i.e. the classic “Autler–Townes” EIT condition, produced only small (except for the absorption reduction associated with partial populating of level $|2\rangle$) modifications to the absorption spectrum (Fig. 2b). In this configuration the Rabi frequency (~ 4 meV) should be just enough to observe some splitting of the line, but this is masked in the experiment by spatio-temporal fluctuations in the beam intensities.

The most striking result occurs when the coupling beam frequency was tuned half-way between E_{12} and E_{23} ($\hbar\omega_c \sim E_{13}/2$) (Fig. 2c). A pronounced (67% reduction in absorption) dip appears in the absorption spectrum. It is spectrally narrower (FWHM ~ 3.6 meV) than the original homogenous linewidth and is absent in spectra taken with the coupling laser detuned by an equal amount below E_{12} ($\hbar\omega_c = 116$ meV, Fig. 4). Its spectral narrowness, the non-obvious relationship between its position (126 meV) and the coupling photon energy (144 meV), both suggest an origin in quantum interference.

3. Theoretical treatment

We theoretically treat the three-level system within a density-matrix formalism whose time evolution, within a rotating frame and under the rotating-wave and relaxation-time approximations, is written as

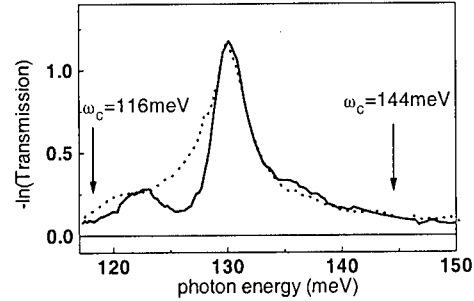


Fig. 4. Comparison between measured absorption spectra with $\omega_c \sim E_{13}/2$ (heavy line) and with, $\omega_c = 116$ meV (light line), i.e. at an equal but opposite detuning from the E_{12} resonance.

$$\begin{aligned}\dot{\rho}_{11} &= \gamma_2 \rho_{22} + i\Omega_{12}(\rho_{12} - \rho_{21}), \\ \dot{\rho}_{22} &= -\gamma_2 \rho_{22} + \gamma_3 \rho_{33} - i\Omega_{12}(\rho_{12} - \rho_{21}) \\ &\quad + i\Omega_{23}(\rho_{23} - \rho_{32}), \\ \dot{\rho}_{33} &= -\gamma_3 \rho_{33} - i\Omega_{23}(\rho_{23} - \rho_{32}), \\ \dot{\rho}_{12} &= (i\Delta_{21} - \gamma_{12}/2)\rho_{12} - i\Omega_{12}(\rho_{22} - \rho_{11}) + i\Omega_{23}\rho_{13}, \\ \dot{\rho}_{13} &= (i\Delta_{31} - \gamma_{13}/2)\rho_{13} - i\Omega_{12}\rho_{23} + i\Omega_{23}\rho_{12}, \\ \dot{\rho}_{23} &= (i\Delta_{32} - \gamma_{23}/2)\rho_{23} - i\Omega_{23}(\rho_{33} - \rho_{22}) - i\Omega_{12}\rho_{13}\end{aligned}$$

together with $\rho_{ij} = \rho_{ji}^*$. Carrier conservation requires that $\sum_{i=1}^3 \rho_{ii} = 1$ and the Ω_{ij} are the Rabi frequencies (assumed real) of the coupling laser field and the $|i\rangle \leftrightarrow |j\rangle$ transition.

In contrast to many previous treatments, these equations allow for the simultaneous coupling between both (1–2 and 2–3) dipole-allowed transitions and the “coupling” laser. This is required in our case because the states are close to being equally spaced in energy and has important consequences as shown below. $\Delta_{21} = \hbar\omega_c - E_{12}$ and $\Delta_{32} = \hbar\omega_c - E_{23}$ are the single-photon detunings and $\Delta_{31} = \Delta_{21} + \Delta_{32}$ the two-photon detuning of the coupling laser frequency from the various electronic resonances.

The γ_i denote the damping of the population states $|i\rangle$, i.e. they are inversely proportional to the intersubband recombination times. The γ_{ij} ($i \neq j$) are the total coherence relaxation rates, given by $\gamma_{12} = (\gamma_2 + \gamma_{12}^{\text{dph}})$, $\gamma_{23} = (\gamma_2 + \gamma_3 + \gamma_{23}^{\text{dph}})$, $\gamma_{13} = (\gamma_3 + \gamma_{13}^{\text{dph}})$, where γ_{ij}^{dph} is the dephasing decay rate of the quantum coherence of the $|i\rangle \leftrightarrow |j\rangle$ transition. In contrast to many atomic schemes the γ_{ij}^{dph} , determined in QWs by electron–electron, interface roughness and phonon scattering processes, are the dominant

contributions to the γ_{ij} and the major obstacle to the observation of coherent effects such as EIT.

We solve these equations numerically in the steady-state limit, i.e. equivalent to assuming a continuous-wave coupling beam in the experiment. The resulting density matrix is then used with linear response theory to calculate the absorption spectrum as a function of ω_p using the quantum regression theorem [23]. Again we adapt the treatment of Ref. [23] to coherently include absorption processes between both of the dipole-allowed QW transitions.

The results of this analysis are also plotted in Fig. 2. In all cases we set $\hbar\Omega_{12} \approx \hbar\Omega_{23} \approx 5$ meV corresponding to the coupling laser intensity used, $\gamma_{12} = \gamma_{23} = \gamma_{13} = 5$ meV and $\gamma_2 \sim \gamma_3 = 1.3$ meV, equivalent to the intersubband relaxation time $\tau = 1$ ps we extract from the samples' saturation characteristics. Intersubband recombination times were measured using the absorption saturation method of Vodopyanov et al. [24].

With these parameters, when $\omega_c = E_{23}$ the theory predicts Autler–Townes splitting but significantly, no coherent EIT. Although not obvious from the figure, the theory curve has the form of two split Lorentzian lines, but the overall quantum coherence is not maintained sufficiently well to give the destructive interference at the line centre which would reduce the absorption below the split-Lorentzian lineshape. Due to spatio-temporal fluctuations in the beam intensities, however (which are assumed constant in the model), even the Autler–Townes splitting is too weak to be observed experimentally (Fig. 2b).

The strongest quantum interference effect is predicted by the theory when the coupling frequency is tuned to the “two-photon resonance”, $\omega_c = E_{13}/2$, i.e. the “phase-locked” regime. This can be understood in terms of a four-photon process (Fig. 5), where the absorption–emission path $1 \rightarrow 3 \rightarrow 2$ interferes destructively with the absorption path $1 \rightarrow 2$. At the same time the “coupling” field has Stark shifted the original “bare” $1 \rightarrow 2$ transition to the red and the $2 \rightarrow 3$ transition to the blue. This results in an overall red shift of the $1 \rightarrow 2$ transition to ~ 125 meV, and a corresponding transparency feature at this energy. The coherence of all the states also appears to be maintained, by the “phase-locked” two-photon coupling, more efficiently than the Autler–Townes case $\omega_c = E_{23}$.

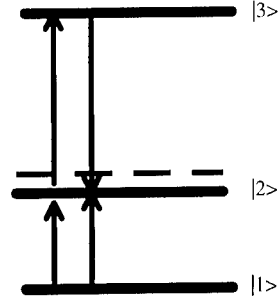


Fig. 5. Schematic of the quantum interference at “two photon resonance”. The dashed line represents the original “bare” energy of state 2, before being optically Stark shifted by the coupling laser.

In the model, progressively detuning away from the $\hbar\omega_c \sim E_{13}/2$ two-photon resonance, destroys the interference effect. Also, at this ω_c , reducing the coupling Rabi frequency by as little as 20% destroys the interference, in good agreement with the intensity dependent measurements shown in (Fig. 6). Both of these facts suggest a strong dependence on two-photon coupling in the interpretation of the results.

A more complete theoretical treatment of this effect would take into account the reality that there are a large number of electron oscillators in these samples. In contrast to the atomic case, these oscillators are strongly coupled to each other by scattering processes which modify the transition energies by “many-body” interactions [25,26] (i.e. Coulomb, exchange and depolarisation energies). Computing the effect of these in the presence of the strong coupling laser field is beyond the scope of this paper.

The dominant inhomogeneous broadening mechanism is conduction band non-parabolicity [27],¹ which contributes an inhomogeneous linewidth component

$$\Delta_{ij}^{\text{npb}} = \hbar^2 k_F^2 / 2M_{ij},$$

where

$$M_{ij} = [m_i^{*-1} - m_j^{*-1}]^{-1},$$

¹ Conduction band non-parabolicity was treated as in Sirtori et al. [27] using the materials parameters of Ref. [9]. Relative to the well bottom, bare energy levels (in-plane effective masses) were $E_1 = 46$ meV ($0.045m_0$); $E_2 = 176$ meV ($0.053m_0$); $E_3 = 338$ meV ($0.061m_0$).

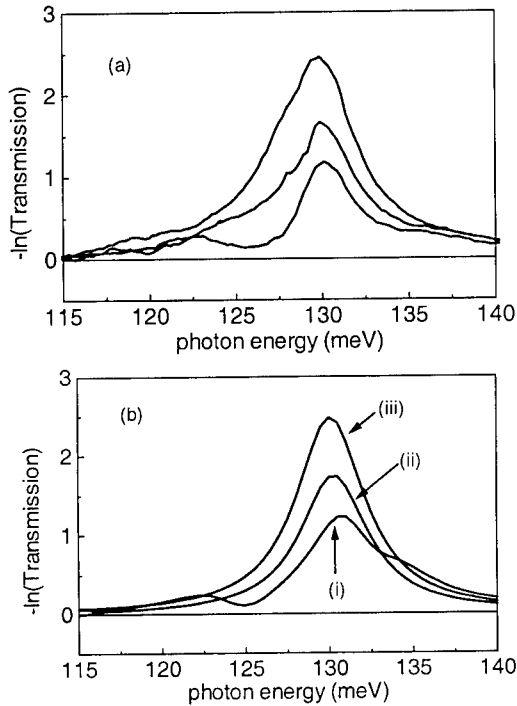


Fig. 6. Experimental (a) and theoretical (b) coupling intensity dependence of the EIT feature for “two-photon resonance” case $\omega_c = E_{13}/2$: (i) $\Omega_{\text{Rabi}} = 4.8$ meV, (ii) $\Omega_{\text{Rabi}} = 1.6$ meV, (iii) $\Omega_{\text{Rabi}} = 0.48$ meV.

amounting to ~ 4.9 meV in these samples. This is sufficiently small compared with the total transition linewidth that the “sole collective excitation” picture, as defined in Refs. [25,26] and assumed in our three-level treatment, should be valid under these measurement conditions.

This “sole collective excitation” picture was also confirmed experimentally, when attempts to observe “spectral holes” burnt into the absorption lineshape by selectively exciting a subset of the subband population, failed. In many cases the lineshape of the excited sample is slightly narrower than the theory predicts, suggesting some form of a co-operative effect within the coherent electron population. Although carrier redistribution within the subbands may alter the transition energies by up to the ~ 5 meV total “many-body” energy, this effect is too small to account for the ω_c resonance behaviour of the “phase-locked” coherence feature we observe.

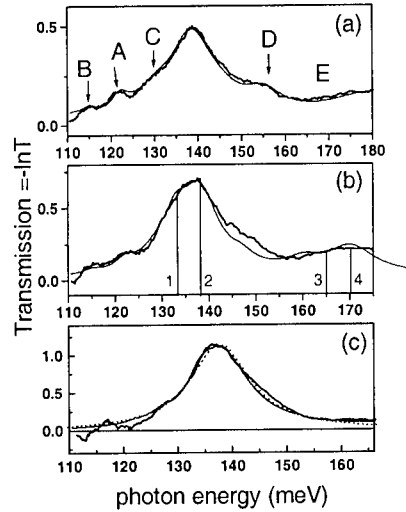


Fig. 7. Sample 1690A; weak probe absorption with a strong saturating pump resonant with the 1–2 transition (a) $100 I_{\text{sat}}$ (b) $10 I_{\text{sat}}$ (c) $1 I_{\text{sat}}$. Thick lines are experimental data and thin lines theoretical fits. All measurements were carried out at 30 K. The letters refer to features described in the text and Fig. 8.

4. Intersubband scattering dynamics measurements

The available pump intensities in the “coupling” beam were approximately 10 times the saturation intensity of the E_{12} transition. Tuning the “coupling” beam to E_{12} results in strong excitation of the 2D electron system and the redistribution of the carriers into high enough k_{11} states for non-parabolicity to invalidate the “the single collective excitation” picture. This allows the electron momentum distributions to be mapped out spectroscopically [27], yielding scattering rate information relevant to QC laser design.

Typical spectra (Fig. 7) show “phonon bumps” in the electron distributions at positions corresponding to the dominant phonon scattering processes in intersubband relaxation. Because $E_{12} \sim 4 \hbar \omega_{\text{LO}}$, modelling the dynamics reduces to 11 coupled rate equations in the initial and final state populations for the six photon transitions labelled in Fig. 8. The solutions yield the ratio of inter- to intra-subband scattering rates, $\tau_{\text{is}}/\tau_{12}$ and the ration of phonon emission to absorption events which in turn yields the non-equilibrium phonon density (Table 1).

The pump–probe experiment shows that for an excited state which is populated with an electron sheet

Table 1

Summary of scattering rate data extracted from rate-equation analysis of pump–probe experiments

Pump intensity/ I_{sat}	ISB pump rate R/ps	n_{p0h}	τ_{12}/ps	τ_{is} emission/ps	τ_{is} absorption/ps
100	0.3	1	0.45	0.05–0.3	0.1–0.6
10	0.1	1	0.45	0.05–0.3	0.1–0.6
1	0.02	0.5	0.6	0.06–0.2	0.2–1.2

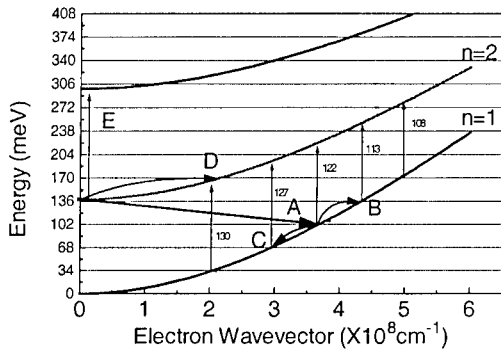


Fig. 8. Theoretical electron dispersion for sample 1690A and the phonon scattering events leading to the spectral features in Fig. 7. The arrows denote the photon transition energies (in meV) at $E = \hbar\omega_{\text{LO}}$ intervals along the subbands.

density $\sim 2 \times 10^{11} \text{ cm}^{-2}$, a non-equilibrium phonon distribution ($n_{\text{ph}} \sim 1$ at 30 K) controls the electron energy distribution [28] in the subbands. The intersubband phonon scattering rate is ~ 400 fs, and the intrasubband phonon scattering rate lies in the range 100–250 fs, and depends on the electron momentum. In this regime, dipole de-phasing rates are determined by intrasubband phonon scattering.

As a result, the $n = 1$ subband minimum can be significantly depleted as electrons are trapped at high lying energy states, leading to lasing without a global k -space population inversion [29] and reduced lasing thresholds for quantum cascade lasers.

5. Concluding remarks

In conclusion, we have observed a sharp interference feature associated with electromagnetically induced quantum interference in QWs, which is not related to saturation or spectral hole burning effects. We found that the induced transparency can be ob-

served when the coupling field is two-photon-resonant with the E_{13} subband transition, this behaviour being fully consistent with a density matrix treatment which simultaneously includes coupling between all states in a three-level system.

This and other intersubband scattering dynamics measurements were made under similar experimental regimes as occur, or as could be engineered to occur if desired, in QC lasers at threshold, and may have significant influence in their future design.

References

- [1] S.E. Harris, Phys. Today 50 (7) (1997) 36.
- [2] J.P. Marangos, J. Mod. Opt. 45 (1998) 471.
- [3] K.-J. Boller, A. Imamoglu, S.E. Harris, Phys. Rev. Lett. 66 (1990) 2593.
- [4] J.E. Field, K.H. Hahn, S.E. Harris, Phys. Rev. Lett. 67 (1991) 3062.
- [5] M.M. Kash et al., Phys. Rev. Lett. 82 (1999) 5229.
- [6] Y. Zhao et al., Phys. Rev. Lett. 79 (1997) 641.
- [7] B.S. Ham, P.R. Hemmer, M.S. Shahriar, Opt. Commun. 144 (1997) 227.
- [8] B.S. Ham, P.R. Hemmer, M.S. Shahriar, Phys. Rev. A 59 (1999) R2583.
- [9] K. Ichimura, K. Yamamoto, N. Gemma, Phys. Rev. A 58 (1998) 4116.
- [10] M. Jain et al., Phys. Rev. Lett. 77 (1996) 4326.
- [11] G. Almogly, A. Yariv, J. Nonlinear Opt. Phys. Mater. 4 (1995) 401.
- [12] G. Padmabandu et al., Phys. Rev. Lett. 76 (1996) 2053.
- [13] Y. Zhao, D. Huang, C. Wu, Opt. Lett. 19 (1994) 816.
- [14] S.M. Sadeghi, J.F. Young, J. Meyer, Phys. Rev. B 56 (R15) (1997) 557.
- [15] A. Imamoglu, R.J. Ram, Opt. Lett. 19 (1994) 1744.
- [16] H. Schmidt, A. Imamoglu, Opt. Commun. 131 (1996) 333.
- [17] J. Faist et al., Nature (London) 390 (1997) 589.
- [18] J. Faist et al., Appl. Phys. Lett. 71 (1997) 3477.
- [19] H. Schmidt, K.L. Campman, A.C. Gossard, A. Imamoglu, Appl. Phys. Lett. 70 (1997) 3455.
- [20] J. Faist et al., Appl. Phys. Lett. 63 (1993) 1354.
- [21] K.L. Vodopyanov, V. Chazapis, Opt. Commun. 136 (1997) 98.

- [22] K.L. Vodopyanov, V. Chazapis, C.C. Phillips, *Appl. Phys. Lett.* 69 (1996) 3405.
- [23] L.M. Narducci et al., *Phys. Rev. A* 42 (1990) 1630.
- [24] K.L. Vodopyanov et al., *Semicond. Sci. Technol.* 12 (1997) 708.
- [25] D.E. Nikonov, A. Imamoglu, L.V. Butov, H. Schmidt, *Phys. Rev. Lett.* 79 (1997) 4633.
- [26] D.E. Nikonov, A. Imamoglu, M.O. Scully, *Phys. Rev. B* 59 (1999) 12 212.
- [27] C. Sirtori, F. Capasso, J. Faist, *Phys. Rev. B* 50 (1994) 8663.
- [28] G.B. Serapiglia, Ph.D. Thesis, London University, 1999.
- [29] J. Faist, F. Capasso, C. Sirtori, D.L. Sivco, A.L. Hutchinson, M.S. Hybertsen, A.Y. Cho, *Phys. Rev. Lett.* 76 (1996) 411.

Fano profile in intersubband transitions in InAs quantum dots

Ph. Lelong^{a,*}, S.-W. Lee^a, K. Hirakawa^b, H. Sakaki^a

^a*Institute of Industrial Science, University of Tokyo, 7-22-1 Roppongi, Minato-ku, Tokyo 106, Japan*

^b*Japan Science and Technology Corporation, 1-4-25 Mejiro, Toshima-ku, Tokyo 171-0031, Japan*

Abstract

We have investigated the infrared photocurrent spectra due to bound-to-continuum intersubband transitions in self-assembled InAs/GaAs quantum dots. It is found that the observed photocurrent spectra exhibit a broad peak followed by a peculiar quenching of their intensity at photon energy around 370 meV. We theoretically demonstrate that such a strong modulation of the intersubband transition spectra is due to Fano resonance which results from the quantum mechanical interference within the continuum. The calculated intersubband transition spectrum is in excellent agreement with experiments. © 2000 Elsevier Science B.V. All rights reserved.

Keywords: InAs quantum dots; Fano resonance; Quantum interference

The advances in nano-fabrication technology have made it possible to grow self-assembled InAs quantum dots (QDs) in the Stranski–Krastanov mode [1]. The physics of QDs have been intensively studied in view of their possible applications to optoelectronic devices, such as memory devices, lasers, infrared photodetectors, etc. Recently, we have realized an infrared photodetector which utilizes a bound-to-continuum intersubband transition in InAs QDs and obtained a large responsivity in the mid-infrared range [2]. The electrons initially localized in an array of QDs are photoionized into a continuum and finally drained laterally by modulation-doped two-dimensional channels [2]. However, a detailed understanding of the intersubband transition process has not been established

yet. Fig. 1 shows the photocurrent spectra measured at various temperatures in a normal incidence geometry. A broad peak in a photon energy range of 100–300 meV is observed as well as a weak broadband photosensitivity above 400 meV. It should be noted in the spectra that there exists a peculiar quenching of the intensity around $\hbar\omega = 370$ meV for the whole temperature range studied, suggesting the intrinsic origin of the phenomenon.

In this work, we have investigated infrared photocurrent spectra by calculating the probability of bound-to-continuum intersubband transitions for one electron trapped in QDs. In quantum wells, it is well known that some states in the continuum above the potential barrier keep the memory of the potential profile, the so-called virtual states or resonances. We suppose a similar behavior takes place for the QDs. We define the resonances as the continuum states

* Corresponding author. Fax: +81-3-5452-5136.

E-mail address: lelong@quanta.rcast.u-tokyo.ac.jp (Ph. Lelong)

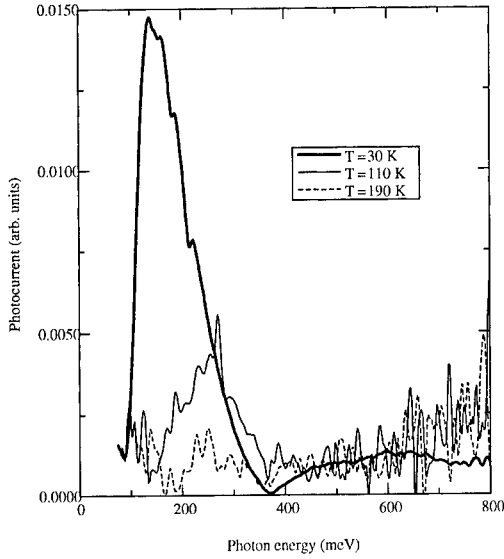


Fig. 1. Photocurrent spectra due to bound-to-continuum intersubband transitions in self-assembled InAs quantum dots measured at various temperatures.

characterized by a maximum of probability to find one electron in the QD. If the resonances are sufficiently well resolved, we can extract these states from the rest of the continuum (\equiv flat continuum) and approximate them as the “bound” states. Nevertheless, they continue to interact with the flat continuum. We theoretically demonstrate that such a strong modulation of intersubband transition spectra is caused by Fano resonances which results from the quantum mechanical interferences between the resonances and the flat continuum. This is a well-known effect initially studied by Fano [3,4] and has been observed in many atomic, molecular, and solid-state systems [5–11]. With a view to analyze the different aspects of this effect, we have made two theoretical approaches to the subject.

In the first one, we have performed a numerical calculation of the probability of intersubband transition as a function of the photon energy, by assuming a system in which one InAs QD is embedded in a large cylinder of GaAs. We have approximated the shape of the QDs by a small disk with a radius r and a height h . This choice offers two advantages: (1) the calculation of the continuum is simplified, while keeping the dot shape re-

alistic, and (2) the related symmetries of the QD allow to discuss the selection rules in the intersubband transitions with respect to the polarization of the light. The conduction band discontinuity at InAs/GaAs interface was assumed to be about $V_0 = 400$ meV and the electron effective mass in the QD to be $m = 0.067m_0$. The QD size is chosen to accommodate one bound state ε_a around 100 meV below the bottom of the GaAs conduction band in order to fit the experimental value. With ($r = 10$ nm, $h = 1.7$ nm) we obtain the first bound state at $\varepsilon_a = 102$ meV and a second one at $\varepsilon_b = 18$ meV. For the sake of simplicity, we have discretized the continuum states by enclosing the QD in a huge cylinder (radius $R = 800$ nm; height $H = 800$ nm). Let us denote the one-electron Hamiltonian by H_c and the potential of the QD by V_{dot}

$$H_c = -\frac{\hbar^2}{2m} \Delta + V(r) \quad \text{with}$$

$$V_{\text{dot}}(\rho, \phi, z) = -V_0 \theta(|z| - h/2) \theta(\rho - r). \quad (1)$$

Because of the cylindrical symmetry of the QD, the electron wave function can be written as

$$\Psi_{nkl}(\rho, \phi, z) = e^{in\phi} \phi_{nk}(\rho) \psi_l(z) \quad \text{with}$$

$$n \in \mathbb{Z}, (k, l) \in \mathbb{N} \quad (2)$$

and is characterized by three quantum numbers n, k, l . ε_{nkl} is the eigenenergy ($\varepsilon_a = \varepsilon_{0,1,1}$ and $|\Psi_{0,1,1}\rangle = |\chi\rangle$). At this point we are now able to show the existence of the resonances. In Fig. 2, we have plotted the probability Prob_{dot} to find one electron in the QD for the continuum states $\{|\Psi_{\pm 1,k,1}\rangle\}_k$ as a function of the photon energy. Several pronounced maxima of probability are observed at 150, 380, 700 meV, etc., defining a series of resonances ($|\varphi_1\rangle, |\varphi_2\rangle, |\varphi_3\rangle$, etc., respectively). In contrast with the sharp line width for the real bound state (about 10 μeV), those for the resonances are in the order of 100 meV.

The electron–photon interaction is expressed as

$$W_{c-\text{photon}} = -\frac{e}{m} (\mathbf{A} \cdot \mathbf{p} + \mathbf{p} \cdot \mathbf{A}), \quad (3)$$

where \mathbf{p} is the momentum of the electron and \mathbf{A} the vector potential of the light. For a typical photon energy range ($\hbar\omega = 100\text{--}1000$ meV), the vector potential \mathbf{A} is assumed to be constant and small (dipole

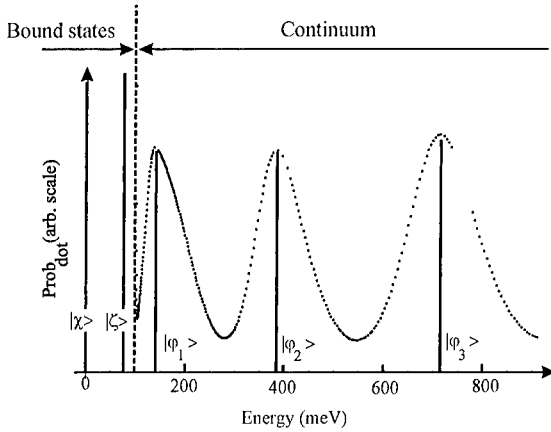


Fig. 2. The energy dependence of the probability of finding one electron in the dot.

approximation). It follows that the term of electron–photon interaction can be treated as a perturbation. By using Fermi’s golden rule, we have calculated the intersubband transition probability:

$$P_1 = \frac{2\pi}{\hbar} \sum_{n,k,l} |\langle \Psi_{n,k,l} | W_{e-photon} | \Psi_{0,1,1} \rangle|^2 \times \delta(\varepsilon_{nkl} - \varepsilon_a - \hbar\omega). \quad (4)$$

Some simplifications appear naturally if we rewrite the electron–photon interaction in a cylindrical coordinate ($p_{\pm} = p_x \pm ip_y$). After some calculation, we found that the probability of absorption P_1 has different selection rules on the quantum number n (angular momentum).

$$P_1 = \frac{2\pi}{\hbar} \sum_{n,k,l} \left[\frac{|A|^2}{4} (|\langle \Psi_{n,k,l} | p_+ | \Psi_{0,1,1} \rangle|^2 \delta_{n-1,0} + |\langle \Psi_{n,k,l} | p_- | \Psi_{0,1,1} \rangle|^2 \delta_{n+1,0}) + |A_z|^2 |\langle \Psi_{n,k,l} | p_z | \Psi_{0,1,1} \rangle|^2 \delta_{n,0} \right] \times \delta(\varepsilon_{nkl} - \varepsilon_a - \hbar\omega). \quad (5)$$

For the intersubband transition process from the ground state in the QD, the quantum number n can take only the following values $n = 0, \pm 1$. For the normal incidence geometry, which we are interested in, the polarization of light is in-plane (xy -direction) and only $n = \pm 1$ is relevant. A typical profile of P_1 for in-plane polarization is plotted in Fig. 3. As seen in

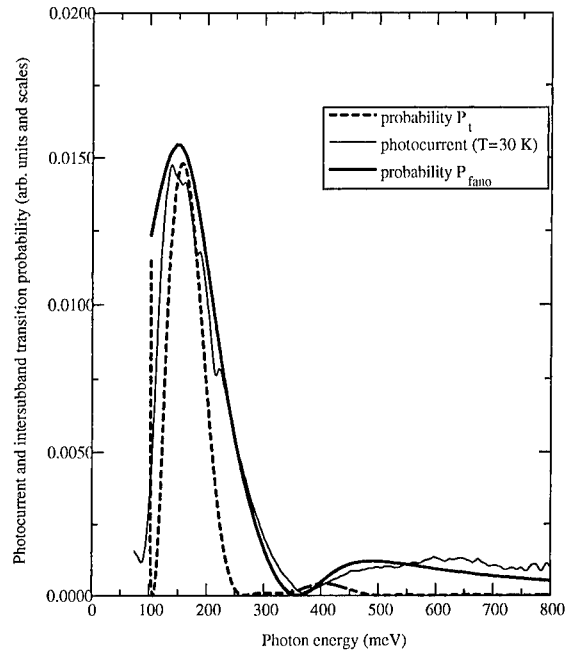


Fig. 3. Photocurrent spectrum measured at 30 K (thin solid line), intersubband transition probability calculated numerically (dashed line) and analytically by Eq. (16) (thick solid line).

the figure, one large peak of absorption is observed, which corresponds to the intersubband transition to the first resonance. Furthermore, the quenching of the transition probability around 370 meV is also well reproduced.

To obtain more insight into the origin of the quenching in the intersubband transition process, we have developed an analytical approach based on the initial model developed by Fano [3]. The resonances are extracted from the continuum and assimilated as “bound” states. We, then, introduce a coupling term between the bound states and the continuum V_{memory} .

Within this framework, the one-electron Hamiltonian H_c can be written as

$$H_c = H_0 + V_{\text{memory}} \quad \text{with } \varepsilon = \langle \Psi | H_c | \Psi \rangle. \quad (6)$$

The Hamiltonian H_0 describes the system in which the continuum states $|k\rangle$ are decoupled from the bound state $|\chi\rangle$ (energy ε_a) and resonances $|\varphi_p\rangle$ (energy ε_p). We also assume that the continuum states $|k\rangle$ are equidistant in energy and separated by an arbitrary

small energy step δ .

$$\langle \chi | H_0 | \chi \rangle = \varepsilon_a \quad \text{and} \quad \langle \varphi_p | H_0 | \varphi_p \rangle = \varepsilon_p,$$

$$p = 1, 2, 3, \dots, \quad (7)$$

$$\langle k | H_0 | k \rangle = k\delta, \quad k = 0, \pm 1, \pm 2, \dots \quad (8)$$

The resonances are assumed to be coupled with the flat continuum by constant matrix elements V due to the pseudo-interaction V_{memory} ,

$$0 = \langle k | V_{\text{memory}} | k \rangle = \langle \varphi_p | V_{\text{memory}} | \varphi_p \rangle, \quad (9)$$

$$V = \langle k | V_{\text{memory}} | \varphi_p \rangle = \langle \varphi_p | V_{\text{memory}} | k \rangle. \quad (10)$$

$$P_{\text{Fano}}(\tilde{\varepsilon}) = \frac{|q_1(\tilde{\varepsilon} - \tilde{\varepsilon}_2) + q_2(\tilde{\varepsilon} - \tilde{\varepsilon}_1) + (\tilde{\varepsilon} - \tilde{\varepsilon}_2)(\tilde{\varepsilon} - \tilde{\varepsilon}_1)|^2}{(2\tilde{\varepsilon} - \tilde{\varepsilon}_2 - \tilde{\varepsilon}_1)^2 + \zeta(\tilde{\varepsilon} - \tilde{\varepsilon}_1)^2 + \zeta(\tilde{\varepsilon} - \tilde{\varepsilon}_2)^2 + (\tilde{\varepsilon} - \tilde{\varepsilon}_2)^2(\tilde{\varepsilon} - \tilde{\varepsilon}_1)^2}. \quad (16)$$

By using the model by Fano, it is possible to calculate the eigenstates and eigenvalues $\{|\Psi\rangle, \varepsilon\}$ of the coupled system. Finally, the bound state $|\chi\rangle$ interacts with both the resonances and the flat continuum by electron–photon interaction $W_{\text{e-photon}}$. The matrix elements for the intersubband transitions from the bound state to the p th resonances and to the flat continuum are denoted by W_p and W , respectively.

$$W_p = \langle \varphi_p | W_{\text{e-photon}} | \chi \rangle = \langle \chi | W_{\text{e-photon}} | \varphi_p \rangle, \quad (11)$$

$$W = \langle k | W_{\text{e-photon}} | \chi \rangle = \langle \chi | W_{\text{e-photon}} | k \rangle. \quad (12)$$

Within this framework we can calculate the intersubband transition probability P_{Fano} from the bound state $|\chi\rangle$ to the continuum $\{|\Psi\rangle, \varepsilon\}$.

$$P_{\text{Fano}} = \frac{|\langle \Psi | W_{\text{e-photon}} | \chi \rangle|^2}{W^2}. \quad (13)$$

In the calculation we took the limit of the “real” continuum. For this procedure we assumed by using Fermi’s golden rule that the probability of transition Γ in a unit time between the resonances and the continuum remains constant in the limit $\delta \rightarrow 0$,

$$\Gamma = \frac{2\pi}{\hbar} \frac{V^2}{\delta} \underset{\delta \rightarrow 0}{=} \text{constant}. \quad (14)$$

We use $\hbar\Gamma$ to normalize the energies and to define the following dimensionless variables:

$$q_p = \frac{\delta}{\pi V} \frac{W_p}{W}, \quad \tilde{\varepsilon} = \frac{2\varepsilon}{\hbar\Gamma}, \quad \tilde{\varepsilon}_p = \frac{2\varepsilon_p}{\hbar\Gamma}, \quad \zeta = \frac{4V^2}{\hbar^2\Gamma^2}, \quad (15)$$

where q_p is the ratio between the matrix element for exciting an electron to the p th resonance and the flat continuum. For a large q , the electron is favorably promoted to the resonances. ζ is related with the line width of the transition probability ($\propto \sqrt{1 + \zeta}$).

From Fig. 2, we observe that the quenching of the photocurrent takes place when the photon excites an electron to a state located between the first two resonances. If we limit our study around this energy range, the photocurrent spectrum will be proportional to the intersubband transition probability, P_{Fano} , which takes into account only the lowest two resonances:

By a correct choice of the dimensionless parameters (the energies and the line width of the resonances were determined from the diagonalization of H_0 and we assumed 10% of size fluctuation of the QDs. Only the ratio q_1/q_2 was used as a fitting parameter), we have calculated the intersubband transition probability. As seen in Fig. 3, the agreement between theory and experiment is excellent. This fact clearly indicates that the quenching of the photocurrent spectra observed at 370 meV is due to Fano resonance.

To conclude, we have investigated the infrared photocurrent spectra due to bound-to-continuum intersubband transitions in self-assembled InAs/GaAs quantum dots. It is found that the observed photocurrent spectra exhibit a broad peak followed by a peculiar quenching of their intensity at photon energy around 370 meV. We have theoretically demonstrated that such a strong modulation of the intersubband transition spectra is due to Fano resonance which results from the quantum mechanical interference within the continuum. The calculated intersubband transition spectrum is in excellent agreement with experiments. We emphasize that the Fano effect is a limiting factor for the sensitivity of QD infrared photodetector. A better understanding of this effect is a sine qua none condition to improve the efficiency of photodetection.

Acknowledgements

The authors thank Prof. M. Helm for many helpful discussions. This work was supported partly by the

Grant-in-Aid from the Ministry of Education, Science, Sports and Culture, Japan and also by CREST of Japan Science and Technology Corporation. One of us (Ph. Lelong.) acknowledges the financial support from the Marubun Research Promotion Foundation.

References

- [1] J.-Y. Marzin, J.M. Gerard, A. Izraël, D. Barrier, G. Bastard, *Phys. Rev. Lett.* 73 (1994) 716.
- [2] S.-W. Lee, K. Hirakawa, Y. Shimada, *Appl. Phys. Lett.* 75 (1999) 1428.
- [3] U. Fano, *Nuovo Cimento* 12 (1935) 156.
- [4] U. Fano, *Phys. Rev.* 124 (1961) 1866.
- [5] S. Glutsch, D.S. Chemla, F. Bechstedt, *Phys. Rev. B* 51 (1995) 16885.
- [6] J. Faist, C. Sirtori, F. Capasso, S.-N.G. Chu, L.N. Pfeiffer, K.W. West, *Optics Lett.* 21 (1996) 985.
- [7] S. Glutsch, U. Siegner, M.-A. Mycek, D.S. Chemla, *Phys. Rev. B* 50 (1994) 17009.
- [8] S. Bar-Ad, P. Kner, M.V. Marquezini, S. Mukamel, D.S. Chemla, *Phys. Rev. Lett.* 78 (1997) 1363.
- [9] C.P. Holfeld, F. Löser, M. Sudzius, K. Leo, D.M. Whittaker, K. Köhler, *Phys. Rev. Lett.* 81 (1998) 874.
- [10] D.Y. Oberli, G. Böhm, G. Weiman, J.A. Brum, *Phys. Rev. B* 49 (1994) 5757.
- [11] U. Siegner, M.-A. Mycek, S. Glutsch, D.S. Chemla, *Phys. Rev. B* 51 (1995) 4953.



ELSEVIER

Physica E 7 (2000) 179–182

PHYSICA E

www.elsevier.nl/locate/physa

Inhomogeneous broadening of intersubband absorption bands of quantum well structures investigated by hole burning

S. Schmidt, J. Kaiser, A. Seilmeier*

Physikalisches Institut, Universität Bayreuth, D-95440 Bayreuth, Germany

Abstract

Transient spectral holes are observed in the intersubband absorption band of a n-modulation-doped GaAs/AlGaAs quantum well structure with 5.9 nm wide wells. At 300 K, the widths of the holes amount to approximately 50% of the width of the roughly 7 meV wide intersubband absorption profile. Increasing inhomogeneous broadening and a decreasing homogeneous width are found with decreasing temperature. Well width fluctuations are discussed as dominant mechanism of the inhomogeneous broadening. © 2000 Elsevier Science B.V. All rights reserved.

Keywords: Hole burning; Inhomogeneous broadening; Ultrafast absorption changes; Picosecond spectroscopy

GaAs/AlGaAs quantum well structures often exhibit intersubband absorption bands with Lorentzian line shape. From this fact, a homogeneous broadening of the transition has been deduced in many cases (e.g. [1]). Particularly in structures with very narrow quantum wells, however, broad intersubband transitions of several meV width are observed and simultaneously lifetimes of a few picoseconds are measured [2]. A comparison of the spectral widths with the lifetimes indicates an inhomogeneous broadening of the intersubband transition.

Generally the frequency positions of the transition lines can be calculated easily, but the origin of the large spectral widths and of the observed shapes are

not understood very well. Interface roughness, and the dependence of the effective mass on the energy have been discussed as relevant broadening mechanisms [3,4]. In this paper spectral hole burning is used to investigate the inhomogeneous broadening. It is shown, that an increased spectral width of the intersubband transition at lower temperatures is due to an increased inhomogeneity. The experiments are performed on a picosecond time scale to meet the requirements of the very short lifetimes of the excited subbands.

The transient population holes are detected in the following way: A first infrared pulse of 2 ps duration and a spectral width of 1.2 meV excites electrons from the lowest to the first excited subband. The subsequent change of the intersubband absorption is measured time and frequency resolved by a second independently tunable infrared picosecond pulse of considerably lower energy. The data are taken on an

* Corresponding author. Tel.: +49-921-55-3162; fax: +49-921-55-3172.

E-mail address: alois.seilmeier@uni-bayreuth.de (A. Seilmeier)

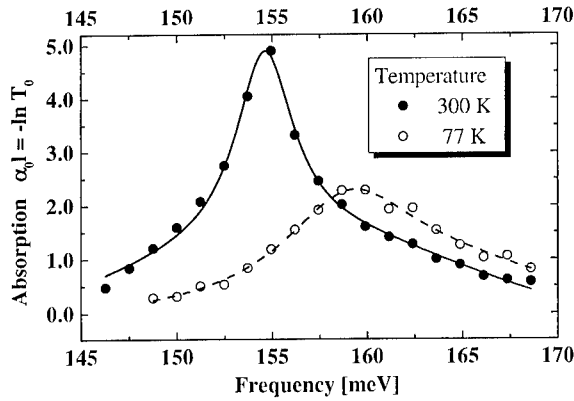


Fig. 1. Intersubband absorption spectra taken at 300 and 77 K. They are measured with picosecond IR pulses of 1.2 meV width. They are identical to spectra taken with a FTIR spectrometer.

n-modulation-doped multiple GaAs/Al_{0.35}Ga_{0.65}As quantum well structure with 5.9 nm wide GaAs quantum wells embedded in between 36 nm thick Al_{0.35}Ga_{0.65}As layers. The central 8 nm of the barriers are doped by Si with a concentration of $3 \times 10^{11} \text{ cm}^{-2}$. At 300 K, the sample shows a broad absorption band of 7 meV width at $h\nu = 154 \text{ meV}$ which is shown in Fig. 1 as solid line. Such broad absorption lines are typical for modulation-doped quantum wells of thicknesses in the order of 6 nm. It is quite interesting to see that the spectral shape is close to a Lorentzian shape. Despite of this fact, we are able to observe spectral holes in the absorption line.

At 77 K, the center frequency shifts to 160 meV, the absorption coefficient decreases and the width increases to 11 meV. The oscillator strength, however, remains the same. Such an unusual temperature dependence is observed in many narrow, n-modulation doped samples with low doping concentration and is not completely understood so far.

At delay time $t_D = 0 \text{ ps}$ population holes in the intersubband absorption band are observed ($T = 300 \text{ K}$). At a relatively low excitation intensity of 400 kW/cm^2 , which is close to the saturation intensity, bleaching of the absorption is found at frequencies close to the pump frequency. In Fig. 2a the change in absorption $\Delta\alpha l = \alpha l - \alpha_0 l$ measured by the weak probe pulse is plotted which is directly proportional to the spectral holes. α and α_0 are the absorption coefficients with and without excitation,

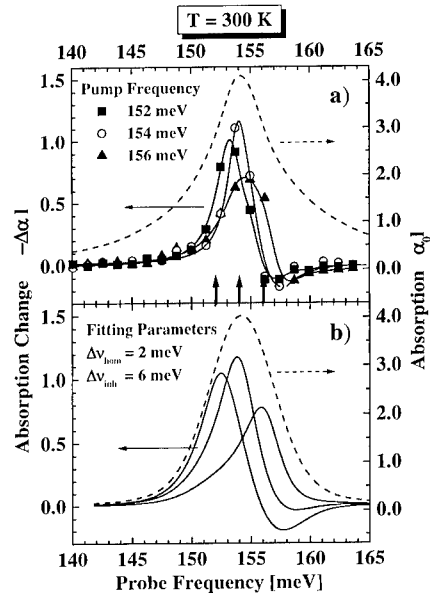


Fig. 2. Hole burning at $T = 300 \text{ K}$. Solid lines: spectra of transient holes after excitation at the three different pump frequencies marked by arrows. Dashed lines: intersubband absorption. The intensity of the excitation pulses amounts to 400 kW/cm^2 . (a) Experimental data; (b) results of numerical simulations according to the model presented in the text with $S_0 = 0.7$ and $\Delta = 0.4 \text{ meV}$.

respectively. The holes are located close to the pump frequencies and exhibit widths of $\sim 4 \text{ meV}$ corresponding to a homogeneous linewidth of roughly 2 meV. Contributions from coherent $\chi^{(3)}$ -processes to the $\Delta\alpha$ -signal are negligible here. They are expected to appear at higher laser intensities [5]. $\chi^{(3)}$ signals generally exhibit narrower line widths and are located exactly at ν_p .

At the blue wings of the hole spectra an increase in absorption is observed. It can be explained by a small blue shift of the whole absorption band due to intersubband excitation. This shift is produced by a transient transfer of electrons in the excited subband to the barrier. Such a transfer is observed mainly in strongly modulation-doped structures [6].

The conditions in our investigations are such that the homogeneous width is comparable to the inhomogeneous broadening and the pump intensity is in the order of the saturation intensity. In this case, a detailed analysis of the experimental data requires a numerical solution of the equations for absorption saturation

in inhomogeneously broadened systems [7,8]. We use the standard steady-state model for a two-level system. The intersubband absorption $\alpha_0(\nu)$ is assumed to be a convolution of a (Gaussian) distribution function G of width Γ_i and a Lorentzian line-shape function L of width Γ_h

$$\alpha_0(\nu) = \alpha_0 \int G(\nu_0 - \nu_c, \Gamma_i) L(\nu - \nu_0, \Gamma_h) d\nu_0.$$

The absorption $\alpha(\nu, \nu_{p0})$ after excitation by an intense pump pulse at frequency ν_{p0} is given by

$$\begin{aligned} \alpha(\nu, \nu_{p0}) = & \alpha_0 \int (G(\nu_0 - \nu_c, \Gamma_i) L(\nu - \nu_0 - \Delta, \Gamma_h) \\ & \times \left(1 - \int [S(\nu_p)/(1 + S(\nu_p))] \right. \\ & \left. \times L(\nu_0 - \nu_p, \Gamma_h^S) d\nu_p \right) d\nu_0, \end{aligned}$$

where $S(\nu_p) = I_p(\nu_p)/I_S$ is the saturation parameter. $I_p(\nu_p)$ is the intensity distribution ($\Delta\nu_p = 1.2$ meV) of the pump pulse at frequency ν_{p0} and I_S is the saturation intensity. $\Gamma_h^S = \Gamma_h(1 + S(\nu_p))$ is the homogeneous line width broadened by saturation. Δ represents the small blue shift of the whole absorption spectrum $\alpha(\nu, \nu_{p0})$ due to intersubband excitation.

The observed hole spectra and the absorption spectra are compared with model calculations shown in Fig. 2b. A homogeneous line width of 2 meV, an inhomogeneous broadening of 6 meV, and a blue shift $\Delta = 0.4$ meV is used. The saturation parameter was chosen to be $S_0 = \int S(\nu_p) d\nu_p = 0.7$. This value nicely compares with a saturation intensity of 400 kW/cm² which was determined in a separate bleaching experiment.

Fig. 3a shows experimental data for $t_D = 0$ ps taken at $T = 77$ K. The lower absorption cross section requires a higher pump intensity of 1.5 MW/cm² to get reliable data. Hole spectra of a width of 3–4 meV are observed which are slightly blue shifted with respect to the pump frequency. Fig. 3b shows the result of the model calculations. The best fit is obtained with $\Gamma_h = 1.5$ meV, $\Gamma_i = 10$ meV, and $S_0 = 1.0$. A parameter $\Delta = 0.4$ meV reproduces the blue shift of the hole spectra and the absorption increase in the blue wings. It is surprising to see an increase of the inhomogeneous broadening and a decrease of the homogeneous width at lower temperatures.

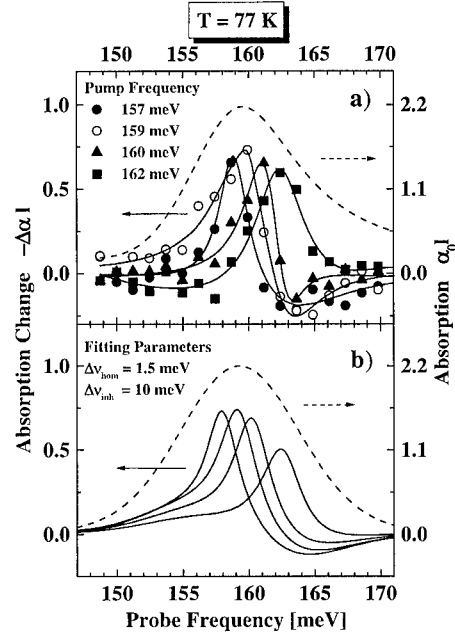


Fig. 3. Hole burning at $T = 77$ K. Spectra of transient holes (solid lines) after excitation with pump pulses of an intensity of 1.5 MW/cm² at four different frequencies. The dashed line represents the intersubband absorption. (a) Experimental data; (b) results of numerical simulations with $S_0 = 1$ and a blue shift of $\Delta = 0.4$ meV using the model presented in the text.

The homogeneous linewidth is larger than the spectral width calculated from the observed sub-band lifetime of 2–3 ps. Obviously, it is determined by dephasing processes with a T_2 time of approximately 0.7 ps; a value which is in rough agreement with the results of Ref. [9]. Possible dephasing mechanisms are electron–electron and intraband–LO phonon scattering. Electron–electron scattering is believed to be the main mechanism since dephasing times of several hundred femtoseconds are expected for our sample parameters. The decrease of the homogeneous width Γ_h at lower temperatures can be explained by an increased Pauli blocking of electron states due to the narrowing of the electron distribution. In this way, less phase space is available for electron–electron scattering which increases the T_2 time. The origin of the inhomogeneous broadening is believed to be mainly due to the interface roughness of the quantum wells. Detailed band structure calculations show that thickness fluctuations of only

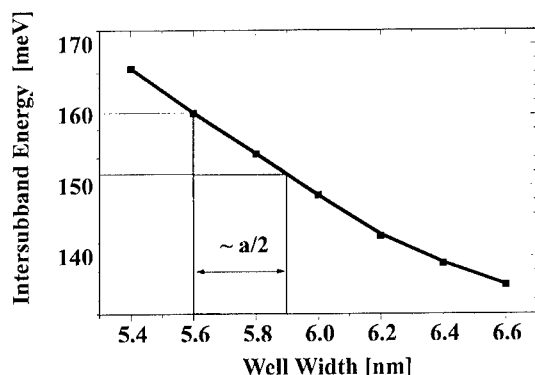


Fig. 4. Intersubband transition energy as a function of the well width self-consistently calculated for n-modulation doped GaAs/Al_{0.35}Ga_{0.65}As quantum wells (barrier width 36 nm, doping concentration $3 \times 10^{11} \text{ cm}^{-2}$). The marked region represents a well width fluctuation of 0.3 nm which leads to a broadening of the transition energy of $\sim 8 \text{ meV}$.

one atomic layer (approximately 0.3 nm) yield an intersubband broadening of $\sim 8 \text{ meV}$ at 300 K (see Fig. 4) which nicely compares with the observed width of the intersubband transition. The rising inhomogeneous broadening with decreasing temperature is not understood finally. A preliminary explanation is as follows: The well width fluctuations lead to a distribution of islands in the quantum wells which exhibits local energy minima in the lowest subband [10]. Lateral transitions between these local minima may require thermal energy which is not available at low temperature. The inhomogeneous broadening at low temperatures represents the distribution of these minima. At higher temperatures, however, transitions between local minima become possible and the electrons accumulate in the islands of the lowest energy resulting in a narrower line width.

Quite interesting is the dynamics of the transient holes which will be discussed in details elsewhere. Increasing the delay time from $t_D = -1$ to 1 ps a growth of the $\Delta\alpha$ amplitude and of the spectral width and a shift of the holes towards the center of the absorption band are observed. These changes are believed to be mainly due to an increasing saturation.

In summary, the presented data clearly show the inhomogeneous broadening of GaAs/AlGaAs intersubband transitions. Work is in progress to get more information on the detailed origin of the inhomogeneous broadening.

References

- [1] J. Faist, F. Capasso, C. Sirtori, D.L. Sivco, A.L. Hutchinson, S.N.G. Chu, A.Y. Cho, *Appl. Phys. Lett.* 63 (1993) 1354.
- [2] A. Seilmeier, U. Plödereder, J. Baier, G. Weimann, in: H. C. Liu, B.F. Levine, J.Y. Anderson (Eds.), *Quantum Well Intersubband Transition Physics and Devices*, NATO ASI Series E 270, Kluwer, Dordrecht, 1994, p. 421.
- [3] K.L. Campman, H. Schmidt, A. Imamoglu, A.C. Gossard, *Appl. Phys. Lett.* 69 (1996) 2554.
- [4] G. Beadie, W.S. Rabinovitch, D.S. Katzer, M. Goldenberg, *Phys. Rev. B* 55 (1997) 9731.
- [5] J. Kaiser, A. Seilmeier, in: S.S. Li, Y.-K. Su (Eds.), *Intersubband Transitions in Quantum Wells: Physics and Devices*, Kluwer, Boston, 1998, p. 147.
- [6] J. Kaiser, A. Seilmeier, *Phys. Stat. Sol. B* 204 (1997) 205.
- [7] W. Demtröder, *Laser Spectroscopy*, Springer, Berlin, 1988.
- [8] H. Graener, G. Seifert, *Chem. Phys. Lett.* 68 (1991) 185.
- [9] R.A. Kaindl, S. Lutgen, M. Woerner, T. Elsaesser, B. Nottelmann, V.M. Axt, T. Kuhn, A. Hase, H. Künzel, *Phys. Rev. Lett.* 80 (1998) 3575.
- [10] R. Gottinger, A. Gold, G. Abstreiter, G. Weimann, W. Schlapp, *Europhys. Lett.* 6 (1988) 183.



ELSEVIER

Physica E 7 (2000) 183–186

PHYSICA E

www.elsevier.nl/locate/physa

Absorption saturation of near-infrared intersubband transition in lattice-matched InGaAs/AlAsSb quantum wells [☆]

A. Neogi^{a,b,*}, H. Yoshida^a, T. Mozume^a, N. Georgiev^{a,b}, T. Akiyama^a, O. Wada^a

^aThe FESTA Laboratories, The Femtosecond Technology Research Association, 5-5 Tokodai,
Tsukuba Ibaraki 300-2635, Japan

^bNew Energy and Industrial Research Development Organization, 1-1-3 Higashi Ikebukuro, Tokyo 170, Japan

Abstract

We report the near-infrared intersubband absorption characteristics in $\text{In}_{0.53}\text{Ga}_{0.47}\text{As}/\text{AlAs}_{0.56}\text{Sb}_{0.44}$ heterostructures lattice matched to InP substrate. The intersubband transition energy increases on reducing the quantum-well width and tends to saturate at around 0.65 eV on further reducing the InGaAs layer thickness due to the influence of the interface fluctuations. We present the first report on intersubband absorption saturation in InGaAs/AlAsSb QWs using a femtosecond light source (~ 200 fs) tuned resonantly to the intersubband transition energy (0.52 eV). We observe a clear absorption saturation behavior of the intersubband transitions. At higher excitation power, a strong absorption due to interband two-photon transitions occurs. The interband two-photon transitions are induced by the intersubband transitions, as the band gap of the InGaAs well layers is resonant to the two-photon transition energy of the intersubband separation of this unique high-conduction band-offset InGaAs/AlAsSb quantum-well system. © 2000 Elsevier Science B.V. All rights reserved.

Keywords: Absorption saturation; Near infrared; InGaAs/AlAsSb quantum well

1. Introduction

Optoelectronic devices based on intersubband transitions (ISB) in the optical communication regime have been receiving increased attention due to its potential in the development of ultrafast switches or modulators [1–3] and flexibility to span a large

wavelength range in a detector array [4]. Intersubband optical transitions for the communication wavelength regime require materials with a large conduction band offset at the heterojunction. Efforts to achieve near-infrared intersubband have been aimed using strained InGaAs/AlAs or more recently AlGaInN/GaN quantum-well structures [2]. However, the large lattice mismatch between the well and the barrier or the substrate in strained-layer systems restricts the total number of well that can be grown, limiting the effective intersubband absorption within the active medium [5,6]. The near-infrared (~ 0.8 eV) intersubband transitions in InGaAs/AlAs quantum

[☆] This work was supported by the New Energy and Industrial Technology Development Organization (NEDO) in the framework of Femtosecond Technology Project.

* Corresponding author. Tel.: +81-298-47-5181; fax: +81-298-47-4417.

E-mail address: arup@festa.or.jp (A. Neogi)

well are also restricted either by the In segregation or carrier leakage [5], whereas in AlGaInN/GaN quantum well the shortest intersubband transition energy reported is 0.42 eV due to the growth of high Al-content layers [2].

InGaAs/AlAsSb quantum wells lattice matched to InP have been found to be ideally suited for near-infrared intersubband optoelectronic devices due to its large conduction band offset [7], a larger $\chi^{(3)}$ [8] and sub-picosecond optical response [9,10]. Despite the potentialities of this material system there are very few reports of its optical properties due to the difficulties involved in growing AlAsSb material that includes two group-V elements with a large miscibility gap [11]. A large intersubband absorption coefficient has been predicted in the communication wavelength regime but it is yet to be actually realized [9]. In this paper, we investigate the interband and intersubband optical properties of $\text{In}_{0.53}\text{Ga}_{0.47}\text{As}/\text{AlAs}_{0.56}\text{Sb}_{0.44}$ quantum wells for its possible use in near-infrared optoelectronic devices. We investigate the well width dependence of the interband characteristics of the material by photoluminescence (PL) spectroscopy and the intersubband transitions using Fourier Transform transmission spectroscopy. We report a large ISB absorption observed in the near-infrared regime from a lattice-matched system. We discuss the probable growth conditions that affect the intersubband transition in this material system. We also present the first report on the influence of the excitation power dependence of the transmission in the presence of the intersubband transition in the InGaAs/AlAsSb material system.

2. Experiment

InGaAs/AlAsSb quantum wells (QWs) were grown on (0 0 1)-oriented semi-insulating InP substrates by MBE using Ga, In and Al as type III species and Sb₄ and As₄ as the group V species without cracking. The details of the growth has been reported elsewhere [12]. The lattice mismatch $\Delta a/a$ of the InGaAs and AlAsSb measured using a high-resolution four-crystal X-ray diffractometer was found to be less than $\pm 3 \times 10^{-3}$. The InGaAs well layers was varied between 15 and 40 Å and the width of the AlAsSb barrier layers was optimized to 88 Å.

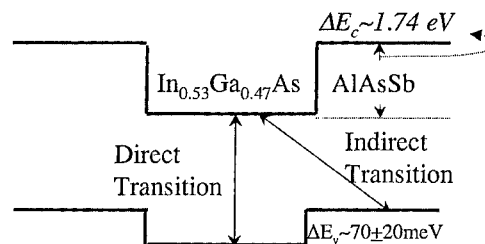


Fig. 1. Band profile of type-II InGaAs/AlAsSb quantum well.

The PL measurements were carried out at 77 K using an argon-ion laser with an emission wavelength at 514.5 nm. The luminescence was dispersed in a 0.64 m monochromator and detected by a cooled Ge detector using conventional lock-in detection.

For detecting the intersubband transitions, near-infrared polarization resolved transmission spectra were measured at room temperature with a BRUKER IFS 66 v/s FTIR using a near-infrared white light source and cooled InSb detector. The samples of 4–5 mm length were lapped to a thickness of 200 μm and the two end facets were polished at 45° to enable normal incident light to pass through a multiple-reflection guided geometry yielding enhanced ISB absorption in the QW.

The power dependence study of the intersubband absorption was performed for a 200 period QW with a well width of 30 Å doped to $1 \times 10^{19} \text{ cm}^{-3}$. An excitation wavelength of 2.4 μm was generated using an optical parametric amplifier (OPA) pumped by a regenerated 800 nm light pulse from a Ti:Sapphire laser. Two hundred femto seconds signal light pulses from the OPA were generated with a repetition rate of 1 kHz with a 100 μm spot and were resonantly tuned to the intersubband energy separation of the well.

3. Results and discussion

A schematic band diagram of the InGaAs/AlAsSb heterostructure is given in Fig. 1. The valence band maximum of the AlAsSb barrier is located above the valence band maximum of the InGaAs, whereas the conduction band minimum resides within the InGaAs layers. This leads to a spatially indirect optical transition for the lowest interband energy levels with a spatial separation of electrons and holes (type II

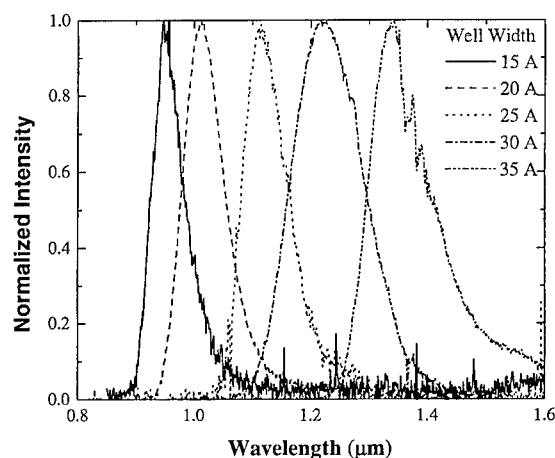


Fig. 2. Well-width dependence of the low-temperature PL spectrum of InGaAs/AlAsSb quantum wells doped to $1 \times 10^{19} \text{ cm}^{-3}$, measured with an excitation power of 2 mW.

transitions). A direct transition (type I) within the InGaAs layer between the confined electron and the quasi-bound state is also feasible [13]. However, in narrow quantum wells, the interband transitions are found to be dominated by a type II transition [13].

Fig. 2 shows the photoluminescence spectra for QWs with varying well width (L_w) with the PL intensity normalized to their respective peak intensities. The excitation of the laser was 2 mW with all the QWs being uniformly doped to 10^{19} cm^{-3} . It is observed that the PL peak position shows an expected blue-shift with the reduction of the quantum well width associated with the increase in the band gap of the InGaAs layers. The PL spectra are relatively wider (~ 80 – 100 meV) compared to conventional AlGaAs/GaAs QWs not only because of the indirect transition of the type II structure but also likely due to the influence of the interface steps associated with the InGaAs/AlAsSb heterojunction. The spectral width of the 30 Å well is relatively wider due to the relatively larger number of well (~ 200 periods) compared to the other samples. This is consistent with the large number of interfaces involved.

Fig. 3 depicts the well-width dependence of the intersubband absorption spectrum where the absorption is estimated from the logarithmic ratio of the TM to the TE light. The QWs are uniformly doped to 10^{19} cm^{-3} with 88 periods. It is observed that

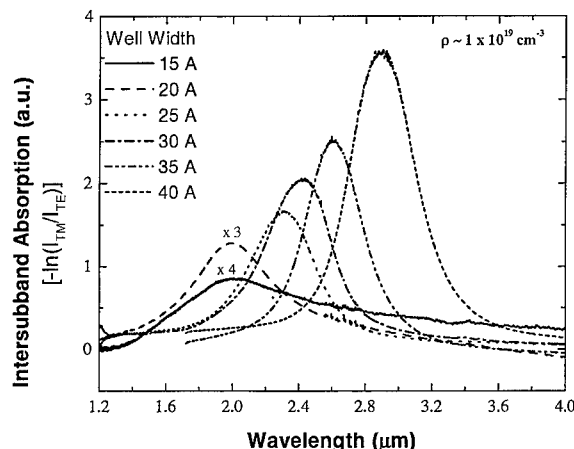


Fig. 3. Well-width dependence of room-temperature intersubband absorption of InGaAs/AlAsSb quantum wells.

the intersubband transition wavelength reduces with the well width and tends to saturate around 1.9 – $2.0 \mu\text{m}$ for well width narrower than 2 nm . The shortest transition wavelength achieved with normal growth was $1.95 \mu\text{m}$ for a 1.5 nm well, and the ISB absorption is considerably higher compared to strained layer QWs [5, 6]. It corresponds to an absorption coefficient of about 5000 cm^{-1} at $2.4 \mu\text{m}$. The observed peak-ISB transition wavelength is red shifted compared to the theoretical estimation based on a simple envelope wave-function approximation. This deviation increases for narrower well as the interface gradient of 2–3 monolayers becomes comparable to the intended well thickness of 5–6 monolayers. The interface quality and the actual well width of the narrow QWs are therefore a suspect. It has also been reported that AlAsSb/InGaAs hetero-interface forms a terrace-like stepped structure [14]. This would result in an increase of the ground-subband potential from the bottom of the conduction band and a lowering of the upper conduction band subband potential on reducing the well width, leading to a saturation of the ISB transition energy. The apparent reduction in ISB absorption with the well width is associated to the decrease in the active layer (effective carrier concentration in the QW) thickness, as the well number has been maintained constant. We have observed that improving the interface quality can further reduce the transition wavelength. Efforts are underway to achieve a consistent and higher ISB absorption at

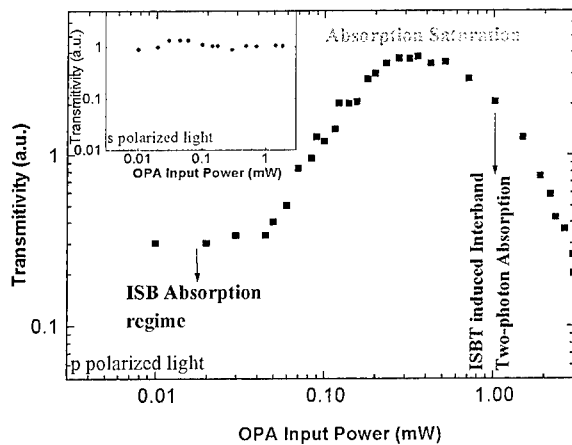


Fig. 4. Power dependence of the transmitted light at $2.4\ \mu\text{m}$ through a 200 period quantum well with a width of $30\ \text{\AA}$; pulse width $\sim 200\ \text{fs}$.

shorter wavelength by optimizing the growth technique by incorporating AlAs between the interface layers or by strain compensation [12].

The ISB transition wavelength can be reduced drastically to the communication wavelength regime by using coupled quantum wells. We have achieved intersubband transition simultaneously at 1.33 and $1.55\ \mu\text{m}$ utilizing the miniband transitions in a coupled quantum well [15].

Fig. 4 shows the power dependence of the transmitted signal at $2.4\ \mu\text{m}$ through a 200 period MQW with a well width of $30\ \text{\AA}$ that exhibits an intersubband absorption at $2.4\ \mu\text{m}$. We observe a saturation behavior of the intersubband absorption on increasing the input power. On increasing the OPA input power beyond a few hundred μW a strong absorption of the signal is observed. This is due to the interband two-photon absorption, which is allowed when the ground state conduction subband is depopulated by optical pumping to the upper state in presence of intersubband transition. The PL spectrum shows that for a $30\ \text{\AA}$ well width MQW the interband gap energy is $1.0\ \text{eV}$, which is exactly at the two-photon resonance of the intersubband separation corresponding to $0.5\ \text{eV}$. As the electron from the first conduction subband state $|c1\rangle$ is excited to the upper state $|c2\rangle$, the interband absorption due to the two-photon process is initiated. In the inset the transmission of s-polarized light is shown. As the s-polarized light does not excite ISB transitions, it does not undergo any absorption due to the

two-photon process as the first conduction subband states are totally occupied in the doped QW. This is a unique feature of this narrow-band gap material system with a large conduction band offset and needs to be investigated in further detail for applying this material for practical devices.

In conclusion, we report the intersubband absorption characteristics in a novel lattice-matched InGaAs/AlAsSb quantum well. The intersubband transition wavelength tends to saturate due to the interface non-abruptness. We observe absorption saturation behavior in this material system for the first time and also observed an intersubband transition-initiated two-photon interband absorption process in a $30\ \text{\AA}$ MQW. As the threshold for the two-photon process is found to be very high compared to the intersubband absorption saturation power, it is not expected to impede the performance of ISB-based optoelectronic devices.

References

- [1] R. Khel Sink, G. Bahir, A. Abare, H. Schmidt, S. DenBaars, J.E. Bowers, Electronic Materials Conference, paper Z9, 1997.
- [2] N. Izuka, N. Suzuki, International Compound Semiconductor Conference, Paper Fr1B3, 1998.
- [3] J.H. Smet, L.H. Peng, Y. Hirayama, C.H. Fonstad, Appl. Phys. Lett. 64 (1994) 986.
- [4] H.C. Liu, International Conference on Mid-infrared Optoelectronics Materials and Devices, paper I5, 1999.
- [5] T. Asano, S. Noda, T. Abe, A. Sasaki, Jpn. J. Appl. Phys. 35 (1996) 1285.
- [6] B. Sung, H.C. Chui, M.M. Fejer, J.S. Harris Jr, Electron Lett. 33 (1997) 818.
- [7] Y. Nakata, Y. Sugiyama, T. Inata, O. Ueda, S. Sasa, S. Muto, T. Fuji, Proc. Mater. Res. Soc. Symp. 198 (1990) 289.
- [8] T. Akiyama, A. Neogi, H. Yoshida, O. Wada, Proc. Conference on Lasers and Electro Optics, USA, 1999, paper CWF 11, p. 108.
- [9] H. Yoshida, T. Mozume, T. Nishimura, O. Wada, Electron. Lett. 34 (1998) 913.
- [10] H. Yoshida, T. Mozume, A. Neogi, O. Wada, Electron. Lett. 35 (1999) 1103.
- [11] S. Nemeth, B. Grietens, H. Bende, G. Borghs, Jpn. J. Appl. Phys. 36 (1997) 3426.
- [12] N. Georgiev, T. Mozume, Appl. Phys. Lett. 75 (1999) 2371.
- [13] T. Mozume, N. Georgiev, T. Nishimura, H. Yoshida, S. Nishikawa, A. Neogi, J. Crystal Growth, in press.
- [14] C. Yang, International Conference on Mid-infrared Optoelectronics Materials and Devices, paper I1, 1999.
- [15] A. Neogi, T. Mozume, H. Yoshida, O. Wada, Photon. Tech. Lett. 11 (6) (1999) 632.



ELSEVIER

Physica E 7 (2000) 187–190

PHYSICA E

www.elsevier.nl/locate/physa

First-order coherent THz optical sideband generation from asymmetric QW intersubband transitions

C. Phillips^{a, *}, M.Y. Su^b, J. Ko^c, L. Coldren^c, M.S. Sherwin^b^aExperimental Solid State Group, Physics Department, Imperial College of Science and Technology, London, SW7 2AZ, UK^bPhysics Department and Center for Terahertz Science and Technology, University of California, Santa Barbara, CA 93106, USA^cMaterials Department, University of California, Santa Barbara, CA 93106, USA

Abstract

We have generated terahertz (THz) optical sidebands on a near-infrared probe beam by driving an excitonic intersubband resonance with THz electric fields. We use THz radiation polarized along the non-centro-symmetric axis of a quantum well system to generate a comb of sidebands $\omega_{\text{sideband}} = \omega_{\text{NIR}} + n\omega_{\text{THz}}$. In exploring the rich polarization of the process's power, and NIR frequency dependences we encounter both an efficient perturbative regime modeled by a $X^{(2)}$ non-linear susceptibility, and a non-perturbative regime which has not been previously explored in driven quantum systems. © 2000 Elsevier Science B.V. All rights reserved.

Keywords: Subbands; Frequency mixing; Terahertz optical sidebands

Recently, two-color frequency mixing experiments have been used to generate “sidebands” on a NIR optical beam, in a terahertz analogue of RF heterodyning. The NIR was resonant with a quantum well interband transition and the THz pump beam interacted with intra-band transitions whose dipole moments, for experimental convenience, were polarized in the well plane [1–3]. In this geometry the intra-band system is centro-symmetric and only even sidebands, $\omega_{\text{sideband}} = \omega_{\text{NIR}} + 2n\omega_{\text{THz}}$ where $\omega_{\text{NIR}}(\omega_{\text{THz}})$ is the frequency of the NIR (THz) beam and $n = 1, 2, \dots$,

were seen. However, the resonance behavior of the sideband emission allowed spectroscopy of the internal structure of magneto-exciton transitions [2].

For the further application of THz EO effects in non-linear spectroscopy and in ultrafast optical phase/amplitude modulation, the ability to excite THz optical sidebands of all orders, particularly the efficient first-order process, is important. By using an asymmetric coupled quantum well (ACQW) structure to break inversion symmetry in the THz dipoles, and by polarizing the THz radiation in the QW normal we here demonstrate, for the first time, resonant THz NIR modulation.

The sample was grown by molecular beam epitaxy on a semi-insulating GaAs substrate. It consists

* Corresponding author. Tel.: +44-171-594-7575; fax: +44-171-594-7580.

E-mail address: chris.phillips@ic.ac.uk (C. Phillips)

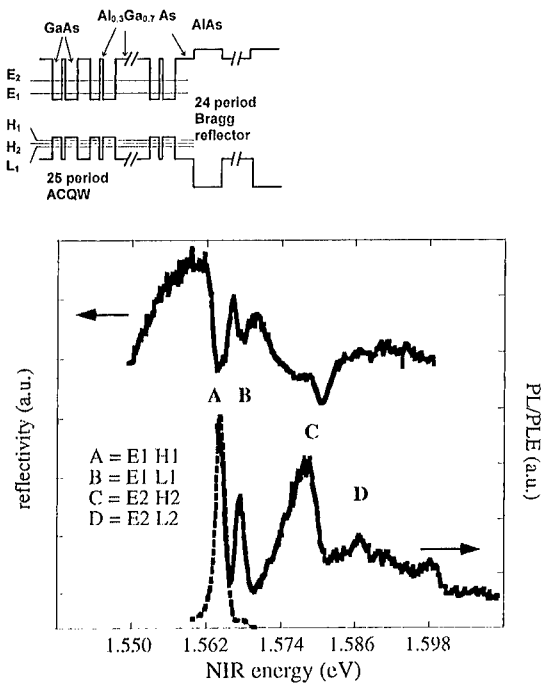


Fig. 1. (a) Schematic of asymmetric coupled quantum well (ACQW) sample on distributed Bragg reflector (DBR) used for sideband generation. (b) CW reflectivity and PL excitation spectra.

of 25 periods of undoped ACQW, each consisting of 7.5 and 8.5 nm GaAs quantum wells separated by a 2.3 nm $\text{Al}_{0.3}\text{Ga}_{0.7}\text{As}$ barrier. The two lowest lying electron (heavy hole) subbands are calculated to be split by 12 meV (3 meV). Below the quantum wells is a distributed Bragg reflector (DBR) consisting of a 24-periods of 66.3 nm AlAs and 58.3 nm $\text{Al}_{0.3}\text{Ga}_{0.7}\text{As}$. The 90 nm wide DBR passband was centered on the low-temperature ACQW band gap (Fig. 1).

The THz sources were the UCSB free-electron lasers, which provide several kilowatts of tunable THz radiation from 0.3–4.5 THz in 2–6 μs pulses at ≈ 1 Hz. The THz beam propagated in the QW plane and was focused onto the cleaved edge of the sample at ≈ 12 K. Simultaneously, ≈ 5 mW of NIR radiation from a tunable Ti : sapphire laser was focused into the same interaction volume in the sample. The diffraction-limited NIR beam propagated at near-normal incidence through the active ACQW region, reflected off the DBR, and made a second

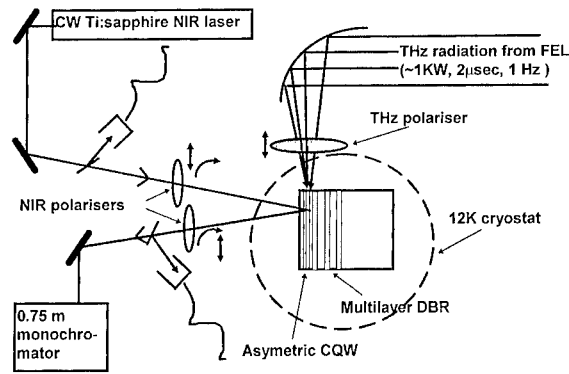


Fig. 2. Experimental geometry.

pass through the ACQW region before being collected by an optical fiber bundle. The collected light was dispersed in a 0.85 m double-monochromator and detected with a cooled GaAs photomultiplier (Fig. 2).

The sidebands were found always to have the same linear and circular polarization state as the incident NIR beam and were detectable only when the THz radiation had a linear polarization component normal to the QW. These facts imply that the sidebands originate from coherent virtual QW transitions which absorb neither energy nor momentum from the optical fields and do not depend on the presence of real excited carriers.

The dependence of the sideband intensity on ω_{NIR} and incident THz power was studied at THz frequencies: 0.7, 1.5, 2.5, 3.1 and 3.4 THz (2.9, 6.2, 10.3, 12.8, 14.0 meV). The results divided naturally into perturbative “high”-frequency ($\omega_{\text{THz}} > 2$ THz) and non-perturbative “low”-frequency (0.7 THz, 1.5 THz) cases (Fig. 3).

The typical “high-frequency power” dependence of the sideband intensity (Fig. 3a) shows accurate linear and quadratic dependences on THz intensity for the 1ω and 2ω sidebands, respectively, characteristic of a perturbative interaction that can be described [4] by non-linear susceptibilities $\chi^{(2)}$ and $\chi^{(3)}$. The low-frequency case (Fig. 3b) is qualitatively different: the simple linear/quadratic power dependence breaks down at low intensities, saturating and starting to oscillate. This regime, characterized by $\mu E_{\text{THz}}/\hbar\omega_{\text{THz}} \approx 1$ where μ is the intersubband dipole moment, and E_{THz} the amplitude of the THz electric

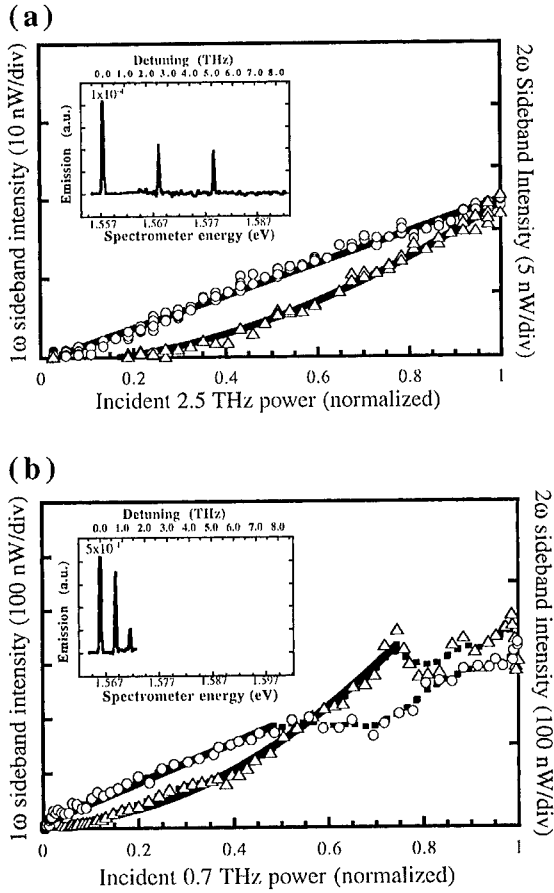


Fig. 3. THz power dependence of the 1ω (circles) and 2ω (triangles) sideband intensities at (a) $\omega_{\text{THz}} = 2.5$ THz and (b) $\omega_{\text{THz}} = 0.7$ THz. Solid lines are linear and quadratic fits, dotted lines are a guide to the eye. Insets: Typical sideband emission spectra. Full THz power is ≈ 2 kW at an intensity of ≈ 2 MW cm $^{-2}$. The NIR intensity was ≈ 250 W cm $^{-2}$.

field [5,6] is easier to access at lower THz frequencies. It marks the boundary between “perturbative” and “non-perturbative” pictures of the strongly driven 2D electronic system.

In a perturbative treatment, which considers only the discrete excitonic states while neglecting the electron–hole interaction and continuum, the second-order susceptibility for the $+1\omega$ sideband is written as follows:

$$X^{(2)}(\omega_{\text{NIR}} + \omega_{\text{THz}}, \omega_{\text{NIR}}, \omega_{\text{THz}}) \propto \sum_{m,n,p,q} \frac{\langle 0|x|E_p H_q\rangle \langle E_p H_q|z|E_m H_n\rangle \langle E_m H_n|x|0\rangle}{(\omega_{pq} - \omega_{\text{NIR}} - \omega_{\text{THz}} + i\Gamma)(\omega_{mn} - \omega_{\text{NIR}} + i\Gamma)}, \quad (1)$$

where $x(z)$ is the dipole moment in the NIR (THz) polarization, $|0\rangle$ is the vacuum state with no excitons $|E_p H_q\rangle$ are excitonic states (including both heavy and light holes), $\hbar\omega_{pq}$ is the energy of the $|E_p H_q\rangle$ state relative to the vacuum and Γ is a phenomenological linewidth.

The electron–heavy hole interband dipole matrix element is given by

$$\langle E_m H_n | z | 0 \rangle = \beta \int \Psi_{E_m}^*(z) \Psi_{H_n}^*(z) dz, \quad (2)$$

where the constant β is the dipole matrix element between electron and heavy-hole band edge Bloch wave functions [7]. The light-hole interband dipole matrix element is given by

$$\langle E_m L_n | z | 0 \rangle = \frac{1}{3} \beta \int \Psi_{E_m}^*(z) \Psi_{L_n}^*(z) dz. \quad (3)$$

The factor of $\frac{1}{3}$ is due to the $Y_{3/2,1/2}$ symmetry of the light-hole band [7,8]. The intersubband dipole matrix element is

$$\begin{aligned} \langle E_p H_q | z | E_m H_n \rangle &= \int \Psi_{E_p}^*(z) z \Psi_{E_m}^*(z) dz \\ &\quad - \int \Psi_{H_q}^*(z) z \Psi_{H_n}^*(z) dz, \end{aligned} \quad (4)$$

where the minus sign reflects the fact that electrons and holes are of opposite charge.

The solid lines in Fig. 4 are the square moduli of $X^{(2)}$ based on Eqs. (1)–(4). The energies $\hbar\omega_{pq} - E_{\text{gap}}$ were calculated by solving the 1D Schrodinger equation for the quantum well using standard values for the electron, heavy- and light-hole effective masses (8). All confined states in the ACQW were included. The values for the band gap E_{gap} and linewidth Γ were determined by measuring the reflectivity spectrum while under THz illumination. At high THz frequencies the main effect of the THz field on the reflection spectrum was a uniform red shift of 1–2 meV of the excitonic features, which is consistent with direct local lattice heating to ≈ 25 K.

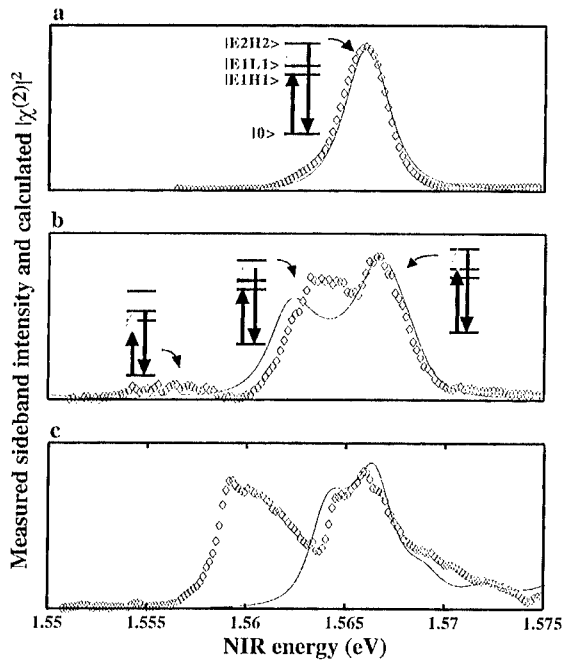


Fig. 4. $+1\omega$ sideband intensity versus ω_{NIR} . Diamonds: data. Line: calculated $|\chi^{(2)}|^2$. (a) $\omega_{\text{THz}} = 3.1$ THz. (b) $\omega_{\text{THz}} = 2.5$ THz. (c) $\omega_{\text{THz}} = 0.7$ THz. Mixing is enhanced when either the NIR fundamental or the sideband is resonant with peaks in the interband DOS, and maximizes when both NIR and THz frequencies simultaneously resonate with interband and intersubband transitions, respectively (e.g. (a), rightmost peak in (b)).

In Fig. 4c $\omega_{\text{THz}} = 0.7$ THz/2.9 meV (the same low-frequency case which displayed the non-monotonic power dependence in Fig. 1b), the NIR resonant

structure shows an additional strong peak not predicted by perturbation theory. This regime, the subject of current active study, involves a rich interplay between non-perturbative modification of the 2D density of states and a strong field THz modulation of the NIR beam (see e.g. Ref. [9]).

In conclusion, we have observed first- and higher-order THz sidebands resonantly generated on a NIR carrier beam for the first time. The experimental evidence implies that they are generated coherently and could find application in a number of interesting coherent spectroscopy and optical information processing schemes, including THz phase and amplitude coherent modulation/demodulation systems.

References

- [1] K.B. Nordstrom, K. Johnsen, S.J. Allen, A.P. Jauho, B. Birnir, J. Kono, T. Noda, H. Akiyama, H. Sakaki, Phys. Rev. Lett. 81 (1998) 457.
- [2] J. Kono, M.Y. Su, T. Inoshita, M.S. Sherwin, S.J. Allen, H. Sakaki, Phys. Rev. Lett. 79 (1997) 1758.
- [3] J. Cerne, J. Kono, T. Inoshita, M.S. Sherwin, M. Sundaram, A.C. Gossard, Appl. Phys. Lett. 70 (1997) 3543.
- [4] R. Boyd, Nonlinear Optics, Academic Press, New York, 1992, p. 102.
- [5] K. Johnsen, A.P. Jauho, Phys. Rev. B 57 (1998) 8860.
- [6] T. Fromherz, Phys. Rev. B 56 (1997) 4772.
- [7] G. Bastard, Wave Mechanics Applied to Semiconductor Heterostructures, Les Editions de Physique, Les Ulis Cedex, 1988, pp. 43–46, 247–249.
- [8] P. Yu, M. Cardona, Fundamentals of Semiconductors, Springer, Heidelberg, 1996, pp. 68–70.
- [9] K. Johnsen, A.-P. Jauho, Phys. Rev. Lett. 83 (1999) 1207.



ELSEVIER

Physica E 7 (2000) 191–199

PHYSICA E

www.elsevier.nl/locate/physce

Collective effects in intersubband transitions

R.J. Warburton^{a,*}, K. Weilhammer^a, C. Jabs^a, J.P. Kotthaus^a, M. Thomas^b, H. Kroemer^b^aCenter for NanoScience and Sektion Physik, LMU, Geschwister-Scholl-Platz 1,
80539 München, Germany^bDepartment of Electrical and Computer Engineering, University of California, Santa Barbara, CA 93106, USA

Abstract

We present experiments on the intersubband resonance (ISR) in InAs/AlSb quantum wells with the aim of understanding the linewidth. We find that fluctuations in the well width dominate the scattering right up to temperatures well beyond room temperature. ISR with two occupied subbands is used to gain insight into these phenomena. We find clear evidence for Landau damping and we argue generally that Landau damping represents the crucial scattering mechanism for all ISRs. The argument is strengthened by considering the intrasubband plasmon, where we also find evidence for Landau damping, in this case in a magnetic field. © 2000 Elsevier Science B.V. All rights reserved.

Keywords: Intersubband resonance; Linewidth; Collective effects; InAs

1. Introduction

It has been known for at least 20 years that intersubband resonance (ISR) is not a single-particle process [1,2]. ISR is a collective phenomenon, more accurately described as a plasmon or charge-density excitation. There are now a number of experiments which demonstrate this point. One example is the ISR in a system with a broad single-particle density of states. This can be achieved in a low-band-gap system such as InAs where the separation between the subbands is smaller at the Fermi wave vector $k = k_f$ than at $k = 0$. In such a case, the ISR is a single, narrow

line: the collective effects collapse all the available oscillator strength into a single mode [3–5]. Another example is to probe the ISR in the non-linear regime with a very intense source. In this case, optical pumping of the carriers weakens the collective effects and the ISR red-shifts [6].

The collective effects shift the energy away from the single-particle energy separating the subbands. This shift however represents typically only a small proportion of the ISR energy as there are two competing effects. The direct electron–electron interaction, often referred to as the depolarisation field in this context, and the exchange–correlation interaction cause blue- and red-shifts, respectively, and tend to cancel [7,8]. This enables the ISR energy to be estimated to the 10% level simply with a single-particle calculation. It is now widespread practice to model all ISRs, in

* Corresponding author. Fax: +49-89-2180-3182.

E-mail address: richard.warburton@physik.uni-muenchen.de (R.J. Warburton)

particular in ISR-based emitters and detectors, with the single-particle states. While this approach may be satisfactory for the ISR energy we argue here that it is very misleading for the scattering mechanisms which determine the ISR linewidth.

The purpose of the present work is to examine the linewidth of the ISR. In the best samples, the ISR linewidth is homogeneously broadened, in which case the linewidth is determined by scattering mechanisms [9,10]. In another terminology, the linewidth is inversely related to the dephasing time of the ISR. There exist some experimental studies of the linewidth: it would appear that the linewidth is determined by elastic, momentum non-conserving scattering off extrinsic defects such as interface roughness or ionised impurities [10]. The temperature dependence has not been extensively explored, but there are some reports that at least for GaAs-based devices the room temperature linewidth is comparable to the low-temperature linewidth [11–13]. Furthermore, the ISR linewidth has no obvious correlation with the transport mobility [10]. Theoretically, we are not aware of a microscopic approach to compute the linewidth. In fact, the ISR linewidth is usually described with the single-particle scattering rates.

We present here a detailed study of ISR of InAs/AlSb quantum wells. We find that the ISR linewidth rises strongly with reducing well width but has a very weak temperature dependence. We argue that the weak temperature dependence cannot be easily understood in a single-particle picture. Instead, we propose a collective picture based on Landau damping. This model is supported by experiments on a quantum well with two occupied subbands where we see the direct consequences of Landau damping [14]. We also present results on the intrasubband plasmon which support our assertion that Landau damping is the crucial scattering mechanism for plasmons in this material system.

2. Samples and experiments

The InAs quantum wells were all grown on GaAs substrates with AlSb barriers. In order to investigate the well width dependence of the ISR, we looked at a number of samples, each with 12 quantum wells and

carrier densities within 10% of 10^{12} cm^{-2} , with well widths 60, 70, 85, 100, 130 and 150 Å. The wells are all δ doped 50 Å away from the interfaces, and the wells are separated by 100 Å of AlSb. One sample has a higher doping concentration and also wider wells, 180 Å. In this case, two subbands are occupied as revealed by a beating in the Shubnikov–de Haas oscillations. By analysing the oscillations we determined the densities of the first and second subbands (labelled 1 and 2) to be $n_1 = 1.89 \times 10^{12} \text{ cm}^{-2}$ and $n_2 = 0.74 \times 10^{12} \text{ cm}^{-2}$, respectively. We have also investigated an additional sample with a single 150 Å InAs quantum well with carrier density $0.9 \times 10^{12} \text{ cm}^{-2}$ and particularly high mobility, ca. $0.5 \times 10^6 \text{ cm}^2/\text{V s}$.

The ISR was excited in three different ways. The first technique was simply to tilt the sample with respect to the incident beam (loosely referred to as Brewster geometry). The second technique was to deposit a thick layer of silver onto the sample surface and to illuminate the bevelled edges of the sample (strip-line geometry). This tended to give very strong resonances and in some cases we deposited only a 0.2 mm wide strip of silver in order to avoid saturation effects. The third technique was to use crossed electric and magnetic field (Voigt geometry) [15]. The magnetic field (up to 12 T) lies in the plane of the quantum well as does the electric field of the light. This geometry gives much weaker resonances than in the strip-line geometry, ruling out saturation effects, and allows the ISR matrix element to be determined simply from the resonance intensity.

The ISRs lie in the mid infrared and were recorded with a Fourier transform spectrometer and variety of detectors (low-temperature Ge : Cu photoconductor, HgCdTe photoconductor and a DLTS detector). A reference spectrum was taken at normal incidence (Brewster geometry), from a sample with a different well width (strip-line geometry), or at zero magnetic field (Voigt geometry).

Related to the ISR is the intrasubband plasmon. However, the energy of the intrasubband plasmon is zero at zero wave vector, and so in order to excite a plasmon we supplied an additional impulse with a metallic grating on the sample surface. The intrasubband plasmon has a much smaller energy than the intersubband plasmon corresponding to wavelengths in the far-infrared region which we detected with a 2 K composite Si bolometer.

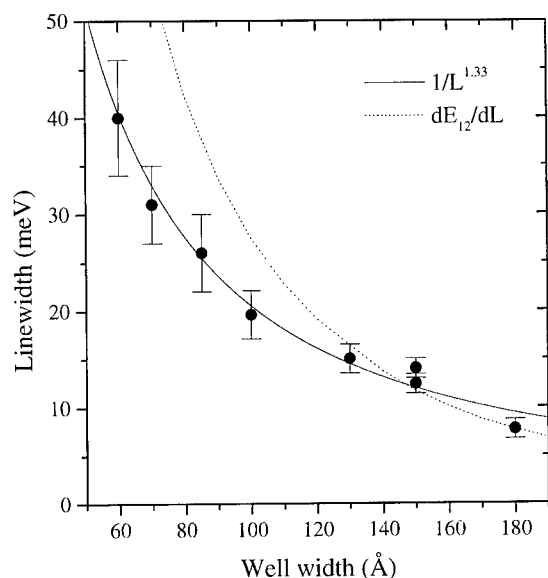


Fig. 1. The linewidth of the intersubband resonance (ISR) against well width. The solid symbols represent the measurements on InAs/AlSb quantum wells at 4.2 K with electron densities around 10^{12} cm^{-2} . The dotted curve is $F \propto dE_{12}/dL$ where the separation between the first and second subbands E_{12} was calculated with the Kane model, and the curve was made to pass through the point for well-width 180 Å. The solid curve is a fit to the experimental data.

For both the ISR and the intrasubband plasmon, the experimental resonances are close to Lorentzian in shape and we therefore infer that the broadening is predominantly homogeneous.

3. The intersubband resonance

3.1. Temperature and well-width dependence of the linewidth

Fig. 1 shows the linewidth of the ISR plotted against well width for a temperature of 4.2 K. It can be seen that the linewidth rises quite rapidly with decreasing well width. The most obvious explanation is that well width fluctuations are responsible for the linewidth because they increase in importance as the well narrows. Other possible scattering mechanisms, for instance off ionised impurities and phonons, would not have such a strong well-width dependence. Fig. 2 shows the linewidth against temperature for the sample with 180

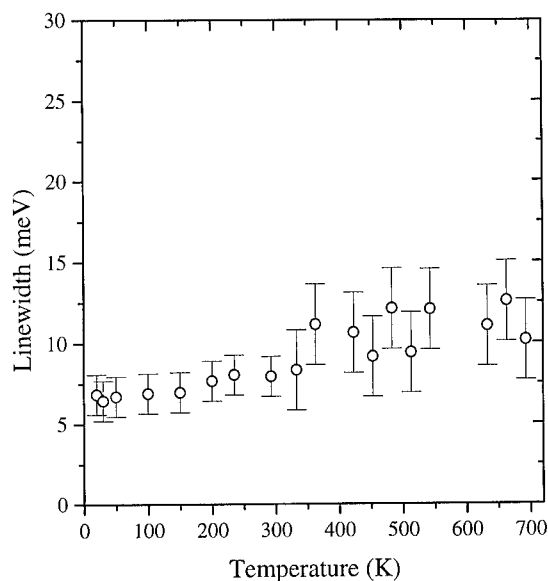


Fig. 2. The ISR linewidth for a 180 Å quantum well with $2.63 \times 10^{12} \text{ cm}^{-2}$ carrier density plotted against temperature. Note that the temperature scale extends to well above room temperature.

Å well width.¹ It can be seen that the linewidth is remarkably insensitive to temperature, increasing by barely 50% right up to 700 K, i.e. well above room temperature. It can therefore be concluded that scattering off well-width fluctuations is the dominant dephasing mechanism even at high temperature. As in Ref. [10] we find no correspondence of the intersubband lifetime with the transport mobility. At low temperature for instance we have two samples with 150 Å well width with transport mobilities differing by an order of magnitude. Nevertheless, the ISR linewidths differ by no more than 10%. As the temperature increases, the transport mobility decreases rapidly as scattering off LO phonons becomes more prevalent yet the ISR linewidth is largely unchanged.

It is difficult to account for the dependence of the ISR linewidth on well width and its independence on temperature in a single-particle model. At low temperature, one would naively expect that the linewidth increases as $1/L^3$. This is too strong a dependence on well width, partly due to the neglect of

¹ Plotted in Fig. 2 is the linewidth of the 2–3 ISR of the sample with two occupied subbands. The sample with 150 Å well width and a singly occupied subband showed essentially the same behaviour.

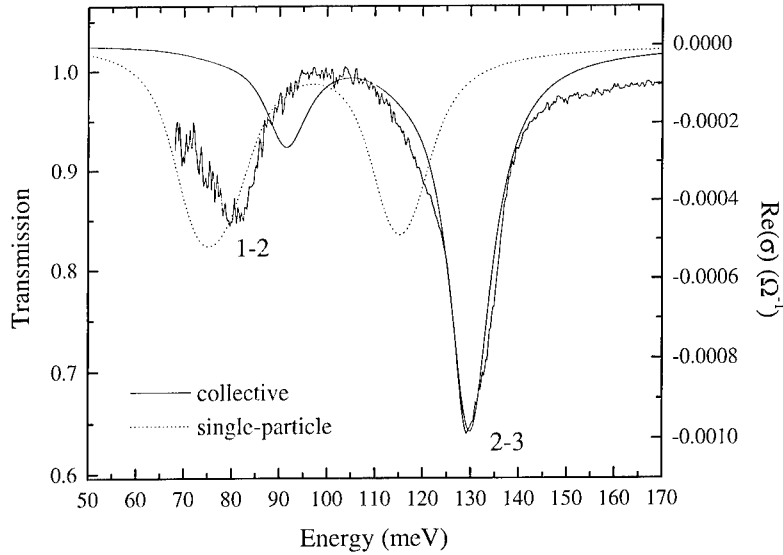


Fig. 3. The measured ISR for a 180 Å InAs quantum well with two occupied subbands. Results of the calculations are also shown: the dotted curve is without collective effects; the solid curve includes collective effects in the self-consistent field approximation (Ando model).

the nonparabolicity in the InAs band structure which weakens the well-width dependence. It is straightforward to incorporate the nonparabolicity with the Kane model [4] and this yields the dotted curve in Fig. 1. The curve rises more rapidly than the experimental data points and this represents a failure of the single-particle picture. The temperature dependence is still more striking. All estimates of the ISR linewidth from LO phonon scattering are in the range of a few meV [9,16]. On increasing the temperature, the LO phonon emission rate should increase as $1 + n_{\text{LO}}$ where n_{LO} is the LO phonon occupation. This factor doubles between 0 and 600 K. Furthermore, absorption of LO phonons should also contribute to the linewidth at elevated temperatures. In other words, in a single-particle picture the ISR linewidth should show a much stronger dependence on temperature than is observed experimentally.

3.2. ISR for two occupied subbands

In order to probe this issue further, we present the ISRs of the sample with two occupied subbands. The transmission spectrum at low temperature is shown in Fig. 3. There are two resonances as expected, one corresponding to the 1–2 ISR, and one to the 2–3 ISR.

It is interesting to note that the 1–2 ISR is weaker than the 2–3 ISR and we first discuss this point.

In a single-particle picture, the oscillator strength of the 1–2 ISR is proportional to $(n_1 - n_2)z_{12}^2 E_{12}$ and the oscillator strength of the 2–3 ISR is proportional to $n_2 z_{23}^2 E_{23} z_{12}$ (z_{23} is z -dipole matrix element between the first and second (second and third) subbands. For the present sample, $(n_1 - n_2) > n_2$ and the matrix elements z_{12} and z_{23} are approximately equal. (Including band nonparabolicity, we calculate $z_{12} = 36.5$ and $z_{23} = 39.5$ Å). Hence, in the single-particle picture the 1–2 : 2–3 intensity ratio should be 1.3 : 1. In the experiment however, the ratio is 0.5 : 1. The explanation is that the depolarisation field not only shifts both the 1–2 and 2–3 ISRs to higher energy but it also couples the two resonances. An analogy with two coupled pendulums can be made: there is an in-phase normal mode (2–3) and an out-of-phase normal mode (1–2). The out-of-phase mode couples weakly to the long wavelength electric field of the light. A sum rule on the oscillator strength is bound to exist so that the 2–3 ISR gains intensity from the 1–2 ISR. It should be noted that the terminology 1–2 and 2–3 is only approximate as the depolarisation field admixes the two ISRs. As the carrier intensity increases, the coupling becomes stronger such that the 2–3 mode takes es-

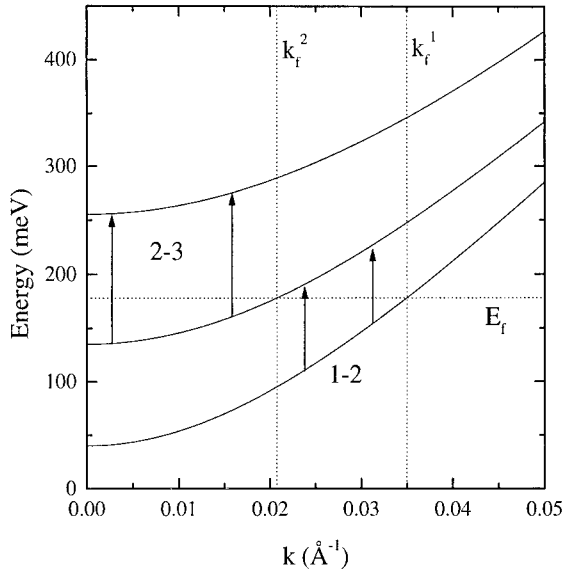


Fig. 4. The in-plane dispersion of the subbands in a 180 Å InAs/AlSb quantum well calculated with four band $\mathbf{k} \cdot \mathbf{p}$ theory. Static many-electron effects have been neglected. The low-temperature Fermi energy E_f and the corresponding Fermi wave vectors k_f^1 and k_f^2 are shown as dotted lines. The energy zero lies at the bottom of the InAs well.

entially all of the oscillator strength. This is exactly what is observed: at $6 \times 10^{12} \text{ cm}^{-2}$ for instance we can only observe a single ISR.

The claim is that the depolarisation field not only quenches the broadening in the single-particle spectrum but also transfers oscillator strength from the 1–2-like ISR to the 2–3-like ISR. To confirm this point, we have carried out calculations in the Ando formalism (self-consistent field approximation) [2]. The formalism was extended to include both multiply occupied subbands and elevated temperatures. At the carrier densities here, the depolarisation field is the dominant collective interaction so for simplicity we have neglected the exciton term. The single-particle states were calculated with the Kane model and their dispersions are shown in Fig. 4. As a check, we fixed the Fermi energy such that the total carrier concentration is $n_1 + n_2 = 2.63 \times 10^{12} \text{ cm}^{-2}$, the experimental value, and compared the calculated $n_1 : n_2$ ratio to the experimental one. The agreement was better than 10%. The Ando theory assumes that all single-particle states have an inhomogeneous width Γ which is state

and temperature independent. The calculation gives most directly the real part of the out-of-plane dynamic conductivity $\Re(\sigma_{zz}(E))$ at zero wave vector $q = 0$. This is linearly related to the absorption; $-\Re(\sigma_{zz}(E))$ can be directly compared to the transmission data.

Fig. 3 shows the results of the calculations taking $\Gamma = 11 \text{ meV}$ to reproduce the experimental linewidth.² At low temperature, we have an excellent agreement with the experimental results supporting the claim that the depolarisation field is responsible for the transfer of intensity from 1–2 to 2–3. The only discrepancy between the calculated and measured spectra is the energy of the 1–2-like mode which is perhaps related to the omission of exchange-correlation effects.

We now turn to the temperature dependence. The experimental data are shown in Fig. 5a. It can be seen that the upper 2–3-like ISR has a linewidth which is only weakly temperature dependent right up to 600 K. Conversely, the lower 1–2-like ISR broadens above 200 K and eventually forms a shoulder of the 2–3-like ISR. Our explanation is that the lower mode becomes degenerate with single-particle transitions as the temperature is increased and this degeneracy dephases the ISR. This is an example of Landau damping which is known from metal physics to be a very effective scatterer of plasma oscillations [17]. In this case, the single-particle transitions are between subbands 2 and 3 at high k which have a low energy because of band nonparabolicity.

Calculations with the Ando formalism reproduce the experimental results very closely, as shown in Fig. 5b. As in the experiment, the lower ISR broadens above 200 K. To confirm our interpretation of Landau damping, we plot in Fig. 6 $\Re(\sigma_{zz})$ against energy without collective effects. There are two main peaks corresponding simply to the 1–2 and 2–3 inter-subband transitions. The peaks are broad due to both the assumed inhomogeneous broadening and the nonparabolicity in the band structure. The calculated energies of the collective modes are shown by the dotted lines. It can be seen that at the 2–3 collective ISR,

² The line width of the 2–3 ISR is ca. 11 meV in this strip-line experiment and is slightly larger than the width determined from the same sample in the Voigt geometry (plotted in Figs. 1 and 2). This is because saturation effects in the strip-line geometry could not be eliminated completely.

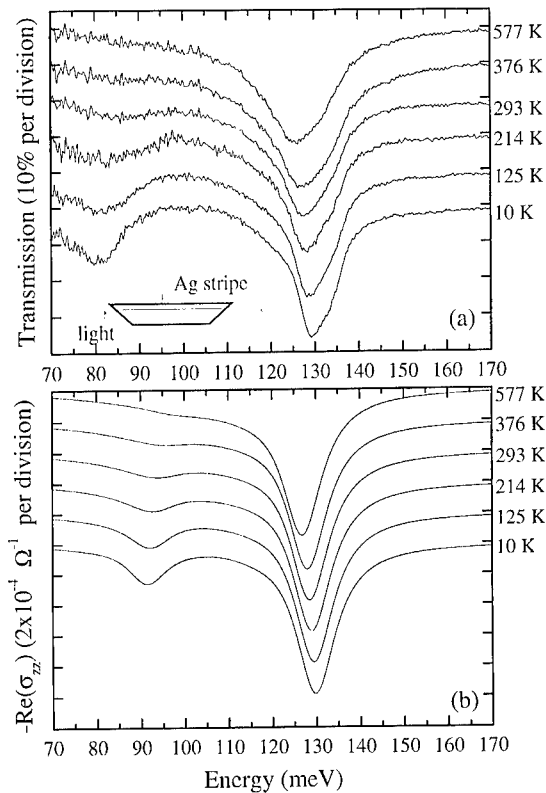


Fig. 5. The temperature dependence of the ISR for the 180 Å InAs quantum well with two occupied subbands: (a) experimental transmission spectra. The spectra are offset from 1 for the various temperatures; (b) calculations of the real part of the dynamic conductivity, σ_{zz} , at zero wave vector in the Ando model. The curves are offset from 0 for clarity.

there is almost no change on increasing the temperature. However, at the energy of the 1–2 collective ISR, the single-particle density of states increases rapidly with increasing temperature. This supports the Landau damping interpretation.

3.3. Discussion of the ISR linewidth

Experiments on the sample with two occupied subbands show that Landau damping represents a strong scattering mechanism of the ISR. In the experiment, the 1–2 mode broadens because it is Landau damped; the 2–3 mode remains sharp because it is not. It is possible to explain, at least qualitatively, the experimental results against temperature and well width also with

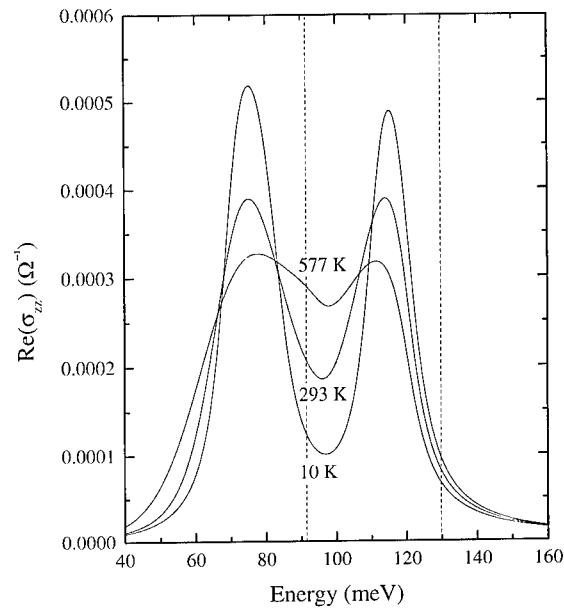


Fig. 6. The calculated real part of the dynamic conductivity, σ_{zz} , without collective effects at three different temperatures. The curves correspond to the density of single-particle transitions with $q = 0$ which form the single-particle background density of states for the calculations in Fig. 5b. The two dotted lines show the energies of the calculated 1–2 and 2–3 collective modes at low temperature.

Landau damping. The starting point is the dispersion relation of the ISR and the underlying single-particle transitions, as shown in Fig. 7 for the simple case of an InAs/AlSb quantum well with a singly occupied subband. The ISR has a very weak dispersion. The single-particle transitions correspond to all possible transitions between occupied and unoccupied states and fall into bands as shown. A number of points can be made with this diagram.

First, the ISR is isolated from the single-particle transitions at $q = 0$. This means that in a pure system, Landau damping cannot take place, i.e. the resonance should be sharp. This is exactly what is observed. Secondly, it is clear why scattering of the ISR with phonons is ineffective. A phonon can only scatter the ISR along its dispersion relation and this severely limits the number of phonons which can participate. Thirdly, an increase of temperature causes states at higher k to be occupied where the subbands are separated by smaller energies through band nonparabolicity. This smears the band of single-particle transitions

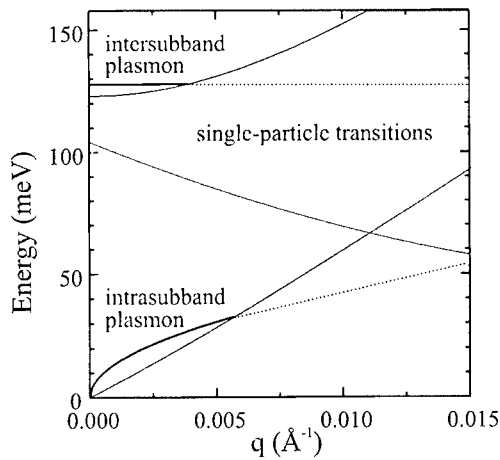


Fig. 7. The energy of the collective modes, the ISR and intrasubband plasmon, against in-plane wave vector, q , along with the single-particle transitions (shaded areas) for a 150 \AA InAs/AlSb quantum well with a singly occupied subband with electron density 10^{12} cm^{-2} .

to lower energies. The important point however is that the ISR mode at $q = 0$ lies above the single-particle transitions and so never becomes degenerate with them, even at very high temperature. This, along with the comment concerning phonon scattering, explains the robustness of the ISR at high temperature. Fourthly, the strong well-width dependence can also be accommodated within this model. Short-range fluctuations in the plane with characteristic length ΔL imply an uncertainty in the in-plane ISR wave vector of $\Delta q \sim \pi/\Delta L$. If this Δq is large enough, the ISR moves into a part of its dispersion where Landau damping occurs. The strong well-width dependence arises from the fact that the depolarisation shift decreases with well width, implying that the mode at $q = 0$ is energetically close to the single-particle states at $q = 0$ for a narrow well. This also means that the intersection of the ISR dispersion curve with the band of single-particle states occurs at smaller q . In other words, a given Δq is more effective in scattering the ISR for a narrow well than for a wide well. Finally, this collective picture is quite different from the usual considerations used to describe the transport mobility where scattering events which degrade the forward momentum are important. It is then no surprise that the ISR linewidth and transport mobility show no obvious correlation.

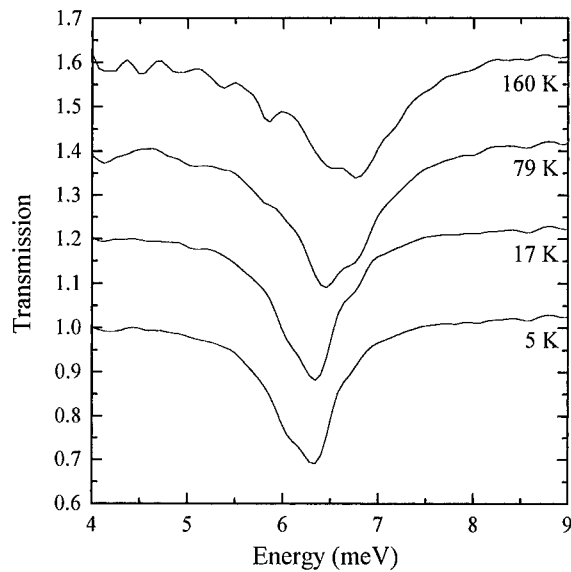


Fig. 8. Transmission spectra of a 150 \AA InAs/AlSb quantum well with electron density 10^{12} cm^{-2} with a metallic grating on the sample surface. The grating has period 1 μm with 0.5 μm thick stripes. The spectra were recorded at various temperatures and are offset from 1 for clarity.

4. The intrasubband plasmon

Fig. 7 shows that there is another plasmon mode in this system in addition to the ISR. This is the intrasubband plasmon which involves excitations only in the occupied subbands and is therefore analogous to plasmons in conventional metals. However, as the subbands are two-dimensional, the dispersion takes on a particular form, varying as \sqrt{q} . We excited a plasmon at $q = 2\pi/d$ with a metallic grating of period d on the sample surface. Fig. 8 shows the transmission of a sample with 1 μm grating on the surface at zero magnetic field ($B = 0$) for several temperatures. The mode at ca. 6 meV is the intrasubband plasmon.

Fig. 8 illustrates that the intrasubband plasmon survives right up to 160 K. It is not as robust at elevated temperatures as the ISR, but at low temperature the intrasubband plasmon does have a smaller linewidth than the ISR. Fig. 9 shows the behaviour of the intrasubband plasmon in a magnetic field, in this case for a sample with 6 μm grating period where in fact at least two intrasubband plasmons can be excited. The strong absorption which increases in energy with increasing

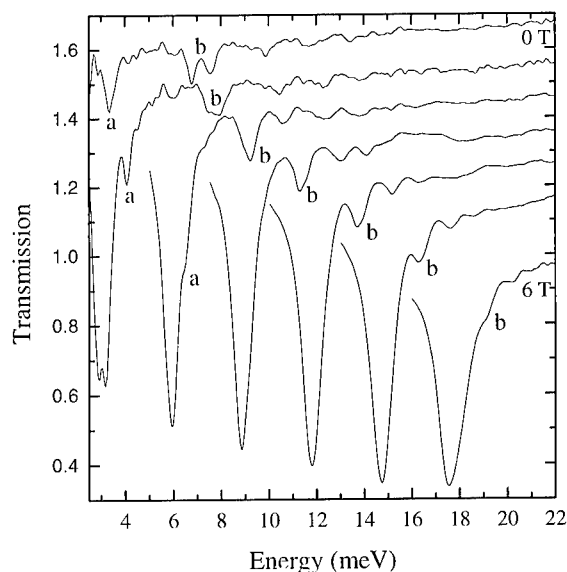


Fig. 9. Transmission spectra of a 150 Å InAs/AlSb quantum well at 4.2 K with electron density 10^{12} cm^{-2} with a metallic grating on the sample surface. The grating has period $6 \mu\text{m}$ with $3 \mu\text{m}$ thick stripes. The data were recorded at magnetic fields 0, 1, 2, 3, 4, 5, and 6 T. The curves are offset from 1 for clarity.

magnetic field is simply the electron–cyclotron resonance. Plasmon a merges with the cyclotron resonance around 2 T; plasmon b at around 6 T. If the plasmons maintained their $B = 0$ linewidths they would be strong enough to be distinguishable from the cyclotron resonance. The results in Fig. 9 imply rather that the plasmons broaden when they are close to the cyclotron resonance. All these effects can be interpreted in terms of Landau damping.

The intrasubband plasmon at low temperature and $B = 0$ T is energetically separated from the single-particle transitions and therefore exhibits a sharp line. As explained above, the ISR mode at $q = 0$ never becomes degenerate with single-particle excitations and this helps to preserve its character at elevated temperature. However, the intrasubband plasmon does become degenerate with some thermally excited single-particle excitations because it inevitably has a finite q . This means that the intrasubband plasmon is more sensitive to thermal smearing of the Fermi distribution than the ISR. The scattering of the ISR is dominated by elastic, momentum nonconserving processes. Our

interpretation is that these processes scatter the ISR along its dispersion curve into a region where the ISR is strongly damped. Following this train of thought, this is less likely to happen to the intrasubband plasmon because its dispersion has a much stronger dependence on wave vector. This would explain why at low temperature the intrasubband plasmon has a smaller linewidth than the ISR. In a magnetic field, the single-particle structure is changed: the available density of states is concentrated into Landau levels. Damping of the intrasubband plasmon can then occur through a degeneracy with transitions between the Landau levels (essentially cyclotron resonance). As the magnetic field increases, the intrasubband plasmon becomes closer energetically to the cyclotron resonance, increasing the damping.

These results are significant as they can be interpreted with the same picture as those on the ISR despite the different energies and dispersions of the two excitations. The two modes are clearly related. It is known for instance that the intrasubband plasmon and the ISR repel each other energetically [18,19]. This simply emphasises the point that the ISR is a form of plasma oscillation and not simply the transition between two quantum states.

5. Conclusions

We have investigated the linewidth of the ISR in InAs/AlSb quantum wells. Experimentally, the linewidth increases with decreasing well width but exhibits only modest changes with increasing temperature even at temperatures well above room temperature. The implication is that well-width fluctuations represent the dominant scattering mechanism at all temperatures. The corollary is that well-width fluctuations must be minimised for the smallest linewidths and optimum device performance. We cannot account for these results on the linewidth with a single-particle model. Instead, we argue that the ISR linewidth is strongly influenced by the collective nature of the ISR. We propose a model based on Landau damping which is inspired by experiments on a sample with two occupied subbands. The model can at least qualitatively account for the experimental results.

Acknowledgements

We would like to thank S.E. Ulloa, K. Kempa, K.L. Campman, A. Imamoğlu, and C. Sirtori for helpful discussions. The work was funded by the Office of Naval Research, the NSF (grant DMF 91-20007), the EEC (R.J.W.'s HCM grant), the Volkswagen Foundation, and the BMBF through a Max Planck Research Award. J.P.K. would like to thank the staff at QUEST for their hospitality.

References

- [1] S.J. Allen et al., *Solid State Commun.* 20 (1976) 425.
- [2] T. Ando, *Z. Physik B* 26 (1977) 263.
- [3] C. Gauer et al., *Phys. Rev. Lett.* 74 (1995) 2772.
- [4] R.J. Warburton et al., *Phys. Rev. B* 53 (1996) 7903.
- [5] M. Załuzny, *Phys. Rev. B* 43 (1991) 4511.
- [6] K. Craig et al., *Phys. Rev. Lett.* 76 (1996) 2382.
- [7] W.L. Bloss, *J. Appl. Phys.* 66 (1989) 3639.
- [8] E. Batke et al., *Phys. Rev. B* 43 (1991) 6812.
- [9] J. Faist et al., *Appl. Phys. Lett.* 63 (1993) 1354.
- [10] K.L. Campman et al., *Appl. Phys. Lett.* 69 (1996) 2554.
- [11] P. von Allmen et al., *Semicond. Sci. Technol.* 3 (1988) 1211.
- [12] M.O. Manasreh et al., *Appl. Phys. Lett.* 57 (1990) 1790.
- [13] D. Huang et al., *Phys. Rev. B* 52 (1995) 14126.
- [14] R.J. Warburton et al., *Phys. Rev. Lett.* 80 (1998) 2185.
- [15] C. Gauer et al., *Europhys. Lett.* 30 (1995) 111.
- [16] R. Ferreira, G. Bastard, *Phys. Rev. B* 40 (1989) 1074.
- [17] G.D. Mahan, *Many-Particle Physics*, Plenum Press, New York, 1993 (Chapter 5).
- [18] S. Das Sarma, *Phys. Rev. B* 29 (1984) 2334.
- [19] S. Oelting et al., *Phys. Rev. Lett.* 56 (1986) 1846.



ELSEVIER

Physica E 7 (2000) 200–203

PHYSICA E

www.elsevier.nl/locate/physe

Direct observation of dynamical screening of the intersubband resonance

S. Graf^{a,*}, H. Sigg^a, K. Köhler^b, W. Bächtold^c^aPaul Scherrer Institute, Laboratory for Micro- and Nanotechnology, CH-5232 Villigen-PSI, Switzerland^bFraunhofer Institut für angewandte Festkörperforschung, Tullastrasse 72, D-79108 Freiburg i.Br., Germany^cLaboratory for Electromagnetic Fields and Microwave Electronics, ETHZ, CH-8092 Zürich, Switzerland

Abstract

We have studied the intersubband resonance of GaAs/AlGaAs multi-quantum well systems by comparing photon drag and absorption spectra. The peak absorption at room temperature is found to be blueshifted from the photon drag resonance by as much as 33 cm^{-1} . We argue that this difference gives directly the depolarization shift. © 2000 Elsevier Science B.V. All rights reserved.

Keywords: Depolarization; Photon drag; Collective effects; Screening

It is by now commonly accepted that the intersubband resonance (ISR) in doped semiconductor quantum well (QW) systems is not a single-particle process but a collective phenomenon designated as a plasmon or charge-density excitation [1]. As a consequence, the resonance energy observed, for example, in a far-infrared (FIR) transmission or absorption experiment, does not occur at the energy given by the single-particle energy level separation. Also, the line width and lineform of the resonance may be affected by collective effects [2].

Numerous works have been devoted to the determination of these collective effects by studying the dependence of the ISR on temperature [3,4],

intensity [5], and carrier density [6–8]. The drawback of these methods is that the single-particle effects are distinguished from the many-body effects using model calculations, which require knowledge of sample parameters such as the electron concentration, effective mass, QW width, barrier heights, etc.

A FIR-based method which gives the undressed intersubband energy is the study of the coupled intersubband Landau level transitions in the limit of high in-plane magnetic fields [9]. The single-particle transition energy is then obtained by a proper extrapolation of the high-field data to zero magnetic field [10].

The purpose of this paper is to show that the photon drag (PD) effect yields a new method to directly observe the depolarization shift. In contrast to all above methods, our measurement can also be performed at room temperature.

* Corresponding author. Tel.: +41-56-310-4566; fax: +41-56-310-2646.

E-mail address: stephan.graf@psi.ch (S. Graf)

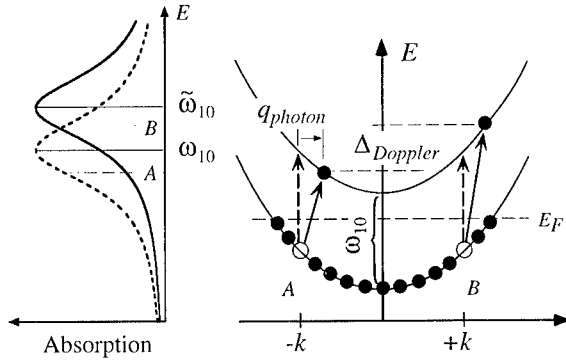


Fig. 1. Energy diagram with the nonvertical transitions between ground and first excited subbands by absorbing IR light with a wave vector q (for clarity, q has been greatly enlarged). Due to the Doppler effect, the absorption energy for a transition A at any negative k is smaller than the corresponding transition B at positive k by $\Delta_D = 2\hbar k q / m^*$. The transition probability (dashed line in the graph to the left) is equal for transitions A and B only at excitation with ω_{10} , although the absorption (full line) is maximal at the so-called dressed ISR $\tilde{\omega}_{10}$.

While the optical properties are related to the plasmon excitation with a virtually negligible propagation vector, the photon drag is a current which is driven by the transfer of momentum from the photon to the electron system. An ISR excited electron with wave vector k_2 leaves an empty state (hole) in the ground subband with $k_1 = k_2 - q$, where $q = 2\pi\nu n/c$ is the photon wave vector with the refractive index n in GaAs, Fig. 1. The thereby excited currents are proportional to the corresponding relaxation time. Since the transition energy depends on the in-plane velocity of the electron in the direction of the light propagation (Doppler effect!), the PD signal should be decomposed into its so-called direct and resonant parts [11–14]. The direct part is a consequence of the direct momentum transfer from the photon to the electron system and is thus proportional to the absorption, full line in the left of Fig. 1, and the photon momentum $p = \hbar q$. The resonant part is due to the Doppler effect and the difference in the subband momentum relaxation rates, $\tau_1 - \tau_2$.

This second contribution reveals the single-electron transition energy ω_{10} , since, its zero crossing corresponds to the energy at which the transition probability (dashed line in the left of Fig. 1) for any negative k (measured with respect to the light prop-

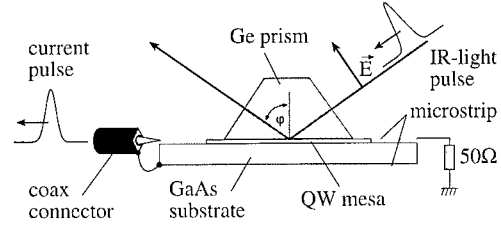


Fig. 2. Setup of the signal detection, where the active QW layer is integrated into a microstrip transmission line. The attenuated total reflection incoupling of the light is accomplished using a Ge-prism placed on top of the sensitive area.

agation direction) is equal to the corresponding transition at positive k (transitions A and B in Fig. 1). The current is obtained by summing over all possible k -states, yielding obviously zero in this case.

The full theoretical treatment of the problem, employing the self-consistent field method, is given by Załuzny [15]. He shows that the ω -dependence of the direct part coincides with the spectral dependence of the IS absorption coefficient. The line shape of the resonant component is no longer exactly antisymmetric, as assumed in the simple case [11,12,14] when omitting the depolarization effect. However, the sign change, which we will determine in the experiment, still occurs at the undressed resonance frequency ω_{10} .

The samples were grown by molecular-beam epitaxy and consist of a 30 period modulation doped multi QW system made of 82 Å GaAs wells and 260 Å $\text{Al}_{0.35}\text{Ga}_{0.65}\text{As}$ barriers, with $0.87 \cdot 10^{12} \text{ cm}^{-2}$ electrons per well. The top and bottom layers adjacent to the multi-QW structure were designed to properly compensate for, surface charge and the background doping in the buffer layer and substrates, respectively. The Fermi energy lies between the first two subbands, and therefore, also at room temperature (RT), a single IS-resonance is observed. The signal detection scheme relies on the integration of the active QW layer into a microstrip, forming a microwave transmission line [16,17] (Fig. 2). Intense far-infrared (FIR) light pulses are provided by the free electron laser of the FOM institute for plasma physics (FELIX). Pulse transients and radiation wavelength used are in the range of 1–5 ps and 8–15 μm , respectively. All the ISR experiments were performed at RT.

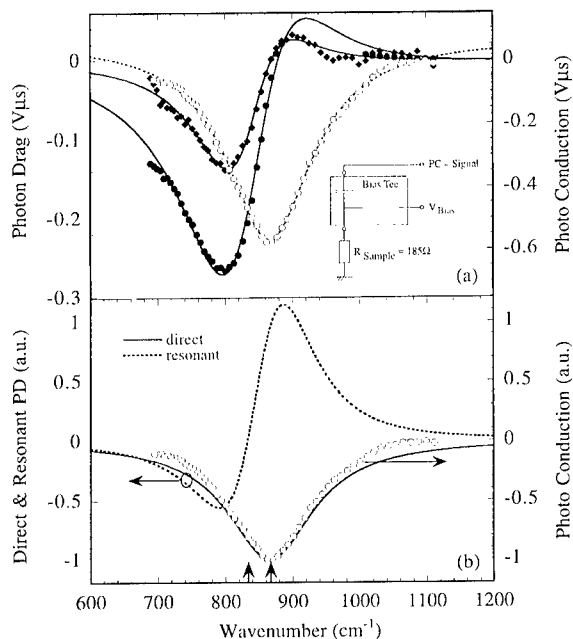


Fig. 3. (a) Intersubband spectra at RT of the GaAs/AlGaAs MQW system obtained under positive, zero and negative bias. The photo conduction (PC) measurement (open circles) performed at ± 0.3 V bias is obtained by subtracting the signals of either polarity. The photon drag (PD) spectra (diamonds), is obtained by adding the signals, and is measured at zero bias (full circles). The inset shows the schematic of the biasing electronic network. (b) The decomposition spectra of the PD fit using the Załuzny model to the data shown in (a). The peak position of the PC spectra (right arrow) is blue shifted from the zero crossing of the resonant PD part (left arrow).

In order to have the same conditions, for an accurate comparison between the PD and the ISR absorption, pulsed photocurrent and photo conduction (PC) measurements have been performed under, respectively, zero, positive or negative bias, Fig. 3 (inset). For better signal to noise ratios, we integrated over the entire macropulse of FELIX.¹ The mechanism of the in-plane PC can be understood as a simple electron heating effect and thus is directly related to the absorbed power. Tedious transmission measurements are circumvented with this method. The PC spectrum, shown in Fig. 3(a) (open circles), has a Lorentzian line shape with the

peak position at 866 cm^{-1} , in good agreement with the resonance position obtained by attenuated total reflection (ATR) measurements with a Fourier transform spectrometer. The constant offset visible far from the resonance stems from the inequality of the conductivity for the two bias polarities. The PD signal has been obtained from the same measurements by adding the signals of each polarity. The spectral response in this way obtained, is corrected for offset and plotted in Fig. 3(a) (diamonds) together with the direct measurement of the photon drag (full circles) at zero bias. The direct signal is stronger, since losses in the biasing electronic network (bias-Tee) were omitted. Unfortunately, some measurement points are missing in the spectrum due to a temporary blackout of the IR source. Aside from this difference in strength, the deviation in the line shape and position is negligible.

Shown in Fig. 3(b) are the direct and resonant parts of the PD, extracted from the fitted experimental PD spectra, applying the theory of Załuzny. The value for the relaxation time ratio is found to be 1.4.² The obtained bare intersubband spacing ω_{10} is found to be 833 cm^{-1} , which corresponds to a shift of the peak resonance from the PC measurement by as much as 33 cm^{-1} (cf. the two arrows of Fig. 3(b)), illustrating the importance of screening even at RT. This value is comparable to the blueshift of 50 cm^{-1} predicted by Załuzny in his recent paper [15]. In his calculation, a slightly narrower QW system has been used, and the temperature has been set to $T = 0 \text{ K}$. According to a previous paper of Załuzny [18], the depolarization shift for comparable QW systems is reduced by approximately 10% at $T = 300 \text{ K}$, in fair agreement with our experiment.

To conclude, the role of collective effects in the ISR has been demonstrated by the comparison of the absorption with the photon drag effect. Our combined ISR experiments on GaAs/AlGaAs QW systems show for the first time that the undressed resonance position is apparent from a direct experiment, providing a benchmark for testing the validity of many-body

¹ FELIX produces micropulses at 1 ns intervals during a macropulse which was here $5.4 \mu\text{s}$ long.

² According to the argumentation given in Ref. [19], the maximum value for the momentum time ratio can be estimated from $\mu_{\text{Hall}}(300 \text{ K}) \simeq 7800 \text{ cm}^2/\text{V s}$ and from the absorption line width $\Gamma_{\text{ATR}} \simeq 19.3 \text{ meV}$, yielding an upper limit of approximately 4.5.

interaction models. This technique has been applied to study the depolarization shift dependence on excitation intensity [20].

Acknowledgements

We gratefully acknowledge the support by the FOM Institute in providing the required beam time on FELIX. Part of the work is supported by the SNF.

References

- [1] T. Ando, A.B. Fowler, F. Stern, *Rev. Mod. Phys.* 54 (1982) 437.
- [2] R.J. Warburton, K. Weilhammer, J.P. Kotthaus, M. Thomas, H. Kroemer, *Phys. Rev. Lett.* 80 (1998) 2185.
- [3] D. Huang, G. Gumbs, M.O. Manasreh, *Phys. Rev. B* 52 (1995) 14 126.
- [4] M.O. Manasreh, F. Szmulowicz, D.W. Fischer, K.R. Evans, C.E. Stutz, *Appl. Phys. Lett.* 57 (1990) 1790.
- [5] K. Craig, B. Galdrikian, J.N. Heyman, A.G. Markelz, J.B. Williams, M.S. Sherwin, K. Campman, P.F. Hopkins, A.C. Gossard, *Phys. Rev. Lett.* 76 (1996) 2382.
- [6] M. Ramsteiner, J.D. Ralston, P. Koidl, B. Dischler, H. Beibl, J. Wagner, H. Ennen, *J. Appl. Phys.* 67 (1990) 3900.
- [7] R. Sasagawa, H. Sugawara, Y. Ohno, H. Nakajima, S. Tsujino, H. Akiyama, H. Sakaki, *Appl. Phys. Lett.* 72 (1998) 719.
- [8] K. Ensslin, D. Heitmann, K. Ploog, *Phys. Rev. B* 39 (1989) 10 879.
- [9] E. Batke, G. Weimann, W. Schlapp, *Phys. Rev. B* 43 (1991) 6812.
- [10] G. Brozak, B.V. Shanabrook, D. Gammon, D.S. Katzer, *Phys. Rev. B* 47 (1993) 9981.
- [11] S. Luryi, *Phys. Rev. Lett.* 58 (1987) 2263.
- [12] M.I. Stockman, L.N. Pandey, T.F. George, *Phys. Rev. Lett.* 65 (1990) 3433.
- [13] A.D. Wieck, H. Sigg, K. Ploog, *Phys. Rev. Lett.* 64 (1990) 463.
- [14] H. Sigg, E. Rosencher, B. Vinter, B. Levine (Eds.), *Intersubband Transitions in Quantum Wells*, Plenum Press, New York, 1992.
- [15] M. Zajączny, *Solid State Commun.* 103 (1997) 435.
- [16] H. Sigg, S. Graf, M. Kwakernaak, B. Margotte, D. Erni, P. van Son, K. Köhler, *Superlattices Microstruct.* 19 (1996) 105.
- [17] H. Sigg, M.H. Kwakernaak, B. Margotte, D. Erni, P. van Son, K. Köhler, *Appl. Phys. Lett.* 67 (1995) 2827.
- [18] M. Zajączny, *Phys. Rev. B* 49 (1994) 2923.
- [19] H. Sigg, P. van Son, K. Köhler, *Surface Science* 361/362 (1996) 468.
- [20] S. Graf, H. Sigg, K. Köhler, W. Bächtold, submitted.



ELSEVIER

Physica E 7 (2000) 204–207

PHYSICA E

www.elsevier.nl/locate/physa

Linewidth and dephasing of THz-frequency collective intersubband transitions in a GaAs/AlGaAs quantum well

J.B. Williams^{a,*}, M.S. Sherwin^a, K.D. Maranowski^b, C. Kadow^b, A.C. Gossard^b^aPhysics Department and Center for Terahertz Science and Technology, University of California, Santa Barbara, CA, USA^bMaterials Department, University of California, Santa Barbara, CA, USA

Abstract

Terahertz-frequency intersubband (ISB) transitions in semiconductor quantum wells are of interest due to the potential for making devices that operate at THz frequencies, and the influence of many-body interactions on the intersubband dynamics. We present measurements of the linear absorption linewidth of ISB transitions in a single 40 nm delta-doped GaAs/Al_{0.3}Ga_{0.7}As square quantum well, with a transition energy of order 10 meV (3 THz). Separate back- and front-gates allow independent control of charge density ($0.1\text{--}1 \times 10^{10} \text{ cm}^{-2}$) and DC bias ($-2.5\text{--}0.5 \text{ mV/nm}$). A picture of scattering of the intersubband plasmon into single-particle excitations qualitatively explains the DC bias dependence of the line-width data. © 2000 Elsevier Science B.V. All rights reserved.

Keywords: Terahertz intersubband transitions; Intersubband linewidth; Collective effects

In an n-type modulation-doped GaAs/AlGaAs quantum well, confinement of electrons to the well breaks the continuum of conduction band states into subbands. Optically excited transitions between subbands are the basis of several promising new devices, such as detectors [1] and quantum cascade lasers [2,3], which would operate at THz frequencies. An important parameter for the operation of the devices is the linewidth of the intersubband (ISB) transition. The quantum well is also interesting in its own right as a model system for testing many-body theories. The

ISB excitation of the quantum well is known to be a collective mode of the 2D electron gas, the ISB plasmon [4]. The width of a homogeneously broadened absorption line is proportional to the dephasing rate of the ISB plasmon. Our goal is to better understand the dephasing of the ISB plasmon at THz frequencies.

The sample used was a 40 nm GaAs square well, grown by molecular beam epitaxy on a semi-insulating substrate. It consists of 100 nm GaAs; 180 nm superlattice (30 periods of 3 nm GaAs, 3 nm Al_{0.3}Ga_{0.7}As); 100 nm Al_{0.3}Ga_{0.7}As; Si delta-doped layer of charge concentration $5 \times 10^{11} \text{ cm}^{-2}$; 10 nm Al_{0.3}Ga_{0.7}As barrier; 8.5 nm GaAs quantum-well backgate; a barrier and doping layer identical to the above; 490 nm Al_{0.3}Ga_{0.7}As; Si delta-doped layer of charge concen-

* Corresponding address: Quantum Institute, University of California, Santa Barbara, CA 93106, USA. Fax: +1-805-893-4170.

E-mail address: jwilliam@physics.ucsb.edu (J.B. Williams)

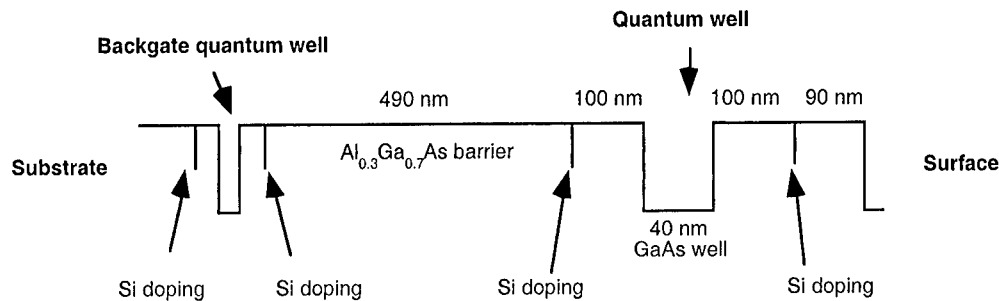


Fig. 1. Conduction band-edge profile.

tration $3 \times 10^{11} \text{ cm}^{-2}$; 100 nm $\text{Al}_{0.3}\text{Ga}_{0.7}\text{As}$ barrier; 40 nm GaAs quantum well; a barrier layer identical to the above; Si delta-doped layer of charge concentration $1 \times 10^{12} \text{ cm}^{-2}$; 90 nm $\text{Al}_{0.3}\text{Ga}_{0.7}\text{As}$; and a 10 nm GaAs capping layer. A sketch of the conduction band is shown in Fig. 1. The backgate is a narrow, doped quantum well which is not optically active at the frequencies of interest, and was used to control the charge density in the wide quantum well via the field effect. There are several conduction subbands in the well, with the energy separation of the lowest two subbands tunable over a range of 10–20 meV. In this work, only the lowest subband was occupied, and we measured only transitions between the lowest two subbands.

A $6 \text{ mm} \times 6 \text{ mm}$ sample was cleaved from the wafer. Separate ohmic contacts were made to the backgate and quantum well. A 200 nm thick Al Schottky contact was evaporated onto the surface of the sample, on a $6 \text{ mm} \times 4 \text{ mm}$ rectangular area, to form the frontgate. Another 200 nm thick layer of Al was evaporated onto the back side of the sample, so that the Al layers on both sides of the semiconductor sample form a parallel-plate waveguide (see Fig. 2).

By controlling the voltages applied to the frontgate, QW, and backgate, the charge density in the well and the DC electric field at the well can be independently varied. Thus, we can independently vary the charge density and DC electric field and examine the behavior of the ISB absorption linewidth.

The charge density in the well was measured using capacitance–voltage profiling. The frontgate and quantum well are two sheets of charge which form a parallel-plate capacitor. Using an AC technique, we

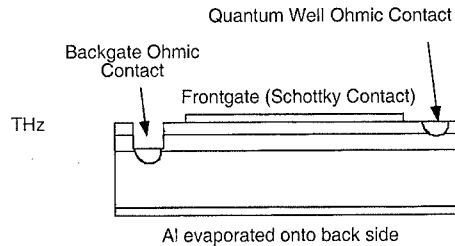


Fig. 2. Cross-section view of processed sample with all contacts indicated, and edge coupling geometry shown.

measure this capacitance versus frontgate voltage, V_{fg} . The capacitance signal is equal to dQ/dV_{fg} , where Q is the charge in the quantum well. This is integrated to find the charge density.

The DC electric field is not measured, but is calculated from the applied gate voltages and sample dimensions using the following formula:

$$\text{field} = \frac{V_{\text{fg}}}{2d_{\text{fg}}} - \frac{V_{\text{bg}}}{2d_{\text{bg}}},$$

where $V_{\text{fg(bg)}}$ is the frontgate (backgate) voltage with respect to the quantum well voltage, and $d_{\text{fg(bg)}}$ is the distance of the frontgate (backgate) from the quantum well. In addition to the applied field there is a fixed, built-in electric field whose magnitude is found from the absorption data to be about 0.3 mV/nm.

The spectra were measured with a Fourier transform IR spectrometer, using the edge-coupling geometry, as shown in Fig. 2. A polarizer was inserted after the sample to select the component of the transmitted light with polarization in the growth direction. The transmitted light was then detected by a bolometer.

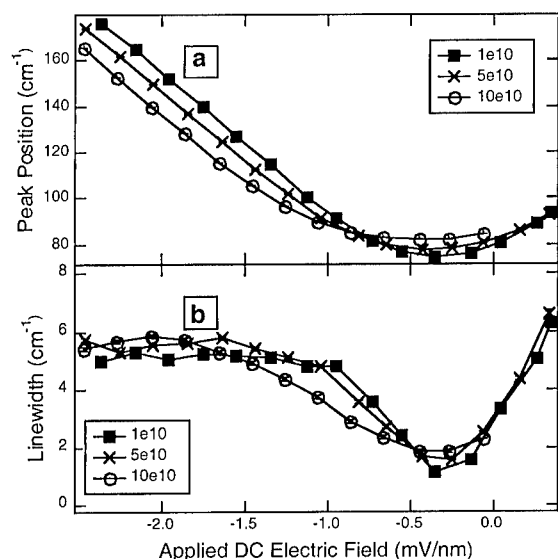


Fig. 3. Position of the absorption peak (a) and half-width at half-max (b) versus applied DC electric field, at charge densities of 1, 5, and $10 \times 10^{10} \text{ cm}^{-2}$.

Each raw spectrum, with electrons in the well, was normalized to the spectrum measured with the well depleted by the gates. The attenuation coefficient is given by

$$\alpha(\omega) = \frac{1}{\text{sample length}} \ln \frac{I(\text{empty})}{I(\text{full})},$$

where ω is the frequency, $I(\text{empty})$ is the transmitted intensity versus frequency with the well depleted of electrons, and $I(\text{full})$ is the transmitted intensity versus frequency with the well full of electrons. From a fit of the absorption spectrum to a Lorentzian line shape function, we obtain the peak position, linewidth, and area of the absorption curve.

The absorption data were measured at a temperature of 2.3 K. The peak positions are plotted against applied DC field, for several charge densities, in Fig. 3a. The peak position is tunable by over a factor of two, from 75 to over 160 cm^{-1} . Since this is a symmetric quantum well, the peak position should be symmetric about its minimum value at zero DC field. The peak position shows the expected quadratic dependence on DC field. However, the minimum occurs at an applied field of -0.3 mV/nm , which implies that the sample has an additional fixed, built-in field of $+0.3 \text{ mV/nm}$.

The linewidths (half-width at half-max) are plotted against applied DC field, for the same set of charge densities, in Fig. 3b. The data shows several interesting features. First, the linewidth has a strong field dependence, dropping dramatically to a minimum at zero bias (minimum which coincides with the minimum in peak position). Second, the field dependence is greater at low charge densities than at high charge densities. Third, the linewidth data are asymmetric about zero field, saturating at $5\text{--}6 \text{ cm}^{-1}$ for negative tilts (more negative frontgate) but appearing to rise higher than that for positive tilts (more positive frontgate).

The existence of a sharp minimum in the field dependence of the linewidth cannot be explained by assuming that the line is inhomogeneously broadened. With the ionized donors 100 nm away from the well, the most likely source of inhomogeneous broadening is an inhomogeneous well-width (electrons in different parts of the sample see a different width, and thus absorb at different frequencies). However, this inhomogeneity would be weakest away from flat-band, when electrons everywhere in the plane are pushed against one side of the well and see a potential which is roughly triangular, independent of the position of the other side of the well. This would lead to a minimum in the linewidth away from flat-band, which is the opposite of what we observe. Thus, we believe that the line is homogeneously broadened, and therefore the linewidth is determined by relaxation dynamics.

The linewidth minimum at flat-band can be qualitatively explained by a model of plasmon scattering [5]. The intersubband excitation created by photon absorption is properly described as a collective mode of the 2DEG, the intersubband plasmon, with wave vector $\mathbf{k} = \mathbf{0}$ (Fig. 4). The plasmon energy is blue-shifted from the $\mathbf{k} = \mathbf{0}$ single-particle excitations, an effect known as the depolarization shift. The plasmon can be dephased by scattering elastically into the continuum of single-particle excitations, if sufficient momentum transfer is supplied. The scattering rate should correlate to q_{min} , the minimum wave vector required for scattering into the SPE continuum; greater q_{min} leads to less scattering. For our well, at constant charge density, q_{min} is maximized at flat-band, as follows: The depolarization shift has a maximum at flat-band, due to the maximum in oscillator strength which occurs

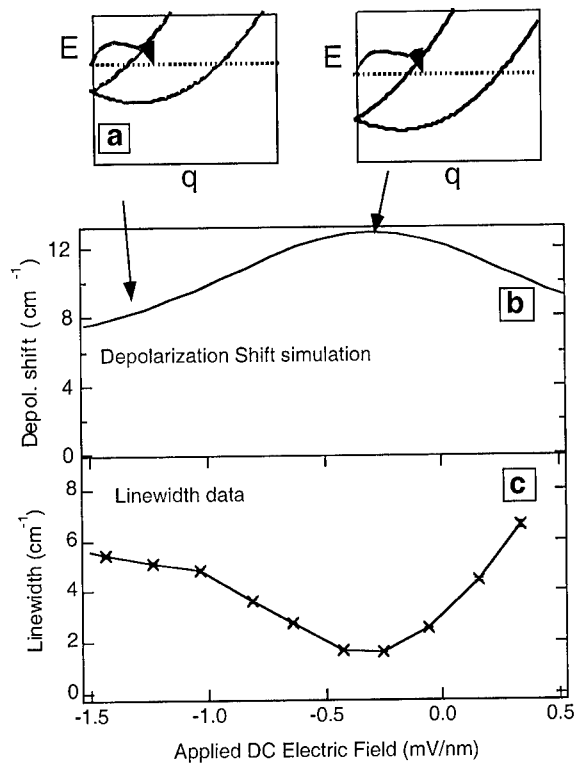


Fig. 4. Scattering of the intersubband plasmon. Plasmon energy is indicated by dotted line, while single-particle excitations lie between the parabolic curves (a). Calculated depolarization shift (b) and measured linewidth (c) versus DC electric field.

when the ground and excited subband wave functions overlap most strongly at flat-band. This maximum in depolarization shift means that q_{\min} has a maximum at flat-band, which explains the observed minimum in linewidth.

Note that increasing the charge density increases the depolarization shift, but does not necessarily increase q_{\min} , since the SPE spectrum becomes broader. Thus, the density dependence in this picture is not obvious.

In conclusion, we find that the absorption linewidth depends strongly on the DC electric field, dropping sharply to as low as 1 cm^{-1} at zero DC bias. The field dependence of the linewidth suggests that the line is homogeneously broadened, and can be qualitatively explained by a model of scattering of the collective ISB plasmon into single-particle excitations. Future work aims to produce a quantitative calculation of the linewidth.

Acknowledgements

This work was funded by NSF-DMR, AFOSR, and ONR-MFEL.

References

- [1] C. Cates, J.B. Williams, M.S. Sherwin, K.D. Maranowski, A.C. Gossard, Proc. SPIE 3617 (1999) 58.
- [2] B. Xu, Q. Hu, M.R. Melloch, Appl. Phys. Lett. 71 (1997) 440.
- [3] M. Rochat, J. Faist, M. Beck, U. Oesterle, M. Illegems, Appl. Phys. Lett. 73 (1998) 3724.
- [4] T. Ando, A.B. Fowler, F. Stern, Rev. Mod. Phys. 54 (2) (1982) 437.
- [5] R.J. Warburton, K. Weilhammer, J.P. Kotthaus, M. Thomas, H. Kroemer, Phys. Rev. Lett. 80 (1998) 2185.



ELSEVIER

Physica E 7 (2000) 208–211

PHYSICA E

www.elsevier.nl/locate/physa

Nonlinear intersubband optical response of multiple-quantum-well structures

M. Załuźny*, C. Nalewajko

Institute of Physics, M. Curie Skłodowska University, pl. M. Curie Skłodowskiej 1, 20-031 Lublin, Poland

Abstract

We present a theoretical formalism, based on the transfer matrix method and the so-called sheet model, which describes light propagation in multiple-quantum-well (MQW) structures in the range of nonlinear intersubband absorption. Intensity of the transmitted light as a function of the input intensity is calculated for typical GaAs/GaAlAs MQW. A comparison with commonly used in literature slowly varying envelope approximation is also given. © 2000 Elsevier Science B.V. All rights reserved.

PACS: 78.66.–w; 42.50.Hz

Keywords: Light propagation; Saturation; Nonlinear response

It has been proved, both theoretically and experimentally, that for high intensities of the infrared radiation the nonlinear saturation of the intersubband optical absorption becomes important [1–6]. The usual theoretical approach to the problem of nonlinear optical response of multiple-quantum-well (MQW) structures is based on the slowly varying envelope approximation (SVEA) (see e.g. Ref. [2]). Here, we present a more general numerical approach to the above-mentioned problem. Our approach is based on the transfer matrix method and the so-called sheet model [7,8]. In this model a quasi-two-dimensional electron gas is approximated by a 2D conducting sheet having intensity-dependent conductivity [5,6].

We will concentrate on a simple transmission geometry similar to that studied theoretically (employing SVEA) by Almogly and Yariv [2].

The system under consideration is formed by a nonlinear MQW structure (occupying the region $0 \leq z < d_{\text{MQW}}$) sandwiched between two semi-infinite dielectrics. To simplify calculations we assume that the conductivity of the 2D sheet is determined only by intersubband transitions. We assume also that the sheets are located in the middle of the wells. Consequently, the whole system can be modeled by a stack of $1, 2, 3, \dots, m$ plane-parallel linear homogeneous layers with the nonlinear sheets located at the interfaces $z_{i,j} = z_{i+1}$, $\mathcal{N} = 1, 2, 3, \dots, N$ where N is the number of quantum wells in the structure. The stack is bounded by ambient (0) and substrate ($m+1$) media.

* Corresponding author. Fax: +48-81-5376191.

E-mail address: zaluzny@tytan.umcs.lublin.pl (M. Załuźny)

When incident light is polarized in the x - z plane there is only the single component of the magnetic field $\mathbf{H}(\mathbf{r}, t) = \mathbf{e}_y H(x, z) e^{-i\omega t}$. Since we are interested in the optical response at frequency ω the following relation between amplitudes of the magnetic field in the q and p ($p > q$) media (layers) may be written [9,8]:

$$\begin{bmatrix} H_{l+}^{(q)} \\ H_{l-}^{(q)} \end{bmatrix} = \mathbf{I}_{q,q+1} \prod_{n=q+1}^{p-1} \mathbf{L}_n \mathbf{I}_{n,n+1} \begin{bmatrix} H_{u+}^{(p)} \\ H_{u-}^{(p)} \end{bmatrix}. \quad (1)$$

In Eq. (1) $H_{\alpha+}^{(j)}$ and $H_{\alpha-}^{(j)}$ ($\alpha = l, u$) are the complex amplitudes of the magnetic field corresponding to the waves traveling in positive and negative z -directions, respectively. The subscript $l(u)$ indicates that we take the complex amplitude with respect to the plane $z_{j,j+1}(z_{j-1,j})$.

The matrix \mathbf{L}_j describes the effect of propagation through a homogeneous layer j . It is given by

$$\mathbf{L}_j = \begin{bmatrix} \exp(-ik_z^{(j)} d_j) & 0 \\ 0 & \exp(ik_z^{(j)} d_j) \end{bmatrix}, \quad (2)$$

where $k_z^{(j)} = (\omega/c) \sqrt{\epsilon_j - \epsilon_w \sin^2(\varphi)}$, φ is the angle of incidence in the ambient medium, ϵ_j (d_j) denotes the dielectric function (thickness) of the j th layer. [We assume that $\epsilon_0 = \epsilon_{m+1} = \epsilon_w$ where $\epsilon_w(\epsilon_b)$ is the dielectric function of the well (barrier) material.]

$\mathbf{I}_{i,j}$ is a 2×2 matrix accounting for the interface between the media i and j ($i = j + 1$). It can be calculated using appropriate boundary conditions.

When $z_{i,j} \neq z_{i+1}$ then [9,8]

$$\mathbf{I}_{i,j} = \frac{1}{t_{ij}} \begin{bmatrix} 1 & r_{ij} \\ r_{ij} & 1 \end{bmatrix}, \quad (3)$$

where $r_{ij} = (k_z^{(i)} \epsilon_j - k_z^{(j)} \epsilon_i) / (k_z^{(i)} \epsilon_j + k_z^{(j)} \epsilon_i)$ and $t_{ij} = 2k_z^{(i)} \epsilon_j / (k_z^{(i)} \epsilon_j + k_z^{(j)} \epsilon_i)$.

When $z_{i,j} = z_{i+1}$ then $\mathbf{I}_{i,j} \equiv \mathbf{I}_{i+1}^{2D}$ takes a more complicated form [8]

$$\mathbf{I}_{i+1}^{2D} = \frac{1}{t_{i+1}^{2D}} \begin{bmatrix} 1 & -r_{i+1}^{2D} \\ r_{i+1}^{2D} & (t_{i+1}^{2D})^2 - (r_{i+1}^{2D})^2 \end{bmatrix} \quad (4)$$

with

$$r_{i+1}^{2D} = \frac{A(\omega, \varphi, |\mathcal{E}_z^{(i+1)}|^2)}{1 + A(\omega, \varphi, |\mathcal{E}_z^{(i+1)}|^2)}, \quad (5)$$

$$t_{i+1}^{2D} = \frac{1}{1 + A(\omega, \varphi, |\mathcal{E}_z^{(i+1)}|^2)} \quad (6)$$

and

$$A(\omega, \varphi, |\mathcal{E}_z^{(i+1)}|^2) = \frac{2\pi \tilde{\sigma}_{zz}^{2D}(\omega, |\mathcal{E}_z^{(i+1)}|^2)}{c \sqrt{\epsilon_w}} \times \tan(\varphi) \sin(\varphi),$$

where $\tilde{\sigma}_{zz}^{2D}(\omega, |\mathcal{E}_z^{(i+1)}|^2)$ is the intensity-dependent 2D conductivity [5,6], $\mathcal{E}_z^{(i+1)} = E_z^{(i+1)+} = E_z^{(i+1)-}$ and $E_z^{(i+1)-}$ ($E_z^{(i+1)+}$) denotes the z component of the electric field before (beyond) the \mathcal{N} th sheet. (Since we consider only the intersubband transitions and $\epsilon_i = \epsilon_j = \epsilon_w$ the normal component of the electric field E_z is continuous during the crossing of the sheet [8].)

In this work we employ a simple one-electron two-subband saturation model for the 2D intersubband conductivity [5,6]

$$\tilde{\sigma}_{zz}^{2D}(\omega, |\mathcal{E}_z^{(i+1)}|^2) = \frac{\sigma_{zz}^{2D}(\omega)}{1 + |\mathcal{E}_z^{(i+1)}|^2 / (\mathcal{E}_z^{\text{sat}})^2 [\delta^2(\omega) + 1]}, \quad (7)$$

where

$$\sigma_{zz}^{2D}(\omega) = \frac{N_S e^2 f_{12} \hbar}{2m\Gamma} \frac{i}{\delta(\omega) + i}. \quad (8)$$

Here $\delta(\omega) = (\hbar\omega - E_{21})/\Gamma$ is the normalized detuning of the incident light from the intersubband energy E_{21} , $\mathcal{E}_z^{\text{sat}} = (\Gamma \bar{\Gamma})^{1/2} / |ez_{12}|$ is a saturation electric field, $f_{12} = 2m\hbar^{-2} E_{21} z_{12}^2$ is the oscillator strength connected with $1 \rightarrow 2$ transitions ($f_{12} \approx 1$), $\tau = \hbar/\Gamma$ is the dephasing time connected with $1 \rightarrow 2$ transitions, $\bar{\tau} = \hbar/\bar{\Gamma}$ is the phenomenological lifetime, e and m are the charge and the effective mass of the electron, respectively, and finally, N_S is the surface electron concentration. (We assume that only ground subband is occupied.)

Since 2D conductivity is the function of $|\mathcal{E}_z|^2$ a recursion method was used to determine the relation between the output light intensity $I^{\text{out}} (= [c/8\pi\sqrt{\epsilon_w}] |H_{u+}^{(m+1)}|^2)$ and the input light intensity $I^{\text{in}} (= [c/8\pi\sqrt{\epsilon_w}] |H_{l+}^{(0)}|^2)$. We move from the output side of the MQW (medium $m+1$) to the input side (medium 0). For given I^{out} ($H_{u+}^{(m+1)}$) one calculates, employing Eqs. (1)–(3) appropriate magnetic field amplitudes and $|\mathcal{E}_z^{(i+1)}|^2$. (Since the substrate is lossless

the phase of $H_{i+}^{(m+1)}$ can be set to zero without loss of generality.) Knowing $|\mathcal{E}_z^{(i)}|^2$, one calculates the intensity-dependent conductivity (7) corresponding to \mathcal{N} th sheet and then using Eqs. (1)–(8) one can calculate appropriate magnetic field amplitudes and $|\mathcal{E}_z^{(i+1)}|^2$. The procedure is continued until the amplitudes $H_{i+}^{(0)}$ and $H_{i-}^{(0)}$ are obtained.

Now, we recall the relation between I^{out} and I^{in} resulting from SVEA [10]

$$-A_{\text{SQW}}(\omega, \varphi)N = \frac{I^{\text{out}} - I^{\text{in}}}{I^{\text{sat}}(\varphi)[\delta^2(\omega) + 1]} + \ln \frac{I^{\text{out}}}{I^{\text{in}}}, \quad (9)$$

where $I^{\text{sat}}(\varphi) = (c\sqrt{\epsilon_w}/8\pi)[\mathcal{E}_z^{\text{sat}}/\sin(\varphi)]^2$ and $A_{\text{SQW}}(\omega, \varphi) = [4\pi\text{Re}\sigma_{zz}^{2D}(\omega)/c\sqrt{\epsilon_w}] \tan(\varphi) \sin(\varphi)$ is the (linear) single QW absorptance.

[Eq. (9) is equivalent to that used by the authors of Ref. [2].]

It is worth noting that SVEA is based on the assumption that the propagation characteristics are determined only by the absorption of light. In other words, in contrast with the sheet model (or effective medium approach), effects connected with the generation of a back-propagation beam (multiple-reflections) are not considered in SVEA [2].

The detailed numerical calculations indicate that, like in the case of the linear absorption, SVEA breaks down only when a structure contains large number of quantum wells and φ is close to (or larger than) the critical angle φ_c . This angle corresponds to the total internal reflection at the interface between the ambient medium and MQW (with $N_s = 0$) treated as uniform uniaxial effective medium (for details see Ref. [8]). (We assume here that $\epsilon_0 = \epsilon_w > \epsilon_b$.) Fig. 1 illustrates the above-mentioned breakdown of SVEA. The numerical results have been obtained taking typical parameters of GaAs/GaAlAs multiple-quantum-well structure: $L_{\text{MQW}} \equiv d_{\text{MQW}}/N = 400 \text{ \AA}$, $L_{\text{QW}} = 85 \text{ \AA}$ (= the thickness of the quantum well), $N_s = 10^{12} \text{ cm}^{-2}$, $f_{12} = 0.9$, $2\Gamma = 11 \text{ meV}$, $E_{21} = 110 \text{ meV}$, $\epsilon_w = 10.9$ and $\epsilon_b = 9.8$. (The above parameters correspond to $I^{\text{sat}}(\varphi) = 2.8 \bar{\Gamma}/\Gamma \sin^2(\varphi) \text{ MW cm}^{-2}$ and $\varphi_c \cong 74^\circ$.) We show the dependence of the output intensity on the input intensity predicted by the sheet model and SVEA at $\varphi = 75^\circ$ for $\delta(\omega) = 0$ and ± 1 when $N = 200$. The violation of SVEA presented in Fig. 1 results mainly from the fact that in the above

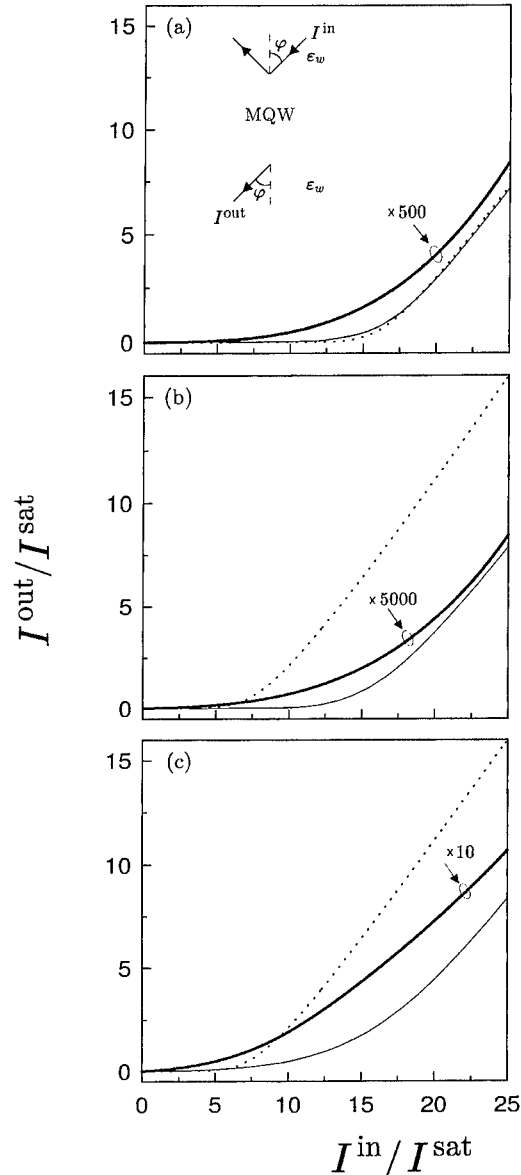


Fig. 1. The dependence of the output intensity on the input intensity [in the unit of saturation intensity $I^{\text{sat}} \equiv I^{\text{sat}}(\varphi = 75^\circ)$] predicted by the sheet model (thick solid curves) and SVEA (dotted curves) for the MQW structure described in the text at $\varphi = 75^\circ$ for different values of the detuning. The geometry is shown in the inset. For comparison we also present the dependence of I^{out} on I^{in} calculated using the sheet model and taking $\epsilon_b = \epsilon_w$ (thin solid curves). (a) $\hbar\omega = E_{21}$. (b) $\hbar\omega = E_{21} + \Gamma$. (c) $\hbar\omega = E_{21} - \Gamma$.

approximation multiple reflections are not taken into account. Let us assume for the moment that $N_S = 0$. When $\varphi > \varphi_c$ and the structure is sufficiently thick, then one can show (employing the effective medium approach) that only very small fraction of the incident light is transmitted (see Fig. 2 in Ref. [8]). The situation changes drastically when we neglect, like in SVEA, the difference between ε_w and ε_b . Then, all light is transmitted through MQW structure. It is the main reason why, even in the presence of the nonlinear intersubband absorption, the difference between the sheet model and SVEA reduces dramatically in the limit $\varepsilon_b \rightarrow \varepsilon_w$.

Although the numerical calculations reported in this paper are made for a single pass transmission geometry, it does not mean that the application of the sheet model is limited only to this geometry. Extension of our approach to other geometries is planned to be presented in a later paper.

References

- [1] F.H. Julien, J.M. Lourtioz, N. Herschkorn, D. Delacourt, J.P. Pocholle, M. Papuchon, R. Planel, G. Le Roux, *Appl. Phys. Lett.* 53 (1988) 116.
- [2] C. Almogly, A. Yariv, *J. Nonlin. Opt. Phys. Mat.* 4 (1995) 401.
- [3] K. Craig, B. Galdrikian, J.N. Heyman, A.G. Markels, J.B. Williams, M.S. Sherwin, K. Capman, P.F. Hopkins, A.G. Gossard, *Phys. Rev. Lett.* 76 (1996) 2382.
- [4] K.L. Vodopyanov, V. Chazapis, C.C. Phillips, B. Sung, J.S. Harris Jr., *Semicond. Sci. Technol.* 12 (1997) 708.
- [5] E.J. Roan, S.L. Chuang, *J. Appl. Phys.* 69 (1991) 3249.
- [6] M. Zakuźny, *Phys. Rev. B* 47 (1993) 3995, *J. Appl. Phys.* 74 (1993) 4716.
- [7] W.L. Mochan, R. Fuchs, R.B. Barrera, *Phys. Rev. B* 27 (1983) 771.
- [8] M. Zakuźny, C. Nalewajko, *Phys. Rev. B* 59 (1999) 13 043.
- [9] M.A. Azzam, N.M. Bashara, *Ellipsometry and Polarized Light*, North-Holland, Amsterdam, 1987.
- [10] M. Zakuźny, C. Nalewajko, to be published.



ELSEVIER

Physica E 7 (2000) 212–215

PHYSICA E

www.elsevier.nl/locate/physa

Second-harmonic generation in quantum wells: the role of many-body effects

Victor Bondarenko^{a,*}, Mirosław Załuźny^b

^aDepartment of Theoretical Physics, Institute of Physics, National Academy of Sciences of Ukraine, 46, prospekt Nauky, Kiev-28, 252650, Ukraine

^bInstitute of Physics, M. Curie-Skłodowska University, pl. M. Curie-Skłodowskiej 1, 20-031, Lublin, Poland

Abstract

We study theoretically the influence of the Coulomb interaction on the second-harmonic generation (SHG) connected with intersubband transitions in asymmetric quantum wells. Our approach is based on the time-dependent local density approximation. Numerical calculations are performed for asymmetric coupled double quantum well structure with small energy separation between ground and excited subbands. It was shown that the Coulomb interaction not only shifts the peak positions in SHG spectrum but also considerably modifies their height. The correct description of the above modification must take into account the nonlinear dependence of the exchange-correlation potential on the electron density. © 2000 Elsevier Science B.V. All rights reserved.

Keywords: Asymmetric quantum wells; Coulomb interaction; Second harmonic generation; Many-body effects

1. Introduction

Recently, Heyman et al. [1] have shown experimentally that in coupled asymmetric double quantum wells (ADQWs) not only the intersubband absorption spectrum but also the second-harmonic generation (SHG) spectrum can be very strongly affected by the Coulomb interaction.

In this paper we present, employing the TDLDA, a derivation of the second-order susceptibility $\chi_{zz}^{(2)}(2\omega)$

connected with SHG in two subband asymmetric QWs. We will show that the expression for $\chi_{zz}^{(2)}(2\omega)$ reported in Ref. [1] is not fully correct.

Our approach is based on the density matrix formulation developed in our previous papers [2,3]. By calculating the contribution of the indirect Coulomb interaction to the self-consistent effective perturbing potential we take into account the ‘additional driving term’ which resulted from the nonlinear dependence of the exchange-correlation potential upon the electron density.

The electron envelope wave function can be written as $|i, \mathbf{k}_{||}\rangle = \exp(i\mathbf{k}_{||}\mathbf{r}_{||})\varphi_i(z)$ where $\mathbf{k}_{||}$ ($\mathbf{r}_{||}$) is the wave vector (position) in the x – y plane. $\varphi_i(z)$ is the solution of the one-dimensional Schrödinger

* Correspondence address: c/o P. Argyrakis, Department of Physics, University of Thessaloniki, 54006, Thessaloniki, Greece. victor@kelfos.physics.auth.gr.

E-mail addresses: bondaren@iop.kiev.ua (V. Bondarenko), zaluzny@tytan.umcs.lublin.pl (M. Załuźny)

equation

$$\left[\frac{p_z^2}{2m} + V_{\text{QW}}(z) + V_{\text{H}}(z) + V_{\text{XC}}(z) \right] \varphi_i(z) = E_i \varphi_i(z), \quad (1)$$

where m is the effective mass of an electron, E_i is the minimum energy of the i th subband, $V_{\text{QW}}(z)$ determines the shape of the confining quantum well potential, $V_{\text{H}}(z)$ is the electrostatic Hartree potential, and $V_{\text{XC}}(z)$ denotes the exchange-correlation potential energy. We adopt a standard parametrized form (originally due to Gunnarson and Lundqvist [4]) for this potential.

The equation of motion for the matrix elements of density matrix ρ [in the representation of $|i, \mathbf{k}_{\parallel}\rangle$ ($i = 1, 2$)] is given by

$$\frac{\partial \rho_{ij}}{\partial t} = \frac{1}{i\hbar} [H^{(0)} + \Delta V, \rho]_{ij} - \frac{\Delta \rho_{ij}}{\tau_{ij}}, \quad (2)$$

where τ_{ii}^{-1} is the relaxation rate from the i th subband, $\tau_{ij}^{-1} = \tau_{ji}^{-1}$ is the off-diagonal elastic dephasing rate connected with $i \rightarrow j$ transitions, $\Delta \rho = \rho - \rho^{(0)}$, $\rho^{(0)}$ and $H^{(0)}$ are the unperturbed density matrix and Hamiltonian, respectively.

The self-consistent effective perturbing potential $\Delta V \equiv \Delta V(z, t)$ can be written in the form

$$\Delta V(z, t) = \Delta V_{\text{EXT}}(z, t) + \Delta V_{\text{H}}(z, t) + \Delta V_{\text{XC}}(z, t), \quad (3)$$

where $\Delta V_{\text{EXT}}(z, t)$ is the external perturbation, ΔV_{H} takes into account the direct Coulomb interaction [which (in the linear approximation) results in the depolarization effect (DE)] whereas ΔV_{XC} describes the contribution of the exchange-correlation interaction [which (in the linear approximation) results in the exciton-like effect (EE)] [5].

The change of the electron distribution $[\Delta n(z, t)]$ induced by $\Delta V(z, t)$ can be expressed through the density matrix as

$$\Delta n(z, t) = \text{Tr}[\Delta \rho \delta(z - z')]. \quad (4)$$

As in most of the previous papers we assume that $\Delta V_{\text{EXT}}(z, t)$ is small. In this limit a self-consistent solution of the problem can be obtained perturbatively by expanding $\Delta \rho$, ΔV and Δn (generally denoted as ΔX) in powers of $\Delta V_{\text{EXT}}(z, t)$ as

$$\Delta X(z, t) = \sum_{n=1,2} X^{(n)}(z, t). \quad (5)$$

Using the usual iterative method and Eqs. (2)–(5) we get

$$\frac{\partial \rho_{ij}^{(n)}}{\partial t} = \frac{1}{i\hbar} [\hat{H}, \rho^{(n)}]_{ij} + \frac{1}{i\hbar} \sum_{k>0} [V^{(k)}, \rho^{(n-k)}]_{ij} - \frac{\rho_{ij}^{(n)}}{\tau_{ij}}. \quad (6)$$

Let us assume that $\Delta V_{\text{EXT}}(z, t) = ez\tilde{E} \exp(-i\omega t) + \text{c.c.}$ When we neglect (for simplicity) the rectification effect then $X^{(n)}(z, t) = X^{(n)}(z, n\omega) \exp(-in\omega t)$.

The surface electronic polarization $[P_s(t)]$ can be also a series of similar expansion. The second-order term $[P_s^{(2)}(t)]$ is connected with $\rho^{(2)}$ by the relation

$$P_s^{(2)}(t) = \frac{-e}{\varepsilon_0} \text{Tr}[\rho^{(2)}(z, t)z] \\ = \varepsilon_0 \chi_{zz}^{(2)}(2\omega) \tilde{E}^2 \exp(-i2\omega t) + \text{c.c.}, \quad (7)$$

where

$$\chi_{zz}^{(2)}(2\omega) = \frac{-e}{\varepsilon_0 \tilde{E}^2} \sum_{i,j} \tilde{\rho}_{ij}^{(2)}(2\omega) z_{ji}, \quad (8)$$

is the SHG surface susceptibility, $z_{ij} = \int \varphi_i(z) z \varphi_j \times (z) dz$ and $\tilde{\rho}_{ij}^{(n)} = 2 \sum_{\mathbf{k}_{\parallel}} \rho_{ij}^{(n)}$.

The direct Coulomb contribution and the exchange-correlation contribution to the n th-order effective potential $V^{(n)}(z, n\omega)$ can be written in terms of $n^{(n)}(z, n\omega)$ as

$$V_{\text{H}}^{(n)}(z, n\omega) = -\frac{e^2}{\varepsilon_0 \varepsilon} \int_{-\infty}^z dz' \int_{-\infty}^{z'} dz'' n^{(n)}(z'', n\omega), \quad (9)$$

$$V_{\text{XC}}^{(n)}(z, n\omega) = V'_{\text{XC}}(z) n^{(n)}(z, n\omega)$$

$$+ \frac{1}{2} V''_{\text{XC}}(z) [n^{(1)}(z, n\omega)]^2 \delta_{n2}, \quad (10)$$

where $V'_{\text{XC}}(z)$, $V''_{\text{XC}}(z)$ are the first and second functional derivatives of $V_{\text{XC}}(z)$ with respect to the equilibrium density distribution of the electrons and ε is the averaged dielectric constant. At this point it is interesting to note that the second term in Eq. (10) accounts for the ‘additional driving term’ (ADT) which represents the nonlinear dependence of the exchange-correlation potential upon the sheet electron density, i.e. the case when $V'_{\text{XC}}(z) \neq 0$. It does not appear in the linear response. Note that in this paper we work in the standard static approximation, i.e. we neglect a frequency dependence of the exchange-correlation potential (for details see Ref. [6]).

Applying Eqs. (6), (8)–(10), the final expression for $\chi_{zz}^{(2)}(2\omega)$ is found to take rather a complicated form:

$$\chi_{zz}^{(2)}(2\omega) = \frac{-e^3 2N_s z_{12}^2 (z_{22} - z_{11})}{\epsilon_0} \frac{E_{21}^2 - (\hbar\omega + i\Gamma)^2}{[\tilde{E}_{21}^2 - (\hbar\omega + i\Gamma)^2]^2} \left\{ \left[\frac{E_{21}^2 + (2\hbar\omega + i\Gamma)(\hbar\omega + i\Gamma)}{\tilde{E}_{21}^2 - (2\hbar\omega + i\Gamma)^2} \frac{\tilde{E}_{21}^2 - (\hbar\omega + i\Gamma)^2}{E_{21}^2 - (\hbar\omega + i\Gamma)^2} \right. \right. \\ \left. \left. + \frac{\hbar\omega + i\Gamma}{2\hbar\omega + i\Gamma} \right] - \frac{z_{12}}{(z_{22} - z_{11})} \frac{\tilde{\alpha}_{21} E_{21} N_s}{\tilde{E}_{21}^2 - (2\hbar\omega + i\Gamma)^2} \left[\frac{E_{21}^2 + (2\hbar\omega + i\Gamma)(\hbar\omega + i\Gamma)}{E_{21}^2 - (\hbar\omega + i\Gamma)^2} + \frac{\hbar\omega + i\Gamma}{2\hbar\omega + i\Gamma} \right] \right. \\ \left. - \frac{z_{12}}{(z_{22} - z_{11})} \frac{4\tilde{Z}_{12} N_s^2 E_{21}^3}{[\tilde{E}_{21}^2 - (2\hbar\omega + i\Gamma)^2][E_{21}^2 - (\hbar\omega + i\Gamma)^2]} \right\}. \quad (11)$$

Here $E_{21} = E_2 - E_1$, N_s is the surface electron concentration (we assume that only ground subband is occupied), $\Gamma = \hbar/\tau_{12}$, $\tilde{\Gamma} = \hbar/\tau_{11} = \hbar/\tau_{22}$, $\tilde{E}_{21} = E_{21}[1 + 2\tilde{\alpha}(1, 2; 1, 2)N_s/E_{21}]^{1/2}$ is the intersubband energy shifted by DE and EE [5], $\tilde{\alpha}_{21} = \tilde{\alpha}(1, 2; 2, 2) - \tilde{\alpha}(1, 2; 1, 1)$, $\tilde{\alpha}(i, j; k, l) = (e^2/\epsilon_0 \epsilon)L(i, j; k, l) + Y(i, j; k, l)$, with

$$L(i, j; k, l) = \int_{-\infty}^{\infty} dz \left(\left[\int_{-\infty}^z dz' \varphi_i(z') \varphi_j(z') \right] \times \left[\int_{-\infty}^z dz' \varphi_k(z') \varphi_l(z') \right] \right), \quad (12)$$

$$Y(i, j; k, l) = \int_{-\infty}^{\infty} dz \varphi_i(z) \varphi_j(z) \varphi_k(z) \varphi_l(z) V'_{XC}(z) \quad (13)$$

and

$$\tilde{Z}_{12} = \frac{1}{2} \int dz [\varphi_1(z) \varphi_2(z)]^3 V''_{XC}(z). \quad (14)$$

For comparison, the authors of Ref. [1] gave (without presenting details of the calculations) the following expression for the susceptibility:

$$\chi_{zz}^{(2)}(2\omega) = \frac{-e^3 N_s 3z_{21}^2 (z_{22} - z_{11})}{\epsilon_0} \times \frac{[(E_{21} + i\Gamma)^2 - (\hbar\omega)^2](E_{21} + i\Gamma)^2}{[(\tilde{E}_{21} + i\Gamma)^2 - (2\hbar\omega)^2][(\tilde{E}_{21} + i\Gamma)^2 - (\hbar\omega)^2]^2}. \quad (15)$$

We should note that in the one-electron approximation [$\Delta V(z, t) = \Delta V_{\text{EXT}}(z, t)$] only Eq. (11) reduces to that derived by Tsang et al. [7]. Nevertheless, numerical calculations show that (in the one-electron limit) the difference between the spectral shapes of $|\chi_{zz}^{(2)}(2\omega)|^2$ resulting from Heyman's and Tsang's expressions is

negligibly small. Unfortunately, Heyman's expression gives incorrect sign for $\text{Im}[\chi_{zz}^{(2)}(2\omega)]$. It is connected

with the fact that Eq. (15) contradicts the well-known rule saying that the poles of the susceptibility should lie in the lower half of the complex-frequency plane [8]. This indicates that the authors of Ref. [1] introduced the damping factor in an incorrect way. It must also be noted that Eq. (15) does not include the ADT.

We have performed numerical calculations for the modulation-doped ADQW (similar to that studied in Ref. [1], with 85 and 75 Å GaAs wells separated by 25 Å $\text{Al}_{0.3}\text{As}_{0.7}\text{Ga}$ barrier taking $\Gamma = 0.42$ meV and $\tilde{\Gamma} = 0.1$ meV. Fig. 1 presents the spectral shape of $|\chi_{zz}^{(2)}(2\omega)|^2$ at $N_s = 2.5 \times 10^{11} \text{ cm}^{-2}$. The peak positions of $|\chi_{zz}^{(2)}(2\omega)|^2$ are denoted by the resonance photon energies $\hbar\omega_{\text{res}}^L$ and $\hbar\omega_{\text{res}}^H$. The calculations indicate (see the inset of Fig. 1) that these energies are very close to $\tilde{E}_{21}/2$ and \tilde{E}_{21} , respectively, but do not coincide with $E_{21}/2$ and E_{21} , as in the one-electron limit. Thus, similar to the case of linear response, the SHG peaks are shifted by the DE and EE. Note that, in the structure considered, the Coulomb correction to the intersubband resonant energy $\Delta E_{21} (= \tilde{E}_{21} - E_{21})$ is comparable with E_{21} .

Inspection of Fig. 1 (see also Ref. [9]) also shows that in contrast with the linear intersubband absorption, the height of the peaks in the SHG spectrum is also very strongly modified by the Coulomb interaction. In the structure considered here this interaction reduces (enhances) the peak at $\hbar\omega_{\text{res}}^L$ ($\hbar\omega_{\text{res}}^H$) even in orders of magnitude. It should be pointed out that such huge changes can be observed only in structures where ΔE_{21} is comparable with or more than E_{21} .

Fig. 1 shows that a correct description of the influence of the exchange-correlation part of the Coulomb

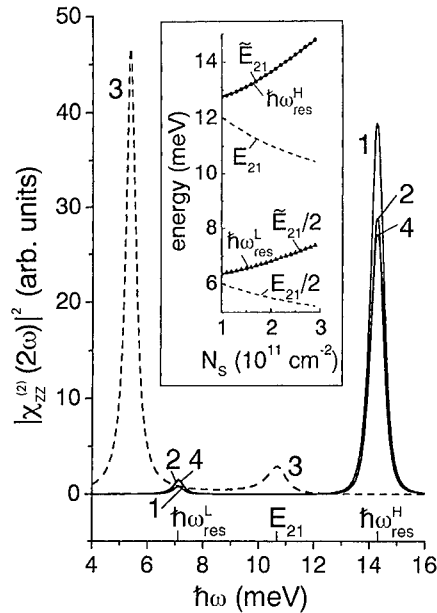


Fig. 1. Spectral dependence of $|\chi_{zz}^{(2)}(2\omega)|^2$ for the ADQW structure described in the text: 'exact' result (curve 1), 'exact' result but without ADT (curve 2), the one-electron approximation result (curve 3). Curve 4 is calculated employing Eq. (15). The inset shows the sheet electron density dependence of the resonance photon energies $\hbar\omega_{res}^L$ and $\hbar\omega_{res}^H$ as well as \tilde{E}_{21} (circles), and $\tilde{E}_{21}/2$ (triangles). For comparison the N_s dependence of E_{21} and $E_{21}/2$ is also given.

interaction on the SHG spectrum must take into account the ADT in the self-consistent perturbing potential [the second term in Eq. (10)]. As was mentioned this term appears due to the nonlinear dependence of the exchange-correlation potential upon the electron density. The ADT does not impact the peak positions at all. However, its influence on the susceptibility peak values is comparable with that induced by the linear term in Eq. (10). This is a novel feature of the exchange-correlation interaction: an effect of nonlinearity of the exchange-correlation potential,

which is different from the DE and EE in its influence on the SH susceptibility.

It is interesting to note that the above-mentioned peak height modification cannot be described even qualitatively by the simple replacement $E_{21} \rightarrow \tilde{E}_{21}$ in the one-electron expression for $\chi_{zz}^{(2)}(2\omega)$.

We would also like to note that the numerical values for $|\chi_{zz}^{(2)}(2\omega)|^2$ predicted by Eq. (15) are not far from those given by Eq. (11) provided that $\Gamma \ll E_{21}$, $\hbar\omega$ is close to the resonance energies, and the ADT is omitted.

In conclusion, the results obtained show that many-body effect can modify dramatically the second-harmonic spectrum of ADQWs when inter-subband resonance frequency of the structure belongs to the terahertz region. Electron–electron interaction not only shifts the peak positions in SHG spectrum but also considerably modifies their height. The direct and exchange-correlation contributions to the Coulomb interaction are always competing in their effect on the SHG spectrum. The indirect interaction is found to demonstrate a novel feature which results from the nonlinearity of the exchange-correlation potential.

References

- [1] J.N. Heyman, K. Craig, B. Galdrikian, M.S. Sherwin, K. Campman, P.F. Hopkins, S. Fafard, A.C. Gossard, Phys. Rev. Lett. 72 (1994) 2183.
- [2] M. Załuźny, Phys. Rev. B 51 (1995) 9757.
- [3] M. Załuźny, V. Bondarenko, J. Appl. Phys. 81 (1997) 3276.
- [4] O. Gunnarson, B.I. Lundqvist, Phys. Rev. B 13 (1976) 4274.
- [5] T. Ando, A. Fowler, F. Stern, Rev. Mod. Phys. 54 (1982) 437.
- [6] E.K.U. Gross, W. Kohn, Adv. Quantum Chem. 21 (1998) 255.
- [7] L. Tsang, D. Ahn, S.L. Chuang, Appl. Phys. Lett. 52 (1988) 697.
- [8] P.N. Butcher, D. Cotter, The Element of Nonlinear Optics, Cambridge University Press, Cambridge, 1993, p. 92.
- [9] M.S. Sherwin, K. Craig, B. Galdrikian, J. Heyman, A. Markelz, K. Campman, S. Fafard, P.F. Hopkins, A. Gossard, Physica D 83 (1995) 229.



ELSEVIER

Physica E 7 (2000) 216–219

PHYSICA E

www.elsevier.nl/locate/physce

Subband selective disorder in a quasi-2D system and its effect on the intersubband spectrum

M. Hackenberg^a, C. Metzner^{a,*}, M. Hofmann^b, G.H. Döhler^a

^a*Institut für Technische Physik I, Universität Erlangen, Erwin-Rommel-Str. 1, 91058 Erlangen, Germany*

^b*Institut für Technische Physik III, Universität Erlangen, Erwin-Rommel-Str. 1, 91058 Erlangen, Germany*

Abstract

We investigate theoretically the intersubband (IS) absorption spectra of a quantum well with a sub-monolayer of barrier material inserted at the well center z_c . This “perturbation layer” creates a random lateral potential modulation with different fluctuation amplitudes Δ_m for the ground ($m = 0$) and first excited ($m = 1$) subband. In the unbiased system, the 0-electrons become in-plane localized by the perturbation ($\Delta_0 > 0$), while the excited subband remains unaffected ($\Delta_1 = 0$), due to the node of its wave function at z_c . In this case of *selective disorder* our calculated IS spectra show at low carrier density a broad peak, reflecting the \vec{k} -spectrum of 0-electron states, in-plane localized in the “void areas” of the perturbation layer. For higher densities, a second, sharper peak occurs at lower energies, due to occupation of extended states. By applying a longitudinal electric field, the fluctuation amplitudes Δ_m of the two subbands can be continuously varied, up to the point where $\Delta_1 = \Delta_0$ (case of *correlated disorder*). The corresponding IS spectra gradually change to a single, very narrow line with an only weak dependence of position and width on carrier density. © 2000 Elsevier Science B.V. All rights reserved.

PACS: 78.20.Bh; 78.20.-e; 71.23.An

Keywords: Disorder; Potential fluctuation; Intersubband spectrum

1. Introduction

Interface roughness is one of the most important factors determining the linewidth of the IS resonance in semiconductor hetero-structures. Using advanced growth techniques, it is now possible to fabricate quantum wells with thickness fluctuations δa of only one atomic monolayer d_M . The lateral potential amplitude

Δ_m corresponding to these fluctuations is not very large in wide quantum wells, because of the small probability density of electrons in the interface region. Consequently, the scattering of electrons by interface defects is often considered as a weak perturbation, contributing to the homogeneous line broadening [1]. This approximation is justified, provided that the lateral “island size” l_0 of the interfaces is small compared to the Fermi-wavelength λ_F of the electron gas.

The situation is different in narrow wells, as they are used in devices with large IS energy differences $\varepsilon_1 - \varepsilon_0$, like, for example, the mid-infrared quantum

* Corresponding author. Tel. +49-9131-852-7282; fax: +49-9131-852-7293.

E-mail address: metzner@physik.uni.erlangen.de (C. Metzner)

cascade laser [2]. In such systems, the interface-induced lateral potential fluctuations can have a considerable amplitude. Then there arises the possibility of in-plane localization of electrons, depending however on the interface correlation length or average island size l_0 .

In the alloy limit $l_0 \rightarrow 0$ (“pseudo-smooth” interfaces), a homogeneous medium approximation is possible and the disorder broadening may be described by an electron self-energy with some finite imaginary part. In this regime, the IS resonance has an almost Lorentzian shape and its linewidth grows with decreasing well thickness.

In the extreme semiclassical limit $l_0 \rightarrow \infty$, the regions of different well thickness $a = a(x, y)$ can be treated like independent subsystems. In such an ideal situation, multiple sharp lines would be expected in the spectrum, reflecting the “quantization” of the well thickness in units of one atomic mono-layer d_M (As already observed in the case of interband luminescence).

Physically more interesting is the regime of coherent multiple scattering, when the island size is finite and comparable to the Fermi-wavelength $l_0 \approx \lambda_F$. In this case, the thicker areas of the well act on the electrons as attractive, lateral “quantum boxes”, causing in-plane localization and a corresponding level quantization. However, there is usually no direct signature of those effects in the IS spectrum, because the lateral potential modulation acts on both subbands simultaneously and in a similar way. It would therefore be desirable to design a system with optical transitions between a strongly disordered subband and some undisturbed “reference level”.

Such a situation can be approximately realized in a (remotely doped) quantum well with high-quality interfaces, in which disorder is purposefully introduced by placing a submonolayer of barrier material in the center z_c of the well. For a content of barrier atoms $x_b > 0.5$, the random voids in the layer will form attractive islands of some typical size l_0 . If the material of the perturbation layer is lattice-matched (no elastic strain), the disorder potential can be modeled by a δ -function along the growth axis. In the lateral directions, it is described by a binary-valued random distribution $U(x, y) \in \{0, 1\}$, with 0 and 1 corresponding to voids and clusters of the inserted layer, respectively. The effective in-plane perturbation acting on an electron with the subband wave function $\varphi_m(z)$

is then given by $V_m(x, y) = \Delta_m U(x, y)$, with the fluctuation amplitude $\Delta_m = V_0 d_M \varphi_m^2(z_c)$, where V_0 is the conduction band discontinuity. This perturbation potential acts selectively on the ground subband $m = 0$, as long as the node of the $m = 1$ -subband coincides with z_c . Note that there is also no intersubband mixing in this case. By applying an electric field, the subband wave functions are deformed, which is equivalent to an external tuning of the perturbation amplitudes Δ_m . Since these quantities determine, both, the degree of localization and the IS correlations, strong effects are expected for the IS spectrum.

In this paper, we analyze the situation described above in realistic computer simulations. First, random atomic in-plane profiles are generated, according to prescribed statistical properties of the perturbation layer, like the island size l_0 and the coverage x_b . For each of these profiles, the effective in-plane potentials (and 0–1 scattering matrix elements) are computed. Then, the Schrödinger equation of the multi-subband system subject to the lateral potential modulation is solved by an exact numerical diagonalization technique, neglecting all effects of the electron-electron interaction (band-bending, screening). The resulting disordered electron states are used to calculate the IS spectrum (for z-polarized light and $T = 0$ K) as a function of carrier density, using Fermi’s Golden Rule (compare Ref. [3]).

The organization of our paper is as follows. Section 2, we introduce our model system and some useful quantities. The results are then presented and discussed in Section 3.

2. The model system

We considered a GaAs quantum well of thickness $a = 10.5$ nm in an AlAs-matrix and assumed perfect (or “pseudo-smooth”) well–barrier interfaces. For reasons of simplicity, the perturbation layer was modeled as a one-monolayer thick AlAs-film with random voids. The voids (lateral quantum boxes) have a quadratic shape with linear dimensions l_0 , are statistically distributed in the plane and cover totally $1 - x_b = 0.3$ of the sheet area. Being interested only in the essential physical features of the system, we assumed that the electric field F and the carrier density n_s can be varied independently.

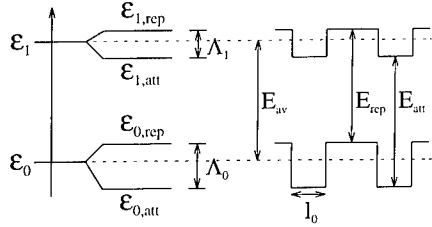


Fig. 1. Schematic lateral modulation of the subband edges and characteristic energies of the model system.

For the discussion of our simulation results it is useful to introduce some characteristic quantities, related to the position dependent subband energy edges $\varepsilon_m(x, y)$ in the laterally modulated quasi-2D system. Fig. 1 shows the splitting of the two undisturbed (= average) subband edges ε_m due to the lateral potential modulation, the fluctuation amplitudes Δ_m and the characteristic transition energies $E_{av} = \varepsilon_1 - \varepsilon_0$, E_{att} and E_{rep} (corresponding, respectively, to the average system, the attractive quantum boxes and the repulsive barrier regions). Note that for $\Delta_0 > \Delta_1$, the relation $E_{rep} < E_{av} < E_{att}$ is valid. Thus, in the semiclassical limit $l_0 \rightarrow \infty$ at sufficient carrier density, one would expect two IS lines below and above the average subband separation. The peak splitting $E_{att} - E_{rep} = \Delta_0 - \Delta_1$ is a direct measure of the “subband selectivity” of the lateral potential modulation. It disappears in the case of perfectly correlated disorder $\Delta_0 = \Delta_1$. However, in the more realistic cases discussed below, the peak positions can deviate from these semiclassical values, due to localization effects.

3. Results and discussion

The central part of Fig. 2 shows the results for the unbiased system, i.e. the case of perfectly *selective disorder* with $\Delta_0 = 27$ meV and $\Delta_1 = 0$. In this system state, the semiclassical transition energies would be $E_{rep} = 83$ meV, $E_{av} = 91$ meV and $E_{att} = 110$ meV.

We first consider a low density of $n_s = 1.9 \times 10^{11} \text{ cm}^{-2}$, where the Fermi level is located in the classically bound energy region $\varepsilon_{0,att} < \Phi < \varepsilon_{0,rep}$. Here we find a broad absorption peak at photon energies slightly below E_{att} . This peak is due to transitions between localized states of the 0-subband, confined

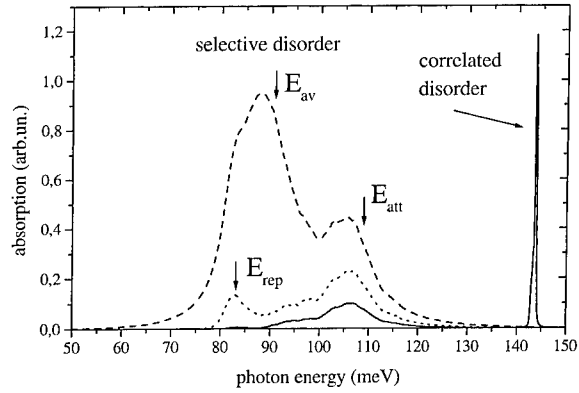


Fig. 2. Calculated IS spectra in the case of *selective disorder* for three different carrier densities: $n_s = 1.9 \times 10^{11} \text{ cm}^{-2}$ (full line), $n_s = 3.8 \times 10^{11} \text{ cm}^{-2}$ (dotted line) and $n_s = 1.9 \times 10^{12} \text{ cm}^{-2}$ (dashed line). The vertical arrows indicate the characteristic transition energies in the semiclassical limit. The sharp peak at 142 meV corresponds to the case of *correlated disorder*.

in the lateral quantum boxes (voids), and delocalized plane-wave states of the undisturbed excited subband (Compare Fig. 3(a)). Note that, in general, each initial state has finite overlap with many plane waves in the 1-subband, reflecting the broad Fourier spectrum of localized wave functions.

At density $n_s = 3.8 \times 10^{11} \text{ cm}^{-2}$, the Fermi level already exceeds the top of the lateral wells ($\Phi > \varepsilon_{0,rep}$) and extended states start to become occupied. The “local kinetic energy” $E_{kin}(x, y) = \Phi - \varepsilon_0(x, y)$ of these Fermi surface states is small in repulsive areas and high in the quantum box regions. Thus, the associated wave functions contain both low and high spatial frequency components and couple to the corresponding plane waves in the 1-subband (see Fig. 3(a)). In the IS spectrum, the low-frequency components produce a relatively narrow peak close to E_{rep} , while there is still some contribution at E_{att} from the quantum box regions.

At even higher densities $n_s = 1.9 \times 10^{12} \text{ cm}^{-2}$, the average kinetic energy of the Fermi edge states is large compared to the potential fluctuations Δ_0 . These states are only weakly modulated by the lateral potential profile and behave almost like in the undisturbed, or average system. Consequently, they contribute to the IS spectrum at energies around E_{av} .

We now turn to the case of perfectly *correlated disorder*, which is realized at an electric field of

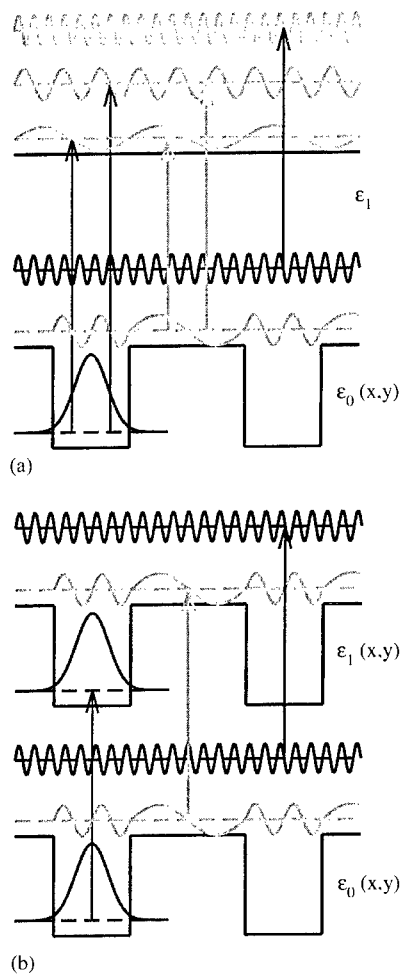


Fig. 3. Schematic explanation of the different contributions to the IS spectrum in the cases of *selective* and *correlated* disorder (Parts (a) and (b), respectively). The transition processes (groups of vertical arrows) depicted from left to right become subsequently active, when the corresponding initial states are occupied with increasing Fermi level.

$F = 260$ kV/cm. As shown in the right part of Fig. 2, the corresponding IS spectrum consists of a single and extremely narrow line, with the position and width depending only weakly on the carrier density. This is due to the parallel fluctuations of the two effective subband edges $\epsilon_1(x, y) - \epsilon_0(x, y) = E_{av} = \text{const}$ (see Ref. [3]). A very similar spectrum of (localized and extended) quantum states is formed in both subbands (see Fig. 3(b)) and IS transitions occur only between “correlated pairs” of wave functions (Small deviations from this rule may occur due to IS mixing effects). Since this special form of disorder shifts the initial and final level by almost the same amount, the transition energy is always close to E_{av} .

We conclude that the realization of our “computer experiment” would provide direct evidence for the IS correlation effects. In the case of selective disorder, the spectra yield information about the atomic “interface” profile of the perturbation layer.

Acknowledgements

One of the authors (C.M.) would like to thank the Deutsche Forschungsgemeinschaft DFG for financial support.

References

- [1] K.L. Campman, H. Schmidt, A. Imamoglu, A.C. Gossard, Appl. Phys. Lett. 69 (17) (1996) 2554.
- [2] J. Faist, F. Capasso, L. Sivco, C. Sirtori, A. Hutchinson, A. Cho, Science 264 (1994) 553.
- [3] C. Metzner, M. Hofmann, G.H. Döhler, Phys. Rev. B 58 (1998) 7188.

Absorption of in-plane polarized light in quasi-2D systems enabled by strong potential fluctuations

C. Steen^a, C. Metzner^{a,*}, M. Hofmann^b, G.H. Döhler^a

^a*Institut für Technische Physik I, Universität Erlangen, Erwin-Rommel-Strasse 1, 91058 Erlangen, Germany*

^b*Institut für Technische Physik III, Universität Erlangen, Erwin-Rommel-Strasse 1, 91058 Erlangen, Germany*

Abstract

We investigate theoretically the absorption of infrared radiation by quasi-2D conduction band electrons in strongly doped semiconductor quantum wells. Due to the break-down of the k -conservation rule in such disordered systems, absorption is possible not only with light polarized in growth direction, but also in the case of in-plane polarization. We start with realistic single particle states, localized in the layer plane by the potential fluctuations of the random impurity distribution. The absorption spectrum for both polarization modes is then calculated on the basis of these electron states, using Fermi's golden rule. For perpendicular polarization, our theory yields the usual resonance line at the intersubband energy separation $\hbar\omega_{\text{res}} = \epsilon_1 - \epsilon_0$, yet asymmetrically broadened by the disorder. The same model system shows for in-plane polarized light a broader absorption band in the low-energy range $0 \leq \hbar\omega < \hbar\omega_{\text{max}}$, which is due to non- k -conserving intra-subband transitions between localized states. With increasing electron density, this spectrum becomes narrower and its peak is red shifted more and more. When the disorder is reduced by modulation doping, intra-subband absorption can be observed only in the range of very small photon energies, e.g. $\hbar\omega_{\text{max}} \rightarrow 0$. Both effects can be explained by considering the properties of the disordered electron states. © 2000 Elsevier Science B.V. All rights reserved.

PACS: 78.20.Bh; 78.20.-e; 71.23.An

Keywords: Disorder; Free-carrier absorption; Intra-subband transition; Potential fluctuation

1. Introduction

In order to study intra-conduction band absorption in quasi-2D systems, the incoming light beam has usually to be polarized *perpendicular* to the electron layer. In this mode, electrons are directly excited from the

ground subband 0 to some higher subband $m > 0$ (or the continuum). In the single-particle picture, this corresponds to “vertical” inter-subband transitions in the $E(k)$ -diagram (energy versus wave vector).

In an ideal system (free electron motion parallel to the layers) and without the assistance of phonons, absorption of *in-plane* polarized light would be impossible, because energy and momentum cannot be conserved in this configuration. This polarization direction, however, becomes effective via higher-order

* Corresponding author. Tel.: +49-9131-852-7282; fax: +49-9131-852-7293.

E-mail address: metzner@physik.uni-en.langen.de (C. Metzner)

transitions, involving the simultaneous scattering with some kind of dynamic or static imperfections.

The free-carrier absorption of in-plane polarized light, assisted by acoustic photons, has already been analyzed by Spector [1], using a second-order golden rule approximation. In the present paper, we investigate the absorption spectrum of heavily doped quantum wells, where scattering with charged impurities provides the necessary momentum transfer for optical intra-subband transition.

It should be noted that a perturbative treatment of the scattering is not possible in our case, because the interaction of the electrons with the impurities can be extremely strong, especially in center doped quantum wells, or in modulation doped structures with thin spacer layers. Actually, in those systems, coherent multiple scattering leads to the formation of in-plane localized electron states, which can consequently not be characterized by a well-defined wave vector k or subband index m . Rather, the whole theory has to be based on these disordered single-particle states from the start. Once the electron-impurity interaction is incorporated exactly into the quantum states, photon-assisted transitions can be computed directly with the first-order golden rule formula.

We use numerically calculated electron states in a finite lateral simulation area with periodic boundary conditions, corresponding to a realistic random distribution of charged donors (cf. Ref. [2]). Static screening of the potential fluctuations is included on the Hartree level [3,4]. For simplicity, we disregard any dynamic electron–electron interactions [5], the electron–phonon coupling and non-parabolicity effects.

The organization of our paper is as follows. In Section 2, we introduce our two-model systems. The results for both models are then presented and discussed in Section 3.

2. The model systems

To extract the fundamental physics of intra-subband absorption, it is convenient to start with a highly simplified (model A). We have considered an AlGaAs–GaAs (effective mass $m_{\text{cl}} = 0.067m_0$) square potential well, characterized by the thickness a and barrier height V_b , which is disturbed by a “co-doping”

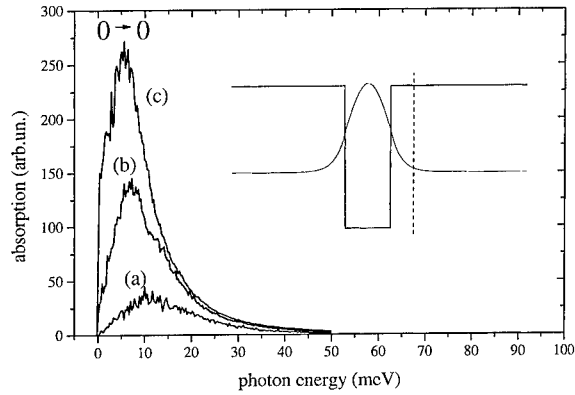


Fig. 1. Intra-subband absorption spectra of model system A with modulation co-doping, for three different electron densities: (a): $n^{(2)} = 0.25 \times 10^{12} \text{ cm}^{-2}$, (b): $n^{(2)} = 0.75 \times 10^{12} \text{ cm}^{-2}$, (c): $n^{(2)} = 1.25 \times 10^{12} \text{ cm}^{-2}$. The system parameters used in the calculations were as follows: $a = 4 \text{ nm}$, $v_b = 230 \text{ meV}$, $N_C^{(2)} = 1.0 \times 10^{12} \text{ cm}^{-2}$, spacer $d = 2 \text{ nm}$.

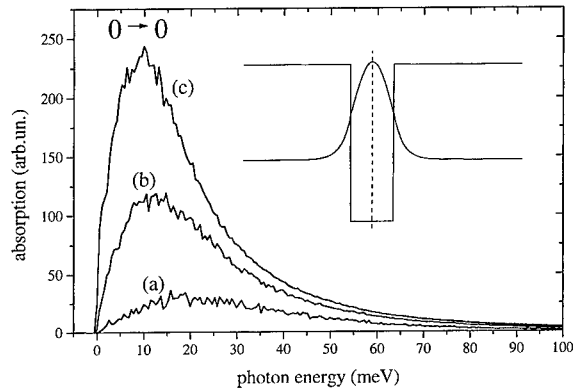


Fig. 2. Like Fig. 1, however with the co-doping layer placed in the center of the quantum well.

δ -layer (compare insets of Figs. 1 and 2). We assume an equal density $N_C^{(2)}$ of charged donors and acceptors, randomly distributed within this layer. Such an exactly compensated doping layer, although difficult to realize in practice, is macroscopically neutral and, thus, causes no band bending in the average conduction band profile. Nevertheless, it creates potential fluctuations similar to the case of ordinary, non-compensated doping. Thus, the fundamental subband structure of the 2D-system does not depend on the z -position of the co-doping layer,

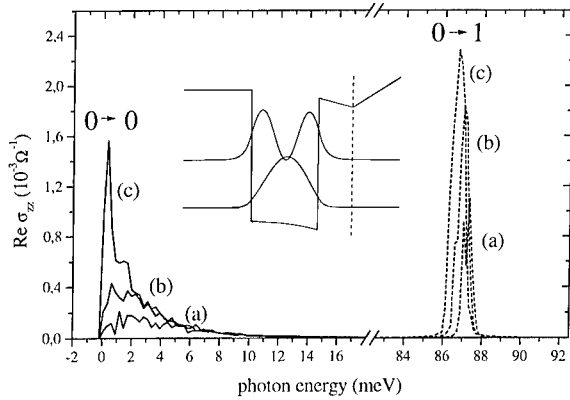


Fig. 3. Intra- (full lines) and inter-subband (dashed lines) absorption spectra of the realistic model B with modulation n -doping ($N_D^{(2)} = 0.75 \times 10^{12} \text{ cm}^{-2}$), for three different electron densities: (a) $0.1N_D^{(2)}$, (b): $0.2N_D^{(2)}$, (c): $0.3N_D^{(2)}$. The system parameters used in the calculations were as follows: $a = 10 \text{ nm}$, $V_b = 230 \text{ meV}$, spacer $d = 5 \text{ nm}$.

relative to the electron gas. Since we also neglect electron–electron interactions in model A, the disordered single particle states for a given set of system parameters can be computed once and for all. The electrons are then filled into this fixed level spectrum, according to a Fermi distribution (at $T = 4 \text{ K}$), and the intra-subband absorption spectra are calculated for different (two-dimensional) carrier densities $n^{(2)}$.

In the next step we consider a more realistic system (model B), a n -type δ -doped quantum well embedded in a field effect transistor structure, in which the carrier density $n^{(2)}$ is controlled by a metallic gate (compare insets of Figs. 3 and 4). In model B we re-calculate the self-consistent band profile for each given $n^{(2)}$ and also include static electronic screening of the potential fluctuations on the level of the Hartree approximation. Note that in this realistic model, while the Fermi level is scanning through the density of states, the quantum states of the electrons are changing. Thus the observed changes in the optical spectra are partly due to “trivial” effects, e.g. the $n^{(2)}$ -dependence of the fundamental subband structure. In model B we include, both, the ground ($m = 0$) and first excited ($m = 1$) subband, so that we can analyze the 0–0 intra-subband and the 0–1 inter-subband absorption processes simultaneously (for in-plane and perpendicular light polarization, respectively).

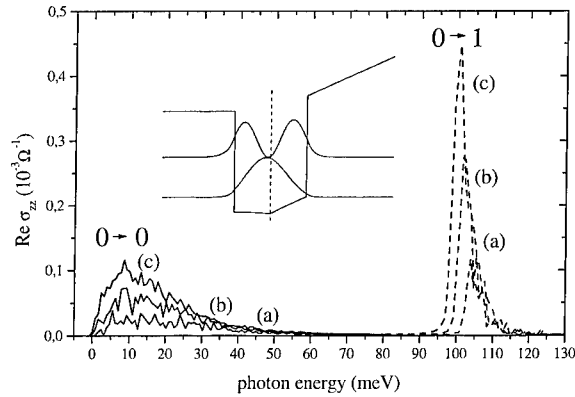


Fig. 4. Like Fig. 3, however with the n -doping layer placed in the center of the quantum well.

3. Results and discussion

The absorption spectra calculated for model system A are presented as a function of electron density in Fig. 1 (modulation co-doping, weaker disorder) and in Fig. 2 (center co-doping, very strong disorder). Generally, the 0–0 transitions occur in the low-frequency range (starting from $\hbar\omega = 0$) and the spectra show an asymmetric line profile, with a long tail on the high-energy side. We can characterize this line shape by the peak photon energy $\hbar\omega_{\text{peak}}$ and the high-energy “limit” of the absorption range $\hbar\omega_{\text{max}}$ (where the absorption has dropped to $\frac{1}{10}$ of its peak value).

In the case of modulation doped systems, we can roughly estimate the high-energy limit for intra-subband transitions by considering the parabolic dispersion relation of free carriers and assuming the electrons initial state at the band minimum ($\mathbf{k} = \mathbf{0}$). By scattering with the charged impurities, the maximum wave vector transfer is here of order $\Delta q_{\text{max}} \approx 1/d$, where d is the spacer layer thickness. With this momentum gain, the electron can be excited up to energies of order $E_{\text{max}} \approx (\hbar\Delta q_{\text{max}})^2 / (2m_{\text{el}})$. For a spacer of $d = 5 \text{ nm}$ we thus obtain $E_{\text{max}} = 23 \text{ meV}$, which is in fair agreement with the observed spectral widths. Correspondingly, with increasing spacer layer d the intra-subband excitations become more and more limited to the range of very long wavelengths (microwave radiation, AC-electric fields).

For systems with small spacer layers (strong disorder), however, the free electron picture is not

applicable any longer, because the carriers become in-plane localized. Approaching the extreme case of center-doping (Fig. 2), the absorption band width saturates at about $\hbar\omega_{\text{max}} \approx 50$ meV, for an electron density of $n^{(2)} = 0.75 \times 10^{12} \text{ cm}^{-2}$.

Note that the low-energy excitations $\hbar\omega \rightarrow 0$ are due to levels slightly below and above the Fermi level Φ . Therefore, the $n^{(2)}$ -dependence of the absorption coefficient at low photon energies reflects specifically the properties of the electron states at the Fermi edge of the disordered quantum spectrum.

Especially, the limiting case at $\hbar\omega = 0$ describes the DC-conduction of the electron system. Although our lateral system size is too small to simulate DC-transport realistically, our results indicate a rather abrupt increase of the absorption coefficient $\alpha(\omega = 0)$ (or, equivalently, of the real part of the dynamic conductivity $\sigma(\omega = 0)$) from zero to a finite value at a certain carrier density $n_{\text{crit}}^{(2)}$. This may be interpreted as an insulator–metal transition, which can also be confirmed by inspecting the nature of the quantum states in vicinity of the critical Fermi level.

In the insulating regime, for low carrier densities (Fermi level located deep in the tail of the broadened density of states), all electrons are localized in individual potential minima. At energies slightly above the Fermi level, no final states with considerable optical matrix element are available, because the corresponding wave functions are localized in spatially separate areas. Only at higher excitation energies, $\hbar\omega \rightarrow \hbar\omega_{\text{peak}}$, optically connected states become accessible. These states are more extended, however, not in the sense of plane waves. Rather, the occupation probability of each of these high-energy (“scarred”) wave functions is spatially distributed over many small resonances, appearing typically above the “valleys” of the 2D potential relief. If one of these resonances is located at the same lateral potential well where the initial electron state is localized, a finite matrix element becomes possible. Thus, for low carrier densities, the maximum absorption is found at higher photon energies.

If more carriers are filled into the (fixed) random potential landscape, the localization radius of the Fermi edge states increases. If the Fermi level reaches the region of the “extended” states described above, optical transitions with lower excitation energy become possible. The corresponding initial and final states have a

subset of their resonance maxima located in the same spatial areas. Correspondingly, $\hbar\omega_{\text{peak}}$ is gradually red shifted with increasing $n^{(2)}$.

We now turn to the results obtained for the more realistic model B. Fig. 3 shows absorption spectra (real part of the dynamic, two-dimensional conductivity σ) calculated for the modulation n-doped sample, both for in-plane (full line) and z-polarized light (dashed line). Note that the integrated absorptions of the inter- and intra-subband spectra are of comparable magnitude. This is, for low carrier densities, a simple consequence of the oscillator strength sum rule.

The 0–1 intersubband resonance is found very close to the undisturbed subband separation $\hbar\omega_{\text{res}} = \varepsilon_1 - \varepsilon_0$. Its asymmetric peak shape and surprisingly small line width (despite the strong potential fluctuations) are due to the intersubband correlation effect, which has already been described in detail before [2].

The 0–0 absorption spectra show basically the same tendencies as in the case of model A, i.e. the dominance of long-wavelength excitations in the high-density regime. A detailed interpretation of these spectra is, however, complicated by the simultaneous effects of the electron–electron interaction (band bending, screening). Especially, a part of the observed absorption peak shift with electron density is now due to changes of the potential profile in the lateral and z-directions.

In heavily doped quantum wells, it should be possible to observe intra-subband transitions with standard far-infrared or RAMAN spectroscopy. In quasi-2D systems with controllable electron density, the derivative of the absorption coefficient with respect to the density (small modulation of $n^{(2)}$ around its mean value at fixed wavelength) would be of special interest. This quantity would yield valuable information about the properties of the disordered electron states at the Fermi level. However, for a direct comparison with experiment in the high density regime, it will be necessary to include dynamic electron–electron interactions into the theory. This work is now in progress.

Acknowledgements

One of the authors (C.M.) would like to thank the Deutsche Forschungsgemeinschaft DFG for financial support.

References

- [1] H.N. Spector, Phys. Rev. B 28 (1983) 971.
- [2] C. Metzner, M. Hofmann, G.H. Döhler, Phys. Rev. B 58 (1998) 7188.
- [3] K. Schröder, C. Metzner, M. Hofmann, G.H. Döhler, Superlattices Microstruct. 21 (1997) 223.
- [4] C. Metzner, M. Hofmann, G.H. Döhler, Superlattices Microstruct. 25 (1999) 239.
- [5] C. Metzner, G.H. Döhler, Phys. Rev. B 60 (1999) 11005.



ELSEVIER

Physica E 7 (2000) 225–228

PHYSICA E

www.elsevier.nl/locate/physce

Inter-subband relaxation due to electron–electron scattering in quantum well structures

K. Kempa*, P. Bakshi, J.R. Engelbrecht, Y. Zhou

Department of Physics, Boston College, Chestnut Hill, MA 02467, USA

Abstract

We present a full RPA formalism, and an efficient computational scheme for the inter-subband relaxation processes due to the electron–electron interactions in quantum well structures. Based on a full self-energy calculation, our formalism includes both single particle (e.g. Auger) and collective (plasmon) processes, and is applicable to strongly inhomogeneous, non-equilibrium steady-state systems. To show the efficacy of our formalism, we analyze two recent experiments which report different scattering rates for similar structures and similar carrier densities. We obtain quantitative agreement with the experimental results, showing that the observed difference is due to different excitation levels of the electron population. We have also shown, that the electron–plasmon scattering dominates inter-subband electron–electron scattering at low temperatures. © 2000 Elsevier Science B.V. All rights reserved.

Keywords: Electron–electron scattering; Auger process; Collective excitations; Plasmons; Self-energy

1. Introduction

Electron–electron scattering dominates the physics of carrier relaxation in quantum nanostructures for which the inter-subband separation is less than the LO phonon energy (~ 35 meV in GaAs). Knowledge of the electron–electron scattering rates is therefore crucial in determining the electrical and thermal transport properties of such structures. This is especially important for structures used as active regions of devices designed for emission of radiation in the THz frequency range [1–3]. Typically, these operate in a non-equilibrium steady state, and in some cases

carry a large electron population in the active region. Then the electron–electron scattering becomes the limiting mechanism in achieving population inversion. Of obvious interest here is the possibility of reducing those electron–electron scattering rates (by appropriate structure design, or excitation scheme) so that a significant inter-subband population inversion can be achieved [2,3]. This could clear the way to a THz laser [2,3].

Experiments show that the inter-subband electron–electron scattering rates in semiconductor quantum well systems can be very high (of the order of 1 meV), almost approaching in some circumstances the inter-subband scattering rate due to emission of LO phonons. However, two recent experiments [4–6], performed on two-subband quantum well structures

* Corresponding author. Fax: +1-617-552-8478.

E-mail address: kempa@bc.edu (K. Kempa)

(with the inter-subband separation below the LO phonon threshold), showed that the inter-subband relaxation rates, due to electron–electron scattering, differed in the two experiments by over an order of magnitude.

We present here an efficient calculation scheme, for the electron–electron scattering rate in quantum well

$$\chi_0(\mathbf{r}, \mathbf{r}', \omega) = \sum_{\mathbf{K}n} \sum_{\mathbf{K}'n'} \frac{(f_{\mathbf{K}n} - f_{\mathbf{K}'n'}) \psi_{\mathbf{K}n}(\mathbf{r}) \psi_{\mathbf{K}'n'}^*(\mathbf{r}') \psi_{\mathbf{K}'n'}(\mathbf{r}) \psi_{\mathbf{K}n}^*(\mathbf{r}')}{\omega + E(\mathbf{K}n) - E(\mathbf{K}'n') + i\delta} \quad (4)$$

systems, which includes both single particle (Auger) and collective (plasmon) processes. Such a complete treatment is essential for a proper analysis of the non-equilibrium steady state systems with significant carrier populations. We apply this formalism to the experimental scenarios of Refs. [3–6].

We consider here a nanostructure in which electrons are trapped, by an arbitrary confining potential, to a finite size domain in z the direction, and are free to move in any direction perpendicular to z . We assume, that the energy spectrum consists of only two subbands, and that the temperature is zero in this part of the paper. The averaged out scattering rate, γ_{scat} , of an electron in the upper of the two subbands ($n = 2$), can be obtained from the imaginary part of the corresponding self-energy, which in RPA has the following form [7,8]:

$$\Sigma(\mathbf{r}, \mathbf{r}', \omega) = \frac{i}{2\pi} \int d\omega' S(\mathbf{r}, \mathbf{r}', \omega') G_0(\mathbf{r}, \mathbf{r}', \omega - \omega'), \quad (1)$$

where the single-particle (noninteracting) propagator is given by

$$G_0(\mathbf{r}, \mathbf{r}', \omega) = \sum_{\mathbf{K}n} \frac{\psi_{\mathbf{K}n}(\mathbf{r}) \psi_{\mathbf{K}n}^*(\mathbf{r}')}{\omega - E(\mathbf{K}n) + i\delta}, \quad (2)$$

where \mathbf{K} is the electron, in-plane, wave vector of the electron, $n = 1, 2$, is the subband index, and $\mathbf{r} = (\mathbf{R}, z)$, where \mathbf{R} is the in-plane position vector. The single-particle energy is $E(\mathbf{K}n) = K^2/2m + \varepsilon_n$ (m is the effective mass, ε_n is the electron energy associated with the motion in z -direction). Throughout we assume that $\hbar = 1$. $\psi_{\mathbf{K}n}(\mathbf{r})$ is the corresponding single-particle eigenfunction of the state \mathbf{K} in the n th subband. The screened interaction $S(\mathbf{r}, \mathbf{r}', \omega)$, is given

in RPA by the Dyson equation

$$S(\mathbf{r}, \mathbf{r}', \omega) = v(\mathbf{r}, \mathbf{r}') + \int d\mathbf{r}'' \int d\mathbf{r}''' v(\mathbf{r}, \mathbf{r}'') \times \chi_0(\mathbf{r}'', \mathbf{r}', \omega) S(\mathbf{r}', \mathbf{r}', \omega), \quad (3)$$

where the Coulomb potential is $v(\mathbf{r}, \mathbf{r}') = e^2/\varepsilon|\mathbf{r} - \mathbf{r}'|$ and the bare susceptibility is

with $f_{\mathbf{K}n}$ are the respective occupation factors, and ε is the dielectric constant of the semiconductor. The expectation value of the self-energy in the state $\mathbf{K}n$ is

$$D(\mathbf{K}n) = \int d\mathbf{r} \int d\mathbf{r}' \Sigma(\mathbf{r}, \mathbf{r}', E(\mathbf{K}n)) \psi_{\mathbf{K}n}(\mathbf{r}) \psi_{\mathbf{K}n}^*(\mathbf{r}') \quad (5)$$

and, finally,

$$\gamma_{\text{scat}} = 1/\tau_{\text{scat}} = -\langle \text{Im}[D(\mathbf{K}2)] \rangle \quad (6)$$

where $\langle \rangle$ means averaging over all states of the upper subband ($n = 2$).

Further algebra is needed, which involves Fourier transforming in-plane quantities and employing the cosine Fourier transforms [9–11] along z , to transform the above equations into an efficient computational scheme [12].

We first apply our formalism to the experimental scenario of Ref. [4], where a double well structure is remotely doped, so that electrons occupy the lower subband up to the Fermi level $E_{F1} = 4$ meV. A beam of THz radiation excites some of the electrons to the upper subband. The inter-subband separation is $\Delta = 11$ meV. All other subbands in this structure are at least 100 meV above this doublet. The occupation of the upper subband (N_2) is controlled by the radiation intensity (I), and can be estimated from the electron flux balance between the two subbands $N_1 \gamma_{\text{THz}} = N_2 \gamma_{\text{scat}}$, where N_1 is the lower subband population, and γ_{THz} , proportional to I , is the up-conversion rate due to the THz radiation. Fig. 1 shows our calculation (circles) of $1/\tau_{\text{scat}}$ versus I compared with the experimental results (squares). The agreement is very good over three orders of magnitude of I .

Next, we apply our formalism to a similar double well, two subband structure of Refs. [5,6]. In this case,

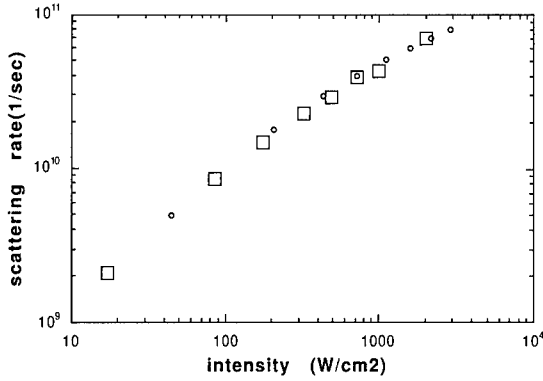


Fig. 1. Inter-subband scattering rate versus intensity of the THz radiations. Circles represent our calculation, and squares the experimental results of Ref. [4].

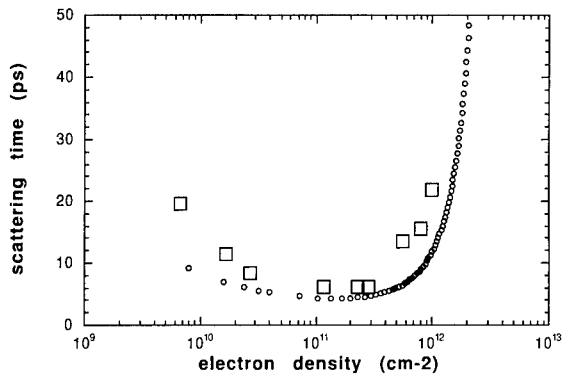


Fig. 2. Inter-subband scattering time versus total electron density. Circles represent our calculation, and squares the experimental results of Refs. [5,6].

a laser beam is used to excite electrons from the valence band into a narrow window which overlaps with both subbands in the conduction band. Since the excitation rate is very fast, the electron population divides, essentially equally (due to the constant density of states), between the two subbands. The final result of our calculation (circles) is shown in Fig. 2, and is in a good quantitative agreement with the experiment (squares).

In the experiment of Ref. [4], for most of the radiation intensities, the electron gas had a smaller population in the upper band, compared to the case of the

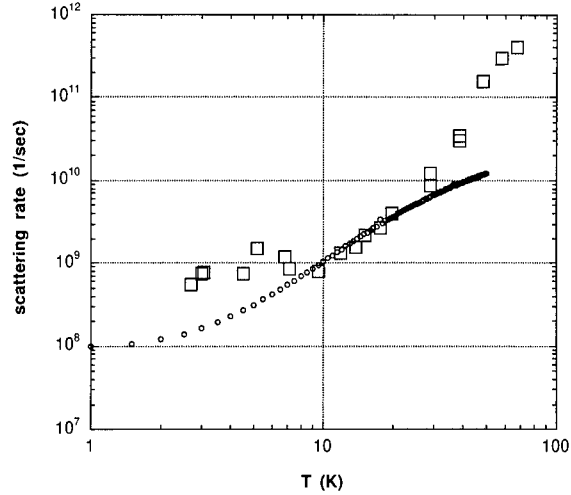


Fig. 3. Inter-subband scattering rate versus temperature. Circles represent our calculation, and squares the experimental results of Ref. [13].

experiment of Refs. [5,6]. Then a simple phase-space blocking argument, combined with the quadratic scaling of the Auger process with the upper band density, explains the smaller scattering rates measured in Ref. [4].

One of the results of the experiment reported in Ref. [4] was the temperature dependence of the inter-subband scattering rate. It was suggested that $\gamma_{\text{scat}} \sim A \exp(-E_{a1}/kT) + B \exp(-E_{a2}/kT)$, with the activation energy $E_{a1} = 2.9$ meV for small temperature (T), and $E_{a2} = 24$ meV for large T . While E_{a2} clearly is due to emission of LO phonons ($\omega_{\text{LO}} = \Delta + E_{a2} = 35$ meV), origin of the lower activation energy E_{a1} remained unexplained. In a later study (Ref. [13]), this low-temperature domain was studied in detail. It was shown, that the temperature dependency in this very low T range ($T < 30$ K), is more complex than earlier suggested on the basis of a very limited number of data points. In fact, the scattering rate seems to follow T^2 dependency, in the temperature range $10 \text{ K} < T < 30 \text{ K}$, before saturating at the level of 10^9 s^{-1} for $T < 10 \text{ K}$ (see Fig. 3, squares).

In order to calculate the temperature dependency of the inter-subband scattering rate, we include temperature in our formalism. Since the experimental scenarios of Refs. [4,13] employ a marginal

excitation of the electron gas (quasi-equilibrium situation), in this study of the temperature dependency, we can employ the Matsubara formalism. More details are given elsewhere (Ref. [12]). The results of our calculations are shown in Fig. 3 (circles), together with the experimental results of Refs. [4,13] (squares). Our calculations agree well with the experiment in the window $10\text{ K} < T < 30\text{ K}$. The higher *observed* scattering rates outside this range, are due to mechanisms not included in our calculations (i.e. LO phonons for $T > 30\text{ K}$, and acoustic phonons for $T < 10\text{ K}$). In our calculation [12] we find that the low-temperature expansion for the electron–electron scattering rate begins with $a + bT^2$. In this range, the electron–electron scattering rate is dominated by the *collective* contribution (i.e. from plasmons and higher-order electron–electron processes), as compared to the Auger process. The relative importance of the collective contribution diminishes for larger T . For the parameters of the experimental scenario of Ref. [13] (areal density of 10^{11} cm^{-2}), however, even at $T = 20\text{ K}$, it amounts to 50% of the total scattering rate. This emphasizes the importance of performing the full self-energy calculations.

In conclusion, we have developed a full RPA formalism, and an efficient computational scheme for calculating the electron–electron scattering rate, which includes both single particle (e.g. Auger) and collective (plasmon) processes. Our calculations are in good quantitative agreement with recent experimental results. We have also shown, that the temperature dependence of the inter-subband electron–electron scattering rate in the quantum well system of Ref. [13], is dominated by the electron–plasmon scattering, i.e. collective effects, below $T = 20\text{ K}$.

Acknowledgements

We wish to thank A. Nazarenko, and K. Unterrainer for helpful discussions. This work was supported by the U.S. Army Research Office under grant number DAAG55-97-1-0021.

References

- [1] M. Rochat, J. Faist, M. Beck, U. Oesterle, M. Illegems, Appl. Phys. Lett. 73 (1998) 3724.
- [2] K. Kempa, P. Bakshi, C.G. Du, G. Feng, A. Scorupsky, G. Strasser, C. Rauch, K. Unterrainer, E. Gornik, J. Appl. Phys. 85 (1999) 3708.
- [3] P. Bakshi, K. Kempa, A. Scorupsky, C.G. Du, G. Feng, R. Zobbl, G. Strasser, C. Rauch, Ch. Pacher, K. Unterrainer, E. Gornik, Appl. Phys. Lett. 75 (1999) 1685.
- [4] J.N. Heyman, K. Unterrainer, K. Craig, B. Galdrikian, M.S. Sherwin, K. Campman, P.F. Hopkins, A.C. Gossard, Phys. Rev. Lett. 74 (1995) 2682.
- [5] M. Hartig, S. Haacke, P.E. Selbmann, B. Deveaud, R.A. Taylor, L. Rota, Phys. Rev. Lett. 80 (1998) 1940.
- [6] M. Hartig, J.D. Ganiere, P.E. Selbmann, S. Haacke, B. Deveaud, L. Rota, Results Presented at the 24th ICPS Conference, Jerusalem, Israel, August 1998, paper TU3-A5.
- [7] J.C. Inkson, Many-Body Theory of Solids, Plenum Press, New York, 1984.
- [8] R.D. Mattuck, A Guide to Feynman Diagrams in the Many-Body Problem, McGraw-Hill, New York, 1976.
- [9] K. Kempa, W.L. Schaich, Phys. Rev. B 34 (1986) 547.
- [10] K. Kempa, D.A. Broido, C. Beckwith, J. Cen, Phys. Rev. B 40 (1989) 8385.
- [11] K.D. Tsuchi, W.W. Plummer, A. Liebsch, E. Pehlke, K. Kempa, P. Bakshi, Surf. Sci. 247 (1991) 302.
- [12] K. Kempa, P. Bakshi, J. Engelbrecht, Y. Zhou, submitted.
- [13] J.N. Heyman, J. Barnhorst, K. Unterrainer, J. Williams, M.S. Sherwin, K. Campman, A.C. Gossard, Physica E 2 (1998) 195.

The intrasubband and intersubband relaxation of nonequilibrium electron populations in wide semiconductor quantum wells

S.-C. Lee*, I. Galbraith

Department of Physics, Heriot-Watt University, Edinburgh EH14 4AS, UK

Abstract

The evolution of nonequilibrium electron distributions in wide GaAs quantum wells, driven by electron–electron scattering processes, is calculated through numerical integration of the Boltzmann collision integrals, by incorporating the multi-subband dynamically screened Coulomb interaction derived in the random phase approximation. We present results for the thermalisation and intersubband population relaxation times of these distributions, for different carrier densities and lattice temperatures, and for different fractions of the population excited into the upper subband, including the highly nonequilibrium case of a population inversion between the subbands. We compare the relative importance of electron–electron and electron–LO-phonon scattering processes in determining the intersubband population relaxation times. The role played by screening in intersubband transitions is discussed. © 2000 Elsevier Science B.V. All rights reserved.

Keywords: Intersubband population relaxation; Electron–electron scattering; Nonequilibrium distributions; Dynamic screening

In the current generation of mid-infrared quantum cascade lasers, which operate through intersubband transitions in the conduction band, electron–LO-phonon scattering is the dominant competing non-radiative process. To extend these devices to longer operating wavelengths in the far-infrared, wider quantum wells are required, resulting in smaller intersubband energy separations. For energy separations less than the LO-phonon energy E_{LO} , the electron–LO-phonon scattering process is suppressed, and intersubband transitions through electron–electron scattering become significant. In this work, we fo-

cus on the electron–electron scattering process. In particular, we investigate the temporal evolution of nonequilibrium electron distributions driven by this process, and the resulting intersubband population relaxation times.

To calculate the evolution of nonequilibrium electron distributions in the quantum well subbands we numerically integrate the multisubband Boltzmann collision rate equations [1,2]. The screened interaction [2,3] between the electrons is modelled with the multisubband dynamic dielectric function derived in the random phase approximation (RPA). The system we will consider is a nonequilibrium electron distribution in a GaAs/ $Al_xGa_{1-x}As$ quantum well with two subbands, and intersubband energy separation

* Corresponding author. Fax: +44-131-451-3136.
E-mail address: toni@phy.hw.ac.uk (S.-C. Lee)

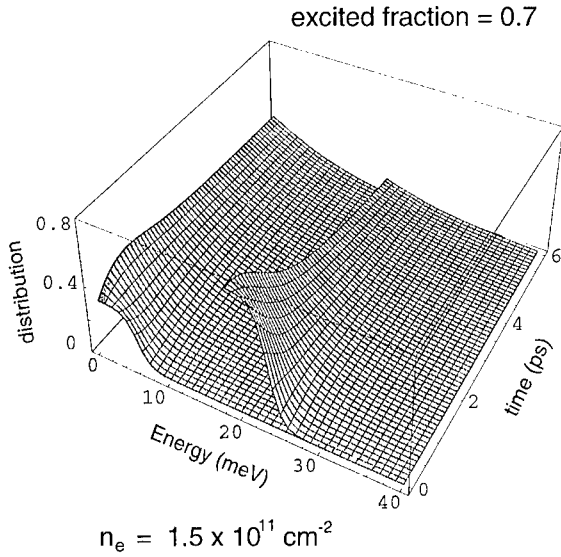


Fig. 1. Evolution of nonequilibrium electron distributions driven by electron–electron scattering. The initial excited carrier fraction is 0.7. $n_e = 1.5 \times 10^{11} \text{ cm}^{-2}$. $L_w = 307 \text{ Å}$.

$\Delta E_{21} < E_{1,0}$. We assume that the well has infinite barriers, and that the electrons obey a parabolic energy dispersion.

We consider first a distribution with a carrier density $n_e = 1.5 \times 10^{11} \text{ cm}^{-2}$, in a well of width $L_w = 307 \text{ Å}$ ($\Delta E_{21} \sim 18 \text{ meV}$). To generate the initial nonequilibrium distributions we promote a fraction of the equilibrium distribution in the lower subband into the upper subband to simulate intersubband excitation by an optical pulse. The temperature of the equilibrium distribution before the excitation is a measure of the width of the nonequilibrium distribution.

Fig. 1 shows the evolution of a highly nonequilibrium distribution in which 70% of the carriers are excited into the upper subband. The lattice temperature T_L is 10 K. Within each subband the distributions reach a quasi-equilibrium in around 2 ps. The overall thermalisation to a single Fermi distribution occurs on a longer time scale, $> 6 \text{ ps}$.

The relaxation time $dn_{2,k}/dt$ of the population $n_{2,k}$ in each k -state in the upper subband is a function of the energy of the state. Hence, there is no single decay time for the transfer of electrons from each state in the upper subband to the lower subband. However, a measure of the decay time for the total population in the upper subband can be obtained by integrating

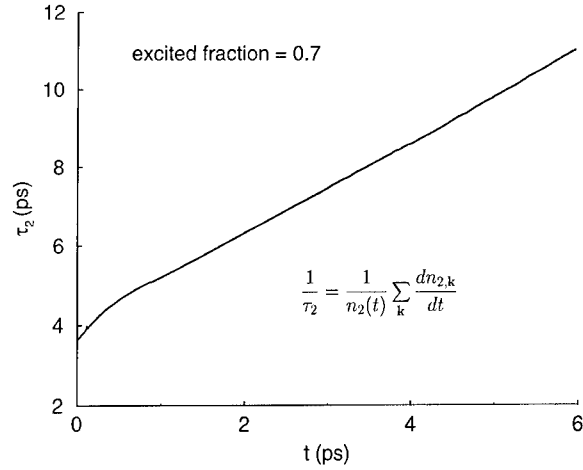


Fig. 2. Intersubband population relaxation times for the electron distributions shown in Fig. 1.

all the rates, $dn_{2,k}/dt$, over the k -states in this subband, and we can define the intersubband population relaxation time $1/\tau_2 = (\sum_k dn_{2,k}/dt)/n_2(t)$, where n_2 is the carrier density in the upper subband. In Fig. 2, we plot τ_2 for the system shown in Fig. 1 as the distributions evolve. Fig. 2 shows that τ_2 is not constant during the evolution, but increases from $\sim 3 \text{ ps}$ at the beginning of the evolution to over 10 ps after a time of 6 ps. Hence, the population decay time is nonexponential and cannot be characterised by a single time.

We now give more detailed results showing initial intersubband population relaxation times $\tau_2^{t=0}$, as a function of carrier density. This would be an appropriate measure of the relaxation time for a nonequilibrium distribution that is maintained in a steady state, for instance, by continual pumping. Fig. 3(a) shows $\tau_2^{t=0}$, plotted against n_e , for $T_L = 10 \text{ K}$, and with different fractions of excited carriers in the upper subband. The results show that the relaxation time decreases with increasing numbers of carriers in the upper subband. This is because the number of scattering partners in the upper subband increases at high excitation, and the number of empty states in the lower subband also increases, which allows scattering into this subband to occur more easily. Looking at the density dependence, we see that intersubband relaxation due to electron–electron scattering is slowest at low densities (10^{10} cm^{-2}) with times ranging from $> 50 \text{ ps}$ to $> 100 \text{ ps}$. The times decrease with increasing density because increasing the number

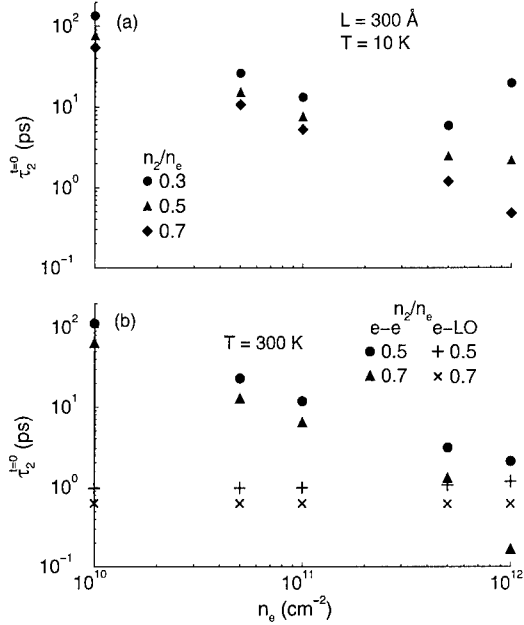


Fig. 3. Intersubband population relaxation times $\tau_2^{l=0}$ versus n_e for different excited carrier fractions in the upper subband (a) $T_L = 10$ K. Electron–electron scattering only. (b) $T_L = 300$ K. Electron–electron and electron–LO-phonon scattering.

of carriers increases the scattering probability. The relaxation times reach a minimum of a few picoseconds to $< \sim 1$ ps at around 10^{12} cm⁻². At higher densities, the intersubband relaxation times start to increase again. This is seen first for the case with lowest excitation $n_2/n_e = 0.3$. This increase is due to state-filling in the lowest subband, which prevents electrons from scattering down into this subband [4].

In a real device operating at room temperature, the electron distributions are more widely spread in energy. In this case, there are electrons with sufficiently high energy in the subbands to emit LO-phonons. In Fig. 3(b), we compare the electron–electron and electron–LO-phonon intersubband relaxation times at 300 K. Again, the relaxation times due to electron–electron scattering decrease from tens of picoseconds at 10^{10} cm⁻² to around 1 ps at 10^{12} cm⁻². The relaxation times due to electron–LO-phonon scattering are subpicosecond and almost constant with density. Thus, at 300 K, electron–LO-phonon scattering dominates at most densities, and the net relaxation times are governed by this process. When the electron–electron scattering rates are a maximum at around 10^{12} cm⁻²,

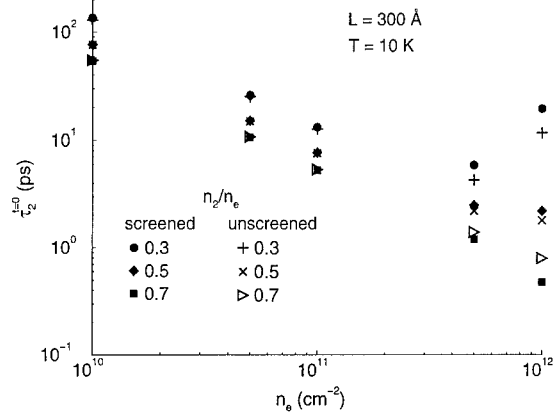


Fig. 4. Intersubband population relaxation times $\tau_2^{l=0}$ versus n_e due to electron–electron scattering calculated with and without screening. $T_L = 10$ K.

the relaxation times due to both scattering processes are similar, and in this case both processes must be considered simultaneously.

Finally, we discuss the screening of the interactions which result in intersubband transitions, and govern the intersubband population relaxation times. It is known that screening for these interactions is relatively unimportant [2,5], in comparison with the case of intrasubband transitions. This is due to the behaviour of the form factor describing the overlap of the electron envelope functions which cancels the $1/q$ divergence of the Coulomb potential when $q \rightarrow 0$. Thus, even in the absence of screening these interactions which lead to intersubband transitions are short-range in nature, and screening has a lesser effect on such a potential.

In Fig. 4, we show again the relaxation times calculated with screening that were shown in Fig. 3(a). We also show in Fig. 4, relaxation times calculated without any screening. At lower densities, the relaxation times calculated with and without screening are almost identical. However, as the density increases above 5×10^{11} cm⁻², the relaxation times from the two calculations start to diverge, as the screening becomes more important at higher densities.

We point out here an interesting effect which is seen most clearly in the results at 10^{12} cm⁻². Looking at the low-excitation case, $n_2/n_e = 0.3$, we find that the relaxation time calculated with screening is longer than in the unscreened case, i.e., the screening has

reduced the strength of the interaction. Considering the high-excitation case with a population inversion, $n_2/n_c = 0.7$, we find the opposite effect. The screening has reduced the relaxation time in comparison with the unscreened case, implying that the screening has increased the interaction strength.

To understand these results, we look at the screened interaction for the intersubband transitions [2], $V_{1212}^s(q, \omega) = V_{1212}(q)/\epsilon(q, \omega)$, where $V_{1212}(q)$ is the unscreened interaction and the subscripts label the subbands of the initial and final states occupied by the two scattering electrons before and after the scattering process. The dynamic dielectric function in the random phase approximation is given by $\epsilon(q, \omega) = 1 - V_{1212}(q)[\Pi_{12}(q, \omega) + \Pi_{21}(q, \omega)]$ where the polarisation function

$$\Pi_{12}(q, \omega) = 2 \sum_k \frac{n_{1,k+q} - n_{2,k}}{E_{1,k+q} - E_{2,k} - \hbar\omega - i\delta}. \quad (1)$$

In the static, long-wavelength limit [2]

$$\epsilon(q \rightarrow 0, \omega = 0) = 1 + \frac{e^2(n_1 - n_2)\mathcal{F}_{1212}(q)}{\epsilon_s \Delta E_{21}} \frac{1}{q}, \quad (2)$$

where n_1 and n_2 are the carrier densities in the lower and upper subbands, respectively. Hence, $\epsilon(q \rightarrow 0, \omega = 0)$ can be greater than or less than one depending on the relative populations of the two subbands, resulting in a screened interaction that is less than or greater than the unscreened interaction. For the case of a population inversion, $n_1 < n_2$, and the interaction is enhanced resulting in the reduced relaxation time seen in Fig. 4 for the high-excitation case $n_2/n_c = 0.7$ at 10^{12} cm^{-2} . We note that the static, long-wavelength approximation given in Eq. (2) is not a realistic approximation for inter-

subband transitions [2]. However, the dependence of the screening on the difference in the distributions in the two subbands is seen also in Eq. (1) at finite q and ω .

In conclusion, we have studied the evolution of nonequilibrium electron distributions in wide semiconductor quantum wells. The evolution is, in general, driven by electron–electron scattering processes, and if the electrons are sufficiently high in energy in the subbands, by electron–LO-phonon scattering processes. In general, when the electron–LO-phonon scattering process can occur, for instance, at 300 K, it will dominate the intersubband relaxation even in wide wells. We find also that screening for intersubband transitions is unimportant at low densities, but at higher densities it may enhance or suppress the interaction, increasing or decreasing intersubband relaxation times, depending on the relative populations in the subbands.

Acknowledgements

Financial support from The Royal Society and the EPSRC is acknowledged.

References

- [1] S.-C. Lee, I. Galbraith, *Phys. Rev. B* 55 (1997) R16025.
- [2] S.-C. Lee, I. Galbraith, *Phys. Rev. B* 59 (1999) 15796.
- [3] P. Sotirelis, P. von Allmen, K. Hess, *Phys. Rev. B* 47 (1993) 12744.
- [4] M. Hartig, J.D. Ganière, P.E. Selbmann, B. Deveaud, L. Rota, *Phys. Rev. B* 60 (1999) 1500.
- [5] M. Dür, S.M. Goodnick, P. Lugli, *Phys. Rev. B* 54 (1996) 17794.



ELSEVIER

Physica E 7 (2000) 233–236

PHYSICA E

www.elsevier.nl/locate/physce

Electron energy relaxation in silicon quantum dots by acoustic and optical phonon scattering

Manfred Dür, Stephen M. Goodnick *

Department of Electrical Engineering, Arizona State University, P.O. Box 875706, Tempe, AZ 85287-5706, USA

Abstract

In the present work, we theoretically investigate the energy relaxation of electrons due to acoustic and optical phonon scattering in quantum-dot systems embedded in a Si metal-oxide-semiconductor structure with (100) surface orientation. The confinement potential normal to the Si/SiO₂ interface is modeled by an infinite triangular quantum well. For the spatial confinement in the lateral directions due to depletion gates we assume a parabolic potential. The calculated transition rates for electron scattering between discrete energy levels in the dot are included in a simple transport model using Monte Carlo techniques to simulate the relaxation of electrons from higher levels back to the ground level. We find that the electron decay shows a non-exponential behavior. The simulated relaxation time strongly depends on the confinement in the lateral directions and may vary by several orders of magnitude. © 2000 Elsevier Science B.V. All rights reserved.

Keywords: Silicon; Quantum dots; Phonon scattering; Monte Carlo method

1. Introduction

The decay of carriers in fully quantized semiconductor systems from excited states to the ground state is of critical importance for potential applications in opto-electronic devices such as infrared lasers and photodetectors. Over the past few years, energy relaxation of electrons in quantum-dot (QD) structures by means of acoustic and optical phonon scattering has been the subject of extensive experimental and theoretical studies. However, most of the work so far has been devoted to QDs in GaAs [1–3]. Relatively

little has been reported concerning QDs in Si [4]. The recent increased interest in QD structures based on the Si metal-oxide-semiconductor (MOS) technology requires more thorough understanding of zero-dimensional transport mechanisms to interpret non-equilibrium measurements currently pursued by various research groups.

In Si, electron–phonon scattering is more complicated than in GaAs because of its multi-valley band structure and ellipsoidal energy surfaces. In the present work, we generalize the theoretical framework for the description of electron–phonon scattering in Si-based QDs to account for these special features not present in GaAs-based structures. The scattering rates are then implemented in a simple transport model utilizing a Monte Carlo approach to simulate the relaxation of a

* Corresponding author. Tel.: +1-480-965-6410; fax: +1-480-965-3837.

E-mail address: stephen.goodnick@asu.edu (S.M. Goodnick)

single electron injected into the QD back to the ground state.

2. Simulated structure and theoretical model

The QD device considered in this paper was fabricated recently [5] and consists of a MOS capacitor with n-type inversion layer on a (100) surface of p-type Si. The strong surface electric field created by the top inversion gate quantizes the motion of electrons normal to the Si/SiO₂ interface. Additional confinement in the lateral directions is achieved with depletion gates in close proximity to the interface. Consequently, the electrons are confined to a very small region (typically on the order of $200 \times 200 \text{ nm}^2$) between the depletion gates leading to the formation of a QD with a completely discrete energy spectrum.

We model the spatial confinement of electrons in the direction normal to the Si/SiO₂ interface, taken as the z -axis, by an infinite triangular quantum well. The triangular potential approximation is a reasonable approximation when the inversion charge is small compared with the depletion charge [6]. As in AlGaAs/GaAs heterojunctions, the quantization of the electronic motion can be controlled by varying the voltage applied to the top electrode. Based on self-consistent calculations of gated QD structures [7], a parabolic form of the potential is assumed for the lateral confinement,

$$V_{\text{lat}} = \frac{1}{2}K_x x^2 + \frac{1}{2}K_y y^2, \quad (1)$$

where K_x and K_y characterize the strength of this confinement. For a (100) surface orientation, the motion of electrons normal to the interface is decoupled from the lateral motion and the envelope wave functions described within the effective mass approximation are products of Airy functions and harmonic oscillator functions. The electronic spectrum of the QD may be labeled by a triple of integers (n_x, n_y, n_z) . n_x and n_y denote harmonic oscillator states with energies $\hbar\omega_x$ and $\hbar\omega_y$. n_z refers to the bound states in the z -direction. In contrast to GaAs, the six-fold ellipsoidal valley structure of Si gives rise to two sets of bound states in the (100) direction, n_z and n'_z , associated with the two-fold degenerate set of valleys projecting with the

longitudinal mass along the (100) axis (n_z), and the four-fold set projecting towards the (100) direction with the transverse mass (n'_z). The lowest lying states correspond to the unprimed states associated with the two-fold degenerate valleys projecting onto the (100) surface with the heavier longitudinal mass.

The interaction of electrons in the dot with bulk-like acoustic and optical phonons is treated within the deformation potential theory. For intravalley transitions, the angular dependence of the deformation potentials is included in the calculation [8], whereas for intervalley transitions we assume constant deformation potentials taken from Ref. [9]. The phonon frequencies are calculated from an adiabatic bond charge model [10]. We use Fermi's golden rule to compute the electron-phonon scattering rates between energy levels in the QD.

3. Results and discussion

Fig. 1 shows the transition rate for electrons scattering from upper to lower levels versus lateral confinement energy in the ground subband ($n_z = 0$) of the unprimed ladder of electric subbands ($m_z = m_{||}$, $m_x = m_y = m_{\perp}$). $m_{||}$ and m_{\perp} are the effective electron masses parallel and perpendicular to the major principal axis of the ellipsoidal valley in Si. The rate is plotted assuming isotropic lateral confinement ($K_x = K_y$). The calculations are performed for an effective electric field in the inversion layer $eF = 10 \text{ meV/nm}$ at a lattice temperature $T = 0 \text{ K}$. As can be seen from this figure, interlevel scattering of electrons is dominated to first order by acoustic phonons including contributions from both longitudinal (LA) and transverse (TA) modes. For the acoustic modes, the characteristic peak occurring between 5 and 6 meV is due to the tradeoff between the inverse q dependence of the matrix element (where q is the effective momentum associated with the difference in energy between initial and final state) which decreases with increasing interlevel spacing, and the overlap integral of the initial and final state which vanishes as the interlevel spacing approaches zero. Intervalley scattering due to longitudinal optical (g-LO) phonons is relatively weak. Because of the almost flat LO-phonon dispersion, this process only occurs in a very narrow range of confinement energies.

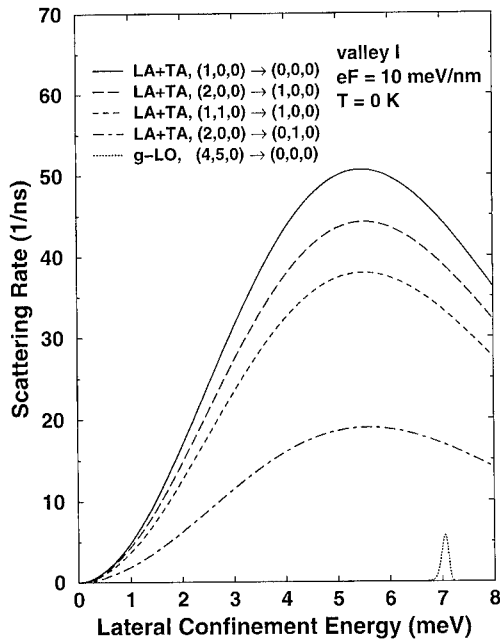


Fig. 1. Transition rate for electron scattering from upper to lower levels as a function of lateral confinement energy in the ground subband of the lowest lying valley.

To simulate interlevel relaxation of electrons due to phonon scattering in a Si QD, the calculated transition rates are included in a simple transport model employing Monte Carlo techniques. In this model, a single electron is placed in an excited QD level at the start of the simulation. The electron then relaxes back to the ground level via lower lying levels by means of phonon scattering events. The scattering events are generated stochastically based upon the quantum mechanical transition probability for each mechanism. Fig. 2 shows the time evolution of the electron energy measured relative to the ground level for various initial electron energies in the case of strong lateral confinement ($\hbar\omega_x = \hbar\omega_y = 2$ meV). The results are averaged over 15 000 QDs and over all degenerate initial levels. The respective relaxation times vary between 50 and 100 ps, consistent with the transition rates given in Fig. 1. Fig. 3 shows the average electron energy versus time for weak lateral confinement ($\hbar\omega_x = \hbar\omega_y = 0.1$ meV) on a semi-logarithmic scale. The interlevel decay of electrons is clearly non-exponential. The relaxation dynamics signifi-

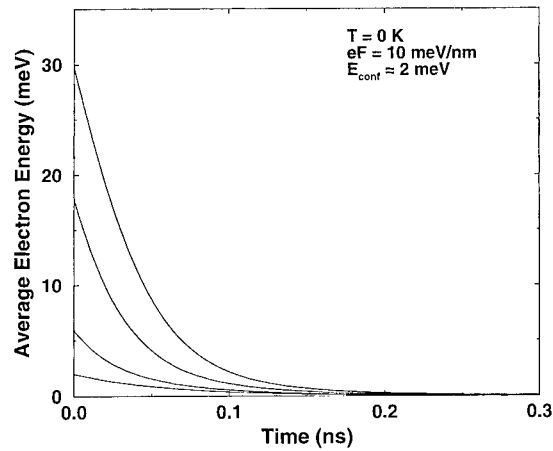


Fig. 2. Average electron energy versus time for strong lateral confinement (linear plot).

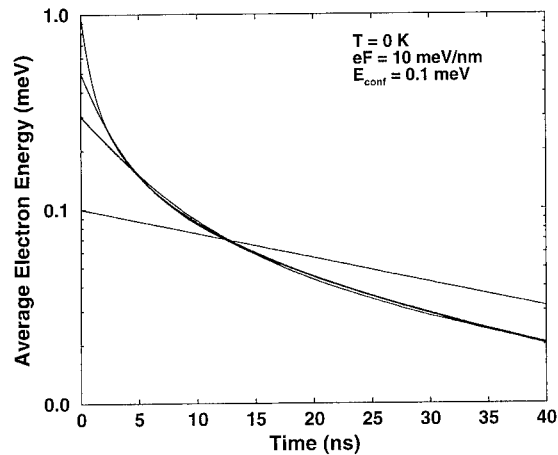


Fig. 3. Average electron energy versus time for weak lateral confinement (semi-logarithmic plot). The electron decay is non-exponential.

cantly slows down as the electron decays towards the ground state. This slowdown is due to the reduced interlevel spacing, which suppresses the electron-phonon scattering rate. The simulated time constants become longer and are on the order of nanoseconds.

Fig. 4 illustrates the effect of non-zero temperature on the relaxation rate for the 2 meV confinement energy case of Fig. 2. Increasing temperature results in an increase of both phonon absorption and emission in the relaxation process, which results in non-zero

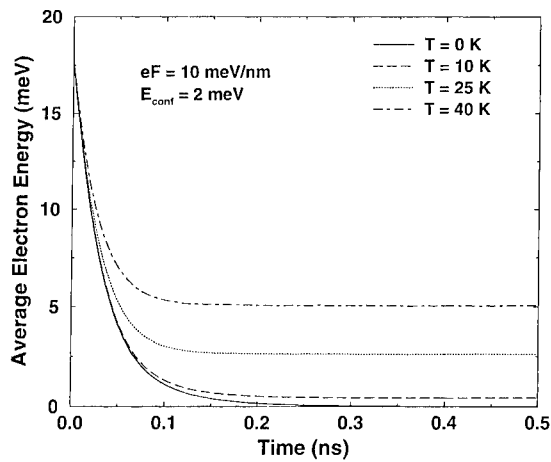


Fig. 4. Average electron energy versus time for the same parameters as Fig. 2, but for different lattice temperatures.

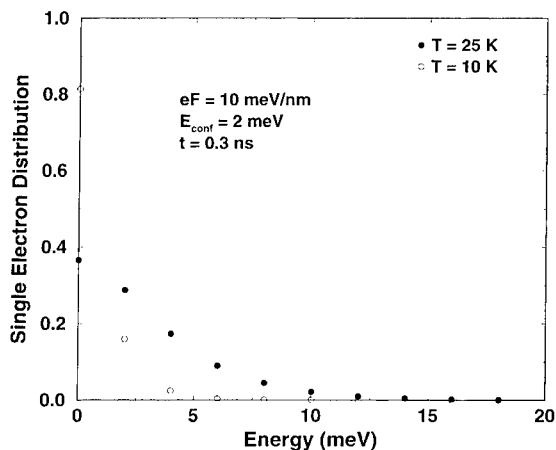


Fig. 5. Plot of the steady-state single-particle level occupancy for two different temperatures corresponding to the parameters of Fig. 2.

energy (relative to the ground level) after long times characteristic of the thermal energy, $k_b T$, due to the balance of absorption and emission events in the dot. This equilibrium state in the dot may be characterized by a distribution function shown in Fig. 5 for two different temperatures. There it is apparent that a Boltzmann-like distribution is established for the occupancy of the different levels, which decreases exponentially with increasing level energy.

Acknowledgements

This work was supported in part by the Office of Naval Research under Contract No. N00014-98-1-0594. Additionally, M.D. would also like to acknowledge the support of the Austrian Science Foundation through the Schrödinger Fellowship J1741-PHY in this work.

References

- [1] U. Bockelmann, *Phys. Rev. B* 50 (1994) 17271.
- [2] H. Benisty, *Phys. Rev. B* 51 (1995) 13281.
- [3] T. Inoshita, H. Sakaki, *Phys. Rev. B* 46 (1992) 7260.
- [4] M. Dür et al., *Nanotechnology* 10 (1999) 142.
- [5] M. Khoury et al., *Appl. Phys. Lett.* 74 (1999) 1576.
- [6] T. Ando et al., *Rev. Mod. Phys.* 54 (1982) 437.
- [7] A. Kumar et al., *Phys. Rev. B* 42 (1990) 5166.
- [8] C. Herring, E. Vogt, *Phys. Rev.* 101 (1956) 944.
- [9] V.V. Mitin, *Z. Phys. B* 60 (1985) 1.
- [10] W. Weber, *Phys. Rev. B* 15 (1977) 4789.



ELSEVIER

Physica E 7 (2000) 237–240

PHYSICA E

www.elsevier.nl/locate/physa

Time-resolved intersubband optical transitions in resonantly optically pumped semiconductor lasers

I. Shtrichman^a, U. Mizrahi^a, D. Gershoni^{a,*}, E. Ehrenfreund^a, K.D. Maranowski^b,
A.C. Gossard^b

^aPhysics Department and Solid State Institute, Technion-Israel Institute of Technology, Haifa 32000, Israel

^bMaterials Department, University of California, Santa Barbara, CA 93106, USA

Abstract

Using picosecond visible-pump mid-infrared-probe technique, we directly measured the photoexcited electron dynamics in the first conduction subband of a GaAs/AlGaAs quantum well laser, below and above its threshold. Our results clearly show that even at low temperatures, under optical excitation into the lowest heavy hole exciton resonance, GaAs/GaAlAs quantum well lasers lase in accordance with the common two-plasma model and not from an excitonic phase. © 2000 Elsevier Science B.V. All rights reserved.

Keywords: Picosecond spectroscopy; Electron–hole plasma; Pump and probe; Excitons

The dynamics of charge carriers and photons in operating semiconductor lasing devices has been studied and investigated very intensively during the last few decades [1–4]. It is commonly accepted that in bulk and hetero-structured semiconductor lasers, stimulated emission and gain is achieved by the creation of electron and hole plasmas which the energy separation between their quasi Fermi levels is larger than the semiconductor fundamental band gap [5]. A characteristic signature of this behavior is the spectral shift towards lower energy of the stimulated emission relative to the spontaneous one. In some special cases,

however, different behavior was noticed [6]. Under these circumstances, where no such spectral shift was observed, other lasing mechanisms were invoked. Mechanisms such as stimulated emission through annihilation of localized excitons [6–8], exciton–exciton interaction, biexciton decay [9,10] exciton–optical-phonon interaction [11], or even exciton condensation [12,13], have been suggested, and their relevance and agreement with the experimental observations were discussed.

To date, all the experimental studies of these systems were based on optical transitions across the fundamental band gap of the lasing device [1–4,14]. In this work we use, for the first time, optical-picosecond pulses to pump the laser, together with a synchronous infrared (IR) pulse, selectively tuned into the quantum

* Corresponding author. Tel.: +972-4-8293693; fax: 972-4-823 5107.

E-mail address: dg@physics.technion.ac.il (D. Gershoni)

structure intersubband optical transition resonance, to directly probe the dynamics of the electronic plasma. In our experiments, the intersubband probe does not create an electron–hole pair but rather induces an optical transition of only one type of photoexcited carrier (an electron in our case). Therefore, the probe pulse is not subjected to the exclusion principle and is extremely sensitive to the momentum state of the carrier whose optical transition is being induced. Thus, a direct measurement of the population of carriers in various momentum states within the first, lasing electronic subband is obtained [15]. In addition, the technique has the advantage of totally different spectral ranges for the pump and the probe beams. This enables a background-free measurements even at resonance, near band-gap pumping.

We study a molecular-beam epitaxy-grown GaAs/AlGaAs heterostructure laser with a periodic quantum structure embedded in its active region. The sample contains 25 periods of 60 Å thick GaAs well followed by 120 Å thick $\text{Al}_{0.33}\text{Ga}_{0.67}\text{As}$ barrier. Two 1 μm thick $\text{Al}_{0.5}\text{Ga}_{0.5}\text{As}$ layers, on each side of the periodic structure separately, confined the optical mode (see inset to Fig. 1). We calculate that at the lasing wavelength (768 nm), 96% of the electromagnetic energy is confined within the active region. Fig. 1 describes schematically the sample. The edges of the sample were cleaved and then polished at 45° to the growth axis in order to form a waveguide for the IR radiation and to enable a considerable electric field component along the growth axis. The substrate was then thinned down and laser bars with 0.6 mm long optical cavities were cleaved. We used a cylindrical lens to focus the pump pulse on the laser bars and monitored the temporally integrated emission along the cavity direction using a monochromator followed by an array of detectors. At the same time, the intersubband photo-induced absorption (PIA) could be determined from the measured transmission of the IR probe pulse through the waveguide. By changing the pump–probe delay time, the temporal evolution of the photoexcited carriers following the excitation pulse was monitored [16]. The temporal and spectral resolution of the experimental setup were 4 ps and 0.8 meV, respectively.

When the focusing lens was oriented perpendicularly to the optical cavity there was no lasing and the integrated emission intensity was almost linear with

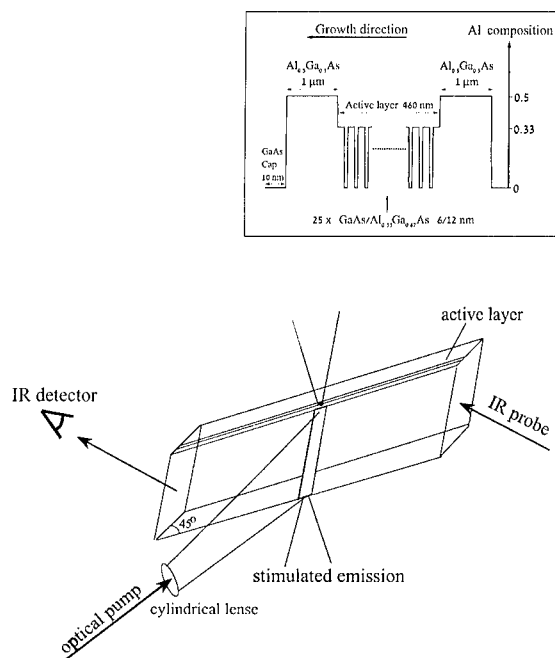


Fig. 1. Schematic description of the experimental arrangement. The pump pulse induces lasing along the cavity direction, while at the same time the intersubband absorption is measured with an IR probe pulse. The inset shows the layers structure.

pump intensity. For a lens orientation along the optical cavity the spectrum evolved with the increase of the excitation density such that above a certain threshold, a low-energy spectral line appeared and lasing action was established. In this case the emission intensity grew very rapidly with the excitation density above threshold. We estimated a typical threshold density of $4.5 \times 10^{11} \text{ cm}^{-2}$ for our laser bars. The lasing emission energy at 10 K was 15 meV below the heavy-hole excitonic resonance (HH1), and 10 meV below the spectral peak of the spontaneous emission.

In Fig. 2 we show the intersubband PIA spectrum (bottom), and its excitation spectrum (top), where the two lowest excitonic resonances HH1, LH1 are clearly resolved. We follow the dynamics of the electronic population in the E1 level, by measuring the PIA transients at various IR wavelengths within the E1–E2 transition resonance. The measured transients are then summed over the whole spectral range of this resonance (8 meV). We pump the sample at the energy of the lowest excitonic

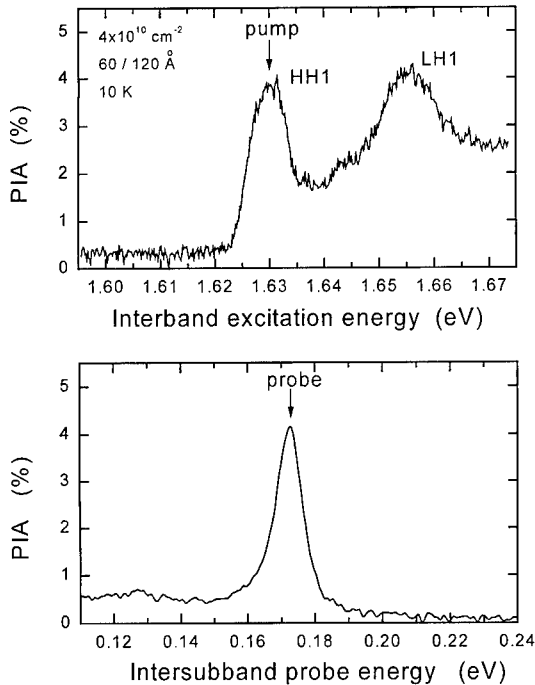


Fig. 2. (bottom) CW measured intersubband PIA spectrum of the laser sample; (top) excitation spectrum of the intersubband PIA measured 60 ps after the excitation pulse.

resonance, HH1. In Fig. 3 we display the spectrally integrated intersubband absorption as a function of time for three different pump intensities. The left panel shows the temporal evolution under non-lasing conditions. The integrated absorption, which is proportional to the electron density in E1, decays exponentially with a characteristic lifetime of $\cong 300$ ps, which is almost excitation density independent. The inset (Fig. 3, left panel) displays the temporally and spectrally integrated intersubband absorption as a function of pump density for this case. We note that the average population of E1 grows sub-linearly with pump intensity due to the bleaching of the excitonic resonance at these high excitation densities [17]. The mid panel of Fig. 3 displays the temporal evolution of the PIA when the orientation of the cylindrical lens was along the optical cavity and efficient feedback was therefore set in. Above threshold (10 mW), lasing action was clearly observed. Below threshold (3 mW), the behavior is identical to that of the previ-

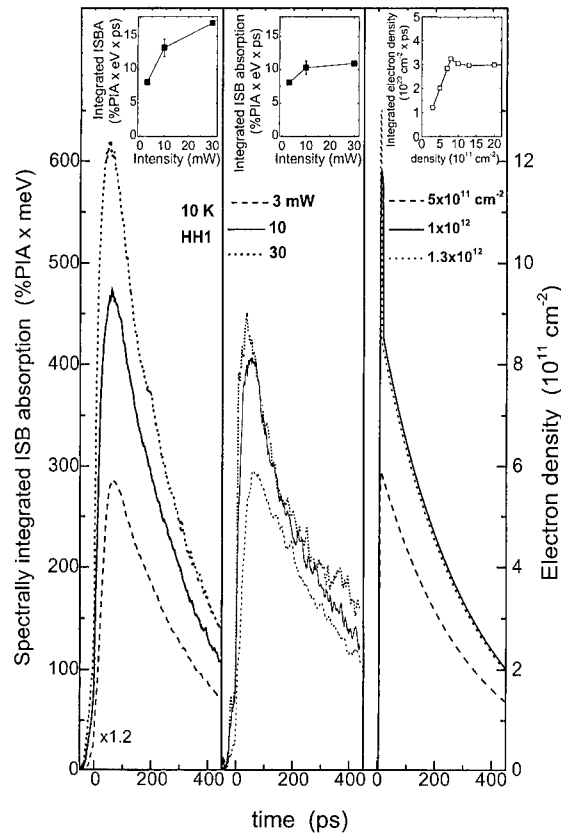


Fig. 3. Spectrally integrated intersubband PIA as a function of time for the "laser" sample at three pump densities: (left (mid) panel) sample in non-lasing (lasing) pumping configuration; (left (mid) inset) temporally and spectrally integrated PIA intensity as a function of pump intensity for non-lasing (lasing) pumping configuration into the HH1 resonance at 10 K; (right panel) calculated electron density from a rate equations model.

ous case. At and above threshold, however, the situation is markedly different. In these cases the stimulated emission significantly limits the density of electrons within the lasing cavity and as a result the PIA signal ceases to increase with the excitation density. The maximum of the PIA remains merely the same, even when the excitation density is increased by a factor of 3. After reaching its maximum, the absorption rapidly drops below a certain level, from where it continues to decay in a similar way to the non-lasing cases. The inset to the mid panel of Fig. 3 shows the temporally and spectrally integrated intersubband absorption as a function of pump density

for this case. We clearly note that above threshold the electronic density is saturated. This saturation is very similar in nature to the well-known above-threshold clamping of the quasi-Fermi level in steady-state operation of semiconductor lasers [14].

Our results can be interpreted in the following way. Right after the above-threshold pump pulse ($\cong 10$ ps) lasing action begins and the E1 level is forced to depopulate at very short times due to the presence of immense number of cavity photons during the lasing action. After the electron density drops below the lasing threshold (at $\cong 60$ ps), the depopulation of E1 is still rapid due to stimulated emission during the intermediate regime. After the electron density drops further ($\cong 150$ ps), spontaneous emission remains the only decay mechanism of the electronic population and the PIA decays similarly to the non-lasing cases.

In order to quantitatively account for these results, we numerically solved three-coupled rate equations for the electrons, holes and photons within our optical cavity. The temporal behavior of the electronic population for various initial pulse densities are displayed in the right panel of Fig. 3. We note that our simple two-plasma rate equations model explains at least semi-quantitatively our experimental measurements. With our limited temporal resolution we cannot resolve experimentally the initial very rapid spike ($\cong 2$ ps) that is clearly seen in the calculated electron density above threshold. However, the clamping of the electron density above threshold to its threshold value is very clear both in the experiment and in the calculation (Fig. 3, right panel inset). We find that the calculated pump densities that are best fitted to the measurements are in very good agreement with our estimated experimental pump densities, when the exciton bleaching phenomenon mentioned above is taken into consideration.

These measurements and calculations demonstrate the validity and usefulness of our novel experimental method for studying the dynamics of carriers within an operating quantum-well-based semiconductor laser.

Specifically, our results clearly show that even at low temperatures, under optical excitation into the

lowest HH exciton resonance, conventional GaAs/GaAlAs quantum well lasers lase in accordance with the common two plasmas model and not from an excitonic phase.

Acknowledgements

The work at Technion was supported by the Israel Science Foundation founded by the Israel Academy of Sciences and Humanities.

References

- [1] T. Takahashi, M. Nishioka, Y. Arakawa, *Appl. Phys. Lett.* 58 (1991) 4.
- [2] T. Sogawa, Y. Arakawa, *IEEE J. Quantum Electron.* 27 (1991) 1648.
- [3] P. Michler, A. Lohner, W.W. Rühle, G. Reiner, *Appl. Phys. Lett.* 66 (1995) 1599.
- [4] F. Sogawa, A. Hangleiter, H. Watabe, Y. Nagamune, M. Nishioka, Y. Arakawa, *Appl. Phys. Lett.* 69 (1996) 3137.
- [5] A. Yariv, *Quantum Electronics*, 3rd Edition, Wiley, Singapore, 1989.
- [6] J. Ding, H. Jeon, T. Ishihara, M. Hagerott, A.V. Nurmikko, H. Luo, N. Samarth, J. Furdyna, *Phys. Rev. Lett.* 69 (1992) 1707.
- [7] K.B. Ozanyan, J.E. Nicholls, M. O'Neill, L. May, J.H.C. Hogg, W.E. Hagston, B. Lunn, D.E. Ashenford, *Appl. Phys. Lett.* 69 (1996) 4230.
- [8] X. Fan, H. Wang, H.Q. Hou, B.E. Hammons, *Phys. Rev. B* 56 (1997) 15256.
- [9] F. Kreller, M. Lowisch, J. Puls, F. Henneberger, *Phys. Rev. Lett.* 75 (1995) 2420.
- [10] V. Kozlov, P. Kelkar, A. Vertikov, A.V. Nurmikko, C.-C. Chu, J. Han, C.G. Hua, R.L. Gunshor, *Phys. Rev. B* 54 (1996) 13932.
- [11] I. Galbraith, S.W. Koch, *J. Crystal Growth* 159 (1996) 667.
- [12] P.B. Littlewood, Xuejun Zhu, *Phys. Scripta T* 68 (1996) 56.
- [13] H. Chu, Y.C. Chang, *Phys. Rev. B* 54 (1996) 5020.
- [14] T. Paoli, *IEEE J. Quantum Electron.* 9 (1973) 267.
- [15] R. Duer, I. Shtrichman, D. Gershoni, E. Ehrenfreund, *Phys. Rev. Lett.* 78 (1997) 3919.
- [16] R. Duer, D. Gershoni, E. Ehrenfreund, *Superlattices Microstruct.* 17 (1995) 5.
- [17] S. Schmitt-Rink, D.S. Chemla, D.A.B. Miller, *Adv. Phys.* 38 (1989) 89.



ELSEVIER

Physica E 7 (2000) 241–244

PHYSICA E

www.elsevier.nl/locate/physa

Emission of mid-infrared radiation and intersubband population inversion in near-infrared laser QW structures

L.E. Vorobjev^a, D.A. Firsov^a, V.A. Shalygin^{b,*}, Zh.I. Alferov^b, N.N. Ledentsov^b,
V.M. Ustinov^b, Yu.M. Shernyakov^b, V.N. Tulupenko^c

^aRadio Physical Department, St. Petersburg State Technical University, St. Petersburg 195251, Russia

^bA.F.Ioffe Institute, St. Petersburg 194021, Russia

^cDonbass State Engineering Academy, Kramatorsk 343913, Ukraine

Abstract

A new possibility to obtain the intersubband population inversion under current injection (or optical pumping) of the electrons into the structure with GaAs/AlGaAs quantum wells (QWs) is discussed. The QWs are embedded into the *i*-layer of a p^+-i-n^+ heterostructure. We consider QWs of funnel shape with three electron levels and find the conditions to realize mid-infrared (MIR)-stimulated emission due to intersubband electron transitions under simultaneous stimulated emission of near-infrared (NIR) radiation due to interband transitions. Experimental data on spontaneous MIR emission from InGaAs/GaAs QWs under simultaneous NIR lasing are presented. © 2000 Elsevier Science B.V. All rights reserved.

Keywords: Near-infrared lasing; Stimulated emission; Current injection; Optical pumping

1. Introduction

MIR semiconductor lasers ($\lambda = 4\text{--}15\text{ }\mu\text{m}$) can find extensive applications in different fields. The development of physics and technology of low-dimensional structures opens up new possibilities in the development of MIR lasers. Many attempts have been made to find structures with quantum wells in which an intraband population inversion between the size-quantization levels in a quantum well can be produced. Studies in this field have already resulted

in the development of quantum cascade lasers [1] and fountain lasers with optical pumping [2].

In this paper we consider the principles of producing intraband population inversion in QWs under current injection of electrons into the *i*-region of a NIR laser heterostructure. Two special features of the appearance of the intraband population inversion can be noted. First, a long-lived energy level (“metastable” level) should exist. Second feature is the simultaneous stimulated emission in the NIR range due to interband optical transitions of electrons ($h\nu \approx E_g$). We calculate the intraband population inversion rate and the optical gain in MIR range for specially designed heterostructures with asymmetric QWs of funnel shape.

* Corresponding author. Fax: +7-812-533-4717.

E-mail address: vadim@twonet.stu.neva.ru (V.A. Shalygin)

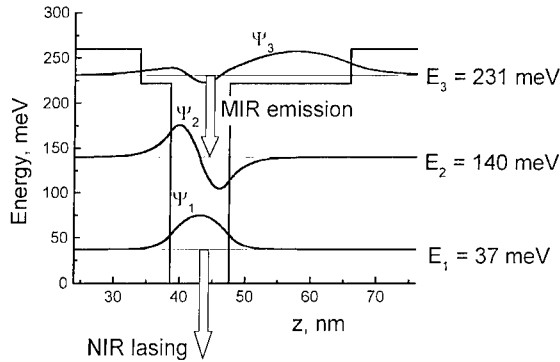


Fig. 1. The configuration of a QW in the form of an asymmetric funnel. The energy levels and wave functions for the electron states are shown.

The threshold injection current for MIR lasing is estimated. Similar calculations are also performed for the case of interband optical pumping of the structure.

As a first step in the creation of MIR laser of new type the experimental data on spontaneous MIR emission from InGaAs/GaAs QWs under simultaneous NIR lasing are presented.

2. Intraband population inversion

Let us consider a p^+-i-n^+ GaAs/AlGaAs NIR laser structure containing a QW in the form of an asymmetric funnel incorporated into its i -layer (Fig. 1). The narrow part of the funnel is formed by a GaAs layer of thickness 9 nm, with two asymmetrically arranged $\text{Al}_{0.29}\text{Ga}_{0.71}\text{As}$ layers of total thickness 23 nm adjacent to it. To the left and right of the QW there are two $\text{Al}_{0.34}\text{Ga}_{0.66}\text{As}$ layers and then two $\text{Al}_x\text{Ga}_{1-x}\text{As}$ layers of variable composition with x varied from 0.34 to 0.9. The variable composition layers form a composite waveguide in i -layer of laser structure both for NIR and MIR radiation.

According to calculations, such a complex QW has three size-quantization levels with energies $E_1 = 37$, $E_2 = 140$ and $E_3 = 231$ meV. Note that the energy spectrum in the region above the barrier is quasi-discrete, with the levels separated by a distance about of 1 meV. The electrons injected into the i -layer occupy the quasi-discrete levels in the region above the barrier and then they are trapped at the E_1 , E_2 and E_3 levels of QW due to scattering by polar optical

(PO) phonons (scattering by acoustic phonons and interface imperfections can be neglected).

Under stationary conditions, the electron concentrations at different levels can be found from the system of rate equations, taking into account only basic processes:

$$\eta \frac{J}{e} A_3 - N_3 W_{23} - N_3 W_{13} - N_3 (\tau_{v3}^{\text{sp}})^{-1} = 0, \quad (1)$$

$$\eta \frac{J}{e} A_2 + N_3 W_{23} - N_2 W_{12} - N_2 (\tau_{v2}^{\text{sp}})^{-1} = 0, \quad (2)$$

$$\eta \frac{J}{e} A_1 + N_3 W_{13} + N_2 W_{12} - N_1 (\tau_{v1}^{\text{sp}})^{-1} - B_1^{\text{st}} n_{\text{NIR}} = 0, \quad (3)$$

where J is injection current density; coefficient η takes into account a decrease in the number of carriers caused by recombination outside the QW; N_i and A_i are the surface electron concentration and probability of trapping at the level E_i ; W_{ji} is the probability of intersubband transitions, τ_{vi}^{sp} is the lifetime of an electron at the level E_i relative to the radiative recombination during spontaneous interband emission. The last term in Eq. (3) describes the depletion of level E_1 due to stimulated NIR emission, where n_{NIR} is the photon density and B_1^{st} is a proportionality coefficient. We consider the case of low temperatures when $k_B T \ll \Delta E_{ij}$, $\hbar\omega_0$ ($\hbar\omega_0$ is the PO phonon energy), so we neglect intersubband thermal excitation and take into account the intersubband transitions due to emission of PO phonons only. The total probability of the transition from the state $E_i(\mathbf{k}_{\perp i})$ to the subband E_j is

$$W_{ji}(\mathbf{k}_{\perp i}) = \frac{2\pi}{\hbar} \sum_{\mathbf{k}_{\perp j}} \sum_{q_z} |C_q|^2 |J_{ji}(q_z)|^2 \cdot \delta_{q_{\perp}, \mathbf{k}_{\perp j} - \mathbf{k}_{\perp i}} \times \delta \left[E_i + \frac{\hbar^2 k_{\perp i}^2}{2m_e} - E_j - \frac{\hbar^2 k_{\perp j}^2}{2m_e} - \hbar\omega_0 \right], \quad (4)$$

where \mathbf{k}_{\perp} is the electron wave vector perpendicular to the axis of growth, and C_q determines the electron-phonon interaction energy

$$|C_q|^2 = \frac{2\pi e^2 \hbar \omega_0}{V(q_{\perp}^2 + q_z^2) \epsilon^*}, \quad \frac{1}{\epsilon^*} = \frac{1}{\epsilon_{\infty}} - \frac{1}{\epsilon_0}, \quad (5)$$

q_{\perp} and q_z are components of the phonon wave vector perpendicular and parallel to the growth axis. The

integral J_{ji} characterizes the overlap of the electron wave functions for levels E_i and E_j :

$$J_{ji}(q_z) = \int \psi_j^*(z) e^{-iq_z z} \psi_i(z) dz. \quad (6)$$

Calculations yield the following results for our QW: $W_{12} = 3 \times 10^{12} \text{ s}^{-1}$; $W_{23} = 2.6 \times 10^{11} \text{ s}^{-1}$; $W_{13} = 8.4 \times 10^{10} \text{ s}^{-1}$, $A_1 = 0.02$; $A_2 = 0.03$; $A_3 = 0.95$. Thus, $W_{13}, W_{23} \ll W_{12}$, and $A_1, A_2 \ll A_3$, and hence, the E_3 level can be called “metastable”. In addition, the probability W_{ii} of intraband transitions exceeds the probability W_{ji} of transitions between subbands: $W_{ii} \gg W_{ji}$. The probability of the radiative interband recombination is relatively small: $(\tau_{v1}^{\text{sp}})^{-1} \simeq 10^9 \text{ s}^{-1}$. Then we obtain for population inversion between E_3 and E_2 levels:

$$N_3 - N_2 \approx \frac{\eta J A_3}{e(W_{13} + W_{23})}. \quad (7)$$

Let us express $N_3 - N_2$ in the terms of threshold current for NIR lasing $J_{\text{th}}^{\text{NIR}}$, which usually is about 200 A/cm^2 in similar NIR lasers. Near the threshold we obtain from Eqs. (1)–(3): $N_{1\text{th}} = \eta J_{\text{th}}^{\text{NIR}} \tau_{v1}^{\text{sp}} / e \approx 5.5 \times 10^{11} \text{ cm}^{-2}$ and $N_3 - N_2 = 1.7 \times 10^9 \text{ cm}^{-2}$ (at $\eta = 0.5$). For $J > J_{\text{th}}^{\text{NIR}}$ the photon density is $n_{\text{NIR}} \sim (J/J_{\text{th}}^{\text{NIR}} - 1)$, and assuming approximately $B_1^{\text{st}} \sim N_1$ [3], we obtain that the electron concentration on the level E_1 is independent of current: $N_1 \simeq \text{const} = N_{1\text{th}}$. For these conditions the population inversion is proportional to the current: $N_3 - N_2 = 1.7 \times 10^9 \text{ cm}^{-2} J/J_{\text{th}}^{\text{NIR}}$, and we can obtain a large optical gain for MIR radiation under transition $E_3 \rightarrow E_2$.

Note once more that the generation of NIR radiation is an important condition for obtaining the population inversion. Stimulated NIR radiation removes electrons from the E_1 level and thus maintains the constant concentration of electrons at this level at $J \gg J_{\text{th}}^{\text{NIR}}$. Otherwise already at $J/J_{\text{th}}^{\text{NIR}}$ the electron concentration would be so high that the thermal excitation to upper levels would reduce the population inversion.

3. Amplification of MIR radiation and lasing

We have designed the heterostructure with 10 QW layers and composite waveguide that confines both MIR and NIR radiation (Figs. 2 and 3). MIR radiation due to transitions $E_3 \rightarrow E_2$ ($\lambda = 14 \mu\text{m}$) has the factor

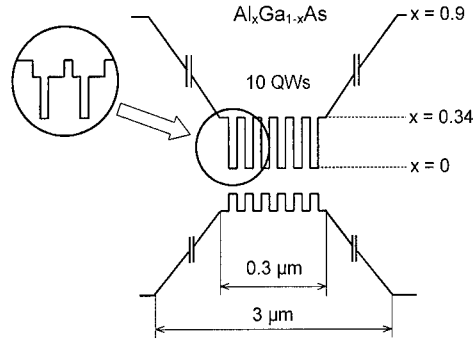


Fig. 2. Design of the composite waveguide that confines both MIR and NIR radiation in the laser structure.

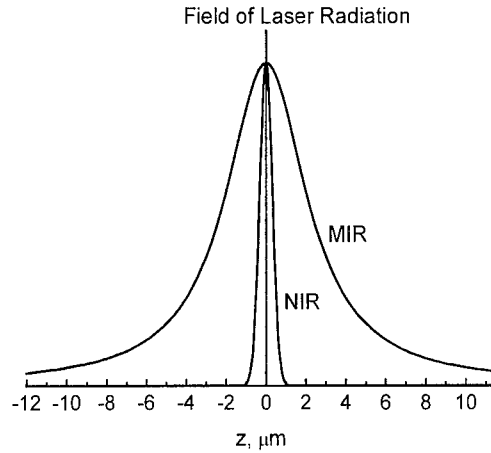


Fig. 3. Field distribution for MIR and NIR radiation in the composite waveguide.

of optical confinement $\Gamma \approx 0.1$. At resonator length about 1.5 mm the lasing condition is satisfied with the optical gain $\alpha_{32} = 68 \text{ cm}^{-1}$.

In accordance with Ref. [4] we can find the gain under direct optical transitions between levels E_3 and E_2 :

$$\alpha_{32} = \frac{4\pi e^2 (N_3 - N_2) \cos^2 \theta}{cn_r L_w} \omega_{32} |Z_{32}|^2 \times \frac{\gamma}{\gamma^2 + (\hbar\omega - \hbar\omega_{32})^2}, \quad (8)$$

where $Z_{32} = \int \psi_3^* z \psi_2 dz = 1.4 \text{ nm}$; θ is the angle between the growth direction and the polarization vector of the wave; γ is the broadening and n_r is the

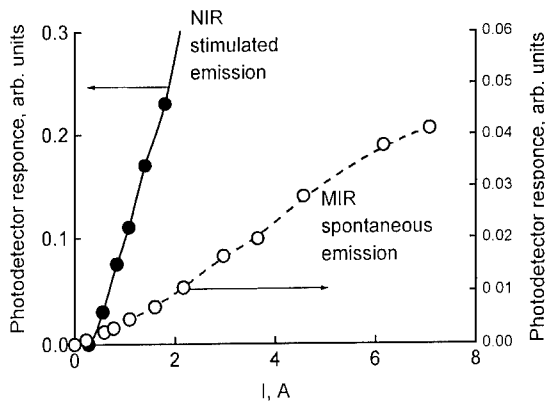


Fig. 4. Intensities of spontaneous intersubband MIR radiation and stimulated interband NIR radiation from the NIR laser structure under current injection.

refraction index. According to calculations the value of optical gain necessary for MIR lasing can be obtained with $N_3 - N_2 = 1.3 \times 10^{10} \text{ cm}^{-2}$.

Since the structure contains 10 QWs we must multiply the right-hand side of Eq. (7) to the factor 0.1 and then we can calculate the threshold current for MIR lasing: $J_{\text{th}}^{\text{MIR}} = 76J_{\text{th}}^{\text{NIR}} = 1.5 \times 10^4 \text{ A/cm}^2$. In the case of interband optical pumping ($h\nu > E_g$) the threshold power of excitation is equal $P_{\text{th}}^{\text{MIR}} = J_{\text{th}}^{\text{MIR}} h\nu/e = 7 \times 10^3 \text{ W/cm}^2$.

4. Spontaneous emission of MIR radiation from NIR laser QW structures

Experimental studies of spontaneous intersubband MIR emission were performed in NIR injection laser with $\text{In}_{0.2}\text{Ga}_{0.8}\text{As}/\text{GaAs}$ QWs embedded into intrinsic layer of p^+-i-n^+ diode structure. The QWs had two electron levels with energy distance between them about 108 meV. The laser had a waveguide only for NIR radiation ($\lambda \approx 0.9 \mu\text{m}$). To detect MIR radiation we used Ge : Cu and Si : B photoresistors. InSb and Ge filters were used to cut-off the stimulated NIR radiation. Using a set of optical filters with different transmission spectra (CaF_2 , BaF_2 , NaCl , and KBr) we have found that the observed MIR radiation lies in the range 9–20 μm . The experimental results are presented in Fig. 4. The dashed line demonstrates stimulated NIR emission, the solid line shows spontaneous MIR

emission. It should be emphasized that MIR emission has no saturation at the currents exceeding the threshold current of NIR lasing more than 20 times. This fact means that electron concentration on the level E_1 does not increase and electron–electron collisions do not influence the population of upper levels. The ground subband always has free states (they are located above the Fermi quasi-level), so intersubband transitions can occur at any current. That is why spontaneous MIR emission from these structures has no threshold. Earlier observed spontaneous MIR emission from $\text{InGaAs}/\text{AlGaAs}$ NIR laser structures with quantum dots had a threshold current close to the threshold of NIR lasing [5].

5. Conclusion

Principles of producing population inversion and generation of MIR radiation using intersubband transitions of electrons in QWs in NIR laser structures are suggested. The first experimental studies of spontaneous MIR emission are performed on similar structures. So, the first step in the development of MIR laser of new type with current or optical pumping has been done.

Acknowledgements

This work was supported in part by RFBR, Grant 99-02-17102; INTAS, Grant 97-0751; Russian Program “Integration”, Grant 75; Program “Physics of Solid State Nanostructures”.

References

- [1] J. Faist, F. Capasso, D.L. Sivco, C. Sirtori, A.L. Hutchinson, A.Y. Cho, *Science* 264 (1994) 553.
- [2] O. Gauthier-Lafaye, P. Boucaud, F.H. Julien, S. Sauvage, S. Cabaret, J.-M. Lourtioz, V. Thierry-Mieg, R. Planel, *Appl. Phys. Lett.* 71 (1997) 3619.
- [3] W. Tsang (Ed.), *Semiconductor injection lasers*, Chapter 2, in: *Semiconductors and Semimetals*, Vol. 22, Academic Press Inc., New York, 1985.
- [4] T. Ando, A. Fowler, F. Stern, *Rev. Modern Phys.* 54 (1982) 437.
- [5] L.E. Vorobjev, D.A. Firsov, V.A. Shalygin, V.N. Tulupenko, Yu.M. Shernyakov, N.N. Ledentsov, V.M. Ustinov, Zh.I. Alferov, *JETP Lett.* 67 (1998) 275.



ELSEVIER

Physica E 7 (2000) 245–249

PHYSICA E

www.elsevier.nl/locate/physa

Modulated resonant Raman and photoluminescence spectroscopy of Bragg confined asymmetric coupled quantum wells

M. Levy^{a,*}, R. Kapon^b, A. Sa'ar^b, R. Beserman^a, V. Thierry-Mieg^c, R. Planel^c

^a*Solid State Institute and Physics Department, Technion, Israel Institute of Technology, Technion City, Haifa 32000, Israel*

^b*Department of Applied Physics, The Fredi and Nadine Hermann School of Applied Science, The Hebrew University of Jerusalem, Jerusalem 91904, Israel*

^c*Laboratoire de Microstructures et Microelectronique – CNRS, 196 Avenue H. Ravera, BP107, 92225 Bagneux, France*

Abstract

Electronic Bragg mirrors were used to confine carriers at energy levels above the barrier height in asymmetric coupled quantum wells. Two classes of above barrier states were resolved by using photoluminescence, photoluminescence excitation and modulated resonant Raman spectroscopy. The first class is Bragg confined levels that are highly localized in the asymmetric quantum wells region and are red shifted when locally excited electric field is generated in the asymmetric coupled quantum well region. The second class of levels that extend mainly above the reflectors is not shifted when the locally excited field is generated. This phenomenon is due to the smaller confinement of the extended states in the asymmetric quantum well region. © 2000 Elsevier Science B.V. All rights reserved.

Keywords: Bragg states; Intersubband transitions; Modulated resonant Raman scattering

The presence of Bragg reflectors on each side of a quantum well (QW) leads to a confinement of the energy levels above the barrier height. Two kinds of states exist: the first group, called Bragg states, are highly localized in the QW region due to the Fabry–Perot effect of the reflectors while the second group forms mini-bands in the continuum that mainly extend over the reflectors. Despite several reports on above the barrier states in Bragg confined structures none of these works provide direct evidence to the existence of two different classes of above the barrier states.

In a previous [1] work we provided experimental evidence to the existences of quasi-continuum and quasi-bound states in an asymmetric coupled QW (ACQW) structure. While quasi-continuum states are localized in the barrier region, quasi-bound states can be viewed as resonances of the QW where a significant fraction of the envelope wave function is localized in the ACQW region. Using the newly developed method of locally modulated resonant Raman spectroscopy (MRRS) we were able to resolve each group of states.

In order to increase the confinement of the quasi-bound states and thus to increase the overlap with bound states we replaced the barriers with

* Corresponding author. Fax: 972-4-8235107.

E-mail address: sslevy@tx.technion.ac.il (M. Levy)

Bragg reflectors. These quarter wavelength structures strongly reduce the envelope wave-function amplitude outside the ACQW and generate a truly bound state in the continuum, called Bragg levels [2,3]. The Bragg reflectors are composed of a finite superlattice (SL) designed so that the barriers (L_B) and wells (L_W) widths in the SL section equal the integer times the electron De-Broglie quarter-wavelength $L_{W,B} = (n \times \lambda_{W,B})/4$. Furthermore, the Bragg levels also obey the Bragg criterion where the ACQW width equals integer times the electron De-Broglie half-wavelength [4–6] $L_{ACQW} = (n \times \lambda_{ACQW})/2$.

In the present work we report a detailed investigation of the confinement of these Bragg levels in the ACQW region. By generating a localized DC electric field in the ACQW region and using the MRRS technique we were able to resolve two classes of states. The first class is a Bragg state confined in the ACQW region and the second class is confined in the reflectors region.

The sample consists of 25 periods of a Bragg confining structure (see Fig. 1) that is composed of an ACQW grown between two GaAs/Al_{0.34}Ga_{0.66}As Bragg mirrors. The ACQW is composed of a 7 nm wide GaAs QW (WQW), a 15 nm Al_{0.2}Ga_{0.8}As intermediate barrier and a 5 nm narrow GaAs QW (NQW). Each Bragg mirror is a 4 period SL where each period consists of 3 nm-GaAs QW and 9 nm-Al_{0.34}Ga_{0.66}As barrier. The sample was n-doped to the level of $2 \times 10^{11} \text{ cm}^{-2}$ in the Bragg confining SL. The whole structure was capped with a 15 nm GaAs layer.

The energy levels and the envelope wave functions were calculated by solving self-consistently the Ben Daniel–Duke Poisson equations for the conduction and the valence envelope functions [7,8] and are shown schematically in Fig. 1. The structure was designed so that the two lowest conduction states E_1 and E_2 are located in the WQW and NQW, respectively. The third conduction subband, E_3 , extends over the entire ACQW and its energy is 115 meV above E_1 . Fig. 1 also shows the Bragg confined level E_B and the two extended levels E_{ex1} and E_{ex2} in the reflector region. The method used to generate the local electric field is also shown schematically in Fig. 1. Carriers located in the ground state (E_1) of the WQW are resonantly excited by a CO₂ laser to E_3 . Some of these carriers loose their energy by phonon assisted relaxation processes and decay to E_2 . Because of the thick barrier

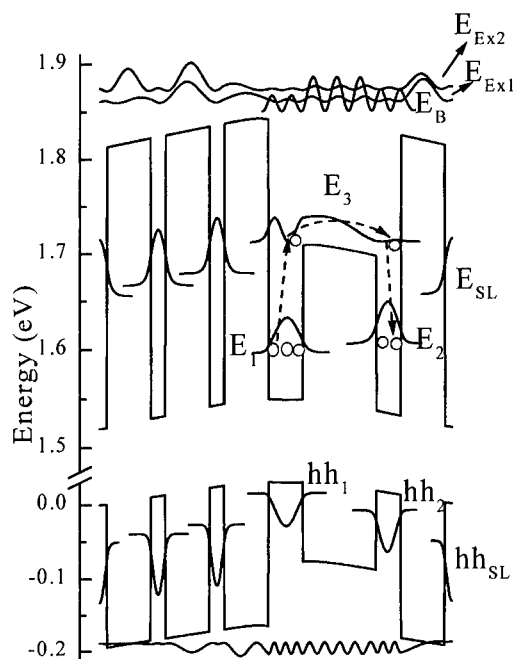


Fig. 1. Schematic description of the energy levels in valence and conduction bands of Bragg confined structure. Also shown is the intersubband excitation process and the charge carrier transfer from the WQW to the NQW. This charge transfer generates the static electric field.

that separates these two levels the relaxation time for electrons in the second level is of the order of several hundreds of picoseconds. As a result in a steady state, there is a net charge transfer from the WQW to the NQW that induces a local electric field across the ACQW. A detailed description of this mechanism including the relevant rate equations is given in Ref. [1].

Using infrared (IR) polarization-resolved absorption spectroscopy we measured the $E_1 : E_3$ transition energy to be 115 meV (see inset of Fig. 2) in good agreement with our calculations. Fig. 2 shows the PL spectrum (a) the PLE (b,c) of the bound states and the PL (d) and PLE (e) spectra of the continuum states. The PL in (a) shows three peaks E_1 , E_2 and E_{SL} at 1.57, 1.605 and 1.705 eV, respectively, which are identified as recombination of bound electrons and holes in the WQW, NQW and bound levels in the Bragg reflectors, respectively. The high-energy part of the PL (d) in Fig. 2 at 2.07 and 2.082 eV is related

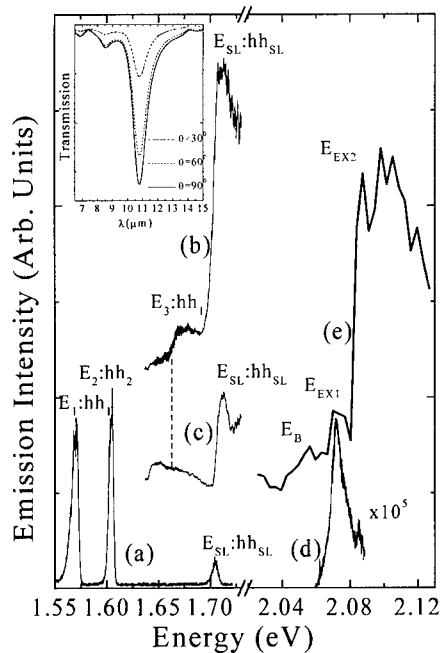


Fig. 2. PL and PLE of bound and above the barrier levels in the Bragg confined structure. (a) PL of the three lowest bound subbands. (b) and (c) PLE of the bound levels monitored at the WQW and NQW respectively. (d) PL of above the barrier states in the reflector region. (e) PLE of above the barrier states monitored at the WQW. The inset shows the intersubband absorption spectrum.

to transitions from E_{ex1} and E_{ex2} , to valence continuum subbands. We monitored the PLE signal at 1.57 eV (WQW) (b) and 1.605 eV (NQW) (c). While the PLE is monitored at the WQW (1.57 eV), we observe a rise in the density of states at an energy of 1.67 eV that corresponds to the $HH_1 : E_3$ transition and is located 115 meV above $E_1 : HH_1$ as expected. This level around 1.67 eV is also seen when the PLE is monitored at 1.605 eV (i.e. the NQW energy). Our findings indicate that, despite that the electron-hole pairs ($HH_1 : E_3$) are initially excited in the WQW, there is an efficient electron transfer to E_2 in the NQW. This is due to the presence of the E_3 electronic level that extend over both WQW and NQW as predicted by our model [1]. Hence, intersubband excitation at 10.6 μm from our CO_2 laser can generate a local dc electric field across the ACQW. The continuum levels E_{ex1} and E_{ex2} are clearly resolved in the PLE spectrum (e) while the Bragg confined level E_B is weakly seen.

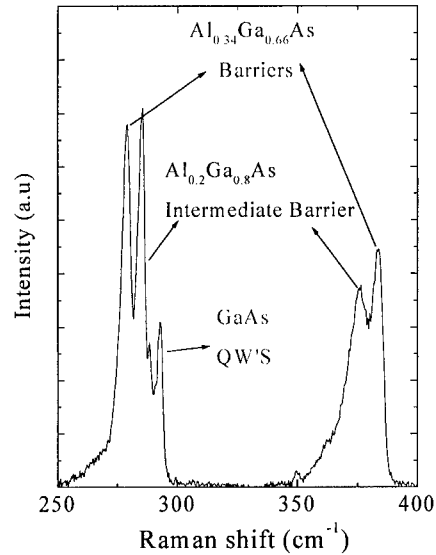


Fig. 3. Raman spectrum of the Bragg confined structure.

Next, the effect of locally modulated DC-electric field on the above the barrier energy levels was investigated using MRRS.

For that purpose we varied the dye laser photon energy in the 1.96–2.16 eV range and by measuring the resonant Raman spectra at 10 K we probed the electronic levels in the continuum. Each electronic level is associated with two resonances in the RRS spectrum [9,10]. The first resonance is achieved when the incident photon energy is close to an electronic transition E_B while the second resonance is achieved when the photon energy is $E_L = E_B + \hbar\omega_{LO}$, where $\hbar\omega_{LO}$ is the energy of the longitudinal (LO) phonon. The Raman spectrum has contributions from three different layers, GaAs, $\text{Al}_{0.2}\text{As}_{0.8}$, and $\text{Al}_{0.34}\text{Ga}_{0.66}\text{As}$ which constitute a single unit cell. Therefore, when recording a single Raman spectrum (Fig. 3), we observe the following phonon vibrations: 292 cm^{-1} (36.2 meV) from the GaAs layers, 285 cm^{-1} (35.3 meV) and 376 cm^{-1} (46.6 meV) which are the GaAs- and AlAs-like modes, of the $\text{Al}_{0.2}\text{As}_{0.8}$ layer, respectively, 280 cm^{-1} (34.7 meV) and 382 cm^{-1} (47.3 meV) are the GaAs- and AlAs-like modes of the $\text{Al}_{0.34}\text{As}_{0.66}\text{As}$ layer, respectively. Fig. 4a and b show the RRS spectra from the GaAs and $\text{Al}_{0.2}\text{As}_{0.8}$ layers, respectively. The Bragg level at 2.52 eV denoted by E_B is seen mainly

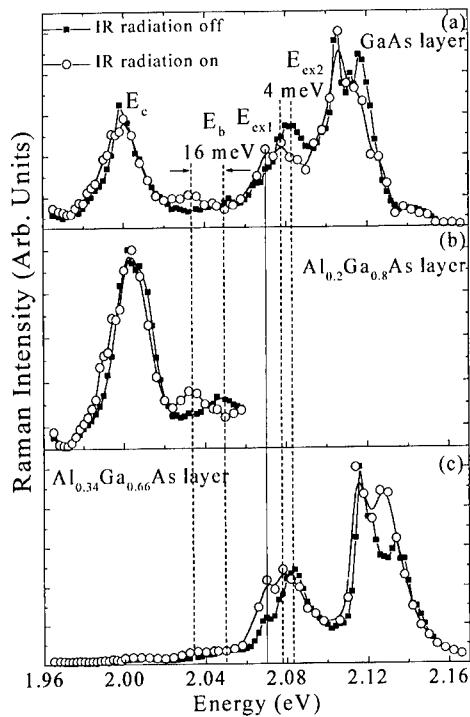


Fig. 4. RRS of the above barrier levels with (solid squares) and without (open circles) IR excitation. (a) RRS from the GaAs layers, (b) RRS from the $\text{Al}_{0.2}\text{Ga}_{0.8}\text{As}$ layers, (c) RRS from the $\text{Al}_{0.34}\text{Ga}_{0.66}\text{As}$ layers.

in these spectra. Furthermore, under infrared excitation of 4 kW/cm^2 , this level is red shifted by 16 meV. The energy levels E_{ex1} at 2.07 eV and E_{ex2} at 2.082 eV were seen in the RRS spectra of all layers but had the largest amplitude in the GaAs layer (Fig. 4a) and $\text{Al}_{0.34}\text{As}_{0.66}\text{As}$ layer (Fig. 4c). Under infrared illumination the level E_{ex1} at 2.07 eV has a very small shift (≤ 1 meV) which cannot be resolved in our experiments. The level E_{ex2} at 2.082 eV red shifts only by 4 meV. The out going beams of these two levels are found at one phonon energy distance above these levels and they are shifted exactly as the incoming beams. Near the continuum onset at 2.007 eV the RRS spectrum show a wide peak. This peak denoted E_c is strongly enhanced in the RRS spectra of the GaAs and $\text{Al}_{0.2}\text{As}_{0.8}\text{As}$ layers, and is very weak in the RRS spectra of the $\text{Al}_{0.34}\text{As}_{0.66}\text{As}$ layers.

Table 1

The calculated γ values for the continuum states

	E_{ex1}	E_{ex2}	E_B
γ	0.13	0.15	0.48

From the RRS results (Fig. 4) we see that under IR illumination the Bragg confined E_B red shifts by 16 meV while the reflector level E_{ex1} is shifted by less than 1 meV. These results can be explained by considering the localization of these states above the barrier levels in the ACQW region. The Bragg confined state is highly localized in the ACQW region. Therefore, under the influence of the local field this level shows a relatively large shift. On the other hand, the extended levels E_{ex1} and E_{ex2} are localized mainly in the reflectors region and therefore, experience much smaller shifts than the Bragg confined level. Our results indicate that the envelope wave function of the level E_{ex2} has a larger overlap with the ACQW and therefore, has a larger shift compared to E_{ex1} .

In order to compare the degree of localization between the Bragg confined level and the reflectors levels we defined the confinement factor, γ , as follows:

$$\gamma = \frac{\int_{\text{asymmetric well}} |\chi_c(z)|^2 dz}{\int_{\text{unit cell}} |\chi_c(z)|^2 dz}, \quad (1)$$

where γ measures the degree of localization of the continuum levels in the ACQW region (where a unit cell is a sum of the ACQW and the SL widths). The calculated values of γ are summarized in Table 1. These values are in good agreement with our experimental results showing that the Bragg level E_B is most localized while E_{ex1} is less localized state in the ACQW.

The linewidths of the electronic levels: E_B , E_{ex1} , E_{ex2} are found to be less than 6 meV, except for E_c which is found to have a line width of 13 meV. The linewidth of E_c suggests that this level is a mini-band formed by the interaction of the electronic wave functions with adjacent unit cells.

In conclusion, by inserting Bragg reflectors in each side of an ACQW and by using modulated

RRS as a probe we see two kinds of confined states. The first kind corresponds to a Bragg level that is confined in the ACQW region. This level was only seen in the RRS profiles of the ACQW layers, and in addition it showed a relatively large red shift when a local static electric field is generated in the ACQW region. The second kind of levels extends mainly in the reflectors region, show a very small shift under the same field. A calculation of the probability to find these states in the ACQW region is in agreement with our interpretation.

Acknowledgements

This research was supported by the Israel Science Foundation founded by the Israel Academy of Science and Humanities.

References

- [1] M. Bendayan, R. Kapon, R. Beserman, A. Sa'ar, R. Planel, *Phys. Rev. B* 56 (1997) 9239.
- [2] M. Zahler, I. Brener, G. Lenz, J. Saltzman, E. Cohen, L. Pfeiffer, *Appl. Phys. Lett.* 61 (1992) 949.
- [3] M. Zahler, E. Cohen, J. Saltzman, E. Linder, E. Maayan, L. Pfeiffer, *Phys. Rev. B* 50 (1994) 5305.
- [4] F. Capasso, C. Sirtori, J. Faist, D.L. Sivco, S.G. Chu, A.Y. Cho, *Nature* 358 (1992) 565.
- [5] C. Sirtori, F. Capasso, J. Faist, D.L. Sivco, S.G. Chu, A.Y. Cho, *Appl. Phys. Lett.* 61 (1992) 898.
- [6] B. Sung, H.C. Chui, E.L. Martinet, J.S. Harris Jr., *Appl. Phys. Lett.* 68 (1996) 2720.
- [7] J. Wang, J.P. Leburton, J.E. Zucker, *IEEE J. Quant. Electron* 30 (1994) 989.
- [8] T. Worren, K.B. Ozanyan, O. Hunderi, F. Martelli, *Phys. Rev. B* 58 (1998) 3977.
- [9] J.E. Zucker, A. Pinczuk, D.S. Chemla, *Phys. Rev. B* 38 (1988) 4287.
- [10] J.E. Zucker, A. Pinczuk, D.S. Chemla, A. Gossard, W. Wiegmann, *Phys. Rev. Lett.* 51 (1983) 1293.



ELSEVIER

Physica E 7 (2000) 250–254

PHYSICA E

www.elsevier.nl/locate/physa

Intersubband electro-absorption and retardation in coupled quantum wells: the role of interface scattering

R. Kapon^a, N. Cohen^a, V. Thierry-Mieg^b, R. Planel^{b,1}, A. Sa'ar^{a,*}

^a*Department of Applied Physics, The Fredi and Nadine Hermann School of Applied Science, The Hebrew University of Jerusalem, Jerusalem 91904, Israel*

^b*Laboratoire de Microstructures et Microelectronique-CNRS, 196 Avenue H. Ravera, BP107, 92225 Bagneux, France*

Abstract

In this work we present a systematic experimental study aimed at resolving the various contributions to electro-optical modulation in a multiple coupled quantum wells structure. Using a set of eight-cross/parallel polarizer-analyzer measurements we were able to resolve the spectral dependence of the DC electric-field-induced absorption and phase-retardation due to intersubband transitions. The results of our experiment were fitted to a model that allows all quantum properties of the structure to vary with the external DC electric field and estimate the contribution of each term to the overall modulation. The experimental results suggest that, apart from the Stark shift of the energy levels, a major contribution to electro-optical modulation comes from line width modulation. We propose a model that correlates this effect with alloy disorder and interface roughness scattering that gives rise to electron dephasing. The larger degree of electron localization near the interfaces in the presence of a DC electric field is responsible for this effect. © 2000 Elsevier Science B.V. All rights reserved.

Keywords: Electro-absorption; Electro-retardation; Intersubband transitions; Interface roughness

The large second-order optical nonlinearities associated with intersubband transitions (ISBTs) in quantum wells (QWs) can be utilized to develop a new class of infrared (IR) nonlinear devices. In particular, IR electro-optical (EO) modulators that are based on these transitions were extensively investigated [1–7]. These modulators have the advantage of being compatible with other ISBT devices such as QWIPs and quantum cascade lasers, for integration purposes.

In this work we investigate experimentally EO modulation in an asymmetric coupled quantum wells (CQWs) structure. In a previous work [8] we found that this structure should deliver efficient EO modulation at the IR wavelengths. However, a careful analysis of the modulation process is essential to resolve both electro-absorption (EA) and electro-retardation (ER) in our sample since both the amplitude and the phase of the optical field are affected by the DC-electric field thus altering the state of polarization of the outgoing IR beam.

The structure used for our experiments consists of 50 periods of CQWs. Each period consists of two

* Corresponding author. Fax: 972-2-5663878.

E-mail address: saar@vms.huji.ac.il (A. Sa'ar)

¹ This paper is dedicated to the memory of Richard Planel, deceased 29 June 1999.

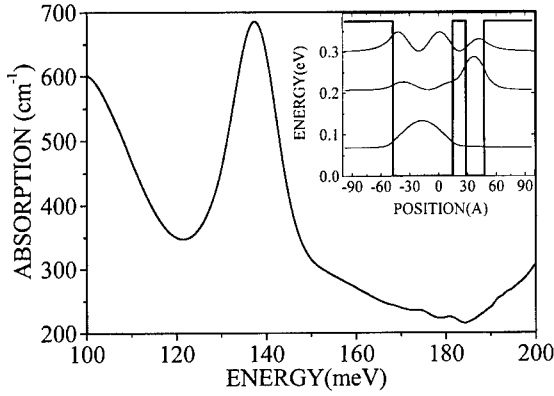


Fig. 1. FTIR linear absorption spectrum of our sample showing the $|1\rangle \rightarrow |3\rangle$ intersubband transition at 137 meV. The inset shows the band structure of the sample together with the calculated energy levels and wave functions.

GaAs QWs, 60 and 20 Å wide, respectively, separated by a 15 Å $\text{Al}_{0.4}\text{Ga}_{0.6}\text{As}$ barrier. A 375 Å thick $\text{Al}_{0.4}\text{Ga}_{0.6}\text{As}$ barrier, modulation doped (n-type) at the center to a level of $n_{2D} = 4 \times 10^{11} \text{ cm}^{-2}$, separates the periods from each other. The entire structure was grown on the top of a semi-insulating (100) GaAs substrate with top and bottom 5000 Å thick heavily doped n-GaAs layers ($n = 1 \times 10^{18} \text{ cm}^{-3}$).

The potential structure together with the allowed energy levels and wave functions, that were calculated using a numerical code that solves the Ben Daniel–Duke and the Poisson equations self-consistently, are shown in the inset of Fig. 1. We found that the structure has three subbands with transition energies of 140 meV for the $|1\rangle \rightarrow |2\rangle$ ISBT and 200 meV for the $|1\rangle \rightarrow |3\rangle$ ISBT at 77 K. Linear-polarization-resolved FTIR absorption measurements, shown in Fig. 1, reveal a strong absorption line at 137 meV with a full-width at half-maximum (FWHM) of 10 meV. This is in good agreement with our energy level calculations. The sample was processed into a $2 \times 5 \text{ mm}^2$ rectangular mesa structure, using standard photolithography and wet chemical etching. Finally, ohmic metal contacts of AuGe/Ni/Au were defined at the bottom and the top mesas. Two parallel edges of

the sample were polished in 45° in the commonly used multi-pass waveguide geometry [8] to allow optical transmission.

The experimental set-up used to measure EO modulation is shown schematically in Fig. 2. IR-radiation from a black body source is focused onto the sample facet using ZnSe lenses. The sample, which is held at a constant temperature of 77 K inside an optical cryostat, is placed between a polarizer (P) and analyzer (A) whose angles can be rotated. In addition a quarter-wave plate ($\lambda/4$) is placed in the optical path. Radiation that emerges from the sample is collected using another ZnSe lens onto a $\frac{1}{8}$ spectrometer followed by a HgCdTe detector.

Two types of measurements were made. In one type of experiments a square wave voltage between 0 and V was applied across the sample at a frequency of 4 kHz and the differential transmission through the sample, ΔT , was measured using a lock-in amplifier. In the second set of measurements the linear transmission, T , was measured using a chopper to modulate the incoming beam while the outgoing signal was measured, again, using a lock-in amplifier. The frequency of modulation was the same for both experiments to eliminate effects of frequency response of the measuring system.

It can be shown that full characterization of a given anisotropic crystal requires a set of nine measurements [9] at different orientations of the polarizer/analyzer/quarter-wave plate. However, in our semiconductor structure, the ISBT selection rules dictate the principal axis [10] so that a set of only six measurements is sufficient to characterize the structure. We denote each configuration of our experimental system by three parameters $(\theta_p, \theta_A, \Gamma_0)$ where θ_p and θ_A are the angles of the polarizer and analyzer relative to the extraordinary axis (growth direction) and Γ_0 is the retardation introduced by the quarter-wave plate. In Ref. [11] we showed that one can use the following relations to deduce the induced absorption and induced retardation from the following set of measurements:

$$\frac{\Delta T(0, 0, 0)}{T(0, 0, 0)} = -\frac{1}{2}\alpha^{(2)}V, \quad (1)$$

$$\frac{-2 \left\{ \left[\Delta T\left(\frac{\pi}{4}, \frac{\pi}{4}, \frac{\pi}{2}\right) - \Delta T\left(\frac{\pi}{4}, -\frac{\pi}{4}, \frac{\pi}{2}\right) \right] - \frac{\Delta T(0, 0, 0)}{2T(0, 0, 0)} \left[T\left(\frac{\pi}{4}, \frac{\pi}{4}, \frac{\pi}{2}\right) - T\left(\frac{\pi}{4}, -\frac{\pi}{4}, \frac{\pi}{2}\right) \right] \right\}}{\left[T\left(\frac{\pi}{4}, \frac{\pi}{4}, 0\right) - T\left(\frac{\pi}{4}, -\frac{\pi}{4}, 0\right) \right]} = \Gamma^{(2)}V, \quad (2)$$

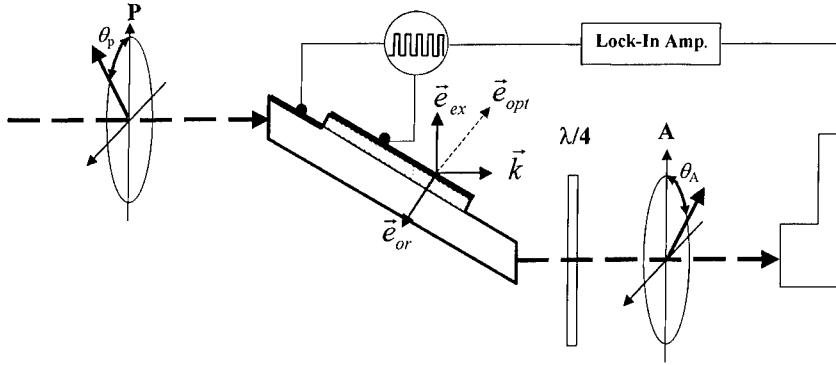


Fig. 2. The experimental set-up: (P) input polarizer, ($\lambda/4$) quarter wavelength plate; (A) output analyzer-polarizer. θ_p and θ_A are the angles of the polarizer and the analyzer relative to the extra-ordinary direction, respectively.

where V is the applied voltage, and $\alpha^{(2)}$ and $\Gamma^{(2)}$ are the electric-field-induced EA and ER coefficients, respectively. In our analysis we plotted $\alpha^{(2)}V$ and $\Gamma^{(2)}V$ versus the applied voltage, for each photon energy, and fitted the data to a linear approximation (see Fig. 2 of Ref. [10]). The slope of the resulting lines are $\alpha^{(2)}$ and $\Gamma^{(2)}$, respectively. The open circles in Fig. 3(a), show the induced EA. A first positive peak at 125 meV and a second negative peak at 137 meV are observed. While the second peak at 137 meV is very close to the resonance of the linear absorption, the first peak at 125 meV is shifted to a significantly lower energy. The results for the induced ER are shown in Fig. 3b in open circles. Here, the first positive ER peak appears at 133 meV while the second negative peak appears at 142 meV.

In order to correlate the experimental results to the physical mechanisms responsible for EO modulation we followed the approach described in Ref. [12]. A first-order expansion (with respect to the DC-electric field) of the linear susceptibility, $\chi^{(1)}(\omega) = \Omega_{21}/(\varepsilon - \varepsilon_{21} - i\gamma_{21})$, yields

$$\chi^{(2)}(\omega) = \left(\frac{\partial \chi^{(1)}}{\partial \varepsilon_{21}} \Delta \varepsilon_{21} + \frac{\partial \chi^{(1)}}{\partial \Omega_{21}} \Delta \Omega_{21} + \frac{\partial \chi^{(1)}}{\partial \gamma_{21}} \Delta \gamma_{21} \right), \quad (3)$$

where

$$\chi_e^{(2)} = \frac{\partial \chi^{(1)}}{\partial \varepsilon_{21}} = \frac{\Omega_{21}}{(\varepsilon - \varepsilon_{21} - i\gamma_{21})^2},$$

$$\chi_\Omega^{(2)} = \frac{\partial \chi^{(1)}}{\partial \Omega_{21}} = \frac{1}{(\varepsilon - \varepsilon_{21} - i\gamma_{21})},$$

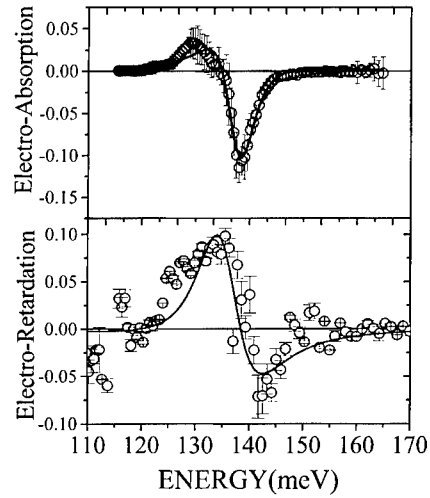


Fig. 3. (a) EA versus the photon energy; (b) ER versus photon energy. Circles denote the measured values while the solid lines represent the best fit of the experimental results to the model.

$$\chi_r^{(2)} = \frac{\partial \chi^{(1)}}{\partial \gamma_{21}} = \frac{i\Omega_{21}}{(\varepsilon - \varepsilon_{21} - i\gamma_{21})^2}, \quad (4)$$

where $\chi^{(2)}(\omega)$ is the second-order EO susceptibility, Ω_{21} is proportional to the transition dipole matrix elements times the population difference of the lowest two subbands, ε_{21} is the transition frequency and γ_{21} is the line width of the transition. In the present analysis we took into account line-width modulation that was not considered in Ref. [12].

In Fig. 4 we plot the real (Fig. 4b) and imaginary (Fig. 4a) parts of each term in Eq. (4) normalized

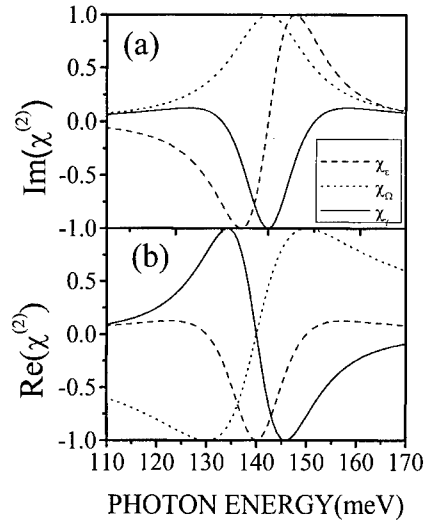


Fig. 4. Spectral behavior of: (a) the imaginary; (b) the real part of the EO susceptibility for modulation arising from changes in γ_{21} (solid line), ε_{21} (dashed line) and Ω_{21} (dotted line).

to their maximum value. Note that each of the contributions to modulation yields a different spectral dependence. Furthermore, since EA is related to the imaginary part of the susceptibility and ER to the real part of the susceptibility, we can fit the experimental results for both the ER and the EA coefficients to Eq. (4). The fitting procedure yields the relative contribution of each term in Eq. (4) to the experimental results. The solid lines in Fig. 3 show the results of the fit where the values of ε_{21} , γ_{21} and Ω_{21} in the absence of a DC-electric field were taken from the linear absorption measurements. The fitting procedure yields: $1/V(\Delta\varepsilon_{21}/\varepsilon_{21}) \cong 4 \times 10^{-3}/V$, $1/V(\Delta\gamma_{21}/\gamma_{21}) \cong 7.6 \times 10^{-2}/V$ and $1/V(\Delta\Omega_{21}/\Omega_{21}) \cong 1 \times 10^{-3}/V$. Thus, close to resonance, EO modulation in our structure is mainly due to line-width broadening.

Let us now compare the experimental results to a model based on a numerical solution of the Ben Daniel–Duke and Poisson equations for our structure. We treated the biased QW as a new structure and numerically calculated ε_{21} and Ω_{21} as a function of the DC-electric field, F . First-order expansion of the form

$$\begin{aligned}\varepsilon_{21}(F) &= \varepsilon_{21}(0) + \frac{\partial \varepsilon_{21}}{\partial F} F + \dots, \\ \Omega_{21}(F) &= \Omega_{21}(0) + \frac{\partial \Omega_{21}}{\partial F} F + \dots\end{aligned}\quad (5)$$

was used to derive the following relations for the modulation coefficients

$$\frac{\Delta\varepsilon_{21}}{\varepsilon_{21}} = \frac{\partial \ln \varepsilon_{21}}{\partial F} F \quad \text{and} \quad \frac{\Delta\Omega_{21}}{\Omega_{21}} = \frac{\partial \ln \Omega_{21}}{\partial F} F. \quad (6)$$

The second term in our expansion is related to quantum interference and carrier density modulation as discussed in Ref. [12]. However, since in our experiment $\varepsilon_2 - \varepsilon_1 \approx 137 \text{ meV} \gg kT \approx 7 \text{ meV}$ we expected carrier density modulation to be negligible.

Line-width broadening may originate in several processes that give rise to electron dephasing [13,14]. In our structure, because of the large number of interfaces and the thin intermediate barrier, we assign line-width broadening to interface roughness and alloy disorder scattering at the interfaces. Following Ando et al. [15] we write line-width broadening due to interface roughness as follows:

$$\begin{aligned}\gamma &= KF_{\text{eff}}^2, \quad \text{where } F_{\text{eff}} = \int dz |\psi(z)|^2 \frac{\partial V}{\partial z} \\ &\cong \sum_j V_0 |\psi(z_j)|^2,\end{aligned}\quad (7)$$

where the summation is over all interfaces, V_0 is the conduction band discontinuity at the interface, $\psi(z)$ is the envelope wave function and for each interface at $z = z_j$ we took $\partial V/\partial z = V_0 \delta(z - z_j)$. Hence, we conclude that the strength of interface roughness scattering has a quadratic dependence on the probability to find the electron at a given interface. Therefore one should expect to find a weak contribution of this scattering process in a rectangular QW where the ground envelope state tends to vanish near the interfaces and a large contribution for QW structures with many interfaces. In our CQW a large probability to find the electron near the interfaces is expected, particularly for the interfaces of the thin intermediate AlGaAs barrier. Taking now, again, the envelope-state to be a function of the DC-electric field and applying the linear expansion procedure (as in Eqs. (5) and (6)) for line-width modulation yields

$$\frac{\Delta\gamma}{\gamma} \cong \frac{\partial \ln(|\psi|^4)}{\partial F} \Big|_{F=0}. \quad (8)$$

Eqs. (6) and (8) can be now used to calculate the various modulation coefficients. Applying the numerical code for our structure yields: $1/V(\Delta\varepsilon_{21}/\varepsilon_{21}) \cong 6 \times 10^{-3}/V$, $1/V(\Delta\gamma_{21}/\gamma_{21}) \cong 1 \times 10^{-1}/V$ and $1/V(\Delta\Omega_{21}/\Omega_{21}) \cong 8.5 \times 10^{-4}/V$ in

reasonably good agreement with our experimental results.

In conclusion, we have presented an experimental technique for measuring the EO modulation based on ISBTs in QWs. Our experiment reveals that both electro-refraction and electro-absorption contribute to EO modulation. Furthermore, we have found that in QW structures with several interfaces the modulation stems mostly from line-width broadening under the application of an external electric field.

References

- [1] P.F. Yuh, K.L. Wang, *IEEE J. Quantum Electron.* 25 (1989) 1671.
- [2] E.B. Dupont, D. Delacourt, M. Papuchon, *IEEE J. Quantum Electron.* 29 (1993) 2313.
- [3] R.P.G. Karunasiri, Y.J. Mii, K.L. Wang, *IEEE Electron Dev. Lett.* 11 (1990) 227.
- [4] C. Sirtori, F. Capasso, D.L. Sivco, A.L. Hutchinson, A.Y. Cho, *Appl. Phys. Lett.* 60 (1992) 151.
- [5] A. Segev, A. Sa'ar, Y. Oiknine-Schlesinger, E. Ehrenfreund, *Superlattices Microstruct.* 19 (1996) 47.
- [6] L.R. Friedman, R.A. Soref, J. Khurgin, *IEEE J. Quantum Electron.* 31 (1995) 219.
- [7] V. Berger, N. Vojdani, D. Delacourt, J.P. Schnell, *Appl. Phys. Lett.* 68 (1996) 1904.
- [8] B.F. Levine, *J. Appl. Phys.* 74 (1993) R1.
- [9] M. Born, E. Wolf, *Principles of Optics*, 3rd Edition, Wiley, New York, 1989.
- [10] D. Kaufman, A. Sa'ar, N. Kuze, *Appl. Phys. Lett.* 64 (1994) 2543.
- [11] R. Kapon, N. Cohen, A. Sa'ar, V. Thierry-Mieg, R. Planel, *Appl. Phys. Lett.* 75 (1999) 1583.
- [12] A. Sa'ar, R. Kapon, *IEEE J. Quantum Electron.* 33 (1997) 1517.
- [13] J. Faist, F. Capasso, C. Sirtori, D.L. Sivco, A.L. Hutchinson, S.N.G. Chu, A.Y. Cho, *Appl. Phys. Lett.* 63 (1993) 1354.
- [14] R.F. Kazarinov, R.A. Suris, *Sov. Phys. Semicond.* 6 (1972) 120.
- [15] T. Ando, A.B. Fowler, F. Stern, *Rev. Mod. Phys.* 54 (1982) 437.



ELSEVIER

Physica E 7 (2000) 255–258

PHYSICA E

www.elsevier.nl/locate/physica

Thermal relaxation processes in $\text{Si}_{1-x}\text{Ge}_x/\text{Si}$ quantum wells studied by inter-subband and inter-valence band spectroscopy

B. Adoram^a, D. Krapf^a, M. Levy^b, R. Beserman^b, S. Thomas^c, K.L. Wang^c, J. Shappir^a,
A. Sa'ar^{a,*}

^a*Department of Applied Physics, The Fredi and Nadine Herrmann School of Applied Science, The Hebrew University of Jerusalem, Jerusalem 91904, Israel*

^b*Solid State Institute and Physics Department, The Technion, Haifa 32000, Israel*

^c*Department of Electrical Engineering, University of California at Los Angeles, CA 90024, USA*

Abstract

In this paper we present a systematic experimental investigation of the optical properties associated with inter-subband and inter-valence band transitions in p-type pseudomorphic $\text{Si}_{1-x}\text{Ge}_x/\text{Si}$ multiple quantum-wells structure under high-temperature thermal treatments. The structure exhibits two types of optical absorption lines: the first obeys the inter-subband selection rules and is assigned to heavy-hole transitions while the second obeys the inter-valence band selection rules and is assigned to transitions between a heavy hole and a mixed spin split off and light-hole state. Annealing treatments reveal two kinds of thermally activated processes. The first process is assigned to strain relaxation while the second is assigned to Si and Ge inter-diffusion. Raman spectroscopy provides additional support to our interpretation of the activation processes. We propose a quantitative model, based on the Bir–Pikus deformation potential to explain the experimental results. © 2000 Elsevier Science B.V. All rights reserved.

Keywords: Silicon–germanium quantum wells; Inter-valence band transitions; Strain relaxation; Inter-diffusion

Pseudomorphic silicon–germanium (SiGe) heterostructures grown on Silicon (Si) substrates have extensively been investigated over the recent years for silicon-based optoelectronic applications. Due to the large valence band discontinuity between Si and SiGe strained alloys, this semiconductor system is suitable for fabricating p-type quantum-well infrared

photodetectors (QWIPs) that can monolithically be integrated with Si-based readout circuits [1]. However, standard Si-processing technology involves high-temperature thermal treatments that may cause a severe degradation in device's performances [2]. Therefore, it is essential to understand how thermal annealing processes [3–5] affect the optical properties associated with transitions within the valence band in SiGe/Si heterostructures.

In this work, we study the influence of thermal annealing processes on the optical transitions within the

* Corresponding author. Tel.: +972-2-6585701; fax: +972-2-5663878.

E-mail address: saar@vms.huji.ac.il (A. Sa'ar)

valance band in p-type pseudomorphic Si/SiGe QWs. Infrared (IR) absorption spectroscopy was applied to probe various thermally activated processes and their influence on the optical properties of these heterostructures.

The sample used for our study was grown by molecular beam epitaxy (MBE) on a high resistivity ($1500 \Omega \text{ cm}$) n-type (100) Si substrate. It consists of 20 periods of SiGe/Si QWs. Each period consists of a 30 \AA wide $\text{Si}_{0.77}\text{Ge}_{0.23}$ QW, boron (p-type) doped to a level of $9.6 \times 10^{11} \text{ cm}^{-2}$ and a 500 \AA undoped Si barrier. In addition, a 300 \AA wide $\text{Si}_{0.77}\text{Ge}_{0.23}$ layer and boron doped to a level of $4 \times 10^{18} \text{ cm}^{-3}$, was grown on top of the QWs. The whole structure is capped with 5000 \AA top and bottom Si contact layers and boron doped to a level of 10^{19} cm^{-3} . Both the contact and the wide well layers are used for detector's application to be discussed elsewhere. IR absorption measurements were recorded using a Perkin-Elmer 2000 Fourier transform infrared spectrometer (FTIR) with the sample polished to standard 45° multi-pass waveguide geometry. In this geometry, the polarization of the IR beam can continuously be changed from s- to p-polarization (i.e. polarization normal and parallel to the growth direction).

Infrared transmission spectra at various polarization angles of the as grown sample were shown elsewhere [6]. In brief, two absorption lines at 3.8 and $6.1 \mu\text{m}$, polarized perpendicular to the growth direction, and an additional line at $10 \mu\text{m}$, polarized parallel to the growth direction have been observed. We assign the $10 \mu\text{m}$ absorption line to the $\text{HH1} \rightarrow \text{HH2}$ inter-subband transition (ISBT) in the QWs, (where HH stands for heavy-hole subbands), while the 6.1 and the $3.8 \mu\text{m}$ absorption lines are assigned to the HH1 to a mixed light hole (LH) and spin-split-off (SO) state ($\text{SO}+\text{LH}$)1 inter-valence band transitions (IVBTs) in the semi-bulk 300 \AA wide SiGe strained layer and the QWs, respectively. The origin of the SO and LH inter-mixing is the QW confinement and the strain [7,8]. The IVBT at $6.1 \mu\text{m}$ fits very well to the energy separation between the HH and SO levels in semi-bulk strained $\text{Si}_{0.77}\text{Ge}_{0.23}$.

Thermal annealing has been performed in a Nitrogen gas ambient furnace for 1 h at temperatures between room temperature and 1060°C and the IR absorption spectra were recorded after each thermal process. At the insets of Figs. 1(a) and (b) we plot

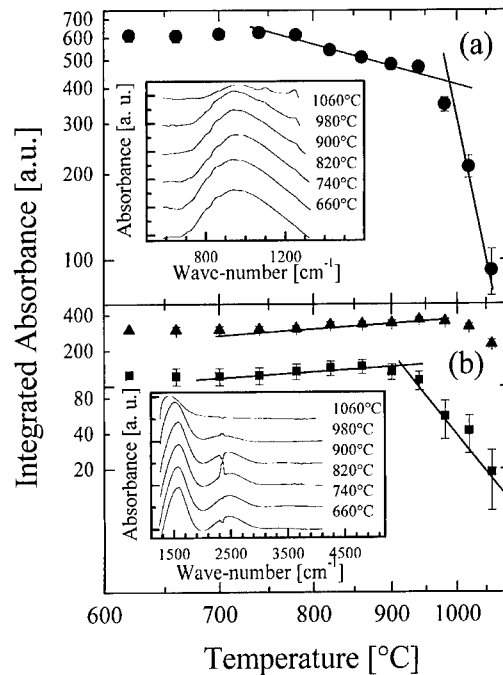


Fig. 1. (a) Arrhenius plot of the ISBT integrated absorbance (●) versus the annealing temperature. The solid lines represent the two activation processes. (b) The same for the QW IVBT (■) and the semi-bulk IVBT (▲). The insets in (a) and (b) show the ISBT and IVBT absorption spectra at various annealing temperatures respectively.

the ISBT and IVBT absorption lines at various temperatures. Let us define the integrated absorbance as the area below each absorption line. Arrhenius plots of the integrated absorbance versus the annealing temperature for the ISBT and IVBT absorption lines are shown in Figs. 1(a) and (b).

Several activation processes can be deduced from these figures. At temperatures higher than 940°C the integrated absorbance of both QW absorption lines decreases with the increasing temperature. The activation energy of both lines is approximately the same, $\Delta E_D \cong (1.9 \pm 0.2) \text{ eV}$. The semi-bulk IVBT ($6.1 \mu\text{m}$) shows a weaker decrease that begins at slightly higher temperatures. In the temperature range, $750\text{--}940^\circ\text{C}$, we observed an additional thermally activated process. Here, the QW ISBT integrated absorbance decreases with the increasing temperature with an activation energy of $\Delta E_S \cong (0.13 \pm 0.02) \text{ eV}$ while the integrated absorbance of both IVBTs increases with the increasing temperature with $\Delta E_S \cong$

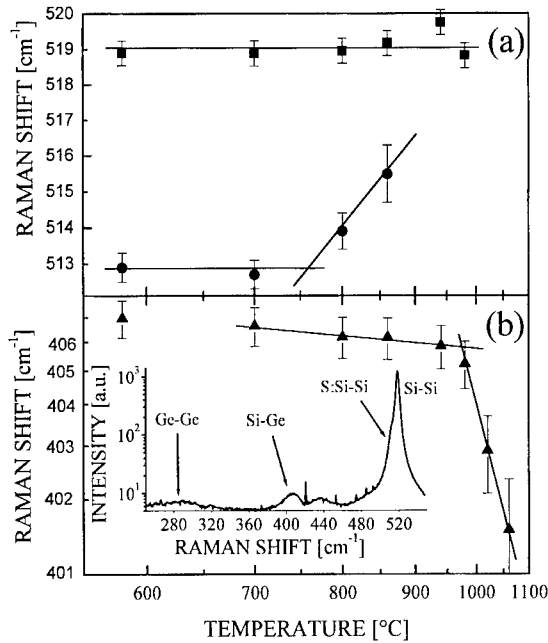


Fig. 2. (a) Raman shifts of the strained (●) and unstrained (■) Si-Si phonon lines. (b) The same for the SiGe phonon line (▲). Inset: a typical Raman spectra after annealing at 700°C.

$-(0.09 \pm 0.02)$ eV. In addition, we did not observe a shift of the QW ISBT peak energy while the IVBT lines show a red shift of the peak energy at temperatures above 800°C (see Figs. 2(b) and 3(b) in Ref. [6]).

The high-temperature activation process is assigned to inter-diffusion of Ge/Si atoms between the strained SiGe QWs and the Si barrier regions. This process causes a destruction of the interfaces between the wells and the barriers, giving rise to a strong alloy disorder scattering that destroys the coherency of the QW electronic states. The activation energy measured for this process is in good agreement with other reports on Ge/Si inter-diffusion in strained layers that were detected by other experimental techniques [9,10]. The semi-bulk IVBT (from the wide well) is expected to be less sensitive to this process since inter-diffusion should destroy the entire SiGe region rather than the interfaces (as is in the case of the 30 Å QW).

The mid-temperature activation process is assigned to thermally activated strain relaxation in the pseudomorphic SiGe layers [3,4,11,12]. To verify this assumption we measured the Raman scattering spectra

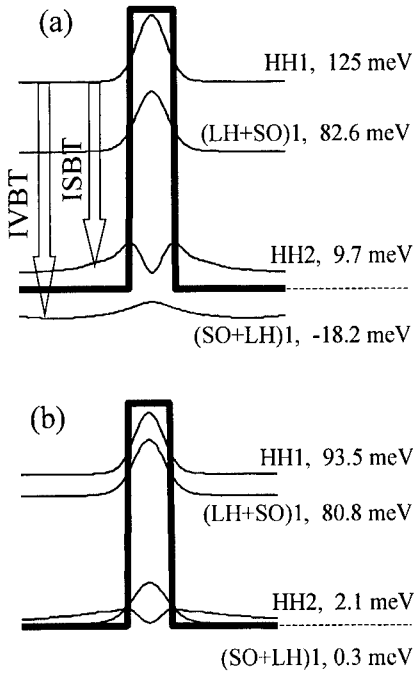


Fig. 3. The square of the envelope wave functions for all bound states at $k_{\perp} = 0$. (a) Fully strained QW. (b) Fully relaxed QW.

of the samples for each annealing temperature. The inset of Fig. 2(b) shows a typical spectrum obtained at 700°C, with the various phonon lines as indicated in the figure. In Fig. 2(a) we plot the strained Si-Si phonon line versus the annealing temperature. With the increasing temperature the strained Si-Si line shifts towards the bulk Si-Si line, until the two lines can not be resolved above 900°C. Fig. 2(b) shows a red shift of the SiGe phonon line as annealing temperature rises. Here again, two activation processes with activation energies of $\Delta E_S \cong (0.11 \pm 0.04)$ eV and $\Delta E_D \cong (2.3 \pm 0.6)$ eV are clearly observed. These two energies are in good agreement with the activation energies observed for the QW ISBT.

In order to understand the influence of strain relaxation on the valence band structure and the various optical transitions involved in our sample, we numerically solved the 6×6 Luttinger-Kohn (LK) Hamiltonian [13] for our $\text{Si}_{1-x}\text{Ge}_x/\text{Si}$ QW structure. In our calculations, we took into account both the confinement potential and the strain deformation potential using the Pikus-Bir Hamiltonian [14]. The solution was derived in a similar manner to that presented in Refs.

[7,8], where a Fourier transform of the envelope wave functions transforms the set of six coupled LK differential equations into an algebraic matrix that can be diagonalized. Both envelope wave functions and energy dispersion relations for all confined levels were numerically calculated.

In Fig. 3 we show the square of the envelope wave functions for all bound states at $k_{\perp} = 0$. Two limiting cases are shown: a fully strained QW and a fully relaxed QW. These two limiting examples serve the purpose of illustrating how strain affects the band structure. First, for a fully relaxed QW, the gap between HH and LH ground states is strongly reduced (in bulk silicon the two bands are degenerated). Second, the HH QW potential becomes shallower in the absence of strain, thus pushing up the HH2 state near the top of the QW. As a result, the HH2 envelope wave function becomes less localized in the QW region. Third, the strain in the QW gives rise to an additional strong mixture between SO and LH. However, once the energy of the mixed states lies above the LH barrier, the LH contribution becomes unlocalized. As a result, the strain causes the entire envelope wave function to be less localized in the QW as illustrated in Fig. 3. During the relaxation the contribution of the LH becomes smaller and the envelope state become more localized in the QW region.

The above effects are responsible to the activation processes observed by the optical absorption measurements. The energy levels involved in the optical transitions, i.e. $\text{HH1} \rightarrow \text{HH2}$ and $\text{HH1} \rightarrow (\text{SO} + \text{LH})1$, are in good agreement with the experimentally observed absorption spectra. Furthermore, the integrated absorbance of the ISBT is proportional to $|\langle \text{HH1} | z | \text{HH2} \rangle|^2$, where $|\text{HH1}\rangle$ and $|\text{HH2}\rangle$ are the envelope wave functions of the lowest HH states. Hence, strain relaxation causes the HH2 envelope to be less localized in the QW and to a decrease of the absorption as observed in the experiment. The integrated absorbance of the IVBTs is proportional to the envelope states overlap $\langle \text{HH1} | (\text{SO} + \text{LH})1 \rangle$ [7,8]. Here, we find that strain relaxation gives rise to a larger degree of envelope state localization. For example, in the two limiting cases shown in Fig. 3 we find that the state $(\text{SO} + \text{LH})1$ consists of 32% SO and 68% LH in the fully strained case while 88% SO and 12% LH is obtained for the fully relaxed structure. Hence, with increasing annealing temperature the contribution of the

localized SO to the overlap integral increases giving rise to an increase of the absorption. Note that this model also explains the red shift of the optical transitions [6].

In summary, we have measured the influence of thermal annealing processes on inter-valence band and inter-subband transitions in pseudomorphic $\text{Si}/\text{Si}_{1-x}\text{Ge}_x$ quantum wells. Two thermally activated processes were resolved. The first process is assigned to strain relaxation that gives rise to a decrease of the ISBT and an increase of IVBTs. At temperatures above 940°C a second aprocess of Si/Ge inter-diffusion was observed. This process destroys the coherency of the QW envelope states giving rise to a rapid decrease of all QW absorption lines.

Acknowledgements

This work was partially supported by grant #5877 of the Israeli Ministry of Science.

References

- [1] R.P.G. Karunasiri, J.S. Park, K.L. Wang, *Appl. Phys. Lett.* 61 (1992) 2434.
- [2] M. Gluck, J. Hersener, H.G. Umbach, J. Rapich, J. Stein, *Solid State Phenom.* 57–58 (1997) 413–418 (1997 Scitec Publishing, Switzerland).
- [3] J.-P. Noel, N.L. Rowell, D.C. Houghton, D.C. Perovic, *Appl. Phys. Lett.* 57 (1990) 1037.
- [4] M.R. Sardela Jr., G.V. Hansson, *J. Vac. Sci. Technol. A* 13 (1995) 314.
- [5] B. Dietrich, E. Bugiel, L. Klatt, G. Lippert, T. Morgenstren, H.J. Osten, P. Zaumseil, *J. Appl. Phys.* 74 (1993) 3177.
- [6] B. Adoram, D. Krapf, J. Shappir, A. Sa'ar, M. Levy, R. Besserman, S.G. Thomas, K.L. Wang, *Appl. Phys. Lett.* 75 (1999) 2232.
- [7] T. Fromherz, E. Koppensteiner, M. Helm, G. Bauer, J.F. Nutzel, G. Abstreiter, *Phys. Rev. B* 50 (1994) 15073.
- [8] T. Fromherz, P. Kruck, M. Helm, G. Bauer, J.F. Nutzel, G. Abstreiter, *Appl. Phys. Lett.* 68 (1997) 3611.
- [9] T. Walter, C.J. Humphreys, A.G. Cullis, D.J. Robbins, *Institute of Physics Conference Series* 157, IOP publishing, Bristol, 1997, pp. 47–54 and references therein.
- [10] K. Dettmer, W. Freiman, M. Levy, Yu.L. Khait, R. Beserman, *Appl. Phys. Lett.* 66 (1995) 2376.
- [11] A. Rodriguez, T. Rodriguez, A. Kling, J.C. Soares, M.F. da Silva, C. Ballesteros, *J. Electron. Mater.* 28 (1999) 77.
- [12] D.J. Lockwood, J.-M. Baribeau, *Phys. Rev. B* 45 (1992) 8565.
- [13] J.M. Luttinger, W. Kohn, *Phys. Rev.* 97 (1955) 869.
- [14] G.L. Bir, G.E. Pikus, *Symmetry and Strain-Induced Effects in Semiconductors*, Wiley, New York, 1974.



ELSEVIER

Physica E 7 (2000) 259–262

PHYSICA E

www.elsevier.nl/locate/physica

Investigation of electric-field-dependent population properties in a GaAs/(Al,Ga)As multiple, asymmetric double quantum well structure by photoluminescence spectroscopy

L. Schrottke *, R. Hey, H.T. Grahn

Paul-Drude-Institut für Festkörperelektronik, Hausvogteiplatz 5–7, 10117 Berlin, Germany

Abstract

Photoluminescence (PL) spectroscopy is used to study the population properties of a multiple, asymmetric GaAs/(Al,Ga)As double quantum well superlattice, which represents a simplified version of the active region of a quantum cascade laser (QCL). In the case of anti-Stokes PL of the narrower well, which is observed for excitation between the excitonic states of the two quantum wells and sufficiently high electric field strengths, the photocarriers are only excited in one of the two wells. The anti-Stokes signal gives direct evidence for transport of electrons *and* holes through the (Al,Ga)As barriers. An analysis of the electric-field dependence of the conventional PL as well as the anti-Stokes PL signal demonstrates that the population of the subbands can be determined in the limit of weak excitation intensity. © 2000 Elsevier Science B.V. All rights reserved.

Keywords: Superlattice; Population; Photoluminescence

1. Introduction

In 1994, the first operating laser based on intersubband transitions, the quantum cascade laser (QCL), was reported by Faist et al. [1]. In addition to its great practical interest, the cascade structure also deserves attention for its basic physical properties. The population of the subbands, e.g., is determined by a complicated interplay of transport and relaxation processes. Photoluminescence (PL) spectroscopy seems to be an appropriate tool to investigate this popu-

lation [2,3], although the excitation of electron–hole pairs is not compatible with the unipolar character of the QCL. In conventional PL experiments, the excitation of electron–hole pairs is approximately equal in all quantum wells (QWs). In contrast, for excitation energies between the excitonic states of the different QWs, electrons and holes are only excited in the wider wells, so that any PL signal from the narrower QWs would give direct evidence of the transport of electrons *and* holes through the barriers. This type of PL signal appears at a higher photon energy than the excitation energy and is therefore referred to as anti-Stokes PL. In order to study the population properties of such structures by PL spectroscopy, the influence of

* Corresponding author. Fax: +49-30-20377-515.

E-mail address: lutz@pdi-berlin.de (L. Schrottke)

hole transport has to be considered. In this paper, we apply anti-Stokes as well as conventional PL spectroscopy on an asymmetric GaAs/(Al,Ga)As double quantum well superlattice, which represents a simplified active region of a QCL. We demonstrate that PL spectroscopy can be applied as a simple measuring technique to characterize the underlying processes, if the excitation intensity is sufficiently low.

2. Experimental

The samples consist of a superlattice structure with a unit cell containing two wells and two barriers, which all have different thicknesses. While the different barrier thickness results in a different transfer rate between the electronic ground states of adjacent wells, different well widths result in different transition energies, which allow to identify the QWs with respect to their injection barrier. We define forward bias as the polarity, for which the electron ground state of the wider well is at a higher energy than the one of the adjacent narrower well, if they are connected by the thin barrier. In this paper, forward bias is denoted by a positive electric field strength.

The $\text{Al}_{0.3}\text{Ga}_{0.7}\text{As}/\text{GaAs}$ superlattice structure forms the intrinsic region of an n^+-i-n^+ structure, which was grown by molecular-beam epitaxy on an n^+ -GaAs substrate. It contains 20 periods each with a 5-nm well, a 10-nm barrier, a 4-nm well, and a 14-nm barrier. The total thickness of the intrinsic region amounts to 735 nm. For the PL experiments, the sample was optically excited with an Ar^+ -laser-pumped Ti:sapphire laser tuned to the excitation energies of 1.625 and 1.722 eV. If not otherwise specified, the laser power was adjusted to about 50 nW with the beam focused to a diameter of about 100 μm .

3. Results and discussions

Fig. 1 shows the observed PL intensity of the two QWs as a function of detection energy and electric field in a gray scale representation for an excitation energy of 1.722 eV. While the low-energy line at 1.615 eV exhibits only two pronounced minima at field strengths near ± 27 kV/cm, the high-energy line at 1.642 eV shows maxima at field strengths of about

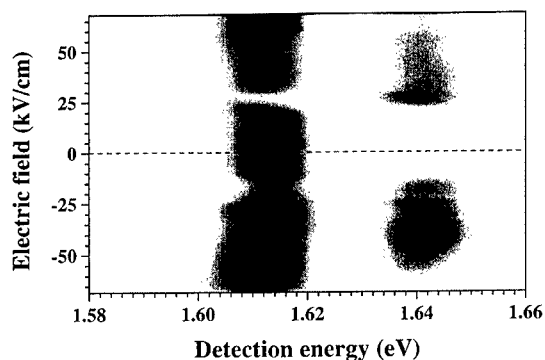


Fig. 1. PL intensity as a function of detection energy and applied electric field measured at a temperature of 5 K for an excitation energy (1.722 eV) above the excitonic states of the two quantum wells. Darker areas correspond to higher intensities, lighter areas to lower intensities.

± 27 and -40 kV/cm. In order to have an experimental quantity that is related to the occupation of the quantum well states, we define the ratio $\rho = I_n/I_w$ of the integrated PL intensity I_n of the narrower and I_w of the wider well, which is shown in Figs. 2(a) and (b) as a function of the applied electric field strength for excitation above and below the ground state of the narrower well, respectively. For both excitation conditions and forward bias, ρ exhibits a clear maximum near 27 kV/cm. A second, smaller maximum exists for excitation of both quantum wells near 5 kV/cm. In reverse bias, ρ appears to have two maxima for both excitation conditions.

The characteristic field strengths, at which electron (forward bias 16, reverse bias 13 kV/cm) or heavy-hole states (forward bias 4.6, reverse bias 5.4 kV/cm) of two adjacent wells are at the same energy, can be correlated with distinct points in the experimental ρ -curves as shown in Figs. 2(a) and (b). Since the PL intensity and hence ρ depend on the product of electron and hole concentrations for each QW, the field dependence of ρ does not directly reflect the occupation of electron or hole states alone. For forward bias above the hole resonance, the preferred hole transport occurs through the thin barrier from the narrower to the wider well so that ρ exhibits a maximum at the resonance condition for holes and a minimum just below the electron resonance. Above this field strength, ρ strongly increases up to 27 kV/cm due to the increased electron trans-

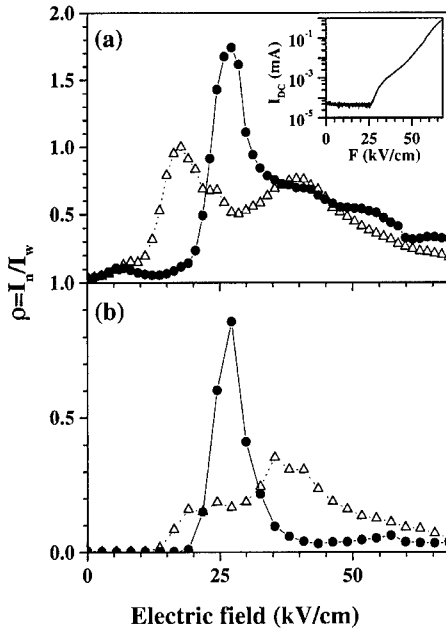


Fig. 2. Ratio $\rho = I_n/I_w$ of the integrated PL intensities of the narrower (I_n) and wider (I_w) QWs for excitation energies of (a) 1.722 and (b) 1.625 eV versus applied electric field for forward (dots) and reverse bias (triangles). In (b), ρ corresponds to the ratio of the anti-Stokes to the Stokes PL intensity. The inset of (a) shows the DC current (I_{DC}) as a function of electric field (F) without laser excitation.

fer from the wider to the narrower well through the thin barrier. The opposite behavior is observed for reverse bias. The strong decrease (increase for reverse bias) of ρ above 27 kV/cm, which results in a maximum (minimum) at this field strength, is probably related to the dramatic increase of the current above 27 kV/cm as shown in the inset of Fig. 2(a), which may lead to a different transfer mechanism through the barriers, e.g., activation by electron impact excitation. A more detailed discussion is presented in Ref. [4].

Within a simple rate equation model for unipolar systems, one expects that the occupation ratio $\eta = n_n/n_w$ of the electronic subband states of adjacent wells is proportional to the ratio t_{wn}/t_{nw} with t_{wn} and t_{nw} denoting the transfer rates from the wider to the narrower well and vice versa, respectively, which depend strongly on the electric field strength. However, probing η with PL spectroscopy would require to include the hole distribution into the model. If ‘combined’

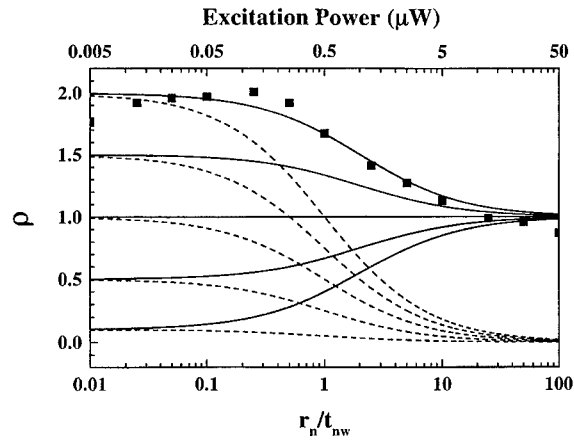


Fig. 3. Calculated values of ρ as a function of r_n/t_{nw} according to the simple model outlined in the text for several values of ν (from top to bottom 2.0, 1.5, 1.0, 0.5, 0.1). The solid lines correspond to excitation in both QWs, the dashed lines to excitation in the wide QWs alone. The experimental values of ρ for an electric field strength of 27 kV/cm as a function of excitation intensity are included as solid squares.

recombination rates r_w and r_n are introduced, which are considered to be proportional to the hole concentrations, but approximately independent of the electronic system, the calculated ρ is a linear function of $\nu = (t_{wn}/t_{nw})(r_n/r_w)$ considering the term r_n/t_{nw} as a parameter. The influence of this term itself is, however, not so obvious. Fig. 3 shows ρ as a function of r_n/t_{nw} for several values of ν . While in the limit of very low hole concentrations, i.e., when $r_n \ll t_{nw}$, which corresponds in our experiment to very low excitation intensities, the measured value ρ is close to the value of t_{wn}/t_{nw} , it tends to unity for higher excitation intensities. The measured excitation intensity dependence of ρ as shown in Fig. 3 for 27 kV/cm agrees well with the calculated dependence of ρ on r_n/t_{nw} . At this field strength, which is still below the strong increase of the current, ρ exhibits its maximum value.

Despite these complex transport behavior, the occupation ratio η can be estimated for field strengths above the electron resonances. Insofar as it is only the barrier thickness (and not the different energetic positions of the electron and hole states in the wells) that determines the transport properties, η can be determined from the measured values of ρ for both polarities in the limit of low excitation intensities

eliminating the proportionality factors. At its maximum, η reaches a value of about 1.8. Note, however, that a precise quantitative discussion would require a detailed numerical analysis taking into account the (electric-field dependent) transfer rates of electron *and* heavy-hole states through the different barriers.

4. Conclusions

In summary, this investigation demonstrates that PL and in particular anti-Stokes PL spectroscopy of asymmetric double quantum well superlattices can be used for a qualitative discussion of the occupation properties of the quantum well states. Characteristic field strengths of the structure can be correlated with extrema in the field dependence of the relative intensity of the two quantum wells. Although

the anti-Stokes PL gives direct evidence that both electrons and holes participate in the transport processes, a strong electric-field-dependent population inhomogeneity was demonstrated for the case of low excitation intensities. Furthermore, anti-Stokes PL seems to be a very useful tool to investigate carrier transfer in such structures.

References

- [1] J. Faist, F. Capasso, D.L. Sivco, C. Sirtori, A.L. Hutchinson, A.Y. Cho, *Science* 264 (1994) 553.
- [2] H.T. Grahn, H. Schneider, W.W. Rühle, K.v. Klitzing, K. Ploog, *Phys. Rev. Lett.* 64 (1990) 2426.
- [3] Y.B. Li, J.W. Cockburn, J.P. Duck, M.J. Birkett, M.S. Skolnick, I.A. Larkin, M. Hopkinson, R. Grey, G. Hill, *Phys. Rev. B* 57 (1998) 6290.
- [4] L. Schrottke, R. Hey, H.T. Grahn, *Phys. Rev. B* 60 (1999) 16635.



ELSEVIER

Physica E 7 (2000) 263–266

PHYSICA E

www.elsevier.nl/locate/physica

Pico-second non-linear optical transmission in an asymmetric triple quantum well structure

N. Sawaki^{a,*}, H.S. Ahn^b, K. Mizutani^a, M. Yamaguchi^a^a*Nagoya University, Department of Electronics, Chikusa-ku, Nagoya 464-8603, Japan*^b*Korea Maritime University, Department of Applied Physics, Yeongdo-ku, Pusan 606-791, South Korea*

Abstract

The transmission of a GaAs/AlGaAs asymmetric triple quantum well structure shows strong nonlinear behavior as a function of the incident laser intensity. The nonlinear behavior is attributed to the Stark shift due to the triple resonance of three electronic states in the conduction band, which is induced by the optical excitation. The pump and probe measurement shows that the build up of internal field in the quantum wells is achieved within a few pico-seconds after the excitation. © 2000 Elsevier Science B.V. All rights reserved.

Keywords: Triple quantum well; Tunneling; Stark shift

1. Introduction

In an application of a coupled quantum well structure to electronic or photonic devices, build up of internal field due to the transfer of electrons between quantum wells will modify the performance/characteristics of the device/structure [1]. If electrons and holes are generated in an asymmetric coupled quantum well by a laser pulse, the electrons will transfer between quantum wells through a thin potential barrier by the resonant tunneling or phonon assisted tunneling process. Then an internal field is achieved by temporal spatial separation of

electrons and holes because of the different tunneling times for electrons and holes.

In this paper, we will demonstrate ultra fast optical response of an asymmetric coupled triple-quantum well (ATQW) by the switching of the subband lineup from off-resonant to resonant state due to the build up of internal field.

2. Sample structure and experimental method

The sample was made by molecular beam epitaxy (MBE) on a semi-insulating (001) GaAs substrate. Fig. 1 shows schematic band structure of the ATQW. Three nominally undoped GaAs quantum wells, of widths 7.6, 8.8 and 10.8 nm and separated by nominally undoped 2 nm-thick

* Corresponding author. Tel.: +81-52-789-3321; fax: +81-52-789-3157.

E-mail address: sawaki@nuee.nagoya-u.ac.jp (N. Sawaki)

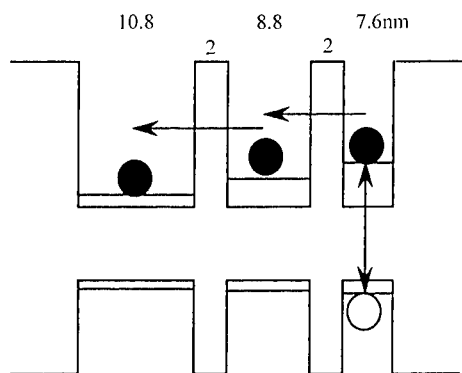


Fig. 1. Schematic band diagram of the ATQW.

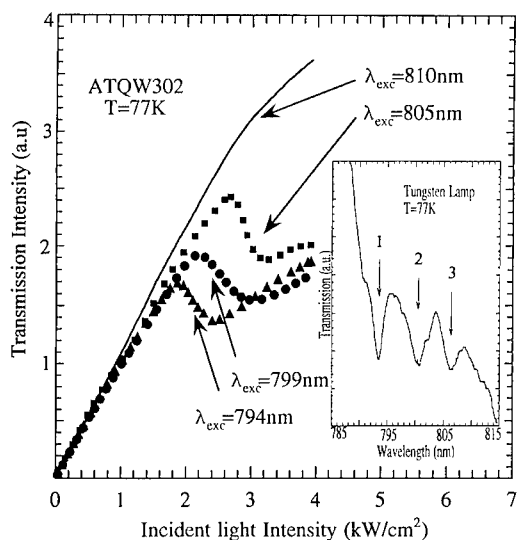


Fig. 2. Non linear transmission of an ATQW.

$\text{Al}_{0.3}\text{Ga}_{0.7}\text{As}$ barrier layers, are embedded between 100 nm-thick $\text{Al}_{0.3}\text{Ga}_{0.7}\text{As}$ cladding layers. The well widths have been designed so that three electronic states will be resonant by a small external electric field [2]. In order to measure the transmission, the GaAs substrate was removed by selective chemical etching. The absorption spectrum of the sample at 77 K indicates spectral peaks at 794, 800 and 806 nm, which are due to excitonic absorption in each quantum well (See the inset of Fig. 2.) It was found that the spectral peak wavelengths exhibit strong quantum confined Stark shift on application of an external electric field perpendicular to the hetero-interface,

and occurrence of the anti-crossing of three electronic levels was confirmed [3].

A mode-locked Ar^+ laser-pumped Ti-sapphire laser (tunable wavelength from 750 to 850 nm at 100 MHz repetition rate) was used as the pump and probe lights. The spectral width of the laser was 0.5 nm and the pulse width was 2.5 ps. The experiments were performed at 77 K by dipping the sample into liquid nitrogen.

3. Optical non-linearity and Stark shift of the spectral peaks by internal field

Fig. 2 shows typical time-integrated transmission versus incident light intensity characteristics of the sample at different wavelengths. At a wavelength of 810 nm, which is longer than the spectral peaks due to the excitonic absorption in the sample but shorter than the fundamental absorption edge of bulk GaAs, the transmission shows slight increase as the incident light intensity increases. This shows that the absorption of GaAs is suppressed by the strong laser beam. Further increase of the incident power enhances the absorption slightly, the variation of which is however monotonous. If the wavelength of the incident beam is short, on the other hand, the sample exhibits anomalous non-linear behavior, i.e., rapid decrease at 2–3 kW/cm^2 . Apparently, the threshold intensity for the rapid decrease depends on the wavelength. This anomalous non-linear behavior is attributed to the modification of the absorption coefficient by the Stark shift of the electronic states.

In order to confirm the mechanism, the integrated photoluminescence (PL) spectra are studied using the laser beam with a wavelength of 794 nm as the excitation source. By this resonant excitation, electrons and holes are generated in the narrowest well as shown in Fig. 1. Because of the short tunneling time of electrons, they are expected to transfer to wide wells leaving holes in the original layer. Then the spatial separation of electrons and holes will produce an electric field in the quantum wells, which in turn will induce the Stark shift of the PL spectral peaks. The phenomenon will persist during the lifetime of holes. In Fig. 3, the PL peak wavelength due to electron–hole recombination in the widest well is plotted as a function of the excitation intensity. In the lower part of the figure, the

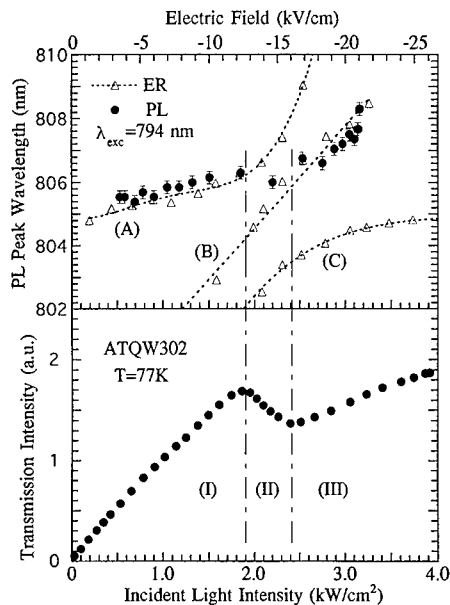


Fig. 3. PL peak shift as a function of excitation intensity.

transmission of the excitation laser beam is shown for comparison. Obviously, the Stark shift is accompanied by the non-linear behavior of the transmission.

The Stark shift of the electronic states on application of an external electric field was investigated in detail [3]. The results of electro-reflectance (ER) measurements have been reproduced in Fig. 3, where the scale of the horizontal axis is adjusted to get the best fit between the ER versus Field characteristics and PL versus excitation intensity characteristics. If the fitting is accepted, at the incident laser power when we have found anomalous non-linear behavior, the triple resonance of three electronic states occurs [4]. It might be surprising that a laser light could produce such a strong internal field in the quantum wells. But simple analysis demonstrates the possibility [5]. If electrons and holes of 10^{11} cm^{-2} are generated by a laser pulse and separated from each other, we may expect an electric field of 14 kV/cm in the AlGaAs layer which is in order of magnitude agreement with the observation. The incident laser intensity is high enough to give rise to a kind of thermal effect. But at region II shown in Fig. 3, we cannot observe red shift of the spectral peak due to the temperature rise. Thus, we may conclude that the anomalous behavior is due to the Stark shift induced by the internal electric field.

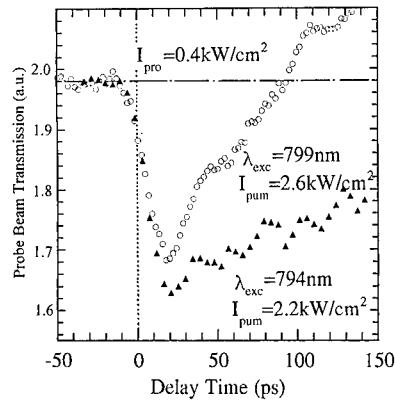


Fig. 4. Time dependence of the probe beam transmission.

4. Picosecond response of the transmission

If the non-linear behavior is due to the spatial separation of the electrons and holes, the appearance of the non-linearity should be determined by the tunneling time of electrons and holes. In this section, the time dependence of the non-linear behavior is investigated with pump and probe method. To do this, the laser pulse train was divided into two beams; a strong pump beam and a weak probe beam which was given a delay time τ . The intensity of the probe beam was less than 0.4 kW/cm^2 . The transmission of the probe beam was measured as a function of the delay time τ .

In Fig. 4, variation of the probe beam intensity is displayed as a function of the delay time. The pump pulse was given at $\tau = 0$. It is notable that the magnitude of the transmission change is as large as 20% of the total transmission, which is more than two orders of magnitude larger than the value expected for the transmission change due to the accumulation of carriers in the conduction band. Moreover, the fast change is an increase of the absorption which is in contrast to the effect expected for the bleaching phenomena [6]. Occasionally, the fast decrease of the transmission was followed by gradual increase, which depended on the wavelength and excitation intensity. If the excitation pump intensity was low, i.e. if it was in the region of (I) in Fig. 3, then we did not observe the rapid decrease but only gradual increase of the probe beam transmission was observed. Thus, the gradual increase of the transmission shown in Fig. 4 is attributed to a kind of bleaching phenomenon.

Second point of the results shown in Fig. 4 is that the maximum change is achieved at 15–20 ps after the excitation. Considering the Gaussian pulse of 2.5 ps duration, the delay is too long to be interpreted by the change of the reflectivity with the carrier density. Since the evolution of the transmission change is not expressed by a simple exponential function, any fitting procedure will not be effective. But the convolution of the results with a Gaussian probe pulse gives a rise time of the order of 8 ps, which should represent the time necessary for the internal field to build up.

Generally, the radiative recombination lifetime in a quantum well is of the order of 1 ns, and the hole tunneling time should be longer than 100 ps [7]. So the hole process will have no effect on the transmission change observed in Fig. 4. In asymmetric coupled quantum wells, the tunneling transfer of electrons should be assisted with emission or absorption of phonons. In the present case the difference between the two energy levels is only several meV which is much smaller than the LO-phonon energy of GaAs, so the optical phonon process should be prohibited at 77 K. On the other hand, the transfer time due to acoustic phonon process is expected to be much longer [8]. Therefore, if the rise time is controlled by the tunneling transfer of electrons, the short time of 8 ps must be due to resonant tunneling process. Various studies on the resonant tunneling of electrons in GaAs QWs suggest that the tunneling escape time through a 2 nm $\text{Al}_{0.3}\text{Ga}_{0.7}\text{As}$ barrier is of the order of 2–3 ps [9], which is shorter than the rise time of 8 ps observed in the present case.

Since the energies in the conduction band are designed so that a weak field could induce the triple resonance, the energy separation between them is not so large. At $t = 0$, when the flat band condition is fulfilled, electrons can transfer with off-resonant condition, which is a rather slow process. As the carrier density in the wide wells, increases the resonant condition will be achieved and the transition will become fast. Thus, the slightly long time constant observed in Fig. 4 may reflect both the off-resonant and resonant conditions. If this is the case, we are observing the transient process of the change in the band line-up in the conduction band, i.e., from the off resonant flat

band condition to the triply resonant states. The detailed study with femtosecond time resolution will be necessary to reveal the line shape of the transmission change. The realization of fast response of the ATQW suggests an application of the structure to an optical device as an alternative to the SEED [10].

5. Conclusion

Nonlinear transmission of a GaAs/AlGaAs asymmetric triple quantum well structure has been investigated using picosecond pump–probe method at 77 K. A rise time as short as 8 ps of the variation of the transmission was demonstrated. The fast response was discussed in terms of the tunneling transfer time of electrons.

Acknowledgements

This work is partly supported by the Grant in Aid from the Ministry of Education, Science, Culture and Sports of Japan.

References

- [1] M. Seto, M. Helm, *Appl. Phys. Lett.* 60 (1992) 859.
- [2] S. Fukuta, H. Goto, N. Sawaki, T. Suzuki, H. Ito, K. Hara, *Semicond. Sci. & Technol.* 8 (1993) 1881.
- [3] N. Sawaki, T. Kidokoro, S. Ohsaki, T. Suzuki, K. Hara, *Physica B* 227 (1996) 384.
- [4] H.S. Ahn, M. Yamaguchi, N. Sawaki, *Jpn. J. Appl. Phys.* 37 (1998) 45.
- [5] H.S. Ahn, M. Yamaguchi, T. Kidokoro, N. Suzuki, K. Hara, *Semicond. Sci. Technol.* 12 (1997) 722.
- [6] A. Miller, D. Craig, E.J. Manning, in: P. Mandel, S.D. Smith, B.S. Wherrett (Eds.), *From Optical Bistability towards Optical Computing*, North-Holland, Amsterdam, 1987 (Chapter 3).
- [7] E.T. Yu, M.K. Jackson, T.C. MacGill, *Appl. Phys. Lett.* 55 (1989) 744.
- [8] N. Sawaki, R. Hoepfel, E. Gornik, H. Kano, *Appl. Phys. Lett.* 55 (1989) 1996.
- [9] M. Nido, M.G.W. Alexander, W.W. Rühle, T. Schweizer, K. Kohler, *Appl. Phys. Lett.* 56 (1990) 355.
- [10] D.A.B. Miller, *Opt. Quantum Electron.* 22 (1990) S61.



ELSEVIER

Physica E 7 (2000) 267–273

PHYSICA E

www.elsevier.nl/locate/physce

Coherent dynamics of photoexcited semiconductor superlattices in homogeneous electric fields

T. Meier*, H.J. Kolbe, A. Thränhardt, G. Weiser, P. Thomas, S.W. Koch

Department of Physics and Material Sciences Center, Philipps University, Renthof 5, D-35032 Marburg, Germany

Abstract

A microscopic many-body theory for the linear and nonlinear optical properties of semiconductor superlattices subjected to electric fields is presented. The approach has been used for the analysis of various processes related to the Bloch-oscillation dynamics of carriers in static fields and for investigating dynamical localization induced by alternating fields. It is shown that the theory describes very well experimental field-modulated absorption spectra of a strongly coupled superlattice. Furthermore, characteristic signatures, such as negative absorption in the short-pulse optical response of superlattices subjected simultaneously to static and alternating electric fields are predicted. © 2000 Elsevier Science B.V. All rights reserved.

Keywords: Semiconductor superlattices; Electric-field-induced effects; Many-body theory

1. Introduction

During the last decade the dynamics of photoexcited carriers in semiconductor superlattices (SL) with electric fields has attracted considerable attention. One of the early objectives was the direct time domain observation of Bloch oscillations (BO), i.e. the coherent AC-motion of carriers induced by a DC electric field, which had been predicted a long time ago [1,2]. The observability of BO as modulations of the time-integrated four-wave-mixing signal in SL was predicted in Ref. [3] and experimentally verified in

Ref. [4]. One year later, also the observation of the coherent intraband emission due to Bloch-oscillating carriers, which typically has a Terahertz frequency, has been reported [5]. During the following years there has been a rapid development in the experimental work on field-induced effects in semiconductor SL. This research led, for example, to the experimental realization of BO at room temperature [6], indicating that they could potentially be used in actual devices. Moreover, BO have been observed in the Terahertz emission of electrons excited high above the band gap resonantly with the edge of the second miniband [7] and the field-induced ionization of excitons in SL has been investigated using four-wave mixing [8]. Quite recently, the spatial displacement of Bloch-oscillating electrons could be measured using

* Corresponding author. Fax: +49-6421-2827076.

E-mail address: torsten.meier@physik.uni-marburg.de (T. Meier)

spectrally resolved four-wave mixing [9]. In the meantime BO have also been seen in atomic systems [10–12], nicely demonstrating that Zener's original prediction is indeed a quite general quantum-mechanical phenomenon that can be observed in a variety of physical systems.

Many details of the experimentally observed temporal traces associated with BO have been interpreted on the basis of theoretical developments, which proceeded parallel to the experimental work. The theory is able to predict and interpret such details as excitonic effects in linear and nonlinear optical signals, as well as the damping of the coherent motion due to electron–phonon and electron–electron scattering and due to the presence of disorder on the basis of a realistic three-dimensional model of a biased SL. For recent reviews on the theoretical developments see Refs. [13–15].

Also in SL in AC electric fields interesting effects may arise. As for example predicted in Refs. [16,17] an AC field with an appropriately chosen amplitude and frequency may induce *dynamical localization* (DL). The strong AC field required for the observation of the predicted effects can be supplied by a free-electron laser. Indeed, such strong AC fields were successfully used to observe multiphoton-assisted tunneling [18], absolute negative conductance [19], and the inverse Bloch-oscillator [20] in SL. Distinct signatures of DL were also found in the measurements reported in Refs. [19,21] and the existence of DL has been verified recently in atomic systems [22,23].

In Section 2 of this paper, we briefly review our theoretical approach which is based on a full anisotropic three-dimensional description of the SL in homogeneous external electric fields and includes many-body Coulomb interactions among the carriers, as well as carrier–LO–phonon interactions [24–29]. We then focus on linear optical absorption spectra of SL in electric fields. It is shown in Section 3 that our theoretical model is able to reproduce the measured DC field-dependent absorption spectra of a strongly coupled GaInAs/InP SL. Even the very sensitive field-modulated spectra, which give direct access to the field-dependence of optical resonances such as energetic shifts, change in strength, and broadening, are reproduced by our model. Numerical results on the short-pulse linear optical absorption spectra of SL subjected simultaneously to AC and DC fields

are presented in Section 4. It is shown, that an AC field component introduces distinct signatures in the absorption spectra. Furthermore, it turns out that the phase of the AC field is relevant and that there may be spectral regions of negative absorption present in the strongly driven system. Our results are briefly summarized in Section 5.

2. Theory

The electronic wave functions used as a basis set to describe anisotropic SL have been described in detail in Ref. [24]. The wave functions are factorized into products of plane waves associated with the two-dimensional motion within the quantum wells that form the SL, and Bloch functions associated with the growth direction. For the in-plane dispersion, i.e. perpendicular to the growth direction, we use an effective mass model, whereas the dispersion in the growth direction of the SL, as well as the corresponding wave functions, are obtained by solving the Kronig–Penney model. Within this model we maintain the anisotropy of the SL and the dispersion has a cylindrical symmetry, i.e. it depends on k_z (z denotes the growth direction) and on the absolute value of k_{xy} [24].

The Hamiltonian governing the coherent dynamics of photoexcited SL includes the single-particle terms of electrons and holes, their interactions due to the Coulomb potential, as well as the optical dipole-coupling between valence and conduction bands induced by the light field [13,15]. Homogeneous electric fields, in general, lead to different types of terms. We take the intraband acceleration due to the electric field into account, as described in Refs. [24–27]. Other terms which describe Zener transitions between bands and subbands and field-induced renormalizations of the bandstructure are neglected because they can be assumed to be of minor importance [25–27]. The resulting Hamiltonian is given explicitly in Refs. [13,15].

As dynamic variables we consider the electron and hole populations as well as the corresponding interband polarizations [13,15,25]:

$$\begin{aligned} f_{i,k}^e &= \langle c_{i,k}^\dagger c_{i,k} \rangle, & f_{j,k}^h &= \langle d_{j,k}^\dagger d_{j,k} \rangle, \\ p_{ji,k} &= \langle d_{j,-k} c_{i,k} \rangle. \end{aligned} \quad (1)$$

Here, $c_{i,k}^\dagger$ ($d_{j,k}^\dagger$) creates and $c_{i,k}$ ($d_{j,k}$) destroys an electron (a hole) with wave vector \mathbf{k} in band $i(j)$. The equations of motion for the quantities in Eq. (1) are obtained from the Heisenberg equation. Due to the many-body Coulomb interaction these two-point variables couple to higher-order correlations, which are represented by four-point functions, i.e. we run into the usual many-body problem of having an infinite hierarchy of equations of motion. To close the equations for our dynamic variables at the lowest level we apply the time-dependent Hartree–Fock approximation, i.e. we factorize four-point variables into products of two-point variables [28]. Within such an approximation scheme, first-order Coulomb terms, which give rise to important excitonic effects, are included. The resulting equations, the multisub-band semiconductor Bloch equations (SBE) including the action of the electric field are given below and have been presented and solved numerically in Refs. [13,15,25,29,30].

$$\left(\frac{\partial}{\partial t} + \frac{e\mathbf{F}}{\hbar} \cdot \nabla_{\mathbf{k}} \right) f_{i,k}^e = \frac{1}{i\hbar} \sum_{j'} (\mathcal{U}_{ij',k} p_{j'i,k}^* - \mathcal{U}_{ij',k}^* p_{j'i,k}) + \left. \frac{\partial f_{i,k}^e}{\partial t} \right|_{\text{coll}}, \quad (2)$$

$$\left(\frac{\partial}{\partial t} + \frac{e\mathbf{F}}{\hbar} \cdot \nabla_{\mathbf{k}} \right) f_{j,-k}^h = \frac{1}{i\hbar} \sum_{i'} (\mathcal{U}_{i'j,k} p_{ji',k}^* - \mathcal{U}_{i'j,k}^* p_{ji',k}) + \left. \frac{\partial f_{j,-k}^h}{\partial t} \right|_{\text{coll}}, \quad (3)$$

$$\left(\frac{\partial}{\partial t} + \frac{e\mathbf{F}}{\hbar} \cdot \nabla_{\mathbf{k}} \right) p_{ji,k} = \frac{1}{i\hbar} \sum_{i'j'} (\mathcal{E}_{ii',k}^e \delta_{jj'} + \mathcal{E}_{jj',-k}^h \delta_{ii'}) p_{j'i',k} + \frac{1}{i\hbar} \mathcal{U}_{ij,k} (1 - f_{i,k}^e - f_{j,-k}^h) + \left. \frac{\partial p_{ji,k}}{\partial t} \right|_{\text{coll}}, \quad (4)$$

where

$$\mathcal{U}_{ij,k} = \mu_{ij,k} E(t) - \sum_{i'j',k'} V^{\text{eh}}(k, -k', -k, k') p_{j'i',k'} \quad (5)$$

and

$$\mathcal{E}_{ii',k}^e = \varepsilon_{i,k}^e \delta_{ii'} - \sum_{i'',k''} V^{\text{ee}}(k, k'', k, k'') f_{i'',k''}^e, \quad (6)$$

$$\mathcal{E}_{jj',k}^h = \varepsilon_{j,k}^h \delta_{jj'} - \sum_{j'',k''} V^{\text{hh}}(k, k'', k, k'') f_{j'',k''}^h,$$

are, respectively, the renormalized Rabi-frequencies (field renormalization) and electron and hole energies (band-gap renormalization) [28]. In Eqs. (2)–(6), V is the Coulomb matrix element, μ is the optical dipole matrix element between conduction and valence-band states, $\varepsilon^{\text{e,h}}$ are the single-particle energies, and \mathbf{F} is the electric field. Effects beyond the Hartree–Fock approximation and further interactions of the carrier with other quasiparticles are formally represented by the collision terms denoted by $|_{\text{coll}}$. The total polarization that determines optical experiments is given by $P = \sum_{ij,k} \mu_{ij,k} p_{ji,k}$.

Besides the terms describing the electronic dynamics alone, also electron–LO–phonon coupling has been treated up to second order within the Markov approximation [24,25,30]. Electron–phonon coupling results in dephasing of both intra- and interband polarizations as well as energy-relaxation processes [24,25,30]. In order to describe highly excited systems we have also included static screening in the model [29,31].

Solving the coherent part of the SL-SBE within the k -space basis as described by Eqs. (2)–(6) yields identical results as using a Wannier–Stark (WS) basis set for the electronic wave functions associated with the growth direction [14,30]. As is discussed in Ref. [30], however, for the case of electron–phonon coupling the numerical results may depend on the basis set due to the Markov approximation used in the second-order description of scattering processes.

Going beyond the Hartree–Fock approximation for the Coulomb interaction by considering second-order terms [32] or even four-point functions [33] is numerically a very demanding task for anisotropic SL even on the fastest supercomputers available nowadays. Therefore, so far no such systematic extension for three-dimensional anisotropic systems has been reported. In Refs. [15,31], however, numerical results on the intraband Terahertz emission including second-order terms within a mean-field approximation, which can be regarded as carrier–carrier scattering events, are presented. Such calculations are

possible, because these terms can be evaluated extremely efficiently via a Monte Carlo simulation. Unfortunately, this is not the case for other terms appearing in the same order of the Coulomb interaction.

3. Field-dependent absorption of a strongly coupled superlattice

In Ref. [34] it is demonstrated that numerical solutions of the SL-SBE reproduce field-dependent and even field-modulated absorption spectra of a GaInAs/InP SL exclusively in the regime of WS localization. Here we show that our theoretical model is able to reproduce the field-modulated absorption spectra of another strongly coupled GaInAs/InP SL consisting of 21-periods with 4.9 nm thick wells of Ga_{0.47}In_{0.53}As and 1.7 nm thick InP barriers, however, over a broad range of field strengths. The miniband width of the electron and heavy-hole bands of the GaInAs/InP SL was estimated from solving the Kronig–Penney model to be 100 and 0.7 meV, respectively.

The experiments are performed at a temperature of $T = 20$ K and the differential electroabsorption spectra are obtained by lock-in technique with a modulation voltage of ± 20 mV corresponding to a modulation field of $\Delta F = \pm 0.25$ kV/cm. To model the differential electroabsorption we first have to consider the field-dependent absorption $\alpha(\omega, F)$. This is obtained from the polarization density $P(\omega, F)/V$ induced by the field $E(\omega)$ via

$$\alpha(\omega, F) = \frac{\omega}{nc} \text{Im} \left\{ \frac{P(\omega, F)}{VE(\omega)} \right\}, \quad (7)$$

where n is the background refractive index. To account for line broadening we use a phenomenological dephasing time $T_2 = 600$ fs in Eq. (4) and further introduce inhomogeneous broadening via averaging the spectra with a Gaussian of 10.6 meV full-width at half-maximum (FWHM). The differential electroabsorption spectrum at the field F is then obtained as the difference of the absorption spectra via

$$\Delta\alpha(\omega, F) = \alpha(\omega, F + \Delta F) - \alpha(\omega, F - \Delta F). \quad (8)$$

A comparison between the experimental and theoretical differential electroabsorption spectra for various fields is displayed in Fig. 1. Considering that

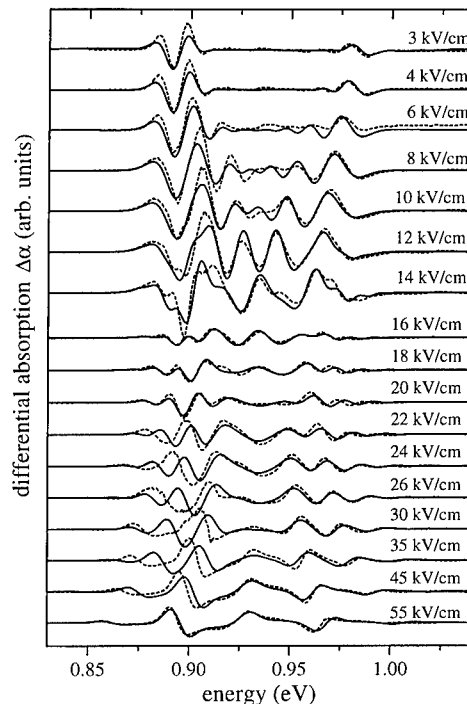


Fig. 1. Experimental (solid) and theoretical (dashed) field-modulated absorption spectra $\Delta\alpha$ of a Ga_{0.47}In_{0.53}As/InP superlattice with 4.9 nm well and 1.7 nm barrier width for various DC fields as indicated in the figure.

differential spectra are very sensitive to even small field-induced absorption changes, we find an amazingly good agreement between experiment and theory over a broad range of fields, covering the weak field Franz–Keldysh regime, as well as intermediate fields up to the strong field regime of WS localization. For small DC field, the field-dependent absorption is dominated by the Franz–Keldysh effect. It leads to well-known modulations of the absorption near the lower and the upper miniband edges, see Fig. 1 for $F = 3$ and 4 kV/cm. For these small fields $\Delta\alpha$ vanishes in the middle of the miniband because of the finite coherence length [35]. With increasing field, the Franz–Keldysh oscillations originating from the lower and the upper miniband edges extend over a broader spectral range and meet in the miniband center, see Fig. 1 for $F \approx 8$ kV/cm. In the intermediate field regime the differential electroabsorption spectra are very complicated and are determined by interferences of both sets of Franz–Keldysh oscillations as

well as oscillations which indicate the onset of WS localization. For even stronger fields, the spectra are dominated by the WS localization, which introduces distinct signatures in the differential electroabsorption spectra [34]. For $F = 55$ kV/cm the central excitonic WS transition $\nu = 0$ which occurs close to the center of the miniband at approximately 0.93 eV, shows a positive $\Delta\alpha$. This means that this transition gains oscillator strength with increasing field as expected for field-induced localization. On the other hand, the first-order excitonic WS transitions $\nu = -1, +1$, which appear for $F = 55$ kV/cm approximately at 0.89 and 0.97 eV, respectively, show a predominantly dispersive $\Delta\alpha$. This lineshape just reflects the shift of these resonances away from band center with increasing field.

Whereas the overall agreement between the experimental and theoretical spectra displayed Fig. 1 is very good and for some fields even excellent, one can see some deviations which are particularly strong near the lower miniband edge between $F = 22$ and 35 kV/cm. At present, we have no obvious explanation for this deviation and further studies are required to clarify this point.

4. Linear spectra of a superlattice in static and alternating fields

For static fields along the growth direction of a SL the field-dependent optical absorption is dominated by the Franz–Keldysh effect in the weak field limit and by the WS localization for rather strong fields [14,15]. AC fields have been shown to reduce the SL miniband width and may even induce a band collapse if the conditions for DL are fulfilled [16,17,25]. Due to the change of the electronic dispersion also the spectral position of the SL exciton shifts with an AC field [25]. If the SL is subjected to both AC and DC fields the SL absorption may show interesting signatures which are discussed in the following.

We use a GaAs/Al_{0.3}Ga_{0.7}As SL with 9.7 nm well and 1.7 nm barrier width. The widths for the lowest electron and heavy-hole minibands are 18 and 2 meV, respectively. The electric field is taken as

$$F(t) = F_{DC} - F_{AC} \sin(\omega_{AC}t + \Phi). \quad (9)$$

With such a field Eq. (4) is solved using $T_2 = 1$ ps for excitation with a short 10 fs optical pulse arriving

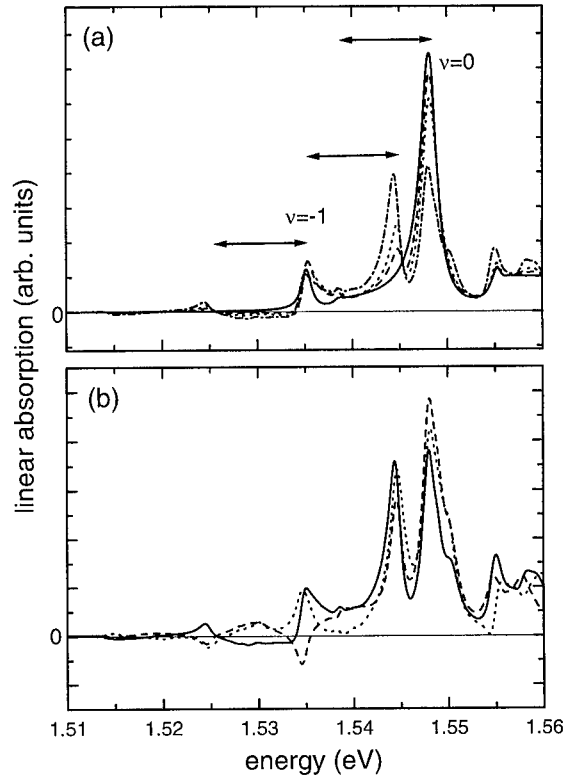


Fig. 2. Absorption spectra of a GaAs/Al_{0.3}Ga_{0.7}As superlattice with 9.7 nm well and 1.7 nm barrier width. The DC field is taken to be 15 kV/cm and the AC field has a frequency of $\hbar\omega_{AC} = 10$ meV. (a) Dependence on the amplitude of AC field for $\Phi = 0$: $F_{AC} = 0$ kV/cm (solid), $F_{AC} = 3$ kV/cm (dashed), $F_{AC} = 5$ kV/cm (dotted), and $F_{AC} = 10$ kV/cm (dashed-dotted). (b) Dependence on phase of AC field for $F_{AC} = 10$ kV/cm: $\Phi = 0$ (solid), $\Phi = -\pi/2$ (dashed), and $\Phi = \pi/2$ (dotted). The arrows indicate spectral positions of photonic sidebands of the $\nu = -1$ and 0 Wannier–Stark transitions.

at $t = 0$ and the linear absorption $\alpha(\omega, F)$ is obtained via Eq. (7).

The absorption spectra with AC and DC field are displayed in Fig. 2. Without any AC field component we see in Fig. 2(a) two peaks in the spectra which are the weak $\nu = -1$ and the strong $\nu = 0$ excitonic WS transitions. With an AC field component additional peaks appear in the spectra which are energetically separated from the $\nu = 0$ and -1 WS excitons by multiples of $\hbar\omega_{AC}$, which is just the photon energy of the AC field. Thus, the absorption maxima in the presence of an AC field can be understood qualitatively simply as photonic sidebands. Related terahertz optical

sidebands have been observed on magnetoexcitons [36]. Another feature present in the spectra in Fig. 2(a) is the appearance of a broad region with negative absorption, i.e. optical gain, spectrally below the $\nu = -1$ WS exciton.

Similar results on negative optical absorption have been reported for the so-called *A*- and *V*-type three level systems that are coherently coupled to strong AC fields. The analysis has shown that in such strongly driven systems it is possible to have negative absorption without an interband population inversion [37,38]. In these systems the population inversion that is usually needed to have negative absorption is replaced by the coherence introduced by an AC field.

As is shown in Fig. 2(b), the absorption line shape depends sensitively on the phase of the AC field with respect to the short optical pulse that measures the absorption. Whereas for $\Phi = 0$ there is a broad spectral region with negative absorption present below the $\nu = -1$ WS exciton, for $\Phi = \pi/2$ and $-\pi/2$ it is absent. For $\Phi = -\pi/2$, on the other hand negative absorption appears directly at the $\nu = -1$ WS exciton and $\hbar\omega_{AC}$ below.

Similar results including the possibility of negative absorption and the phase sensitivity of the absorption spectra have been presented recently in Ref. [39] on the basis of a simplified model that considered only the 1s excitons. The results presented here include higher exciton and continuum states allowing us to give a much more realistic description of the absorption spectra. For example, the *broad* spectral region of negative absorption that has been discussed above is probably missed if only the 1s excitons are considered.

5. Summary

In this paper, we briefly review a theoretical approach, based on the anisotropic three-dimensional description of the SL in homogeneous external electric fields, which allows us to calculate linear and non-linear optical properties. We focus on two examples of linear optical absorption spectra of SL in electric fields. It is demonstrated that the model appropriately describes field-modulated absorption spectra of a strongly coupled GaInAs/InP SL. Numerical results on the short-pulse linear optical absorption spectra of SL subjected simultaneously to AC and DC fields re-

veal that strong high-frequency AC fields introduce distinct signatures in the absorption spectra if a DC field is present. In particular, the possibility of having negative absorption has been demonstrated.

Acknowledgements

This work is supported by the Deutsche Forschungsgemeinschaft through the Sonderforschungsbereich 383 and the Leibniz prize, and by the Max-Planck Research Prize of the Max-Planck Society and the Humboldt Foundation.

References

- [1] F. Bloch, Z. Phys. 52 (1928) 555.
- [2] C. Zener, Proc. Roy. Soc. A 145 (1934) 523.
- [3] G. von Plessen, P. Thomas, Phys. Rev. B 45 (1992) 9185.
- [4] J. Feldmann, K. Leo, J. Shah, D.A.B. Miller, J.E. Cunningham, T. Meier, G. von Plessen, A. Schulze, P. Thomas, S. Schmitt-Rink, Phys. Rev. B 46 (1992) 7252.
- [5] C. Waschke, H.G. Roskos, R. Schwedler, K. Leo, H. Kurz, K. Köhler, Phys. Rev. Lett. 70 (1993) 3319.
- [6] T. Dekorsy, R. Ott, H. Kurz, Phys. Rev. B 51 (1995) 17275.
- [7] H.G. Roskos, C. Waschke, R. Schwedler, P. Leisching, Y. Dhaibi, H. Kurz, K. Köhler, Superlattices Microstruct. 15 (1994) 281.
- [8] G. von Plessen, T. Meier, M. Koch, J. Feldmann, P. Thomas, S.W. Koch, E.O. Göbel, K.W. Goossen, L.M. Kuo, R.F. Kopf, Phys. Rev. B 53 (1996) 13688.
- [9] V.G. Lyssenko, G. Valusis, F. Löser, T. Hasche, K. Leo, M.M. Dignam, K. Köhler, Phys. Rev. Lett. 79 (1997) 301.
- [10] M.B. Dahan, E. Peik, J. Reichel, Y. Castin, C. Salomon, Phys. Rev. Lett. 76 (1996) 4508.
- [11] K.P. Marzlin, J. Audretsch, Europhys. Lett. 36 (1996) 43.
- [12] M.G. Raizen, C. Salomon, Qian Niu, Phys. Today 50 (1997) 30.
- [13] T. Meier, P. Thomas, S.W. Koch, Phys. Low-Dimensional Struct. 3/4 (1998) 1.
- [14] J. Hader, P. Thomas, S.W. Koch, Prog. Quantum Electron. 22 (1998) 123.
- [15] T. Meier, P. Thomas, S.W. Koch, in: K.T. Tsien (Ed.), *Ultrafast Processes in Semiconductors*, Springer, New York, in press.
- [16] D.H. Dunlap, V.M. Kenkre, Phys. Rev. B 34 (1996) 3525.
- [17] M. Holthaus, Phys. Rev. Lett. 69 (1992) 351.
- [18] B.J. Keay, S.J. Allen, J. Galan, J.P. Kaminski, K.L. Chapman, A.C. Gossard, U. Bhattacharya, M.J.W. Rodwell, Phys. Rev. Lett. 75 (1995) 4098.
- [19] B.J. Keay, S. Zeuner, S.J. Allen, K.D. Maranowski, A.C. Gossard, U. Bhattacharya, M.J.W. Rodwell, Phys. Rev. Lett. 75 (1995) 4102.

- [20] K. Unterrainer, B.J. Keay, M.C. Wanke, S.J. Allen, D. Leonard, G. Medeiros-Ribeiro, U. Bhattacharya, M.J.W. Rodwell, *Phys. Rev. Lett.* 76 (1996) 1973.
- [21] S. Winnerl, E. Schomburg, J. Grenzer, H.-J. Regl, A.A. Ignatov, K.F. Renk, D.P. Pavelev, Y. Koschurinov, B. Melzer, V. Ustinov, S. Ivanov, S. Schaposchnikov, P.S. Kopev, *Superlattices Microstruct.* 21 (1997) 91.
- [22] B.G. Klappauf, W.H. Oskay, D.A. Steck, M.G. Raizen, *Phys. Rev. Lett.* 81 (1998) 1203.
- [23] B.G. Klappauf, W.H. Oskay, D.A. Steck, M.G. Raizen, *Phys. Rev. Lett.* 82 (1999) 241.
- [24] F. Rossi, T. Meier, P. Thomas, S.W. Koch, *Phys. Rev. B* 51 (1995) 16943.
- [25] T. Meier, F. Rossi, P. Thomas, S.W. Koch, *Phys. Rev. Lett.* 75 (1995) 2558.
- [26] T. Meier, G. von Plessen, P. Thomas, S.W. Koch, *Phys. Rev. Lett.* 73 (1994) 902.
- [27] T. Meier, G. von Plessen, P. Thomas, S.W. Koch, *Phys. Rev. B* 51 (1995) 14490.
- [28] H. Haug, S.W. Koch, *Quantum Theory of the Optical and Electronic Properties of Semiconductors*, World Scientific, Singapore, 1994.
- [29] K.-C. Je, T. Meier, F. Rossi, S.W. Koch, *Appl. Phys. Lett.* 67 (1995) 2978.
- [30] J. Hader, T. Meier, S.W. Koch, F. Rossi, N. Linder, *Phys. Rev. B* 55 (1997) 13799.
- [31] F. Rossi, M. Gulia, P.E. Selbmann, E. Molinari, T. Meier, P. Thomas, S.W. Koch, in: M. Scheffler, R. Zimmermann (Eds.), *The Physics of Semiconductors, Proceedings of the 23rd ICPS*, World Scientific, Singapore, 1996, pp. 1775–1778.
- [32] F. Jahnke, M. Kira, S.W. Koch, G. Khitrova, E.K. Lindmark, T.R. Nelson, D.V. Wick, J.D. Berger, O. Lyngnes, H.M. Gibbs, K. Tai, *Phys. Rev. Lett.* 77 (1996) 5257.
- [33] C. Sieh, T. Meier, F. Jahnke, A. Knorr, S.W. Koch, P. Brick, M. Hübner, C. Ell, J. Prineas, G. Khitrova, H.M. Gibbs, *Phys. Rev. Lett.* 82 (1999) 3112.
- [34] A. Thränhardt, H.J. Kolbe, J. Hader, T. Meier, G. Weiser, S.W. Koch, *Appl. Phys. Lett.* 73 (1998) 2612.
- [35] A. Jaeger, G. Weiser, P. Wiedmann, I. Gyuro, E. Zielinski, *J. Phys.: Condens. Matter* 8 (1996) 6779.
- [36] J. Kono, M.Y. Su, T. Inoshita, T. Nado, M.S. Sherwin, S.J. Allen, H. Sakaki, *Phys. Rev. Lett.* 79 (1997) 1758.
- [37] S.E. Harris, *Phys. Rev. Lett.* 62 (1989) 1033.
- [38] M.O. Scully, S.-Y. Zhu, A. Gavrielides, *Phys. Rev. Lett.* 62 (1995) 2813.
- [39] M.M. Dignam, *Phys. Rev. B* 59 (1999) 5770.



ELSEVIER

Physica E 7 (2000) 274–278

PHYSICA E

www.elsevier.nl/locate/physce

Interminiband spectroscopy of biased superlattices

M. Helm^{a,*}, W. Hilber^a, G. Strasser^b, R. De Meester^c, F.M. Peeters^c, A. Wacker^d

^a*Institut für Halbleiter- und Festkörperphysik, Universität Linz, A-4040 Linz, Austria*

^b*Institut für Festkörperelektronik, TU Wien, A-1040 Wien, Austria*

^c*Department of Physics, University of Antwerp, B-2610 Antwerpen, Belgium*

^d*Institut für Theoretische Physik, TU Berlin, D-10623 Berlin, Germany*

Abstract

We study the interminiband absorption in a GaAs/AlGaAs superlattice under the application of an electric field along the growth axis. While transport shows domain formation and next-nearest tunneling of electrons, the infrared absorption spectrum is strongly modified and reveals transitions to Zener-coupled Wannier–Stark ladders far in the continuum. © 2000 Elsevier Science B.V. All rights reserved.

Keywords: Superlattice; Wannier–Stark ladder; Interminiband absorption; Tunneling

Upon application of an electric field along the growth axis, intersubband transitions exhibit Stark shifts [1,2], transfer of oscillator strengths in coupled quantum wells [3], or localization-induced line-narrowing of transitions into the continuum [4]. Strongly coupled superlattices (SLs) behave differently in several respects. First, the intersubband absorption is known to extend over a certain spectral width, which corresponds to the widths of the minibands involved in the transition. It has been shown that the oscillator strength is distributed over the mini-Brillouin zone, with the maximum at the zone-edge [5,6]. This has found application in superlattice cascade lasers [7]. In a vertical electric field,

they show negative differential resistance (NDR) [8], Bloch oscillations [9] and the formation of a Wannier–Stark ladder (WSL) [10,11]. These phenomena have been studied using transport [8] and infrared emission (in doped SLs) [12] as well as by optical methods (in undoped SLs) [9]. The evolution of the inter-miniband absorption spectrum in a vertical electric field, however, has not been studied to date. Yet it could yield new insight into the above phenomena, especially when transport and infrared optical techniques are combined. In the mid-infrared one can use the inter-miniband absorption spectrum to observe the modification of the electron distribution function in the electric field [13] or the break-up of the minibands into Wannier–Stark ladders. In the far-infrared (or THz) it has been predicted that, under conditions of NDR and Bloch oscillations, optical gain occurs below the Bloch frequency [14].

* Corresponding author. Tel.: +43-732-2468-9602; fax: +43-732-2468-650.

E-mail address: m.helm@hlphys.uni-linz.ac.at (M. Helm)

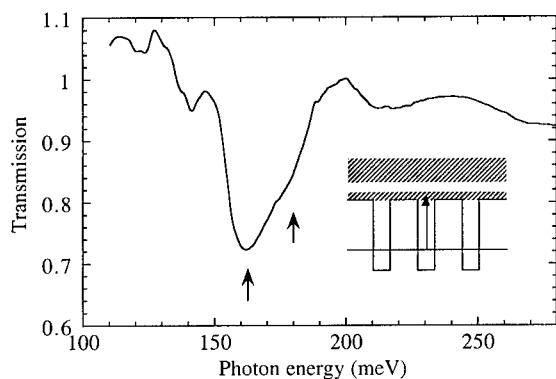


Fig. 1. Interminiband transmission spectrum for zero electric field. The inset shows a schematic of the absorption process. The main absorption and the high-energy shoulder, related to the critical points, are indicated by arrows.

Here we report on an experiment, which combines transport and intersubband absorption in a biased superlattice. Due to the high currents, inevitably occurring in vertical transport of strongly coupled superlattices, it is difficult to use the same sample also for IR absorption measurements, which usually require a relatively large sample size. Therefore we designed a SL (300 periods of 50 Å GaAs and 80 Å $\text{Al}_{0.29}\text{Ga}_{0.71}\text{As}$) with a relatively narrow first miniband (width $\Delta_1 = 1.2$ meV), to keep the current density low, but a rather wide second miniband ($\Delta_2 = 30$ meV), to achieve strong coupling between the adjacent wells via the excited states. The doping was $n = 2.25 \times 10^{11} \text{ cm}^{-2}$ per period. The second miniband is located right above the barriers in the continuum (see inset of Fig. 1).

Fig. 1 shows the zero-field interminiband absorption spectrum of the superlattice, obtained by the ratio of the p-polarized (active) to the s-polarized (inactive) transmission signal, measured in a multi-pass waveguide geometry on a sample with several etched 1-mm² mesas. The main absorption maximum at 162 meV and the high-energy shoulder at 180 meV (both indicated by arrows in Fig. 1) are due to the well-known singularities of the joint density of states at the center and the edge of the mini-Brillouin zone, respectively. (A calculated zero-field interminiband absorption spectrum is shown below in the lowest curve of Fig. 4.)

Due to the relatively narrow width of the first miniband, we can expect sequential tunneling rather than

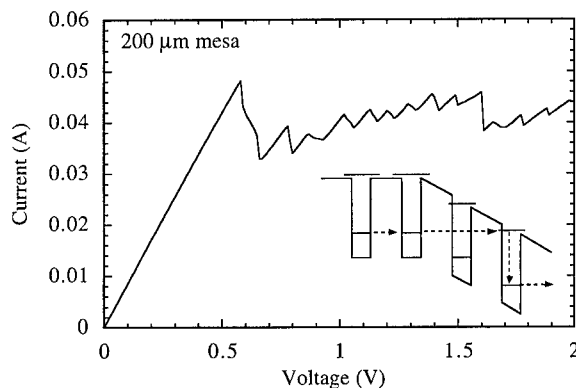


Fig. 2. Low-bias part of the SL current-voltage characteristic measured on a 200 μm mesa at $T = 10$ K. The spacing of the sharp NDRs is ≈ 90 meV. The inset shows the conduction-band edge near the boundary of the low- and high-field domain together with a schematic of the transport process.

miniband transport to be the transport mechanism at low bias [15]. This is also evident in the current-voltage characteristic, which, after an ohmic onset, exhibits 300 sharp NDRs with a spacing of approximately 90 meV (shown in Fig. 2 only up to 2 V). At $300 \times 90 \text{ mV} = 27 \text{ V}$ the current rises steeply [16] (not shown). Such a behavior is well known in weakly coupled SLs and is due to sequential tunneling and domain formation [17,18]. The present case, however, is quite distinct, since from the NDR spacing of 90 meV (i.e. half the subband spacing), it follows that in the high-field domain the electrons tunnel to the second subband in the *next-nearest* SL period (and not the adjacent period, as usually observed, see inset of Fig. 2).

The IR absorption experiments under bias were performed on 1-mm²-size mesas with a Bruker IFS66 Fourier-transform spectrometer operated in a gated step-scan mode [13]. The transmission was measured during the 10-μs voltage pulse and some 10 μs later as a reference. The resulting transmission change $T(F)/T(F=0)$ is plotted in Fig. 3 for a series of bias voltages. Note that the minima in the signal correspond to decreased transmission, i.e. they essentially correspond to absorption lines induced by the electric field (marked by arrows). The spectral positions of the differential absorption features hardly change with bias voltage, but their magnitude increases and reaches up to 30%

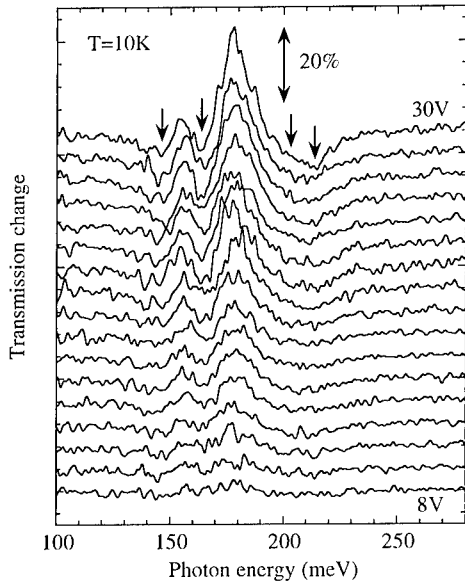


Fig. 3. Differential transmission spectrum ($T(F)/T(0)$) of the superlattice for a series of bias voltages between 8 and 30 V. Minima essentially correspond to electric-field-induced absorption lines (marked by arrows).

at the highest voltage. This is a consequence of the non-homogeneous electric-field distribution in the SL. In the present range of bias voltages, the SL consists of a low-field domain, where the electric field is nearly zero (ground-state-to-ground-state tunneling) and a high-field domain, where the electric field is approximately $F = (E_{21})/ed = 85 \text{ mV}/130 \text{ \AA} = 65 \text{ kV/cm}$ (tunneling into the second subband in the next-nearest SL period). Increasing the voltage only increases the relative length of the high-electric-field domain, resulting in a larger optical signal.

Understanding the transmission spectra of Fig. 3 requires a calculation of the absorption coefficient, α , under bias. This has been performed using a finite system of 19 SL periods and a phenomenological Lorentzian broadening of $\Gamma = 7 \text{ meV}$ (HWHM) of each transition [16]. The result is plotted in Fig. 4 for electric fields from $F = 0$ up to $F = 70 \text{ kV/cm}$. Only up to 20 kV/cm the splitting of the interminiband absorption into a regular WSL can be observed. At higher fields, strong mixing of several continuum WSLs occurs due to Zener coupling [19]. For direct comparison with the experiment, the quantity $\alpha(0) - \alpha(F)$, which is proportional to the measured transmission change

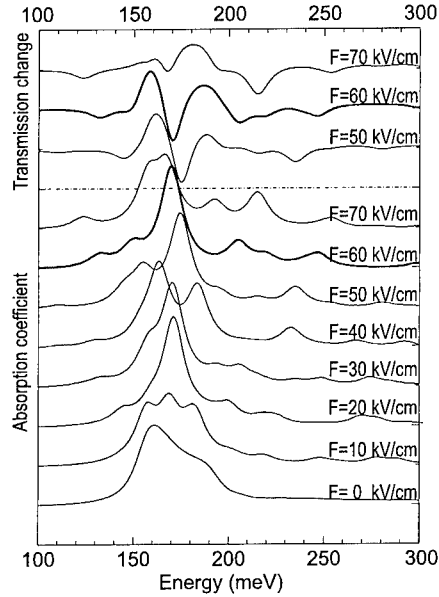


Fig. 4. Absorption coefficient calculated for electric fields from 0 to 70 kV/cm. In addition, the transmission change is shown for 50, 60, and 70 kV/cm in the upper panel to facilitate comparison with the experiment (see text). The experimentally relevant 60 kV/cm spectra are plotted with thicker lines (compare with Fig. 2).

$T(F)/T(0)$, is plotted in the upper panel of Fig. 4. Most of the experimental features can be reasonably well reproduced for a field of $F = 60 \text{ kV/cm}$ (drawn by thicker lines for clarity); only the maximum at $\approx 180 \text{ meV}$ is larger than predicted. The above field corresponds to a voltage drop of 80 meV per SL period, which is very close to half the energy separation E_{21} , and thus confirms the tunneling to the next-nearest SL period.

A more graphical understanding of the transitions dominating the absorption spectrum can be obtained by using a classification of the energy levels in terms of pure WSL quantum numbers, $E_{m,p} = \varepsilon_m + peFd$ (neglecting the interaction due to Zener coupling for the moment) [10]. Such an assignment can be done by inspecting in detail the wave functions and oscillator strengths over several SL periods and is shown in Fig. 5. (Transitions from a state $|m = 1, p\rangle$ to $|m', p'\rangle$ are written as $(m', p' - p)$ for brevity.) The main parts of the relevant wave functions are indicated by bold lines and the calculated absorption coefficient is shown for comparison. The main observed transitions (indicated by arrows) are, from low to high energies,

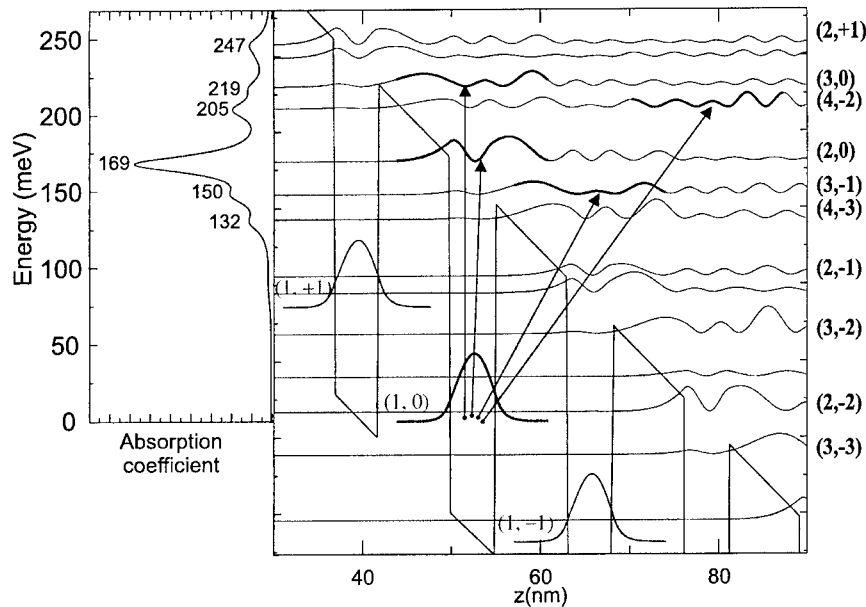


Fig. 5. Conduction-band profile, energy levels and squared wave functions drawn for four superlattice periods with an electric field of 60 kV/cm. The experimentally observed transitions are indicated by arrows and the main parts of the respective wave functions are shown by thicker lines. The numbers on the right represent an (approximate) assignment in terms of WS states (see text). In addition, the calculated absorption coefficient is shown on the left for comparison, including the peak photon energies.

$(3, -1)$, $(2, 0)$ (this is the main vertical intersubband transition), $(4, -2)$, and $(3, 0)$.

As seen in Fig. 5, the continuum WSL wave functions display the character of both the localized WSL- and the free-electron-like states. Note also that due to the finiteness of the structure used in the calculation, no perfect periodicity of the solution for the wave functions under a translation $z \rightarrow z + d$ and $E \rightarrow E - eFd$ is obtained. In the absorption coefficient (which is the *observable* quantity) this symmetry is however recovered, when calculated with a finite Γ . This shows the relation of Γ to the coherence length; when Γ is very small, the wave functions more easily feel the edges of the finite SL [20].

In summary, we have reported on a combined measurement of transport and intersubband absorption in a biased SL, and observed Wannier–Stark ladders in the continuum as well as the next-nearest-neighbor tunneling. Extension of the present technique to the far-IR spectral region and applied to more strongly coupled SLs may unveil the intra-miniband spectral response [21], and possibly gain, of a superlattice under Bloch-oscillation conditions.

Acknowledgements

This work was supported by the FWF, the GMe (both Austria), and the FWO-VI (Belgium). R.D.M. is supported by IWT (Belgium).

References

- [1] A. Harwit, J.S. Harris Jr., Appl. Phys. Lett. 50 (1987) 685.
- [2] Y. Mii et al., Appl. Phys. Lett. 56 (1990) 1986.
- [3] J. Faist, F. Capasso, A.L. Hutchinson, L.N. Pfeiffer, K.W. West, Phys. Rev. Lett. 71 (1993) 3573.
- [4] C. Sirtori, J. Faist, F. Capasso, D.L. Sivco, A.Y. Cho, Appl. Phys. Lett. 62 (1993) 1931.
- [5] M. Helm et al., Phys. Rev. B 48 (1993) 1601.
- [6] M. Helm, Semicond. Sci. Technol. 10 (1995) 557.
- [7] G. Scamarcio, F. Capasso, C. Sirtori, J. Faist, A.L. Hutchinson, D.L. Sivco, A.Y. Cho, Science 276 (1997) 773.
- [8] A. Sibille et al., Superlattices Microstruct. 13 (1993) 247.
- [9] K. Leo, Semicond. Sci. Technol. 13 (1998) 249 and references therein.
- [10] E.E. Mendez, F. Agullo-Rueda, J.M. Hong, Phys. Rev. Lett. 60 (1988) 2426.
- [11] P. Voisin et al., Phys. Rev. Lett. 61 (1988) 1639.
- [12] G. Scamarcio, F. Capasso, A.L. Hutchinson, D.L. Sivco, A.Y. Cho, Phys. Rev. B 57 (1998) R6811.

- [13] W. Hilber, M. Helm, K. Alavi, R.N. Pathak, Appl. Phys. Lett. 69 (1996) 2528.
- [14] S.J. Allen et al., Semicond. Sci. Technol. 7 (1992) B1.
- [15] A. Wacker, A.-P. Jauho, Phys. Rev. Lett. 80 (1998) 369.
- [16] M. Helm, W. Hilber, G. Strasser, R. De Meester, F.M. Peeters, A. Wacker, Phys. Rev. Lett. 82 (1999) 3120.
- [17] H.T. Grahn, H. Schneider, K. von Klitzing, Phys. Rev. B 41 (1990) 2890.
- [18] S.H. Kwok et al., Phys. Rev. B 51 (1995) 9943.
- [19] A. Sibille, J.F. Palmier, F. Laruelle, Phys. Rev. Lett. 80 (1998) 4506.
- [20] C. Rauch, G. Strasser, K. Unterrainer, W. Boxleitner, E. Gornik, A. Wacker, Phys. Rev. Lett. 81 (1998) 3495.
- [21] G. Brozak, M. Helm, F. DeRosa, C.H. Perry, M. Koza, R. Bhat, S.J. Allen Jr., Phys. Rev. Lett. 64 (1990) 3163.



ELSEVIER

Physica E 7 (2000) 279–284

PHYSICA E

www.elsevier.nl/locate/physa

Coupled Bloch-phonon oscillations in GaAs/AlGaAs superlattices: theory and experiment

T. Dekorsy^{a,*}, A. Bartels^a, H. Kurz^a, A.W. Ghosh^b, L. Jönsson^b, J.W. Wilkins^b, K. Köhler^c,
R. Hey^d, K. Ploog^d

^a*Institut für Halbleitertechnik II, RWTH Aachen, Sommerfeldstr. 24, D-52056 Aachen, Germany*

^b*Department of Physics, Ohio State University, 174 West 18th Avenue, Columbus, OH 43210, USA*

^c*Fraunhofer-Institut für Angewandte Festkörperphysik, D-79108 Freiburg, Germany*

^d*Paul Drude Institut für Festkörperphysik, D-10117 Berlin, Germany*

Abstract

We report on the femtosecond dynamics of coherent Bloch oscillations in GaAs/Al_xGa_{1-x}As superlattices. In a superlattice with a miniband width equal to the optical phonon energy of GaAs the Bloch frequency can be tuned into resonance with the LO phonon by an applied electric field. We observe a strong coupling between Bloch oscillations and phonons leading to the coherent excitation of optical phonons when both are brought into resonance. This phenomenon is analyzed theoretically on the base of a microscopic Hamiltonian for the electron–phonon interaction in the superlattice. We show that coupled modes are described by a nonlinear pendulum coupled linearly to an oscillator representing the phonons. Under resonance condition the amplitudes of both modes increase and sidebands appear. The theoretical results are compared to the experimental observations. © 2000 Elsevier Science B.V. All rights reserved.

Keywords: Bloch oscillations; Electron–phonon coupling; Superlattices; THz dynamics

1. Introduction

Bloch oscillations of electrons in superlattices have been convincingly demonstrated in femtosecond time-resolved experiments like four wave mixing [1,2], THz emission [3], and transmissive electro-optic sampling (TEOS) [4]. TEOS experiments monitor the

change in transmission of a time-delayed circularly polarized probe pulse through a biased superlattice after photoexcitation with a linearly polarized pump pulse. The transmission change is affected directly by longitudinal field oscillations in the superlattice that occur at THz frequencies. This involves Bloch oscillations, plasmons, longitudinal optical phonons, all of which exist in the THz regime. In particular, the first two modes are tunable and can be brought into resonance via the change of an external applied electric field and the change of carrier density,

* Corresponding author. Tel.: +49-241-80806; fax: +49-241-8888246.

E-mail address: dekorsy@iht-ii.rwth-aachen.de (T. Dekorsy)

respectively. The coupling between the modes is expected to result in a modification of the mode amplitudes and broadenings of the spectral response.

In this paper, we describe recent experimental and theoretical progress made towards the understanding of these interactions. Besides the fundamental physical interest, such mode-coupling is crucial to understand for designing THz devices operating on Bloch oscillators. Our results can be summarized as follows: starting with a microscopic Hamiltonian describing electrons and phonons interacting with each other in a superlattice under an external DC field, we establish that the Bloch oscillating electrons behave like a nonlinear pendulum coupled linearly to an oscillator representing the phonons. We solve the equations perturbatively in the limit of low density and establish that contrary to conventional expectations with mode-coupling the coupled Bloch-phonon modes do not have a gap in their frequency spectra at resonance as the external field is varied. Instead, the coupling manifests itself through a resonant enhancement of the amplitudes of both the Bloch oscillation and the phonon modes. In addition, sidebands of varying heights and widths are generated near resonance due to parametric Bloch-phonon coupling. The theoretical results are compared to experiments performed in a GaAs/Al_xGa_{1-x}As superlattice with a first electronic miniband width equal to the LO phonon energy of GaAs. This miniband width allows us to tune the Bloch frequency into resonance with the LO phonon.

2. Theoretical description of Bloch-phonon equations

We consider a system of collision-free superlattice electrons with a tight-binding kinetic energy $\epsilon_k = -(A/2)\cos kd$, interacting through a Coulomb repulsion $V_q = 4\pi e^2/q^2$ and coupled to an external DC field E_0 along the growth direction of the superlattice through a dipole matrix $\mu_{kk'} = (ie/\hbar)\delta_{kk'}\partial/\partial k$. The scalar notation k refers here to the momentum component along the growth direction of the superlattice. We also introduce a set of dispersionless LO phonons of frequency ω_{LO} , stretched by an external DC field through a phonon dipole moment μ_q per unit cell, and coupled to electrons through a Fröhlich polar coupling $M_q = -i\sqrt{4\pi e^2\hbar\omega_{LO}/2\epsilon_p q^2}$, with $1/\epsilon_p \equiv$

$1/\epsilon_\infty - 1/\epsilon_0$, the subscripts ∞ and 0 corresponding, respectively, to high- and low-frequency dielectric constants of the superlattice. The Hamiltonian then is

$$\begin{aligned} \mathcal{H} = & \sum_k \epsilon_k c_k^\dagger c_k + \frac{1}{2} \sum_{q, k, k'} V_q c_{k+q}^\dagger c_{k'-q}^\dagger c_k c_{k'} \\ & - E_0 \sum_{k, k'} \mu_{k, k'} c_k^\dagger c_{k'} + \sum_q \hbar \omega_{LO} b_q^\dagger b_q \\ & - E_0 \sum_q \mu_q (b_q + b_q^\dagger) + \sum_{k, q} M_q c_k^\dagger c_{k+q} (b_q + b_{-q}^\dagger). \end{aligned} \quad (1)$$

We use the Hamiltonian to write down the equations for the electron density matrix $N_{KQ} \equiv \langle c_{K+Q/2}^\dagger c_{K-Q/2} \rangle$. We factorize all four-operator expectation values into products of two-operator expectation values using the random phase approximation, which allows us to describe the dynamics in terms of the mean-field polarization $P = \mu n = (ie/\hbar) \sum_K \partial N_{KQ} / \partial Q|_{Q=0}$. Note that we are employing for convenience the ‘center-of-mass’ and ‘relative’ coordinates $K = (k + k')/2$ and $q = k - k'$. We also ignore electron–phonon correlations, which allows us to factorize terms like $\langle c^\dagger c b \rangle \approx \langle c^\dagger c \rangle \langle b \rangle$. The equation for the distribution function $f_K = N_{K0}$ then is

$$\left[\frac{\partial}{\partial t} + \frac{eE(t)}{\hbar} \frac{\partial}{\partial K} \right] N_{K0} = -\frac{i}{\hbar} \sum_q M_q (B_q + B_{-q}^*) \times [N_{K-q/2, q} - N_{K+q/2, q}], \quad (2)$$

where $B_q = \langle b_q \rangle$ and B_q^* are the amplitudes of the *coherent* phonons, and $E(t) = E_0 - 4\pi P(t)$. In the long-wavelength limit $q \rightarrow 0$, expanding the terms in the square bracket about $q = 0$ leads to a cancellation of the divergence in $M_q \propto 1/q$, leading to a modified pendulum equation for the net vector potential $\eta(t) = ed/\hbar \int_0^t dt' E(t')$. Since the stretching $w \propto B_0 + B_0^*$ of the polar ions also contributes to the net electric field: $\dot{\eta} = (ed/\hbar)(E_0 - 4\pi n\mu) - Cw$, with $C = \sqrt{\omega_{LO}^2 - \omega_{TO}^2}$ non-zero because the transverse phonons oscillate at the bare frequency ω_{TO} while the longitudinal phonons oscillate at a larger frequency ω_{LO} due to the extra stretching from the polar fields. The transverse and longitudinal phonon frequencies satisfy the Lyddane–Sachs–Teller relation: $\omega_{LO}/\omega_{TO} = \sqrt{\epsilon_0/\epsilon_\infty}$ [5]. The result of this

calculation describes a pendulum (electronic mode) linearly coupled to an oscillator (LO phonon mode):

$$\begin{aligned}\ddot{\eta} + \omega_{\text{pl}}^2 \sin \eta &= -C\dot{w}, \\ \ddot{w} + \omega_{\text{TO}}^2 w &= C\dot{\eta},\end{aligned}\quad (3)$$

where ω_{pl} is the plasma frequency. For the boundary conditions we assume an impulsive generation of LO phonons [6,7], and no initial polarization induced by the photoexcitation process itself: $\eta(0) = \dot{\eta}(0) = 0$, $w(0) = C\omega_{\text{B}}/\omega_{\text{LO}}^2$, and $\dot{w}(0) = \tilde{\omega}_{\text{B}} = \omega_{\text{B}}\epsilon_{\infty}/\epsilon_0$, where ω_{B} is the Bloch frequency. The system of equations (3) can then be solved in the low-density limit ($\omega_{\text{pl}} \ll \omega_{\text{B}}$) by a perturbative expansion in the small parameter $\omega_{\text{pl}}/\tilde{\omega}_{\text{B}}$. We expand the variables as follows:

$$\begin{aligned}\eta(t) &= \eta_0(t) + \left(\frac{\omega_{\text{pl}}}{\tilde{\omega}_{\text{B}}}\right)^2 \eta_1(t) + \dots, \\ w(t) &= w_0(t) + \left(\frac{\omega_{\text{pl}}}{\tilde{\omega}_{\text{B}}}\right)^2 w_1(t) + \dots\end{aligned}\quad (4)$$

and solve for $\eta(t)$ and $w(t)$ perturbatively in the small parameter $(\omega_{\text{pl}}/\tilde{\omega}_{\text{B}})^2$. The result of the calculation is as follows:

$$\begin{aligned}\eta_0(t) &= \tilde{\omega}_{\text{B}} t, \\ w_0(t) &= \frac{C\omega_{\text{B}}}{\omega_{\text{LO}}^2}, \\ \eta_1(t) &= \tilde{\omega}_{\text{B}} \left(\frac{\omega_{\text{TO}}^2 - \tilde{\omega}_{\text{B}}^2}{\omega_{\text{LO}}^2 - \tilde{\omega}_{\text{B}}^2} \right) \left[\frac{\sin(\tilde{\omega}_{\text{B}} t)}{\tilde{\omega}_{\text{B}}} - t \right] \\ &\quad + \frac{C^2 \tilde{\omega}_{\text{B}}^3}{\omega_{\text{LO}}^2 (\omega_{\text{LO}}^2 - \tilde{\omega}_{\text{B}}^2)} \left[\frac{\sin(\omega_{\text{LO}} t)}{\omega_{\text{LO}}} - t \right], \\ w_1(t) &= \frac{C\tilde{\omega}_{\text{B}}}{\omega_{\text{LO}}^2 - \tilde{\omega}_{\text{B}}^2} [\cos(\tilde{\omega}_{\text{B}} t) - 1] \\ &\quad - \frac{C\tilde{\omega}_{\text{B}}^3}{\omega_{\text{LO}}^2 (\omega_{\text{LO}}^2 - \tilde{\omega}_{\text{B}}^2)} [\cos(\omega_{\text{LO}} t) - 1].\end{aligned}\quad (5)$$

The zeroth-order corrections in the plasma frequency show that in the absence of screening charges ($\omega_{\text{pl}} = 0$), there are no oscillations in the system, just

a stretch of the ions within each unit cell, proportional to the external field. Dynamics is introduced once electrons are photoexcited into the conduction miniband, i.e., through the terms η_1 and w_1 . This leads to Bloch oscillations in $\dot{\eta}_1$ while w_1 exhibits signatures of LO phonons. The LO phonons are excited coherently, because the ionic displacement w is proportional to $\langle b_0^\dagger + b_0 \rangle$, which is non-zero [8]. Prior to the excitation, the stretch of the ions is given by $w_0 = C\omega_{\text{B}}/\omega_{\text{LO}}^2$. Ultrafast screening by the photoexcited charges leads to a new reduced equilibrium value of magnitude $C\omega_{\text{B}}/\omega_{\text{LO}}^2 [1 - \omega_{\text{pl}}^2/\omega_{\text{B}}\tilde{\omega}_{\text{B}}]$, obtained from the DC component of w . It is this impulsive change in equilibrium stretching that excites the phonons coherently at frequency ω_{LO} .

Although the perturbation theory breaks down at resonance $\tilde{\omega}_{\text{B}} \approx \omega_{\text{LO}}$ as can be seen clearly from the divergences in η and w , we can get an idea about the field dependencies of these quantities away from resonance. For the Bloch oscillations, we look at the part of $\dot{\eta}$ that oscillates at ω_{B} , which yields the corresponding Fourier amplitude. The coefficient of the $\cos \tilde{\omega}_{\text{B}} t$ term in $\dot{\eta}(t)$ is given by $(\omega_{\text{pl}}^2/\tilde{\omega}_{\text{B}})([\omega_{\text{TO}}^2 - \tilde{\omega}_{\text{B}}^2]/[\omega_{\text{LO}}^2 - \tilde{\omega}_{\text{B}}^2])$. The second factor in the round brackets is the resonance factor, which leads to a peak at resonance ($\tilde{\omega}_{\text{B}} \approx \omega_{\text{LO}}$). The prefactor $\omega_{\text{pl}}^2/\tilde{\omega}_{\text{B}}$ gives the familiar result that the Bloch oscillation amplitude varies as Δ/E_0 for a superlattice with miniband width Δ and external field E_0 . Thus, the Bloch amplitude has a peak superimposed on a decreasing structure when plotted versus the bias voltage. For the phonon mode, as obtained from the ω_{LO} component of $w(t)$, the amplitude varies as $\sim \omega_{\text{B}}$ for small fields and $\sim 1/\omega_{\text{B}}$ for large fields, leading to a relatively weak dependence on field, except a strong enhancement at resonance. Evidently, the amplitudes diverge at resonance, indicating that a more careful numerical analysis, taking into account the specific details of the measurement process and collisions, is needed to get agreement with experiments.

For small plasmon frequencies, the perturbation theory does not allow for any change in the resonance frequencies due to coupling. The oscillations are at frequencies ω_{LO} and $\tilde{\omega}_{\text{B}}$. There is no mode at the TO frequency. This is expected, since Fröhlich polar phonons couple only with longitudinal modes. The transverse mode that arises in plasmon–phonon dispersions, for example, are basically longitudinal

phonons oscillating at the bare TO frequency due to electronic screening. For a fixed plasma frequency, however, varying the Bloch frequency parametrically does not alter the screening, hence we do not expect the TO modes to emerge. The Bloch frequency enters only through the initial conditions in Eq. (3), and not directly in the equations themselves, which explains why merely varying the Bloch frequency does not open up a gap in the frequency spectrum plotted versus ω_B . Bloch oscillations thus couple with phonons in a way that is qualitatively different from plasmon–phonon modes [9]. Bloch oscillations arise simply because the sample is periodic, while the LO and plasma oscillations arise due to actual restoring forces associated with oscillator-like motions. The coupling manifests itself through a non-monotonic field dependence of the individual peak amplitudes plotted for varying fields.

The coupling of Bloch oscillations and phonons also occurs through the appearance of Bloch-phonon sidebands due to the parametric coupling between the two modes through the sine term in the equations of motion, which tends to mix modes. For example, let us substitute $\eta(t) \approx \tilde{\omega}_B t + \alpha_0 \tilde{\omega}_B \sin(\tilde{\omega}_B t) + \beta_0 \sin(\omega_{LO} t)$ in the equation for η in Eq. (3), where α_0 and β_0 are obtained from our perturbative solution for η . This gives

$$\begin{aligned}
 -Cw &= \alpha_0 \tilde{\omega}_B \cos(\tilde{\omega}_B t) + \beta_0 \omega_{LO} \cos(\omega_{LO} t) \\
 &- \omega_{pl}^2 \sum_{m=-\infty}^{\infty} \sum_{p=-\infty}^{\infty} \left[\frac{J_{m-1}(\alpha_0) J_p(\beta_0)}{m\tilde{\omega}_B + p\omega_{LO}} \right] \\
 &\times \cos(m\tilde{\omega}_B + p\omega_{LO})t. \quad (6)
 \end{aligned}$$

As one can see from the last term, the response has sidebands at positions $m\tilde{\omega}_B + n\omega_{LO}$ for integer m and n , arising out of the Bloch-phonon couplings. An investigation of the arguments of the Bessel terms reveals that the sidebands are prominent near resonance, at plasma frequencies larger than the collision rate but small enough to not screen out the Bloch oscillations. The sidebands demonstrate that Bloch oscillations couple with phonons even in the absence of a gap in the spectrum. Collisions, however, will tend to wash away the sidebands. Fig. 1 shows Bloch-phonon sidebands for $\nu_{pl} = 2$ THz, obtained by a numerical solution of the Bloch-phonon coupled equations of motion in the absence of collisions.

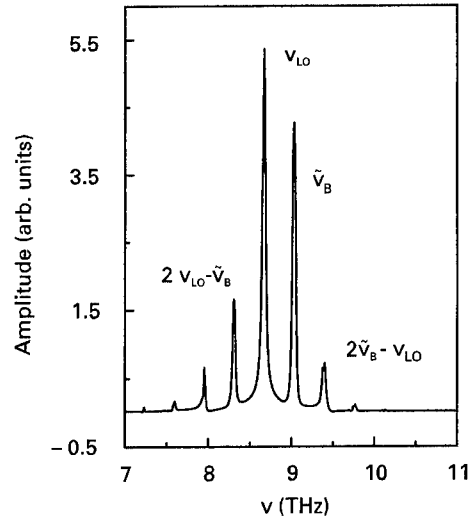


Fig. 1. Bloch-phonon sidebands arising out of parametric coupling between LO phonons and Bloch oscillations in absence of collisions for a plasma frequency $\nu_{pl} = 2$ THz and a Bloch frequency $\nu_B = 11.4$ THz.

3. Experimental results

We perform TEOS experiments for the investigation of Bloch-phonon coupling, since it is sensitive to the internal longitudinal polarization along the growth direction of the superlattices [4]. The laser source is a Kerr-lens mode-locked Ti:sapphire laser delivering optical pulses of 50 fs duration corresponding to a spectral width of 40 meV. The broadband laser spectrum is tuned to the first interband transitions in the superlattice, i.e. from the first heavy-hole to the first electron states. The short pulse prepares a coherent superposition of electronic Wannier–Stark states in the biased superlattice [10,11]. The heavy holes are already fully localized at the electric fields under consideration. A coherent electronic wavepacket is created which performs spatial oscillations along the superlattice growth direction with the Bloch frequency [12]. The investigated sample consists of 35 periods GaAs wells of 6.7 nm width and $\text{Al}_{0.3}\text{Ga}_{0.7}\text{As}$ barriers of 1.7 nm width. The coupling of the lowest quantized electronic levels in the quantum wells forms an electronic miniband of 36 meV width which equals the LO phonon energy in bulk GaAs. For applying a static

electric field, the superlattice is embedded in a Schottky diode. This miniband width allows to tune the Bloch frequency into resonance with the LO phonon. This is not possible for smaller miniband widths since for such superlattices the wave functions are already fully localized so that no oscillating wavepacket with the phonon frequency can be excited. On the other hand, larger miniband widths are inherently associated with stronger dephasing times. Hence, the choice of a minibandwidth equal to the phonon energy is a trade-off concerning the visibility of Bloch-phonon coupling.

Figs. 2(a) and (b) depict the time-domain TEOS data and the corresponding frequency domain responses recorded at an excitation density of $1 \times 10^{10} \text{ cm}^{-2}$ at 10 K. This excitation density corresponds to a plasma frequency much lower than the phonon frequency, so that coupling with plasmons can be neglected in the frequency range close to the optical phonon resonance. The data are shown for different voltages applied to the sample. For the voltages range below -3.8 V , the data are dominated by the rapidly dephasing electronic coherence of the Bloch oscillations with a dephasing time of $(400 \pm 50) \text{ fs}$. The frequency of the oscillations increases with increasing bias voltage according to $v_B = eEd/h$ as expected for Bloch oscillations. At reverse bias voltages larger than -4.0 V , oscillations appear, which can be traced over more than 10 ps in contrast to the subpicosecond dephasing of the Bloch oscillations at lower voltages. The Fourier transforms show at -4.0 V a strong maximum at the LO phonon. At -4.2 V the signal is fully dominated by the long-living oscillation with LO frequency. At this voltage the Bloch frequency is in resonance with the LO phonon. The change from the electronic coherence with a sub-ps dephasing time to the long living phonon oscillations becomes also clearly visible in the frequency domain data (Fig. 2(b)). The pure electronic coherence is associated with the broad spectral peak while the spectral width of the coherent phonon oscillation is determined by the finite time-window of the measurement. Higher reverse bias voltages could not be applied to the sample due to the occurrence of breakdown of the Schottky diode. In addition, we infer from CW electr-absorption measurements that at higher internal electric fields the electronic states become fully localized.

The experimental results clearly demonstrate a coupling of Bloch oscillations to LO phonons under resonance conditions. The observed generation of coherent phonons under resonance conditions confirms the theoretical result of an enhancement of the LO phonon amplitude. The enhancement of the Bloch amplitude under resonance conditions cannot be deduced from the experiments. One reason is the miniband width which equals the LO phonon energy leading to a strong localization of the Wannier–Stark wave functions close to resonance. Another reason is the expected strong dephasing of the Bloch oscillations when the carriers can energetically relax between adjacent Wannier–Stark levels by LO phonon emission [13]. Both of these aspects are not included in the theoretical model so far. The appearance of sidebands also cannot be deduced from the experimental data, which is attributed to the rapid dephasing of the electronic coherence in the experiments. These discrepancies demonstrate the importance to include collision effects in the theory.

4. Conclusions

The theoretical analysis of the polar coupling between Bloch oscillations and LO phonons in a superlattice leads to a resonance and sidebands. The coupling of Bloch oscillations with LO phonons can be described by the linear coupling of a pendulum (electronic mode) with an oscillator (phonon mode). Perturbation theory in the small parameter $(\omega_{\text{pl}}/\tilde{\omega}_{\text{B}})^2$ reveals that near the Bloch-phonon resonance, there is no gap in the spectrum, but the amplitudes of the Bloch and phonon modes diverge. The absence of the gap is due to the fact that the Bloch oscillation is not an elementary excitation that could cause a level repulsion with the phonons, but merely a periodic response of electrons to a periodic array of quantum wells. The resonant enhancement of the individual Fourier amplitudes indicates coupling between Bloch oscillations and LO phonons. However, the perturbation theory breaks down at resonance. Thus, a more detailed analysis will need to incorporate collisions in the equations of motion, followed by numerical modeling. The coupling of Bloch oscillations is confirmed by the experimental results obtained in a superlattice with 36 meV electronic miniband width.

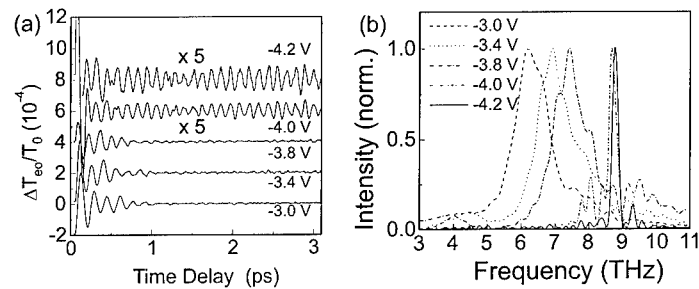


Fig. 2. (a) Coupled Bloch-phonon oscillations at 10 K lattice temperature for an excitation density of $1 \times 10^{10} \text{ cm}^{-2}$ for different voltages applied. The data at -4.0 and -4.2 V are magnified by a factor of 5. (b) Normalized Fourier transforms of the data in (a).

Acknowledgements

This work was supported in part by the German Volkswagen Foundation and the United States National Science Foundation (PHY-9722127). AB thanks the Konrad-Adenauer Stiftung for financial support. AWG thanks the Ohio State University Presidential Fellowship for support.

References

- [1] J. Feldmann, K. Leo, J. Shah, D.A.B. Miller, J.E. Cunningham, S. Schmitt-Rink, T. Meier, G. von Plessen, A. Schulze, P. Thomas, *Phys. Rev. B* 46 (1992) 7252.
- [2] K. Leo, P. Haring Bolivar, F. Brüggemann, R. Schwedler, K. Köhler, *Solid State Commun.* 84 (1992) 943.
- [3] C. Waschke, H.G. Roskos, R. Schwedler, K. Leo, H. Kurz, K. Köhler, *Phys. Rev. Lett.* 70 (1993) 3319.
- [4] T. Dekorsy, P. Leisching, H. Kurz, K. Köhler, *Phys. Rev. B* 50 (1994) 8106.
- [5] M. Born, K. Huang, *Dynamical Theory of Crystal Lattices*, Clarendon Press, Oxford, 1954.
- [6] A.V. Kuznetsov, C.J. Stanton, *Phys. Rev. B* 51 (1995) 7555.
- [7] G.C. Cho, W. Kütt, H. Kurz, *Phys. Rev. Lett.* 65 (1990) 764.
- [8] A.V. Kuznetsov, C.J. Stanton, *Phys. Rev. Lett.* 73 (1994) 3243.
- [9] A. Mooradian, A.L. McWhorter, *Phys. Rev. Lett.* 19 (1967) 849.
- [10] E.E. Mendez, F. Agulló-Rueda, J.M. Hong, *Phys. Rev. Lett.* 60 (1988) 2426.
- [11] P. Voisin, J. Bleuse, C. Bouche, S. Gaillard, C. Alibert, A. Regreny, *Phys. Rev. Lett.* 61 (1988) 1639.
- [12] G. Bastard, R. Ferreira, in: G. Fasol, A. Fasolini (Eds.), *Spectroscopy of Semiconductor Microstructures*, Plenum Press, New York, 1989, p. 333.
- [13] J. Hader, T. Meier, S.W. Koch, F. Rossi, N. Linder, *Phys. Rev. B* 55 (1997) 13 799.



ELSEVIER

Physica E 7 (2000) 285–288

PHYSICA E

www.elsevier.nl/locate/physce

Generation and manipulation of Bloch wave packets

F. Löser^{a,*}, M. Sudzius^a, B. Rosam^a, V.G. Lyssenko^a, Y. Kosevich^b, M.M. Dignam^c,
K. Köhler^d, K. Leo^a

^a*Institut für Angewandte Photophysik, Technische Universität Dresden, 01062 Dresden, Germany*

^b*Max-Planck-Institut für Physik komplexer Systeme, 01187 Dresden, Germany*

^c*Physics Department, Lakehead University, Thunder Bay, Ont., Canada P7B 5E1*

^d*Fraunhofer-Institut für Angewandte Festkörperphysik, 79108 Freiburg, Germany*

Abstract

We show how the spatial dynamics of a Bloch oscillating wave packet can directly be measured and manipulated by means of optical techniques. For excitation below and above the Wannier–Stark ladder (WSL) center, the wave packet performs harmonic oscillations, following the predictions of Zener; for excitation near the WSL center the wave packet is in the so-called breathing mode: a symmetric oscillation with virtually zero center of mass motion. How the position and line width of the excitation laser changes the initially excited wave packets and their dynamics will be discussed. © 2000 Elsevier Science B.V. All rights reserved.

Keywords: Bloch oscillations; Superlattices; Spatial displacement; Time-resolved spectroscopy

1. Introduction

Recently, the dynamics of wave packets in semiconductor systems have been intensively investigated. Due to the improved excitation and detection systems detailed studies of the formation, dynamics and dependence on initial conditions could be achieved. On the other hand, semiconductor heterostructures have introduced the possibility to create highly tailored structures for experiments needing special energetic and spatial structures.

The periodicity of such an artificial semiconductor system opens the opportunity to observe a bundle of new physical phenomena. The periodic electron motion, the so-called Bloch oscillation (BO), predicted from the work of Bloch [1] and Zener [2] in the 1930s are one of these interesting effects relying on a periodic structure. Zener proposed that a particle in a periodic potential subjected to an electric field will oscillate in real space.

In a semiclassical picture: if an electron is “put” at $k = 0$ and the electric field is switched on quasi-instantaneously, the electron moves with constant k -space velocity. Due to the periodicity of the band structure it oscillates in real space with the period

$$\tau_B = h/eFd \quad (1)$$

* Corresponding author. Tel.: +49-351-463-2464; fax: +49-351-463-7065.

E-mail address: loeser@iapp.de (F. Löser)

and a total spatial amplitude

$$L = \Delta/eF, \quad (2)$$

where F is the applied electric field, d the lattice period, and Δ the width of the band.

In a quantum mechanical picture, the BO can be described as time evolution of an electronic wave packet composed of the eigenstates of the full Hamiltonian (including electric field). These so-called Wannier–Stark-ladder (WSL) states [3] form a equally spaced ladder-like structure with the energy spacing:

$$\Delta E = eFd. \quad (3)$$

Bloch oscillations are thus equivalent to quantum beats (QB) of the WSL states, provided that the amplitudes of the contributing WSL states were chosen in such a way that a periodic spatial motion results.

Such oscillations are only existent, as long as the coherence of the wave packet is not destroyed by scattering, otherwise a standard transport picture applies. A suitable system to observe BO was proposed and built by Esaki and Tsu [4]. The semiconductor superlattice (SSL) with miniband width in the range of tens of meV and large lattice constants in the order of tens of Angstrom allow an electron to complete a full BO cycle before it is scattered. In such an SSL, the frequency domain equivalent of the BO, the WSL was observed by Mendez and coworkers [5] by optical experiments as ladder of transitions:

$$E_n = E_0 + neFd, \quad n = 0, \pm 1, \pm 2, \dots, \quad (4)$$

where n is the ladder index and E_0 is the energy of the direct transition with electron and hole in the same well, labeled by $n = 0$.

Optical experiments using short laser pulses with broad spectra were used to create Bloch wave packets by excitation of adjacent WSL levels. The wave packet dynamics was then detected by several time-resolved techniques like four-wave-mixing (FWM) [6,7] and the detection of the terahertz radiation emitted from the oscillating electrons [8,9].

Theoretical investigations on the wave packet amplitude and its dependence on excitation conditions, Coulomb interactions and the SL parameters [10–12] were recently performed. The total spatial amplitude as maximal center of mass motion of the wave packet is expected to strongly depend on the initial properties of the wave packet. For a symmetrical excited wave

packet, the so-called breathing mode, was predicted: the constituents move symmetrically with respect to the WSL center and, therefore, prevent a center of mass motion of the wave packet. Furthermore, the excitonic interactions lead to redistribution of the oscillator strength to transitions with negative index, and are assumed to drastically change the dynamics [11].

2. Experimental method

Recently, we have introduced a method to directly trace the center-of-mass motion of wave packets in biased SSL using the Wannier–Stark ladder field dependence as sensitive dipole field detector [13]. The oscillating dipole, caused by the moving electrons and nearly static holes, is superimposed on the static bias field and does slightly shift the WSL transitions in energy as a function of delay. The displacement can be calculated with only carrier density as parameter from this peak shift. For details about the experiment and the displacement calculation see Ref. [13]. Fig. 1 shows the Bloch electron displacement and confirm the harmonic spatial motion as predicted by Zener.

The experiments are performed using GaAs/Al_{0.3}Ga_{0.7}As superlattices with different lattice constants. We discuss here results taken with an SL with 67 Å well and 17 Å barrier width. A Kronig–Penney calculation yields a miniband width of 38 meV. The

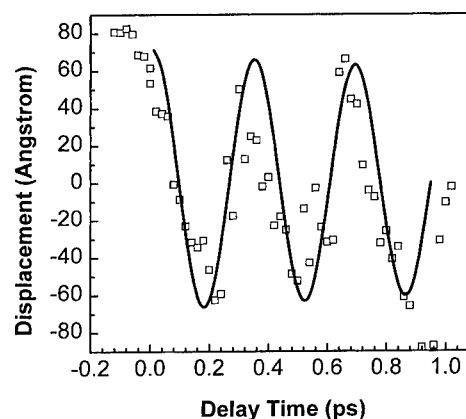


Fig. 1. Displacement of the electron wave packet in a 67/17 Å GaAs/AlGaAs superlattice as function of delay time calculated from peak shift. The measurements are performed at 10 K, with bias field of 16.5 kV/cm and an excitation density (in the first well) of $1.7 \times 10^{10} \text{ cm}^{-2}$.

maximal spectral laser width (FWHM) is with 21 meV sufficiently smaller than the miniband width and thus enabling a selective excitation of WSL transitions. For the experiments a standard transmission FWM geometry is used and the emitted third-order polarization was spectrally resolved. The samples were held at about 10 K.

3. Results and discussion

In this paper, we show that the amplitude of the wave packet can be tuned between breathing mode oscillations and harmonic spatial oscillations. Fig. 2 displays the spectrally resolved FWM signal (solid lines) for different excitation conditions showing the heavy-hole (hh) transitions labeled as hh_n , where n is the index as defined in Eq. (4). Shown are the three main situations (a) excitation energetically below, (b) close to the center and (c) above the center of the WSL.

The amplitude dependence on laser position is shown in Fig. 3 for a bias field of 15 kV/cm and a carrier density $9 \times 10^9 \text{ cm}^{-2}$. The excitation position is defined as the difference of the laser position with respect to the experimentally observed hh_0 transition in units of the WSL splitting. From the peak shift the displacement was calculated as mentioned above. Both the curves shown, belonging to laser widths of 12 and 21 meV, respectively, show a pronounced

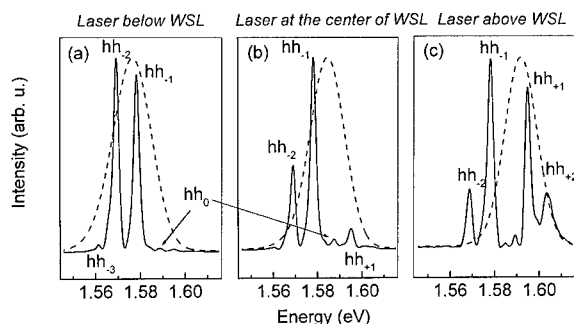


Fig. 2. Laser excitation conditions: FWM spectra (solid lines) showing the WSL heavy-hole (hh) transitions. Three typical examples for laser excitation are shown (dashed lines): below the center of the WSL (a), close to the center (b), and above the center (c). The relative laser position is defined in units of the WSL splitting with respect to the experimentally observed hh_0 transition.

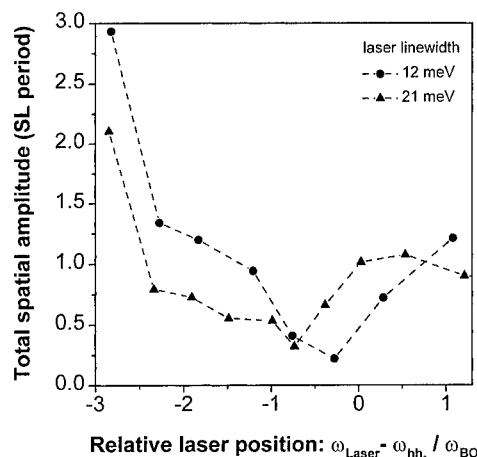


Fig. 3. Experimentally determined amplitude of the Bloch oscillating wave packet as function of the excitation energy for two spectral width of the laser at a field of 15.2 kV/cm. The energy is given in units of the WSL splitting relative to the experimentally observed hh_0 transition.

minimum with nearly zero amplitude. In either cases, the position of the minimum with respect to the WSL center is clearly shifted below the center, and is significantly more for the broader laser spectrum. For excitation well below and above the center of the WSL the amplitudes increases. The semiclassical amplitude would be at about 3.5 SL periods.

Theoretical calculations taking excitonic interactions into account and including dephasing phenomenologically clearly reproduce the amplitude minimum, but expect this above the center [11,14]. All our experiments, performed for various scattering times and laser line widths, show the minimum below the WSL center. A new theoretical approach including scattering and the influence of the background plasma on the basis of Boltzmann equation [15] is able to qualitatively reproduce the experimental data and explains dependencies on the experimental excitation conditions like, e.g., the laser line width [16]. It turns out that just a drastic change of the interminiband relaxation time would lead to a significant change of the minimum position. This drastic variation could not be realized by the typical excitation conditions in such FWM experiments neither by temperature nor by intensity change. For a detailed understanding further investigations including a quantitative analysis are necessary and promising.

In conclusion, we have shown that the amplitude of optically excited wave packets in superlattices can be controlled between true Bloch oscillations with a center of mass motion and symmetric breathing modes and discussed relevant parameters which influence this. For a more detailed understanding of processes influencing the dynamics a new theoretical approach has to be used.

Acknowledgements

We thank R.B. Liu, D. Meinhold, and T. Hasche for fruitful discussions. Support from the Deutsche Forschungsgemeinschaft (Schwerpunkt “Quantenkohärenz”) and the Volkswagen Stiftung is gratefully acknowledged.

References

- [1] F. Bloch, *Z. Phys.* 52 (1928) 555.
- [2] C. Zener, *Proc. R. Soc. London, Ser. A* 145 (1932) 523.
- [3] G.H. Wannier, *Phys. Rev.* 117 (1960) 432.
- [4] L. Esaki, R. Tsu, *IBM J. Res. Dev.* 14 (1970) 61.
- [5] E.E. Mendez, F. Agullo-Rueda, J.M. Hong, *Phys. Rev. Lett.* 60 (1988) 2426.
- [6] J. Feldmann, K. Leo, J. Shah, D.A.B. Miller, J.E. Cunningham, T. Meier, G.v. Plessen, A. Schulze, P. Thomas, S. Schmitt-Rink, *Phys. Rev. B* 46 (1992) 7252.
- [7] K. Leo, P. Haring Bolivar, F. Brüggemann, R. Schwedler, K. Köhler, *Solid State Commun.* 84 (1992) 943.
- [8] C. Waschke, H.G. Roskos, R. Schwedler, K. Leo, H. Kurz, K. Köhler, *Phys. Rev. Lett.* 70 (1993) 3319.
- [9] R. Martini, G. Klose, H.G. Roskos, H. Kurz, H.T. Grah, R. Hey, *Phys. Rev. B* 54 (1996) R14 325.
- [10] G. Bastard, R. Ferreira, in: G. Fasol, A. Fasolino (Eds.), *Spectroscopy of Semiconductor Microstructures*, Vol. 206 of NATO Advanced Study Institute, Series B: Physics, Plenum Press, New York, 1989, p. 333.
- [11] M.M. Dignam, J.E. Sipe, J. Shah, *Phys. Rev. B* 49 (1994) 10 502.
- [12] A.M. Bouchard, M. Luban, *Phys. Rev. B* 52 (1995) 5105.
- [13] V.G. Lyssenko, G. Valusis, F. Löser, T. Hasche, M.M. Dignam, K. Köhler, *Phys. Rev. Lett.* 79 (1997) 301.
- [14] M. Sudzius, V.G. Lyssenko, F. Löser, K. Leo, M.M. Dignam, K. Köhler, *Phys. Rev. B* 57 (1998) R12 693.
- [15] Y. Kosevich, unpublished.
- [16] F. Löser, K. Leo, Y. Kosevich, M.M. Dignam, K. Köhler, unpublished.

Evolution of energy levels of a GaAs/AlGaAs superlattice under the influence of a strong magnetic field

T. Bauer^{a,*}, A.B. Hummel^a, H.G. Roskos^a, K. Köhler^b

^a*Physikalisches Institut der Johann Wolfgang Goethe-Universität, Robert-Mayer-Str. 2–4, D-60325 Frankfurt am Main, Germany*

^b*Fraunhofer-Institut für Angewandte Festkörperphysik, Tullastr. 72, 79108 Freiburg, Germany*

Abstract

We present photocurrent spectra of the Wannier–Stark ladder of a GaAs/AlGaAs superlattice in a magnetic field up to 9 T and oriented along the growth direction of the superlattice. The Landau and Wannier–Stark quantization directions are perpendicular to each other. The salient observation is the evolution of Landau fans for the different Wannier–Stark transitions, with the Landau fan assigned to the spatially direct Wannier–Stark-ladder transitions being very pronounced quite in contrast to the Landau fans for the spatially indirect Wannier–Stark transitions which are weak. © 2000 Elsevier Science B.V. All rights reserved.

Keywords: Superlattices; Magnetic field; Wannier–Stark ladder; Landau quantization

Semiconductor superlattices have been investigated intensively as model structures for coherent wave packet dynamics of electrons in a periodic potential. The application of a DC electrical bias field along the surface normal, i.e., the growth direction of the superlattice, leads to localization of the wave functions and the development of a ladder of energy states, the so-called Wannier–Stark ladder [1–4] (see Fig. 1). Simultaneous excitation of several Wannier–Stark-ladder states creates wave packets which subsequently perform spatial oscillations known as Bloch oscillations [5–11].

In preparation for time-resolved studies of the influence of an additional strong magnetic field on the coherence of the charge carriers performing Bloch oscillations, this paper presents an experimental analysis of the evolution of a superlattice's energy levels and their oscillator strength as a function of the magnetic field up to 9 T. The influence of the magnetic field depends on its orientation with respect to the direction of the electrical bias field. A magnetic-field oriented parallel to the electrical field quantizes the motion of the electrons within the planes of the superlattice and hence leads to a quasi-zero-dimensional confinement of the charge carriers. This alignment of the magnetic field parallel to the electrical field (see Fig. 1) is termed “Faraday geometry”. It is the geometry which is investigated in this paper. If the

* Corresponding author. Tel.: +49-(0)69-798-22035; fax: +49-(0)69-798-28448.

E-mail address: t.bauer@physik.uni-frankfurt.de (T. Bauer)

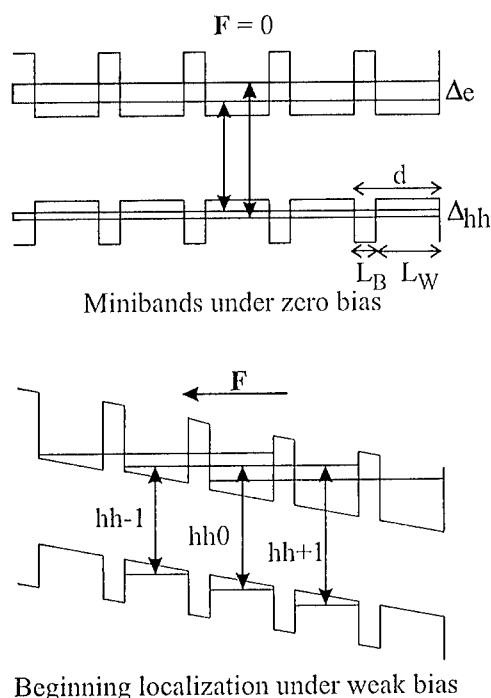


Fig. 1. Schematic representation of Wannier–Stark quantization in a GaAs/AlGaAs superlattice under the influence of a DC electrical field. The nomenclature of relevant interband transitions between Wannier–Stark states is indicated in the lower part of the figure. The spatially direct transitions are labeled by “0”, the spatially indirect transitions by negative integers (reduced transition energy), respectively, positive integers (increased transition energy).

magnetic field is oriented perpendicular to the electrical field (“Voigt geometry”), the situation is more complex because the carriers are confined in one direction by both the electrical and magnetic field, and strong mixing effects are expected between Wannier–Stark quantization and Landau quantization. This situation will be the subject of future studies.

The investigated superlattice sample consists of 35 periods of 9.7-nm-wide GaAs wells separated by 1.7-nm-wide $Al_{0.3}Ga_{0.7}As$ barriers. It is a superlattice with a moderate coupling strength between the wells as indicated by the width of the first electron miniband of 18 meV. The undoped superlattice was grown by molecular beam epitaxy on an n^+ -doped GaAs substrate (doping density: $2\text{--}4 \times 10^{18} \text{ cm}^{-3}$). It is embedded between undoped GaAs buffer layers with a thickness of 250 nm (top layer) and 350 nm (bottom layer). An electrical bias field can be applied

between the substrate and a semitransparent Schottky contact on top of the wafer. The semitransparent Schottky contact consists of a 1-nm-thick Cr layer and a 5-nm-thick Au film, the backside metallization of a 200-nm-thick alloyed AuGe film.

Photocurrent spectra are recorded with the help of a 30-W halogen lamp, a 0.5-m monochromator with a 1200-lines/mm grating and a low-noise voltage/current converter followed by a lock-in amplifier. The photon energy is tuned from 1.531 to 1.698 eV with a spectral resolution better than 0.16 meV. The polarization of the light is linear in order to excite both σ^+ - and σ^- -transitions. The excitation spot on the sample has a rectangular shape with a length of 8 mm and a width of 1.5 mm; because of the rather large spot size, broadening of the spectral features by residual spatial inhomogeneities of the superlattice parameters cannot be ruled out but does not appear to be significant. The excitation density is about $5 \times 10^6 \text{ cm}^{-2}$, estimated for carrier lifetimes of about 200 ps and 35 nW excitation power.

The sample is mounted in a He magnet cryostat with a superconducting split-coil magnet which allows to apply a magnetic field of up to 9 T at the sample. In this study, the magnetic field is oriented parallel to the electrical field ($E \parallel B$, Faraday geometry), hence, the Wannier–Stark and Landau quantization directions are orthogonal to each other. The sample temperature is kept at 8 K.

Fig. 2 shows measured photocurrent spectra for magnetic fields from 0 to 9 T. The data were taken without an external voltage applied to the sample. The good signal-to-noise ratio (up to 1000:1 peak to peak) achieved both by averaging multiple scans and by spectral oversampling allows even weak transitions to be observed in the data.

The photocurrent spectrum for vanishing magnetic field is dominated by the lowest excitonic Wannier–Stark transitions, the spatially direct 1shh0 and 1slh0 transitions (at 1.553 and 1.567 eV, respectively), and the spatially indirect 1shh-1 transition (at 1.545 eV), similar to results previously reported in Refs. [12,13]. hh and lh denote the heavy-hole and light-hole valence bands, respectively. The trailing numbers are the Wannier–Stark ladder indices as illustrated in Fig. 1. 1s specifies the excitonic ground state, ns , with $n > 1$, the excited exciton states. The Wannier–Stark splitting of 7.3 meV between the 1shh0 transition and the

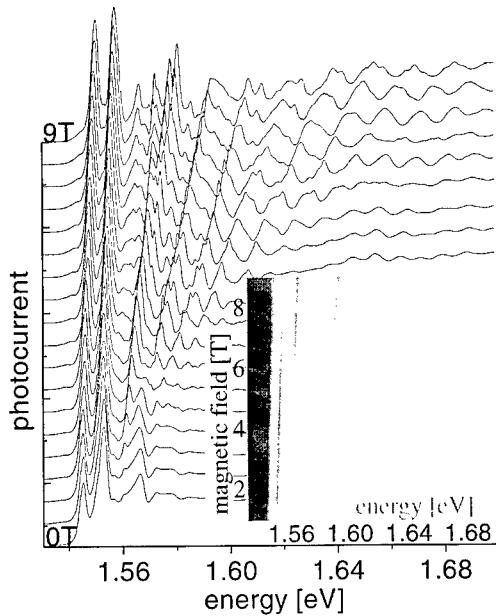


Fig. 2. Photocurrent spectra taken over the range from 1.531 to 1.698 eV for magnetic fields from 0 to 9 T with increment 0.5 T at fixed electrical field of 10 kV/cm. The inset shows a contour plot of the data of the main panel. The three strong peaks at 0 T (going from low to high energy) are associated with the 1shh-1, 1shh0, and 1shh+1 transitions.

1shh-1 transition is a result of the intrinsic electrical Schottky field of about 10 kV/cm.

The magnetic field induces additional quantization as well as lifting of degeneracies [14]. The spectra for high magnetic fields are rather complex. The salient feature is the appearance of a Landau fan for the hh0 transition which can be seen best in the gray-scale-encoded representation of the data in the inset of Fig. 2. With increasing magnetic field, more and more transitions of the fan become visible. At 9 T, we can identify up to ten hh0 Landau transitions extending over the whole energy range investigated in this study. The magnetic-field dependence of the spectral position of each Landau transition depends on the index of the exciton state it evolves from. While the lowest transition, developing out of the 1shh0 transition, experiences only a weak diamagnetic shift, the transitions evolving out of high-index n shh0 exciton transitions (with $n \gg 1$) shift with a large gradient to higher energies. Within the limitations given by the overlap and the (anti)crossing of

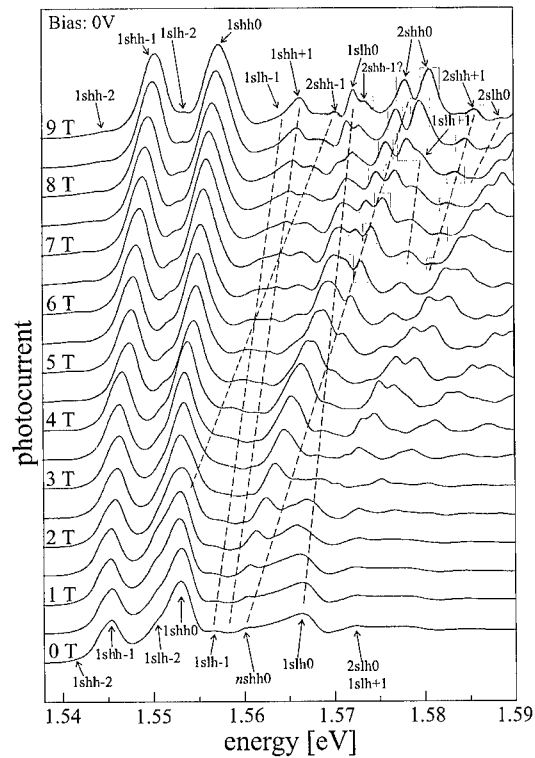


Fig. 3. Segment of the photocurrent spectra of the preceding figure, representing a zoom into the photon-energy range from 1.541 to 1.596 eV.

transitions it appears that the magnetic-field dependence for $n > 1$ is linear, with a slope as given by the expression derived with a single-particle model $E_m(B) = (m + 1/2)\hbar eB/\mu^*$, with μ^* denoting the reduced electron and hole mass and m indicating the Landau quantum index ($m = n - 1 = 0, 1, 2, \dots$) corresponding to the 1s, 2s, 3s, ... excitonic states [15–17]. The oscillator strength for all spatially direct hh Wannier–Stark transitions rises with increasing magnetic field because of the change in dimensionality known from investigations of 2D systems [18–21].

In addition to the Landau fan for the spatially direct Wannier–Stark transitions, one can identify 2s rungs of at least two more Landau fans. These rungs assigned to the spatially indirect hh-1 and hh+1 Wannier–Stark transitions are indicated by dark gray boxes in Fig. 3 which presents a magnified view of the data of Fig. 2 in the vicinity of the bandedge. The identification of the 2shh-1 transition is somewhat ambiguous because

the assignment can be made to either one of two lines marked in Fig. 3.

It is remarkable that the identification of Landau fans for the spatially indirect Wannier–Stark transitions is quite difficult. This is most unexpected for the hh-1 transitions because the lowest 1shh-1 transition is rather strong at the electrical field of 10 kV/cm even without magnetic field and becomes even more prominent with rising magnetic field. In fact, its oscillator strength increases more strongly with the magnetic field than the oscillator strength of the spatially direct 1shh0 transition. One might expect that the hh-1 Landau fan should evolve with similar clarity as the hh0 Landau fan, shifted to lower energy by the Wannier–Stark splitting which remains nearly unaffected by the magnetic field. The fact that the Landau fan for the hh-1 transition is resolved only in part, can only be explained as evidence for a large difference in oscillator strength between the higher-index hh-1 Landau transitions as compared to the 1shh-1 transition. Similar arguments hold for the other Wannier–Stark transitions. This experimental observation is corroborated by yet unpublished model calculations performed by Glutsch with methods described in Ref. [22] for the parameters of our experiment.

Fig. 3 allows to discern clearly a number of additional aspects of the spectra. The preeminent features are the following: (i) The 1s transitions do not evolve linearly with magnetic field. The diamagnetic shift is weak at low field but becomes stronger at higher magnetic field. Such a field dependence is theoretically expected for two-dimensional [23–26] and three-dimensional [19] excitons. (ii) The spectra are rich in the occurrence of crossings and anticrossings of transitions. A preeminent example is the anticrossing of the fundamental light-hole transition 1slh0 with the 2shh0 transition at a magnetic field around 4.5 T. (iii) The line width of the 1s transitions determined by fitting a Lorentzian to the experimental data amounts to 3–4 meV. In general, the width of most lines seems to remain constant with increasing magnetic field, although narrower lines emerge at higher magnetic fields such as the double-peak structure in the region around 1.58 eV consisting of two lines with a bandwidth of 2–2.5 meV for each line. The double peak is indicated in Fig. 3 by light-gray boxes. It can be identified as the 2shh0 doublet (originating from the π shh0 continuum at 0 T) with the splitting result-

ing mainly from the lifting of the angular-momentum degeneracy in the valence band by the magnetic field. The splitting energy is 2.5 meV at 9 T and is in the range of values expected from experimental and theoretical data obtained for uncoupled [18] and coupled [19] quantum wells. Angular-momentum splitting is expected to occur for all Wannier–Stark transitions. The amount of the splitting, however, appears to be too small for most transitions visible in Fig. 3 to induce more than a broadening of the lines even at 9 T. A more detailed analysis of the angular-momentum splitting requires excitation of the transitions by circularly polarized light which will be performed in future work.

Acknowledgements

We gratefully acknowledge numerous discussions with S. Glutsch (University of Jena) and with L. Bányai, G. Meinert, and H. Haug (University of Frankfurt). This work is supported by the Schwerpunktprogramm “Quantenkohärenz in Halbleitern” of the Deutsche Forschungsgemeinschaft.

References

- [1] E.O. Kane, *J. Phys. Chem. Solids* 12 (1959) 181.
- [2] J. Bleuse, G. Bastard, B. Voisin, *Phys. Rev. Lett.* 60 (1988) 220.
- [3] E.E. Mendez, F. Agulló-Rueda, J.M. Hong, *Phys. Rev. Lett.* 60 (1988) 2426.
- [4] E.E. Mendez, G. Bastard, *Phys. Today* 6 (1993) 34.
- [5] C. Waschke, H.G. Roskos, R. Schwedler, K. Leo, H. Kurz, K. Köhler, *Phys. Rev. Lett.* 70 (1993) 3319.
- [6] J. Feldmann, K. Leo, J. Shah, D.A.B. Miller, J.E. Cunningham, T. Meier, G. von Plessen, A. Schulze, P. Thomas, S. Schmitt-Rink, *Phys. Rev. B* 46 (1992) 7252.
- [7] M. Dignam, J.E. Sipe, J. Shah, *Phys. Rev. B* 49 (1994) 10 502.
- [8] R. Martini, G. Klose, H.G. Roskos, H. Kurz, H.T. Grahn, R. Hey, *Phys. Rev. B* 54 (1996) R14 325.
- [9] P. Haring Bolivar, F. Wolter, A. Müller, H.G. Roskos, H. Kurz, K. Köhler, *Phys. Rev. Lett.* 78 (1997) 2232.
- [10] F. Wolter, H.G. Roskos, P. Haring Bolivar, G. Bartels, H. Kurz, K. Köhler, H.T. Grahn, R. Hey, *Phys. Stat. Sol. B* 204 (1997) 83.
- [11] V.G. Lyssenko, G. Valusis, F. Löser, T. Hasche, K. Leo, M.M. Dignam, K. Köhler, *Phys. Rev. Lett.* 79 (1997) 301.
- [12] F. Agulló-Rueda, E.E. Mendez, J.M. Hong, *Phys. Rev. B* 40 (1989) 1357.

- [13] K. Fujiwara, K. Kawashima, T. Yamamoto, N. Sano, R. Cingolani, H.T. Grahn, K. Ploog, *Phys. Rev. B* 49 (1994) 1809.
- [14] L.D. Landau, E.M. Lifshitz, in: *Quantum Mechanics*, Pergamon Press, Oxford, 1965.
- [15] D.C. Reynolds, D.C. Look, B. Jogai, C.E. Stutz, R. Jones, K.K. Bajaj, *Phys. Rev. B* 50 (1994) 11 710.
- [16] J.R. Nicholas, in: P. Bhattacharya (Ed.), *EMIS Datareviews No. 15: Properties of III–V Quantum Wells and Superlattices*, INSPEC, London, 1996.
- [17] D.C. Reynolds, D.C. Look, B. Jogai, C.E. Stutz, *Phys. Rev. B* 48 (1993) 17 168.
- [18] S. Schmitt-Rink, J.B. Stark, W.H. Knox, D.S. Chemla, W. Schäfer, *J. Appl. Phys. A* 53 (1991) 491.
- [19] H. Chu, Y.-C. Chang, *Phys. Rev. B* 40 (1989) 5497.
- [20] C. Stafford, S. Schmitt-Rink, W. Schäfer, *Phys. Rev. B* 41 (1990) 10 000.
- [21] J.B. Stark, W.H. Knox, D.S. Chemla, W. Schäfer, S. Schmitt-Rink, C. Stafford, *Phys. Rev. Lett.* 65 (1990) 3033.
- [22] S. Glutsch, D.S. Chemla, F. Bechstedt, *Phys. Rev. B* 54 (1996) 11 592.
- [23] O. Akimoto, H. Hasegawa, *J. Phys. Soc. Japan* 22 (1967) 181.
- [24] M. Shinada, K. Tanaka, *J. Phys. Soc. Japan* 29 (1970) 1258.
- [25] A.H. MacDonald, D.S. Ritchie, *Phys. Rev. B* 33 (1986) 8336.
- [26] A.B. Dzyubenko, A.L. Yablonskii, *Phys. Rev. B* 53 (1996) 16 355.



ELSEVIER

Physica E 7 (2000) 294–298

PHYSICA E

www.elsevier.nl/locate/physce

Negative differential resistance of a 2D electron gas in a 1D miniband

R.A. Deutschmann^{a,*}, W. Wegscheider^{a,b}, M. Rother^a, M. Bichler^a, G. Abstreiter^a

^aWalter Schottky Institut, Technische Universität München, Am Coulombwall, 85748 Garching, Germany

^bUniversität Regensburg, Universitätsstr. 31, 93040 Regensburg, Germany

Abstract

We experimentally investigate the miniband transport in a novel kind of superlattice fabricated by the “cleaved edge overgrowth” method. The structure represents a field effect transistor, where the channel consists of an MBE-grown superlattice perpendicular to the current flow. By means of the gate the Fermi energy can be adjusted between the bottom of the first miniband and into the minigap. We observe pronounced negative differential resistance at electric fields across the superlattice as low as 160 V/cm. From magnetotransport measurements a relation between the applied gate voltage and the position of the Fermi energy in the artificial band structure is established. Electron mobility depending on the Fermi energy is deduced separately from Shubnikov–de Haas oscillations, from the voltage at the peak current and from the low-field resistance. © 2000 Elsevier Science B.V. All rights reserved.

Keywords: Superlattice; Miniband transport; Negative differential resistance; Bloch oscillations

1. Introduction

Man made periodic potentials have long been of great interest for fundamental research and in view of applications. On the one hand epitaxially grown semiconductor superlattices (SLs) have revealed a large variety of effects in electronic transport [1], but so far research has mainly concentrated on systems with Fermi energy close to the miniband minimum. Additionally for a given sample the Fermi energy is usually fixed. On the other hand in surface lateral superlattices the Fermi energy is adjustable, but at the price of a

rather large periodicity and shallow potential modulation which leads to a large number of occupied bands [2]. We have extended a sample structure developed by Störmer et al. [3] to combine attractive features of both: A two-dimensional electron system (2DES) resides in an atomically precise superlattice, the Fermi energy of which can continuously be adjusted over a wide range by a gate, and the bandstructure of which can be engineered by heterostructure MBE growth. This sample design allows us to study superlattice DC transport as well as magnetotransport properties of a single partially or fully filled band.

2. Sample design and measurement technique

Our samples consist of an MBE grown undoped $100 \times 119 \text{ Å}$ GaAs/31 Å $\text{Al}_{0.32}\text{Ga}_{0.68}\text{As}$ SL sand-

* Corresponding author. Tel.: +49-89-28912756; fax: +49-89-3206620.

E-mail address: rainer.deutschmann@wsi.tu-muenchen.de (R.A. Deutschmann)

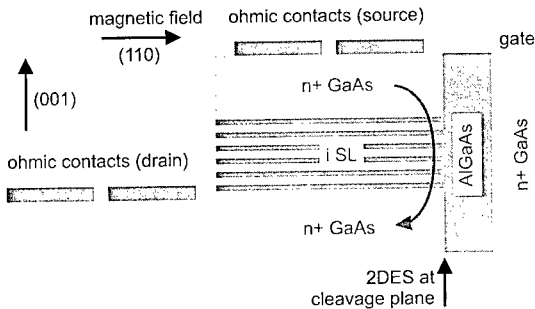


Fig. 1. Sample structure. First in the (001) direction the undoped SL is grown between two n+ GaAs contacts. After cleaving the sample, on the (110) face the gate is grown. At positive gate voltages a two-dimensional electron gas is induced in the SL at the interface to the AlGaAs. The magnetic field is applied perpendicular to the 2DES.

wiched between two 100 nm undoped GaAs layers and two 1 μm n+ GaAs layers grown on semi-insulating (001) GaAs substrate, as shown in Fig. 1. The two doped layers serve as source and drain contacts. After in situ cleaving the sample, an $\text{Al}_{0.32}\text{Ga}_{0.68}\text{As}$ spacer layer is grown on the freshly exposed (110) plane, followed by a 15 nm undoped and a 100 nm n+ GaAs layer, which serves as a gate. After wet chemical etching source, drain and gate are finally contacted by evaporating GeAu.

Experiments were performed at liquid helium temperatures in a four point contact measurement scheme with two contacts each on source and drain. The samples have to be cooled below liquid nitrogen temperatures to avoid thermally activated bulk leakage currents between source and drain. By applying a positive voltage U_g to the gate with respect to source and drain a two-dimensional electron gas can be induced in the SL below the gate. Electrons thus travel in an *undoped* SL from source to drain, while their density can continuously be controlled by the gate. These features make our samples distinct from conventional MBE grown GaAs/AlGaAs SLs used for transport experiments. On the other hand our samples can be viewed as surface lateral SL with strong potential modulation and shorter period as can conventionally be obtained. In DC measurements one set of contacts was used to apply the voltage and measure the current I_{sd} , with the other set of contacts the true voltage drop U_{sd} across the SL was measured. Additionally the sheet resistance of the GaAs contact layers was accounted for

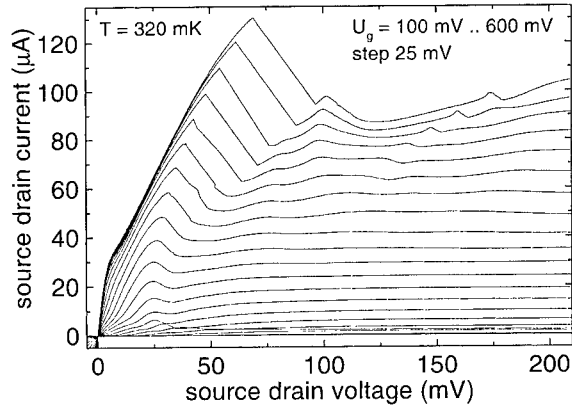


Fig. 2. Current voltage relation for gate voltages between 100 and 600 mV. A region of negative differential resistance at very low electric fields across the SL is observed, the position of which depends on the gate voltage.

by subtracting the appropriate voltage drop. Magneto-transport measurements were also performed in four point geometry with the magnetic field oriented perpendicular to the 2DES.

3. Experimental results

The DC current voltage relation of the transistor for U_g between 100 and 600 mV is shown in Fig. 2. At first sight the curve resembles that of a conventional transistor, with an ohmic current increase at low source drain voltages, saturation at high source drain voltages, an orderly increase of the saturation current with gate voltage, but with an additional region of negative differential resistance (NDR). A closer look reveals four different regimes depending on the gate voltage. For $U_g < 170$ mV no NDR is present. For U_g between 170 and 240 mV NDR develops, the peak current I_{peak} increases, the peak voltage U_{peak} decreases. Subsequently up to $U_g = 400$ mV the voltage U_{peak} remains almost constant at about 25 mV. Finally for even higher U_g the voltage U_{peak} increases again, and instability is observed for $U_{sd} > U_{\text{peak}}$ which causes I_{sd} to drop and U_{sd} to rise abruptly. Additionally a kink is observed in I_{sd} at $U_{sd} = 5$ mV, the origin of which is unclear.

As a first remark we note that for $U_g = 0$ mV practically no leakage current I_{sd} is detected for voltages U_{sd} we are concerned with here. However, for $U_{sd} > 1.1$

V, a gate voltage independent sudden increase of I_{sd} is observed, followed by an instability similar to the one discussed above. This effect is attributed to electrons being injected into the bulk SL from the contact at large U_{sd} . A second remark is concerned with the energetic barrier between source and drain, which prevents bulk leakage current and is determined by the energetic position of the first miniband with respect to the Fermi level in the doped GaAs contacts. At low electron densities ($U_g < 200$ mV) and small U_{sd} this barrier is significant also in the electron channel and causes non-ohmic increase of I_{sd} with U_{sd} .

Information about the relation between U_g and the electron density in the channel n_s was obtained by magnetotransport measurements. We found clear Shubnikov–de Haas (SdH) oscillations in the longitudinal magnetoresistance ρ_{xx} from which three kinds of information can be deduced. First, from the periodicity of the oscillations the electron density was determined to $n_s = (5.7 \pm 0.1) \times U_g 10^{11} \text{ V}^{-1} \text{ cm}^{-2}$ which agrees reasonably well with the result obtained from a capacitor model. The spacing between the maxima of ρ_{xx} was perfectly constant for all U_g when plotted against inverse magnetic field. Second, from the onset of the SdH oscillations a rough estimate of the electron mobility in the SL can be obtained, which will be discussed below. Third, a characteristic positive magnetoresistance and a quenching of the SdH oscillations are observed in the SdH curves when U_g is raised above a critical voltage. This behavior is expected for a system with open electron orbits [4].

4. Discussion

The one-dimensional band structure of the given SL is readily obtained by a Kronig–Penney calculation, which yields a width for the first miniband of $\Delta = 3.8$ meV, separated from the second miniband by a 60 meV one-dimensional minigap. The first excited level of the triangular field effect potential is expected at about 15 meV above the first miniband. Since there is still free electron movement possible perpendicular to the SL parallel to the cleavage plane, the energy-momentum relation is given by

$$E(k_x, k_z) = \frac{\hbar^2 k_x^2}{2m^*} + \frac{\Delta}{2}(1 - \cos(k_z d)),$$

where $d = 150$ Å is the SL period, k_x and k_z are the electron momenta in the free and SL direction, respectively. In order to establish a relation between the Fermi energy E_f and n_s we have determined the density of states (DOS) numerically, which is displayed together with the first miniband in Fig. 3. The DOS has a logarithmic singularity at the top of the miniband, but there are states in the minigap [5].

Experimentally, the onset of the positive magnetoresistance occurred at $U_g = 450$ mV, corresponding to $n_s = 2.5 \times 10^{11} \text{ cm}^{-2}$. On the other hand, given the DOS, we can calculate n_s for $E_f = \Delta$ and we find $n_s = 2.3 \times 10^{11} \text{ cm}^{-2}$ in quite good agreement with the experiment. Thus we know that for any $U_g < 450$ mV, E_f will be in the first miniband, whereas for $U_g > 450$ mV the minigap will be occupied.

We now proceed to extracting the apparent electron mobility depending on U_g from the data, which can be done in three different ways. First the condition $\omega_c \tau \geq 1$ for the appearance of SdH oscillations, with ω_c the cyclotron frequency and τ the scattering time, yields a lower bound of the electron mobility $\mu_{sdH} = 1/B_c$ given the critical magnetic field B_c at the onset of the SdH oscillations. It is well known that this procedure considerably underestimates the true mobility of the carriers [6]. Second in the Esaki and Tsu model [7] the expression $\mu_{ET} = eA\tau d^2/2\hbar^2$ is found where τ can be determined from $U_{peak} = l\hbar/e\tau d$, where $l = 1.5$ µm is the SL thickness. Although the low temperature may justify the use of the Esaki–Tsu model over more sophisticated models, again the obtained mobility will likely be underestimated. This is because the finite Fermi energy has not been taken into account in the calculation. Third we can estimate the mobility from the slope $1/R$ of the ohmic increase of I_{sd} at small U_{sd} from $\mu_R = l/Rn_s eb$, where $b = 240$ µm is the channel width.

In Fig. 4 we have plotted the values of μ obtained as described above. Both μ_{sdH} and μ_{ET} are of the same magnitude and have qualitatively the same behavior with U_g . For small band filling μ_{sdH} and μ_{ET} first increase, then remain constant, and decrease for E_f close to and in the minigap. μ_R in contrast is drastically smaller and shows a very different dependence on U_g with three different linear regimes. The small magnitude of μ_R explains why I_{peak} is much smaller than expected from the Esaki–Tsu model. So far we do not have an appropriate model for these findings.

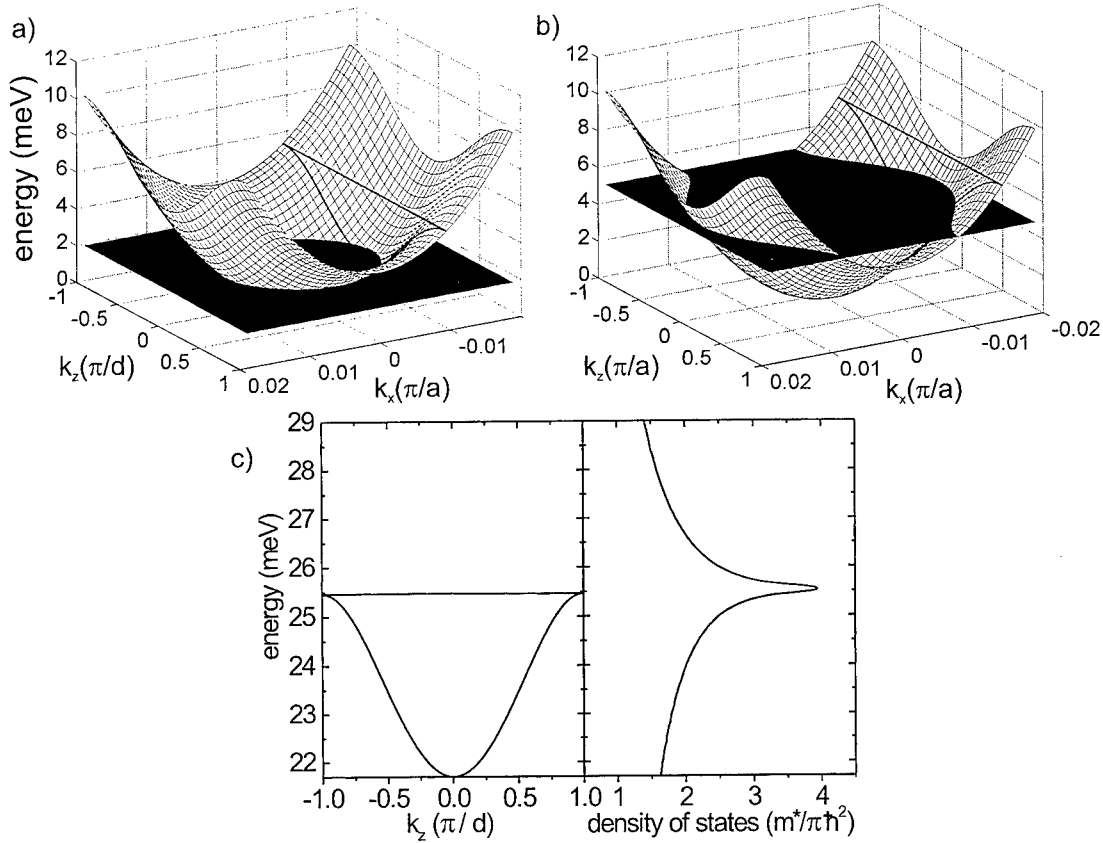


Fig. 3. Shape and density of states of the first miniband: (a) Situation for $E_f = \Delta/2$. Schematically the trajectory of one electron for an electric field along the SL and long scattering time is depicted. a is the lattice constant of GaAs. (b) Situation for $E_f > \Delta$. It can be seen that electron transport and NDR is still possible. (c) Band structure along the SL direction and density of states, normalized to the DOS of a 2DES.

Electrons in a SL are expected to perform Bloch oscillations (BO) when $\omega_{BO}\tau \geq 1$, where $\omega_{BO} = eFd/\hbar$. For $U_g = 375$ mV we have found $\mu_{SdH} = 4$ m²/Vs, from which follows $\tau = m^*\mu/e = 1.5$ ps, with $m^* = 0.067m_e$ conservatively taken. BOs can thus be expected for $U_{sd} > 43$ mV with a minimum frequency of $f_{BO} = 100$ GHz, assuming a constant electric field in the SL. The localization length $\lambda = \Delta/eF$ in this case is 9 periods of the SL, thus ensuring to be far away from Wannier–Stark localization. Of course the problem of incoherent radiation remains.

In conclusion we have presented a novel SL device which gives control over the electric field across the SL as well as the position of the Fermi energy of a

2DES in the SL. Starting at electron densities as low as 0.9×10^{11} cm⁻² NDR is observed. The electric field across the SL at the peak current remains approximately constant at 160 V/cm as long as E_f lies in the miniband, and increases when E_f is raised above the miniband. Surprisingly even when E_f lies in the minigap NDR is persistent. From U_{peak} , from SdH measurements and from the low-field resistance the electron mobility is deduced, respectively. It is found that μ_{ET} and μ_{SdH} both have a maximum when E_f lies in the miniband, whereas μ_R develops a much smaller maximum when E_f lies in the minigap. The presented device may serve as textbook example for 2D electronic transport in a partially or fully filled miniband.

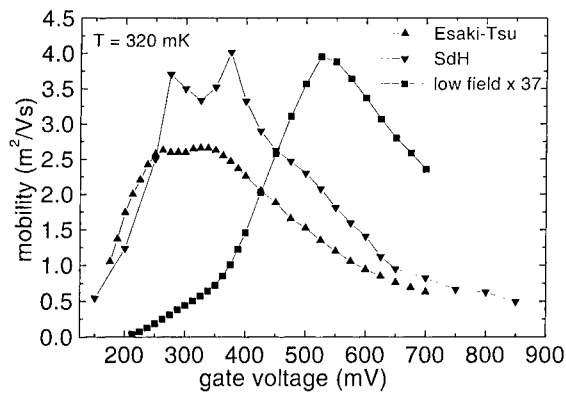


Fig. 4. Electron mobility determined from the position of the current maximum, from the onset of the SdH oscillations, and from the low-field resistance. Note that the low-field resistance is enhanced by a factor of 37.

Acknowledgements

We gratefully acknowledge the support by the DFG via SFB 348 and the BMBF through contract 01 BM 630/1.

References

- [1] H. Grahn (Ed.), *Semiconductor Superlattices, Growth and Electronic Properties*, World Scientific, Singapore, 1995.
- [2] R.R. Gerhardts, D. Weiss, K. von Klitzing, *Phys. Rev. Lett.* 62 (1989) 1173.
- [3] H.L. Störmer et al., *Appl. Phys. Lett.* 58 (1991) 726.
- [4] R.A. Deutschmann et al., *Physica E* 6 (2000) 561.
- [5] T. Ando, *J. Phys. Soc. Japan* 47 (1979) 1595.
- [6] S. Das Sarma, F. Stern, *Phys. Rev. B* 32 (1985) 8442 and references therein.
- [7] L. Esaki, R. Tsu, *IBM J. Res. Dev.* 14 (1970) 61.



ELSEVIER

Physica E 7 (2000) 299–301

PHYSICA E

www.elsevier.nl/locate/physa

Dynamics of electric field domain walls in semiconductor superlattices

David Sánchez^a, Miguel Moscoso^{b, 1}, Luis L. Bonilla^{b, 1}, Gloria Platero^{a, *}, Ramón Aguado^a

^a*Instituto de Ciencia de Materiales (CSIC), Cantoblanco, 28049 Madrid, Spain*

^b*Escuela Politécnica Superior, Universidad Carlos III de Madrid, Avenida de la Universidad 20, 28911 Leganés, Spain*

Abstract

A self-consistent microscopic model of sequential tunneling in superlattices is employed to investigate self-sustained current oscillations. Current spikes – high-frequency modulation due to well-to-well hopping of charge monopole domain walls – are naturally reproduced. Moreover, as the contact doping shrinks, the recycling and motion of charge dipoles resulting in a lower-frequency oscillatory mode is predicted. For low contact doping, this mode dominates and monopole oscillations disappear. At intermediate doping, hysteresis between both the oscillatory modes may be possible. © 2000 Elsevier Science B.V. All rights reserved.

Keywords: Superlattices; High field effects; Tunneling domains

Vertical transport in weakly coupled semiconductor doped superlattices (SLs) has been shown to display nonlinear phenomena such as electric field domain formation, multistability, self-sustained current oscillations, and driven and undriven chaos [1]. When the carrier density is set below a critical value, self-sustained oscillations of the current may appear in voltage biased SLs. They are due to the periodic dynamics of the domain wall (DW), which consists in a charge monopole accumulation layer or

a *monopole*, separating two nearly constant electric field domains [2]. Monopole motion and recycling have been experimentally shown by counting the spikes – high-frequency modulation – superimposed on one period of the current self-oscillations: current spikes correspond to well-to-well hopping of a DW through the SL [3]. Our purpose is to extend the model proposed in Ref. [4] for the stationary case to include the time dependence of the current. We analyze the tunneling current through the SL by means of the transfer Hamiltonian. The dynamics is considered in the model through the Ampère's law for the total current density $J = J(t)$:

$$J = J_{i-1,i} + \frac{\varepsilon}{d} \frac{dV_i}{dt}. \quad (1)$$

* Corresponding author. Fax: +34-91-3720623.

E-mail address: gloria@marenostrium.icmm.csic.es (G. Platero)

¹ Also at Unidad Asociada al Instituto de Ciencia de Materiales (CSIC).

Here $J_{i-1,i}$ is the tunneling current density through the i th barrier of thickness d :

$$J_{i,i+1} = \frac{2e\hbar k_B T}{\pi^2 m^*} \times \sum_{j=1}^{n_{\max}} \int \frac{\gamma}{[(\varepsilon - \varepsilon_{ri}^j)^2 + \gamma^2]} \frac{\gamma}{[(\varepsilon - \varepsilon_{ri+1}^j)^2 + \gamma^2]} \times T_{i+1}(\varepsilon) \ln \left[\frac{1 + e^{(E_{\text{eq}i} - \varepsilon)/k_B T}}{1 + e^{(E_{\text{eq}i+1} - \varepsilon)/k_B T}} \right] d\varepsilon, \quad (2)$$

where ε_{ri}^j is the j th resonant state of the i th well (n_{\max} is the number of subbands participating in the transport) and $T_i(\varepsilon)$ is the transmission through the i th barrier. Note that only the lowest resonant level is assumed to be populated. Scattering is treated phenomenologically by considering the spectral functions of the wells as Lorentzians (γ is the half width). The last term in Eq. (1) is the displacement current at the i th barrier where the potential drop is V_i and ε is the static permittivity. We include the Coulomb interaction in a mean field approximation by means of discrete Poisson equations relating the potential drops in wells, barriers and contacts. The boundary conditions at the contacts describe the lengths of the depletion and accumulation layers as well as the charge density at the leads. The final set of equations solved self-consistently [4]. We have studied a 50-well 13.3 nm GaAs/2.7 nm AlAs SL at $T = 0$ K [3]. Doping in the wells and in the contacts are $N_w = 2 \times 10^{10} \text{ cm}^{-2}$ and $N_c = 2 \times 10^{16} \text{ cm}^{-3}$.

For the sake of brevity, the monopole-mediated self-oscillations are not depicted here, and can be found elsewhere [5]. Instead, we shall focus on dipole self-oscillations akin to those in the Gun effect [2]. Since an advantage of our present model over other discrete ones [1,2] is the microscopic modelling of boundary conditions, we can study what happens when contact doping is changed. The result is that dipole-mediated self-oscillations appear as the emitter doping is lowered below a certain value. There is a range of voltages for which dipole and monopole oscillations coexist as stable solutions. When the emitter doping is further lowered, only the dipole self-oscillations remain. Fig. 1 presents data in the crossover range (below $N_c = 4.1 \times 10^{16} \text{ cm}^{-3}$ and above $N_c = 1.7 \times 10^{16} \text{ cm}^{-3}$ for the second plateau) for the sample values given above, applying a DC bias voltage of 5.5 V. These self-oscillations have

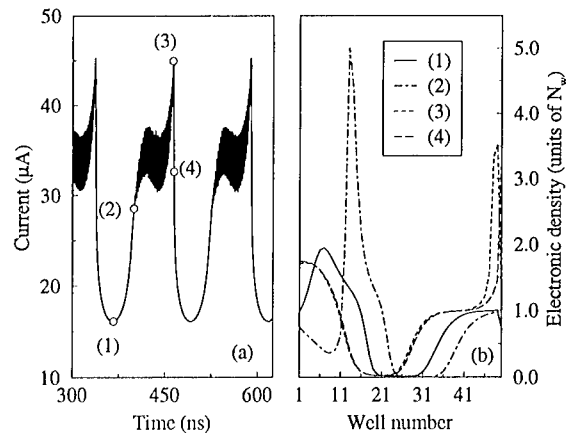


Fig. 1. (a) Dipole-mediated self-sustained oscillations of the total current through the SL. Bias is 5.5 V and the contact doping is $N_c = 2 \times 10^{16} \text{ cm}^{-3}$. (b) Evolution of the well density at the times marked in (a). When a sharp accumulation layer is formed at (2), it starts to get through the SL and spikes arise. The DW leaves a depletion region on its wake (see (3)). Eventually, it dies in the collector at (4) while it is recycled at the emitter (more clearly seen in (1)).

not been observed so far in experiments due to the high contact doping adopted in all the present experimental settings. What is remarkable in Fig. 1(a) (as compared to previous studies) are the spikes superimposed on one side of the oscillations. Such spikes have been observed experimentally and attributed to well-to-well hopping of the DW [3]. Between each two peaks of $J(t)$, we observe 36 additional spikes. Thus dipole recycling and motion occur on almost the whole SL (roughly between the 10th and the 50th well) and accompany the current oscillation. In the experiments performed up to now, self-oscillations present a markedly smaller number of spikes, indicating that they are due to monopole recycling [3,2].

Fig. 2(a) depicts a zoom of the spikes in Fig. 1(a). They have a frequency of about 500 MHz and an amplitude of 5.5 μA . Fig. 2(b) shows the charge density profile at four different times of a current spike marked in Fig. 2(a). Notice that the electron density in Fig. 2(b) is larger than the well doping at only three wells (24, 25 and 26) during the times recorded in Fig. 2(a). The contributions of tunneling and displacement currents to $J(t)$ in Eq. (1) are depicted in Figs. 2(c) and (d).

The spikes reflect the two-stage hopping motion – fast time scale – of the DW. During the stage where

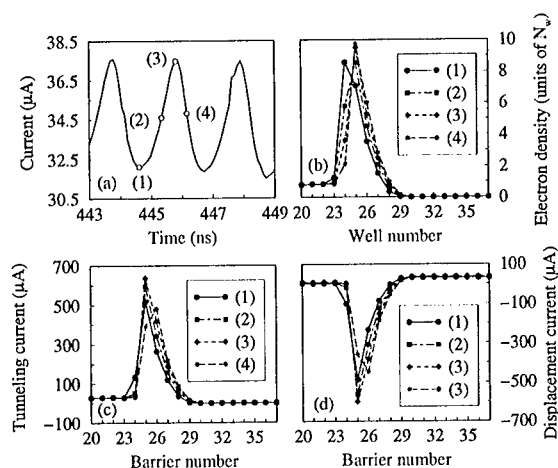


Fig. 2. (a) Zoom of Fig. 1(a) showing the spikes of the current. (b) Electron density profiles (in units of the doping at the wells), (c) tunneling current, and (d) displacement current at the times marked in (a). Notice that after the 29th well the SL is significantly depleted of electrons.

the current rises, charge is mainly transferred through a single barrier, for at time (1) (minimum of the current) the charge accumulates mainly at the i th well (the 24th well in Fig. 2(b)) and then electrons tunnel from this well to the next one, the $(i + 1)$ th, where most of the charge is located at time (3) (maximum of the current). Between times (1) and (3), the tunneling current is maximal where the displacement current is minimal and the total current increases. After that, some charge flows to the next well [time (4)] but both, tunneling and displacement currents, are smaller than what they are previously. This occurs because the potential drop at barrier $(i + 2)$ (in the high field domain) is larger than at barrier $(i + 1)$. Then there is a smaller overlap between the resonant levels

of nearby wells – the tunneling current decreases – and the displacement current and, eventually, $J(t)$ decreases. This stage lasts until well i is drained, and most of the charge is concentrated at wells $(i + 1)$ (the local maximum of charge) and $(i + 2)$ (slightly smaller charge). Then the next current spike starts.

In summary, we have thoroughly performed an analysis of the time-dependent features of a biased SL. Experimentally observed high-frequency oscillations superimposed on natural oscillations are naturally obtained. For the first time, novel charge density wave dynamics (dipole-like current oscillations) is observed when contact doping is lowered sufficiently. The crossover between monopole and dipole solutions is a function of the sample parameters. Further study of such dependence is the aim of a future work.

Acknowledgements

We thank Rosa López and Prof. Holger Grahn for helpful discussions. This work has been supported by the DGES (Spain) grants PB97-0088 and PB96-0875, by the European Union TMR contracts ERB FMBX-CT97-0157 and FMRX-CT98-0180 and by the Community of Madrid, project 07N/0026/1998.

References

- [1] A. Wacker, in: E. Schöll (Ed.), *Theory and Transport Properties of Semiconductor Nanostructures*, Chapman & Hall, New York, 1998 (Chapter 10) and references cited therein.
- [2] L.L. Bonilla et al., *SIAM J. Appl. Math.* 57 (1997) 1588.
- [3] J. Kastrop et al., *Phys. Rev. B* 55 (1997) 2476.
- [4] R. Aguado et al., *Phys. Rev. B* 55 (1997) R16053.
- [5] D. Sánchez et al., *Phys. Rev. B* 60 (1999) 4489.

PHYSICA E

INSTRUCTIONS TO AUTHORS

The "Instructions to Authors" (including the full addresses of the Editors) can also be found on the World Wide Web at: <http://www.elsevier.nl/locate/physce>.

Submission of papers

Manuscripts (one original + two copies) should be sent to one of the following regular editors:

Prof. T. Ando, Tokyo
Prof. T. Chakraborty, Taramani, Chennai
Prof. B.D. McCombe, Buffalo, NY
Prof. M.A. Reed, New Haven, CT
Prof. D. Weiss, Regensburg
(Addresses: see p. 2 of cover)

Original material: Submission of a manuscript implies that it is not being simultaneously considered for publication elsewhere and that the authors have obtained the necessary authority for publication.

Types of contributions

Original research papers and letters to the editors are welcomed. Both should contain an Abstract (of up to 200 words) and a Conclusions section, which, particularly in the case of theoretical papers, translates the results into terms readily accessible to most readers.

Manuscript preparation

All manuscripts should be written in proper English. The paper copies of the text should be prepared with double line spacing and wide margins, on numbered sheets.

Structure: Please adhere to the following order of presentation: Article title, Author(s), Affiliation(s), Abstract, PACS codes and keywords, Main text, Acknowledgements, Appendices, References, Figure captions, Tables.

Corresponding author: The name, complete postal address, telephone and fax numbers and the E-mail address of the corresponding author should be given on the first page of the manuscript.

PACS codes/keywords: Please supply one or more relevant PACS-1995 classification codes and 3-4 keywords of your own choice for indexing purposes.

References: References to other work should be consecutively numbered in the text using square brackets and listed by number in the Reference list.

Illustrations

Illustrations should also be submitted in triplicate: one master set and two sets of copies. The *line drawings* in the master set

should be original laser printer or plotter output or drawn black india ink, with careful lettering, large enough (3-5 mm) to remain legible after reduction for printing. The *photographs* should be originals, with somewhat more contrast than is required in the printed version. They should be unmounted unless part of a composite figure. Any scale markers should be inserted on the photograph itself, not drawn below it.

Colour plates: Figures may be published in colour, if this is judged essential by the editor. The Publisher and the author will each bear part of the extra costs involved. Further information is available from the publisher.

After acceptance

Notification: You will be notified by the editor of the journal of the acceptance of your article.

Copyright transfer: In the course of the production process you will be asked to transfer the copyright of the article to the publisher. This transfer will ensure the widest possible dissemination of information.

Electronic manuscripts

The Publisher welcomes the receipt of an electronic version of your accepted manuscript. If there is not already a copy of this (on diskette) with the journal editor at the time the manuscript is being refereed, you are invited to send a file with the text of the accepted manuscript directly to the Publisher on diskette (allowed formats 3.5" or 5.25" MS-DOS, or 3.5" Macintosh) to the address given below. Please note that no deviations from the version accepted by the editor of the journal are permissible without the prior and explicit approval of the editor. Such changes should be clearly indicated on an accompanying printout of the file.

Author benefits

No page charges: Publishing in Physica E is free of charge.

Free offprints: The corresponding author will receive 25 offprints free of charge. An offprint order form will be supplied by the publisher for ordering any additional paid offprints.

Discount: Contributors to Elsevier Science journals are entitled to a 30% discount on all Elsevier Science books.

Further information (after acceptance):

Issue Manager Physica E
Elsevier Science B.V.
P.O. Box 2759
1000 CT Amsterdam
The Netherlands
Telefax: + 31-20-485 2319
E-mail: j.leest@elsevier.nl



North-Holland, an imprint of Elsevier Science